The extremes of accretion : understanding super-Eddington accretion and feedback phenomena in Ultraluminous X-ray Sources

Andrés Gúrpide Lasheras

To cite this version:

Andrés Gúrpide Lasheras. The extremes of accretion : understanding super-Eddington accretion and feedback phenomena in Ultraluminous X-ray Sources. Cosmology and Extra-Galactic Astrophysics [astro-ph.CO]. Université Paul Sabatier - Toulouse III, 2021. English. NNT : 2021TOU30268 . tel-03689746

HAL Id: tel-03689746
https://theses.hal.science/tel-03689746v1

Submitted on 7 Jun 2022

THÈSE

En vue de l'obtention du

DOCTORAT DE L'UNIVERSITÉ DE TOULOUSE

Délivré par : *l'Université Toulouse 3 Paul Sabatier (UT3 Paul Sabatier)*

Présentée et soutenue le *25 Novembre 2021* **par :**

Andrés Gúrpide Lasheras

Les extrêmes de l'accrétion: comprendre l'accrétion super-Eddington et les processus de rétroaction dans les sources ultra-lumineuses en X

The extremes of accretion: understanding super-Eddington accretion and feedback phenomena in Ultraluminous X-ray Sources

---

JURY

GENEVIÈVE SOUCAIL	Présidente	Astronome
TIMOTHY PAUL ROBERTS	Rapporteur	Professeur
CHRISTIAN MOTCH	Rapporteur	Professeur Emeritus
MATTEO BACHETTI	Examinateur	Chargé de Recherche
VICTORIA GRINGBERG	Examinatrice	Liaison Scientifique
JEAN-FRANÇOIS OLIVE	Directeur de thèse	Professeur
OLIVIER GODET	Co-Directeur de thèse	Maître de Conférences

École doctorale et spécialité :
SDU2E : Astrophysique, Sciences de l'Espace, Planétologie
Unité de Recherche :
Institut de Recherche en Astrophysique et Planétologie (UMR 5277)
Directeur(s) de Thèse :
Olivier Godet et *Jean-François Olive*
Rapporteurs :
Timothy Paul Roberts et *Christian Motch*

"Astronomy compels the soul to look upwards and leads us from this world to another." – Plato, *The Republic*

Acknowledgements

First and foremost, I would like to thank both my supervisors, Jean-François Olive and Olivier Godet, for letting me the opportunity to carry out this PhD in such an exciting field that is the study of Ultraluminous X-ray sources. I think there was a constant encouragement to do even better, to refine what I had done, to check every possible imaginable source of uncertainty and to rewrite every single sentence in a clearer way. While this is any PhD student's nightmare (and it was for some time), if there is any quality to be found in this thesis and everything that has been published along with it, it's in great part thanks to this attitude that has striven me to do better. This has been immensely valuable for my formation as a scientist and I hope my work will be a reflection of these values. They both have also encouraged me to look beyond my field of expertise and strive to become and all-encompassing astrophysicist, which I hope to become one day. I would like to thank them also for the flexibility I was given to pursue my own ideas and organise myself as I felt at best, without any pressure whatsoever. This, I believe, has been a key component in the success of this thesis.

I would also like to thank all researchers at IRAP with whom I have collaborated in one way or another, be it direct work or simply through informal discussion. I could not have wished for a better work environment. In particular, I'd like to thank Thierry Contini, again, for his extreme friendliness and for taking the time to evaluate my thesis by assisting at every thesis committee, it was a pleasure to have him on board. On the work side, I'd also like to thank my pupil M. Parra (aka "basically a worse version of Andrés"), because even if we worked together for a short period of time, he made a very valuable contribution to the last Chapter of this thesis. I wish him success in his career which I have no doubt he will have. I was also honored with an amazing office mate, Soheila, from whom I learned a lot and to whom I wish the best too.

Finally on the academic side, I'd like to thank all the members of the jury for taking the time to review my work and provide thoughtful comments to improve upon. I'd like to thank as well a long list of researchers I have contacted during this thesis asking for comment, doubts or help. All of them have been extremely helpful and it has been great to see that the community is willing to help each other in this great endeavour that is the study of the Universe!

On the emotional side of things, I'd like to thank all the fellow PhD students from Dr. Gabi's PhD diaries (formerly Gabi's PhD diaries) because, for a PhD, almost as important as having someone with whom to have fun, is to have one shoulder (preferably many and from other PhD students) where to cry on. Gabi and Abe acted like the matriarch and patriarch of the whole PhD group, the more experienced fellows which essentially acted like a warning sign of what was to come in the following years. Sacha and Sujay had their role as my elder brothers, whereas Sid and Alessio were more like my twins. They were a constant source of support and fun throughout this journey and I hope we get to catch up often. Another special character in this journey has been (soon Dr.) J. Sebastien, which stood up with me in Roche till the very end of my days and with whom I had an immense pleasure sharing morning coffees, football games (when he used to come) and Sake Sushis (even if Eat Thai will always be better). It is also in great part thanks to him that I was able to finally learn this broken language that is French. Merci mec.

Finally, my last words go to my friends, my girlfriend and my family, they all have been an enormous source of support and I know having completed this Chapter of my life makes them immensely proud. Big part of the joy I felt right is therefore thanks to them and I hope we get to celebrate many more Chapters in life.

Abstract

Au centre de la plupart des galaxies massives se trouve un trou noir supermassif (TNSM) avec des masses entre $10^{6-10}\,M_\odot$. Le trou noir (TN) central agit comme un énorme réservoir d'énergie. Ainsi les processus d'accrétion de matière permettent de convertir efficacement une partie de l'énergie potentielle gravitationnelle du gaz accrété sous forme d'intenses rayonnements et de puissants vents/jets qui vont induire des phénomènes de *rétroaction* dans leurs environnements à de multiples échelles. L'étude de ce phénomène est donc cruciale pour comprendre comment les TN ont participé à la formation des grandes structures de l'Univers observable aujourd'hui. L'étude de l'univers lointain ou primordial a révélé que les TNSM avec des masses de $10^{8-9}\,M_\odot$ existaient déjà lorsque l'Univers n'avait que 5% de son âge actuel, suggérant que les TN ont dû croître extrêmement rapidement. Encore aujourd'hui, les mécanismes de croissance de ces trous noirs, notamment via l'accrétion super-Eddington, reste encore mal compris. De multiples questions subsistent quant à la stabilité de l'accrétion super-Eddington, car l'immense quantité de rayonnements qu'elle engendre devrait repousser le gaz accrété, réduisant voire même stoppant net la croissance des TN. S'il est impossible d'étudier en détail ces premiers TNSM avec l'instrumentation actuelle, trouver des systèmes analogues subissant une *accrétion super-Eddington* offrirait l'opportunité d'étudier indirectement l'apport de ce régime d'accrétion extrême dans la croissance des TNSM. Or, après deux décennies d'étude, il existe maintenant des preuves solides que la plupart des sources ultra-lumineuses en X (ULX), généralement localisées hors du noyau de leur galaxie hôte, sont des systèmes accrétant à des taux super-Eddington de manière *stable.* Certaines de ces sources possèdent également des bulles très larges (centaines de parsec) de gaz ionisés permettant d'étudier les phénomènes de rétroaction induits par les vents puissants et les rayonnements intenses prévenant de la source centrale. Pourtant, ces sources énigmatiques ont déconcerté les astronomes depuis leur découverte : la nature de l'accréteur dans la plupart d'entre elles reste inconnue, tandis que quelques unes montrent des pulsations en rayons X indiquant que l'accréteur est une étoile à neutrons (EN). De plus, les géométries des flots d'accrétion leur permettant d'atteindre des luminosités aussi extrêmes et sa dépendance avec la nature de l'accréteur sont encore mal contraintes.

Cette thèse a pour ambition d'aider à mieux comprendre les propriétés de l'accrétion super-Eddington dans les ULXs et les phénomènes de rétroaction associés sur de multiples échelles spatiales au moyen d'études multi-longueur d'onde (optique, X et dans une moindre mesure les UV). Cette thèse est divisée en deux volets. Dans le premier, j'ai exploité les grandes quantités de données d'archive offertes par les principaux télescopes à rayons X (*XMM-Newton*, *Chandra* et *NuSTAR*) pour réaliser une étude détaillée des transitions spectrales d'un large échantillon d'ULXs, afin de tester quel modèle d'émission serait le plus à même de reproduire les données. Pour la plupart des sources, j'ai montré que leurs transitions spectrales sont mieux décrites par des modèles invoquant une émission anisotrope induite par des vents – dont les géométries sont capatibles avec les prédictions théoriques et les simulations numériques de disques avec des taux d'accrétion super-Eddington – autour de EN faiblement magnétisées ($B < 10^{12}$ G) ou de TN accrétants. La variabilité spectrale observées dans l'échantillon pourraient être dues à des différences dans l'intensité du champ magnétique. La richesse des données me permet également d'examiner les différences/similitudes spectrales entre les ULX à ENs connues et celles pour lesquelles l'accréteur est inconnu; ce qui m'a permis de révéler un nouveau candidat de ce type. Ce travail est suivi d'une étude approfondie de deux ULX, Holmberg II X–1 & NGC 5204 X–1, pour laquelle j'ai exploité la cadence d'observation élevée du *Swift*-XRT pour révéler que ces deux sources suivent un cycle évolutif spectral récurrent dans l'espace dureté – luminosité en X. Il s'agit du premier cycle évolutif mis en évidence pour une source super-Eddington. Les transitions spectrales et la variabilité associées au cycle sont discutées dans le cadre de l'accrétion super-Eddington, en invoquant des changements de taux d'accrétion et un degré variable d'obscuration par les vents super-Eddington. Le deuxième volet de cette thèse se concentre sur l'exploration des données d'archive du *Multi-Unit Spectroscopic Explorer* (MUSE) sur le *Very Large Telescope* (VLT) en mettant l'accent sur la caractérisation des principales sources d'ionisation/excitation du gaz nébulaire en utilisant une série de diagnostics spectraux et en comparant les rapports de raies mesurées avec les modèles prédisant l'émission attendue pour du gaz choqué. Le résultat principal de cette partie est la découverte d'une bulle gonflée par des chocs s'étendant sur des centaines de parsecs autour de l'ULX NGC 1313 X–1. Je montre que la puissance mécanique estimée attribuée à l'éjection de vents par la source centrale est supérieure à la puissance radiative, suggérant que dans le régime super-Eddington, la rétroaction mécanique pourrait être plus importante que la rétroaction radiative.

Abstract

Sitting at the center of most massive galaxies lies a supermassive black hole (SMBH) with masses $10^{6-10}\,M_{\odot}$. The central black hole (BH) acts as an enormous reservoir of energy, when accreting gas from the galaxy and efficiently converting part of the energy into radiation, outflows and jets. Studying this fundamental process involved in the growth of the central BH and its *feedback* into the galaxy is crucial to understand how BHs shaped the large-scale structures of the Universe as we observe them today. Surprisingly, the deepest infrared surveys have revealed that SMBHs with masses $10^{8-9}\,M_{\odot}$ were already present when the Universe was only 5% of its current age, suggesting that these BHs must have grown extremely fast. However, the extreme accretion regime that would be required to allow these BHs to grow so fast is poorly understood. Questions remain about its sustainability, as the copious amount of radiation produced at such high accretion rates are expected to blow off the infalling gas, reducing or even halting the growth rate of the BH. While studying these early SMBHs in detail is not feasible with current instrumentation, nearby systems undergoing *super-Eddington accretion* sustained over several decades are good laboratories to indirectly study this critical epoch. After two decades of studies, there is now firm evidence supporting that most of the Ultraluminous X-ray sources (ULXs) typically found in external galaxies are accreting binary systems undergoing sustained super-Eddington accretion. Much like a scaled-down version of a SMBH, the copious amounts of radiation and outflows these mighty sources produce can ionize large nebulae of gas extending hundreds of parsecs in size, offering an observational template to study the feedback and efficiency of the super-Eddington regime. Yet these enigmatic sources have been puzzling astronomers since their discovery: the nature of the accretor in most of them remains unknown, while a few show X-ray pulsations indicative of a neutron star (NS) accretor. Moreover, the accretion flow geometry allowing them to reach such extreme luminosities and its dependency with the nature of the accretor is still highly debated.

This thesis presents a multi-wavelength study combining X-rays, optical and to lesser extent UV, in an effort to shed light on the engines behind ULXs, the properties of their inflows and outflows as well the feedback signatures in their surroundings. The two main lines of investigation are presented. In the first one, I exploited the extensive archival data offered by the major X-ray telescopes (*XMM-Newton*, *Chandra* and *NuSTAR*) to present a comprehensive study of the long-term spectral transitions of a broad sample of high-quality data ULXs, including known pulsating NS-ULXs, in order to test which of the current models to explain their extreme luminosities fit the data best. The analysis suggest that for the most part, their spectral transitions are best described by models invoking anisotropic emission induced by super-Eddington winds, with accreting lowly magnetised ($B < 10^{12}$ G) NSs or BHs as their engines. The spectral-variability differences observed across the sample might be due to differences in the magnetic field strength. The wealth of data serves also to examine the spectral differences/similarities between the known NS-ULXs and those for which the accretor is unknown, revealing a potential new NS-ULX. This work is followed by an in-depth study of two archetypal ULXs, Holmberg II X–1 and NGC 5204 X–1, where I exploited the high-observing cadence of *Swift*-XRT to reveal that these two sources follow a spectral recurrent evolutionary cycle. The spectral transitions and variability associated with the cycle is discussed in the framework of super-Eddington accretion, by invoking mass-accretion rate changes and varying degree of obscuration by the super-Eddington winds. The second part of this thesis focuses on exploring the archival data from the Multi-Unit Spectroscopic Explorer (MUSE) at the Very Large Telescope (VLT) to study the feedback properties of super-Eddington winds at larger scales, with focus on characterising the main sources of ionization of the nebular gas through state-of-the art spatially-resolved gas diagnostics and comparisons with emission radiative-shock models. The main result of this work focuses around the discovery of a shock-powered bubble nebula extending hundreds of parsecs around the ULX NGC 1313 X-1. The estimated mechanical power attributed to the outflow is in excess of the radiative power, suggesting that in the super-Eddington regime the mechanical feedback by outflows and jets may be more prevalent than the radiative feedback.

Contents

List of Acronyms

Athena	Advanced Telescope for High-ENergy Astrophysics
ACIS	Advanced CCD Imaging Spectrometer
ACS	Advanced Camera for Surveys
AGN	Active Galactic Nucleus
AO	Adaptive Optics
BH	Black Hole
BHT	Black Hole Transient
BPT	Baldwin-Philips-Terlevich
CCD	Charged Coupled Device
CXO	Chandra X-Ray Observatory
EPIC	European photon imaging camera
ESA	European Space Agency
ESO	European Southern Observatory
FOV	Field of View
FWHM	Full Width at Half maximum
GBHB	Galactic Black Hole Binary
GR	General Relativity
GRB	Gamma-Ray Burst
GTI	Good Time Interval
GW	Graviational Wave
HID	Hardness-Intensity Diagram
HMXB	High-Mass X-ray Binary
HLX	Hyper Luminous X-ray source
HRC	High-Resolution Camera
HRMA	High Resolution Mirror Assembly
HS	High-soft State
HST	*Hubble Space Telescope*
IFU	Integral field Unit
IMBH	Intermediate-Mass Black Hole
ISCO	Innermost Stable Circular Orbit
ISM	Interstellar Medium
MHD	Magneto-Hydrodynamic
MOS	Metal Oxide Semi-conductor
MUSE	Multi-Unit Spectroscopic Explorer
NFM	Narrow Field Mode
NS	Neutron Star
NuSTAR	*Nuclear Spectroscopic Telescope Array*
LIGO	Laser Interferometer Gravitational-Wave Observatory
LMXB	Low-Mass X-ray Binary
LS	Low-hard State
PSF	Point Spread Function
PF	Pulsed Fraction
PULX	Pulsating Ultraluminous X-ray source
RGS	Reflection Grating Spectrometer
RHD	Radiative Hydrodynamic
RMHD	Radiative Magneto-Hydrodynamic
SIM	Science Instrument Module

SMBH	Supermassive Black Hole
SNR	Supernova Remnant
SED	Spectral Energy Density
TDE	Tidal Disruption Event
XRT	X-Ray Telescope
ULX	Ultraluminous X-ray Source
ULXP	Ultraluminous X-ray Pulsar
UV	Ultraviolet
UVIS	Ultraviolet and Visible
VLT	Very Large Telescope
WD	White Dwarf
WFC	Wide Field Camera
WFM	Wide Field Mode
WR	Wolf Rayet
XRB	X-ray Binary

Chapter 1

Introduction

Astrophysicists can be regarded as 'historians' of the Universe. Much like biology aims to understand how life originated and evolved on Earth, astrophysics ultimate goal (arguably quite an ambitious one) is to understand how the entire Universe originated and evolved. In the quest for tracing back the history of the Universe, astrophysicists, in particular astronomers—those that used to look through telescopes, now through computer screens, like the present author—may have an edge over historians and biologist in their respective fields: we can look back in time. Not because of some advanced technology other fields lack, but because it so happens that the information we collect, mostly photons —but also gravitational waves and particles—, has to traverse the vast distances of the Universe before reaching us. For instance, if the Sun were to suddenly switch off, it would take approximately eight minutes for us here on Earth to realize, because that is the time it takes for the light to travel the Sun-Earth distance. This implies that looking into the distant Universe, is equivalent to taking a snapshot from the past, allowing astronomers to study the conditions of the Universe when it was still relatively young.

One of the brightest ($L \sim 10^{11-13}\,L_\odot$[1]) and more distant objects astronomers can observe are 'accreting' Supermassive Black Holes (SMBHs), also known as 'quasars'. These Black Holes (BHs) with masses in the $\sim$$10^{6-9}$ M$_\odot$ range sit at the center of most massive galaxies, such as the SMBH Sagittarius A* at the center of our own galaxy ($M \sim 3 \times 10^6$ M$_\odot$; Schödel et al., 2002; Ghez et al., 1998) or the SMBH at the center of M87, whose shadow was recently imaged by the Event Horizon Telescope (6×10^9 M$_\odot$; Event Horizon Telescope Collaboration et al., 2019). When 'active', that is, when gas is falling onto them, these SMBHs efficiently convert part of the infalling gas into radiation across the entire electromagnetic spectrum, in a process called 'accretion'[2]. The luminosity produced in this manner is so intense that these central SMBHs, also termed Active Galactic Nuclei (AGNs), can outshine the entire luminosity produced by all the stars from their host galaxy, allowing astronomers to observe their light across cosmological distances, up to redshift ~ 7 (Mortlock et al., 2011; Bañados et al., 2017). Several relationships between the central BH mass and the properties of the stars in the central part of the host galaxy have been established in the past three decades (e.g. Gültekin et al., 2009), suggesting that, notwithstanding their small sizes[3], these SMBHs are able to exert an enormous influence on their host galaxy and beyond, up to hundreds of lightyear scales (e.g. Begelman, 2003). This *feedback*, that is, the redistribution of the energy by the central BH back into the galaxy and into the gas within the galaxy cluster, is thought to be mediated by accretion/ejection processes: the host galaxy provides a vast reservoir of gas to feed and grow the central BH, while the BH through the accretion process will extract part of the gravitational energy of the infalling gas and convert it into radiation, but also into other forms of mechanical energy, such as astrophysical jets—relativistic ejection of collimated charged particles— or powerful outflows of gas, some expected to form as the radiation pressure exceeds the inward force of gravity as we shall see later. In this manner, an accreting SMBH can regulate and influence various processes inside its host galaxy, such as triggering or quenching star formation and/or enriching the interstellar/intergalactic gas (e.g. Kormendy & Ho, 2013).

This process is beautifully exemplified by the multi-wavelength observations of the well-studied SMBH ($\sim 10^8$ M$_\odot$; Marconi et al., 2006) at the center of the galaxy Centaurus A shown in Figure 1.1. The image shows a composite of optical, infrared (Weiß et al., 2008) and X-ray bands (Kraft et al., 2001) illustrating how the intense radiation field and the jets emanating from the central BH, extending thousands of lightyears in radius, influence the entire galaxy and beyond.

---

[1] $L_\odot$: Solar luminosity $\sim 4 \times 10^{33}$ erg/s.

[2] Not to be confused with Hawking radiation (Hawking, 1975), which is due to relativistic quantum effects near the event horizon of the BH, that are far from being perceptible.

[3] A typical 10^8 M$_\odot$ non-spinning BH has event horizon of $\sim 3 \times 10^{-5}$ lightyears.

Figure 1.1: A composite X-ray (blue), submillimetre (orange) and optical (real color) image showing the jets emaciating from the active SMBH Centarus A. Credit: ESO/WFI (Optical); MPIfR/ESO/APEX/(Submillimetre; Weiß et al., 2008); NASA/CXC/CfA/(X-rays Kraft et al., 2001). Une image composite aux rayons X (bleu), submillimétrique (orange) et optique (couleur réelle) montrant les jets émaciés du SMBH actif Centarus A.

1.1 The Puzzling Growth of Supermassive Black Holes

In an effort to understand this process, astronomers have started to look back in time, when the Universe was still relatively young. By mining the deepest infrared surveys, astronomers are trying to detect the most distant (or youngest) accreting SMBHs in the Universe. These searches have revealed the presence of SMBHs with masses in the $10^{8-9}\,\mathrm{M}_\odot$ range when the Universe was only 5% (at redshift $z \sim 7$) of its current age (Mortlock et al., 2011; Bañados et al., 2017). Considering that BHs are typically formed with $\lesssim 100\,\mathrm{M}_\odot$ as the end point of stellar evolution of massive stars (Fryer & Kalogera, 2001), it is hard to conceive how such massive BHs could be formed already at such early stages of the Universe. A number of scenarios have been proposed to solve this puzzle, which broadly rely on some possibility of forming much more massive BHs, multiple merger events between individual BHs and/or stars, or a very efficient way to transfer mass to the BH through the accretion process (see Greene et al., 2020, for a review).

It is speculated that more massive BHs could have been formed in the early Universe due to the low-metallicity environment. The so-called 'direct collapse' scenario postulates that primordial dense hydrogen gas in the early Universe could have collapsed directly onto a BH of $10^{4-6}\,\mathrm{M}_\odot$ (e.g. Agarwal et al., 2012). In such pristine gas, fragmentation into smaller clumps (and therefore the formation of multiple individual stars) is prevented if the gas is kept relatively hot ($T \geqslant 10^4\,\mathrm{K}$). This can be achieved in the absence of efficient coolants, namely metals and molecular hydrogen. As sated, a low-metallicity environment is a reasonable expectation in such gaseous proto-galaxies. On the other hand, a strong photo-dissociating radiation field (Lyman–Werner photons with energy between 11.2 eV and 13.6 eV) is needed to prevent the formation of molecular hydrogen. In addition, because the gas needs to get rid of the angular momentum before collapsing, it is found that a low initial spin of the gas halo is required to allow the gas to collapse in a reasonable timescale (Eisenstein & Loeb, 1995). The mechanism of transport of angular momentum could be analogue to that invoked in accretion disks (Shakura & Sunyaev, 1973; Eisenstein & Loeb, 1995) (which we shall discuss in Section 2) but the exact mechanism is still a matter of debate (Lodato & Natarajan, 2006). These two conditions could in principle allow the gas cloud to grow larger, and after accumulation in the center, form a central massive object of the order of

$10^{4-6}\,\mathrm{M}_\odot$. This scenario is highly debated as finely tuned conditions seem to be required for it to work, such as the elevated Lyman-Werner photon field required to match the number of observed BHs (Habouzit et al., 2016).

Another similar argument is the notion that the first generation of stars, the so-called Population III stars, formed in a metal-free environment, much different from the environment and the conditions in which stars form in the present-day Universe (Population I). This could allow the formation of more massive stars because, as stated above, clouds of gas need to cool down to fragment, and therefore the absence of metals could allow these clouds of gas to grow larger before fragmenting. Additionally, the absence of metals reduces the opacity of the star thereby reducing mass loss through line-driven stellar winds during its lifetime (Kudritzki, 2002). It is estimated that these primordial stars could have reached masses up to $260\,\mathrm{M}_\odot$, leaving a BH remnant of $\sim 100\,\mathrm{M}_\odot$(Heger et al., 2003). Some works suggest that even stars with masses up to $\sim 1000\,\mathrm{M}_\odot$ could have been formed (Ohkubo et al., 2009) but this has been challenged by simulations showing that these stars would instead form in smaller binary systems with masses in the 10–100 $\mathrm{M}_\odot$ range (see Mezcua, 2017, and references therein).

The formation of more massive BHs would alleviate the rapid growth needed to form the SMBHs at such early redshift, but the evidence for this new class of BHs, the so-called Intermediate-Mass Black Holes (IMBHs) ($10^{2-5}\,\mathrm{M}_\odot$; see Mezcua, 2017, for a review), remains elusive. These IMBHs are the missing link between the 'stellar-mass' BHs, those formed at the end of a star's life, and the aforementioned SMBHs. A few strong IMBH candidates exist such ESO 243–9 HLX-1 (Farrell et al., 2009; Godet et al., 2012) but only recently the Laser Interferometer Gravitational-Wave Observatory (LIGO)-VIRGO collaboration detected a Graviational Wave (GW) BH-BH merger event, where two massive ($> 65\,\mathrm{M}_\odot$) BHs coalesced to form an IMBH with $M = 142^{+28}_{-16}\,\mathrm{M}_\odot$[4] (Abbott et al., 2020).

But even if such massive BHs were formed in the early Universe as a result of more massive Population III stars, which is still a matter of debated (see Volonteri, 2010, and references therein), these BHs seeds would still need to grow very rapidly. One possibility would be through multiple encounters in dense stellar clusters, where most massive stars would sink into the gravitational potential of the cluster and undergo a runaway process, forming an IMBH (Zwart & McMillan, 2002; Miller & Hamilton, 2002). These proto-galaxies were rich in gas and might have provided important reservoirs of gas to feed the newly formed IMBH.

Let us now illustrate in more detail why the detection of these early SMBHs is also challenging to explain invoking only accretion of matter. To illustrate this in more detail, let us introduce a key concept around which this thesis revolves: the so-called 'Eddington limit' or 'Eddington luminosity'. In general, the Eddington limit applies whenever there is a balance between gravitational force and the force induced by radiation pressure. By balancing these two forces, one obtains the theoretical maximum luminosity an object can attain, as higher luminosities would lead to some material being expelled from the system, in turn reducing the luminosity. This can be the case around a star, which was the first consideration of Sir Arthur Eddington in deriving this limiting luminosity. Shakura & Sunyaev (1973) considered that a similar balance between the radiation produced in the accretion process and gravity must take place around compact objects. As the accretion luminosity exceeds the Eddington limit, the radiation pressure can eject the infalling gas, halting or reducing the accretion growth efficiency and in way, perhaps even self-regulating the accretion process. Because more massive compact objects have stronger gravitational potentials, they also possess higher Eddington luminosities and therefore can in principle accrete at faster rates. A mathematical derivation of the Eddington limit is presented later in Chapter 2.

With this 'limitation' in mind, we can now trace back what initial mass would be required to form these SMBHs found at $z \sim 7$. Assuming 10% of the supplied gas is converted into radiation (a reasonable value as we shall see later in Chapter 2) and that these BHs accreted matter continuously at the maximum accretion rate set by the Eddington-limit, a BH with $M \gtrsim 1000\,\mathrm{M}_\odot$would be required already at $z = 40$ (around 65 Gyr after the Big Bang; e.g. Bañados et al., 2017). This is of course, implausible, as even the first population of stars are expected to start forming at $z \sim 30$ (Xu et al., 2013), but this calculation has two implicit assumptions based on standard accretion theory, that will be extensively discussed throughout this thesis. First, it assumes that the accretion luminosity grows proportionally to the mass-accretion rate and secondly, it assumes that the classical Eddington limit sets a hard limit on the maximum accretion-rate an object can attain. The former assumption may be reasonable when the mass-transfer rate is well below the Eddington limit as we will see in Chapter 2. However, in reality, the Eddington limit may simply provide an estimate as to when radiation pressure (and other effects) will start to affect the dynamics of the accretion flow. Indeed, some transient systems are observed to exceed the Eddington limit over short timescales (few days) such as Tidal Disruption Events (TDEs) (Lin et al., 2020), Gamma-Ray Bursts (GRBs) (Vedrenne & Atteia, 2009), or some binary systems in which the companion is a Be type star (Vasilopoulos et al., 2020b). The problem is rather that our understanding of how the accretion flow will be affected as we approach the Eddington limit is uncertain. Estimations based on more realistic theoretical models (which we shall cover in detail in Section 2.2) show that a few episodes of moderate super-Eddington accretion (3–4 times above the classical Eddington limit) could easily grow a $100\,\mathrm{M}_\odot$ into a $10^9\,\mathrm{M}_\odot$ in a period of ~ 500 Myr (Madau et al., 2014), suggesting that super-Eddington accretion could

---

[4] 90% confidence level uncertainty.

have played a crucial role in the early growth of the primordial BHs. However, the strong radiation pressure is expected to blow-off the infalling gas, casting doubts on the sustainability of this process to be an efficient mechanism to grow BHs. But if mass-transfers in excess of the Eddington limit can be fed into a BH in a relatively sustained manner, the tight constraints on the mass of the BH seeds imposed by the detection of these SMBHs in the early Universe could be relaxed. Therefore, constraining its duty cycle, sustainability and growth efficiency of this process is of enormous interest to understand the early growth of the SMBHs as well as their influence in shaping the large scale structures in the Universe through feedback mechanisms.

Unfortunately, due to the enormous distances involved, directly studying the SMBH growth mechanisms in the early Universe is unfeasible with current instrumentation. Fortunately, there is now mounting evidence of a type of nearby systems displaying sustained super-Eddington accretion over year/timescales, allowing us to study in detail the properties of this extreme process and to assess its relevance for the growth of SMBHs. These are an enigmatic class of binary systems, typically found in the outskirst of external galaxies, dubbed Ultraluminous X-ray Sources (ULXs) (Makishima et al., 2000). As their name suggest, the main defining property of these systems, especially when discovered, was their abnormally bright X-ray luminosities (10^{39-41} erg/s) when compared to accreting stellar-mass compact object commonly found in our Galaxy. These abnormal luminosities lead the community to initially think that these were the long-sought IMBHs, as more massive objects would naturally explain their higher luminosities, without violating the Eddington limit. As we will see later in Chapter 3, while there might be some good IMBHs candidates among the ULX population, notably the brightest ones ($> 10^{41}$ erg/s), the evidence in favour of most of these sources as super-Eddington accretors is mounting. Moreover, as opposed to some transient sources that may exceed their Eddington luminosities for a brief period of time during outburst, many of these systems are instead *persistent* and hence ideal to understand sustained super-Eddington over decade-timescales.

The focus of this thesis is therefore the study of these enigmatic sources in order to characterize the properties of the super-Eddington accretion flows, paving the way to decipher the role of this process in the growth of the SMBHs and the formation of large structures in the Universe. In this regard, I present a multi-wavelength study of a sample of sources with the aim of understanding the underlying physical process enabling the Eddington limit to be overcome, characterizing the properties of their inflows and outflows as well as the feedback on the environment. In addition, in order to demonstrate that ULXs could be considered as analogs for our understanding of the growth of SMBHs in the early Universe, it is important to decipher the nature of the accretor powering ULXs. However, after roughly three decades of studies the nature of the accretor in most of these systems remains unknown. Only in 2014 X-ray pulsations were detected in a ULX for the first time (as I will discuss in Chapter 3) and now we know that around seven of them are powered by accreting Neutron Stars (NSs). These discoveries have opened up new questions regarding our understanding of the nature of ULXs: what is the fraction of NSs to BHs in ULX systems? What differences in their observational properties could be seen between such systems and what does this tell us on the differences on the accretion flow geometry (inflows and outflows) and the amount of energy released back into the Interstellar Medium (ISM)? Some theoretical works suggest that some ULXs could be powered by accreting highly magnetised NSs, suggesting that these system could also be of interest to study extreme magnetised accretion. Another interesting aspect is their powerful radiative and mechanical feedback, suggesting that they may even shape some galaxy properties (e.g. Simmonds et al., 2021), much like a scaled-down version of SMBHs. In fact, it is precisely this scale-invariant property of accretion, notably for BH-ULXs, that may allow us to extrapolate our findings to the large-mass regime. But before we dive into this fascinating topic, let us briefly see how BHs, and more generally compact objects – which also include White Dwarfs (WDs) and NSs – are formed.

1.2 The Death of a Star, the Birth of a Black Hole

Compact objects are formed as the endpoint of stellar evolution. They are also known as ‘stellar remnants’, because they are essentially what is left after a star has gone through all its evolutionary stages and consumed its nuclear fuel. Stars are powered by thermonuclear reactions in their core, which keeps them in hydrostatic equilibrium throughout most of their lives, as the radiation produced in the nuclear reactions balances the inward force of gravity. As the star exhausts all of its nuclear fuel in the core, the core contracts as it is no longer supported against its own gravity. Generally, the larger the mass of the core of the star at the end of its life, the stronger the pressure will be needed to sustain it against its own gravity. Typically, stars with initial masses below $\sim 8\,\mathrm{M}_{\odot}$ will form what is known as a WD, a stellar remnant sustained by the ‘electron degeneracy pressure’ (Fowler, 1926), a repulsive force that arises under extreme conditions of pressure due to Pauli’s exclusion principle, which states that fermions (electrons in this case) cannot occupy the same quantum state. This implies that there is a maximum mass a white dwarf can withhold without collapsing, known as the Chandrasekhar limit (Chandrasekhar, 1931). This limit is around $1.4\,\mathrm{M}_{\odot}$, although the exact value depends on the chemical composition and the angular momentum of the star. WDs have typical radii $\gtrsim 0.3\%\ R_{\odot}$. For stars with initial masses $\sim 8\,\mathrm{M}_{\odot} < M < 25\,\mathrm{M}_{\odot}$, the remnant will be a NS, although the exact composition of its core is still not known. In this case the higher temperature within the core enables the star to synthesize heavier elements up to nickel (Ni^{56}), which quickly decays into iron. Beyond this point, nucleosynthesis becomes an endothermic reaction and radiation pressure can no longer prevent the iron core from collapsing. Here the electron degeneracy pressure is not sufficient to prevent the collapse, but as the matter is further compressed two other forces arise: the strong force, which confines quarks into hadrons and becomes repulsive at such short distances, and the neutron degeneracy pressure, the analogue to the electron degeneracy pressure but for neutrons. Oppenheimer & Volkoff (1939) and Tolman (1939) first considered the maximum mass a NS could withhold under the assumption that it was sustained by the neutron degeneracy pressure, but the upper limit was found to be lower than that of the Chandrasekhar limit. Later refinements taking into account the repulsive strong force estimate an upper limit of $\sim 1.5\,\mathrm{M}_\odot < M_{\mathrm{NS}} < 3\,\mathrm{M}_\odot$, depending on the equation of state defining the interior of the NS and its rotation. The typical radii for a NS range from 5 to 14 km. Above this mass limit, Oppenheimer & Snyder (1939) showed that there is no physical mean to avoid the gravitational collapse of the core, and the star leaves a BH as a remnant. Except for stars with initial masses above $\sim 40\,\mathrm{M}_\odot$ (although the exact limit will depend again on the metallicity), which can collapse directly onto a BH, stars will generally undergo a supernova explosion towards the last stages of their evolution (see their Figure Heger et al., 2003).

1.3 Thesis outline

This thesis is divided as follows: Chapter 2, 3 & 4 provide the necessary details to understand the studies I carried out and describe in Chapters 5 & 6. More specifically, Chapter 2 explains the physics and observational phenomenology of accretion around compact objects, with special attention to the differences between what is understood as the sub- and super-Eddington accretion regimes, both theoretically and observationally. Chapter 3 describes briefly the historical background behind ULXs, their basic definition and the current evidence in favour of ULXs as super-Eddington accretors. I also discuss many of the observational evidence and its links with the theory described in the previous Chapter. Some other aspects such as the nature of the accretor are also discussed. Chapter 4 provides a detailed description of all the instrumentation used in this work and how each instrument is useful in each own aspect for the study of ULXs.

Chapters 5 & 6 describe the work I carried out to try to tackle the questions outlined in the Introduction of this thesis. The first Chapter of these two focuses on the studies carried out in X-rays in order to understand the accretion in-/out-flow geometries and the nature of the accretor in ULXs. The second Chapter focuses on the study on the feedback imprints on the environment of ULXs carried out in the optical, to constrain the radiative and mechanical output of these sources. Finally the last Chapter, Chapter 7, offers a general conclusion on the entire work and suggest some avenues to be pursued in the future.

Introduction

Les astrophysiciens peuvent être considérés comme des « historiens » de l'Univers. Tout comme la biologie vise à comprendre comment la vie est née et a évolué sur Terre, le but ultime de l'astrophysique (sans doute assez ambitieux) est de comprendre comment l'Univers entier est né et a évolué. Dans la quête de retracer l'histoire de l'Univers, les astrophysiciens, en particulier les astronomes−ceux qui regardaient à travers des télescopes, maintenant à travers des écrans d'ordinateur, comme le présent auteur− peuvent avoir un avantage sur les historiens et les biologistes dans leur champs respectifs : nous pouvons remonter dans le temps. Non pas à cause d'une technologie de pointe qui manque à d'autres domaines, mais parce qu'il se trouve que les informations que nous collectons, principalement des photons − mais aussi des ondes gravitationnelles et des particules−, doivent parcourir les vastes distances de l'Univers avant de nous atteindre. Par exemple, si le Soleil s'éteint soudainement, il nous faudrait environ huit minutes ici sur Terre pour nous en rendre compte, car c'est le temps qu'il faut à la lumière pour parcourir la distance Soleil-Terre. Cela implique que regarder dans l'Univers lointain équivaut à prendre un instantané du passé, permettant aux astronomes d'étudier les conditions de l'Univers lorsqu'il était encore relativement jeune.

L'un des plus brillants ($L \sim 10^{11-13}\,L_\odot$[5]) et les objets plus éloignés que les astronomes peuvent observer sont « accrétés » SMBHs, également connus sous le nom de 'quasars'. Ces BHs avec des masses de l'ordre de $\sim 10^{6-9}$ M$_\odot$ se trouvent au centre de la plupart des galaxies massives, comme le SMBH Sagittaire A* au centre de notre propre galaxie ($M \sim 3 \times 10^6$ M$_\odot$; Schödel et al., 2002; Ghez et al., 1998) ou le SMBH au centre de M87, dont l'ombre a été récemment imagée par le télescope Event Horizon (6×10^9 M$_\odot$; Event Horizon Telescope Collaboration et al., 2019). Lorsqu'ils sont 'actifs', c'est-à-dire lorsque du gaz tombe sur eux, ces SMBHs convertissent efficacement une partie du gaz entrant en rayonnement sur tout le spectre électromagnétique, dans un processus appelé 'accrétion'[6]. La luminosité produite de cette manière est si intense que ces SMBHs centraux, également appelés AGNs, peuvent surpasser toute la luminosité produite par toutes les étoiles de leur galaxie hôte, permettant aux astronomes d'observer leur lumière à travers des distances cosmologiques , jusqu'au redshift ~ 7 (Mortlock et al., 2011; Bañados et al., 2017). Plusieurs relations entre la masse centrale BH et les propriétés des étoiles dans la partie centrale de la galaxie hôte ont été établies au cours des trois dernières décennies (eg Gültekin et al., 2009), suggérant que, malgré leurs petites tailles[7], ces SMBHs sont capables d'exercer un énorme influence sur leur galaxie hôte et au-delà, jusqu'à des centaines d'échelles d'années-lumière (eg Begelman, 2003). On pense que ce *feedback*, c'est-à-dire la redistribution de l'énergie par le BH central dans la galaxie et dans le gaz au sein de l'amas de galaxies, est médié par des processus d'accrétion/éjection : la galaxie hôte fournit un vaste réservoir de gaz pour alimenter et faire croître le BH central, tandis que le BH par le processus d'accrétion extraira une partie de l'énergie gravitationnelle du gaz entrant et le convertira en rayonnement, mais aussi en d'autres formes d'énergie mécanique, telles que les jets astrophysiques−éjection relativiste de particules chargées collimatées− ou de puissants écoulements de gaz, certains devraient se former lorsque la pression de rayonnement dépasse la force de gravité vers l'intérieur, comme nous le verrons plus tard. De cette manière, un SMBHs accréteur peut réguler et influencer divers processus à l'intérieur de sa galaxie hôte, tels que le déclenchement ou l'extinction de la formation d'étoiles et/ou l'enrichissement du gaz interstellaire/intergalactique (e.g. Kormendy & Ho, 2013).

Ce processus est magnifiquement illustré par les observations multi-longueurs d'onde du bien étudié SMBH ($\sim 10^8$ M$_\odot$; Marconi et al., 2006) au centre de la galaxie Centaurus A illustré à la figure 1.1. L'image montre un composite de bandes optiques, infrarouges (Weiß et al., 2008) et de rayons X (Kraft et al., 2001) illustrant comment le champ de rayonnement intense et les jets émanant du centre BH, s'étendant sur des milliers d'années-lumière de rayon, peut influencer toute la galaxie et au-delà.

---

[5] $L_\odot$: Luminosité solaire $\sim 4 \times 10^{33}$ erg/s.

[6] À ne pas confondre avec le rayonnement de Hawking (Hawking, 1975), qui est dû à des effets quantiques relativistes près de l'horizon des événements de la BH, qui sont loin d'être perceptibles.

[7] Un typique 10^8 M$_\odot$ non-tournant BH a un horizon des événements de $\sim 3 \times 10^{-5}$ années-lumière.

La croissance déroutante des trous noirs supermassifs

Afin de comprendre ce processus, les astronomes ont commencé à remonter le temps, lorsque l'Univers était encore relativement jeune. En exploitant les relevés infrarouges les plus profonds, les astronomes tentent de détecter le SMBHs accréteur le plus éloigné (ou le plus jeune) de l'Univers. Ces recherches ont révélé la présence de SMBHs avec $10^{8-9}\,\mathrm{M}_\odot$ alors que l'Univers n'était qu'à 5% (au redshift $z \sim 7$) de son âge (Mortlock et al., 2011; Bañados et al., 2017). Considérant que BHs sont typiquement formés avec $\lesssim 100\,\mathrm{M}_\odot$ comme point final de l'évolution stellaire des étoiles massives (Fryer & Kalogera, 2001), il est difficile de concevoir comment un tel massif BHs pourrait déjà être formé à ces premiers stades de l'Univers. Un certain nombre de scénarios ont été proposés pour résoudre ce puzzle, qui reposent largement sur une possibilité de former des BHs beaucoup plus massifs, de multiples événements de fusion entre des BHs individuels et/ou des étoiles, ou un moyen très efficace de transférer la masse à la BH par le processus d'accrétion (voir Greene et al., 2020, pour une revue).

On suppose que des BHs plus massifs auraient pu se former dans l'Univers primitif en raison de l'environnement à faible métallicité. Le scénario dit 'd'effondrement direct' postule que l'hydrogène gazeux dense primordial dans l'Univers primordial aurait pu s'effondrer directement sur un BH de $10^{4-6}\,\mathrm{M}_\odot$ (e.g. Agarwal et al., 2012). Dans un tel gaz vierge, la fragmentation en amas plus petits (et donc la formation de plusieurs étoiles individuelles) est empêchée si le gaz est maintenu relativement chaud ($T \geqslant 10^4\,\mathrm{K}$). Ceci peut être réalisé en l'absence de réfrigérants efficaces, à savoir les métaux et l'hydrogène moléculaire. Comme rassasié, un environnement à faible métallicité est une attente raisonnable dans de telles proto-galaxies gazeuses. D'autre part, un fort champ de rayonnement photo-dissociant (photons de Lyman-Werner avec une énergie comprise entre 11.2 eV et 13.6 eV) est nécessaire pour empêcher la formation d'hydrogène moléculaire. De plus, comme le gaz doit se débarrasser du moment angulaire avant de s'effondrer, on constate qu'un faible spin initial du halo gazeux est nécessaire pour permettre au gaz de s'effondrer dans un délai raisonnable (Eisenstein & Loeb, 1995). Le mécanisme de transport du moment angulaire pourrait être analogue à celui invoqué dans les disques d'accrétion (Shakura & Sunyaev, 1973; Eisenstein & Loeb, 1995) (dont nous parlerons dans la section 2) mais le mécanisme exact est encore sujet à débat (Lodato & Natarajan, 2006). Ces deux conditions pourraient en principe permettre au nuage de gaz de s'agrandir, et après accumulation au centre, de former un objet massif central de l'ordre de $10^{4-6}\,\mathrm{M}_\odot$. Ce scénario est très débattu car des conditions finement réglées semblent être nécessaires pour qu'il fonctionne, comme le champ photonique élevé de Lyman-Werner requis pour correspondre au nombre de BHs observés (Habouzit et al., 2016).

Un autre argument similaire est l'idée que la première génération d'étoiles, les étoiles dites de la Population III, se sont formées dans un environnement sans métal, très différent de l'environnement et des conditions dans lesquelles les étoiles se forment dans l'Univers actuel (Population I). Cela pourrait permettre la formation d'étoiles plus massives car, comme indiqué ci-dessus, les nuages de gaz ont besoin de se refroidir pour se fragmenter, et donc l'absence de métaux pourrait permettre à ces nuages de gaz de grossir avant de se fragmenter. De plus, l'absence de métaux réduit l'opacité de l'étoile, réduisant ainsi la perte de masse due aux vents stellaires entraînés par les lignes au cours de sa durée de vie (Kudritzki, 2002). On estime que ces étoiles primordiales auraient pu atteindre des masses allant jusqu'à $260\,\mathrm{M}_\odot$, laissant un BH vestige de $\sim 100\,\mathrm{M}_\odot$(Heger et al., 2003). Certains travaux suggèrent que même des étoiles avec des masses allant jusqu'à $\sim 1000\,\mathrm{M}_\odot$ auraient pu se former (Ohkubo et al., 2009) mais cela a été contesté par des simulations montrant que ces étoiles se formeraient plutôt dans des systèmes binaires plus petits avec des masses en la plage $10\text{–}100\,\mathrm{M}_\odot$ (voir Mezcua, 2017, et les références qui s'y trouvent).

La formation de BHs plus massives atténuerait la croissance rapide nécessaire pour former le SMBHs à un redshift aussi précoce, puisque la preuve de cette nouvelle classe de BHs, la soi-disant IMBHs ($10^{2-5}\,\mathrm{M}_\odot$; voir Mezcua, 2017, pour un examen), reste insaisissable. Ces IMBHs sont le chaînon manquant entre la 'masse stellaire' BHs, celles formées à la fin de la vie d'une étoile, et la SMBHs susmentionnée. Quelques candidats IMBH forts existent tels ESO 243–9 HLX-1 (Farrell et al., 2009; Godet et al., 2012) mais ce n'est que récemment que la collaboration LIGO-VIRGO a détecté un GW événement de fusion BH-BH, où deux énormes ($> 65\,\mathrm{M}_\odot$) BHs se sont fusionnés pour former un IMBH avec $M = 142^{+28}_{-16}\,\mathrm{M}_\odot$[8] (Abbott et al., 2020).

Mais même si un BH aussi massif se formait au début de l'Univers à la suite d'étoiles plus massives de la Population III, ce qui fait toujours l'objet de débats (voir Volonteri, 2010, et les références qui y sont contenues), ces graines BH auraient toujours besoin de croître très rapidement. Une possibilité serait à travers des rencontres multiples dans des amas stellaires denses, où les étoiles les plus massives s'enfonceraient dans le potentiel gravitationnel de l'amas et subiraient un processus d'emballement, formant un IMBH (Zwart & McMillan, 2002; Miller & Hamilton, 2002). Ces proto-galaxies étaient riches en gaz et auraient pu fournir d'importants réservoirs de gaz pour alimenter le IMBH nouvellement formé.

Illustrons maintenant plus en détail pourquoi ces détections précoces sont également difficiles à expliquer en invoquant uniquement l'accrétion de matière. Pour illustrer cela plus en détail, introduisons un concept clé

---

[8] 90% d'incertitude du niveau de confiance.

autour duquel s'articule cette thèse : la soi-disant 'limite d'Eddington' ou 'luminosité d'Eddington'. En général, la limite d'Eddington s'applique chaque fois qu'il existe un équilibre entre la force gravitationnelle et la force induite par la pression de rayonnement. En équilibrant ces deux forces, on obtient la luminosité maximale théorique qu'un objet peut atteindre, car des luminosités plus élevées entraîneraient l'expulsion de certains matériaux du système, réduisant à leur tour la luminosité. Cela peut être le cas autour d'une étoile, ce qui a été la première considération de Sir Arthur Eddington pour dériver cette luminosité limite. Shakura & Sunyaev (1973) considérait qu'un équilibre similaire entre le rayonnement produit dans le processus d'accrétion et la gravité doit avoir lieu autour d'objets compacts. Lorsque la luminosité de l'accrétion dépasse cette valeur, la pression de rayonnement peut éjecter le gaz entrant, arrêtant ou réduisant l'efficacité de croissance de l'accrétion et, peut-être même, autorégulant le processus d'accrétion. Parce que les objets compacts plus massifs ont des potentiels gravitationnels plus forts, ils possèdent également des luminosités d'Eddington plus élevées et peuvent donc en principe s'accumuler à des vitesses plus rapides. Une dérivation mathématique de la limite d'Eddington est présentée plus loin dans le Chapitre 2.

Avec cette 'limitation' à l'esprit, nous pouvons maintenant retracer quelle masse initiale serait nécessaire pour former ces SMBHs trouvés à $z \sim 7$. En supposant que 10% du gaz fourni soit converti en rayonnement (une valeur raisonnable comme nous le verrons plus loin dans le Chapitre 2) et que ces BHs ont accrété de la matière en continu au taux d'accrétion maximum fixé par la limite d'Eddington, un BH avec $M \gtrsim 1000\,\mathrm{M}_\odot$serait déjà requis à $z = 40$ (environ 65 Gyr après le Big Bang ; par exemple Bañados et al., 2017). Ceci est bien sûr invraisemblable, car même la première population d'étoiles devrait commencer à se former à $z \sim 30$ (Xu et al., 2013), mais ce calcul a deux hypothèses implicites basées sur la théorie d'accrétion standard , qui sera largement discuté tout au long de cette thèse : il suppose que la luminosité d'accrétion augmente proportionnellement au taux d'accrétion en masse et que la limite classique d'Eddington fixe une limite stricte au taux d'accrétion maximum qu'un objet peut atteindre. La première peut être une hypothèse raisonnable lorsque le taux de transfert de masse est bien inférieur à la limite d'Eddington comme nous le verrons au Chapitre 2. Cependant, en réalité, la limite d'Eddington peut simplement fournir une estimation du moment où la pression de rayonnement (et d'autres effets) commencera à affecter la dynamique du flux d'accrétion. En effet, certains systèmes transitoires sont observés dépassant la limite d'Eddington sur des échelles de temps courtes (quelques jours) tels que TDEs (Lin et al., 2020), GRBs (Vedrenne & Atteia, 2009) , ou certains systèmes binaires dans lesquels le compagnon est une étoile de type Be (Vasilopoulos et al., 2020b). Le problème est plutôt que notre compréhension de la façon dont le flux d'accrétion sera affecté à l'approche de la limite d'Eddington est incertaine. Des estimations basées sur des modèles théoriques plus réalistes (que nous aborderons en détail dans le Chapitre 2.2) montrent que quelques épisodes d'accrétion modérée de super-Eddington (3–4 fois au-dessus de la limite classique d'Eddington) pourraient facilement se développer un $100\,\mathrm{M}_\odot$ dans un $10^9\,\mathrm{M}_\odot$ dans une période de ~ 500 Myr (Madau et al., 2014), suggérant que l'accrétion super-Eddington aurait pu jouer un rôle crucial rôle dans la croissance précoce du BHs primordial. Cependant, on s'attend à ce que la forte pression de radiation souffle le gaz entrant, jetant des doutes sur la durabilité de ce processus comme mécanisme efficace pour faire croître BHs. Mais si les transferts de masse dépassant la limite d'Eddington peuvent être introduits dans un BH d'une manière relativement soutenue, les contraintes strictes sur la masse des germes de BH imposées par la détection de ces SMBHs dans l'Univers primitif pourrait être relâché. Par conséquent, la limitation de son cycle d'utilisation, de la durabilité et de l'efficacité de croissance de ce processus est d'un intérêt énorme pour comprendre la croissance précoce du SMBH ainsi que leur influence sur la formation des structures à grande échelle dans l'Univers par le biais de mécanismes de rétroaction.

Malheureusement, en raison des énormes distances impliquées, l'étude directe des mécanismes de croissance de SMBH dans l'Univers primitif est impossible avec l'instrumentation actuelle. Heureusement, il existe maintenant des preuves croissantes d'un type de systèmes proches affichant une accrétion soutenue de super-Eddington au cours de l'année/des échelles de temps, ce qui nous permet d'étudier en détail les propriétés de ce processus extrême et d'évaluer sa pertinence pour la croissance de SMBHs. Il s'agit d'une classe énigmatique de systèmes binaires, typiquement trouvés dans la périphérie des galaxies externes, surnommé ULXs (Makishima et al., 2000). Comme leur nom l'indique, la principale propriété déterminante de ces systèmes, en particulier lorsqu'ils ont été découverts, était leur luminosité anormalement brillante aux rayons X (10^{39-41} erg/s) par rapport à l'accrétion d'un objet compact de masse stellaire. que l'on trouve couramment dans notre Galaxie. Ces luminosités anormales conduisent la communauté à penser initialement qu'il s'agissait des IMBHs tant recherchés, car des objets plus massifs expliqueraient naturellement leurs luminosités plus élevées, sans violer la limite d'Eddington. Comme nous le verrons plus tard dans le Chapitre 3, alors qu'il pourrait y avoir de bons candidats IMBHs parmi la population ULX, notamment les plus brillants ($> 10^{41}$ erg/s), les preuves en faveur de la plupart de ces sources en tant que super-accréteurs d'Eddington s'accumulent. De plus, contrairement à certaines sources transitoires qui peuvent dépasser leurs luminosités d'Eddington pendant une brève période pendant l'explosion, bon nombre de ces systèmes sont plutôt *persistants* et donc idéaux pour comprendre le super-Eddington soutenu sur des décennies.

L'objectif de cette thèse est donc l'étude de ces sources énigmatiques afin de caractériser les propriétés des flux d'accrétion super-Eddington, ouvrant ainsi la voie à décrypter le rôle de ce processus dans la croissance de la SMBHs et de la formation de grandes structures dans l'Univers. A cet égard, je présente une étude multi-longueurs d'onde d'un échantillon de sources dans le but de comprendre le processus physique sous-jacent permettant de dépasser la limite d'Eddington, en caractérisant les propriétés de leurs flux entrants et sortants ainsi que les retours sur l'environnement. Afin de démontrer que ULXs pourrait être considéré comme des analogues pour notre compréhension de la croissance de SMBHs dans l'Univers primordial, il est important de déchiffrer la nature de l'accréteur dans ULXs. Mais après environ trois décennies d'études, la nature de l'accréteur dans la plupart de ces systèmes reste inconnue. Seulement En 2014, des pulsations de rayons X ont été détectées dans un ULX pour la première fois (comme je le discuterai au Chapitre 3) et nous savons maintenant qu'environ sept d'entre elles sont alimentées par des étoiles à neutrons en accrétion. Ces découvertes ont ouvert de nouvelles questions : quelle est la fraction de NSs à BHs dans les systèmes ULX ? Quelles différences dans leurs propriétés d'observation pourraient être observées entre de tels systèmes et qu'est-ce que cela nous dit sur les différences sur la géométrie du flux d'accrétion (entrées et sorties) et la quantité d'énergie libérée dans le ISM ? Certains travaux théoriques suggèrent que certains ULXs pourraient accréter des NSs hautement magnétisés, suggérant que ces systèmes pourraient également être intéressants pour étudier l'accrétion magnétisée extrême. Un autre aspect intéressant est leurs puissants pouvoirs radiatifs et mécaniques, suggérant qu'ils peuvent même façonner certaines propriétés des galaxies (e.g. Simmonds et al., 2021), un peu comme une version réduite de SMBHs. En fait, c'est précisément cette propriété d'accrétion invariante à l'échelle, notamment pour BH-ULXs, qui peut nous permettre d'extrapoler nos résultats au régime des grandes masses. Mais avant de nous plonger dans ce sujet fascinant, voyons brièvement comment se forment les BHs, et plus généralement les objets compacts, qui incluent également les naines blanches et les étoiles à neutrons.

La mort d'une étolie, la naissance d'un trou noir

Les objets compacts sont formés comme le point final de l'évolution stellaire. Ils sont également connus sous le nom de « restes stellaires », car ils sont essentiellement ce qui reste après qu'une étoile a traversé toutes ses étapes d'évolution et a consommé son combustible nucléaire. Les étoiles sont alimentées par des réactions thermonucléaires dans leur noyau, ce qui les maintient en équilibre hydrostatique pendant la majeure partie de leur vie, car le rayonnement produit dans les réactions nucléaires équilibre la force de gravité vers l'intérieur. Au fur et à mesure que l'étoile épuise tout son combustible nucléaire dans le cœur, le cœur se contracte car il n'est plus soutenu par sa propre gravité. En général, plus la masse du noyau de l'étoile en fin de vie est grande, plus la pression sera forte pour la maintenir contre sa propre gravité. Typiquement, les étoiles avec des masses initiales inférieures à $\sim 8\,\mathrm{M}_{\odot}$ formeront ce qu'on appelle un WD, un vestige stellaire soutenu par la 'pression de dégénérescence électronique' (Fowler, 1926), une force répulsive qui survient dans des conditions de pression extrêmes en raison du principe d'exclusion de Pauli, qui stipule que les fermions (les électrons dans ce cas) ne peuvent pas occuper le même état quantique. Cela implique qu'il existe une masse maximale qu'une naine blanche peut retenir sans s'effondrer, connue sous le nom de limite de Chandrasekhar (Chandrasekhar, 1931). Cette limite est d'environ $1{,}4\,\mathrm{M}_{\odot}$, bien que la valeur exacte dépende de la composition chimique et du moment cinétique de l'étoile. WD ont des rayons typiques $\gtrsim 0.3\%\ R_{\odot}$. Pour les étoiles avec des masses initiales $\sim 8\,\mathrm{M}_{\odot} < M < 25\,\mathrm{M}_{\odot}$, le reste sera un NS, bien que la composition exacte de son noyau soit toujours pas connu. Dans ce cas, la température plus élevée à l'intérieur du noyau permet à l'étoile de synthétiser des éléments plus lourds jusqu'au nickel (Ni^{56}), qui se désintègre rapidement en fer. Au-delà de ce point, la nucléosynthèse devient une réaction endothermique et la pression de radiation ne peut plus empêcher le noyau de fer de s'effondrer. Ici, la pression de dégénérescence des électrons n'est pas suffisante pour empêcher l'effondrement, mais à mesure que la matière est davantage comprimée, deux autres forces apparaissent : la force forte, qui devient répulsive à de si courtes distances et la pression de dégénérescence des neutrons, l'analogue de la pression de dégénérescence des électrons mais pour les neutrons. Oppenheimer & Volkoff (1939) et Tolman (1939) ont d'abord considéré la masse maximale qu'un NS pouvait retenir en supposant qu'elle était soutenue par la pression de dégénérescence des neutrons, mais la limite supérieure s'est avérée inférieure à celle de la limite de Chandrasekhar. Des raffinements ultérieurs prenant en compte la force répulsive forte estiment une limite supérieure de $\sim 1.5\,\mathrm{M}_{\odot} < M_{\mathrm{NS}} < 3\,\mathrm{M}_{\odot}$, en fonction de l'équation d'état définissant l'intérieur du NS et sa rotation. Les rayons typiques pour un NS vont de 5 à 14 km. Au-dessus de cette limite de masse, Oppenheimer & Snyder (1939) a montré qu'il n'y a aucun moyen physique d'éviter l'effondrement gravitationnel du noyau, et l'étoile laisse un BH comme vestige. À l'exception des étoiles dont la masse initiale est supérieure à $\sim 40\,\mathrm{M}_{\odot}$ (bien que la limite exacte dépendra encore de la métallicité), qui peuvent s'effondrer directement sur un BH, l'étoile subira généralement une explosion de supernova vers les dernières étapes de leur évolution (voir leur Figure; Heger et al., 2003).

Schéma de thèse

Cette thèse est divisée comme suit : Les Chapitres 2, 3 & 4 apportent les précisions nécessaires à la compréhension des études que j'ai menées et décrites dans les Chapitres 5 & 6. Plus précisément, le Chapitre 2 explique la physique et la phénoménologie observationnelle de l'accrétion autour d'objets compacts, avec une attention particulière aux différences entre ce qui est compris comme les régimes d'accrétion sous et super-Eddington, à la fois théoriquement et observationnellement. Le Chapitre 3 décrit brièvement le contexte historique derrière ULXs, leur définition de base et les preuves actuelles en faveur de ULXs en tant que super-accréteurs d'Eddington. Je discute également de nombreuses preuves d'observation et de leurs liens avec la théorie décrite dans le Chapitre précédent. D'autres aspects tels que la nature de l'accréteur sont également discutés. Le Chapitre 4 fournit une description détaillée de toute l'instrumentation utilisée dans ce travail et comment chaque instrument est utile dans chaque aspect propre à l'étude de ULXs.

Les Chapitres 5 & 6 décrivent le travail que j'ai effectué pour tenter d'aborder les questions exposées dans l'introduction de cette thèse. Le premier Chapitre de ces deux Chapitres se concentre sur les études menées en rayons X afin de comprendre les géométries d'accrétion en entrée/sortie et la nature de l'accréteur dans ULXs. Le deuxième Chapitre porte sur l'étude des empreintes de rétroaction sur l'environnement de ULXs réalisée dans l'optique, pour contraindre le rendement radiatif et mécanique de ces sources. Enfin, le dernier Chapitre, le Chapitre 7, propose une conclusion générale sur l'ensemble du travail et suggère quelques pistes à poursuivre dans le futur.

Chapter 2

Accretion

Accretion is an ubiquitous process in the Universe that takes place in a variety of systems and scales, such as in the formation of planetary systems and stars, in galaxies accreting from big reservoirs of gas and around compact objects, the latter being the focus of this thesis. In the most simple cases, accretion simply leads to the accumulation of matter under the influence of gravity. However, the picture around compact objects is in general more complex as the gravitational energy is efficiently converted into radiation. This is because compact objects generally accrete matter from a companion star or a gas reservoir, which carries some angular momentum. The angular momentum prevents the material from free falling into the compact object, which would otherwise fall onto it without noticeable effects in the case of a BH. For this reason, accretion around compact objects generally occurs through a disk, in which angular momentum can be slowly redistributed from the inner parts to the outer parts via viscous processes, enabling the gas to be finally accreted.

Another key difference of accretion around compact objects is due to their defining property: their compactness. This is generally defined as the mass to radius ratio ($\Xi \propto M/R_*$) of the object. Because the terminal velocity of an object falling from infinity is proportional to $\sqrt{M/R_*}$, accreting material around compact objects can reach extreme velocities before reaching the surface (or event horizon) of the accreting object. This makes compact objects enormous reservoirs of gravitational energy and accretion an extremely efficient process to extract it as we shall see below in more depth. Their compactness also leads to strong relativistic effects to be noticeable around them, making them ideal laboratories to test General Relativity (GR) (e.g. Event Horizon Telescope Collaboration et al., 2019).

The theory of accretion around BHs and NSs was developed around the late 70s, when it was already noticed that the release of gravitational energy around compact objects could produce copious amounts of radiation, suggesting that BHs and NSs could become powerful X-ray emitters and even outshine their companion stars (e.g. Lynden-Bell, 1969; Pringle & Rees, 1972; Shakura & Sunyaev, 1973). These authors already noted that a mechanism of loss of angular momentum was needed for the material to be accreted onto the compact object, but the mechanism and its efficiency were unclear at the time (and are still a matter of debate today), which hampered the development of a full theory of accretion. A breakthrough in our understanding of accretion was made in the seminal paper by Shakura & Sunyaev (1973), who were able to derive the structure and the spectrum of the disk by parametrising the efficiency of the unknown mechanism of angular momentum transfer as we shall see in more detail below. These authors considered the case in which a compact object accretes material from a star, the donor, in a gravitationally bound binary system. These systems are broadly termed X-ray Binaries (XRBs), which are strongly linked to ULXs as we shall see in Chapter 3. Generally speaking, XRBs can be divided into two classes depending on the way the material flows onto the compact object (Frank et al., 2002):

- *Roche lobe overflow*: The donor is close enough to the accretor so that the gravitational pull of the compact object is stronger than the gravitation force holding the star together. The outer layers of the star will be stripped away and start flowing onto the compact object.
- *Stellar wind accretion*: This happens when the wind from the companion is partially captured by the gravitational pull of the compact object. This typically occurs when the donor is a massive ($M > 8M_\odot$) star with strong winds.

Typically, but not always, Roche lobe overflow binary systems have $q < 1$ where $q = M_2/M_1$ and where M_1 and M_2 are the mass of the compact object and the donor star, respectively. Systems with $q < 1$ are termed Low-Mass X-ray Binaries (LMXBs). Instead, systems where the donor is heavier than the compact object (i.e. $q > 1$) are referred as High-Mass X-ray Binaries (HMXBs). These systems typically accrete via stellar-wind accretion, but HMXBs in which the donor fills its Roche lobe overflow do exist too, as it is likely the case in the X-ray binary SS433, which is discussed in detail in Section 3.2.5.

Accretion via Roche lobe overflow is generally better understood, so let us now focus in this to illustrate how accretion proceeds and how the emission is produced around the compact object. Consider the orbit of a test

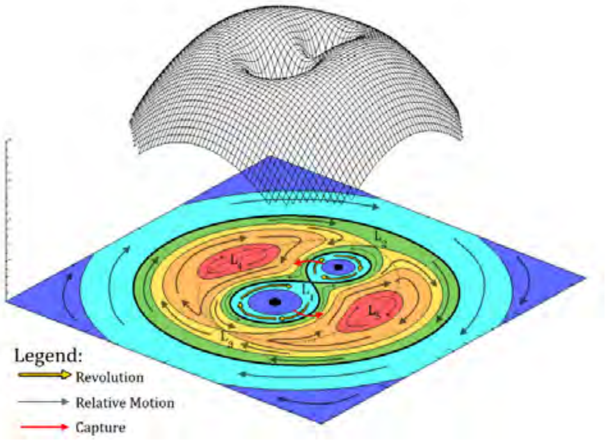

Figure 2.1: Equipotential surfaces in a binary system. The L1 Lagrange point is the point through which mass transfer can occur. The inner bold black line indicates the Roche lobe. From Wikimedia Commons.

particle under the influence of the gravitational potential created by the two bodies orbiting each other. Figure 2.1 shows the equipotential surfaces of the gravitational potential created by the two bodies orbiting each other, assuming the orbits of the two bodies around the system center of mass to be circular and regarding the bodies as point-like masses. The motion of matter is dominated by these equipotential surfaces and the contour of the Roche lobe (inner bold line in the Figure).

Broadly speaking, if the companion star does not fill its Roche lobe, transfer of matter could still occur in the form of wind capture accretion as stated above. But if for instance, the star expands during some stage of its stellar evolution, it may grow to fill its Roche lobe and accretion will proceed via Roche lobe overflow. The material beyond the L_1 Lagrange point, which is a saddle point of the potential created by the two bodies, will start to sink in the gravitational potential of the accretor and mass transfer will continue for as long as the donor fills its Roche lobe.

As stated earlier, the transferred material has specific angular momentum and will not fall directly onto the accretor. Instead, the particles will follow an elliptical orbital motion around the object. The presence of the donor makes these elliptical orbits to precess slowly and a continuous stream of gas will therefore intersect with itself, resulting in dissipation of energy via shocks. This lost of energy will circularize the orbits, forming a ring around the central object at R_{circ} with Keplerian velocity given by:

$$v_\phi(R_{\mathrm{circ}}) = \left(\frac{GM}{R_{\mathrm{circ}}}\right)^{1/2} \tag{2.1}$$

Shakura & Sunyaev (1973) considered the energy dissipation and the transport of angular momentum within the ring that leads to the formation of an accretion disk. They speculated that the physical mechanism responsible for the transfer of angular momentum could be linked to the magnetic fields tangled within the accreting plasma and turbulent motion within the flow, but without making strong assumptions about the exact mechanism, they only parametrised its efficiency. Because the Keplerian law implies differential rotation, tangential stresses between adjacent annuli within the ring could transport the angular momentum from the inner parts of the ring to the outer parts of the ring. As a result, the inner sections of the ring would slow down and spiral inwards as the angular momentum is transferred to the outer sections, that will in turn spiral outwards. Shakura & Sunyaev (1973) argued that this runaway process could spread the initial ring at $R = R_{\mathrm{circ}}$ to both smaller and larger radii forming an accretion disk. Because of viscous dissipation within the disk, matter falling onto the compact object would heat up and radiate a fraction of its energy in cooling down. This is the origin of the luminosity we observe from accretion disks and which allows astronomers to 'observe' and study compact objects. As stated earlier, even if the exact mechanism of transport of angular momentum (and its efficiency) was not known, Shakura & Sunyaev (1973) were able to derive the structure and the spectrum of the disk by parametrising the efficiency of this mechanism.

To do so, Shakura & Sunyaev (1973) considered on the one hand the tangential stresses introduced by the magnetic field tangled within the plasma (see also Lynden-Bell, 1969). The Maxwell stress is:

$$w = -\frac{B_r B_\phi}{4\pi} = -\frac{B^2}{4\pi} \tag{2.2}$$

where B_r and B_ϕ are the radial and azimuthal components of the magnetic field and where we have assumed $B_r = B_\phi = B$.

On the other hand, turbulent motion will also introduce tangential stresses between adjacent annuli. Assuming a turbulent cell of the order of the disk half-thickness (H), the turbulent viscosity can be expressed as $\eta_{\rm t} = \rho v_{\rm t} H$, where ρ is the density of the gas and $v_{\rm t}$ the turbulent velocity. The disk half-thickness can be obtained by simply assuming hydrostatic equilibrium:

$$H(R) = \frac{v_{\rm s}}{v_\phi} R \tag{2.3}$$

where $v_{\rm s}$ is the sound speed. Thus for the turbulent tangential stress we have:

$$w = -\eta_{\rm t} R \frac{d\omega}{dR} \sim -\eta_{\rm t} R \frac{v_\phi}{R} = -\rho v_{\rm t} H R \frac{v_\phi}{R} = -\rho v_{\rm t} v_{\rm s} \tag{2.4}$$

where ω is the Keplerian angular velocity and where we have used the expressions for $\eta_{\rm t}$ and H. Now we can write the total tangential stress as the sum of the contribution from the magnetic and turbulent stresses:

$$w = -\frac{B^2}{4\pi} - \rho {v_{\rm s}}^2 \frac{v_{\rm t}}{v_{\rm s}} = -\rho v_{\rm s}^2 \left(\frac{B^2}{4\pi \rho v_{\rm s}^2} + \frac{v_{\rm t}}{v_{\rm s}} \right) = -\alpha \rho v_{\rm s}^2 \tag{2.5}$$

with $\alpha = \frac{B^2}{4\pi\rho v_{\rm s}^2} + \frac{v_{\rm t}}{v_{\rm s}}$, a dimensionless parameter that sets the efficiency of the transport of angular momentum. This prescription allowed Shakura & Sunyaev (1973) to derive the emitted spectrum and structure of the disk without making strong assumptions on the exact mechanism of angular momentum transfer as we shall see below. Physical constraints suggest that $\alpha < 1$ although the exact value is still a matter of debate (e.g. King et al., 2007). This type of solution is known as the 'alpha prescription'.

A physical mechanism to provide the required angular momentum transfer was put forward later by Balbus & Hawley (1991), who suggested that magneto-rotational instabilities could be an effective mechanism of angular momentum transfer. Briefly, fluid elements from adjacent annuli are connected by magnetic field lines embedded in the plasma. Due to differential rotation, the inner fluid elements will spiral faster than the outer ones, increasing their displacement. The magnetic tension connecting the fluid elements will act as a restorative force, trying to bring these two elements together. To do so, the inner element will be slowed down whereas the outer element will be accelerated. In turn, this will increase their displacement as the inner element will move radially inwards whereas the outer element will move outwards. This will create a runaway process in which the inner annuli will transfer the angular momentum to outer radii, allowing the gas to accrete radially. This mechanism is often used to provide the necessary transfer of angular momentum in numerical simulations (e.g. Jiang et al., 2014).

The efficiency to which the mass is converted to radiation is also strongly dependent on the nature of the compact object. Consider some gas ($\rm M_g$) that falls from L_1 with zero velocity up to the surface or event horizon of the accretor (R_*). The gain in kinetic energy is $\frac{GMM_{\rm g}}{R_*}$. Thus the available energy that *could* be converted into radiation is:

$$L_{\rm acc} = \frac{GM\dot{M}}{R_*} \tag{2.6}$$

where $\dot{M}$ is the accretion rate i.e. mass accreted per unit of time. We see thus that the larger the compactness of the accretor, the more efficient the process is. The amount of gravitational potential energy (or mass) converted into radiation is usually referred as the accretion efficiency, which in Newtonian mechanics can be expressed as $\eta = \frac{GM}{R_* c^2}$. For a disk around a BH R_* is usually the Innermost Stable Circular Orbit (ISCO) of the disk ($R_{\rm isco}$) and one needs to take relativistic corrections into account (e.g. Teukolsky & Shapiro, 1983). For a non-rotating BH, $R_{\rm isco} = 3\,\rm R_S$ where $\rm R_S$ is the Schwarzschild radius ($\rm R_S = \frac{2GM}{c^2}$) and for a maximally spinning Kerr BH $R_{\rm isco} = \rm R_S/2$. Thus, for a non-rotating BH the efficiency is around 6% and for a Kerr BH can go up to $\sim$ 42% (Frank et al., 2002). For comparison, thermonuclear fusion of hydrogen, the most efficient nuclear reaction, the amount of mass that gets converted into energy is only of the order of 0.7%, making accretion around compact objects an extremely efficient process.

As stated in the Introduction, a key concept around which this thesis revolves is the Eddington limit or luminosity, which applies whenever there is a balance between gravitational force and the force induced by radiation pressure. This can be the case around stars or accreting compact objects. Let us now first derive mathematically the classical Eddington limit to illustrate this concept in the case of accretion, which is the relevant case for this work. Consider radial accretion (Bondi, 1952) of gas onto an spherical object of radius (R_*) at a steady rate ($\dot{M}$). Under these circumstances, the accretion luminosity is given by Equation 2.6, which we can rewrite it in terms of the accretion efficiency:

$$L_{\rm acc} = \frac{GM\dot{M}}{R_*} = \eta \dot{M} c^2 \tag{2.7}$$

Assuming the accreting material to be mainly fully ionized hydrogen, the photons transfer momentum to the free electrons through Thomson scattering, since the scattering cross-section for protons is a factor $(m_e/m_p)^2$ smaller, where $m_e/m_p \approx 5\times10^{-4}$ is the ratio of the electron and proton masses. The attractive electrostatic Coulomb force between the electrons and protons means that as they move out the electrons drag the protons with them. Thus, the radiation pushes out electron-proton pairs against the total gravitational force $GM(m_p+m_e)/r^2 \cong GMm_p/r^2$

where r is the radial spherical coordinate. With the previous considerations, equating the gravitational force and the force induced by radiation pressure we find:

$$\frac{GM\,m_p}{r^2} = \frac{L_{Edd}\,\sigma_T}{4\pi\,r^2 c} \rightarrow L_{\rm Edd} = \frac{4\pi\,GM\,m_p c}{\sigma_T} \cong 1.3\times 10^{38}\left(\frac{M}{M_\odot}\right)\,\text{erg/s} \tag{2.8}$$

where $L_{\rm Edd}$ is the Eddington luminosity and σ_T is the Thomson scattering cross-section. At greater luminosities, the outward pressure of radiation will start to blow off the infalling material. In reality, the gas will have different sources of opacity and abundances, the gas will not fall steadily and the geometry of the accretion flow around compact objects generally differs from the spherical case as stated above, but the Eddington limit offers a good first order approximation (see e.g. Steinhardt & Elvis, 2010). In fact, numerical Radiative Magneto-Hydrodynamic (RMHD) simulations have shown that it is precisely the disk geometry of the accretion flow that allows the transfer of matter to surpass the Eddington limit (Ohsuga & Mineshige, 2007). Because photons in the disk escape preferentially in the direction perpendicular to the disk plane, they do not completely counteract the radial force of gravity acting on the inflow material as it is assumed in the classical Eddington limit.

The limiting accretion mass-transfer set by the classical Eddington limit ($\dot{M}_{\rm Edd}$) can be found using Equations 2.7 and 2.8 and assuming a certain accretion efficiency given by the compactness of the accretor:

$$L_{\rm acc} = \eta\dot{M}c^2 \rightarrow L_{\rm acc}(\dot{M}_{\rm Edd}) = L_{\rm Edd} \rightarrow \dot{M}_{\rm Edd} = \frac{L_{\rm Edd}}{\eta c^2} \tag{2.9}$$

and it is convenient to finally define a dimensionless mass-transfer rate $\dot{m} = \dot{M}/\dot{M}_{\rm Edd}$. For $\dot{m}$ well below 1, a source is said to accrete in the sub-Eddington regime, where the effects of the radiation force on the accreting material can be ignored or will be relatively small. However, as $\dot{m}$ increases above 1, the accreting source will enter the super-Eddington regime, where the effects of the radiation pressure and advection will become important as we shall see below in more detail. The aim of this thesis is to broaden our understanding of the super-Eddington regime, of which the foundation was also described in the seminal paper of Shakura & Sunyaev (1973). We will see that other effects such as advection and/or the presence of strong magnetic fields might complicate the picture described here.

2.1 Sub-Eddington accretion

In the sub-Eddington regime, the disk is supported by gas and radiation pressures, which balance the vertical force of gravity. For $\dot{m} << 1$, the disk is said to be 'thin' i.e. H/R << 1. In this approximation, the loss of angular momentum (related to Equation 2.5) causes the gas to increase its kinetic energy and its thermal energy, that can be radiated through the surface of the disk. The radiated flux per unit surface through one side of the disk can be written as (Shakura & Sunyaev, 1973):

$$Q^+(R) = \frac{3}{8\pi}\dot{M}\frac{GM}{R^3}\left[1-\left(\frac{R_{\rm in}}{R}\right)^{1/2}\right] \tag{2.10}$$

where $R_{\rm in}$ is the innermost radius of the disk. The left panel on Figure 2.2 shows the dependency of Q^+ with radius for different mass-accretion rates for a $10\,\mathrm{M}_\odot$ non-spinning BH. The vertical dashed lines indicate where 50% of the radiation flux is emitted. We see thus that most of the emission is emitted in the regions close to the compact object ($R < 6\,R_{\rm in}$). Integrating Equation 2.10 gives the total luminosity of the disk

$$L = 2\int_{R_{\rm in}}^{R_{\rm out}} 2\pi R\;Q^+(R)dR = \dot{M}\,\frac{GM}{2R_{\rm in}} = \dot{M}\eta c^2 = \frac{\dot{M}}{\dot{M}_{\rm c}}L_{\rm Edd} = \dot{m}L_{\rm Edd} \tag{2.11}$$

where the factor 2 comes from taking into account both sides of the disk and we have assumed $R_{\rm out}\rightarrow\infty$. Thus in the sub-Eddington regime the luminosity grows linearly with the accretion rate.

The dependency on the disk temperature with radius and mass-accretion rate can be obtained by assuming that the gas in the disk is optically thick and photons reach thermal equilibrium with the accreting gas before escaping. We can therefore assume that each annuli emits as a black body:

$$\sigma T^4 = Q^+ \rightarrow T(R) = \left\{\frac{3GM\dot{M}}{8\pi R^3\sigma}\left[1-\left(\frac{R_{\rm in}}{R}\right)^{1/2}\right]\right\}^{1/4} \tag{2.12}$$

where σ is the Stephan-Boltzmann constant and where we have used Equation 2.10. The right panel on Figure 2.2 shows the temperature profile of the disk. It is easy to see that BHs will have a peak temperature of $\sim 10^6$ K.

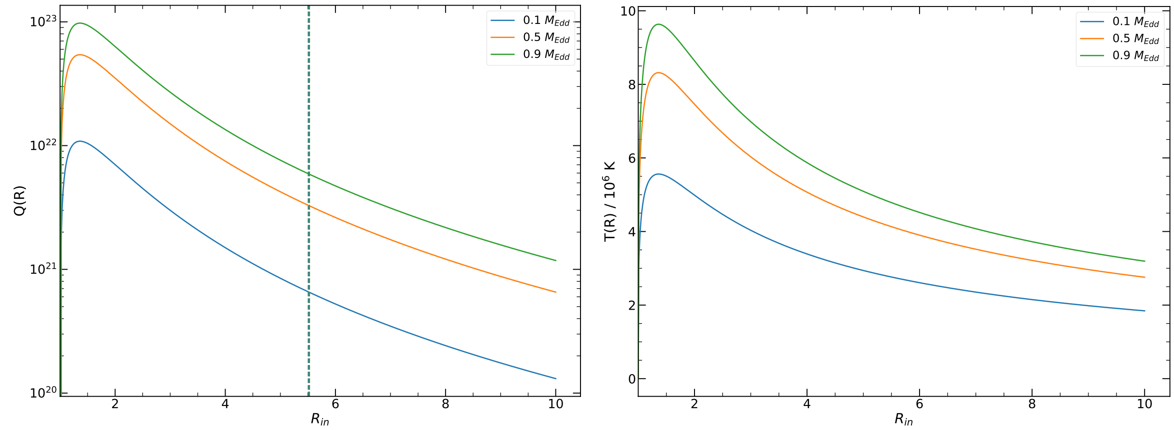

Figure 2.2: *Right*: Radiation flux per unit surface emitted through one side of the disk (left) and temperature profile (right) of the disk for different mass-accretion rates. Calculations are shown for a non-spinning $10\,\mathrm{M}_\odot$ BH.

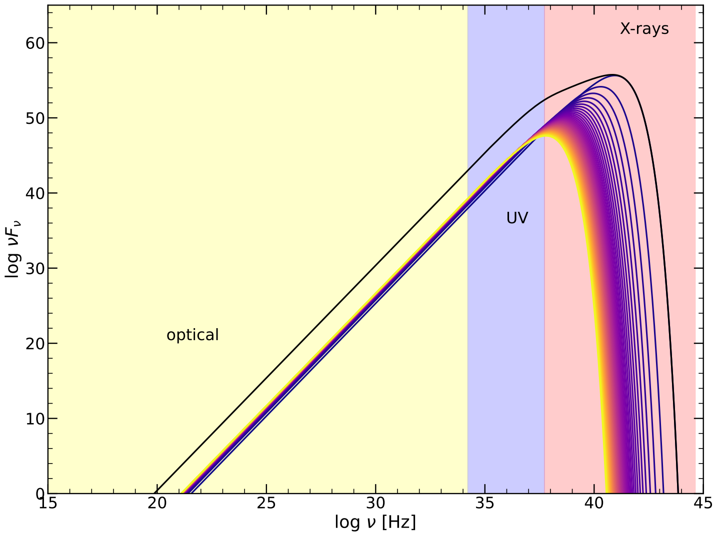

Figure 2.3: The spectrum of an optically thick, geometrically thin accretion disk in which all the emission is radiated locally. The integrated spectrum (black solid line) is composed of multiple annuli of different radii emitting as black bodies (coloured lines). A range from $2R_{\rm in}$ up to $50R_{\rm in}$ every $4R_{\rm in}$ from blue to yellow is shown.

Because we have approximated each annulus as emitting as a black body, the emission spectrum per area element of the disk is:

$$I_\nu = B_\nu[T(R)] = \frac{2h\nu^3}{c^2(e^{h\nu/kT(R)}-1)}\mathrm{ergs}^{-1}\mathrm{cm}^{-2}\mathrm{Hz}^{-1}\mathrm{sr}^{-1} \tag{2.13}$$

where h is the Planck constant, ν is the frequency and k is the Boltzmann constant. For an observer at a distance D seeing the disk whose normal has an angle i with respect to the line of sight (which we could assume corresponds to the binary inclination, but it is not always necessarily the case), the disk subtends a solid angle of $2\pi\, RdR\cos i\, D$. Therefore, the flux at a given frequency is:

$$F_\nu = \frac{4\pi h\cos i\ \nu^3}{c^2D^2}\int_{R_{\rm in}}^{R_{\rm out}}\frac{RdR}{e^{h\nu/kT(R)}-1} \tag{2.14}$$

which is illustrated in Figure 2.3 again for a non-spinning $10\,\mathrm{M}_\odot$ BH, accreting at $0.5\dot{M}_{\rm Edd}$. The peak of the emission occurs in the soft X-ray band, at around 1.6 keV. For a NS the peak would be at ~ 2 keV due to their smaller disk inner radii.

There are several implementations of the standard thin accretion disk in XSPEC (Arnaud, 1996), the X-ray spectral fitting package widely used in X-ray astronomy and in this work. A widely used implementation is the `diskbb` model (Mitsuda et al., 1984). This implementation differs slightly from the Shakura & Sunyaev (1973) solution because it assumes a *non-zero* boundary conditions, to simplify Equation 2.12 into (see Zimmerman et al., 2005, for a detail discussion):

$$T(r) = \left\{ \frac{3GM\dot{M}}{8\pi R^3 \sigma} \right\}^{1/4} \tag{2.15}$$

which is a reasonable approximation for $R >> R_{\mathrm{in}}$. However, given its simplicity, fast computation and early adoption it is still widely used, notably for consistency with previous works. The exact solution to the Shakura & Sunyaev (1973) with zero-boundary conditions is given by the `ezdiskbb` model (Zimmerman et al., 2005) in XSPEC. The main difference between the two is that the `ezdiskbb` gives values for the disk inner radius about 2.2 times smaller. Other more complex implementations also exist, taking into account relativistic effects and/or self-irradiation by the inner disk photons of the outer regions of the disk, but are not as relevant for the present work.

Observationally however, the accretion process around compact objects has been shown to be more complex than implied by standard disk theory. As we will see in the next Sections, the X-ray spectra of BHs and NSs often present additional components beyond the standard disk, some of which are well reproduced in terms of Compton scattering processes. Compton scattering is the scattering of a photon by a free charged particle. This generally occurs between photons and free electrons, but can also occur between photons and bound electrons when the photon energy is much larger than the binding energy of the electron. For low-energy photons (i.e. visible/UV range) this interaction is elastic and is generally termed Thomson scattering. For X-ray and γ-rays, the interaction is inelastic and is generally termed Compton scattering. If the photon transfers energy to the electron, this is referred as Compton scattering or down-scattering. If the electron transfer energy to the photon, this is referred to as inverse Compton or up-scattering.

These systems also show the presence of outflows like equatorial disk winds or collimated relativistic jets, suggesting that part of the gravitational energy is channeled in the form of mechanical energy. Both the launching mechanism of the winds and jets are highly debated. Winds could be launched by magneto-centrifugal forces, X-ray heating and expansion of the outer layers of the disk (thermal winds) or by the radiation pressure (e.g. Miller et al., 2006; Ponti et al., 2012; Higginbottom et al., 2017), the latter being more relevant for the super-Eddington regime as we will see in Section 2.2. Winds in XRBs are preferentially observed in high inclination systems, suggesting that these winds are mostly emitted equatorially (Ponti et al., 2012; Díaz Trigo & Boirin, 2016). Conversely, jets are thought to be collimated along the rotational axis of the compact object by twisted magnetic fields accelerating the plasma, which become coiled up due to the rotation of the ergosphere of a spining BH (Blandford & Znajek, 1977) or due to the rotation of the accretion flow itself (Blandford & Payne, 1982).

2.1.1 Observational Properties of Accreting Black Holes

There are around 22 dynamically confirmed BH X-ray binary systems, that amount to 60 if candidates are included (e.g. Corral-Santana et al., 2016; Casares et al., 2017). The majority (around 80% of them) are transient systems, termed Black Hole Transients (BHTs), which are all LMXBs. The persistent systems are all except XTE J1819.3–2525 HMXBs (Casares et al., 2017). BHTs spend most of their time in quiescence with $L_{\mathrm{X}} \sim 10^{30-33}$ erg/s (around $10^{-8} - 10^{-5}$ L_{Edd}), undergoing episodic outbursts that last weeks to months where the system can reach luminosities sometimes close to Eddington (e.g. Done & Gierliński, 2003; McClintock & Remillard, 2006). These outbursts typically follow a common well-defined pattern termed 'q-diagram' (e.g. Homan et al., 2001; Fender et al., 2004; Belloni, 2010) because of the shape the outburst describes when the variations in the X-ray luminosity (or count rate) are represented against the so-called 'X-ray color'. The X-ray color or 'hardness ratio' is simply the ratio between the count rates in two energy bands: a low-energy or 'soft' band and a high-energy or 'hard band'. A cartoon of a typical BHT outburst is shown in Figure 2.4, where the famous q-diagram is represented. This type of diagram is termed Hardness-Intensity Diagram (HID) and is useful in tracking the evolution of a source brightness and spectral shape. The presence of *hysteresis* in these cycles strongly suggests that the properties of the accretion flow are not uniquely defined by the mass-transfer rate.

The BHTs states are defined in terms of luminosity, spectral shape, timing properties and also radio emission, which are thought to be connected to changes in the accretion flow geometry (e.g. Fender et al., 2004). The X-ray spectra of BHTs are generally fitted with a multicolor disk black body with characteristic temperature of 0.1–1 keV, arising from the accretion disk, and a powerlaw with a cutoff component at tens or hundreds of keV, arising from hot electrons upscattering disk photons (Gilfanov, 2010). The cutoff of the powerlaw sometimes is associated with the temperature of the electrons, which could be present in an optically thin rarefied cloud of plasma surrounding the compact object termed 'corona' (e.g. Gilfanov, 2010). A possible explanation for the corona is the presence of a hot, low-density, optically thin advection-dominated flow [1] (Narayan & Yi, 1995) in the inner regions closest to the compact object, but the exact geometry and origin of this corona remains uncertain (see Done et al., 2007, for a more detailed discussion on the physical properties of this inner flow). For instance, this model does not explain the jet launching mechanism. An alternative scenario has been proposed in which the inner regions

---

[1] I discuss advection in more detail in the context of super-Eddington regime, noting that it is also a relevant process at low-mass accretion rate as we see here.

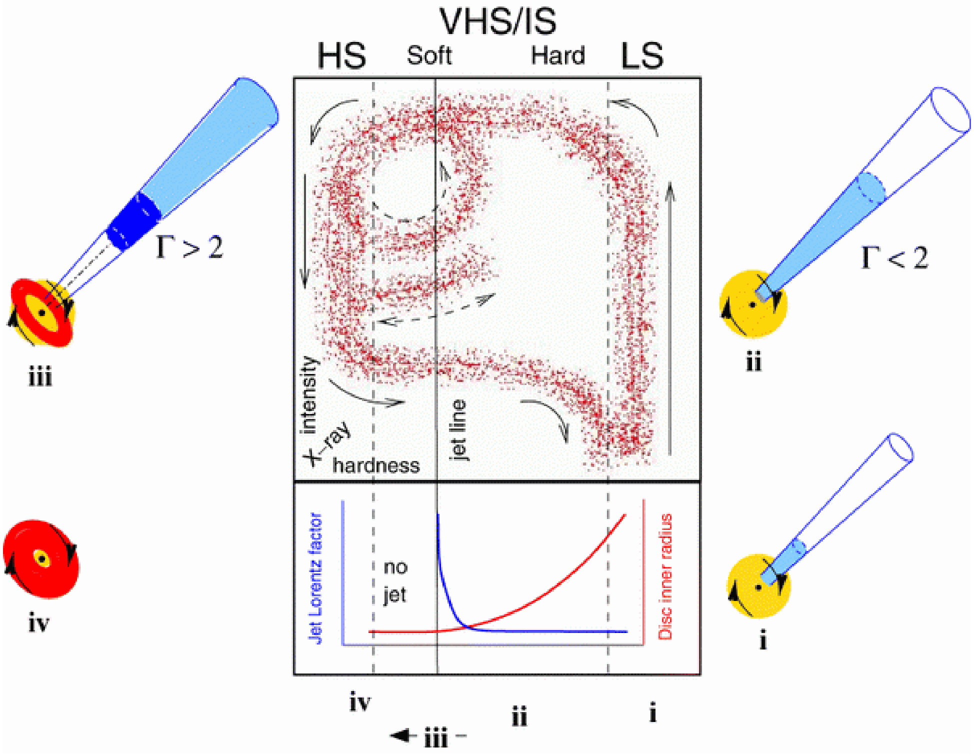

Figure 2.4: Schematic of the evolution of a BHT during outburst. The upper panel shows the intensity as a function of the X-ray color or hardness ratio. The various spectral states are indicated HS (high-soft state), LS (low-hard state) and the intermediate states, the VHS (very high state) and the IS (intermediate state). The lower panel shows the Lorentz factor of the jet and the inner disk radius as the source traverses the different states. The outer cartoons show a schematic of the accretion flow-jet coupling. The Figure is taken from Fender et al. (2004).

of the accretion flow closer to the compact object are strongly magnetized and act as the jet launching site (see e.g. Marino et al., 2021, and references therein). Another famously adopted model for the corona is the so called ‘lamppost’ corona, a point-like source on the rotational axis of the compact object (e.g. Dauser et al., 2013) which sometimes it is argued could be the base of the jet (Wang et al., 2021). The disk and the corona components vary during the outburst and allow astronomers to define some common properties across different systems, which I will briefly summarize below. Another common hallmark of the X-ray spectra of X-ray binaries is the presence of ‘reflection’ features, which are thought to arise due to the illumination of the disk by the hot corona. The hot photons from the corona will be reflected off the disk via Compton scattering, while others will be absorbed and re-emitted in the form of fluorescence lines of heavy elements (e.g. Gilfanov, 2010). The strongest of these lines is the Fe K-α line at 6.4 keV, whose modelling can be used to infer the spin of the BH (e.g. Dauser et al., 2013).

The spectral changes are always accompanied with changes in the timing properties of the source (e.g. Belloni, 2010), that are as useful as the spectral information in probing the physical conditions of the accretion flow and discriminating the different source states. However, for brevity and because the aim of this Section is to highlight the *spectral* differences that exist between sub-Eddington X-ray binaries and ULXs, which are more relevant for the present work, I will focus only on the spectral properties describing the evolution a source follows during outburst.

A typical BH outburst can be described as follows: at low mass-transfer rates, the source is in the Low-hard State (LS) with a low X-ray luminosity in the ~ 0.1–10 keV band and a hard spectrum. This state is dominated by the hard powerlaw component ($> 80\%$ of the flux at 2–20 keV) with a spectral index in the range $1.5 < \Gamma < 2.1$ (McClintock & Remillard, 2006; Belloni, 2010). It is somewhat agreed that in this low luminous hard state the disk is truncated far from the BH ($\sim$100R$_\mathrm{g}$; Figure 2.4) due to the generally low mass-accretion rate (Done et al., 2007), albeit some works contradict this hypothesis as they find that the disk extends close to the R_isco in the LS (e.g. García et al., 2015; Wang et al., 2021) and other scenarios have been proposed as stated above. The low-density hot inner flow (or corona) inverse Compton scatters the soft photons from the disk. Because the disk is truncated and most of the soft X-ray photons are Compton scattered, the spectrum is dominated by the hard component. This state is also associated with quasi-steady radio jet emission (Figure 2.4; Fender et al., 2004).

As the mass-accretion rate increases the disk moves inwards, increasing the number of soft photons that are inverse Compton scattered. The electrons in the hot inner flow cool more efficiently thanks to the additional contribution from the disk photons and thus the spectrum softens. Here the source start to traverse to the left in the HID and will be found in one of the intermediate states, between the LS (right vertical track in the HID in Figure 2.4) and the High-soft State (HS) (left-most parts of the HID). The powerlaw now has an index of $2.4 < \Gamma < 2.5$ and the thermal disk component is now clearly detected (e.g. Belloni, 2010). The steady jet persists as the source keeps softening.

At the so-called ‘jet line’ (Figure 2.4), the jet reaches its maximum power, seen as an increase in the Lorentz factor (bottom panel in Figure 2.4). As the source crosses the jet line, it enters the HS or thermal dominant state (McClintock & Remillard, 2006) where the jet is quenched (e.g. Fender et al., 1999) and the disk extends until the innermost stable orbit. Here the disk dominates the spectrum with a temperature of 0.7–1.5 keV, with a faint powerlaw with $2.1 < \Gamma < 4.8$ contributing only to 25% of the emission in the $2-20$ keV band (Remillard & McClintock, 2006). The attribution to the thermal component to the thin Shakura & Sunyaev disk is supported by the variation of the disk luminosity as $L_\mathrm{disk} \propto T^4$ (Kubota et al., 2001; Gierliński & Done, 2004) in this state, as expected for an accretion disk with constant emitting area. If the distance to the source and the inclination of the disk is known, spectral fitting of the disk component allows to estimate the R_isco, giving some constraints on the BH mass, which will ultimately depend on the spin, since R_isco depends on the spin. Alternatively, if the mass is known from dynamical mass measurements, the spin of the BH can be measured. Note that this measurement is only valid if we are certain that the disk extends to the innermost stable orbit! This will be relevant in Chapter 3 when discussing the first attempts to interpret the ULX spectra.

This picture describes the evolution of most BHTs found in our Galaxy. There are however, some exceptions. For instance, the BHTs LMXB GRS 1915+105 never reaches the LS (Belloni, 2010) and instead switches between three peculiar states corresponding to intermediate states between the high-soft and the low-hard states (Belloni et al., 2000). Interestingly, GRS 1915+105 can reach Eddington or slightly above Eddington luminosities (Done et al., 2004) and is considered a prototypical example of a *microquasar* (e.g. Middleton et al., 2006), because of its nearly persistent relativistic jet emission (Fender et al., 1999). Another Galactic BH binary system belonging to the microquasar realm is SS433, which is suggested to be a persistent super-Eddington accretor (e.g. Fabrika, 2004). These type of Galactic sources might be analogous to the ULXs found in other galaxies (e.g. King & Puchnarewicz, 2002), and I will briefly discuss such link in more detail in Section 3.2.5. Note however that accreting NSs also display relativistic jets (e.g. Coriat et al., 2019). NSs are less radio loud than BHs for a given X-ray luminosity, which is argued to be due to the presence of a hard surface, making them more radiatively efficient (Migliari & Fender, 2006), as we will see below.

2.1.2 Observational Properties of Accreting Neutron stars

NSs differ from BHs in two important aspects: they have a hard surface and they can possess magnetic fields, with strengths up to $B \sim 10^{14-15}$ G, which can disrupt the accretion flow (Pringle & Rees, 1972; Ghosh et al., 1977). These two properties lead to observational effects which are unique signatures of accreting NSs.

Let us now focus on the case of NSs with $B \lesssim 10^{10}$ G, in which the disk may extend all the way to the NS surface (e.g. Popham & Sunyaev, 2001). These type of lowly magnetised NSs are commonly found in LMXBs systems, which can be subdivided into 'atolls' and 'Z' sources, because of the different shapes their evolutionary patterns formed in a colour-colour diagram (e.g. van der Klis, 1989). The difference between the two is due to different mass-accretion rate, being $\lesssim 0.01\,\dot{M}_{\rm Edd}$ in atolls and $\gtrsim 0.1\,\dot{M}_{\rm Edd}$ in Z sources. These sources can be fitted with the same models employed for BHs, a multicolour accretion disk with Comptonized emission and some lines modelling the reflection features (e.g. Done & Gierliński, 2003), suggesting that because NSs have similar gravitational potential to BHs, the accretion flow is somewhat similar. However, because of the presence of a hard surface, the rapidly spinning gas from the disk has to decelerate before accreting onto the NS surface. In the case of BH, if the disk extends to the $R_{\rm isco}$, the material after $R_{\rm in}$ will fall without appreciable effect. Instead, in the case of a NS the decelerating material will form the so-called 'boundary layer' close to the NS surface (e.g. Frank et al., 2002). In the Newtonian approximation, about half of the gravitational energy is radiated in the disk, as the binding energy of a particle of mass m at $R_{\rm in}$ is $GMm/2R_{\rm in}$. The other half can be radiated in the boundary layer and at the NS surface (e.g. Popham & Sunyaev, 2001) and might explain why NS X-ray binaries are generally brighter (when scaled by their lower Eddington ratios) than BHs (e.g. Done & Gierliński, 2003). The physical conditions of the boundary layer are complex and depend on several parameters such as the NS spin, radius and the mass-accretion rate, but it has been argued that this additional emitting component provides a distinct spectral shape and variability unique to accreting NSs, and may offer means to distinguish between accreting BHs and NSs through X-ray spectroscopy (Done & Gierliński, 2003). This was one of the motivations of my first work during this thesis, to try to distinguish BH-ULX from NS-ULX through X-ray spectroscopy (see Section 5).

Another observational effect due to the NS surface is the presence of 'type I' X-ray bursts that last typically from tens to hundreds of seconds (e.g. Galloway et al., 2008; Pastor-Marazuela et al., 2020). These are caused by thermonuclear bursts as the accreting material is compressed against the surface of the NS. The temperature of the gas increases to the point where a thermonuclear flash can be triggered, suddenly increasing the X-ray luminosity by two orders of magnitude (Frank et al., 2002).

Let us now focus on highly magnetised NSs ($B \gtrsim 10^{10}$ G), in which the disk will be disrupted and forced to follow the magnetic field lines (e.g. Pringle & Rees, 1972). These are generally younger systems than their LMXBs counterparts and are found in HMXB systems. The radius at which the disk is truncated is called the 'magnetospheric radius' and can be found by balancing the gas ram pressure with the magnetic pressure (Ghosh et al., 1977). In the spherical case, following (Frank et al., 2002), we can write:

$$\rho v = \frac{\dot{M}}{4\pi r^2} \tag{2.16}$$

and assume v is equal to the free-fall velocity. Therefore, the gas ram pressure can be written as:

$$\rho v^2 = \frac{(2GM_{\rm NS})^{1/2}\dot{M}}{4\pi r^{5/2}} \tag{2.17}$$

The magnetic pressure is given by:

$$P_{\rm mag} = \frac{B^2}{8\pi} \tag{2.18}$$

for which we assume a dipole-like magnetic field $B = B_* R_{\rm NS}^3/r^3$ where B_* is the magnetic field at the NS surface and $R_{\rm NS}$ is the NS radius. Now we can find the radius at which Equation 2.17 is equal to Equation 2.18, obtaining:

$$R_{\rm m} = \xi \left(\frac{R_{\rm NS}^{12} B_*^4}{2GM_{\rm NS}\dot{M}^2} \right)^{1/7} \tag{2.19}$$

where we have introduced a dimensionless factor ξ which takes into account deviations from the spherical case (ξ =1). For accretion disks, $\xi = 0.5$ (Ghosh et al., 1977).

Within $R_{\rm m}$, the gas will accrete onto the magnetic poles of the NS as the gas is forced to follow the magnetic field lines. At $\dot{M} < \dot{M}_{\rm Edd}$, the gas free-falls onto the NS surface where it releases its energy, forming two hot spots (in the simple case of a dipolar magnetic field), where the radiation is able to escape in the direction parallel to the magnetic field (Basko & Sunyaev, 1976). Due to the misalignment of the NS rotational axis with the magnetic axis, the rotation of the NS will give rise to the characteristic X-ray pulsations (X-ray pulsars), again a unique signature of NSs. Because of the dependency of $R_{\rm m}$ with the mass-accretion rate, some atolls also show pulsations, even if their magnetic fields are much lower than accreting X-ray pulsars found in HMXBs.

As $\dot{M}$ approaches $\dot{M}_{\rm Edd}$, a shock front will develop above the NS surface in which the optical depth to Thomson scattering will reach ~ 1. The gas beyond the shock slowly sinks as it is decelerated by the interaction with the photons and can thus radiate its gravitational energy locally. This leads to the formation of an 'accretion column' above the NS surface, that is sustained by magnetic pressure (Basko & Sunyaev, 1976). However, the photons can no longer escape in the direction parallel to the magnetic field and instead escape in this case through the sides of the accretion column, giving also raise to X-ray pulsations.

Accreting X-ray pulsars are generally fitted with a powerlaw with a cutoff in the 10–30 keV range (Coburn et al., 2002; Caballero & Wilms, 2012), which sometimes requires the addition of a soft thermal component with kT $\sim$ 0.1 keV (Hickox et al., 2004). The cutoff power law is a proxy for the complex hard X-ray emission from the accretion column, whereas the soft component is attributed to reflection of this hard X-ray emission off the disk, which becomes important at high luminosities (e.g. Hickox et al., 2004). A model to reproduce the emission from the accretion column in which the radiative shock dominates the emission has been put forward by Becker & Wolff (2007), in which the resulting spectrum is a combination of thermal Comptonization of seed Bremsstrahlung, black body and cyclotron seed photons. We shall later see in Chapter 3 that there might be some similarities between the accreting X-ray pulsar and ULX spectra.

Basko & Sunyaev (1976) showed through theoretical estimates that because the magnetic pressure would sustain the accretion column against the radiation pressure, accreting X-ray pulsars could in principle exceed the classical Eddington limit by a factor of a few. Because magnetic fields are known to reduce the electron scattering opacity (Canuto et al., 1971; Basko & Sunyaev, 1976), of which the Eddington limit depends inversely on (cf. Equation 2.8), in principle highly-magnetised NSs would be more likely to exceed their Eddington luminosities. We shall discuss this in more detail in the context of super-Eddington accretion in Section 2.2.1.

Another important phenomenon linked to highly magnetised NSs, and perhaps relevant for ULXs (see Section 3.3) is the so-called 'propeller regime' (Pringle & Rees, 1972; Illarionov & Sunyaev, 1975). This occurs when the centrifugal barrier of the magnetosphere prevents further infalling of gas onto the NS, halting accretion with the subsequent drop in luminosity. More specifically, this occurs when the co-rotation radius:

$$R_{\rm C} = \left(\frac{GMP^2}{4\pi^2}\right)^{1/3} \tag{2.20}$$

the radius at which the Keplerian disk velocity is equal to the rotation of the NS, is smaller than the magnetospheric radius (cf. Equation 5.1). Here P is the NS rotation period. A transition to the propeller regime can cause the X-ray emission to dramatically drop by a factor $\sim$ 10-100 (e.g. Campana et al., 2002; Tsygankov et al., 2016a). In principle, during accretion phases the gas will transfer angular momentum to the NS, causing it to spin up. During the propeller regime one may expect the NS to instead spin down as the rotational energy is radiated away. The different modes of accretion outlined here as a function of magnetic field, namely, disk accretion, magnetically channeled accretion onto the poles and the transition to the propeller regime are well reproduced in GR-MHD simulations (see calculations by Parfrey & Tchekhovskoy, 2017).

2.2 Super-Eddington accretion

Since $\dot{m}$ only depends on the mass-transfer from the companion, there is no reason for this value to be limited at 1, and in fact it can greatly exceed this value. King (2002) suggested that mass-transfer rates up to 10^{-3} M$_\odot$/yr[2] can be achieved in HMXBs systems as the donor evolves from the main sequence to the giant branch (crossing the Hertzsprung gap) and expands to fill its Roche lobe. Rappaport et al. (2005) showed through binary synthesis that mass-transfer rates to provide ULX luminosities (up to 10^{42} erg/s) could indeed be achieved in such a way, but that these phases would be short lived ($\sim 10^5$ yr). The same authors found that much longer ULX phases could be achieved for donors with masses $M \gtrsim 10$M$_\odot$ during hydrogen nuclear burning. Mass-transfer rates in the range of $\sim 10^{-6} - 10^{-4}$ M$_\odot$/yr during a few 10^4 yrs were also found by Wiktorowicz et al. (2015) for 11M$_\odot$ donors. We see thus that $\dot{m}$ can easily reach up to 1000 for a set of physically plausible models.

As $\dot{m}$ approaches 1, the prescription given in Section 2.1 will no longer be valid as radiation pressure and advection will affect the disk structure and emitted spectrum compared to the sub-Eddington regime. The radiation pressure inflates the disk in the inner regions, helping support against its own gravity, meaning that the condition H/R << 1 is no longer satisfied. One can imagine that because the gas is optically thick and due to the increased scale height of the disk as it becomes more radiation pressure supported, photons now have to undergo multiple scatterings before reaching the surface of the disk. This implies that advection, the horizontal transport of radiation (or heat), will affect the local radiated flux at each radius. This can be expressed as:

$$Q_{\rm rad} = Q^+ - Q_{adv} \tag{2.21}$$

---

[2] The Eddington rate for a non-spinning BH is around 4 × 10^{-7} M$_\odot$/yr, so this corresponds to $\dot{m} \sim 2000$.

. In the case of BHs this effect is particularly important due to the absence of a solid surface. If the photon diffusion time becomes larger than the accretion timescale, photons are now advected into the BH before they can reach the surface of the disk. This provides an additional cooling mechanism for the disk, which becomes radiatively inefficient above the Eddington mass-transfer rate. The radius at which this effect becomes important is called the trapping radius (Begelman, 1979), which increases proportional to $\dot{m}$ in a disk (Abramowicz et al., 1988; Ohsuga et al., 2002). This implies that the luminosity when $\dot{m} \gtrsim 1$, does no longer grow linearly with $\dot{m}$, but instead photon trapping effects only allow the luminosity to increase logarithmically. Disk solutions that take into account this effect are termed 'slim' disks (see Abramowicz et al., 1988, and references therein), because the loss of radiation due to advection implies that the disk is radiatively inefficient H/R $\lesssim 1$ i.e. the disk becomes slim as opposed to thin. It is worth mentioning that 3D RMHD simulations have shown that vertical advection caused by magnetic-buoyancy can reduce the effects of photon trapping around BHs in the super-Eddington regime (Jiang et al., 2014).

The effects of advection can be taken into account using the `diskpbb` (Watarai et al., 2000) model in XSPEC, a generalization of the `diskbb` model which allows to vary the radial temperature profile as $T \propto R^{-p}$, where p is a parameter of the model and for which $p = 0.75$ represents the case of the standard `diskbb`. Watarai et al. (2000) showed that the effects of advection (e.g. Narayan & Yi, 1995) cause the temperature profile of the disk to be flatter compared to the standard value of 0.75. Watarai et al. (2000) showed that the case where $p = 0.5$ is expected for an advection-dominated disk.

However, one can also imagine that instead the radiation pressure will blow off some of the excess gas. This was the solution given by Shakura & Sunyaev (1973), who assumed that all the emission is radiated locally i.e. neglecting the effects of advection and photon trapping effects and assuming that all the excess energy goes into powering the outflows. Here because the disk is radiatively efficient, the disk is said to become 'thick' i.e. $H/R >> 1$. More specifically, because the energy flux in the Shakura & Sunyaev (1973) is proportional to R^{-3} $\left(1-(R_{\rm in}/R)^{1/2}\right)$ (see Eq. 2.10), the outer regions of the disk can remain thin even if $\dot{m} >> 1$. Therefore, the prescription given in the previous Section will remain valid for these regions. However, in the inner regions radiation will inflate the disk as the scale height is proportional to $\dot{m}$ (Shakura & Sunyaev, 1973). The disk scale height becomes of the order of its radius at the so-called spherization radius:

$$R_{\rm sp} = \frac{9}{4}\dot{m} \tag{2.22}$$

at which radius the integrated disk luminosity reaches the Eddington value. Thus, in the inner regions to $R_{\rm sph}$ the radiation pressure will blow off the excess gas, such that the mass-transfer rate decreases linearly with R as:

$$\dot{M}(R < R_{\rm sp}) = \dot{M}_0 \frac{R}{R_{\rm sp}} \tag{2.23}$$

where $\dot{M}_0$ is the mass-transfer at the outer disk radius. The luminosity in the inner parts of the supercritical disk exceed the Eddington value logarithmically as $L_{\rm Edd} \ln \dot{m}$. Therefore, the total luminosity of the disk in the super-Eddington regime given by Shakura & Sunyaev (1973) is:

$$L_{\rm disk} = L_{\rm Edd} + L_{\rm Edd} \ln \dot{m} = L_{\rm Edd}(1 + \ln \dot{m}) \tag{2.24}$$

We see that in both schools of thought the luminosity only grows logarithmically with $\dot{m}$ when $\dot{m} > 1$. In the former case, the excess radiation is lost to advection whereas in the latter case the excess radiation powers the outflow. Lipunova (1999) and Poutanen et al. (2007) derived the solution for a disk in which both outflows and advection affect its structure, by removing angular momentum and by affecting the local radiation flux. The fraction of energy that powers the outflow compared to that which is radiated is a free parameter of the model (ϵ_w), reflecting that the exact underlying physics are still unknown. The solution given by Poutanen et al. (2007) differs slightly from the set of Equations given above, but the main relevant conclusions are qualitatively similar: the presence of $R_{\rm sph}$ growing with $\dot{m}$, but with a more complex dependency introduced by the parameter ϵ_w, a mass-transfer decreasing with radius within $R_{\rm sph}$ and a logarithmic dependence of $L_{\rm disk}$ with $\dot{m}$. The mass-transfer rate as a function of radii within $R_{\rm sph}$ can be approximated as a linear function (Poutanen et al., 2007):

$$\dot{m(R)} = \dot{m}_{\rm in} + (\dot{m}_0 - \dot{m}_{\rm in})\frac{R}{R_{\rm sph}} \tag{2.25}$$

where $\dot{m}_{\rm in}$ is the mass-transfer rate at the inner disk radius (i.e. the mass-accretion rate) whose exact value depends on ϵ_w and $\dot{m}_0$. Figure 2.5 compares the differences in the fraction of matter accreted by the compact object to that transfered for the theoretical prescriptions of Shakura & Sunyaev (1973) and Poutanen et al. (2007). In both cases the mass-transfer rate within $R_{\rm sph}$ decreases linearly (or approximately). However, while Shakura & Sunyaev (1973) assumes that the mass accreted by the compact object is nearly zero, this is not the case in the Poutanen et al. (2007) model, as part of the matter will be advected into the BH instead of expelled in the outflow. The exact value will depend on the unknown value of ϵ_w, for which simultaneous measurements of $L_{\rm rad}$ and $L_{\rm wind}$ might be able to offer some constraints. As we will see in Section 3.2.3 and Chapter 6, the nebulae found around ULXs provide means to estimate the mechanical power of the wind and are thus of great

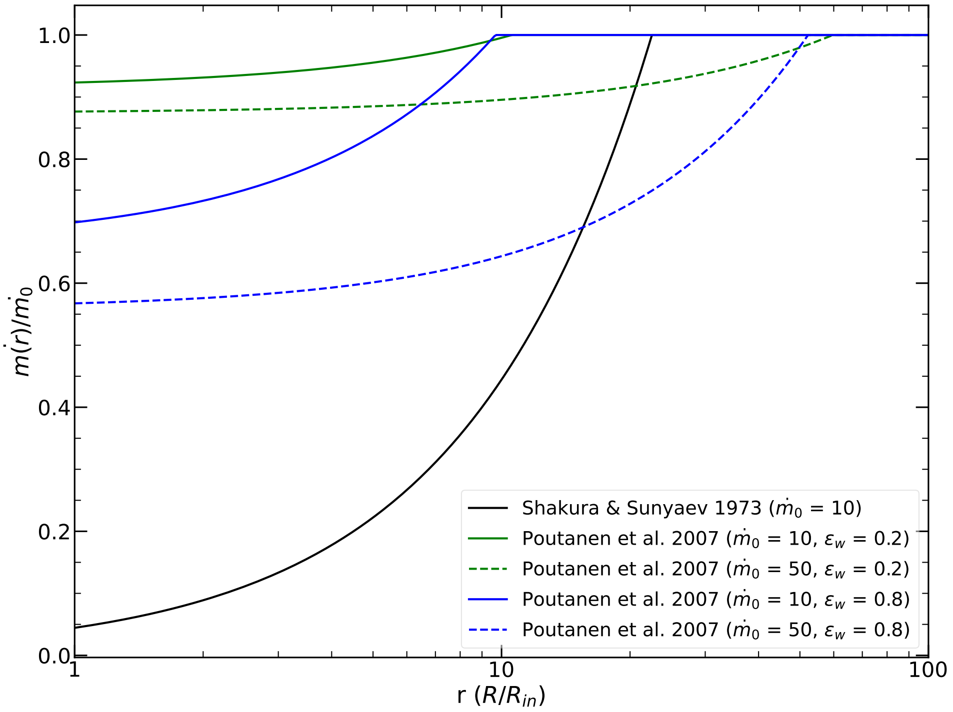

Figure 2.5: Comparison of the ratio of mass-accreted by the compact object to that transfered by the companion ($\dot{m}_0$) for the supercritical disk of Shakura & Sunyaev (1973), in which advection is neglected and all the energy excess powers the outflow, and that of Poutanen et al. (2007), which takes into account advection and where only a certain fraction of the excess energy (parametrised as ϵ_w) goes into power the outflow. Calculations are carried out for a 10M$_\odot$ non-spinning BH and for $\dot{m}_0 = 10$ in the case of Shakura & Sunyaev (1973) and for $\dot{m}_0 = 10$ and 50 in the case of Poutanen et al. (2007).

interest to constrain this parameter.

An important consideration made by Shakura & Sunyaev (1973) and worked out in more details by Poutanen et al. (2007) is the fact that the presence of outflows introduce highly anisotropic emission. Let us explain how this occurs in detail. The outflow velocity in the direction perpendicular to the plane is expected to be proportional to the local Keplerian velocity $\sqrt{\frac{GM}{R}}$ (Shakura & Sunyaev, 1973; Poutanen et al., 2007). Thus, due to angular momentum conservation, the outflow leaves the disk spiraling outwards, forming an evacuated cone around the rotational axis of the object. The outflow is expected to be optically thin to electron scattering only within a narrow angle around the rotational axis of the compact object (Poutanen et al., 2007), due to the lower mass outflow rate there and faster outflow speeds closer to the compact object. Moreover, theoretical calculations by the same authors show that the optical depth to electron scattering of the outflow is expected to be an order of magnitude higher than in the direction parallel to the disk plane compared to the perpendicular direction. This can be understood due to the denser and slower velocity outflow close to the disk plane, compared to the vertical direction. As a result, the conical structure of the wind introduces highly anisotropic emission: observers looking down the optically thin funnel will observe the hard X-ray radiation produced in the vicinity of the compact object whereas observers at high inclinations will observe mostly the reprocessed softer emission of the outflow. This implies that the observed flux not only depends on $\dot{m}$ but also has a strong dependence on the viewing angle.

Photon trapping effects and the conical structure of the outflow inducing anisotropic emission have extensively been confirmed in numerical RMHD simulations (e.g. Ohsuga et al., 2005; Ohsuga & Mineshige, 2007; Takeuchi et al., 2013; C. McKinney et al., 2013). The outflow speeds found in these works reach 10s of the speed light, in agreement with some theoretical estimates (e.g. Shakura & Sunyaev, 1973; King & Muldrew, 2016). The radiation efficiencies found are typically low, of the order of a few percent (C. McKinney et al., 2013; Jiang et al., 2014; Sądowski & Narayan, 2016). For instance, for a 10 M$_\odot$ BH with $\dot{m} = 10$, typical integrated luminosities are only of the order of 2–3 $L_{\rm Edd}$ (e.g. Narayan et al., 2017). However, many of these works also find that the luminosity an observer would infer observing along the polar direction assuming isotropic emission could easily reach a factor 10 or 100 of the classical Eddington limit (e.g. Ohsuga et al., 2005; Narayan et al., 2017). This occurs because the funnel walls are optically thick, and thus the emission from the inner parts of the disk is collimated or Compton scattered by and off the wind walls mostly into the polar directions (King, 2009).

Because mass-transfers in excess of the Eddington value are required to produce the conical funnel structure, King (2009) argues that strong beaming is a natural consequence of super-Eddington accretion. Because the observed flux is generally converted into luminosity assuming isotropic emission, if the emission is emitted in a given preferential direction, as could be the case with the supercritical funnel, then the estimated luminosity under the assumption of isotropic emission ($L_{\rm iso}$) might be an overestimate of the true emitted luminosity (L). Mathematically, this can be simply expressed as:

$$L = L_{\rm iso} b \tag{2.26}$$

where b is known as the beaming factor and reaches a value of 0.5 around standard thin disks (e.g. Kaaret et al., 2017), for instance. It is thus suggested that Equation 2.24 should be modified as (e.g. King, 2008):

$$L = \frac{L_{\rm Edd}}{b}(1 + \ln \dot{m}) \tag{2.27}$$

to take into account this effect when estimating the emitted luminosity[3]. Moreover, King (2009) argues that the opening angle of the funnel decreases with the accretion rate and this is indeed supported by RMHD simulations (Kawashima et al., 2012; Narayan et al., 2017). It is thus natural to think that the degree of beaming b and the mass-transfer rate should be linked. Based on theoretical arguments and observational constraints from ULXs (see Chapter 3), King (2009) finds a scaling of the form $b \propto \dot{m}^{-2}$ and thus Equation 2.27 can be rewritten as:

$$L = \frac{L_{\rm Edd}\dot{m}^2}{73}(1 + \ln \dot{m}) \tag{2.28}$$

where I have used $b = \frac{73}{\dot{m}^2}$ valid for $\dot{m} > 8.5$ (King, 2009). The implications of these results is that supercritically accreting NSs should *appear* brighter than supercritically accreting BHs when fed with the same $\dot{M}$-values, as the radiation will be confined into a smaller angle in the NS case, outweighing their lower Eddington luminosities. For instance, a 10 $M_\odot$ BH with $\dot{m} = 15$ will have the same apparent luminosity as for a NS (2 $M_\odot$) with $\dot{m} = 30$, although it is unclear whether this model could also be applied to NSs as we shall see in Section 2.2.1.

The degree to which the emission in the super-Eddington regime is beamed remains unclear as well as its dependency with the viewing angle. We can compare results from numerical simulations with the theoretical prescription given by King (2009). Ohsuga et al. (2005), using 2D Radiative Hydrodynamic (RHD) simulations and taking into account photon trapping effects, find that for $\dot{m} = 1000$ the luminosity for a $10\,M_\odot$ BH is $\sim 5\,L_{\rm Edd}$, but the inferred isotropic luminosity for a face-on observer can reach $55\,L_{\rm Edd}$, implying a $b \approx 0.01$. Narayan et al. (2017) using 2D RMHD simulations find that for a $10\,M_\odot$ BH with much lower $\dot{m} = 10$, the radiation luminosity is $\sim 2.3 \times 10^{39}$ erg/s, but a favourable observer looking at i=10° would infer $L \sim 10^{40}$, implying a beaming factor of $b = 0.2$. However, using the theoretical estimates of King (2009), we would obtain much larger beaming factors of 0.000073 and 0.73 in the former and latter case respectively. A counter example of a simulation finding larger beaming factors than those predicted by Equation 2.28 is the work of Abarca et al. (2021), who found beaming factors of ~ 0.02 employing 2.5D GR-Magneto-Hydrodynamic (MHD) simulations of a super-critically accreting magnetised ($B \sim 2\times 10^{10}$ G) NS with $\dot{m}$= 20 (cf. $b \sim 0.2$ with Equation 2.28). It is also expected that at very high-mass transfer rates the funnel will become filled with more gas, becoming ultimately optically thick (Narayan et al., 2017), masking the X-ray radiation from the central regions creating a drop in luminosity. We see thus that this remains an unsolved issue and moreover the picture could be differ in the case of a NS accretor as we shall see below.

The outflow is expected to be highly dynamical and patchy, formed of clumps with an optical thickness ~ 1 according to MHD simulations (Takeuchi et al., 2013). The shape of the clumps is expected to be elongated in the outflow direction with a covering factor of ~ 0.3. Passage of clumps along the line of sight could induce short-term variability, as has been invoked for ULXs (Takeuchi et al., 2013; Middleton et al., 2015a) which we shall see in more detail in Section 3.2.1.

2.2.1 Neutron Stars

It is yet not clear whether the picture described above could apply to NSs. Shakura & Sunyaev (1973) argued that the equations used to describe supercritical flows would only need to be modified by scaling the appropriate equations by the mass of the compact object, but NSs differ in two other important aspects with respect to BHs: the presence of a solid surface and the presence of strong magnetic fields. It is generally assumed that far from the NS where the magnetic field is weak, the accretion flow would indeed follow the same geometry as outlined in the previous Section. In this regard, Takahashi et al. (2018) provided an interesting comparison between super-Eddington accretion around a non-magnetised NS and a BH using 2D GR-RMHD simulations. The authors found that indeed the formation of a polar funnel with strong outflows also occurs around NSs.

---

[3] Note that if we consider that only the emission within $R_{\rm sph}$ is beamed then $L = L_{\rm Edd}(1 + \frac{\ln \dot{m}}{b})$ might be more physically motivated.

Because NSs are more radiatively efficient compared to BHs due to the excess radiation produced at the surface of the NS, the authors found that more powerful outflows are launched around non-magnetised NSs compared to BHs. The same authors also found that the funnel is wider in NSs, which might be at odds with the scaling suggested by (King, 2009, see Equation 2.28). Interestingly, their simulations also showed that the accretion flow around the NS is self-regulated in the manner envisaged by Shakura & Sunyaev (1973) i.e. the arrival of more material leads to stronger outflows so that the net mass-accretion rate is always kept around the critical value.

But as we have seen in Section 2.1.2 the magnetic field pressure will force the accreting material to follow the magnetic field lines and to be accreted onto the magnetic polar caps of the NS. King & Lasota (2016) argued that because the magnetic field interaction with the accretion disk will only be effective close to the accretor, the accretion flow will become supercritical regardless of the nature of the accretor and thus the formalism envisaged by Shakura & Sunyaev (1973) for super-Eddington accretion should still apply beyond R_{m}. Because beaming implicitly requires the formation of thick accretion disk and thus the disk to be truncated by the magnetic field within R_{sph}, King & Lasota (2019) suggested that weak magnetic fields are a necessary condition for NS to reach highly super-Eddington luminosities. Within R_{m}, the accretion flow will be forced to follow the magnetic field lines and the formation of an accretion column is expected as for the sub-Eddington regime case (King et al., 2017).

The somewhat opposing view is that it is precisely strong magnetic fields the necessary condition that allows NS to overcome the Eddington limit. Magnetic fields are known to reduce the electron scattering opacity and more matter could flow unimpeded by the radiation field in the presence of strong magnetic fields (Canuto et al., 1971; Basko & Sunyaev, 1976). Mushtukov et al. (2015) considered the accretion column model from Basko & Sunyaev (1976) and found through numerical estimates an scaling of the order of $L \sim 0.35\ B^{3/4}$, where L and B are given in units of 10^{39} erg/s and 10^{12} G, respectively. This implies that strongly magnetised NS with $10^{13} < B < 10^{14}$ G can reach luminosities in the 10^{39-40} erg/s range. Moreover, Mushtukov et al. (2015) showed that the disk is truncated by the magnetic field before it becomes thick (i.e. $R_{\mathrm{m}} > R_{\mathrm{sph}}$) implying that this solution is self-consistent.

RHD simulations of magnetised accretion columns in the super-Eddington regime show that the gas initially free-falls onto the NS poles, but then a shock region is formed close to the NS surface where the gas starts to be pushed upwards, decelerating it close to the NS surface (Kawashima et al., 2016). These authors found that most of the radiation is dissipated in this shocked region through the sides of the column as envisaged by Basko & Sunyaev (1976). Despite the high-mass accretion rate ($\dot{m}$= 10–100), the isotropic luminosity produced is kept around $\sim 3\ L_{\mathrm{Edd}}$. However, because the radiation is confined to a small area around the sides of the accretion column, the inferred luminosity is boosted in these directions, and would give the appearance of emitting close to $300 L_{\mathrm{Edd}}$ if an observer assumes isotropic emission. We see thus that accretion columns can provide means to beam the emission too.

However, the emission from the accretion column might be affected by the material within the magnetosphere of the NS. Mushtukov et al. (2017) argues that at super-Eddington mass-transfers the accumulation of matter within the magnetosphere will lead to the formation of a closed optically thick envelope around the NS as the material is forced to follow the magnetic field lines. The envelope emits as a multicolor blackbody, as it is expected to have a latitudinal temperature gradient and its rotation can also produce pulsations, with more sinusoidal-like profiles compared to accretion columns. The radiation produced at the accretion column closer to the NS might escape freely or be reprocessed by the envelope, affecting the emergent spectrum. Hybrid models considering outflows and optically thick envelopes also exit (Mushtukov et al., 2019). The authors considered the model from Lipunova (1999); Poutanen et al. (2007) to investigate how mass loss within $R_{\mathrm{sph}} <$ R $< R_{\mathrm{m}}$ would affect the luminosity of the NS and the optical thickness of the envelope. Mushtukov et al. (2019) found that the final luminosity depends on the strength of the NS magnetic field and the mass-transfer rate of the donor. This is easily understood due to the dependence of R_{m} on B and on the mass-transfer rate (Equation 5.1), which will be modified by Equation 2.25. The exact value of R_{m} can be calculated re-writing Equation 5.1 using Equation 2.25:

$$\dot{m}(R_{\mathrm{m}}) = \dot{m}_{\mathrm{in}} + (\dot{m}_0 - \dot{m}_{\mathrm{in}})\frac{R_{\mathrm{m}}}{R_{\mathrm{sph}}} \tag{2.29}$$

Because R_{m} depends itself on $\dot{m}$ at R_{m}, the equation has to be solved numerically (Mushtukov et al., 2019). In Figure 2.6 I show the dependency of $\dot{m}_{\mathrm{in}}$ with $\dot{m}_0$ in the presence of magnetic fields.

Essentially, for very large magnetic fields ($B \sim 10^{14}$ G), the condition $R_{\mathrm{m}} > R_{\mathrm{sph}}$ is fulfilled for any reasonable value of $\dot{m}_0$, and mass loss in the disk is negligible. Instead, lowly magnetised ($B \lesssim 10^{12}$ G) NSs with high $\dot{m}_0$ values (~ 100) will lose more mass in the outflow and thus have reduced mass-accretion rates. For large $\dot{m}_0$, the presence of the magnetic field will not have a strong impact and the solution given by Poutanen et al. (2007) is recovered. Note that because large magnetic fields can truncate the disk before it becomes supercritical, the model of Mushtukov et al. (2017, 2019) instead predicts low degree of beaming, with most of the radiation being emitted within R_{m}. In other words, strong magnetic fields would suppress mass loss and beaming by the outflow. Finally it must be noted that the dependency of R_{m} on the mass-accretion rate will be more complex than given by Equation 5.1 in the super-Eddington regime. The radiation pressure will affect the balance between the gas ram pressure and magnetic pressure and therefore modify the dependency of R_{m} on the accretion rate.

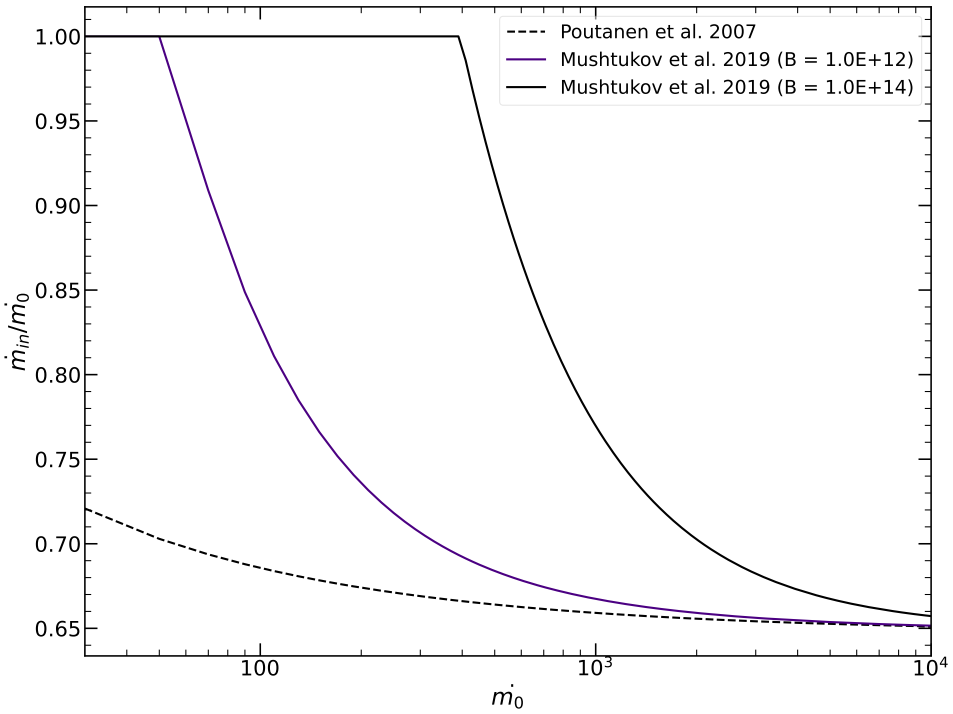

Figure 2.6: Mass-accretion rate ($\dot{m}_{\rm in}$) as a function of the input mass-transfer rate ($\dot{m}_0$) for different values of the magnetic field. We have assumed a NS with $M = 1.4 M_\odot$, $R = 10^6$ cm, $\xi = 1$, more appropriate for the nearly spherical super-Eddington accretion flow (Shakura & Sunyaev, 1973; Mushtukov et al., 2017) and $\epsilon_w = 0.5$ for the calculations.

Chashkina et al. (2019) argue that because the pressure inside the disk depends on the scale-height, the exact dependency of $R_{\rm m}$ on the accretion rate will have a strong dependency on the level of advection and outflows in the disk (i.e. whether the disk is slim or thick) as well as on the interplay between $R_{\rm m}$ and $R_{\rm sph}$(i.e. on whether the disk actually becomes thick before being disrupted by the magnetic field). Thus the exact dependency of $R_{\rm m}$ on $\dot{m}$, will depend strongly on B as well (see their Figure 12 for more details Chashkina et al., 2019).

Chapter 3

Ultraluminous X-ray Sources

ULXs were discovered towards the end of the 1970s when the *Einstein Observatory* telescope (Giacconi et al., 1979), when the first imaging X-ray telescope allowed for the first time to study the X-ray emission of external galaxies (see Fabbiano, 1989, for a review on these observations). These early observations revealed the presence of X-ray extended emission with $L_\mathrm{X} \gtrsim 10^{39}$ erg/s in most normal galaxies, suggested to be due to a mixed contribution from unresolved point-like sources. Indeed, these early works also revealed the presence of about 36 off nuclear point-like sources with X-ray luminosities exceeding the Eddington limit for NS $\sim 2 \times 10^{38}$ erg/s (assuming a $2\,\mathrm{M}_\odot$ mass), with some reaching L_X as high as 10^{39} erg/s. The first and most straightforward explanation in order not to violate the classical Eddington limit, was that these sources hosted more massive ($\gtrsim 100\,\mathrm{M}_\odot$) BHs accreting at sub-Eddington rates (Colbert & Mushotzky, 1999; Makishima et al., 2000). But even these early works already noted that some fine tuning was required to explain *both* the high luminosities and spectral properties. Makishima et al. (2000), who coined the term ultraluminous compact X-ray sources which later become simply ULXs, found that the early ULX spectra obtained with the Japanese *ASCA* telescope (Tanaka et al., 1994) could be well modelled with an optically thick accretion disks with inner disk temperatures ($T_\mathrm{in} \gtrsim 1$ keV), supporting the presence of IMBHs. However, these authors also noted that this interpretation was problematic, as the combination of high luminosities and high temperatures compared to Galactic Black Hole Binarys (GBHBs) required either the Eddington limit to be violated or an abnormal combination of rapidly spinning and massive BHs of up to $\sim 100\,\mathrm{M}_\odot$.

3.1 Basic definition

ULXs are simply defined as extragalactic off-nuclear point-like X-ray sources exceeding the Eddington limit for a $\sim 20\,\mathrm{M}_\odot$ BH ($\sim 2.5 \times 10^{39}$ erg/s). At least historically, this was around the limit of the heaviest accreting BH known at the time (Shahbaz et al. (1994); Remillard & McClintock (2006); see also the case of IC 10 X–1 Silverman & Filippenko (2008), albeit its mass estimate might be unreliable as I discuss in Section 3.3), and thus implied that ULXs represented a different class of objects. Because of this empirical definition, the term ULX encompasses a variety of objects with different properties. Typically, they can be further subdivided into two physically motivated categories: a minority reaching $L_\mathrm{X} \gtrsim 10^{41}$ erg/s dubbed Hyper Luminous X-ray sources (HLXs) (Gao et al., 2003) which typically, but not always, show properties indicating IMBHs accreting in the sub-Eddington regime, and those with $10^{39} < L_\mathrm{X} < 10^{41}$ erg/s, which typically show properties consistent with stellar-mass compact object accreting in the super-Eddington regime and which are are the focus of this work. A good argument for this subdivision is the tentative break found in the X-ray luminosity distribution function found at around 2×10^{40} erg/s in some large-sample studies of ULXs (Swartz et al., 2011) and HMXBs (Mineo et al., 2012), which indicates two distinct classes of objects or a change in the physical processes powering these objects above and below the break. Those above the break, show transitions or temporal properties that seem to be consistent with the expectation of a scaled-up version of GBHBs (e.g. Farrell et al., 2009; Godet et al., 2009; Pasham et al., 2014) and/or show evidence for cooler accretion disks (e.g. Feng & Kaaret, 2010; Servillat et al., 2011; Godet et al., 2012; Lin et al., 2020) which suggest masses in the IMBH range. Instead, we will see below that while the nature of the accretor in most ULXs below remains largely unknown (see Section 3.3), their properties are hard to reconcile with IMBHs accreting at sub-Eddington rates. The growing evidence and advancements in our understanding of the super-Eddington regime suggest that most ULXs host stellar-mass compact objects accreting at super-Eddington rates in a more or less sustained way. Some of this evidence include their atypical X-ray spectral states compared to sub-Eddington X-ray binaries (Section 3.2.1), the detection of pulsations providing direct evidence that some of these systems host accreting NSs (Section 3.2.2), their optical spectra (Section 3.2.4) and the presence of large scale ($\sim$ 50–400 pc) bubbles of ionized gas around a handful of them (Section 3.2.3). For this reason, and due to their sustained luminosities well above 10^{39} erg/s over several decades in some instances (see Section 3.2.1) ULXs represent one of the best laboratories to study *sustained* super-Eddington accretion in the nearby Universe.

It must also be noted that census of ULXs typically contain a fraction of 10–20% of contaminants (e.g. Swartz et al., 2011; Kovlakas et al., 2020). These can include misclassified background AGNs, Supernova Remnants (SNRs) and foreground stars, since most of the ULXs are found through statistical association of X-ray sources with galaxy catalogs. In Section 6.3, I show how combining Multi-Unit Spectroscopic Explorer (MUSE) and X-ray observations we can potentially help cleaning the ULX sample, by showing a specific case of an AGN likely disguised as a ULX.

Throughout this work, the term ULX will be used to refer to the sources showing the properties outlined in this Chapter, whereas the term HLX will be reserved to refer to those sources showing properties consistent with IMBH candidates accreting at sub-Eddington rates.

3.2 Evidence for Super-Eddington Accretion

Because the X-ray luminosity may not be necessarily a good proxy for the accretion rate, especially in the super-Eddington accretion regime (as discussed in Section 2.2), establishing the supercritical nature of an accreting source requires knowledge of its mass and its mass-accretion accretion rate. While this has yet to be achieved in ULXs (although see Section 3.2.5), there is mounting evidence in support of most ULXs being supercritical accretors as I explain below.

3.2.1 The X-ray spectrum

We have seen that the early interpretation of ULXs as accreting IMBHs candidates was subject to some caveats as it required an abnormal fine tuning of both the spin and the mass of the BH in order to explain their properties. The first *XMM-Newton* high-quality ULX spectra were fitted with a soft optically thick accretion disk and a high-energy powerlaw (e.g. Kaaret et al., 2003), a model commonly employed to fit GBHBs spectra (e.g. Remillard & McClintock, 2006). These fits resulted in remarkably cool ($kT_{\rm in} \sim 0.1$–0.3 keV) accretion disks, which was argued to provide evidence for ULXs harbouring BHs in the intermediate mass regime (e.g. Miller et al., 2004). However, this interpretation was problematic because as opposed to GBHBs, where the disk dominates the low-energy emission in the soft state, the powerlaw also dominated the low-energy range in ULXs. As stated in Section 2.1.1, inferring the inner disk radius from the soft component is only valid if the source is found in the soft state, where the disk extends to the $R_{\rm isco}$, making the inferred inner disk radius dubious (e.g. Roberts et al., 2005). Additionally, the powerlaw, often interpreted as Comptonization of soft disk photons in GBHBs, extended well below the peak energy of the disk, rendering this interpretation unphysical. Furthermore, later works showed that the interpretation of the soft component as an optically thick accretion disk around an IMBH was subject to several caveats (e.g. Gonçalves & Soria, 2006; Stobbart et al., 2006; Kajava & Poutanen, 2009). For instance, Gonçalves & Soria (2006) showed that the ULX spectra could be equally well fitted with a powerlaw and an accretion disk with negative normalization i.e. acting as an absorption component to the powerlaw. Along the same lines, Stobbart et al. (2006); Kajava & Poutanen (2009) showed that the IMBH model (i.e. a disk with a high-energy powerlaw) did not follow the $L \propto T^4$ expected for the standard thin accretion disk. But perhaps the most important piece of evidence against the IMBH interpretation was the departure of the high-energy emission from a powerlaw at around 2–7 keV, revealed in high-quality *XMM-Newton* observations (e.g. Stobbart et al., 2006; Gladstone et al., 2009). This high-energy turnover or cutoff has since become the landmark of the canonical ULXs spectra and suggested that ULXs were in an atypical spectral state, unseen in X-ray binaries, termed *ultraluminous state* (Gladstone et al., 2009). This curvature has been robustly confirmed thanks to the advent of the *Nuclear Spectroscopic Telescope Array* (*NuSTAR*) (Section 4.1.3 provides detailed information on this mission) (Bachetti et al., 2013; Rana et al., 2015; Mukherjee et al., 2015), that allowed to extend the observable bandpass above 10 keV with high signal-to-noise ratio. A spectrum of the archetypal ULX NGC 1313 X-1 in the 0.3–10 keV band is shown in Figure 3.1 fitted with an absorbed soft accretion disk and a hard powerlaw using XSPEC (`tbabs`$\otimes$ (`diskbb` + `powerlaw`). Along with the spectral turnover at high-energies, other common properties of the ULX spectra can be seen such the low-energy residuals around 1 keV.

NuSTAR observations have revealed other intriguing features of the ULX spectra. Most of the ULXs observed by the *NuSTAR* observatory so far[1], along with the turnover, require an additional high-energy powerlaw component to model the spectrum above 10 keV (e.g. Mukherjee et al., 2015; Krivonos & Sazonov, 2016; Walton et al., 2017, 2018c; Brightman et al., 2020b; Gúrpide et al., 2021a). The origin of this component remains uncertain, but some clues about its nature come from the fact that this component has been shown to display remarkable little variability, albeit the spectrum changing clearly below $\sim$ 8 keV (Walton et al., 2017, 2020; Gúrpide et al., 2021a). Based on this observational evidence, I discuss its possible nature in Section 5.1.4.5.

---

[1] Around thirteen ULXs have observed by *NuSTAR* with high-signal-to noise ratio, of which $\sim$ eleven show this additional spectral component.

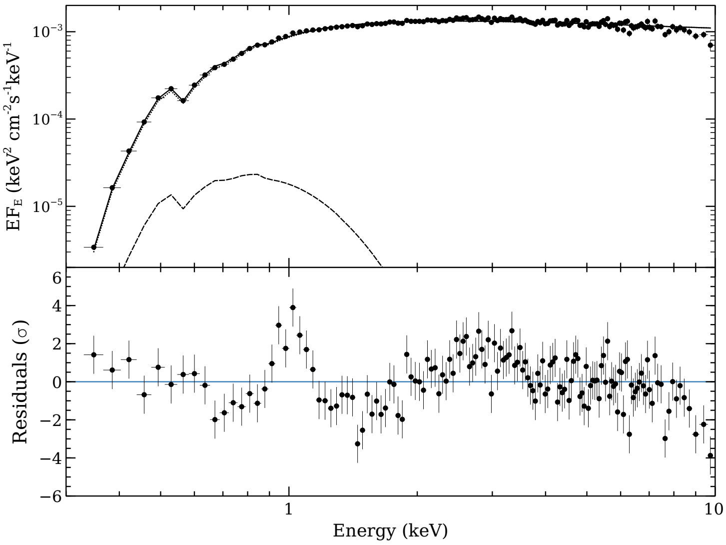

Figure 3.1: Unfolded *XMM-Newton*-EPIC pn spectrum of the ULX NGC 1313 X–1 (obs id 0803990101) fitted with an absorbed accretion disk model (dashed line) and a powerlaw (dotted line). The total model is shown by a solid line. The high-energy curvature can be seen along with low-energy residuals. The data have been rebinned to a minimum significance of 10σ and a minimum count rate of 25 photons per bin.

Long-term studies using *Swift*-X-Ray Telescope (XRT) supported the atypical spectral states seen in spectroscopic studies of ULXs. Many of them were found to be persistently accreting above 10^{39} erg/s over year timescales, showing little or unusual variability compared to X-ray binaries (Kaaret & Feng, 2009; Vierdayanti et al., 2010; Grisé et al., 2010, 2013). This growing observational evidence suggested that ULXs are indeed a different class of sources with respect to sub-Eddington accreting sources, likely to be powered by super-Eddington accretion. Because of the anisotropic emission expected in this extreme regime of accretion (Section 2.2), it was quickly realized that the viewing angle should play an important role in shaping the variability and energy spectra of ULXs (e.g. Abolmasov et al., 2009). In the second part of Chapter 5, I explored the *Swift*-XRT data to provide a coherent picture in order to explain the evolution of the ULX spectra based on changes in the mass-transfer rate and the accretion flow geometry.

The ULX spectra in the 0.3–10 keV band is generally interpreted using two phenomenological model components. The softer component, modelled as black-body emission or a multi-color accretion disk, shows temperatures in the 0.3-0.6 keV range and is ascribed to the emission from the wind photosphere (e.g. Poutanen et al., 2007; Kajava & Poutanen, 2009). The second component can be modelled as another multi-color standard accretion disk (e.g. Gúrpide et al., 2021a), a slim advection-dominated accretion disk (Luangtip et al., 2016) with characteristic temperature of 1–2 keV, thermal Comptonization (Middleton et al., 2015a) or a powerlaw with a cutoff at $\sim$ 3–7 keV (e.g. Gladstone et al., 2009). This hard component is generally ascribed to the emission from the inner parts of the supercritical disk (Poutanen et al., 2007) affected by down-scattering in the wind and advection effects (e.g. Middleton et al., 2015a). As I discuss below and in Chapter 5 the presence of NSs in some ULXs has reignited the debate as to how to interpret the ULX X-ray spectra, which in the absence of physically motivated models remains an unsolved issue. However, in Section 5.2.3.3, I show that a self-consistent and physically motivated model (Abolmasov et al., 2009) can also be used to interpret the ULX spectra.

3.2.1.1 Spectral states

A systematic and empirical classification scheme of the ULXs was first proposed by Sutton et al. (2013) based on the results from Gladstone et al. (2009). ULXs could be mainly found in three spectral regimes: *broadened disk*, *hard ultraluminous* (HUL) and *soft ultraluminous* (SUL). The latter two are mainly distinguished based on the exponent (Γ) of the powerlaw ($\Gamma_{\text{SUL}} > 2 > \Gamma_{\text{HUL}}$) when fitted with a cool accretion disk ($T_{\text{in}} < 0.5$ keV) and a powerlaw at high-energies (Figure 3.2). The former can be fitted with the same model, but the disk provides the curvature at high-energies, whereas the powerlaw fits the soft excess on top of it i.e. these components are swapped with respect to the other two regimes. The spectra can be thus described with a single broadened disk component. The broadened disk regime is thought to correspond to sources close to or at the Eddington limit (Sutton et al., 2013; Middleton et al., 2013), powered by slim accretion disks. Regarding the HUL and SUL states, the authors considered the theoretical arguments from Poutanen et al. (2007); King (2008, 2009) and results from RHD simulations of super-Eddington accretion flows (Kawashima et al., 2012; Takeuchi et al., 2013)

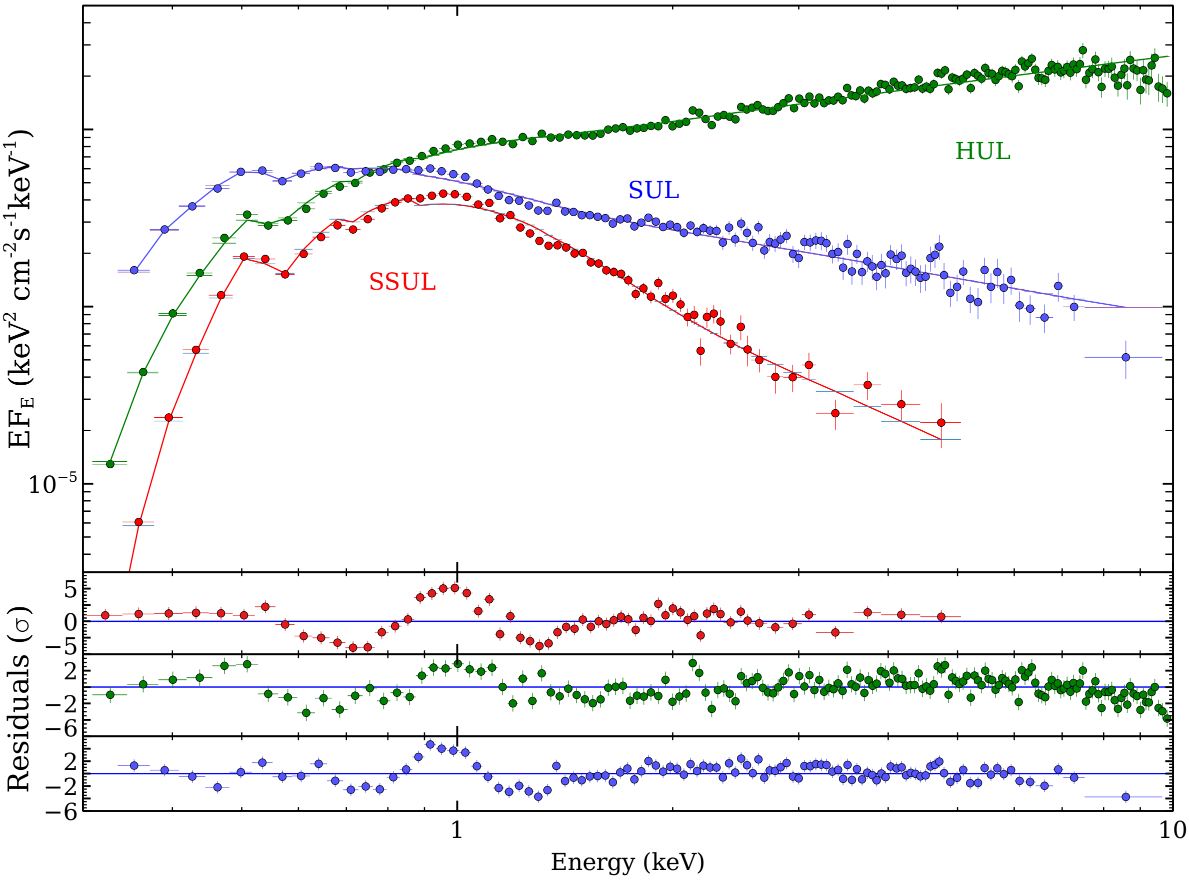

Figure 3.2: Unfolded *XMM-Newton*-EPIC pn spectra of the ULXs Holmberg IX X–1 (green color, obsid 0200980101), NGC 5408 X–1 (blue color, obsid 0302900101) and NGC 247 ULX–1 (red color, obsid 0844860501) fitted with an absorbed accretion disk model (dashed line) and a powerlaw (dotted line) for display purposes. Each source represents one of the following canonical ULX spectral states: the hard ultraluminous (HUL), the soft ultraluminous (SUL) and the supersoft ultraluminous regimes (SSUL). The data have been rebinned to a minimum significance of 5σ and a minimum count rate of 25 photons per bin.

to suggest that the different variability and hardness observed in the two spectral regimes could be explained by the different viewing angle of the systems. ULXs in the HUL regime were characterized by low levels of short-term variability and a hard spectrum, which could be explained by a line of sight looking directly into the inner hot regions of the accretion flow (Middleton et al., 2015a) (see also Section 2.2). Instead, sources in SUL regime showed high levels of short-term variability in the high-energy band and a spectrum dominated by the soft component associated to the wind. A line of sight close or beyond the opening angle of the wind funnel could account for the soft spectrum and the high-energy variability, interpreted as extrinsic variability produced by clumps of wind intermittently obscuring the hard component. The lack of eclipses in the X-ray lightcurves in the Walton et al. (2011) ULX catalogue (Middleton & King, 2016) supports the notion of relatively low-viewing angles, although see Section 5.3.1.

Interestingly, this picture may explain the properties of a subset of ULXs, characterized by an extremely soft spectrum that shows little or no emission above 2 keV and that can be fitted with a single black-body like spectrum with ($kT_{\rm bb} \approx 0.05$–0.2 keV). These sources are termed supersoft ULXs or ultraluminous supersoft sources (ULSs; e.g. Urquhart & Soria, 2016, see Figure 3.2) and sit at around 10^{39} erg/s (Zhou et al., 2019). It has been suggested that ULSs are simply an extension of the SUL and HUL states, in which the sources are viewed at very high inclination angles and/or high accretion rates (inducing a closing of the funnel), in which the inner regions of the accretion flow is reprocessed through Compton down-scattering in the optically thick wind/outflows, giving them a supersoft ultraluminous (SSUL) appearance (Urquhart & Soria, 2016). In this regard, the ULS in NGC 247 (Feng et al., 2016) shows transitions between the SUL and the SSUL regimes (see also the case of the ULS M101; Urquhart & Soria, 2016), supporting this link between standard ULXs and ULSs. Furthermore, recently similar mildly relativistic blueshifted absorption features as those seen in standard ULXs have been reported in NGC 247 (Pinto et al., 2021), which are discussed in more detail in Section 3.2.4. Lastly, a further connection between ULS and ULX may be argued based on the detection of a jet detection in the optical

Table 3.1: Summary of the main properties of the known PULXs. The values are orientative as many are model dependent (such as $L_{\rm X}$) or are variable (such as $P_{\rm spin}$ and $\dot{\nu}$). $\dot{\nu}$ correspond to the secular values when available.

Source	$L_{\rm X}$ peak 10^{39} erg/s	$P_{\rm spin}$ s	ν Hz	$\dot{\nu}^a$ $10^{-10}\,{\rm Hz\,s^{-1}}$	$P_{\rm orb}$ days	$P_{\rm superorb}$ days
M82 X–2[1,2,3]	20	1.38	0.72	–0.6	2.53	60
NGC 7793 P13[4,5,6,7]	9	0.42	2.38	0.38	63.9	66.8
M51 ULX–7[8, 9]	8	2.79	0.36	3.5	1.99	39
NGC 5907 ULX1[10,11,12]	100	1.13	8.1	100	5.3	78
NGC 1313 X–2[12]	10	1.45	–	65–150	<6.1	-
NGC 300 ULX1[13,14,15]	3	31	0.03	4.2	292–766	-
NGC 7793 ULX-4[16]	3.4	0.39	2.52	–	-	-

Notes. (a) Average secular spin torque over year timescales. References: (1) Bachetti et al. (2014) (2) Brightman et al. (2019) (3) Bachetti et al. (2020) (4) Fürst et al. (2016) (5) Israel et al. (2017b) (6) Fürst et al. (2018) (7) Fuerst et al. (2021) (8) Rodríguez-Castillo et al. (2020) (9) Vasilopoulos et al. (2020a) (10) Israel et al. (2017a) (11) Walton et al. (2016a) (12) Sathyaprakash et al. (2019) (13) Carpano et al. (2018) (14) Vasilopoulos et al. (2018) (15) Heida et al. (2019) (16) Quintin et al. (2021)

in the ULS in M81 (Liu et al., 2015), revealed as a strong shift ($v = 0.17\,c$) in the Hα line, such as those observed in the Galactic supercritically accreting source SS433, which I discuss further in Section 3.2.5.

In the second work of Chapter 5, I was able to identify two archetypal ULXs that seem to transit through the three canonical spectral states (HUL-SUL-SSUL). As we shall see later, these results provide strong supporting evidence to the idea that there is indeed a link between standard ULXs and ULSs.

3.2.2 The Discovery of Pulsating Ultraluminous X-ray Sources

The *NuSTAR* observatory was found to be particularly useful in the study of ULXs not only thanks to its high-energy spectral capabilities, but also due to its superb timing resolution reaching tens of microseconds (Bachetti et al., 2021). A breakthrough discovery was made when pulsations were detected in the light curve of the ULX M82 X–2 during an observation targeted to observe the supernova SN2014J in M82 (Bachetti et al., 2014). Since then, pulsations have been detected in six additional ULXs: NGC 7793 P13 (Fürst et al., 2016; Israel et al., 2017a), NGC 5907 ULX1 (Israel et al., 2017b), NGC 300 ULX1 (Carpano et al., 2018), NGC 1313 X—2 (Sathyaprakash et al., 2019), M51 ULX7 (Rodríguez-Castillo et al., 2020) and finally NGC 7793 ULX 3 (Quintin et al., 2021) (see also Section 5.3.2). The main properties of these sources are summarized in Table 3.1.

The discovery of NS-ULXs represents the first direct evidence for ULXs being powered by super-Eddington accretion, as these reach luminosities of factors 100–500 above the classical Eddington limit for a NS (see Table 3.1) and the mass of a NS is constrained to be $\sim$ 2 M$_\odot$. A common characteristic of these pulsating ULXs (PULXs), also termed Ultraluminous X-ray Pulsars (ULXPs), is their strong secular ($\sim$ month/years) spin torques ($|\dot{\nu}| > 10^{11}$ Hz/s). These are generally associated with transfer of angular momentum from accreted matter to the NS surface, causing it to spin-up or down. In addition, the orbital motion of the NS causes the photons time of arrival to be modulated by the Doppler effect, introducing an instantaneous $\dot{\nu}$, that further complicates the detection of pulsations. For this reason, standard tests to detect coherent signals often fail to detect them (e.g. Doroshenko et al., 2015), because the signal spreads over N Fourier bins, where $N = \dot{\nu} T_{\rm obs}^2$, during the course of an observation of length $T_{\rm obs}$. Only when the photon arrival times are corrected for the spin derivative, the signal can be recovered (e.g. Rodríguez-Castillo et al., 2020). But because the spin derivative is not known a priori, these searches require to blindly scan a large 2D P–$\dot{P}$ parameter space. The detection of pulsations is further complicated by the generally low pulsed fractions (PFs $\sim$ 5%–15%) found in PULXs and their extragalactic distances. Rodríguez-Castillo et al. (2020) estimated that from all the ULXs that had sufficiently long exposures for which a PFs as low as 5% could have been detected, 25% are confirmed NSs. Because of the difficulty in detecting pulsations, the nature of the accretor in most ULXs remains unknown (which is discussed in more detail in Section 3.3).

The timing solutions obtained to recover the pulse signal often allow observers to derive the orbital period too (Table 3.1). Intriguingly, many PULXs also show periodicities on timescales of a few months (Table 3.1), on top of the orbital period, which are termed ‘super-orbital periods’. The origin of these super-orbital periods is yet unknown (although see Section 5.2.4), but it also seems to be a common feature of these sources and also in other ULXs for which the accretor is unknown (e.g. Weng & Feng, 2018) (see the also second work in Chapter 5 for a potential new detection and a discussion on possibly origin of the superorbital periods)

It must be noted that super-orbital periods are also found in ‘classical’ Galactic X-ray binaries. These are found in both HMXBs and LMXBs, but they seem to occupy different regions in the orbital-superorbital period plane (Corbet & Krimm, 2013), suggesting perhaps a different mechanism at play. Famous examples include Her X-1, an intermediate-mass system hosting an accreting NS with a 1.70 d orbital period and a 35 d super-orbital modulation (e.g. Staubert et al., 2013), or the 162 d precessing jets of SS433, a likely BH-HMXB system with an orbital period of 13 days, which I discuss in Section 3.2.5 due to its relevance in the context of ULXs.

Another common characteristic of these PULXs is their high-levels of variability over year timescales, reaching two orders of magnitude in many instances (e.g. Walton et al., 2015; Vasilopoulos et al., 2021). This in stark contrast to other ULXs that have observed persistently above $L_X > 10^{39}$ erg/s (e.g. Kaaret & Feng, 2009; Grisé et al., 2010), although this is also observed in the PULX NGC 1313 X–2 (see Section 5.1.4.3). Many of the dramatic flux variations Pulsating Ultraluminous X-ray sources (PULXs) undergo have been frequently ascribed to transitions to the propeller regime (see the case of M51 ULX–7 in Section 5.3.1). As explained in Section 2.1.2, this occurs when the magnetospheric radius (the inner disk radius of the accretion disk) becomes larger than the co-rotation radius. In this configuration, the centrifugal barrier created by the NS spin is expected to cause the accreting material to be expelled from the system, halting accretion with the subsequent drop in X-ray luminosity (Illarionov & Sunyaev, 1975). This phenomenon was invoked to explain the bi-modal flux modulation seen in M82 X–2 (Tsygankov et al., 2016b), but these transitions have been later shown to be periodic (Brightman et al., 2019). This would therefore require some mechanism of periodic mass-transfer or another phenomenon producing the periodic flux modulation, such as precession of the accretion flow.

It has to be noted however that the PULX in NGC 300 shows continuous spin-up rate despite the flux dropping by a factor > 50 (Vasilopoulos et al., 2020b). The spin-up indicates that accretion has continued uninterrupted despite the flux changes, at odds with the expectation of a propeller state transition. Similar results have been reported for NGC 7793 P13 (Fuerst et al., 2021), suggesting that we are observing the effects of obscuring material blocking our line of sight, possibly due to precession of the accretion disk.

3.2.2.1 Strongly or Weakly Magnetized Neutron Stars?

The discovery of NS-ULXs has spurred a debate as to what mechanism allows NS to reach such high luminosities. As we have discussed in Sections 2.1.2 and 2.2.1, because magnetic fields are known to reduce the cross-section to Thomson scattering, strong magnetic fields are a compelling mechanisms to circumvent the Eddington limit. Several theoretical works support this view (Dall'Osso et al., 2015; Mushtukov et al., 2015, 2017) and suggest that PULX harbour NSs with magnetic fields of the order of $B \gtrsim 10^{13}$ G. Instead, King & Lasota (2016, 2019) argue that *weak* magnetic fields $B \sim 10^{11}$ are needed to explain the strong luminosities in PULXs. King & Lasota (2016) argue that super-Eddington mass-transfer rates is what gives ULXs their apparent properties. Because the magnetic field interaction with the accretion flow will only be effective close to the NS, the accretion flow will become supercritical regardless of the nature of the accretor. Therefore the formalism envisaged by Shakura & Sunyaev (1973) for super-Eddington accretion should still apply. King & Lasota (2016, 2019), by solving self-consistently the Equations from Shakura & Sunyaev (1973) linked to the beaming formalism from King (2009), argue that a supercritical disk is needed to provide the necessary beaming factors to explain the observed luminosities, resulting in R_{sph} always being larger than R_{m}.

Mushtukov et al. (2021) tested the accretion flow geometry proposed by King & Lasota (2016, 2019) through Monte-Carlo ray tracing simulations of a NS pulsar whose emission is beamed by a large-scale height disk, by focusing on the relationship between beaming and the observed Pulsed Fraction (PF). Mushtukov et al. (2021) found that strong beaming factors occur as a result of multiple Thomson scatterings within the funnel walls and as a result, this is necessarily accompanied by a dilution of the observed PF. The authors concluded that the detection of PFs above $\sim 10\%$ (e.g. Fuerst et al., 2021) is at odds with the strong beaming factors implied by King & Lasota (2020). Similar discussions also exist from an observational point of view when interpreting the ULX X-ray spectra (e.g. Koliopanos et al., 2017; Walton et al., 2018c), which is discussed in more details in Chapter 5.

3.2.3 Impact on the Surroundings

Further indirect evidence of ULXs accreting at super-Eddington rates comes from radio and optical observations. Optical observations have revealed the presence of tens to hundred parsec bubbles or cavities (e.g. Pakull & Mirioni, 2002; Grisé et al., 2012; Soria et al., 2021) surrounding a handful of ULXs (see Figure 3.3). Many ULX bubbles were initially classified as SNRs (Matonick & Fesen, 1997) because these are typically identified on the basis of a high [S II]/H$\alpha \gtrsim 0.4$ ratio, an indicator of shock-ionized gas. But some of these authors already noted the presence of suspiciously large (with diameters > 100 pc) SNRs in their samples. Subsequent studies revealed that many of these abnormally large SNRs are in fact associated with microquasars or ULXs, with jets and winds carving the ISM, such as the microquasar NGC 7793 S26 (Pakull et al., 2010), the bubble around the ULX in NGC 5585 (Soria et al., 2021) or the double-double microquasar NGC 300 S10 (Urquhart et al., 2019). Other notable examples of early misclassification include the bubbles around the ULXs IC 342 X-1 (Roberts et al., 2003; Cseh

Table 3.2: Summary of the main properties of some of the known ULX bubbles (not exhaustive). The values are orientative.

Source	Size pc×pc	Line	Ionization[a]	SNR[b] 10^{50} erg	Kinetic[c] 10^{39} erg/s	Radio	Size pc×pc
NGC 1313 X-2[1,2]	500×340	Hα	Shock	200	1–10	–	–
Ho IX X-1[1,2,3]	290×440	Hα	Shock	110	1–10	Yes	200×300
NGC 5204 X–1[1]	360×360	Hα	Photo	–	–	–	–
Holmberg II X–1[1,4,5,6]	20×50	HeIIλ4686	Photo	–	–	Jets	81×40
IC 342 X-1[1,2,5,7]	190×190	Hα	Shock	500	3.4	Yes	300×150
NGC 5408 X-1[4,8,9]	60×60	[OIII]λ5007	Photo	–	–	Yes	35×46
NGC 6946 ULX 1 (X-1)[10,11]	20×34	Hα	Photo	–	–	–	–
M81 X–6[2]	260×350	Hα	SNR?	–	–	–	–
NGC 5585 ULX[12]	350×220	Hα	Shock	–	16–3.2	Yes	300×230

Notes. (a) Most dominant ionization process (b) This refers to the energy required assuming the bubble was created by a supernova explosion. (c) Mechanical energy required assuming the bubble was carved by a wind or a jet activity over the bubble lifetime. References: (1) Pakull & Mirioni (2002) (2) Ramsey et al. (2006) (3) Berghea et al. (2020) (4) Lehmann et al. (2005) (5) Cseh et al. (2012) (6) Egorov et al. (2017) (7) Feng & Kaaret (2008) (8) Grisé et al. (2012) (9) Lang et al. (2007) (10) Abolmasov et al. (2006) (11) Kaaret et al. (2010) (12) Soria et al. (2021) .

et al., 2012), Holmberg IX X-1 (Miller, 1995; Grisé et al., 2011) and NGC 6946 X-1 (Blair et al., 2001; Abolmasov et al., 2008). It is now generally established that their sizes and energetics are generally too large compared to known SNRs (e.g. Berghea et al., 2020). Several of these nebulae show strongly broadened (Full Width at Half maximum (FWHM) $\sim$ 100–200 km/s) Balmer lines and the presence of low ionization species such as [S II] and [O I] lines, indicative of shocks or expanding velocities (e.g. Abolmasov et al., 2007a; Urquhart et al., 2018). The mechanical powers inferred from the shock velocities and the observed line luminosities in these bubbles are often comparable or superior to the X-ray luminosities ($P_{\rm mec} \sim 10^{39-40}$ erg/s; Abolmasov et al., 2007a; Cseh et al., 2012; Urquhart et al., 2018; Soria et al., 2021). A summary of the most well studied nebulae are summarized in Table 3.2.

Perhaps surprisingly, others show bright HeIIλ4686 lines and high [O III]/Hβ ratios ($\gtrsim 3$) or low [S II]/Hα ratios ($\ll 1$), suggesting instead that photoionization is the main source of excitation (e.g. Lehmann et al., 2005; Cseh et al., 2012). In these cases, the HeIIλ4686 line acts as a photo counter of the extreme UV and soft X-ray photons, as this line is produced via the recombination of the doubly ionized He^{++}, which requires photons in excess of 54 eV. Because of this property, the HeIIλ4686 line acts not only as a tracer of hard ionizing photons but can be used to estimate whether the emission from ULXs is isotropic or not, as the nebula reprocesses the emission from the ULX in all directions. This property has been used to estimate the flux seen by the nebula from a handful of ULXs (e.g. Kaaret et al., 2004) which seem to agree well with the inferred X-ray luminosity from observations under the assumption of isotropic emission, suggesting that beaming is not important for these sources. However, it has to be noted that the HeIIλ4686 is mostly sensitive to the far UV and soft X-ray radiation, as the photoionization cross-section of He falls off as ν^3 (Osterbrock & Ferland, 2006). Thus, the HeIIλ4686 line may probe mostly the soft emission arising in the wind (as discussed in Section 3.2.1), which is expected to be more or less isotropic (Poutanen et al., 2007). Instead, it is the hard X-ray radiation produced in the inner parts of the accretion flow that is argued to be anisotropic in the super-Eddington regime (e.g. Middleton et al., 2015a).

The observed lines can nevertheless be used to estimate independently the Spectral Energy Density (SED) of the ULX as seen by the nebula. In this regard, Abolmasov et al. (2008) showed that the extreme UV flux extrapolated from the best-fit accretion disk in the X-ray band (Roberts & Colbert, 2003) for the ULX in NGC 6946 (see Table 3.2) could not explain the observed line ratios in the nebula. Instead, an extreme UV source with $L_{UV} \sim 10^{40}$ erg/s is required. Thus once again, this is incompatible with the IMBH scenario proposed based on the cool accretion disk ($T_{\rm in} = 0.15\,$keV; Roberts & Colbert, 2003) inferred from X-ray spectroscopy. Indeed, *Hubble Space Telescope* (*HST*) observation in the far Ultraviolet (UV) by Kaaret et al. (2010) revealed the presence of the fist ultraluminous UV source, in good agreement with the predictions made by Abolmasov et al. (2008) based on the nebular emission.

Therefore the study of the nebulae around ULXs has the potential to provide compelling evidence for further constraining the accretion flow geometry and energetics in the super-Eddington regime through the estimate of the degree of anisotropy of the ULX emission, the presence of strong outflows and their mechanical energy compared to the energy radiated. Additionally, the line maps and the kinematic data allows to identify the presence of winds/jets activity associated with the ULX and the scale of its impact, thereby putting constraints on the role of super-Eddington winds to reprocess baryons on large spatial scales. For this reason,

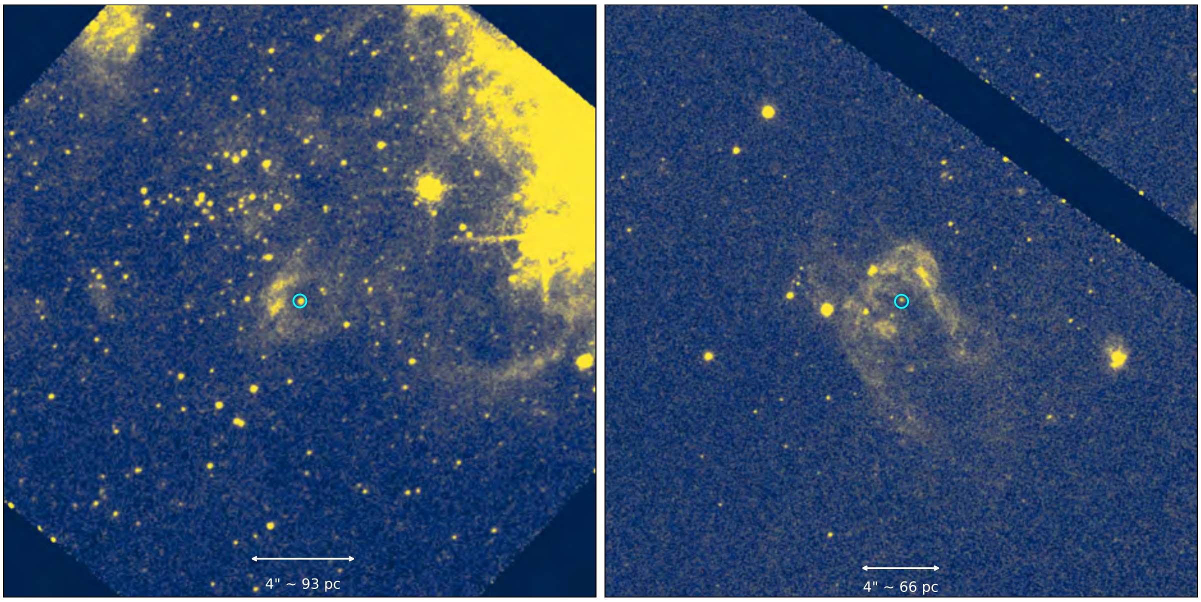

Figure 3.3: Archival optical from the *Hubble Space Telescope* images of the nebulae around NGC 5408 X-1 (left) and IC 342 X–1 (right). The position of the ULXs is shown by a cyan circle in both cases. The image of NGC 5408 X–1 is taken with the Wide Field Camera (WFC) 3/UV and Visible (UVIS) channel in the F502N filter ([OIII]λ5007 line) whereas the image of IC 342 X–1 is taken with Advanced Camera for Surveys (ACS)/WFC in the F658N filter (Hα + the two [NII] lines). In both images, north is up and east is left. See Table 3.2 for more information.

Integral field Unit (IFU) data is particularly compelling for these type of studies and is the main focus of Chapter 6.

It must be noted that some XRBs are also associated with optical and/or radio bubbles. Famous cases are the BH binary system Cygnus X–1 (Russell et al., 2007) or the NS binary system Circinus X–1 (Coriat et al., 2019). However, these are dwarfed in terms of sizes and energetics when compared to those found around ULXs. For instance, the jet-powered nebula around Cygnus X–1 has a diameter of $\sim 4\,$pc and an average jet power of (4–14) $\times\ 10^{36}$ erg/s (Russell et al., 2007). The radio jets of Circinus X–1 extend only around 1 pc and are distorting a larger nebula of similar size, that is thought to be the SNR that gave birth to the compact object (Heinz et al., 2013; Coriat et al., 2019)[2]. Given the young age of the system ($< 4600\,$yr), it is argued that Circinus X–1 might be an earlier version of an SS433-like system (Heinz et al., 2013). SS433 is in turn the only system in our galaxy with a nebula and jet power comparable to that found in ULXs. We shall see such links in more detail in Section 3.2.5.

3.2.4 Evidence for Outflows

A key observational missing piece of evidence to support ULXs as super-Eddington accretors was the direct detection of radiatively accelerated winds expected to be ejected at such high-Eddington ratios as explained in Section 2.2. These features could be revealed as strongly redshifted and/or blueshifted lines emitted in optically thin phases of the wind.

As stated in Section 3.2.1 and shown in Figures 3.1 and 3.2, a common feature seen in high-quality data Charged Coupled Device (CCD) spectra of ULXs are the strong residuals at low energies, with often absorption-looking features around them. These residuals have been seen in both *Chandra* (Roberts et al., 2006) and *XMM-Newton* CCD spectra (e.g. Middleton et al., 2014, 2015a; Pinto et al., 2017), clearly ruling out an instrumental origin. The origin of these residuals was highly debated, as CCD spectra lacked the resolving power to distinguish between broadened absorption lines caused by a fast moving wind (e.g. Middleton et al., 2014) or due to the presence of multiple unresolved lines.

Pinto et al. (2016) analysed the high-resolution *XMM-Newton* grating spectra from the ULXs NGC 1313 X–1, NGC 5408 X–1 and NGC 6946 ULX1 to understand the origin of such residuals. After combining several exposures totaling $\gtrsim 100\,$ks, they found strongly blueshifted absorption lines with $v \sim 0.2\,c$ in the XMM-RGS spectra of NGC 1313 X-1 and NGC 5408 X-1, as well rest-frame emission lines. The absorption lines could be interpreted as due to an outflowing wind while the rest-frame emission lines could be attributed to shock-heated nearby gas. Similar residuals have also been resolved in the ULX in NGC 55 (Pinto et al., 2017), whose soft appearance has been attributed to partial absorption by the wind reprocessing the hard X-ray emission. Later

---

[2] No jet power is estimated in the work of Coriat et al. (2019).

dedicated campaigns seem to confirm these results and reported that the lines are variable with the X-ray continuum, providing clear evidence that the lines are intrinsic to the ULX (Pinto et al., 2020b). These lines have also been recently reported in the first ULS (see Section 3.2.1.1) NGC 247 ULX–1 (Pinto et al., 2021), that shows absorption lines with mildly relativistic velocities of $\sim -0.17\,c$. On the hard X-ray band, Walton et al. (2016b) also reported the presence of an absorption iron feature with $E = 8.77\,\mathrm{keV}$ in the combined *XMM-Newton* and *NuSTAR* data from NGC 1313 X–1, suggesting the presence of an outflow with similar velocities to those found in the Reflection Grating Spectrometer (RGS) data by Pinto et al. (2016). The presence of these winds is in good agreement with those expected from super-Eddington accretion flow simulations (e.g. Ohsuga et al., 2005; Takeuchi et al., 2013; Takahashi & Ohsuga, 2017). The estimated mechanical power of the winds seems to exceed the radiative luminosity (Walton et al., 2016b; Pinto et al., 2020a). In Section 6.2, I was able to detect a shocked bubble around the NGC 1313 X–1 using MUSE data, providing additional evidence for the presence of winds. This allowed me to provide an independent estimate of the wind mechanical power, which was found to be in very good agreement with those reported by Walton et al. (2016b) and Pinto et al. (2020a).

Additional evidence for such winds may come from optical spectroscopy of the ULX counterparts. Fabrika et al. (2015) showed that the optical spectra of eight ULXs (all ever observed in this wavelength) are remarkably similar with Hα and HeIIλ4686 broadened lines with FWHM of $\sim$ 200–1400 km/s. Fabrika et al. (2015) showed that these lines are similar to those seen in stars with hot outflowing winds such as late nitrogen Wolf Rayet (WR) stars. However, these lines are unlikely to arise from the companion star, as wind loss by a WR star is unlikely to provide the needed mass-transfer rate to explain the observed luminosities (Fabrika et al., 2015). Instead, it is argued that these lines arise in radiatively accelerated winds launched from the accretion disk, in good agreement with the predictions made by Shakura & Sunyaev (1973). This is supported by the fact that the broadening found in the HeIIλ4686 lines is smaller than that of the Hα lines. If these lines were produced in the accretion disk, HeIIλ4686 would be expected to be broader, as it is produced in hotter regions closer to the accretor, due to its higher ionization potential. Instead, Fabrika et al. (2015) argued that because these lines are produced in radiatively accelerated winds, Hα lines are more strongly broadened as they are emitted further away from the compact object in areas of higher acceleration, whereas HeIIλ4686 is emitted in slower phases of the wind closer to the compact object. Similar WR-looking optical lines are seen also in the galactic supercritical accretor S433, whose connection with ULXs I discuss below.

3.2.5 Links with the Supercritical Accreting Galactic Source SS433

SS433 is a Galactic HMXB system with a period of $\sim$ 13 days, considered as being the primary example of a supercritical accreting system (see Fabrika, 2004, for a review). The companion star is an A-giant of $\sim 10\,\mathrm{M}_\odot$(Goranskij, 2011) and the nature of the compact star remains unknown, although dynamical estimates and a secular increase in the orbital period suggest the presence of a BH (Goranskij, 2011; Cherepashchuk et al., 2021). Albeit its X-ray luminosity only reaches 10^{36} erg/s, well below the 10^{39} erg/s ULX threshold, the mass outflow rate has been measured to be about $\sim 2\text{–}3 \times 10^{-4}\mathrm{M}_\odot$/yr (van den Heuvel, 1981; Fuchs et al., 2006), which is around 300 times the critical Eddington value for a $10\,\mathrm{M}_\odot$ stellar-mass BH, suggesting that the mass-transfer rate is super-Eddington. Its inclination has been measured to be 78.8 degrees (Margon & Anderson, 1989) and it has thus been suggested that the X-ray faintness of SS433 could be simply due to our unfavourable viewing angle (e.g. King & Puchnarewicz, 2002; Poutanen et al., 2007). This is because at such high-accretion rates the system is expected to be enshrouded by an optically thick wind (Poutanen et al., 2007) and only at low inclination angles we are able to observe directly the hot X-ray emission coming from the inner part of the accretion disk, possibly enhanced by geometrical beaming (King, 2009). Its strong UV luminosity of $\sim 10^{40}$ erg/s (Dolan et al., 1997) is thus attributed to the wind photosphere (Poutanen et al., 2007).

SS433 is also well-known because of its precessing jets, whose precessing period has been measured to be 162 days thanks to the observed Doppler shift in the optical lines emitted within the jet. The jets have a velocity of $\sim 0.26\,c$ and inflate a seashell shaped radio bubble of hundreds of parsecs scale termed W50 (Dubner et al., 1998). W50 requires an average mechanical power of 10^{39} erg/s to be inflated, which is thought to be due to the activity of the equatorial winds and jets, albeit the role of the SNR in the formation of W50 is unclear (Fabrika, 2004). In particular, hydrodynamics simulations by Goodall et al. (2011) suggest that the central roughly spheroid shape of W50 corresponds to the SNR that gave birth to the compact object, whereas the jets have distorted it and formed the elongated lobes around it. Conversely, Ohmura et al. (2021) argues that the activity of the jets, their lateral expansion and their backflows are sufficient to explain the morphology of the nebula.

Many of the properties of SS433 are reminiscent to those observed in ULXs. Optical and radio bubbles are also observed in ULXs, with similar energetics and sizes as we have seen in Section 3.2.3. Radio jets have been detected in Holmberg II X–1 with an average jet power of 2×10^{39} erg/s. Similar Doppler shift in the Hα line with v $\sim$ –0.17c as those seen in SS433 has also been reported in the ULS in M81 (Liu et al., 2015, see Section 3.2.1.1). Equatorial winds with velocities in the 100–1300 km/s have been resolved in SS433 (Paragi et al., 1999; Fabrika, 2004). These similarities led to some authors to attempt to study the apparent luminosity SS433 would have if viewed face-on. Waisberg et al. (2019) studied the irradiation of the jet optical bullets along the rotational axis of the compact object. Based on the observed emission lines, in particular the hydrogen and He lines,

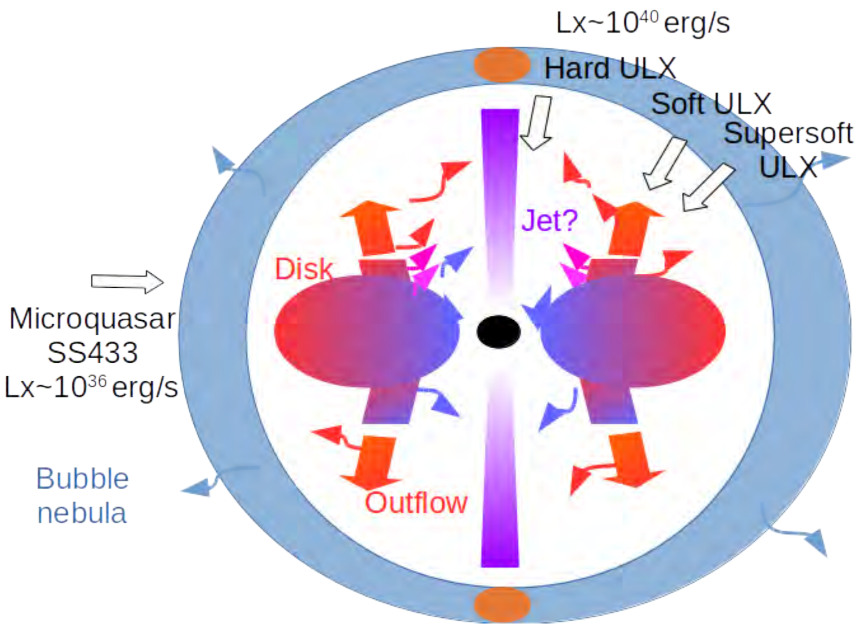

Figure 3.4: Schematic (not to scale) showing the geometry of a supercritical disk with the inclination dependent spectral states of ULXs. The viewing angle of the microquasar SS433 (with an incliantion of 79°) is also shown. The radiatively-driven disk winds and jets and strong radiation are expected to carve and ionize the ISM. The compact object could also be a NS in which the picture may substantially change as discussed throughout the Chapter.

and assuming a hard ULX spectrum for SS433, the authors concluded that the inferred X-ray luminosity for a face-on observer would be $\gtrsim 10^{40}$ erg/s. Similarly, Middleton et al. (2021) performed spectral-timing analysis of dedicated *NuSTAR* observations, which revealed the presence of 100 s lags associated with outflowing material with velocities of 0.14–0.29 c, similar to those seen in ULXs (see Section 3.2.4). The authors estimated the opening angle of the wind cone and luminosity of the reflection component through spectral fitting. Using the Monte-Carlo simulations envisaged by Dauser et al. (2017) to reproduce the reflected emission from a wind-like funnel structure, and the known inclination of SS433, Middleton et al. (2021) inferred face-on luminosity of $> 10^{39}$ erg/s. While these results remain highly uncertain as proper modelling of the reflected emission is needed and the Dauser et al. (2017) model is a simplification based on achromatic scattering, the similar properties between SS433 and ULXs may be regarded as further evidence supporting the idea that ULXs are supercritically accreting systems. A cartoon summary of what has been discussed so far is presented in Figure 3.4.

3.3 The Nature of the Accretor

So far, the nature of the accretor in most ULXs remains unknown. Beyond the detection of pulsations, the most standard method to determine the nature of the accretor is through dynamical mass measurements. Determining the optical counterpart of the X-ray detection is the first challenge, as several counterparts are typically found within the location error circle and ULX counterparts are relatively faint (Gladstone et al., 2013). A unique counterpart is sometimes possible to identify combining the subarcsecond resolution of *Chandra* for the X-ray imaging (Section 4.1.2) and the *HST* for optical imaging (Section 4.2.1) (e.g. Liu et al., 2004; Yang et al., 2011; Gladstone et al., 2013). After the counterpart has been identified, the radial velocity curve of a particular bright emission line can be obtained through several spectroscopy measurements. Several attempts to obtain radial velocity curves have turned inconclusive (Roberts et al., 2011; Cseh et al., 2013) or ruled out by further studies, as it was the case in the PULX NGC 1313 X–2 (Liu et al., 2008; Zampieri et al., 2012; Sathyaprakash et al., 2019). Roberts et al. (2011) suggested that the lack of periodic variability in the HeIIλ4686 line from the optical counterparts in Holmberg IX X–1 and NGC 1313 X–2 could be due to the systems being close to face-on. Holmberg IX X–1 and NGC 1313 X–2 were also analysed in Gúrpide et al. (2021a) and for the former, I found the high-energy emission ($\gtrsim$ 10 keV) to be remarkable stable (see also Walton et al., 2017) which as described in Section 5.1.4.4.1 could indeed imply a low-viewing angle.

A notable exception is the study of Motch et al. (2014), that was able to determine the orbital period of the ULX NGC 7793 P13 to be ≈ 64 days. The companion star was identified as B9Ia type, constraining the mass of the accretor to be below 15 M$_\odot$. Later, the detection of pulsations in NGC 7793 P13 firmly confirmed these results (Fürst et al., 2016).

However, the detection of BH–ULX systems remains elusive. Liu et al. (2013) reported the first detection of a BH–ULX system, based on the detection of a 8.2 day period in the ULS in M101 and the identification of the counterpart as a WR star. With these constraints, the accretor should have a minimum mass of $5\,M_\odot$, clearly ruling out a NS accretor. However, Laycock et al. (2015) argued that the radial velocity curve based of the Doppler shifts of the HeIIλ4686 line in systems with WR companions actually probes the motion of the outflowing wind from the star, instead of the motion of the star itself. As explained by the authors, because the wind is highly ionized due to the X-ray radiation from the compact object, only the part of the wind shielded by the WR star is able to produce the HeIIλ 4686 line. This can explain why the radial velocity curve of the HeIIλ4686 line in IC 10 X–1 (another WR companion system) is offset by one quarter with respect to the X-ray eclipses (see their Figure 1). Under these new considerations, the mass determination in the ULS M101 might need to be revisited.

Another way to tackle the problem is through population synthesis studies. Wiktorowicz et al. (2019) examined the fraction of observed NS to BH in the ULX population, assuming the emission can be beamed at super-Eddington mass-transfer rates using the formalism derived by (King, 2009). They predicted that the fraction of observed NS–ULX is typically $\approx$ 7–20% whereas BH–ULXs usually dominate the observed population (although there are differences depending on the assumptions on metallicity and star-forming rates). This is because BHs require lower mass-transfer rates to reach super-Eddington luminosities and thus they are more easily observed. Instead, NSs need beaming factors $\lesssim 0.7$ to reach the ULX luminosity threshold. This additionally implies that a higher fraction of NSs might be hidden from our view due to misalignment of the emission beam and our line of sight.

The difficulty in detecting pulsations in ULXs has led several authors to investigate other means of identifying NS-ULXs. Walton et al. (2018c) showed that the spectral shape of those ULXs for which broadband X-ray spectroscopy was available were remarkably similar to the known PULXs (see also Pintore et al., 2017; Koliopanos et al., 2017), suggesting that the ULX population may be dominated by NSs. Because of the differences in long-term variability between PULXs and other ULXs (see Section 5.1.4.1), I explored this in more details by taking into account the *spectral variability* in Chapter 5. These also led some authors to explore high-levels of variability as a proxy for detecting PULXs (Song et al., 2020) and in fact it was the main motivation to investigate the presence of pulsations in the newly discovered transient ULX in NGC 7793 (ULX 4; see Section 5.3.2).

Spectral fitting in X-rays can also shed some light on the nature of the accretor. In Galactic X-ray binaries, the estimated disk inner radius, the modelling of certain lines (in particular the Fe Kα line at 6.4 keV), the study of spectral transitions—as we have seen in Section 2.1.2 with the work of Done & Gierliński (2003)− or the identification of the q-shape diagram in an X-ray source (Zhang et al., 2020) can provide clues about the nature of the accretor. However, for ULXs, the identification of the various emission components is still a matter of debate as we have discussed in Section 3.2.1. Moreover, the modelling of the spectra lacks physically motivated models to extract quantitative information about the accretion flow properties. However, comparison of sources for which the accretor is unknown and with known NS-ULXs may provide indirect hints, which was one of the main motivations of the first work of Chapter 5. Moreover, I also attempted to apply a physically motivated in the second work of Chapter 5, from which I could retrieve meaningful parameters about the accretion flow geometry.

Chapter 4

Instrumentation

During this thesis I made used of multi-wavelength data to try to characterize the inner hot regions of the accretion flow around ULXs as well as optical/UV data to try to understand their environment and their impact on their surroundings. For spectroscopic studies of ULXs in the soft X-rays, I made used of the X-ray Multi-mirror Mission Newton (Section 4.1.1) and the Chandra X-ray observatory (Section 4.1.2). These observations were often complemented in the hard X-ray band with data from the *NuSTAR* (Section 4.1.3, that allowed me to constrain the spectral emission from 0.3 keV to ∼ 30 keV. The Neil Gehrels Swift Observatory (Section 4.1.4) was used mainly for photometry in order to characterize long-term trends in the soft X-rays. In the optical/UV, I made used of the high-spatial resolution of the *HST* (Section 4.2.1) for accurate astrometry determination and photometry measurements to complement the imaging-spectral capabilities of the MUSE at the Very Large Telescope (VLT) (Section 4.2.2). This Chapter outlines the main capabilities of these instruments, why they were chose for this study and and how they were used for the purpose of this study. The main steps followed in the data reduction will be outline in Chapters 5 and Chapter 6, in order to avoid redundancies. Note that in some cases the data used in this work was already reduced by the automatic pipeline. Such was the case for the *Swift*/XRT, the *HST* and MUSE data. In addition to using mainly archival data during my PhD, I led several proposals that are also outlined in this Chapter in the corresponding instrument Sections.

4.1 X-ray instruments

4.1.1 The X-ray Multi-mirror Mission Newton

The X-ray Multi-mirror Mission Newton (*XMM-Newton*; Jansen et al., 2001) is one of the cornerstone space observatories launched by the European Space Agency (ESA) on December 10th 1999. The main goal of the mission was to allow high-quality spectroscopy of faint sources and for this reason, *XMM-Newton* was build with the largest effective area of a focusing telescope (1550 cm^2 at 1.5 keV). The telescope has a focal length of 7.5 m and weighs 4 tonnes, making it still the largest telescope ever launched by the ESA.

The spacecraft carries three co-aligned X-ray telescopes consisting of 58 Wolter type I, which combine nested paraboloids and hyperboloids in a coaxial and cofocal configuration to focus the highly energetic X-rays, thereby increasing the effective reflecting area of the telescope. Each telescope has a different X-ray detector in its focal plane, so that all instruments on board can perform simultaneous observations.

The focal plane instruments for the three X-ray mirrors systems were provided by The European photon imaging camera (EPIC) consortium. These instruments were two Metal Oxide Semi-conductor (MOS) CCDs, referred as the MOS cameras (Turner et al., 2001), and a PN CCD camera referred as the PN camera (Strüder et al., 2001), all of them covering the soft X-ray band (∼ 0.3–10 keV). The two telescopes carrying the MOS cameras also have grating assemblies in their light paths, diffracting part of the incoming radiation onto a secondary focus (Figure 4.1). These are the RGSs (Herder et al., 2001), the high spectral resolution spectrometers on board *XMM-Newton* covering the 0.35−2.5 keV range. Approximately 44% of the incoming light is focused onto the MOS cameras while 40% is dispersed by the grating array onto a linear strip of CCDs. The telescope with the full photon flux operates the PN as an imaging X-ray spectrometer and has the highest effective area of all X-ray instruments onboard (∼ 1200 cm^2 at 1 keV compared to 300 cm^2 and 100 cm^2 for each of the MOS and RGS cameras respectively). A comparison between all the effective areas of the non-dispersive detectors used in this work is provided in Figure 4.2.

The EPIC cameras provide imaging with moderate angular resolution, with a Point Spread Function (PSF)

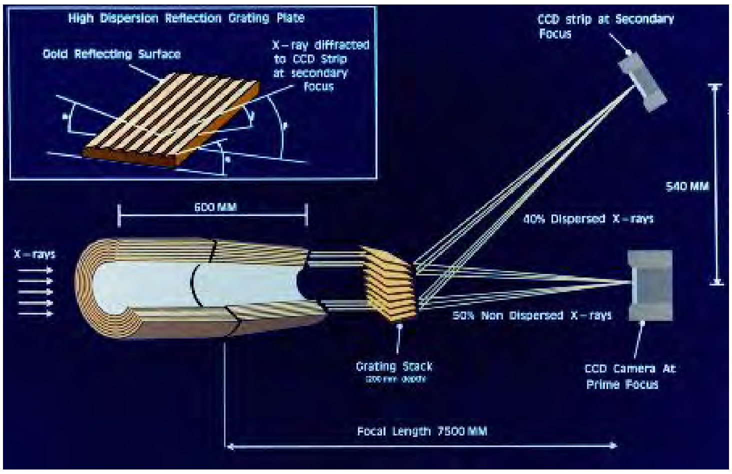

Figure 4.1: Schematic of the light path in the *XMM-Newton* telescopes carrying the Reflection Grating Spectrometers and the MOS cameras illustrating how part of the incoming light is dispersed onto the secondary focus. Credit: ESA.

FWHM ~ 6.6" at 1.5 keV for PN[1] over a 30' Field of View (FOV), and moderate resolution spectroscopy ($E/\Delta E$ ~ 20–50) while the RGS provides dispersive high-resolution X-ray spectroscopy ($E/\Delta E$ = 100 to 500). The PN has a good timing resolution below 200 ms, whereas the MOS cameras have 2.6 s timing resolution in the nominal Full Frame mode[2]. The large effective area of the PN and its subsecond timing resolution makes the de-facto instrument to carry out pulsation searches in ULXs (e.g. Rodríguez-Castillo et al., 2020).

Unless constrained by crowded fields, *XMM-Newton* high throughput makes it probably the most suitable soft X-ray observatory for the study of the ULX continuum. Moreover, the simultaneity of the three EPIC cameras maximizes the scientific return in each exposure and allows to combine the information from all three cameras to obtain high signal-to-noise ratio spectroscopic data. This is demonstrated in Chapter 5, where I exploit *XMM-Newton* outstanding capabilities for the study of the ULX spectral transitions. Additionally, *XMM-Newton* suffers much less from pile-up[3] compared to *Chandra* Advanced CCD Imaging Spectrometer (ACIS) detector (See Section 4.1.2; one or two orders of magnitude less for the same flux level[4]), which can be a problem for bright ULXs, as I explain in Section 5.1.2.

Alongside the X-ray telescopes, there is the Optical/UV Monitor Telescope (XMM–OM; Mason et al., 2001) that provides simultaneous coverage in the 150–650 nm optical/UV bands of a 17 × 17 arcmin FOV centered on the X–ray field of view. However, its limited spatial resolution (PSF with a FWHM of ~ 1.5 arcsec) generally renders it unsuitable for the study of ULXs, given their extragalactic distances and rather faint optical counterparts. For this reason, I generally used the *HST* (described in Section 4.2.1) when needing high-spatial resolution data.

4.1.1.1 Proposals

After Gúrpide et al. (2021a) (see Section 5.1), I led a *XMM-Newton* proposal (AO19) to request two 35 ks *XMM-Newton* observations of the NS-ULX candidate M81 X-6 (see Section 5.3.2) in order to: 1) confirm the accretor as a NS through the detection of X-ray pulsations; 2) probe the appearance of pulsations (or pulse-fraction variability) with the source spectral state in order to constrain system parameters such as the inclination and the role of outflows in diluting the pulsed emission. The panel recognized the importance of the science case but unfortunately, because of the short exposures requested (the observing constraints only allowed to perform 35 ks or less exposures) and the fact that the source had already been observed for 70 ks, the proposal was deemed too risky. Additionally, the contribution to knowledge was considered only incremental as the lack of pulsation could not rule out a NS as the accretor.

4.1.2 The Chandra X-Ray Observatory

The (Chandra X-Ray Observatory (CXO); Weisskopf et al., 2000) was launched in 1999 July 23, joining the *Hubble* (See Section 4.2.1) and the now de-comissioned *Compton Gamma-Ray observatory* as one of four NASA's

---

[1] The MOS cameras have similar angular resolution only slightly improved due to their smaller pixel size. See `https://xmm-tools.cosmos.esa.int/external/xmm_user_support/documentation/uhb/onaxisxraypsf.html` for more details on the angular resolution of EPIC cameras.

[2] `https://xmm-tools.cosmos.esa.int/external/xmm_user_support/documentation/uhb/epicmode.html.`

[3] Pile-up occurs when two close-in-time photons get registered as a single photon with energy equal to the sum of the two incident photons. This leads to spectral distortion and loss of counts.

[4] `https://xmm-tools.cosmos.esa.int/external/xmm_user_support/documentation/uhb/pileupcomp.html`

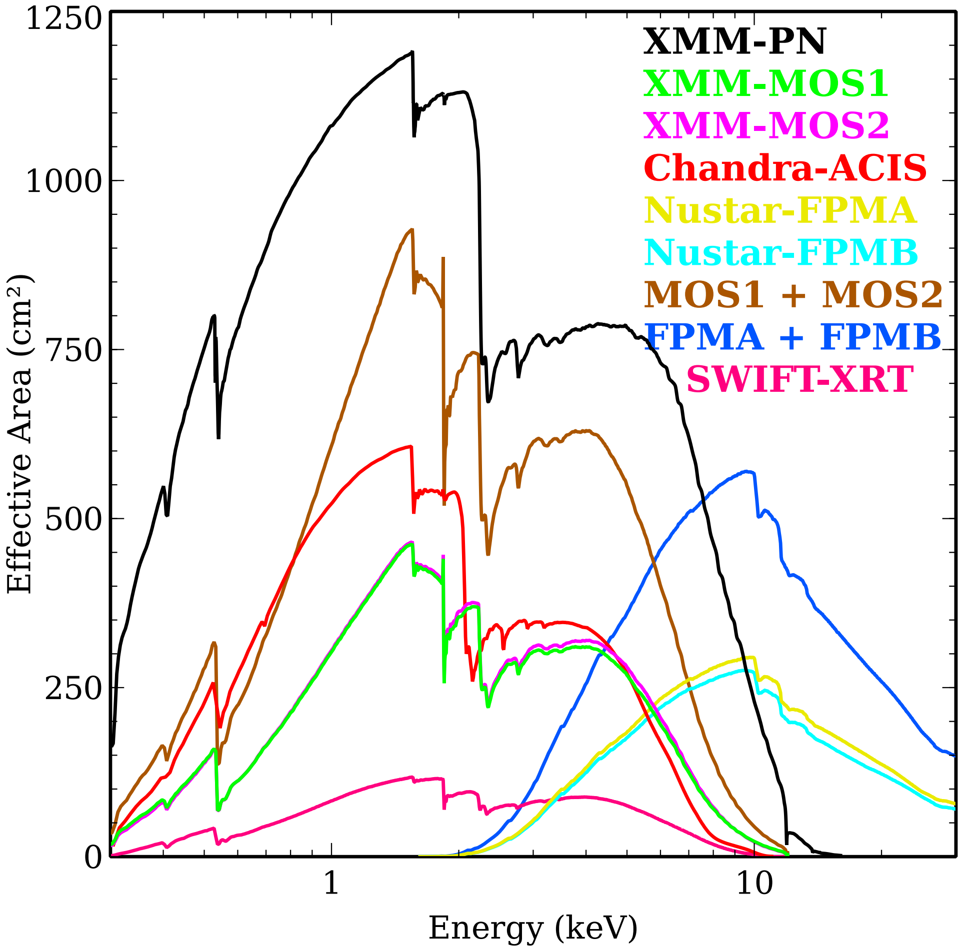

Figure 4.2: A comparison between the effective area of all the non-dispersive X–ray instruments used in this work.

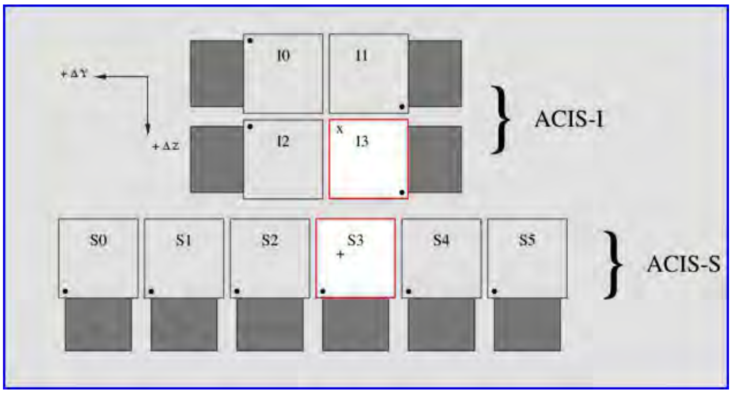

Figure 4.3: ACIS focal plane chip layout showing the Imaging detectors (labelled with an I) and the Spectroscopic detectors (labelled with an S). The detectors with a star indicate the respective aimpoints (I optimizing FOV and S optimizing energy resolution). Credit: NASA/Chandra X-ray Center.

Great Observatories, a large program first proposed in 1976 dedicated to deploy four separate telescopes to cover the gamma-/X-rays, visible and infrared bands[5]. *Chandra* provides coverage in the $\sim$ 0.08–10 keV band, by focusing X-rays with a single telescope comprised of 4 concentric grazing incident Wolter Type-I mirrors called the High Resolution Mirror Assembly (HRMA). The mirrors have an effective area of $\sim$ 800 cm^2 at 1.5 keV, a factor $\sim$ 2 lower than *XMM-Newton*. Two objective transmission gratings (OTGs) are available to be inserted into the converging beam of the HRMA where they disperse the X-rays on the focal plane. These are the Low–Energy Transmission Grating (LETG; Brinkman et al., 2000), that provides high resolving power at low-energies ($E/\Delta E$ > 1000 over the 0.07–0.15 keV band) and moderate resolution (20 $\times$ λ over the $\sim$ 0.2–10 keV), and the High-Energy Transmission Grating (HETG; Canizares et al., 2005), that covers the 0.4–8 keV range with a resolution up to 1000. Given the low effective area of such instruments ($<$ 200 cm^2) below 2 keV, where ULXs are usually the brightest, and the large number of counts usually required for high-resolution spectroscopy, the gratings in *Chandra* are in general not suitable to perform high-resolution spectroscopy of ULXs.

At the focal plane there is the Science Instrument Module (SIM), which houses two detectors: the High-Resolution Camera (HRC) and the ACIS. The SIM has a mechanism to swap the instruments at the focal plane, meaning that by design, only one instrument is operational in each observation. Each of the two instruments have two types of detectors: an Imaging (I) detector and a Spectroscopic (S) (see Figure 4.3). The S chips are arranged on a strip and are meant to serve as the readout of the dispersed photons if one of the gratings is chosen to be placed in the converging beam. Instead the I detectors are placed on a square shape to maximize the FOV. The HRC–S effective area peaks at 1 keV ($\sim$ 200 cm^2) and therefore is most suitable to be used as the readout of the LETG. In contrast, the ACIS–S camera is well suited to be used with the HETG, as its effective area peaks at higher energies (see Figure 4.2).

The virtue of *Chandra* lies in its ability to resolve crowded fields thanks to its sub-arcsecond angular resolution. The HRC-I provides the highest angular resolution (PSF $\sim$ 0.5 arcsec FWHM at 1.5 keV; an order of magnitude greater than that of *XMM-Newton*) and largest FOV (30$\times$30 arcmin), although the energy resolution is rather poor ($E/\Delta E = 1$ over the entire energy band) and provides low effective area above 1 keV (less than 100 cm^2 above 1 keV). The ACIS camera still provides superb angular resolution (PSF $\sim$ 1 arcsec FWHM at 1.5 keV) with improved energy resolution ($E/\Delta E = 15$ at 1 keV) and effective area (340 cm^2 at 1 keV, see Figure 4.2). The higher throughput and higher energy resolution of the ACIS camera makes it the preferred instrument for the observation of ULXs, since achieving the highest angular resolution is not critical for the study of faint distance point-like sources. The *Chandra* spectra of ULXs are typically not as constraining as those obtained with *XMM-Newton*, given its overall lower effective area. However, relying on *XMM-Newton* might not be optimal in crowded fields or in the presence of diffuse emission. In these cases, the higher angular resolution of *Chandra* can be more desirable to obtain cleaner spectra of the target. Such is the case for the PULX M82 X–2 (Brightman et al., 2016b), whose emission can only be resolved by *Chandra*, or the case of the PULX M51 ULX–7 as we will see in Section 5.1.3.1.1. Lastly, as stated in Section 4.1.1, *Chandra* is more sensitive to pile-up, which can be a problem for bright ULXs (see Section 5.1.2). This is because the ACIS camera has a much slower read-out timescale of 3.2 s.

---

[5] The dedicated infrared mission was the *Spitzer* telescope, that was launched after *Chandra* in 2003 and de-comissioned in 2020

4.1.3 The *Nuclear Spectroscopy Telescope Array*

The *Nuclear Spectroscopy Telescope Array* (*NuSTAR*; Harrison et al., 2013) is a small explorer NASA mission launched on 2012 June 13. It is the first high-energy (3–79 keV band) telescope with focusing capabilities in orbit, representing a breakthrough improvement of two orders of magnitude or more in sensitivity and angular resolution compared to traditional collimated or coded mask high-energy instruments. Two 133 nested multilayer-coated Wolter-I conical mirrors focus the hard X-rays onto two independent solid-state focal plane detectors, providing an angular resolution of 18" FWHM at 10 keV (Madsen et al., 2015), an energy resolution of $E/\Delta E \sim$ 25–66 and an instrument effective area of $\sim$ 600 cm^2 at 10 keV (see Figure 4.2). Both mirrors and focal planes are identical, enabling the users to gain sensitivity by merging their images, although in practice this is not recommended [6].

The subarcminute angular resolution, together with the large collective area at high-energies make of *NuSTAR* the ideal observatory to access the $>$ 10 keV ULX emission, given that their Mpc distances and the high-energy spectral cutoff (see Section 3.2.1.1) results in faint emission above 10 keV. Coordinated observations with soft X-ray observatories such as *XMM-Newton* or *Chandra* allow to constrain the broadband 0.3–30 keV X-ray continuum, as above 30 keV the source emission usually drops below the background in the *NuSTAR* band.

4.1.3.1 Proposals

After Gúrpide et al. (2021a) and while working on Gúrpide et al. (2021b), we requested a 20 × 2.5 ks *Swift*-XRT monitoring over a 200 day period of the ULX NGC 5204 X-1 to trigger a 200 ks *NuSTAR* observation when the source entered the soft/bright spectral state (see Chapter 5) to investigate the variability above 10 keV during the evolutionary cycle. We proposed to: 1) assess the variability (or lack of) of the high-energy emission ($>$ 10 keV) between the newly observed spectral state and the one already probed by old *NuSTAR* observations (see Gúrpide et al. (2021a) and Section 5.1.4.5 for a discussion on the variability of the high-energy tail); 2) characterize its full evolutionary hysteresis cycle (see Section 5.2), by tracking its hardness/flux variability with *Swift*; and 3) carry out pulse searches in the new *NuSTAR* dataset of this yet unobserved spectral state. This *NuSTAR* data could allow us to discriminate the nature of the accretor by means of studying the high-energy ($>$ 10 keV) spectral stability, that was argued to be a signature of BH-ULXs (Gúrpide et al., 2021a). Instead, the presence of pulsations would indicate a NS-ULX accretor and would provide clues about the nature of the high-energy emission, possibly ruling out its stability as a BH-ULX signature. Finally, we consider that observing the evolutionary cycle in ULXs is important for the understanding of the accretion flow geometry in the super-Eddington regime around compact objects. The proposal was rejected because there was no guarantee that the proposal would be successful. We argued that based on the $\sim$ 200 day periodicity, there was some guarantee that the source would be observed transiting between the soft states. However, the periodicity had not been computed under the null hypothesis of red-noise, something we worked on in Chapter 5.2.3.1 Section 5.2.3.2.3. Additionally, NGC 5204 X–1 had already been observed for roughly 200 days, where the hardness-raio did not show strong variability (for more details see the Section 5.2).

4.1.4 The Neil Gehrels *Swift* observatory

The Neil Gehrels *Swift* observatory (Gehrels et al., 2004) is a multi-wavelength medium-sized explorer selected by NASA, which leads an international collaboration that developed the instrumentation and data reduction pipeline. *Swift* was launched into a low-Earth orbit on November 20, 2004 with its main focus to detect, localize and determine the redshift of GRBs (Vedrenne & Atteia, 2009) to rapidly distribute the information to the ground for multi-wavelength follow-up observations to help understand their origin and their use as cosmological probes, as well as the physics of ultra-relativistic jets. The spacecraft is designed to allow for rapid slew maneuvers so the telescope could be triggered by transient events and be pointed within 20–70 seconds.

Swift carries three instruments: the Burst Alert Telescope (BAT; Barthelmy et al., 2005), a hard X-ray coded mask operating in the 15–150 keV range, the X-ray Telescope (XRT; Burrows et al., 2005), a focusing X-ray telescope operating in the 0.2–10 keV band, and the Optical/UV Telescope (Roming et al., 2005), a replica of the XMM-OM co-aligned with the XRT. BAT is a wide FOV instrument (1.4 sr) that acts as the GRB trigger detector to slew and repoint the *Swift* telescope to the detected position of the GRB. The XRT uses a grazing incidence Wolter-I telescope to focus the soft X-rays onto a single CCD detector, that has the same design as the *XMM-Newton* MOS CCDs. The telescope has a 23.6 × 23.6 arcmin FOV and an angular resolution of 8.8" FWHM PSF. After the slew maneuver, the XRT measures fluxes, spectra and light curves of the GRB within 20–70 s after the BAT alert. The X-ray counterpart position is measured to $\lesssim$ 5" accuracy. Finally, the UVOT will provide positions of less than 0.3" accuracy by using background stars, which will ensure that the GRB host galaxy can be identified. The stars in the FOV can be later compared to more precise *HST* (see Section 4.2.1) images to refine the GRB position within the galaxy.

---

[6] `https://heasarc.gsfc.nasa.gov/docs/nustar/nustar_faq.html#AplusB`

In general, due to the low throughput (Figure 4.2) of the *Swift* telescope, performing spectroscopic studies of ULXs with XRT is not optimal. However, *Swift* unique rapid pointing capabilities coupled with the ability to schedule high-observing cadence monitoring is particularly compelling to track sources over long periods of time ($\sim$ few months) in both optical/UV and X-rays. For this, *Swift* can be pointed at the source every few days for a few ks to obtain just photometric measurements in the UV and the X–ray bands. These high-cadence monitoring programs have proven particularly useful to discover orbital (Motch et al., 2014) and superorbital periods (see Vasilopoulos et al., 2020a, or later Section 5.2.3.1) in ULXs. Moreover, the short exposures can be later easily stacked by segregating the data by means of hardness-ratio and/or count rate. If enough observations are stacked, a higher S/N spectrum can be obtained and the source spectral state can be constrained (see Luangtip et al., 2016, for an example).

4.1.4.1 Proposals

Albeit in Section 5.2 (Gúrpide et al., 2021b), we showed clearly that NGC 5204 X–1 followed the same pattern as Holmberg II X–1 (see Section 5.1.4.4), the *Swift*-XRT monitoring of NGC 5204 X–1 did not capture the cycle in full. I led a proposal to request 60 × 3ks observations (Cycle 17) spaced between 2 and 10 days to monitor NGC 5204 X–1 with *Swift*-XRT in order to characterize its full evolutionary cycle, by tracking both its rapid and long-term hardness/flux variability. We also aimed to reliably assess the presence of the super-orbital period and its link with the observed ULX spectral states. Unfortunately, the proposal was rejected as it was not shown with enough clarity how the new *Swift* monitoring would reliable distinguish the source spectral state and thus improve the current monitoring. The proposal has been resubmitted for cycle 18.

4.2 Optical/UV instruments

4.2.1 The Hubble Space Telescope

Named after the famous astronomer Edwin Hubble, the *HST* is the only space telescope specifically designed to be upgraded, repaired and maintained by astronauts while in orbit. Soon after its launch in 1990, a focusing problem caused the telescope to fail to deliver the sharp images it has been designed for. The PSF was measured to be of $\sim$ 1 arcsec, compared to the expected 0.1 arcsec. Investigation of the problem revealed a defect in the polishing of the primary mirror, which was causing the images to suffer from spherical aberration. A service manned mission was planned and the scientific instruments were replaced by new ones purposely designed to compensate the aberration caused by the mirrors. After this initial setback, the mission was a success and after thirty years of operations, the *HST* continues to deliver outstanding images and is still actively used in several research programs, such as the Frontier Field Program, which aims to study the most distant and faintest galaxies by taking deep images of blank fields. The telescope has been visited five times throughout its life in order to upgrade the scientific instruments and repair the system components. This long-term design of the *HST* mission have made it the longest lasting space mission ever.

Hubble carries a single Cassegrain reflector telescope with a 2.4 m primary mirror. The mirrors focus the light onto five science cameras and spectrographs currently covering the infra-red, optical and UV bands. Table 4.1 offers a summary of the main instruments currently onboard. Additionally, there is the Fine Guidance Sensors that can be used for precise astrometry measurements, although the main objective of these sensors is to keep the telescope in a stable and accurate pointing position throughout the observation (with an accuracy of $\sim$0.01 arcsec).

The *HST* has been extensively used in the study of ULXs, owing to its ability to resolve crowded fields. Its superb subangular resolution, thanks to its privileged position beyond distorting atmospheric effects, has allowed to resolve and identify ULX optical counterparts (e.g. Liu et al., 2004; Kuntz et al., 2005; Yang et al., 2011; Gladstone et al., 2013), obtain photometric (e.g. Grisé et al., 2008) and spectroscopic measurements (Tao et al., 2012) in the UV/optical wavelengths and study the regions of ionized gas frequently found around them (e.g. Kaaret et al., 2004; Grisé et al., 2012, see also Section 3.2.3). Much of this has been thanks to the Wide Field Camera (WFC)3 (Dressel, 2012) and the Advanced Camera for Surveys (ACS) (Ryon, 2021) (and its predecessors), as it is also the case in Sections 3.2.3 5.2.3.3.

4.2.2 The Multi-Unit Spectroscopic Explorer

The MUSE (Bacon et al., 2010) is a second-generation VLT IFU operating in the optical and near infra red range (480–930 nm in the nominal mode, sampled at 1.25 Å). The instrument is mounted in one of the four 8.2 m units (UT4, Yepun telescope) at the Paranal observatory in Chile, and it saw its first light on 31 January 2014. MUSE is the first instrument to combine simultaneously imaging and spectroscopic capabilities over a large field of view, with high spatial resolution, moderate resolving power and a large spectral range. The instrument was primarily designed to study the distant and faint galaxies through the detection of the Lyman-α hydrogen line over a wide range of redshifts ($2.9 < z < 6.65$). In the nearby universe, MUSE allows the study of AGN feedback,

Instrument	Detector	Wavelength Range nm	FOV arcsec^2	Pixel Size arcsec
Advanced Camera for Surveys	Wide Field Camera	350–1050	202×202	0.05
	High Resolution Channel†	200–1050	29.1×26.1	0.028×0.025
	Solar Blind Channel	115–180	34.59×30.8	0.034×0.030
Wide Field Camera 3	Ultraviolet and Visible (UVIS)	200–1000	162×162	0.04
	NIR	850–1700	123×137	0.13
Cosmic Origin Spectrograph	FUV	115–205	–	–
	NUV	170–320	–	–
Space Telescope Imaging Spectrograph†	CCD	1650–11000	52×52	0.05
	FUV–MAMA	150–1740	25×25	0.025
Near Infrared Camera and Multi-Object Spectrometer†	Low Resolution Camera	800–2500	51.5×51.5	0.2
	Medium Resolution Camera		17.5×7.5	0.075
	High Resolution Camera		11.0×11.0	0.043

Table 4.1: Current instruments onboard *HST*. †Instrument no longer operational.

	Wide Field Mode	Narrow Field Mode
FOV	1×1 arcmin^2	7.5×7.5 arcsec^2
Pixel scale (arcsec)	0.2	0.025
PSF (arcsec)	$\sim$ 0.5–1.5	$\sim$ 0.5–1
PSF–AO (arcsec)	$\sim$0.3–1	0.05–0.08

Table 4.2: Summary of the properties of the MUSE observing modes.

stellar kinematics and populations, star-forming regions, etc.

MUSE has two main modes of observation: the Wide Field Mode (WFM)[7] and the Narrow Field Mode (NFM). The characteristics of each observing mode are summarized in Table 4.2. MUSE was operated under natural seeing conditions at Paranal ($\sim$ 0.5–1.5") until October 2017, when an Adaptive Optics (AO) facility was installed at the UT4. The AO system is aimed to improve the PSF in the WFM by a factor of $\sim$ 2, whereas in the case of the NFM it can reach up to the sampling limit ($\sim$ 50 mas) in favourable seeing conditions ($\sim$ 0.5").

In order to achieve its spectro-imaging capabilities a series of subcomponents first split the incoming light from the FOV in 24 horizontal subfields (see Figure 4.5). This is done by the MUSE field splitter unit (Laurent et al., 2014), depicted in Figure 4.6. The 24 mirrors of the Field Separator reflect the light by the appropriate angle, feeding each sub field into 24 independent IFUs. Each IFU is composed by an image slicer, a spectrograph and a CCD detector. The slicer at the IFU further cuts each subfield into 48 0.2" slits (Figure 4.5). The spectrograph disperses the light of each mini slit in the perpendicular direction onto the CCD detector, achieving a resolving power of $\sim$ 3000 at 7500 Å (see Figure 4.4[8]). Finally, the data is conveniently rearranged in a 3D datacube by the automatic reduction pipeline developed by Weilbacher et al. (2020). The pipeline also produces an accompanying cube with the associated uncertainties for each spaxel. These cube dataproducts can be publicly accessed through the European Southern Observatory (ESO) archive science portal[9], which is the data I made use of in this work.

MUSE simultaneous spectro-imaging capabilities and coverage of the main nebular lines used for gas diagnostics in the Baldwin-Philips-Terlevich (BPT) (Baldwin et al., 1981) diagrams make it a very attractive instrument for the study of the structures of ionized gas around ULXs (see Section 3.2.3) and their environment. We will see

---

[7] For the WFM mode there is an extended mode that allows to extend the blue coverage down to 465 nm.

[8] https://www.eso.org/sci/facilities/paranal/instruments/muse/doc/ESO-261650_MUSE_User_Manual.pdf

[9] http://archive.eso.org/cms.html

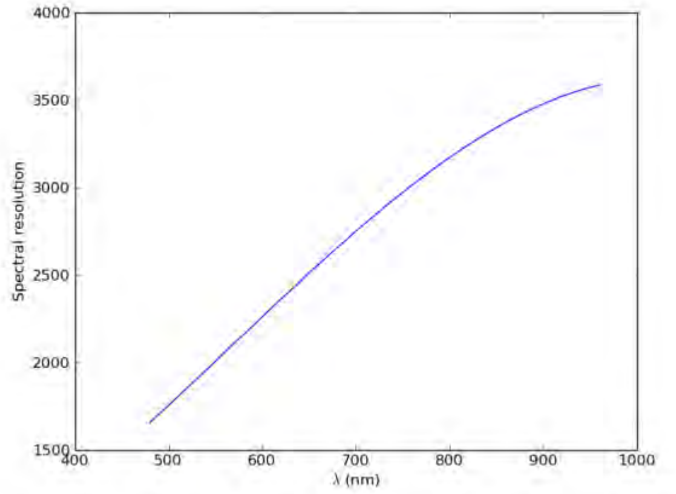

Figure 4.4: MUSE spectral resolution ($R = \Delta\lambda/\lambda$) as a function of wavelength. Credit: ESO.

in Chapter 6 how I exploited MUSE capabilities to analyse these ionized bubbles around ULXs.

4.2.2.1 Proposals

In order to acquire new data to carry out this project, I looked for nearby (<10 Mpc) ULXs with a confirmed optical nebula around, that could be suitable to be observed with MUSE in the NFM. This would give us a view of the kinematics and energetics of the gas around ULXs with unprecedented level of details, allowing us to study the impact of the radiation and/or outflows on the environment. For this, the AO system requires a natural guiding star sufficiently bright ($7 <$ H band Vega magnitude < 14) at 3.5 arcsec from the center of the FOV [10]. Despite these tight observing constraints, (note the the small FOV of MUSE in the NFM in Table 4.2), we were lucky enough to find one target meeting all the requirements: NGC 5408 X–1. This ULX has a ~ 60 pc optical bubble (Grisé et al., 2012) with associated radio emission (Lang et al., 2007). High-resolution spectroscopy in X-rays may have revealed the presence of blueshifted absorption and emission rest-frame features, that have been interpreted as due to an outflowing component with velocities of $\sim$0.2 c shock-heating the surrounding gas Pinto et al. (2016). These properties make NGC 5408 X–1 and excellent candidate for our study. Our goal is to study the physical conditions of the gas through 2D velocity fields, spatially-resolved BPT diagrams, measurements of the electron density, etc. Unfortunately, the proposal has been rejected three times now, last time because of the challenging observing strategy, but it has been resubmitted for Period 109, as the constraints on the guiding star have been relaxed.

---

[10] This has been extended to 5 arcsec in the 2021 March call

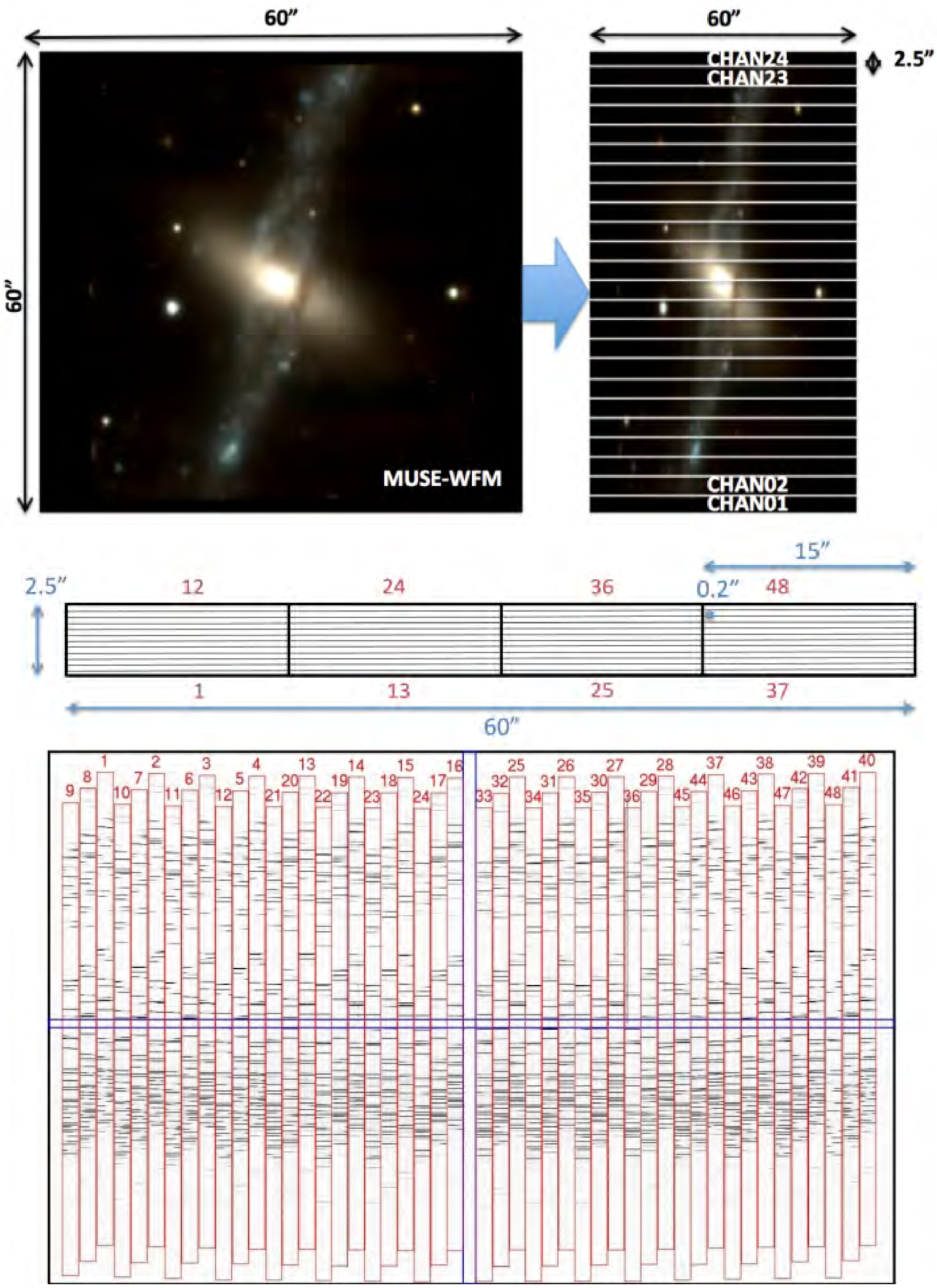

Figure 4.5: Overview of the splitting of the FOV. The top panel shows the splitting of the FOV produced by the MUSE field splitter (Figure 4.6 into the 24 horizontal sub-fields. The middle panel shows the different 48 mini slits produced by the image slicer for one of the 24 sub-fields. The bottom panel shows how the mini slits are arranged and have been dispersed on the CCD detector, with the wavelength increasing from bottom to top for each mini slit. Credit: ESO.

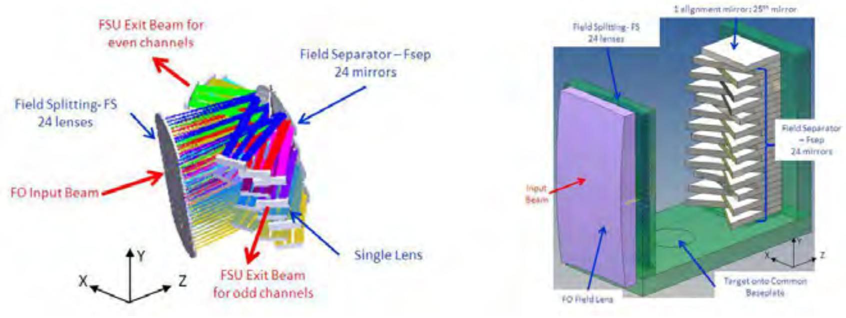

Figure 4.6: 3D schematics of the MUSE field splitter unit that reflects the light of the FOV into 24 different horizontal sub-fields. Figure taken from Laurent et al. (2014).

Chapter 5

Long-term X-ray Evolution of Ultraluminous X-ray Sources

The first part of my PhD thesis focused on characterizing the accretion flow geometry that allows ULXs to reach such extreme luminosities as well as the nature of the accretor (NS or BH). As we have seen in Chapter 3, several scenarios have been proposed in the literature (e.g. Mushtukov et al., 2017; King & Lasota, 2020; Mushtukov et al., 2021) with regards the accretion flow geometry powering ULXs. For this reason I investigated what scenario could best account for the observed spectral variability in X-rays best. X-rays allows us to examine the inner hot regions of the accretion flow and as such, they provide with valuable information about the physical conditions of the gas being accreted as well as the nature of the compact object. The first study was dedicated to characterize the spectral changes seen in the long-term in a sample of 17 ULXs with high-quality spectral data that had been observed in at least five instances, so we could sample a wide range of spectral states. Because we also analysed several confirmed NS-ULXs, we could make use of this extensive study to observe differences between PULXs and ULXs for which the accretor was unknown and thus highlight sources that could be good candidates for being NS-ULXs.

The main results were that PULXs are among the hardest sources in the ULX sample. Moreover, I found that harder PULXs showed less variability in terms of hardness ratio than softer PULXs. I suggested that because magnetic fields are known to suppress outflows (as explained in Section 2.2.1), softer PULXs are consistent with lowly magnetised NS, in which outflows produced anisotropic emission (observed as strong hardness variations) and softer emission due to Compton-down scattering of the accretion column (presumably hard emission) in the cool electrons of the outflow. Instead, highly magnetised NSs might power the hardest ULXs, such that outflows are suppressed and lead to low variability in terms of hardness. Our findings suggested that most of the ULXs in our sample were either consistent with BHs or lowly magnetised NSs, given their softer appearance. We finally were able to provide some evidence for a potential NS candidate, M81 X–6, and a candidate system hosting a BH-ULX, M83 ULX1.

During this first study (Gúrpide et al., 2021a), I discovered that two archetypal ULXs, Holmberg II X–1 and NGC 5204 X–1, not only followed a strikingly similar evolution but also showed an interesting recurrent pattern in a HID. This was hard to see given the sparsity of the *XMM-Newton* and *Chandra* observations and I therefore decided to do a follow-up study (Gúrpide et al., 2021b) where I characterized more precisely this pattern using the high-cadence monitoring offered by *Swift*-XRT. I also analysed the light curves of these two sources looking for potential periodic variability using Lomb-Scargle periodograms and Gaussian process modelling. I found that these two sources transited through the three canonical ULX states: the hard, soft and supersoft ultraluminous regimes (recall Section 3.2.1). This provided firm evidence in support that supersoft ULXs are essentially an extension of ULXs viewed at higher inclinations or with higher-mass accretion rates. The cycle could be characterized by a low variable hard ultraluminous state and recurrent and rapid (as short as $\sim$ 1000 ks in some cases) transitions between the two soft states. I suggested that the spectral transition from hard ultraluminous to soft ultraluminous could be due to an increase of the mass-accretion rate and narrowing of the funnel (recall also Section 2.2). Because the funnel is wide open in the hard ultralumious state, there is little variability as the wind is unlikely to enter the line of sight. As it narrows as the mass-accretion rate increases, the wind will start to intermittently cross the line of sight, providing a natural way to explain the transitions between the two states. However, I also found tentative evidence for a periodicity linked to the transitions between the two states, and if confirmed, this would require another mechanism to explain them, which could be linked to precession of the supercritical funnel. We also found that the cycle is likely to be periodic, but more data might be needed to robustly confirm it.

In both cases, I led the study by performing the complete spectral and temporal analysis and by writing the first version of both full manuscripts.

5.1 Long-term X-ray spectral evolution of ultraluminous X-ray sources: implications on the accretion flow geometry and the nature of the accretor

A. Gúrpide[1], O.Godet[1], F. Koliopanos[1], N. Webb[1] and J.-F. Olive[1]

[1]Institut de Recherche en Astrophysique et Planétologie, Université de Toulouse, UPS/CNRS/CNES, 9 Avenue du Colonel Roche, BP44346, F-31028 Toulouse Cedex 4, France

Accepted to A&A 23th of February 2021

Abstract

The discovery of pulsations in several ultraluminous X-ray sources (ULXs) has demonstrated that a fraction of them are powered by super-Eddington accretion onto neutron stars (NSs). This has raised questions regarding the NS to black hole (BH) ratio within the ULX population and the physical mechanism that allows ULXs to reach luminosities well in excess of their Eddington luminosity. Is this latter the presence of strong magnetic fields or rather the presence of strong outflows that collimate the emission towards the observer? In order to distinguish between these scenarios, namely, supercritically accreting BHs, weakly magnetised NSs, or strongly magnetised NSs, we study the long-term X-ray spectral evolution of a sample of 17 ULXs with good long-term coverage, 6 of which are known to host NSs. At the same time, this study serves as a baseline to identify potential new NS-ULX candidates. We combine archival data from *Chandra*, *XMM-Newton*, and *NuSTAR* observatories in order to sample a wide range of spectral states for each source. We track the evolution of each source in a hardness–luminosity diagram (HLD) in order to identify spectral changes, and show that these can be used to constrain the accretion flow geometry, and in some cases the nature of the accretor. We find NS-ULXs to be among the hardest sources in our sample with highly variable high-energy emission. On this basis, we identify M81 X-6 as a strong NS-ULX candidate, whose variability is shown to be akin to that of NGC 1313 X-2. For most softer sources with an unknown accretor, we identify the presence of three markedly different spectral states, which we interpret by invoking changes in the mass-accretion rate and obscuration by the supercritical wind/funnel structure. Finally, we report on a lack of variability at high energies ($\gtrsim$ 10 keV) in NGC 1313 X-1 and Holmberg IX X-1, which we argue may offer a means to differentiate BH-ULXs from NS-ULXs. We support a scenario in which the hardest sources in our sample might be powered by strongly magnetised NSs, meaning that the high-energy emission is dominated by the hard direct emission from the accretion column. Instead, softer sources may be explained by weakly magnetised NSs or BHs, in which the presence of outflows naturally explains their softer spectra through Compton down-scattering, their spectral transitions, and the dilution of the pulsed-emission should some of these sources contain NSs.

5.1.1 Introduction

Ultraluminous X-ray sources (ULXs) are defined as extragalactic off-nuclear point-like sources with an X-ray luminosity in excess of $\sim 10^{39}$ erg/s (see Kaaret et al., 2017, for a review); although there is now evidence for a Galactic ULX (Wilson-Hodge et al., 2018). Their nature remains for the most part unknown, and given this empirical definition they likely constitute a heterogeneous population of objects. It was initially proposed that ULXs could be powered by accreting intermediate-mass black holes (IMBHs:$\sim$ 100 – 10^5 $M_{\odot}$; see Mezcua, 2017, for a review) in the sub-Eddington regime (Colbert & Mushotzky, 1999; Matsumoto et al., 2001). The best ULX IMBH candidates may be those at the high-end of the high-mass X-ray binary (HMXB) luminosity distribution (e.g. Mineo et al., 2012), reaching $L_{\rm X} \geq 10^{41}$ erg/s in some cases. Some of these objects show transitions or temporal properties that seem to be consistent with the expectation of a scaled-up version of Galactic black hole binaries (GBHBs; e.g. Farrell et al., 2009; Godet et al., 2009; Pasham et al., 2014) and/or show evidence for cooler accretion disks (e.g. Feng & Kaaret, 2010; Servillat et al., 2011; Godet et al., 2012; Lin et al., 2020) which suggest masses in the IMBH regime.

However, it was soon realised that the bulk of the ULX population ($10^{39} < L_{\rm X} < 10^{41}$ erg/s) did not comply with the canonical states seen in GBHBs (e.g. Stobbart et al., 2006; Gladstone et al., 2009; Grisé et al., 2010). It was therefore suggested that stellar-mass black holes (BHs) fed at super-Eddington mass-transfer rates could power these sources (Shakura & Sunyaev, 1973; King & Pounds, 2003; Poutanen et al., 2007), with geometrical beaming possibly further enhancing the observed luminosity (King et al., 2001). In this scenario, the intense radiation pressure blows off some of the excess gas in the form of a wind or outflow, which can become optically thick to the hard radiation emitted in the inner parts of the disk (Poutanen et al., 2007). The wind is expected to form a conic structure around the rotational axis of the compact object due to angular momentum conservation, producing highly anisotropic emission. It was then proposed that the short-term variability and the differences in spectral shape in a broad ULX sample could be understood in terms of different viewing angles and mass-accretion rates (Sutton et al., 2013; Middleton et al., 2015a) with those ULXs with $L_{\rm X} \sim 10^{39}$ erg/s showing a behaviour more consistent with stellar-mass BHs accreting close to or at their Eddington limit (e.g. Middleton et al., 2011b). These studies were later extended to include ultraluminous supersoft sources (ULSs) (Urquhart & Soria, 2016), which are interpreted as sources in which the inclination of the system and/or the accretion rate are so high that the inner disk emission is completely reprocessed by the optically thick wind, with some sources possibly showing transitions between a ULX-like spectrum and a ULS state (Feng et al., 2016). Indeed, numerical simulations of super-Eddington accretion onto BHs have shown extensively that the viewing angle has a strong impact on the observed spectrum (e.g. Ohsuga & Mineshige, 2007; Sądowski et al., 2015; Ogawa et al., 2017). For this reason, it has been suggested that overall ULXs belong to a homogeneous class of objects, including stellar-mass BHs or weakly magnetised neutron stars (NSs), being fed at super-Eddington mass-transfer rates (King & Lasota, 2016; King et al., 2017; Pinto et al., 2020a). Observational evidence supporting winds associated with super-Eddington accretion comes from high-resolution X-ray spectroscopy studies, which revealed absorption and emission features suggesting the presence of strong ionised winds colliding with the circumstellar medium (Pinto et al., 2016, 2017, 2020b).

However, while it was generally accepted that accreting stellar-mass BHs were the engines behind ULXs below 10^{41} erg/s (e.g. Poutanen et al., 2007; Gladstone et al., 2009; Pintore et al., 2014), the discovery of X-ray pulsations in one ULX (Bachetti et al., 2014) showed that NSs can also attain super-Eddington luminosities. Motivated by the discovery of (now) five more pulsating ULXs (PULXs; Fürst et al., 2016; Israel et al., 2017a,b; Carpano et al., 2018; Sathyaprakash et al., 2019; Rodríguez-Castillo et al., 2020) and the possible confirmation of another NS-ULX through the identification of a cyclotron line (Brightman et al., 2018), several authors have highlighted the remarkable X-ray spectral similarity of the ULX sample with those with detected pulsations (Pintore et al., 2017; Koliopanos et al., 2017; Walton et al., 2018c), suggesting that NS-ULX may dominate the ULX population. Yet, there is still some debate over the driving mechanism responsible for their extreme luminosities.

Pintore et al. (2017) suggested that the accretion column could be responsible for the hard emission in ULXs, as their X-ray emission could be described with a model commonly used to fit Galactic X-ray pulsars. Instead, based on the theoretical calculations carried out by Mushtukov et al. (2017), Koliopanos et al. (2017) argued that the ULX spectra are consistent with accreting highly magnetised NSs (B>10^{12} G), as the 0.3 – 10 keV band can be described by two thermal components. In this scenario, the soft thermal component arises from a truncated accretion disk at the magnetospheric radius (Ghosh & Lamb, 1978) while the hard emission is produced in an optically thick envelope as the accreting material is forced to follow the magnetic field lines, creating a closed envelope around the NS. The rotation of the envelope, which is due to the coupling with the NS through the magnetic field lines, and its latitudinal temperature gradient could explain the sinusoidal profiles seen in PULXs (e.g. Fürst et al., 2018), provided that the NS rotational axis is misaligned with the magnetic field axis. Alternatively, Walton et al. (2018c), following the arguments from King & Lasota (2016) and King et al. (2017), showed that the interplay between the mass-accretion rate and magnetic field strength could explain the lack or presence of pulsations in ULXs, suggesting that ULXs might instead be powered by weakly magnetised NSs. This in turn may explain the different spectral shape of those ULXs for which broadband spectroscopy data are available compared to the PULXs.

However, the long-term evolution of PULXs is marked by variability of two orders of magnitude or more in flux (Israel et al., 2017a,b) while other ULXs show variations of a factor of five or less on timescales of years (Grisé et al., 2013; Luangtip et al., 2016; Pinto et al., 2020b) with PULXs also being somewhat harder than the rest of the population (Pintore et al., 2017). Whether these represent differences in the nature of the accretor or are due to a disfavourable viewing angle (e.g. King & Lasota, 2020) is still not fully understood (e.g. Walton et al., 2018c). If beaming is a natural consequence of super-Eddington mass transfer (King, 2009), theoretical studies show that the fraction of observed BH-ULXs could be higher than NS-ULXs (Middleton & King, 2017). Similarly, binary population synthesis studies suggest that BH-ULXs could even dominate the observed ULX population (Wiktorowicz et al., 2019), as NSs need stronger beaming factors to reach $L_X > 10^{39}$ erg/s. However, evidence for supercritically accreting stellar-mass BHs remains elusive. The best observational evidence for such BH-ULX systems might be M101 ULX-1, which was estimated to host a ~ 20 M$_\odot$ BH, although its dynamical mass determination was challenged by Laycock et al. (2015). Constraining the BH-to-NS ratio in ULXs can lead to important clues about the formation path leading to such systems and their connection with HMXBs (e.g. Mineo et al., 2012) and the formation of BH-BH and BH-NS systems.

Therefore, while the spectral resemblance of the ULX population is undeniable, tracing their long-term evolution could be key to understanding the geometry of the accretion flow and discriminating between super-Eddington accretion models and the nature of the accretor. To this end, we present a comprehensive study of the long-term spectral evolution of a representative sample of 17 ULXs (including 6 NS-ULXs) in the $10^{39} < L_x < 10^{41}$ erg/s range in an effort to gain insight into the accretion flow geometry as well as the nature of the accretor. More specifically, we focus on studying the spectral evolution of each source in an attempt to assess which scenario best describes the variability observed: super-Eddington accretion onto a highly magnetised NS, a weakly magnetised NS, or a BH. This in turn provides clues about the nature of the accretor, and by comparing its evolution with the known PULXs, we can identify potential strong NS-ULX candidates. To do so, we build a phenomenological model taking into account the new information obtained on the ULX broadband emission with *NuSTAR* (Bachetti et al., 2014; Walton et al., 2015; Mukherjee et al., 2015; Walton et al., 2020) and track their spectral changes in a hardness–luminosity diagram (HLD).

We describe the sample of sources selected for this work and the data reduction in Section 5.1.2. In Section 5.1.3 we describe the data analysis and results. We discuss our results in Section 5.1.4 and present our conclusions in Section 5.1.5.

5.1.2 Sample selection and data reduction

5.1.2.1 Sample selection

In order to have a representative sample of the possible range of spectral variability of each source, we searched the literature for sources that have been observed on at least five occasions, well-spaced in time, by either *XMM-Newton* (Jansen et al., 2001) or *Chandra* (Weisskopf et al., 2000). We further required that they have either: high-quality *XMM-Newton* data (with $\gtrsim$ 10000 total counts in pn) or simultaneous broadband coverage with *NuSTAR* (Harrison et al., 2013) in at least one epoch. We were less stringent with the data constraints on the PULXs, because they are the only sources for which the nature of the accretor is known and thus they will be crucial for our study. We discarded M82 X–2 from the current PULXs sample (NGC 7793 P13, NGC 5907 ULX1, NGC 300 ULX1, M51 ULX–7, NGC 1313 X–2 and M82 X–2), as this source is only resolved by *Chandra* and its spectra are frequently affected by pile-up. Its emission is also often contaminated with nearby sources and diffuse emission of unknown origin (Brightman et al., 2016a), precluding a clean detailed spectral analysis of the source. Another source of interest is M51 ULX–8, which was identified as harbouring an accreting NS through the detection of a cyclotron resonance feature (Brightman et al., 2018), although no pulsations have been reported to date. We therefore included this source in our sample to further investigate its spectral properties with respect to the PULXs.

For those ULXs for which the accretor is unknown, we included at least two sources from each of the different spectral regimes proposed by Sutton et al. (2013) in order to have a representative characterisation of the ULX population. We also made sure to include those sources showing evidence for super-Eddington outflows with 3σ detections (Pinto et al., 2016, 2017). Thus, we also included NGC 55 ULX1, even if it does not meet our criterion of having more than three epochs. The final sample selected for this study is presented in Table 5.1.

Finally, we note that the luminosities reported for NGC 5907 ULX1 in this work are subject to an additional source of uncertainty, as there is a large discrepancy in the distance measurements to the host galaxy. The distance measurements range from ~17 (Tully et al., 2016) to $\sim$ 12.9 Mpc (Crook et al., 2007) which can boost the inferred luminosity by a factor of $\sim$ 1.7. Here we adopted the most recent estimate of 17.06 by Tully et al. (2016).

5.1.2.2 Data reduction

XMM-Newton data reduction was carried out using SAS version 17.0.0. We produced calibrated event files from EPIC-pn (Strüder et al., 2001) and MOS (Turner et al., 2001) cameras with the latest calibration files as of March 2018 using the tasks *epproc* and *emproc* (version 2.24.1), respectively. We selected events from patterns 0 to 4 for pn and patterns ≤ 12 for the MOS cameras. The standard filters were used to remove pixels flagged as bad and those close to the CCD gaps. We created high-energy ($10 - 12$ keV) light curves from single pattern events from the full field of view to assess the presence of high-background particle flaring periods that could contaminate our spectra. We filtered these periods by removing times where the count rate was above a certain threshold by visually inspecting the light curves. These thresholds varied for each observation, and ranged from ~ 0.3 cts s^{-1} to 1.2 cts s^{-1} and from ~ 0.2 cts s^{-1} to 0.5 cts s^{-1} for the pn and MOS respectively.

Generally, we extracted source events from circular regions with a radius of 40" and 30" for pn and MOS respectively owing to their different angular resolution, rejecting observations in which the source fell on a chip gap. We reduced the source regions to avoid contamination from nearby sources, chip-gaps, or in cases where the source was faint in order to increase the S/N, but always ensuring that at least 50% of the PSF was enclosed. We used elliptical regions in cases where the source was placed at large off-axis angles, resulting in a distorted PSF. This was the case, for example, for the pn observations 0657801601 and 0657802001 of Holmberg IX X-1, observations 0112521001, 0112521101, 0657801801, 0657802001, 0657802201, 0693850801, 0693850901, 0693851001, and 0693851101 of M81 X-6, and observation 0656580601 of Circinus ULX 5. The background region was selected from a larger circular source-free region and on the same chip as the source when possible. For the pn, we also tried to select the background region from the same distance to the readout node as for the source region. Finally, for M51 ULX-7, we used regions of ∼20" and ∼ 25" for pn and MOS detectors respectively, to reduce contamination from the diffuse emission in which the source is immersed (Rodríguez-Castillo et al., 2020). We discuss possible contamination by the diffuse emission and its treatment in Section 5.1.3.1.1.

We noted also that Holmberg IX X-1 and Holmberg II X-1 were bright enough on some occasions to cause pile-up in the *XMM-Newton* detectors. We assessed the importance of pile-up using the tool *epatplot* (version 1.22) when the source count rate was above the recommended values[1]. In order to mitigate its effects, we excised the inner core of the PSF using an annular extraction region. The inner excised radius was never below 10.25" and 2.75" for the pn and the MOS cameras respectively, to avoid introducing inaccuracies in the flux estimation, as recommended[2].

We finally used the tasks *rmfgen* (version 2.8.1) and *arfgen* (version 1.98.3) to generate redistribution matrices and auxiliary response files, respectively. We regrouped our spectra to have a minimum of 20 counts per bin to allow the use of χ^2 minimisation and also avoided oversampling the instrumental resolution by setting a minimum channel width of one-third of the FWHM energy resolution.

We reprocessed the *Chandra* data using the script *chandra_repro* with calibration files from *CALDB* 4.8.2. We used extraction regions given by the tool *wavdetect* to extract source events. Background regions were selected from roughly three-times-larger, circular, nearby source-free regions. The level of pile-up was assessed by inspecting the images created using the *pileup_map*[3] tool. We rejected observations with a pile-up fraction $\gtrsim$ 5%. We only considered observations that registered ≥ 1000 counts, as we found that below this threshold data were of too poor a quality to robustly discriminate between different models. All data were also rebinned to a minimum of 20 counts per bin.

NuSTAR data were processed using the *NuSTAR* Data Analysis Software version 1.8.0 with *CALDB* version 1.0.2. We extracted source and background spectra using nuproducts with the standard filters. Source events were selected from a circular region of ∼ 60". The only exception was NGC 1313 X-1, for which we followed Walton et al. (2016b) and chose a region of 40 – 50" to reduce contamination from a nearby source (see Bachetti et al., 2013). Background regions were selected from larger circular source-free regions and on the same chip as the source but as far away as possible to avoid contamination from the source itself. We regrouped the *NuSTAR* spectra to 40 counts per bin, owing to the lower energy resolution compared to the *EPIC* cameras. For this work, we only considered *NuSTAR* observations for which simultaneous soft X-ray coverage with *XMM-Newton* was available. A summary of all observations considered can be found in Table 5.1.

5.1.3 Data analysis and results

We used the X-ray spectral fitting package XSPEC (Arnaud, 1996) version 12.10.1f for spectral fitting and quote uncertainties on spectral parameters at the 90% confidence level for a single parameter of interest, unless stated otherwise. All fluxes were estimated using the pseudo-model `cflux` in XSPEC.

In general, we fitted EPIC data and the ACIS data in the 0.3 – 10 keV range. For the sources with the highest absorption columns (NGC 5907 ULX1, IC 342 X-1 and Circinus ULX5), we inspected the *epatplot* to choose the most suitable energy range to perform spectral fitting on the EPIC data. For IC 342 X-1 and Circinus ULX5, we noticed strong deviations from the observed pattern distributions with respect to the epatplot model below ∼ 0.4 keV. This is to be expected because the low-energy part of these absorbed spectra is likely dominated by the charge redistribution tail (and possibly noise). We therefore restricted the lower energy range to 0.4 keV for these two sources. For *NuSTAR*, we typically considered the 3 – 35 keV range, although to avoid including bins with negative number of counts in the χ^2 minimisation we restricted the high-end of the energy range to those bins where the net number of counts was positive.

When simultaneously fitting spectra from different instruments from the same epoch, we attempted to compensate for calibration uncertainties by introducing a multiplicative cross-normalisation factor that was allowed to vary between the different instruments. This factor was frozen to unity for the pn (or the two MOS detectors if no pn data was available). We used the same factor for the MOS detectors as we found them to be generally in good agreement, while FPMA and FPMB each had their own separate constant, as recommended[4]. The agree-

---

[1] https://xmm-tools.cosmos.esa.int/external/xmm_user_support/documentation/uhb/epicmode.html

[2] https://www.cosmos.esa.int/web/xmm-newton/sas-thread-epatplot

[3] https://cxc.harvard.edu/ciao/ahelp/pileup_map.html

[4] https://heasarc.gsfc.nasa.gov/docs/nustar/nustar_faq.html

ment between the pn and the MOS cameras was usually within errors, with a few cases in M81 X–6 where the disagreement reached 10% because of the highly elliptical distorted PSF caused by the off-axis position of the source on the detectors. The value of the cross-normalisation factor between *EPIC* data and *NuSTAR* detectors was typically in agreement within the errors, reaching a 5-20% disagreement in some cases, with the largest values found when the source was highly off-axis on the *NuSTAR* detectors.

Finally, we fitted together, that is, we assumed the same spectral model for two or more datasets if they were close in time (separated by a few days) and if after inspecting each observation separately we found no significant variation in flux and spectral parameters. This is also noted in Table 5.1 where we quote the different datasets that have been fitted together based on the above. Throughout this work, we use the word *epoch* to refer to all datasets that have been fitted together assuming the same model.

5.1.3.1 Spectral modelling

5.1.3.1.1 Choice of model: Our first aim was to characterise the long-term spectral evolution of our sample in a simple and coherent manner by studying variations of the spectral components (i.e. luminosity, radius, temperature, etc.). As the latest studies revealed that the 0.3 – 10 keV band can be modelled by two thermal components (e.g. Mukherjee et al., 2015; Koliopanos et al., 2017, 2019; Walton et al., 2020), which can reproduce the curvature seen at high-energies, we first considered a phenomenological model based on two multi-colour blackbody disks (`diskbb` in XSPEC; Mitsuda et al., 1984) to fit the data in this band, taking into account interstellar absorption by neutral hydrogen with two absorbing components `tbabs` in XSPEC. One was frozen at the Galactic value along the source line of sight (see Table 5.1), and the other one was left free to vary to take into account possible absorption from the host galaxy and the system itself. We adopted abundances given by Wilms et al. (2000) and cross-sections given by Verner et al. (1996) as recommended.

While other models have been commonly adopted to reproduce the hard emission ($\sim$ 2 keV – 10 keV) in ULXs, like Comptonisation of soft disk photons in a warm optically thick corona or a more phenomenological power law, we preferred the `diskbb` over these for various reasons. First of all, a warm optically thick corona up-scattering photons from the disk is merely a proxy to reproduce the curvature seen at high energies, as its physical interpretation is subject to several caveats (see Koliopanos et al., 2017, and references therein). Additionally, broadband spectroscopic studies have shown how this model fails to reproduce the spectral shape of ULXs (Walton et al., 2015; Mukherjee et al., 2015). Therefore, for the purpose of reproducing the spectral curvature in (at least) the *XMM-Newton* band, the `diskbb` has been shown to be equally valid with only two parameters. The power law (or a power law with a cutoff for the same matter) unphysically diverges towards low energies, thus taking up flux from the soft component and causing the absorption column to be overestimated.

Another advantage of the dual thermal component is that thanks to its simplicity, it can be used as a proxy to represent more complex models. For instance, in the context of super-Eddington accretion, the soft black body has been frequently associated with an outflow, while the hard one has been associated with emission from the inner parts of the accretion flow (e.g. Walton et al., 2014). Alternatively, Koliopanos et al. (2017) associated the soft component with an accretion disk truncated at the magnetospheric radius, and attributed the hard component to the emission from the magnetospheric envelope (Mushtukov et al., 2017). The `diskbb` also allows us to easily test theoretical predictions by studying the evolution of its temperature with its luminosity as we show in Sections 5.1.3.4 and 5.1.3.5.

However, visual inspection of the fit residuals revealed strong residuals at high energies in the 0.3 – 10 keV band in some epochs, indicating that our phenomenological model is not able to reproduce the emission at high energies. We show this for two high-quality observations of Holmberg II X-1 and NGC 5408 X-1 in Fig 5.1. This is perhaps not surprising, as broadband studies using *NuSTAR* data have revealed the presence of a faint hard power-law-like excess dominating above $\sim$ 10 keV (e.g. Mukherjee et al., 2015; Walton et al., 2015, 2017). We find that for those epochs for which we have broadband coverage with *NuSTAR*, this excess can be well modelled as Comptonisation of the hot thermal component as noted by previous studies. As the nature of this Comptonisation component is still poorly understood (Walton et al., 2017) and given the lack of broadband coverage for most of the observations considered here, we decided to use the `simpl` model (Steiner et al., 2009) to reproduce it, as this latter does not assume any geometry but simply scatters a fraction of photons (f_{scat}) of the seed component towards high energies, emulating a power-law component with a certain Γ, with the advantage that it does not diverge towards low energies.

In order to identify those epochs for which the `simpl` model component is required, we would ideally rely on Monte-Carlo simulations. However, given the large number of datasets considered here this is not feasible. Instead, to obtain an estimate as to when the data quality allows us to constrain this component, we performed an F-test between the dual-thermal model described above and the model `tbabs`⊗`tbabs`⊗(`diskbb` + `simpl`⊗`diskbb`) and decided to include the `simpl` model only if the probability of rejecting ($P_{\rm rej}$) the simpler model was $\sim 3\ \sigma$. We also included the `simpl` model for observations with $P_{\rm rej}$ slightly below this value if we were able to constrain its parameters using near-in-time observations with $P_{\rm rej} > 3\ \sigma$ (see below). Similarly, we excluded the `simpl` component in some cases with $P_{\rm rej} > 3\ \sigma$ if its parameters are largely unconstrained. We are aware that this is not an appropriate use of the F-test, however the presence of this component was already shown to be significant by Walton et al. (2018c) and indeed we found that this component was required to fit the highest quality datasets. We are not claiming to confirm this component as present or not, but instead we used these values as a reference

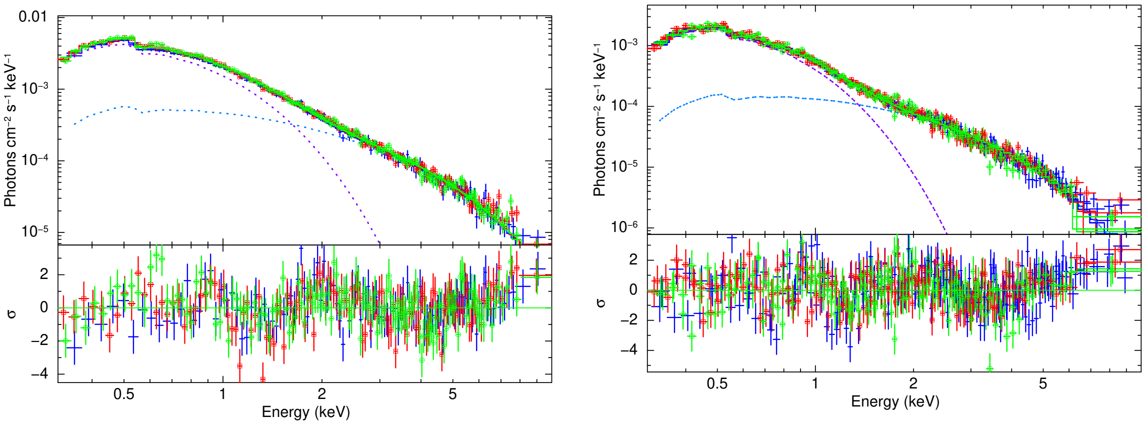

Figure 5.1: Unfolded pn (blue), MOS1(red), and MO2 (green) spectra fitted with an absorbed dual thermal component (`tbabs`⊗`tbabs`⊗(`diskbb`+ `diskbb`) on *(left)* observation 0200470101 of Holmberg II X-1 ($\chi^2{}_r \sim 1.34$) and *(right)* observations 0723130301 and 0723130401 of NGC 5408 X-1 ($\chi^2{}_r \sim 1.5$), which we fit together given the lack of variability (see Section 5.1.3). Data have been visually rebinned to have at least 3 σ significance and a minimum of 35 counts per bin. Some clear residuals are seen at high energies indicating that the model is inadequate.

indicating when the data quality allows this component to be constrained. We present the result of this F-test in Table 5.7 where we also indicate for which observations we finally included this component.

For NGC 7793 P13 we found that this component is largely unconstrained even in the broadband datasets, resulting in no fit improvement when adding this component. The broadband datasets yield fits with $\chi^2_r \sim 1.1$ with the dual-thermal model alone, which are statistically acceptable, and so we decided not to add this component.

Furthermore, as the `simpl` model is mostly responsible for the emission above $\sim$ 8 keV in our modelling, its parameters are not well constrained when *Chandra* or *XMM-Newton* data are considered alone, and only in long *XMM-Newton* exposures with $>$ 40000 counts in pn can we constrain both f_{scat} and Γ simultaneously. We also found good consistency between the Γ-values in several epochs and that most sources are found recurrently at similar fluxes and hardness ratios (see Section 5.4). We therefore tied Γ across epochs where the source is found at similar flux and hardness ratio, while leaving f_{scat} and the rest of the parameters free to vary. By doing so we were able to use the broadband information provided by *NuSTAR* to have some constraints on those epochs where this information is not available. For NGC 1313 X-1, after checking the consistency of Γ across epochs and bearing in mind that its variability above 10 keV has been shown to be small (Walton et al., 2020), we tied Γ for all observations where the `simpl` model is used. For NGC 5408 X-1 and NGC 6946 X-1, we also found very little variability at high-energies and therefore we again tied Γ across all observations where we added the `simpl` model. Finally, for NGC 1313 X-2, we also found that the same Γ-value can be tied for the four epochs for which we included the `simpl` model, although in this case the source shows a certain variability at high energies (see Section 5.1.3.3).

For M81 X-6, M51 ULX-7, M51 ULX-8, and M83 ULX1, given the lack of broadband coverage and that the dual-thermal model gave an acceptable fit to the data, we found no need to try to improve the fit by adding the `simpl` model and therefore we did not explore this option. As stated in Section 5.1.2, the *XMM-Newton* observations of M51 ULX-7 might be contaminated by some diffuse emission. To quantify the possible contamination from this diffuse emission, we extracted two MOS1 and MOS2 spectra (from obs id 0824450901) from two circular (25" in radius) regions located 34" from the source in two different directions. We fitted both emission spectra with a powerlaw and a `mekal` model subject to Galactic absorption only. The spectral parameters of both spectra are consistent within errors with $\Gamma = 2.9^{+0.4}_{-0.6}$ and 2.8±0.3, and plasma temperature = 0.28±0.03 keV and $0.27^{+0.04}_{-0.03}$ keV for region 1 and 2 respectively. We therefore ruled out strong spatial variations and computed the luminosity of region 1. We find a total unabsorbed luminosity of $(4.9^{+0.7}_{-0.3}) \times 10^{38}$ erg/s in the 0.3 – 10 keV band, with the soft band (0.3 – 1.5 keV) being approximately five times brighter than the hard band. We therefore estimate that the diffuse emission can make the source appear $\sim$ 25% softer in the *XMM-Newton* observations, given that M51 ULX-7 has a typical luminosity of 4 × 10^{39} erg/s. We therefore added this diffuse emission model as a fixed additive component to the M51 ULX-7 continuum in all *XMM-Newton* observations and decided to discard obsids 0677980701, 0677980801, and 0830191401 when the source was at its lowest.

Finally, some sources show strong residuals at soft energies, which have been associated with unresolved emission and absorption lines produced in an outflow colliding with the circumstellar gas (Pinto et al., 2016, 2017, 2020b). In most cases, we ignored them, as we are interested in the continuum emission and this will not affect our results. There are two exceptions to this: for NGC 5408 X-1, including a Gaussian emission line at $\sim$ 1 keV leads to a $\Delta\chi^2$ improvement that ranges from $\sim$ 50 to 122 (for 3 extra degrees of freedom) depending on the observation. We therefore decided to also determine the parameters of this Gaussian in the joint fit of the high-quality datasets by tying together all its parameters. We obtain E = 0.947±0.005 keV, σ = 78±6 eV and

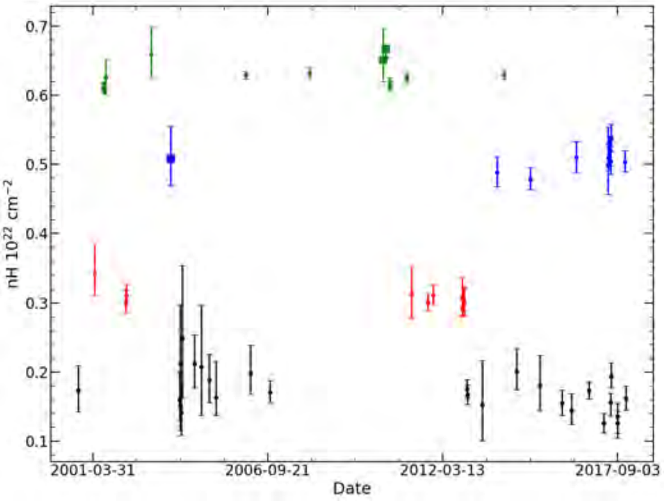

Figure 5.2: Evolution of the local absorption column over time for NGC 5408 X-1 (green), NGC 7793 P13 (blue), Holmberg IX X-1 (red), and NGC 1313 X-2 (black) shifted by 0.2 10^{22} cm^{-2} for clarity. All spectra have been fitted with a model consisting of an absorbed dual `diskbb` model in the 0.3 – 8 keV band. Errors are shown at 3σ confidence level. Circles and squares correspond to *XMM-Newton* and *Chandra* data respectively.

normalisation = $2.7^{+0.3}_{-0.2} \times 10^{-5}$ photons/cm^2/s. For NGC 5204 X-1, we also included a Gaussian emission line for the *Chandra* obsid 3933 following Roberts et al. (2006) as we again note similar strong residuals. In this case we obtain E = 0.97±0.02 keV, $\sigma = 56^{+24}_{-21}$ eV and normalisation = 2±1 × 10^{-5} photons/cm^2/s, consistent with the values reported by Roberts et al. (2006).

5.1.3.1.2 Treatment of the absorption column: There is still no consensus as to whether the local absorption column in ULXs is variable (e.g. Kajava & Poutanen, 2009) or not (e.g. Miller et al., 2013). The main argument for variability of the absorption column is the contribution from outflows (e.g. Kajava & Poutanen, 2009; Middleton et al., 2015b), which could imprint stochastic variability in $n_{\rm H}$ due to wind clumps crossing our line of sight (Takeuchi et al., 2013; Middleton et al., 2015a) depending on their column density and ionisation state. Alternatively, Middleton et al. (2015b) argued that some expelled gas could cool down far from the source and contribute to the neutral absorption column. If this is the case, it is then not clear over what timescale $n_{\rm H}$ would react to instantaneous changes in the mass-accretion rate.

To make matters more complicated, Miller et al. (2009), studying absorption edges at high spectral resolution in X-rays, showed that the absorption column remains stable throughout spectral changes in a set of X-ray binaries, and that changes in the soft component must come from changes in the source spectrum and not from the absorption column itself.

In view of these complications, we attempted to study variations in $n_{\rm H}$ by fitting all epochs individually for each source using the dual-thermal component over the 0.3 – 8 keV band, so as to use the same model for all epochs and avoid introducing artificial changes in $n_{\rm H}$ due to the different energy ranges considered when using *NuSTAR* data. We find that in general, the values of the absorption column for a given source are consistent within 3σ errors over all epochs, which we show in Figure 5.2 for four sources in our sample. Small discrepancies can be attributed to low data quality (e.g. short exposure *Chandra* observations and/or calibration uncertainties) rather than real physical-$n_{\rm H}$ changes. For NGC 5408 X-1, when fitting the 0.3 – 8 keV band with the dual-thermal model we still see strong residuals at high energies, which may indicate that the dual-thermal model cannot adequately fit the 0.3 – 8 keV band. We therefore repeated the study of the $n_{\rm H}$ variations replacing the hard `diskbb` with a power law with a high-energy cutoff (`cutoffpl` in XSPEC) to ensure that the lack of mismodelling of the high-energy emission does not affect the $n_{\rm H}$ variations (or lack of) found before. With this model we again find all $n_{\rm H}$ values consistent at the 3 σ level.

Conversely, we did find evidence for variability in the absorption column of NGC 1313 X-1 and NGC 55 ULX1 when following the same approach, where variations above the 3σ confidence level were seen (see the arrows in Figure 5.3). However, given the phenomenological nature of our model, we cannot rule out the possibility that these discrepancies are due to a change in the underlying continuum, therefore changing the parameter degeneracies.

For the other sources not discussed here, we do not find such strong evidence for variability in the absorption column as for the sources discussed above, although in some cases this could be due to poorly constrained model parameters. Therefore, in view of the above considerations, we consider that the absorption column can be assumed to be constant for the most part, with the exception of epoch 2004-08-23 of NGC 1313 X-1 and epoch 2010-05-24 of NGC 55 ULX1. In these cases we allowed $n_{\rm H}$ to vary together with the continuum parameters as

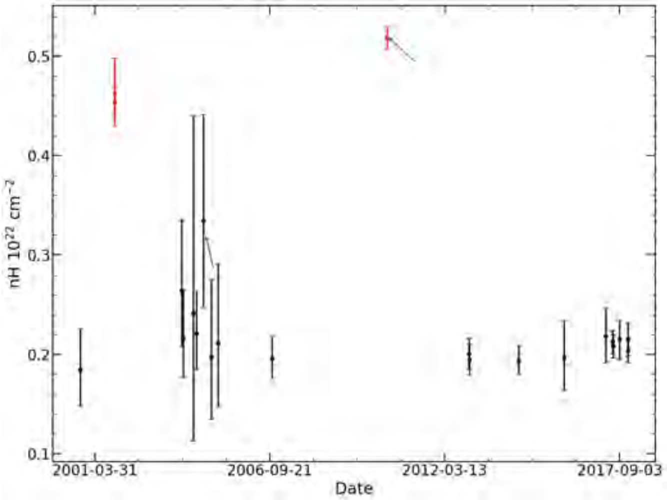

Figure 5.3: As in Figure 5.2 but for NGC 1313 X-1 (black) and NGC 55 ULX1 (red). Arrows indicate epochs where a 3 σ significant change is seen with respect to some other epochs (see text for details).

this is preferred by the fit. We find $\Delta\chi^2$ improvements of $\sim$ 25 and 15 for NGC 1313 X-1 and NGC 55 ULX1 respectively when leaving $n_{\rm H}$ free, compared to the case where $n_{\rm H}$ is frozen to the average value (see following section). We discuss this in more detail in Section 5.1.4.4.

5.1.3.1.3 Spectral fitting approach: Ideally, we would jointly fit all datasets for each source, tying the $n_{\rm H}$ and Γ across certain datasets as explained above. However, such a procedure would be computationally prohibitive. As the joint fit will mostly be driven by those datasets with higher data quality, in order to reduce the computational burden of this approach we decided to do our spectral fitting in two steps: we first jointly fitted those datasets with better statistics, tying together Γ across those epochs where the source is found at similar flux and hardness ratio and $n_{\rm H}$ across *all* epochs, while leaving the remaining parameters free to vary. We typically consider three to eight datasets for each source, which includes those observations with the longest *XMM-Newton* exposures when the three EPIC cameras are operational, those for which simultaneous *NuSTAR* coverage is available and in some rare cases, the longest *Chandra* observations. We next fitted the remaining observations of lower data quality individually with $n_{\rm H}$ and Γ frozen at the values found in the joint fit. The results of the joint and the subsequent individual fits are reported in Table 5.2.

For Circinus ULX5, the joint-fit approach results in largely unconstrained parameters for the low-energy components at soft energies. This is likely due to a combination of the calibration uncertainties at low energies (see Section 5.1.3) and the high absorption column along the line of sight ($n_{\rm HGal}$ = 50.6$\times$ 10^{20} cm^{-2}; HI4PI Collaboration et al., 2016). We therefore considered only epoch 2013-02-03 to constrain $n_{\rm H}$ as it offers the best constrains on the broadband emission.

5.1.3.2 Hardness–luminosity diagram

As a first source classification and in order to highlight the differences and similarities between the sources in our sample, we started by building a HLD similar to that often used for X-ray binaries (Done & Gierliński, 2003) and also for ULXs (e.g. Sutton et al., 2013). We did this by computing unabsorbed fluxes rather than counts because relying on count rates is not feasible given the different instruments employed for this work. Furthermore, fluxes have the advantage that they can be corrected for absorption column. To do this, we retrieved the total unabsorbed luminosity in the 0.3 – 10 keV band from the `tbabs`$\otimes$`tbabs`$\otimes$(`diskbb` + `simpl`$\otimes$`diskbb` or `diskbb`) depending on the epoch. The hardness ratio is computed as the ratio of unabsorbed fluxes in a soft band (0.3 – 1.5 keV) and a hard band (1.5 – 10 keV). This is motivated by the fact that the pulsating component in PULXs has been shown to dominate at high energies (e.g. Israel et al., 2017a; Walton et al., 2018b) and thus we may expect to highlight the differences between pulsating and non-pulsating sources, while the soft component in ULXs usually stops dominating above $\sim$ 1 keV.

Indeed, the results presented in Figure 5.4 and Table 5.3 show clearly that PULXs are harder than the rest of the sample, with some interesting exceptions. In general, PULXs harden in the 0.3–10 keV band with luminosity with high levels of flux variability. We find that most of the population reaches a maximum luminosity of $\sim 2 \times 10^{40}$ erg/s, with just Holmberg IX X-1 and NGC 5907 ULX1 above this value. This is also highlighted in Figure 5.5, where a drop in sources reaching a maximum luminosity $\sim 2 \times 10^{40}$ erg/s is clearly seen.

Lastly, we note that as we have rejected observations below $\sim$ 1000 counts, transitions to the off states below $\sim 10^{39}$ erg/s like those seen for NGC 5907 ULX-1 (Israel et al., 2017a), NGC 7793 P13 (Israel et al., 2017b), or M51 ULX-7 (Brightman et al., 2020a) are not reflected in this diagram.

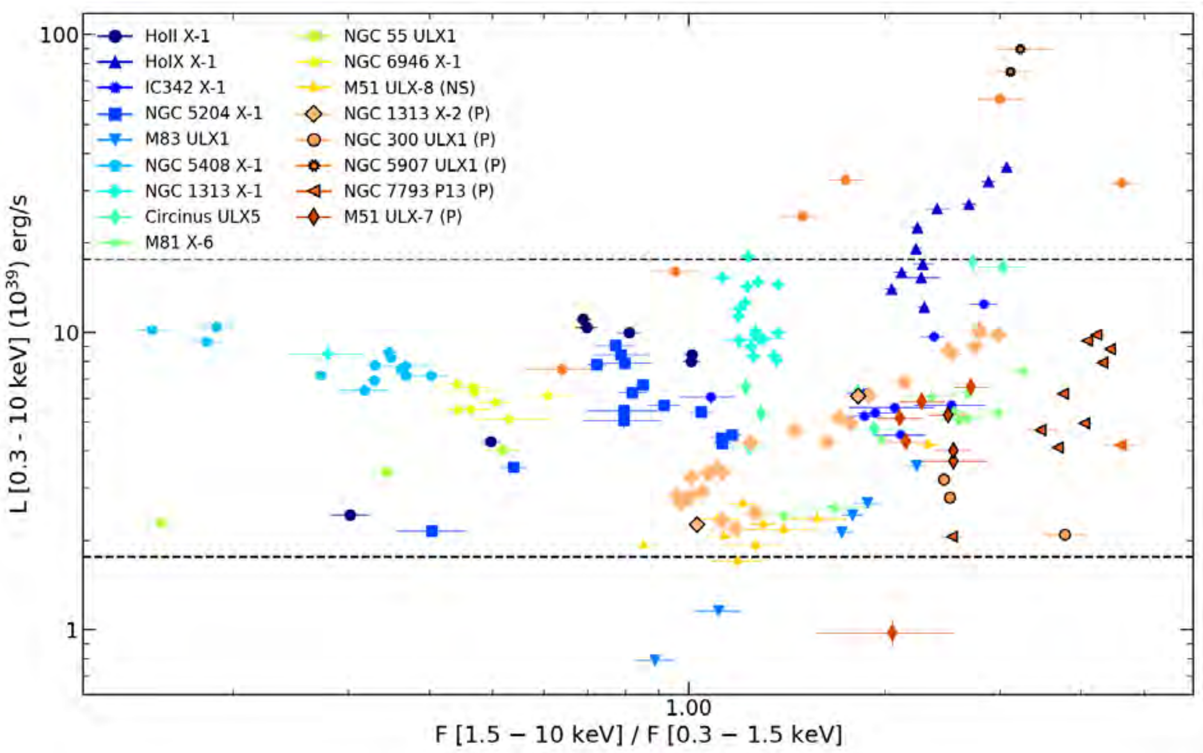

Figure 5.4: Hardness–luminosity diagram for the ULX sample selected for this study. All fluxes and luminosities are unabsorbed. PULXs are shown in shades of orange and the epochs for which pulsations have been reported in the literature (Israel et al., 2017a; Fürst et al., 2018; Carpano et al., 2018; Vasilopoulos et al., 2018; Sathyaprakash et al., 2019; Rodríguez-Castillo et al., 2020) are highlighted by a black edge around the marker. The dashed black lines indicate respectively 10 and 100 times the Eddington limit for a NS ($\sim 2\times 10^{38}$ erg/s).

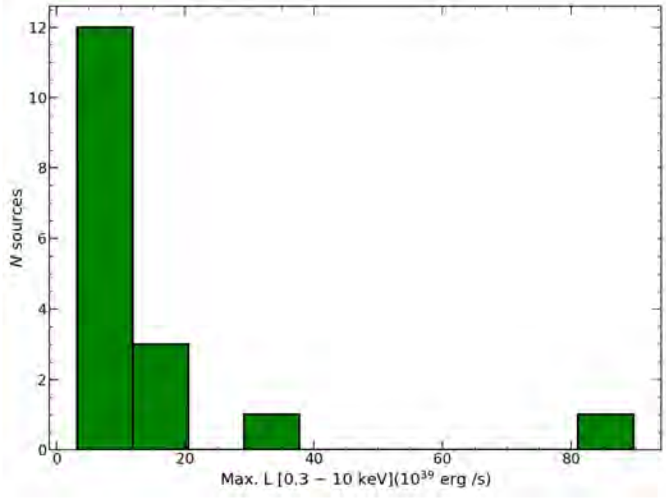

Figure 5.5: Histogram of the maximum unabsorbed luminosity in the 0.3 – 10 keV band attained by each source considered in this work. A clear drop of sources with L≥ 2 × 10^{40} erg/s is seen.

5.1.3.3 Spectral transitions

We also present the temporal evolution of each individual source in the HLD in Figure 5.6, along with the unfolded spectra of some selected epochs. For this, we selected two to four clearly distinct spectral states based on the HLD in order to highlight the possible range of spectral variability of each source. When possible, we selected observations for which *NuSTAR* data are available so that the broadband variability can be observed. We caution that given the sparse monitoring offered by *XMM-Newton* and *Chandra* in some cases, care must be taken when looking at the source variations in the HLD. Arrows indicate the chronological order but in many cases we cannot guarantee that the source did not evolve differently between the epochs considered here.

5.1.3.4 Spectral evolution of the soft thermal component

Several authors have attempted to study the nature of the soft component in ULX spectra by investigating its evolution on the luminosity–temperature (L–T) plane (e.g. Kajava & Poutanen, 2009; Miller et al., 2013). However, these studies have frequently yielded contradictory results and thus there is still no consensus on its true nature. We therefore investigated the correlation of the bolometric luminosity of the cool `diskbb` component with its temperature. We did this by retrieving unabsorbed luminosities of the `diskbb` component in the 0.01 – 100 keV[5]. All fluxes are reported in Table 5.3. We did not attempt to derive any correlation for NGC 55 ULX1 and NGC 300 ULX1 because of the limited number of observations available for these sources.

We next assessed whether L-T are correlated by running a Spearman correlation test[6]. The results are reported in Table 5.4. Five of our sources show a strong positive L–T correlation (Spearman correlation ≥ 0.5 and a p-value of $\lesssim 0.05$). For these, we fitted a power law using the `python` routine *odr*[7], which takes into account both errors on x and y variables (see Figure 5.7 and Table 5.4 for the results). In order to investigate whether these correlations were driven by the degeneracy between $\mathrm{T_{soft}}$ and its normalisation, we derived 99% χ^2 confidence contours around the best-fit $\mathrm{T_{soft}}$ and its normalisation for those sources showing a positive L–T correlation. Given the extensive computational time required by the `steppar` command in XSPEC, we did this only for some selected epochs, ensuring that at least one was from the joint fit. The results are shown in Figure 5.8 for NGC 1313 X-1, Holmberg IX X-1, Holmberg II X-1, and NGC 5204 X-1, where we also overlaid the best-fit $\mathrm{T_{soft}}$ and normalisation from all epochs. In *all* cases where a positive L–T correlation is observed, including IC 342 X-1, which we did not show for brevity, a strong degeneracy between the T_{soft} and its normalisation is observed, highly correlated with the datapoints from the individual observations, indicating that the L–T correlations are simply due to a degeneracy between these two parameters.

For M81 X-6, while the correlation test could indicate a positive correlation, visual inspection of the data clearly reveals that there is no apparent trend (see Figure 5.9). We recall that the Spearman's test coefficient does not take into account errors on the parameters and hence these values need to be treated with caution. In fact, the fit with the power law yields a large error on the index $\alpha = 2.5 \pm 2.0$ (90% confidence level), while the normalisation is consistent with zero.

5.1.3.5 Spectral evolution of the hard thermal component

Similarly, we studied the hard thermal component evolution in the L–T plane. In cases where we employed the `simpl` model on this component, we retrieved the *intrinsic* flux of the hard `diskbb` using `cflux` as `simpl`$\otimes$`cflux`$\otimes$`diskbb` and freezing the normalisation of the `diskbb`. Derived fluxes are presented in Table 5.3 and the results from the L–T correlation are shown in Table 5.5.

Most of the sources show no clear correlation in the hard thermal component. The only exception is M83 ULX1, which shows a strong positive correlation (Spearman correlation of 0.94 with a p-value = 0.005, see Figure 5.10). We again computed χ^2 contours around the best-fit temperature and normalisation for some selected epochs and overlaid the results from the spectral fitting on them as shown in Figure 5.10. In this case, it seems that the degeneracy between these two parameters is not driving the existing correlation.

While NGC 6946 X-1 might seem positively correlated based on the Spearman test alone, examination of the data clearly reveals that there is an overall lack of strong variation of the hard component in most observations (see Figure 5.11). Furthermore, we note a certain bias in those observations for which we have not included the `simpl` model, as the temperature of the hard `diskbb` appears to be systematically higher, as the `diskbb` is pushed towards high energies because of the lack of an additional high-energy component.

5.1.4 Discussion

We examined the long-term spectral evolution of a sample of sources containing known PULXs and ULXs for which the accretor is unknown, in order to gain insight into their nature and the accretion processes driving their extreme luminosities. While our spectral fitting approach is phenomenological, we attempted to understand the nature of the soft and the hard components by means of L–T correlations. The positive L–T correlations for the soft component found in Section 5.1.3.4 are broadly consistent with previous results reported by Miller et al.

---

[5] For the jointly fitted data, this flux calculation is done taking into account errors associated with all tied parameters.

[6] `https://docs.scipy.org/doc/scipy-0.14.0/reference/generated/scipy.stats.spearmanr.html`

[7] https://docs.scipy.org/doc/scipy/reference/odr.html

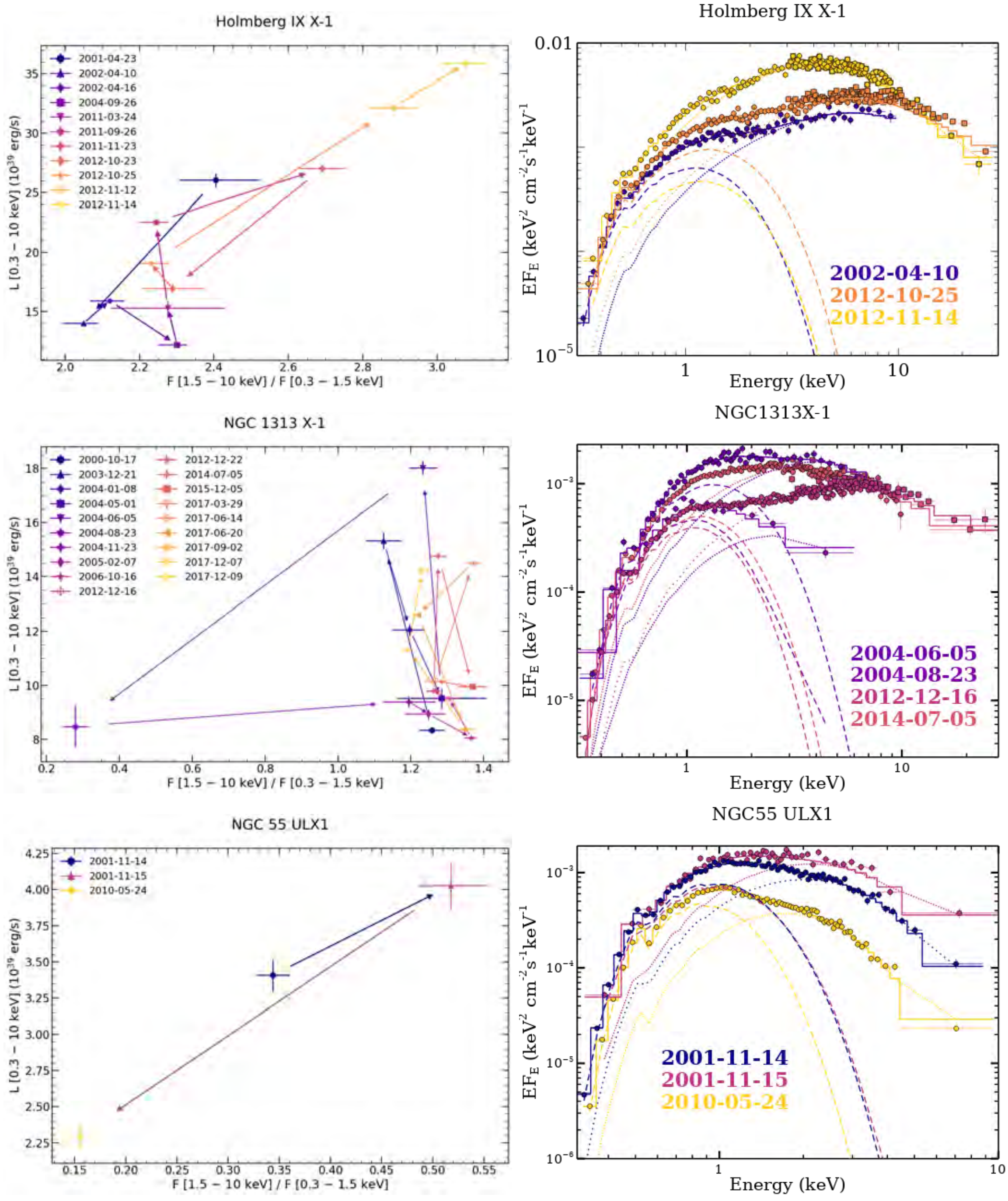

Figure 5.6: Left: Temporal tracks on the HLD. Filled coloured markers indicate fluxes obtained from *XMM-Newton* data, unfilled markers indicate fluxes obtained from joint *XMM-Newton-NuSTAR* data, and black-filled markers indicate fluxes obtained from *Chandra* data. The legend indicates the date of the epoch in each case. Right: Unfolded spectra for selected epochs in which the source has experienced strong changes, following the same colour-code as for the left panels. Selected epochs are indicated in the legend. For the EPIC data, only pn is shown (circles) or MOS1 if pn is not available (as triangles up). In cases where we have used *NuSTAR* data, FPMA is shown, represented as squares and with the same colour as pn. *Chandra* data are shown with downward-pointing triangles. The soft and hard `diskbb` model components are shown with a dashed line and dotted line respectively, while the total model is shown with a solid line. For epochs where the `simpl` model has been used see Table 5.2. Data have been rebinned for clarity.

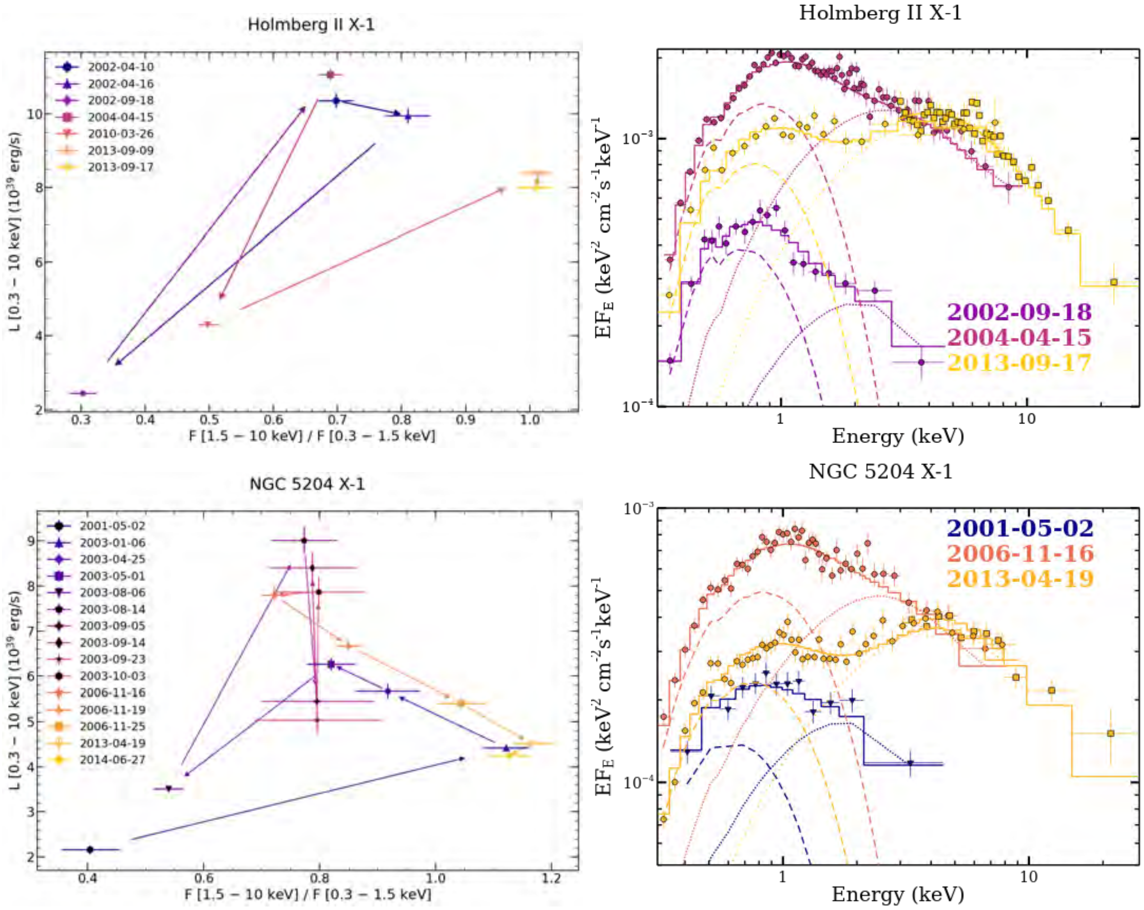

Figure 5.6: Continued

Table 5.4: Results of the L-T correlation for the soft thermal component. We quote the Spearman's rank correlation coefficient, the false-alarm probability (p-value) and the index (α) of the L$\propto T^{\alpha}$ relationship with its 90% confidence level uncertainty.

Source	Spearman	p-value	α
NGC 7793 P13	–0.13	0.73	-^{a}
NGC 5907 ULX1	0.57	0.14	-^{a}
NGC 5408 X-1	–0.14	0.65	-^{a}
Circinus ULX5	0.32	0.5	-^{a}
HoIX X-1	0.87	0.0005	1.31 ± 0.14
M81 X-6	0.65	0.04	-^{b}
IC342 X-1	0.67	0.05	1.27±0.28
NGC 1313 X-1	0.68	0.001	1.69 ± 0.13
NGC 5204 X-1	0.80	0.00001	3.55 ± 0.43
Ho II X-1	0.96	0.0005	3.26± 0.39
NGC 1313 X-2	0.25	0.21	-^{a}
NGC 6946 X-1	0.45	0.26	-^{a}
M83 ULX1	0.71	0.11	-^{a}
M51 ULX-7	–0.22	0.52	-^{a}
M51 ULX-8	0.54	0.108	-^{a}

Notes. $^{(a)}$ Non-correlated source. $^{(b)}$ Not considered correlated due to uncertainties.

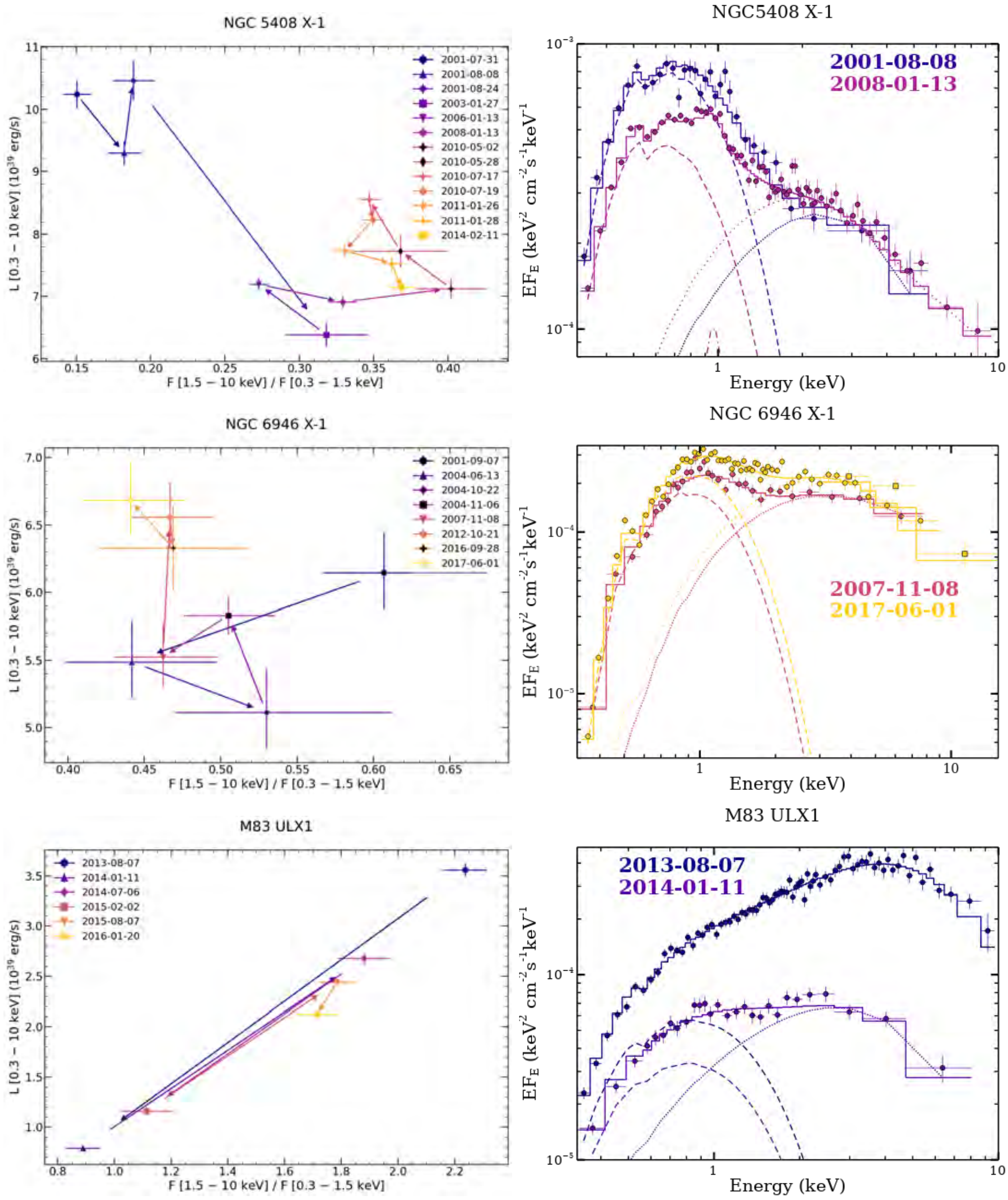

Figure 5.6: Continued

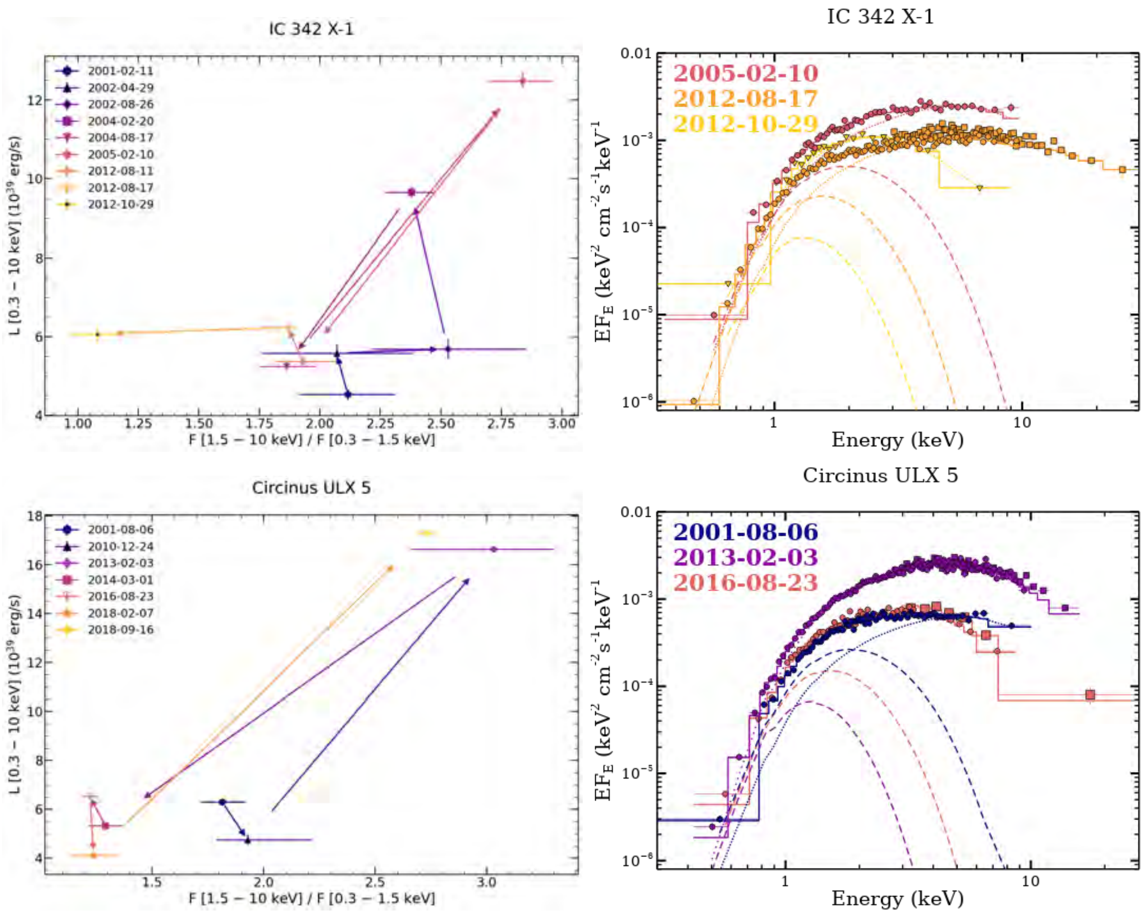

Figure 5.6: Continued

Table 5.5: Results of the L–T correlation for the hard thermal component. Columns as per Table 5.4.

Source	Spearman	p-value	α
NGC 7793 P13	0.45	0.19	-[a]
NGC 5907 ULX1	0.52	0.18	-[a]
NGC 5408 X-1	0.49	0.01	-[a]
Circinus ULX5	–0.46	0.29	-[a]
Ho IX X-1	0.31	0.38	-[a]
M81 X-6	–0.08	0.83	-[a]
IC342 X-1	0.05	0.91	-[a]
NGC 1313 X-1	0.3	0.2	-[a]
NGC 5204 X-1	0.15	0.58	-[a]
Ho II X-1	–0.37	0.47	-[a]
NGC 1313 X-2	–0.07	0.73	-[a]
NGC 6946 X-1	0.90	0.002	-[b]
M83 ULX1	0.94	0.005	4.36 ± 0.70
M51 ULX-7	–0.12	0.75	-[a]
M51 ULX-8	–0.17	0.67	-[a]

Notes. (a) Non-correlated source. (b) Not considered correlated due to uncertainties (see text for details)

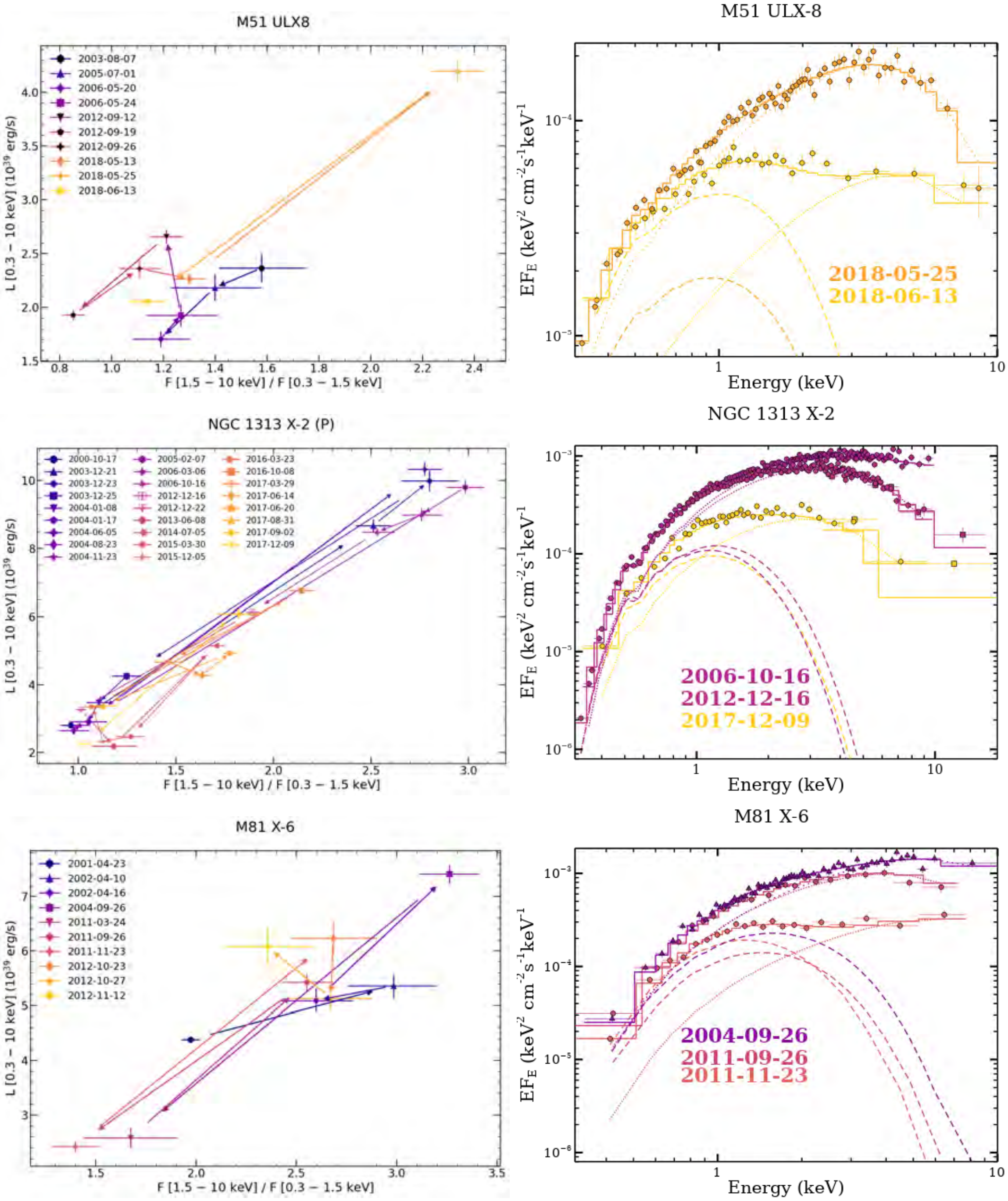

Figure 5.6: Continued

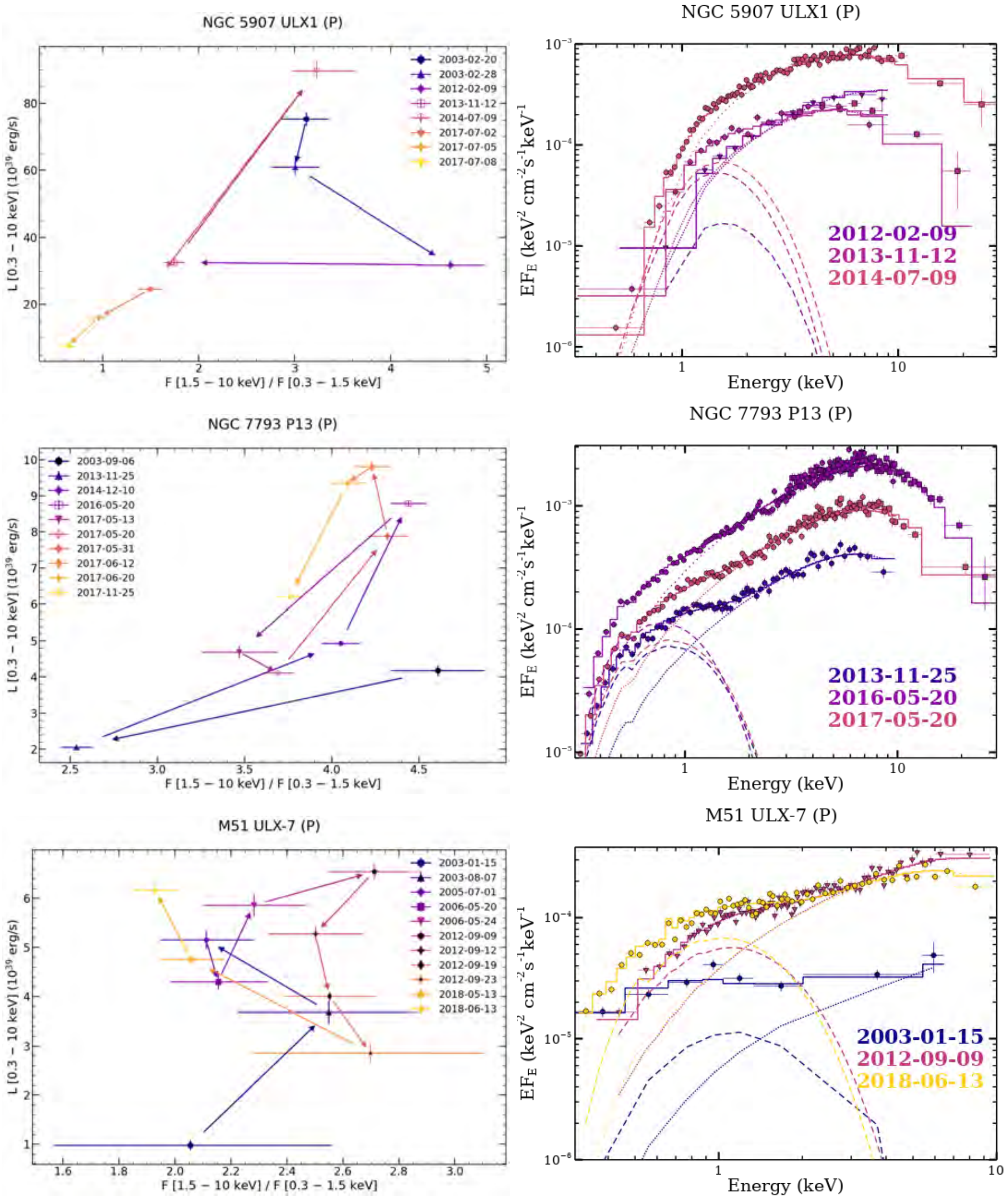

Figure 5.6: Continued

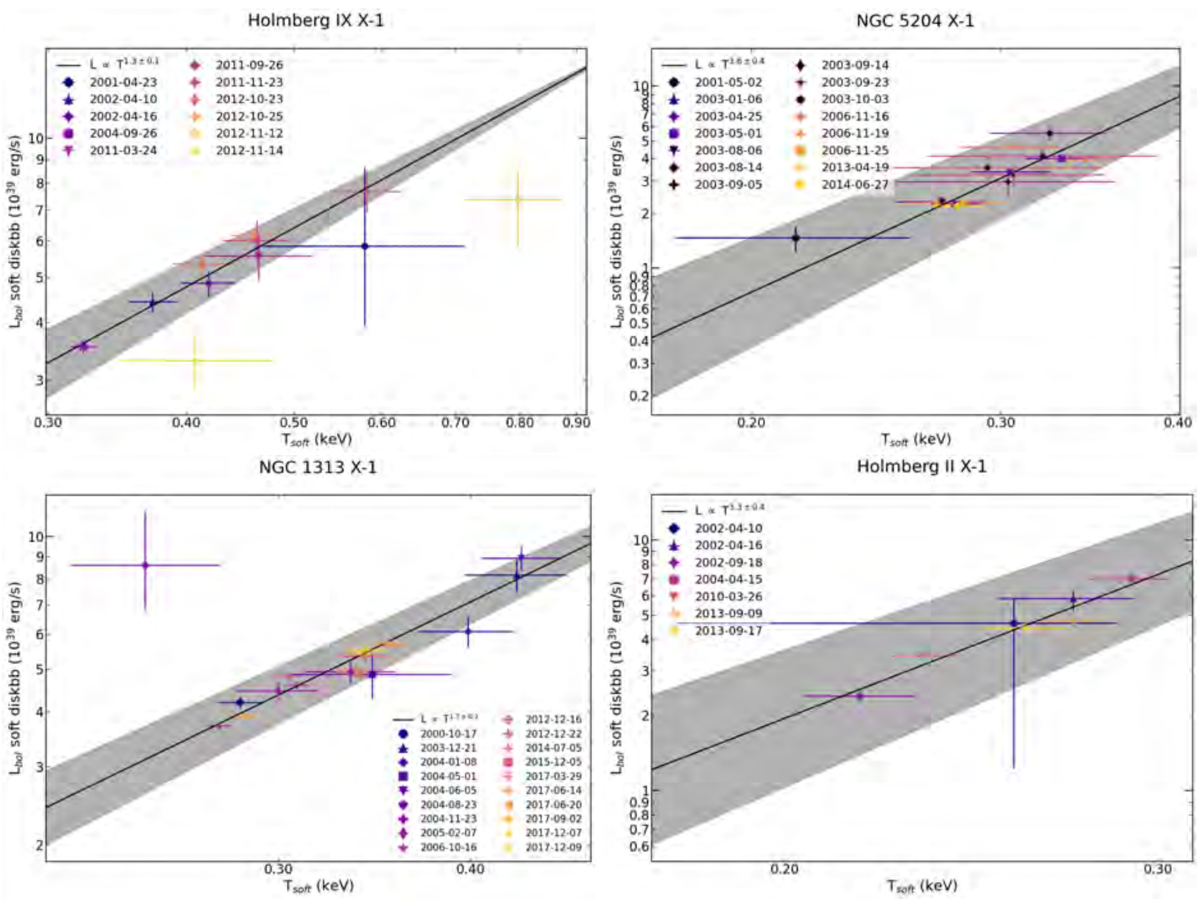

Figure 5.7: Examples of sources showing a positive correlation between the soft `diskbb` component unabsorbed bolometric luminosity and its temperature. The black line shows the best-fit power law with grey shaded areas indicating the 90% confidence interval on the exponent. Symbols are coloured as per Figure 5.6. The data have been fitted with the model `tbabs`⊗ `tbabs`⊗ (`diskbb` + `simpl` ⊗`diskbb` or `tbabs`⊗ `tbabs`⊗ (`diskbb` + `diskbb`) (see text for details).

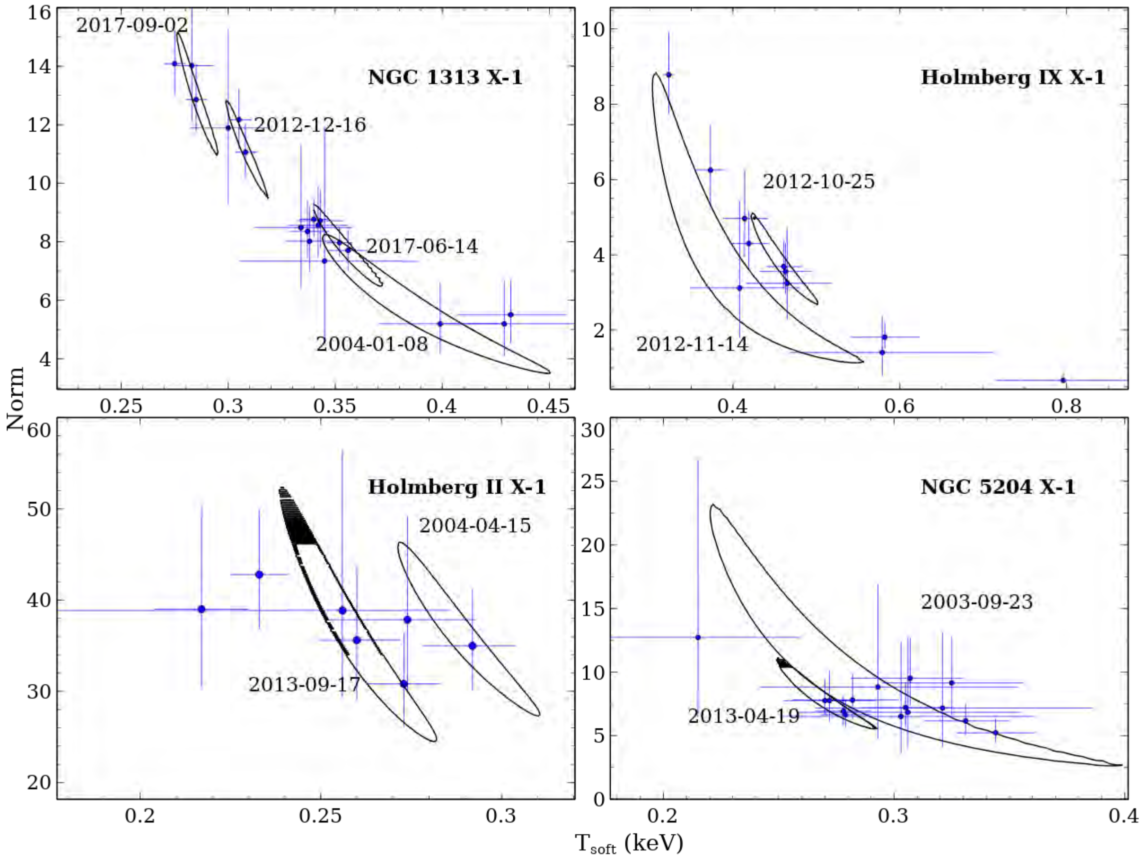

Figure 5.8: 99% χ^2 contours (solid black lines) between T$_{\rm soft}$ and its normalisation for sources showing a positive L–T correlation. For each source, two to four different epochs are represented with the epoch indicated next to the contour. A clear anti-correlation is seen in all cases that closely follows the best-fit values from all the epochs (blue datapoints, 90% confidence level error bars), which indicates that the L–T positive correlation is due to the degeneracy between these two parameters. For the sake of readability, we have ignored epoch 2004-06-05 in the panel of NGC 1313 X-1 as it had a much higher normalisation ($\sim$ 51) compared to the other observations.

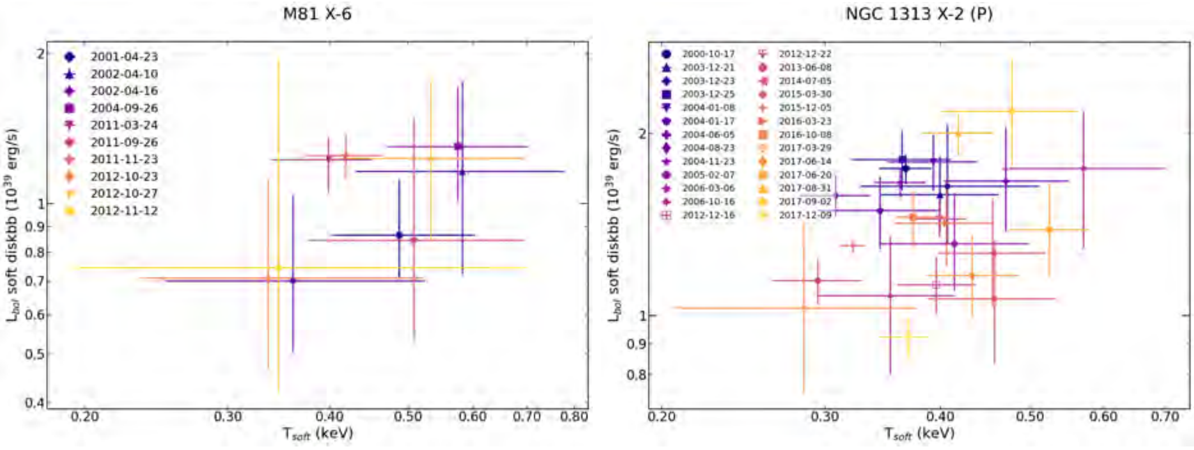

Figure 5.9: As for Figure 5.7 but for sources showing no correlation between the soft `diskbb` bolometric luminosity and its temperature.

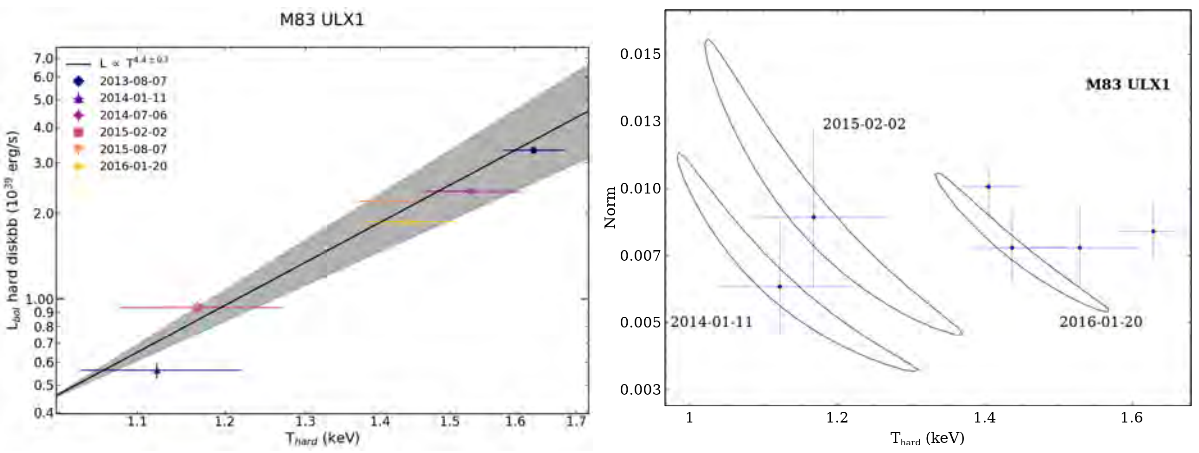

Figure 5.10: Left: As for Figure 5.7 but for M83 ULX1 for the hard `diskbb`. Right: As for Figure 5.8 but for the countours around the best-fit T_{hard} and its normalisation for three selected epochs of M83 ULX1. The degeneracy between these two parameters can be ruled out as the cause of the positive L–T correlation.

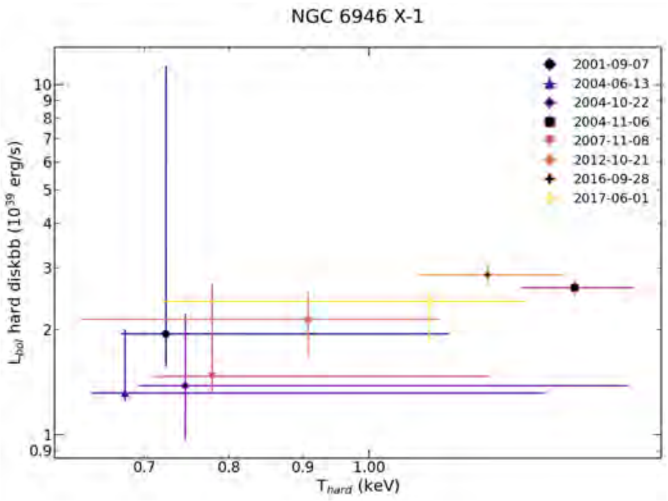

Figure 5.11: Bolometric luminosity of the hard `diskbb` component as a function of its temperature for NGC 6946 X-1. Because of the uncertainties associated with the parameters, we do not consider these two quantities to be correlated (see text for details). Symbols as per Figure 5.6.

(2013), who studied a similar sample of sources and also assumed a constant absorption column, albeit using a different model based on an accretion disk whose photons are Compton-up scattered by an optically thick corona of hot ($T_\mathrm{e} > 2$ keV) electrons. Similar correlations were also reported for NGC 5204 X-1 and Holmberg II X-1 by Feng & Kaaret (2009) using an absorbed `diskbb` and a power law. These correlations have frequently been used to argue in favour of an accretion disk as the nature of the soft component in ULXs. However, our analysis reveals that these are driven by the existing degeneracy (see Figure 5.8) between the temperature of the soft component and its normalisation and therefore these relationships cannot be used reliably to support this scenario. Indeed, it has been shown that depending on the assumption of the underlying model, the correlation can disappear entirely (see e.g. Luangtip et al. (2016); Walton et al. (2020); see also Gonçalves & Soria (2006) for a discussion on the weaknesses of associating the soft component with an accretion disk). Nevertheless, these correlations might be useful to identify sources evolving in a similar fashion.

Conversely, the positive L–T correlation found for the hard thermal component of M83 ULX1 might have a physical origin, as we argue in Section 5.1.4.6, given that this correlation is not driven by the existing degeneracy between the parameters (see Figure 5.10).

Similarly, Kajava & Poutanen (2009) used the found negative L–T correlation for the soft component to argue in favour of an outflow as the nature of the soft component. However, this result was likely artificially created by employing a power law for the high-energy emission while leaving the absorption column free to vary. We therefore suggest that the beaming formalism derived by King (2009) using the results from Kajava & Poutanen (2009), linking the mass-transfer rate ($\dot{m}_0$) with the beaming factor (b) for super-Eddington accretion onto BHs or weakly magnetised NSs, should be revisited in view of these new results. Overall, our study suggests that given the limitation from using phenomenological models to describe the ULX continuum, the observed changes in the best-fit spectral parameters may not be the most appropriate way to build a physical picture for our sources. For this reason, most of our discussion will be based on the variability observed in terms of luminosity and hardness ratios (see Figures 5.4 and 5.6).

Figures 5.4 and 5.5 show that most sources seem to have a maximum luminosity of roughly 2×10^{40} erg/s. M51 ULX-7 and M82 X-2 (the other PULX not analysed in this work) also reach luminosities of a few $\times\, 10^{40}$ erg/s (Brightman et al., 2016a, 2020a). While the sample presented here is rather small in a statistical sense, it confers the advantage that we can take into account the long-term variability of each source; it is also free of contaminants and the absorption column has been carefully estimated. On this basis, our work seems to support larger sample studies (Swartz et al., 2011), where a possible cutoff at around 2×10^{40} erg/s was observed in the luminosity function of a sample of 107 ULX candidates. Mineo et al. (2012) showed that ULXs seem to extend the X-ray luminosity function of HMXBs up to a possible energy cutoff also at around 2×10^{40} erg/s, supporting the idea that ULXs are an evolutionary stage of HMXBs. Thus, ULXs might be related to systems where the companion star expands and starts to fill its Roche Lobe as suggested by King & Lasota (2020). As NS accretors are more numerous among HMXBs (e.g. Casares et al., 2017), it is possible that a substantial fraction of ULXs with $\mathrm{L_x} \sim 10^{39-41}$ erg/s could host a NS. However, we stress that given the limited sample studied here, we may be running into small numbers when distinguishing a cutoff distribution from a power-law one (Walton et al., 2011).

A luminosity cutoff around 2×10^{40} erg/s would be consistent with the maximum accretion luminosity NSs can attain according to Mushtukov et al. (2015). These latter authors considered the accretion column model proposed by Basko & Sunyaev (1976) and the reduction of the electron scattering cross-section in the presence of high-magnetic fields that allows the Eddington limit to be overcome. Mushtukov et al. (2015) suggest that NSs could reach $\sim 10^{40}$ erg/s for a reasonable parameter space of magnetic fields and spin periods. Indeed, the hard component (the `diskbb` or the more complex `simpl⊗diskbb` when applicable) that we would associate with the accretion column (e.g. Walton et al., 2018a) reaches a maximum luminosity of $\sim 10^{40}$ erg/s in NGC 7793 P13, M51 ULX-7, and NGC 1313 X-2. However, the fact that we find a PULX (NGC 5907 ULX1) also above the break is problematic. The hard component is a factor of about eight above this theoretical value. It is possible that by assuming isotropic emission in our luminosity calculations, we may be overestimating the luminosity of the accretion column. We discuss this in more detail in Section 5.1.4.1.

On the other hand, general relativistic radiation magnetohydrodynamic (GRRMHD) numerical simulations of super-Eddington accretion onto BHs also predict saturation of the maximum luminosity with the mass-accretion rate (Narayan et al., 2017), as the models of these latter authors start to become radiatively inefficient above $\sim 10\ \dot{M}_\mathrm{Edd}$. Their simulations show that the observed luminosity saturates at 2×10^{40} erg/s for a 10 $\mathrm{M}_\odot$ BH viewed close to face-on, which might be supported by our observations.

The mass-transfer rate ($\dot{m}_0$) in ULXs is generally accepted to be super-Eddington, even if the sustainability of such a process at such extremes over long timescales (sometimes over several decades) has still to be understood. Models put forward to explain the emission of super-Eddington accretion onto BHs predict that as the mass-transfer rate increases beyond the classical Eddington limit, a radiatively driven outflow will be launched from within the spherisation radius (R_sph), the radius at which the disk reaches the local Eddington limit (Shakura & Sunyaev, 1973; Poutanen et al., 2007). The outflow leaves an optically thin funnel around the rotational axis of the compact object, so that at low inclinations we see a hard spectrum dominated by the inner parts of the disk (Hard ULXs: Sutton et al., 2013). At higher inclinations the outflow becomes optically thick to Thomson scattering (Poutanen et al., 2007) and thus an observer at such inclinations should see a softer and fainter spectrum (soft ULXs: Sutton et al., 2013) as most of the emission will be Compton down-scattered in the wind before reaching the observer (Middleton et al., 2015a; Kawashima et al., 2012). A corollary of this scenario is that as the wind funnel narrows as the mass-accretion rate increases (King, 2009; Kawashima et al., 2012) and the wind starts to enter our line of sight, the contribution from the soft component will dominate the emission, as the wind starts to down-scatter out of the line-of-sight part of the hard emission. Therefore, a source with a hard ULX aspect could shift to a soft ULX aspect under certain conditions. A similar effect can occur if the source precesses (Abolmasov et al., 2009; Middleton et al., 2015a), but we may see differences in the long-term variability between these two scenarios. The increase in the mass-accretion is also expected to increase the Thomson optical thickness of the gas within the funnel, preventing high-energy photons from escaping to the observer without being scattered (Narayan et al., 2017; Kawashima et al., 2012). It is argued that, in extreme cases, either due to a high-mass accretion rate or/and higher inclination angle, a source may appear as a super-soft ultraluminous source (ULS) (Urquhart & Soria, 2016), where most of the emission comes from the wind photosphere.

One key observational property of the presence of the funnel-like structure created by strong outflows is highly anisotropic emission. While a relationship between anisotropy and super-Eddington mass-transfer rates may be a natural consequence of super-Eddington accretion onto BHs (King, 2009), NS may have means to circumnavigate this relationship. Crucially, in the presence of a strong magnetic field, the disk might be truncated before radiation pressure starts to be sufficient to inflate the disk and drive strong outflows (e.g. Chashkina et al., 2019). This occurs when the magnetospheric radius, given by

$$R_{\mathrm{m}} = \xi \left(\frac{R_{\mathrm{NS}}^{12} B^4}{2GM_{\mathrm{NS}}\dot{M}^2} \right)^{1/7}, \tag{5.1}$$

where $\mathrm{R_{NS}}$ is the radius of the NS, B is its magnetic field, $\mathrm{M_{NS}}$ is the mass of the NS, $\dot{M}$ is the mass accretion rate at $\mathrm{R_m}$, and ξ is a dimensionless parameter that takes into account the geometry of the accretion flow and is usually assumed to be 0.5 for an accretion disk (Ghosh et al., 1977), is larger than the spherisation radius (R_{sph}). R_{sph} in turn has a linear dependence on $\dot{m}_0$. This offers a means for a NS to be fed at high-mass transfer rates, while largely reducing anisotropy. On the other hand, we may expect that for weakly magnetised NSs, the disk becomes super-critical given the dependency of R_{m} on B. In this case, the emission will be collimated by the outflow in a similar fashion to super-critically accreting BHs (e.g. King et al., 2017; Takahashi & Ohsuga, 2017). Additionally, we may expect a NS with strong outflows to appear softer, as outflows will Compton down-scatter the emission from the accretion column.

We can therefore make use of the long-term variability observed in the HLD to discuss which scenario best describes the variability observed in each source: super-Eddington accretion onto BHs, weakly magnetised NSs, or highly magnetised NSs. At the same time, the wealth of data analysed in this work allows us to identify groups of sources showing common evolution and similar spectral states, while identifying new NS-ULX candidates based on their similarity with the PULXs. Given that our analysis focuses on discussing the spectral transitions observed in the HLD (see Figure 5.6), our study is less constraining for NGC 6946 X-1 and NGC 5408 X-1[8], given the lack of marked spectral states. We therefore do not attempt to offer any interpretation for these two sources.

Finally, a common characteristic of the PULXs seems to be a hard spectrum accompanied with high levels of variability at high energies ($\gtrsim$ 6 keV; see last four sources in Figure 5.6 and also Figure 1 from Pintore et al., 2017). On this basis, we argue that M81 X-6 constitutes the best NS-ULX candidate from our sample, given its harder spectrum *and* its high spectral variability at high energies as we discuss in Section 5.1.4.3. This high-energy component is likely associated with emission from the accretion column in the case of PULXs (Walton et al., 2018b,c) and may offer means to distinguish NS- and BH-ULXs (which we discuss in Section 5.1.4.5). While IC 342 X-1 and Circinus ULX5 also show a hard spectrum with high levels of variability at high energies, they both show a soft and dim state that we argue is akin to that seen in NGC 1313 X-1, a much softer source with relatively stable high-energy emission (see Figure 5.6), and therefore we discuss them in Section 5.1.4.4.1. Nevertheless, we stress that the spectral similarity across the sample is undeniable as also noticed in previous studies (e.g. Pintore et al., 2017; Walton et al., 2018c).

5.1.4.1 Pulsating ultraluminous X-ray sources

Remarkably, our analysis shows (Figure 5.4) that PULXs are among the hardest sources in our sample, something also noted by Pintore et al. (2017) employing a colour-colour diagram. Interestingly, PULXs with higher pulse fractions, such as for example NGC 7793 P13 (PF∼20%; Israel et al., 2017b), M51 ULX-7 (PF∼12%; Rodríguez-Castillo et al., 2020), and NGC 300 ULX1 (PF∼50%; Carpano et al., 2018), tend to appear harder (see Figure 5.4) while the softest PULX in our sample, NGC 1313 X-2, has the lowest pulse fraction (PF∼5% Sathyaprakash et al., 2019). Figure 5.6 shows that harder PULXs show little variability in the HLD (see the case of NGC 7793 P13 and M51 ULX-7[9]), while in contrast NGC 1313 X-2 shows strong changes in hardness by a factor of about three, without entering into the propeller regime. Below, we discuss whether these differences in the long-term evolution could be explained by the different interplay between R_{m} and R_{sph}. We note that in the super-Eddington regime, the interaction between the magnetic field and the disk is likely to be more complex than as predicted by Equation 5.1 as radiation pressure can dominate over the gas ram pressure (Takahashi & Ohsuga, 2017; Chashkina et al.,

---

[8] We note that the increase in luminosity of NGC 5408 X-1 in 2001 is less certain given the short exposure of the 2001 observations and our assumption of constant n_{H}.

[9] We note that epochs 2003-01-15 and 2013-11-25 of NGC 7793 P13 and M51 ULX-7, where the sources are found in a softer and dimmer state, are likely associated with the sources resuming from the propeller regime.

2019) but for the qualitative picture discussed here we neglect these facts. For NGC 300 ULX1, given the limited number of observations, we cannot offer a detailed discussion as for the other sources and therefore we do not consider this source further.

NGC 1313 X-2: $R_{\rm m} < R_{\rm sph}$ – This source shows a strong bi-modal behaviour in the HLD (see Figure 5.6 and also Feng & Kaaret, 2006; Pintore & Zampieri, 2012) that is likely associated with the 158-day quasi-periodicity reported by Weng & Feng (2018) using *Swift*-XRT data, although an association is not straightforward because several periodicities are found in the periodogram presented by the authors. Our analysis reveals that this bi-modal behaviour is driven by a highly variable hard component while the soft emission is rather stable (the soft `diskbb` varies by a factor $\lesssim 2$ in luminosity while the hard component luminosity varies by a factor $\lesssim 5$, see Figure 5.9). This bi-modal behaviour is confirmed by *Swift*-XRT long-term monitoring (Weng & Feng, 2018).

This variability is unlikely to be produced by the propeller effect, where the centrifugal barrier of the magnetosphere prevents further infalling of gas onto the NS (Illarionov & Sunyaev, 1975), because for a period of $\sim$ 1.47 s (Sathyaprakash et al., 2019), we should expect a drop in luminosity by a factor of $\sim$ 220 (see for instance equation 5 from Tsygankov et al., 2016b) assuming a NS radius of 10 km and a mass of 1.4 $M_\odot$, whereas the observed drop in luminosity from brightest to dimmest is only about a factor of five (using the luminosities in the 0.3 – 10 keV band from epochs 2006-03-06 and 2013-06-08). Instead, the absence of transitions to the propeller regime can be used to set constraints on the maximum magnetic field of the source, because we require that the magnetospheric radius is always smaller than the co-rotation radius, the radius at which the Keplerian disk velocity is equal to the rotation of the NS. We therefore require that at the minimum luminosity observed in the source, $R_{\rm m} < R_{\rm C}$. We can rearrange equation (37) from Mushtukov et al. (2015) to derive an upper limit on the magnetic field strength:

$$B_{12} \lesssim 3.8 \times \xi^{-7/4} m^{1/3} R_6^{-5/2} P^{7/6} L_{intr}^{1/2}, \tag{5.2}$$

where L_{intr} is the minimum intrinsic luminosity in units of 10^{39} erg/s, B_{12} is the magnetic field in units of 10^{12} G, R_6 is the NS radius in units of 10^6 cm, m is the NS mass in $M_\odot$, P is the period in seconds, and ξ is the same dimensionless parameter as for Equation 5.1 which we take again to be 0.5. We can express the intrinsic luminosity in terms of the observed luminosity taking into account a beaming factor (b) (e.g. King & Lasota, 2020) so that $L_{\rm intr} = b\,L_{\rm observed}$ with $b \leq 1$. Setting $L_{\rm observed} = 2.2 \pm 0.1$ (from epoch 2013-06-08), $R_6 = 1$, $m = 1.4$, and $P = 1.47$ s we obtain an upper limit on the magnetic field of $B = (b^{1/2} 33.0 \pm 0.7) \times 10^{12}$ G. This suggests that we can rule out extreme magnetic fields ($B \geq 10^{13}$ G) for moderate values of b ($\lesssim 0.1$).

Therefore, the hardening of the source with luminosity might instead support a scenario in which a conical outflow from a supercritical disk imprints highly anisotropic emission. Changes in the viewing angle due to the source precession and a varying degree of down-scattering in the wind could therefore explain the variability of the source. For a discussion on possible mechanisms for precession in ULXs we refer the reader to Vasilopoulos et al. (2020a). The stability of the soft component and the fact that the changes in HR and luminosity are likely driven by a super-orbital period support the hypothesis that changes in the mass-accretion rate are not the main source of variability. Additionally, the presence of strong outflows may be supported by the residuals observed at soft energies around 1 keV (see Figure 5.12) in the epoch with the longest exposure (2017-06-20), reminiscent of those seen in NGC 5408 X-1 and NGC 55 ULX 1 (Middleton et al., 2014; Pinto et al., 2016, 2017).

Overall the variability of the source and its low pulse-fraction ($\sim$ 5%) support a scenario in which NGC 1313 X-2 is a weakly magnetised NS, in which $R_{\rm sph} > R_{\rm m}$ and therefore outflows and precession cause the emission to be highly anisotropic. This is also supported by the recent ray tracing Monte-Carlo simulations of Mushtukov et al. (2021), showing that larger scale-height flows lead to lower pulse-fraction due to the increased number of scatterings.

NGC 7793 P13 and *M51 ULX-7*: $R_{\rm m} > R_{\rm sph}$ – Conversely, both the long-term evolution of NGC 7793 P13 and M51 ULX-7 show little variability in terms of hardness ratio, although they are also associated with super-orbital periodicities of 66.9 days (see Fürst et al., 2018, Figure 5) in the case of NGC 7793P13 and 39 days in the case of M51 ULX-7 (Vasilopoulos et al., 2020a). Indeed, long-term *Swift*-XRT monitoring shows no clear bi-modal behaviour (Weng & Feng, 2018) in a hardness–intensity diagram in the case of NGC 7793 P13. Both sources also show a very hot hard component ($T_{\rm hard} \sim 3$ keV), although it is unclear whether the absence of a third, high-energy component may have boosted the inferred temperature. In a similar way as for NGC 1313 X-2, most of the luminosity variability is again seen in the hard component (the soft component varies by a factor of about two and the hard component by a factor of about five). However, for NGC 7793 P13 and M51 ULX-7, the soft component does seem to brighten with source luminosity.

The lack of HR variability might indicate that anisotropic emission caused by the wind funnel is not important in these sources. As stated before, in the presence of a strong magnetic field, the disk might be truncated before radiation pressure starts to be sufficient to inflate the disk and drive the strong outflow. Assuming the geometry of the accretion flow outside $R_{\rm m}$ is similar to that of supercritically accreting BHs, our soft `diskbb` could represent the emission from the outer regions of the accretion disk, with partial reprocessing by the wind if $R_{\rm m} > R_{\rm sph}$ (Kitaki et al., 2017). If we consider this model component to provide a rough estimate of the size of this emitting region, a larger emitting area compared to NGC 1313 X-2 —for which we have argued that outflows are important— could indicate that the disk is being truncated further from the accretor in the case of NGC 7793 P13 and M51 ULX-7. To illustrate this, we compute the mean radius of the inner disk given by the soft `diskbb` normalisation (N) from all epochs. Using

$$R_{\rm in} = \sqrt{N/\cos i} \times D_{10} \times f_{\rm col}^2, \tag{5.3}$$

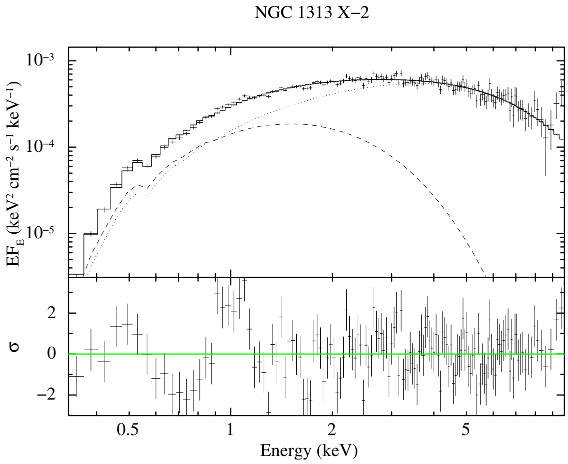

Figure 5.12: Unfolded spectra of NGC 1313 X-2 of epoch 2017-06-20 (only pn is shown for clarity) fitted with an absorbed dual thermal component. The soft and hard `diskbb` components are shown with the dashed and dotted lines respectively, while the total model is shown with a solid line. Strong residuals are seen at soft energies at around 1 keV.

where i is the inclination of the system, D_{10} is its distance in units of 10 kpc, and $f_{\rm col}$ is the colour correction factor (Shimura & Takahara, 1995), which we take as 1.8 (e.g. Gierliński & Done, 2004) throughout this paper, gives $1637^{+106}_{-66}(\cos i)^{-1/2}$ km, 1975^{+197}_{-134}, and $2257^{+125}_{-104}(\cos i)^{-1/2}$ km for NGC 1313 X-2, M51 ULX-7, and NGC 7793 P13, respectively. Naively assuming this radius gives a rough estimate of the size of the magnetospheric radius ($R_{\rm m}$), it may indicate a higher mass-accretion rate for NGC 1313 X-2 (and/or a lower magnetic field strength) and thus a scenario in which the disk becomes thick and outflows cause anisotropic emission. Instead, the larger radius of NGC 7793 P13 and M51 ULX-7 may suggest that either the mass-accretion rate is lower or the magnetic field strength is higher, which can result in the disk remaining geometrically thin (see also Chashkina et al., 2017) and therefore in reduced anisotropy. We note that these would support previous studies by Koliopanos et al. (2017), where the same relationships for $R_{\rm m}$ and $R_{\rm sph}$ were found for NGC 7793 P13 and NGC 1313 X-2 (see their Table 2 and 4).

Assuming the mass-accretion rate varies within a similar range in the three sources, a stronger magnetic field in NGC 7793 P13 and M51 ULX-7 is also supported by the fact both sources undergo periods of inactivity to $\lesssim 10^{38}$ erg/s, likely associated with the propeller regime (e.g. Fürst et al., 2016; Vasilopoulos et al., 2021), indicating that the condition $R_{\rm m} > R_{\rm C}$ is more easily achieved. Furthermore, the lower pulse-fraction of NGC 1313 X-2 compared to that of NGC 7793 P13 and M51 ULX-7 is consistent with less material reaching the magnetosphere and thus the accretion column, as a result of the mass loss in the disk. Therefore, the emission at high energies is not only intrinsically diminished but also down-scattered in the outflow (Mushtukov et al., 2021), which might explain why NGC 1313 X-2 is generally softer than NGC 7793 P13 and M51 ULX-7.

We therefore suggest that the magnetic field in NGC 7793 P13 and M51 ULX-7 is likely to be higher than that of NGC 1313 X-2, meaning that $R_{\rm m} > R_{\rm sph}$. The low degree of beaming and high magnetic field implied by this solution are in agreement with previous magnetic field estimates (Vasilopoulos et al., 2020a; Rodríguez-Castillo et al., 2020) that suggested a magnetic field of $\sim 10^{13}$ G in M51 ULX-7.

NGC 5907 ULX1: $R_{\rm m} \sim R_{\rm sph}$ – Contrary to the rest of PULXs in our sample, the luminosity of NGC 5907 ULX1 clearly exceeds 10^{40} erg/s. The variability between the observations clustered at $L_X \sim (6–8) \times 10^{40}$ erg/s (epochs 2003 and 2014) and epoch 2012 was shown to be associated with different phases of the 78-day super-orbital period (Walton et al., 2016a) of the source by Fürst et al. (2017). This suggests that these changes are not due to a change in the mass-accretion rate and instead suggests changes in the viewing angle as the sources precesses. It has been speculated that the extreme luminosity of the source could be due to a high degree of beaming (e.g. King et al., 2017; King & Lasota, 2019), in which the super-orbital modulation was due to a conical outflow beaming the emission into and out of our line of sight (e.g. Dauser et al., 2017). However, our Figure 5.6 shows that the source is harder when it becomes dimmer in epoch 2012-02-09 (see also Figure 3 from Sutton et al., 2013) compared to epochs in 2003 and 2014, and thus these changes associated with the super-orbital period may be hard to reconcile with changes imprinted by the precession of an outflowing cone, as we would expect a softer emission at low luminosities. This might imply that $R_{\rm sph} \leq R_{\rm m}$ is likely in the case of NGC 5907 ULX1.

We note that other mechanisms could also cause the luminosity to be overestimated under the assumption of isotropic emission. In reality, the emission from the accretion column is not expected to be emitted isotropically. Instead, radiation-hydrodynamic simulations of super-Eddington accretion onto magnetised NSs by Kawashima et al. (2016) show that the accretion column is expected to have a flat emission profile along its sides, as the emission is only able to escape through the lateral sides of the confined material within it. This naturally creates highly anisotropic emission and can cause the observed emission to be greatly in excess of the Eddington limit.

A high $\dot{m}_0$ is still likely required to produce the observed luminosities. This may require the presence of a strong magnetic field so that the disk is truncated roughly at the point where it becomes supercritical. Thus, as suggested previously (Walton et al., 2018c; King & Lasota, 2019), $R_{\mathrm{sph}} \sim R_{\mathrm{m}}$ seems a plausible condition to explain the high luminosity of NGC 5907 ULX1.

5.1.4.2 The non-pulsating NS: M51 ULX8

This source was identified as a NS through the identification of a possible cyclotron resonance feature (Brightman et al., 2018) [10]. We note that its position in the HLD (see Figure 5.4) may be consistent with a lack of pulsations (Brightman et al., 2018), as this source is markedly dimmer and softer than the overall PULX sample, and sources with higher pulse fractions tend to sit in the harder end of the diagram, as stated before. However, given the apparent lack of variability, it is hard to make a comparison between this source and other PULXs in our sample. Strong variability is only observed for M51 ULX8 in epoch 2018-05-25, where the hard component increased by a factor of two in luminosity. Its behaviour is somewhat similar to that of NGC 1313 X-2 and M81 X-6, the latter we argue is a good PULX candidate (see Section 5.1.4.3), although we lack enough observations of the source at higher luminosities to confirm this similarity. The soft component also shows little variability and no clear correlation, suggesting again a link between these three sources, which would favour a weakly magnetised NS in M51 ULX8 in agreement with the study presented by Middleton et al. (2019a). Should this be the case, then long-term monitoring of the source will be crucial to attempt to identify any quasi-periodicity similar to those seen in NGC 1313 X-2 and M81 X-6.

5.1.4.3 PULX candidates

M81 X-6 – As stated above, M81 X-6 constitutes our best NS-ULX candidate. The spectral evolution and the track in the HLD for this source are strikingly similar to those of NGC 1313 X-2 (Figure 5.6). Both sources transit back and forth from a soft (HR $\lesssim$ 1.5) and low-luminosity state ($\lesssim 4 \times 10^{39}$ erg/s) to a hard (HR $\sim$ 3) and brighter state. The similar temperature, luminosity range, and variability (or lack of it) of the soft component also suggests a link between these two sources. Instead, the variability is driven mostly by the hard component (the soft `diskbb` changes by a factor $\lesssim 2$ in luminosity while the hard component luminosity varies by a factor $\lesssim 5$ in both sources). Furthermore, the variability of M81 X-6 is also likely associated with a 115-day quasi-periodicity (Weng & Feng, 2018) compatible with the one seen in NGC 1313 X-2. Given the similarity of these two sources, we suggest that M81 X-6 also harbours a weakly magnetised NS, meaning that the presence of strong outflows along with source precession may account for its spectral variability.

Prompted by this similarity, we searched for coherent pulsations in M81 X-6 using the code HENDRICS (Bachetti, 2018) which is based on the publicly available Python library Stingray (Huppenkothen et al., 2019). Unfortunately, all but one of the observations have less than 5000 counts in pn, and typically 10000 counts seem to be required in order to detect pulsations (Rodríguez-Castillo et al., 2020). We therefore searched in the observation with the longest exposure ($\sim$ 73 ks in pn, see Table 5.1 and Figure 5.6 epoch 2001-04-23, HR $\sim$ 2, $L \sim 4 \times 10^{39}$ erg/s) suitable for pulse searches, assuming M81 X-6 has a period and period derivative similar to the other PULXs. We used the *Chandra* coordinates given by Swartz et al. (2003) to extract barycentred corrected events in the 0.2 – 12 keV band. We ran HENDRICS on the unbinned event file searching for coherent pulsations in the 0.2 – 8 Hz range based on previous PULX detections and using the Z^2 statistic (Buccheri et al., 1983) suitable for sinusoidal pulses. The search was performed using the option *fast*, which optimises the search in the f–$\dot{f}$ space and reduces the computational time tenfold compared to a classical search. We found no detection above the 3σ level. We ran the same search in the four longest Good Time Interval (GTI) intervals, ranging from 20 ks to 40 ks, as pulsations in PULXs have been shown to vary during the course of an observation (e.g. Bachetti et al., 2020), but again we did not find any significant detections. Overall there is no peak that can be robustly identified as several peaks with similar Z^2 power are found, well below the 3σ level. We also looked in the pn data of the individual observations with shorter exposures, but found no significant detections. We performed a last search looking into the 0.02 – 0.2 Hz range to look for longer periods as those seen in NGC 300 ULX1 (see e.g. Vasilopoulos et al., 2018), with similar results. This could indicate that pulsations in this source are as elusive and faint as those found in NGC 1313 X-2 (Sathyaprakash et al., 2019) and that deep exposures with the source on-axis or deeper searches correcting for the orbital parameters will be required to detect pulsations.

Alternatively, the spectral state of the source may play a role in the detectability of the pulsations. Considering the case of NGC 1313 X-2, the epochs when pulsations were detected by Sathyaprakash et al. (2019) are 2017-09-02 and 2017-12-09 (i.e. the last two epochs in Figure 5.6). The authors also found that the pulse fraction (and hardness, as shown in this work, Figure 5.4) decreases with the source luminosity. As argued before, we understand the hardening of the source as a decrease in the viewing angle as the system precesses. Considering the pulse-fraction calculations for super-critical accretion columns proposed by Inoue et al. (2020), this might imply that the angle between the rotational axis and the magnetic field axis (Θ_B) is greater than the angle between the observer's line of sight and the rotational axis (Θ_{obs}; e.g. $\Theta_B > 30^\circ$ and $\Theta_{\mathrm{obs}} < 30^\circ$, see Figure 5 from Inoue et al., 2020). Assuming the same applies to M81-X6, this could imply that pulsations are more likely to be found in softer and dimmer states (HR $\sim$ 1.5, L $\sim 2.5 \times 10^{39}$ erg/s) where we expect the pulse fraction to be higher.

---

[10] *Chandra* obs id 13813, where the putative line was identified by Brightman et al. (2018) was not considered in this work due to a certain degree of pile-up affecting the observation.

If, instead, the dilution of the pulsed emission is mainly due to a stochastic process such as multiple scatterings through the wind, then it may be possible to find a PULX in similar spectral states, with and without pulsations. Nevertheless, studying the dependence of the appearance of pulsations on the source spectral states seems a promising tool to put constraints on the accretion flow geometry in PULXs.

5.1.4.4 Geometrical effects of a supercritical funnel

Several of the softer sources for which the accretor is unknown show a common pattern in their long-term evolution: three distinct spectral states, two of them at similar low luminosities but distinct hardness and a third one at a higher luminosity (see e.g. NGC 1313 X-1, Circinus ULX5 and IC342 X-1 in Figure 5.6). Two other sources that also show three marked spectral states are Holmberg II X-1 and NGC 5204 X-1, although the luminosity of the dimmer states differs in this case by a factor of between approximately two and four. The difference in luminosity between one of the two dim states and the bright state might be naturally explained by changes in $\dot{m}_0$. However, the presence of an additional dim state requires another explanation. A supercritical funnel, as we discuss below, may offer an explanation for these three states either through obscuration as $\dot{m}_0$ increases (sources in Section 5.1.4.4.1) or changes in the inclination of the system (sources in Section 5.1.4.4.2). Given some of the common transitions and other spectral properties as we show below, we discuss NGC 1313 X-1, Holmberg IX X-1, NGC 55 ULX1, Circinus ULX5, and IC 342 X-1 together in Section 5.1.4.4.1 and Holmberg II X-1 and NGC 5204 X-1 in Section 5.1.4.4.2.

Here, we use NGC 1313 X-1 as our benchmark to discuss some of the transitions observed to the soft and dim states. In some cases, the timescale between these transitions and the duration of each state are poorly constrained because of the sparsity of our data. However, in a few cases, as for NGC 5204 X-1 and NGC 1313 X-1, the sampling rate is high enough for us to observe the source switching from one state to another and therefore we refer to these changes as transitions.

5.1.4.4.1 Optically thick funnels: *NGC 1313 X-1* and *Holmberg IX X-1* – As we show later, NGC 1313 X-1 undergoes a transition similar to that observed in the super-soft ULXs in NGC 247 Feng et al. (2016) and M101 (Soria & Kong, 2016), which are seen to transit from ULSs to a soft ULX spectrum. A similar transition is also seen in NGC 55 ULX1 (Pinto et al., 2017) (and in this work as we argue later), although the source would still be classified as a ULX when in this dim state. These transitions are all marked by an increase in the size of the emitting region of the soft component and a decrease in temperature, interpreted as an expansion of the wind photosphere as the spherisation radius increases with the corresponding decrease in temperature (Poutanen et al., 2007). While the ULXs in M101 and NGC 247 are frequently thought to be viewed at high inclinations (e.g. Ogawa et al., 2017), NGC 1313 X-1 is likely viewed down the optically thin funnel (e.g. Poutanen et al., 2007; Narayan et al., 2017), so that the hard component dominates the emission (epoch 2012-12-16 in Figure 5.6).

The spectral transitions of NGC 1313 X-1 between the low state (L$\sim$ 8 $\times$ 10^{39} erg/s, epoch 2012-12-06) and the high state (L$\sim$ 18 $\times$ 10^{39} erg/s, epoch 2004-06-05) have been frequently interpreted as the wind entering our line due to a narrowing of the funnel as the mass-accretion rate increases (e.g. Sutton et al., 2013). However, the fact that the high-energy emission ($\gtrsim$ 10 keV) remains relatively stable may be at odds with this interpretation, as we should expect the wind to down-scatter (Kawashima et al., 2012; Middleton et al., 2015a) or even absorb (Abolmasov et al., 2009) the high-energy emission from the inner parts of the accretion flow. We should also expect the increase in the mass-transfer rate to lead to an increase in the Thomson scattering optical depth of the funnel (Kawashima et al., 2012), also causing the high-energy emission to drop.

The physical processes at play to produce these high-energy photons are still poorly understood (e.g. Walton et al., 2020) but it is generally accepted that this emission is produced in the vicinity of the accretor (e.g. Kawashima et al., 2012; Takahashi et al., 2016; Walton et al., 2020). For the remainder of this part, we assume that this high-energy component is indeed produced in the inner regions of the accretion flow and focus on the influence of the wind and funnel structure on the spectra, rather than on the origin of this emission, which is discussed in Section 5.1.4.5.

The fact that the high-energy component remains stable could therefore imply that the gas within the funnel has remained optically thin over a certain range of mass-transfer rate, and that the inclination of the system (i) remains well below the half-opening angle of the funnel (θ_f). The second condition is required so that the higher degree of beaming caused by the reduction of θ_f, will only result in an increase in the amount of photons that are down-scattered off the wind walls into the observer's line of sight, with the wind remaining out of the line of sight. As the optical depth of the wind is lowest near the rotational axis of the compact object (Poutanen et al., 2007), the emission from the innermost regions is more likely to reach the observer without suffering severe energy losses (Kawashima et al., 2012). This may support the conclusions of previous works suggesting that NGC 1313 X-1 is seen at low viewing angles (e.g. Middleton et al., 2015a).

The lack of obscuration of the high-energy emission suggests that the mass-accretion rate has to be moderate ($\dot{M} \lesssim 10\ \dot{M}_\mathrm{Edd}$) [11] as for higher mass-transfer rates the gas within the funnel is expected to become optically thick (Narayan et al., 2017). Therefore, regardless of the exact nature of this high-energy power-law tail, we argue that despite the increase in mass-accretion rate in NGC 1313 X-1 up to epoch 2004-06-05, the physical conditions within the funnel have remained stable. The similar persistent high-energy emission seen in Holmberg IX X–1

---

[11] Here we adopt the definition of $\dot{M}$ of (Narayan et al., 2017) where $\dot{M} = \frac{L_\mathrm{Edd}}{\eta c^2}$ and η depends on the BH spin.

and the similar L–T positive correlation suggest a similar evolution in both sources, although NGC 1313 X–1 is seen in an obscured state (see below) not seen in Holmberg IX X–1. We discuss the possible differences between these two sources in more detail in Section 5.1.4.5, focussing on the nature of the high-energy tail.

Interestingly, after NGC 1313 X–1 reaches its maximum luminosity (epoch 2004-06-05), it becomes extremely soft and its luminosity decreases (epoch 2004-08-23 – *obscured state*). This spectral transition (we note that these two observations are just two months apart) can be understood if a further increase in the mass-accretion rate leads to a narrowing of the opening angle of the funnel as the wind becomes more mass loaded, to the point where the gas within the funnel becomes optically thick to the high-energy radiation. This implies that now $\theta_f < i$ and thus the wind effectively enters the line of sight and starts obscuring the inner accretion flow. The optical depth of the wind in the direction parallel to the disk is also expected to be an order of magnitude higher than in the perpendicular direction (Poutanen et al., 2007). High-energy photons are now heavily down-scattered or absorbed and therefore we mostly observe the soft emission from the expanded wind photosphere, as supported by the increase in the normalisation of the soft component (from $\sim$ 5 to $\sim$ 50 before and after the obscuration respectively).

This transition is also in good agreement with the GRRMHD simulations presented by Narayan et al. (2017) of super-Eddington accretion onto BHs. The authors observe a transition from a hard spectrum to a very soft one, as the mass accretion rate increases ($\dot{M} \sim 23\ \dot{M}_{\rm Edd}$ from their simulations) and the gas within the funnel becomes optically thick (see their Figure 9). Furthermore, their simulations also show that the luminosity for an observer with a line of sight close to the rotational axis of the accretor ($i \sim 10^\circ$) is capped at around 2×10^{40} erg/s, which is in very good agreement with the maximum luminosity observed in NGC 1313 X-1. Their simulations also predict an increase in the spectral emission at low energies ($\lesssim$ 0.6 keV), which seem at odds with our observations, where the luminosity of the soft component has remained stable compared to the brightest state. However, we note that Kawashima et al. (2012), who found qualitatively the same results as Narayan et al. (2017) for high-mass transfer rates ($\gtrsim 23\ \dot{M}_{\rm Edd}$), do not observe an increase in luminosity at low energies. It is also possible that because of the expansion of the photosphere, the soft component peaks now in the extreme UV and therefore we cannot reliably assess whether the luminosity of the soft component has increased given our limited bandpass.

Numerical simulations by Ogawa et al. (2017) also predict a steep decline in the high-energy emission as the outflow photosphere enters the line of sight. We find that the temperature of the hard `diskbb` diminishes from 1.6±0.1 keV in epoch 2004-06-05 to $0.92^{+0.10}_{-0.08}$ keV in epoch 2004-08-23 and its unabsorbed bolometric luminosity decays from (11.2±0.6) × 10^{39} erg/s to (2.9±0.4) × 10^{39} erg/s, which seems to support this interpretation.

NGC 55 ULX1 – Similarly, we argue that the soft and dim spectral state observed in NGC 55 ULX1 is analogous to the obscured state observed in NGC 1313 X-1. In both cases, we observe a possible increase in the neutral absorption column (see Section 5.1.3.1.2). Although this might be model dependent (this is discussed further below), it suggests that their spectra have evolved in a similar manner. The ratio of unabsorbed bolometric fluxes in the obscured state are $F_{\rm harddiskbb}/F_{\rm softdiskbb} = 0.34^{+0.12}_{-0.08}$ and $0.29^{+0.01}_{-0.02}$ in NGC 1313 X-1 (epoch 2004-08-23) and NGC 55 ULX1 (epoch 2010-05-24), respectively. This is a factor of about three lower in both cases compared to when the sources were at their brightest, and indicates that the hard component is responsible for the drop in luminosity. We again see an increase in the normalisation of the soft `diskbb` (see also Pintore et al., 2015) akin to the transitions seen in the ULXs in M101 and NGC 247 (Feng et al., 2016; Soria & Kong, 2016). The increase in the neutral absorption column may indicate that now we see parts of the wind less exposed to the central source (Pinto et al., 2020a), where self-absorption could start to be important, although more physically motivated models are needed to address this. The presence of outflows is supported by studies using high-resolution spectroscopy (Pinto et al., 2017, 2020b) which might have revealed the presence of soft residuals associated with outflowing winds in NGC 1313 X-1 and NGC 55 ULX1. Their similar transitions highlighted here therefore support the unification scenario proposed by (Middleton et al., 2015a; Pinto et al., 2020a).

IC 342 X-1 and *Circinus ULX5* – As shown in Figure 5.6, IC 342 X-1 and Circinus ULX5 not only share a very similar evolution in the HLD, but are also found in a soft and dim state (epochs 2012-10-29 and 2016-08-23 for IC 342 X-1 and Circinus ULX5 respectively) reminiscent again of the obscured state seen in NGC 1313 X-1. When both sources are hard and dim (e.g. epochs 2012-08-07 and 2001-08-06 for IC 342 X-1 and Circinus ULX5 respectively) the mass-transfer rate is likely to be low, similar to that of NGC 1313 X-1 in epoch 2012-12-16. The brighter and harder states (epochs 2005-02-10 and 2013-02-30 for IC 342 X-1 and Circinus ULX5 respectively) might correspond to an increase in the mass-transfer rate while the softest and dimmest states are likely again due to the central source being obscured by the funnel becoming optically thick at high-transfer rates. This is supported by the diminishing of the hard component in both temperature and luminosity. In this case, we do not see an increase in the local $n_{\rm H}$-value as for NGC 1313 X-1 or NGC 55 ULX1, which could strengthen the similarities of these obscured states, but we note that these are the two sources with the largest $n_{\rm HGal}$-values ($\gtrsim 30 \times 10^{20}$ cm^{-2}) in our sample and that we noted some calibration uncertainties at low energies (see Section 5.1.2.2). Nevertheless, these sources show that both archetypal soft ULXs (e.g. NGC 55 ULX1) and hard ULXs (e.g. IC 342 X-1) undergo a similar type of transition.

5.1.4.4.2 Inclination effects:

Holmberg II X-1 and *NGC 5204 X-1* – The similarities between Holmberg II X-1 and NGC 5204 X-1 are clear when looking at their long-term evolution in the HLD (see also the similarity between the three spectra shown in Figure 5.6) and are further supported by the similar L–T correlations found for the soft `diskbb` ($\alpha_{\rm NGC5204X\text{-}1} = 3.6\pm0.4$, $\alpha_{\rm HolmbergIIX\text{-}1} = 3.3\pm0.4$). Therefore, regardless of the physical processes powering these two sources, these similarities strongly suggest that we are witnessing the same type of source and/or accretion flow (see also Gúrpide et al. in *prep*).

In epochs 2004-04-15 and 2006-11-16 of Holmberg II X-1 and NGC 5204 X-1 respectively, both sources are found with a hard spectrum and an intermediate luminosity – *hard/intermediate* state. Again, we favour a low viewing angle for NGC 1313 X-1 as the hard component dominates the emission, although the inclination in this case may be higher than for NGC 1313 X-1 given their softer spectra. As both these sources move in the HLD (see 2003 *XMM-Newton* epochs for NGC 5204 X-1 for the transition) from these epochs to softer spectra and brighter luminosities — *bright/soft state* (e.g. epochs 2004-04-15 and 2006-11-16 for Holmberg II X-1 and NGC 5204 X-1 respectively)—, the temperature of the hard component decreases as seen in NGC 1313 X-1[12], while the soft component increases in temperature and luminosity (see Table 5.2). Similarly, most of the variability between these two epochs is seen at mid to soft energies ($\sim 0.3 - 5$ keV), whereas the high-energy emission ($\gtrsim 5$ keV) shows little variability. We argue that these transitions are due once again to an increase in the mass-accretion rate as the slight softening of both sources at high energy and the increase in the soft component seem to match the evolution presented by Kawashima et al. (2012) (see their Figure 2). In this case, the small dimming seen at high energies ($\gtrsim 10$ keV; see especially spectra for Holmberg II X-1) may be due to the fact that our line of sight may now be grazing the optically thick walls of the wind, and thus some of the high-energy photons from the inner parts of the accretion flow are now being Compton down-scattered by the wind. The transitions from hard/intermediate to soft/bright in NGC 5204 X-1 were also reported by Sutton et al. (2013) in terms of hard and soft ULX transitions.

Our study shows that these sources are also seen to transit from bright/soft to another state that we term *dim/soft* (epochs 2002-09-18 and 2001-05-02 for Holmberg II X-1 and NGC 5204 X-1 respectively) and vice versa. For NGC 5204 X-1, this is also seen in the *Chandra* observations of 2003 (see also the full set of *Chandra* observations presented by Roberts et al. (2006)[13]). For Holmberg II X-1, this is also seen in 2010 (see also the 2009/2010 *Swift*-XRT monitoring of Holmberg II X-1 in Grisé et al., 2010).

While there are certain similarities between these transitions and that seen in NGC 1313 X-1 in the obscured state, namely a softening and dimming of the source, we also find certain differences that may indicate that these transitions are not due to the same phenomenon as for NGC 1313 X-1. From the bright/soft state to the dim/soft state, the entire spectrum seems to have diminished in luminosity in the case of Holmberg II X-1 and NGC 5204 X-1 (see the spectra from Figure 5.6), while for NGC 1313 X-1 we show that it was the hard component that is mostly responsible for the dimming. Indeed, the soft `diskbb` is the faintest in the dim/soft state, while the temperature of the hard `diskbb` remains consistent within errors with respect to the bright/soft state (for both Holmberg II X-1 and NGC 5204 X-1). If the funnel has become optically thick due to an increase in the mass-transfer rate and is now obscuring the hard emission, we should expect the soft component to be relatively stable as seen in NGC 1313 X-1. Therefore, the dimming of this component may be at odds with this interpretation.

It is worth noting that the spectral evolution of NGC 5204 X-1 and Holmberg II X-1 from bright/soft to dim/soft bears some resemblance with how the inclination affects the spectral shape (see e.g. Kawashima et al., 2012; Kitaki et al., 2017; Narayan et al., 2017), which could suggest that changes in the inclination are responsible for these spectral changes. Indeed, numerical simulations by Narayan et al. (2017) predict a decrease by about one order of magnitude in luminosity between a source with a face-on aspect and a source viewed at high inclinations ($i > 30°$), which is consistent with our observations of the transitions from bright/soft to dim/soft. However, if the inclination of the system is indeed changing because of precession of the supercritical funnel, we should expect these changes to be associated with some periodicity. Thus, the fact that these transitions do not seem to be periodic (Grisé et al., 2010) may be at odds with the effects of a precessing funnel (albeit see Gúrpide et al. in *prep*).

These transitions were also shown to occur rapidly, in some cases on timescales shorter than half a day (Grisé et al., 2010). This short-term variability may be expected if dense clumps of the wind are intersecting our line of sight (Takeuchi et al., 2013; Middleton et al., 2015a) or if our line of sight is rapidly changing between seeing down the funnel and seeing through the wind walls, which is expected if our line of sight grazes the wind as argued above. More information on and monitoring of the timescale of these transitions is needed to address this issue and therefore this will be further studied in a forthcoming publication.

5.1.4.5 Origin of the high-energy tail

As stated above, NGC 1313 X-1 and Holmberg IX X-1 show a remarkably stable emission above ∼8 keV, although the sources are clearly varying at lower energies. Several physical processes have been proposed to explain the high-energy emission in ULXs; here we attempt to discuss its nature based on this observed stability.

Crucially, the absence of a hard surface in BHs naturally offers an explanation for the presence of a stable emission component: advection and photon trapping effects (Abramowicz et al., 1988; Ohsuga & Mineshige, 2007). In the super-Eddington regime, the diffusion photon time in the vicinity of the BH is expected to be greater than the accretion timescale, while part of the excess energy will go into powering the outflow, so that the luminosity

---

[12] For NGC 5204 X-1, see those epochs of higher quality as the epochs when `simpl` was not included tend to appear with artificially hotter temperatures for the hard `diskbb`.

[13] Although these transitions were well sampled by *Chandra* at the end of 2003, we were not able to use the short exposure ($\sim$ 5ks) observations when the source was caught repeatedly in the low state given the limited number of counts registered.

only increases logarithmically with the mass-transfer rate (Poutanen et al., 2007):

$$L \sim L_{\mathrm{Edd}}(1 + x \ln \dot{m}_0), \tag{5.4}$$

where $x = 1$ if only advection is considered or $x = 0.6$ if all the energy goes into powering the wind. Theoretical works show that this can lead to saturation of the continuum in the hard X-ray band for stellar-mass BHs (Feng et al., 2019) and therefore this stability at high-energies may provide a way of differentiating BH- from NS-ULXs, as NSs have no means of swallowing any excess energy. Therefore, if we assume the high-energy emission is rather insensitive to $\dot{m}_0$ as suggested by the stability of the high-energy component in Holmberg IX X-1 and NGC 1313 X-1, we suggest that the former might harbour a heavier BH than the latter given its brighter high-energy component (around a factor $\sim$ 1.6).

Alternatively, Kawashima et al. (2012) and Kitaki et al. (2017), based on numerical radiation hydrodynamic (RHD) simulations of super-Eddington accretion onto BHs, showed that an overheated region (T $\sim$ 8 keV) is formed in the vicinity of the BH, where a shock is produced in the region where the outflow collides with the inflow. Photons from the disk entering this overheated region will gain energy through multiple Compton up-scatterings prior to escaping through the funnel or the wind itself (where they will undergo Compton down-scattering). Photons escaping mostly through the funnel will be less affected by Compton down-scattering and will be observed as a high-energy power-law tail in the spectrum. Kitaki et al. (2017) argued that the temperature of this region is independent of the BH mass, resulting in a similar spectral shape for the high-energy tail regardless of the BH mass. Therefore, provided that the mass-transfer rate between two given sources is similar, the luminosity of this high-energy component may provide a means to estimate the BH mass ratio between two given sources. The two sources for which this stability is best observed, NGC 1313 X-1 and Holmberg IX X-1, indeed show a similar slope for the hard tail, $\Gamma_{\mathrm{NGC1313X\text{-}1}}{=}2.90^{+0.05}_{-0.04}$, $\Gamma_{\mathrm{1HolmbergIXX\text{-}1}}{=}2.9^{+0.2}_{-0.3}$, and $\Gamma_{\mathrm{2HolmbergIXX\text{-}1}}{=}3.4^{+0.2}_{-0.3}$ where 1 and 2 indicate the two different Γ values we used for the low- and high-flux epochs, respectively. If we instead refit all the high-quality data sets of Holmberg IX X-1 assuming one single value for Γ tied between all epochs, we obtain Γ=3.1±0.2 with $\chi^2_r = 1.06$ for 3722 degrees of freedom, consistent with the slope found in NGC 1313 X-1. Therefore, the brighter luminosity of the high-energy component in Holmberg IX X-1 would again suggest that Holmberg IX X-1 harbours a heavier BH compared to NGC 1313 X-1.

It is however not clear yet how the physical properties of this overheated region change with the mass-transfer rate. Assuming the overheated region is indeed responsible for the stable high-energy tail, then its physical properties should also be rather insensitive to the mass-transfer rate. Given that the overheated region is formed because of the shock of the outflows colliding with the inflow, we may also expect one to form around weakly magnetised NSs too. However, it remains to be seen whether or not the physical conditions within this overheated region and the funnel can lead to the formation of a similar high-energy power-law tail as predicted for supercritically accreting BHs.

Lastly, in the case of accretion onto NS magnetic poles, the accretion column is expected to be responsible for the emission at high energies (Walton et al., 2018c). Unfortunately, simulated spectra from super-critically accreting NSs from numerical simulations are still under study (e.g. Takahashi & Ohsuga, 2017; Takahashi et al., 2018) and it is currently hard to know how the emission from the accretion column reacts to changes in the mass-transfer rate and magnetic field strength. Nevertheless, if the accretion column is responsible for the stable emission observed in these sources, it is still unclear why we observe this difference in terms of stability between PULXs and sources like NGC 1313 X-1 and Holmberg IX X-1.

5.1.4.6 M83 ULX1: a stellar-mass black hole?

This source sits at the lower end of the ULX luminosity distribution. We found the maximum unabsorbed luminosity of M83 ULX1 to be $\sim 3.5 \times 10^{39}$ erg/s, close to the maximum observed luminosity of $\sim 4.5 \times 10^{39}$ erg/s by Soria et al. (2015), although this was computed using a power law which could have boosted the unabsorbed luminosity. This maximum luminosity, using Eddington mass scaling, suggests an accretor of $\sim$ 25 $\mathrm{M}_\odot$. We also found that the hard `diskbb` component follows $\mathrm{L}_{\mathrm{hard}} \propto \mathrm{T}_{\mathrm{hard}}^{4.4\pm0.7}$, which, as suggested by Figure 5.10, does not seem to be spuriously created by existing degeneracies. This may suggest that this component arises from an accretion disk with constant inner radius. This fact together with its low maximum luminosity, may suggest that we are witnessing a BH accreting close to the Eddington-limit, as binary synthesis population studies predict that BH-ULXs tend to emit isotropically, because super-Eddington mass-transfer rates (a factor of approximately eight above the classical Eddington limit) are harder to obtain from binary population evolution in the case of BHs (Wiktorowicz et al., 2019).

We therefore consider the possibility that the source could be accreting close to the Eddington-limit. If so, then we could expect the accretion disk to deviate from the standard thin accretion disk as radiation pressure inflates the disk making it geometrically slim or thick. This may lead to a departure of the radial temperature index (p) of –0.75 for a standard thin accretion disk (Shakura & Sunyaev, 1973), implicitly assumed in the `diskbb` model. In order to explore such deviations, we refitted all our data with an absorbed broadened disk model (`diskpbb` in XSPEC). As in Section 5.1.3, we assumed again constant absorption column and we jointly fitted our data tying n_{H} across all datasets with the `diskpbb` model. We obtained an excellent fit with $\chi^2 \sim 1.02$ for 1493 degrees of freedom (parameters are listed in Table 5.6).

The overall evolution of M83 ULX1 is very similar to that seen in the $\sim$ 10 $\mathrm{M}_\odot$ BH XTE J1550–564 (Kubota & Makishima, 2004). Our hard `diskbb` when using the dual-thermal component shows constant inner-disk radius,

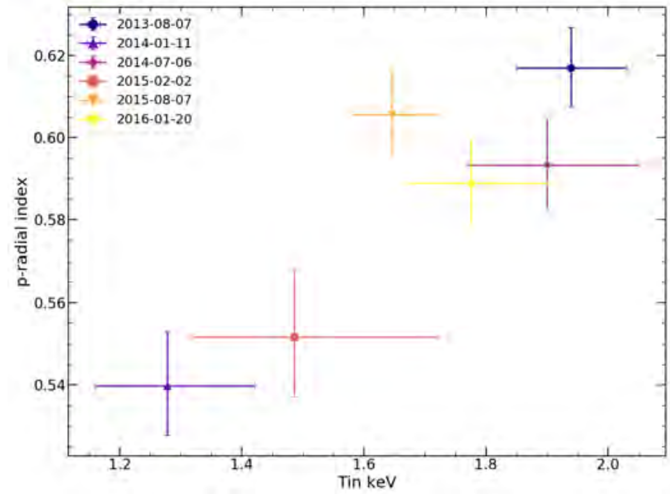

Figure 5.13: Dependency of the p radial index of the `diskpbb` with its temperature for M83 ULX1 (see text for details). This dependency is similar to that seen in stellar-mass BHs in the standard regime (Kubota & Makishima, 2004). Symbols are as per Figure 5.7.

Table 5.6: Results from jointly fitting all datasets of M83 ULX1 with an absorbed `diskpbb` model.

Epoch	$n_{\rm H}$ 10^{20} cm^{-2}	T$_{\rm in}$ keV	p	norm 10^{-4}
1X	3.2 ± 0.7	1.94 ± 0.09	0.62 ± 0.01	24^{+6}_{-5}
2X		1.3 ± 0.1	0.54 ± 0.01	16^{+9}_{-6}
3X		$1.9^{+0.2}_{-0.1}$	0.59 ± 0.01	17^{+7}_{-5}
4X		1.5 ± 0.2	$0.55^{+0.02}_{-0.01}$	14^{+11}_{-7}
5X		1.65 ± 0.07	0.61 ± 0.01	30^{+7}_{-6}
6X		1.8 ± 0.1	0.59 ± 0.01	17^{+6}_{-5}
χ^2_r				1.02
dof				1493

closely following the L$\propto$ T^4 relationship as XTE J1550–564 in the *standard* regime (i.e. when $L_{\rm disk} \propto$ T^4; e.g. period 3 in Kubota & Makishima, 2004)[14]. Additionally, when using the `diskpbb` model, the temperature increases with the radial index p of the `diskpbb` (Figure 5.13) as seen in XTE J1550–564 and LMC X-3 when fitted with the same model (see their Figure 9). Kubota & Makishima (2004) argued that this increase in p with temperature is an artefact caused by the limited bandpass and the fact that the radial dependency is flatter near the innermost disk radius than the –0.75 given by the `diskbb` approximation. Our `diskpbb` L–T relationship follows α = 3.0 ± 0.6 (90% confidence level) with Spearman's test coefficient of 0.94, again with roughly constant normalisation, suggesting that we are witnessing the innermost stable orbit as in XTE J1550–564 and LMC X-3 in the standard regime. A typical value of the normalisation $N \sim 0.002$, corresponds to R$_{\rm in}$ $\sim$ 95 $(\cos i)^{-1/2}$ km, assuming $f_{\rm col}$ = 1.8 as above. If we assume that the constant radius we observe corresponds to the innermost stable orbit for a non-spinning BH, then R$_{\rm in}$ = $R_{\rm isco}$ = 3R$_{\rm S}$, and we obtain a BH mass estimate of $\sim$ 10 $(\cos i)^{-1/2}$ M$_\odot$. This mass estimate would be a factor of six larger if we consider instead a maximally spinning Kerr BH.

A further constraint on the mass of the BH comes from the fact that Kubota & Makishima (2004) argued that a source enters the *anomalous regime* when L$_{\rm diskb}$ / L$_{\rm Edd}$ $\sim$ 0.4. Therefore, given that L$_{\rm disk}$ $\sim$ 4 × 10^{39} erg/s, then the mass of the M83 ULX1 could be of the order of 60 M$_\odot$, which could easily be accounted for with reasonable values of inclination and spin of the BH. We note that it is unlikely that the source is in the anomalous state as we should expect p to decrease with temperature, as this parameter starts to deviate from the standard value for a thin disk of –0.75 (Kubota & Makishima, 2004; Shakura & Sunyaev, 1973), which is at odds with our observations (Figure 5.13).

Although the exact mass estimate is rather uncertain, we conclude that the behaviour of this source is consistent with a massive stellar-mass BH accreting close to the Eddington limit in the high/soft state, given its similar evolution with accreting BHs in the standard regime. This conclusion is in agreement with previous studies by Soria et al. (2015) and other studies suggesting that sources below 3 × 10^{39} erg/s could be consistent with massive BHs accreting close to the Eddington limit (Middleton et al., 2013; Sutton et al., 2013). Such massive BHs might not be rare given the BH masses estimated from gravitational wave events (Abbott et al., 2019).

5.1.5 Conclusions

We present a thorough study of the long-term spectral evolution of a representative sample of ULXs and PULXs using data from *XMM-Newton*, *Chandra*, and *NuSTAR*. By studying their spectral states and transitions, we are able to explain the main sources of variability in these sources, which can be summarised as changes in the mass-transfer rate, changes in the degree of beaming, precession, and obscuration by the optically thick parts of the wind as this latter becomes more mass loaded.

We show that PULXs are among the hardest sources in the sample and discuss their evolution in terms of the interplay between the magnetospheric radius and the spherisation radius. We favour a scenario in which the softest PULX, NGC 1313 X-2, is consistent with a weakly magnetised NS so that $R_{\rm sph} > R_{\rm m}$ and the wind/funnel structure is responsible for imprinting highly anisotropic emission as the source precesses, given the wide HR variability the source spans. This interpretation can explain the significantly softer spectra of NGC 1313 X-2 and its lower pulse fraction, as the primary emission from the accretion column is expected to be down-scattered in the cool electrons of the outflow. Additionally, the lack of transitions to the propeller regime in NGC 1313 X-2 supports this interpretation, as the weak magnetic field (or high-mass transfer rate) implied by the condition $R_{\rm sph}> R_{\rm m}$ will naturally lead to smaller magnetospheric radii, making transitions to the propeller regime less likely to occur. Instead, the hardest PULXs, NGC 7793 P13 and M51-ULX7, are consistent with being strongly magnetised, meaning that $R_{\rm m} > R_{\rm sph}$ given the lack of HR variability, which we interpret as lack of strong anisotropy. In this scenario, the accretion disk is being truncated before it becomes supercritical, suppressing the anisotropy that the funnel/wind structure would otherwise imprint. For NGC 5907 ULX1, we show that in epochs associated with the super-orbital variability, the source appears harder when dimmer. This is hard to reconcile with the anisotropy expected from the funnel/wind structure in which we expect the source to become harder when brighter (as for NGC 1313 X-2). Still, a high-mass transfer rate is required to explain its high luminosity and therefore we conclude that $R_{\rm sph}\sim R_{\rm m}$ is a plausible condition to explain the source variability.

By comparing the evolution of PULXs with the sources in our sample, we are able to identify a strong NS candidate with very similar evolution to that seen in NGC 1313 X-2: M81 X-6. Although we are not able to detect pulsations in the source, it is possible that longer exposures sampling the source in different spectral states may be needed to detect pulsations. Additionally, deeper pulse searches taking into account orbital parameters corrections may be needed.

Most of the softer sources for which the accretor is unknown show three markedly different spectral states: one at highest luminosity and two at similar low luminosities but different hardness ratio. A supercritical funnel can offer an explanation of such degeneracy between luminosity and hardness, because a source is expected to be dim at both low mass-transfer rates and when the gas within the funnel becomes optically thick at high mass-transfer rates, causing the hard radiation from the inner regions of the accretion flow to be abruptly obscured. This could explain the evolution seen in NGC 1313 X-1, NGC 55 ULX1, IC 342 X-1, and Circinus ULX5. For Holmberg II X-1 and NGC 5204 X-1, these transitions may be better explained if our line of sight is grazing the half-opening

---

[14] We note that Kubota & Makishima (2004) uses RXTE that covers the 3–20 keV range and thus their soft component corresponds roughly to our hard component.

angle of the funnel, so that our view of the accretion flow rapidly transits between seeing down the funnel and seeing through the optically thick wind walls as the source precesses. Future higher cadence monitoring of these transitions will be key to determining the exact nature of these transitions, by studying both their timescale and the source evolution preceding and following them. Nevertheless, these transitions are suggestive of strong winds in these sources, which together with their softer appearance compared to most PULXs supports a scenario in which the sources considered here are powered by weakly magnetised NSs or BHs.

Finally, we report on the stability of the high-energy emission ($\gtrsim$ 10 keV) in some of the sources in our sample. Notably, none of the PULXs show such stability, although further high-quality *NuSTAR* observations are needed to probe the different spectral states of both PULXs and those sources for which the accretor is unknown. BHs are favoured candidates to explain this stability, as they naturally offer a means to swallow any excess radiation, stabilising the output radiation even as the mass-transfer rate increases. Should this be the case, this high-energy emission may help to identify BH-ULXs. On the other hand, should some of these sources host NSs, then this stability may offer interesting clues about the accretion flow geometry around NSs in the super-Eddington regime. Nevertheless, we stress the importance of obtaining future *NuSTAR* observations as we may expect to see most of the observational differences between BH- and NS-ULXs at high energies, where the mechanism responsible for the emission is expected to differ (i.e. an accretion column compared to the case of the inner regions of the accretion disk around a BH).

Acknowledgements

The authors would like to thank the anonymous referee for his comments and suggestions that helped improve the quality of the manuscript. A. Gúrpide would like to thank M. Bachetti for his help and assistance during the search of pulsations and to I. Pastor-Marazuela for the computational resources provided. NW acknowledges support by the CNES. This work made used of the free software Veusz developed by J. Sanders to produce some of the plots.

Table 5.1: Sample of sources selected for this study with their respective distance, Galactic absorption (Kalberla et al., 2005; HI4PI Collaboration et al., 2016), and log of observations considered. For each particular epoch, the number of Xs, Ns, or Cs indicates the number of *XMM-Newton*, *NuSTAR*, and *Chandra* observations, respectively, that have been fitted together.

Epoch	Telescope	Instrument	Date	Obs. ID	Good Exp (ks)
Holmberg II X−1 (D = 3.27 Mpc^{a}, n_{H} = 3.7 × 10^{20} cm^{-2})					
1X	*XMM-Newton*	pn/MOS1/MOS2	2002-04-10	0112520601	4.6/9.5/9.6
2X	*XMM-Newton*	pn/MOS1/MOS2	2002-04-16	0112520701	3.7/5.1/5.7
3X	*XMM-Newton*	pn/MOS1/MOS2	2002-09-18	0112520901	3.8/5.8/6.5
4X	*XMM-Newton*	pn/MOS1/MOS2	2004-04-15	0200470101	35.0/49.6/51.1
5X	*XMM-Newton*	pn/MOS1/MOS2	2010-03-26	0561580401	21.7/39.6/40.7
6XNN	*XMM-Newton*	pn/MOS1/MOS2	2013-09-09	0724810101	4.6/6.6/6.6
	NuSTAR	FPMA/FPMB	2013-09-09	30001031002	31.4/31.3
	NuSTAR	FPMA/FPMB	2013-09-09	30001031003	79.4/79.3
7XN	*XMM-Newton*	pn/MOS1/MOS2	2013-09-17	0724810301	5.8/8.6/9.3
	NuSTAR	FPMA/FPMB	2013-09-17	30001031005	111.1/111.0
Holmberg IX X−1 (D = 3.77 Mpc^{a}, n_{H} = 5.5 × 10^{20} cm^{-2})					
1X	*XMM-Newton*	-/MOS1/MOS2	2001-04-23	0111800101	-/17.0/15.1
2X	*XMM-Newton*	pn/MOS1/MOS2	2002-04-10	0112521001	7.0/10.0/10.0
3X	*XMM-Newton*	pn/MOS1/MOS2	2002-04-16	0112521101	7.6/9.4/9.3
4X	*XMM-Newton*	pn/MOS1/MOS2	2004-09-26	0200980101	64.2/88.9/93.7
5X	*XMM-Newton*	pn/-/-	2011-03-24	0657802001	2.9/-/-
6X	*XMM-Newton*	pn/MOS1/MOS2	2011-09-26	0657801801	10.3/15.3/15.3
7X	*XMM-Newton*	pn/MOS1/MOS2	2011-11-23	0657802201	13.1/15.9/15.9
8X	*XMM-Newton*	pn/MOS1/MOS2	2012-10-23	0693850801	5.9/8.7/10.8
9XXNN	*XMM-Newton*	pn/MOS1/MOS2	2012-10-25	0693850901	5.5/11.6/13.0
	XMM-Newton	pn/MOS1/MOS2	2012-10-27	0693851001	3.9/9.3/10.5
	NuSTAR	FPMA/FPMB	2012-10-26	30002033003	88.1/88.0
	NuSTAR	FPMA/FPMB	2012-10-26	30002033002	31.2/31.2
10XNN	*XMM-Newton*	pn/MOS1/MOS2	2012-11-12	0693851701	7.1/9.5/9.5
	NuSTAR	FPMA/FPMB	2012-11-11	30002033005	40.7/40.8
	NuSTAR	FPMA/FPMB	2012-11-11	30002033006	35.2/35.2
11XXNN	*XMM-Newton*	pn/MOS1/MOS2	2012-11-14	0693851801	6.8/8.8/8.8
	XMM-Newton	pn/MOS1/MOS2	2012-11-16	0693851101	2.9/4.9/5.0
	NuSTAR	FPMA/FPMB	2012-11-14	30002033008	14.5/14.5
	NuSTAR	FPMA/FPMB	2012-11-15	30002033010	49.0/49.0
IC 342 X−1 (D = 3.39 Mpc^{a}, n_{H} = 30.5 × 10^{20} cm^{-2})					
1X	*XMM-Newton*	pn/MOS1/MOS2	2001-02-11	0093640901	4.8/9.5/9.5
2X	*XMM-Newton*	pn/MOS1/MOS2	2004-02-20	0206890101	10.2/21.9/21.8
3X	*XMM-Newton*	pn/MOS1/MOS2	2004-08-17	0206890201	17.0/23.4/23.4
4X	*XMM-Newton*	pn/MOS1/MOS2	2005-02-10	0206890401	6.2/8.2/8.7
5XNN	*XMM-Newton*	pn/MOS1/MOS2	2012-08-11	0693850601	37.5/45.2/44.9
	NuSTAR	FPMA/FPMB	2012-08-10	30002032002	21.0/21.0
	NuSTAR	FPMA/FPMB	2012-08-10	30002032003	98.6/98.7
6XN	*XMM-Newton*	pn/MOS1/MOS2	2012-08-17	0693851301	33.3/40.6/42.4
	NuSTAR	FPMA/FPMB	2012-08-16	30002032005	127.4/127.4
1C	*Chandra*	ACIS	2002-04-29	2916	9.3
2C	*Chandra*	ACIS	2002-08-26	2917	9.9
3C	*Chandra*	ACIS	2012-10-29	13686	9.1
NGC 5204 X−1 (D = 4.59 Mpc^{c}, n_{H} = 1.8 × 10^{20} cm^{-2})					
1X	*XMM-Newton*	pn/MOS1/MOS2	2003-01-06	0142770101	15.3/18.5/18.5
2X	*XMM-Newton*	pn/MOS1/MOS2	2003-04-25	0142770301	3.5/7.4/6.9
3X	*XMM-Newton*	pn/MOS1/MOS2	2003-05-01	0150650301	4.8/8.2/8.2
4X	*XMM-Newton*	pn/MOS1/MOS2	2006-11-16	0405690101	7.8/5.8/5.8
5X	*XMM-Newton*	pn/MOS1/MOS2	2006-11-19	0405690201	30.9/40.9/41.5
6X	*XMM-Newton*	pn/MOS1/MOS2	2006-11-25	0405690501	20.4/29.7/29.7
7XXNN	*XMM-Newton*	pn/MOS1/MOS2	2013-04-21	0693851401	13.4/16.4/16.5

Table 5.1: Continued.

	XMM-Newton	pn/MOS1/MOS2	2013-04-29	0693850701	10.0/14.2/15.4
	NuSTAR	FPMA/FPMB	2013-04-19	30002037002	96.0/95.8
	NuSTAR	FPMA/FPMB	2013-04-29	30002037004	89.0/88.9
8X	*XMM-Newton*	pn/MOS1/MOS2	2014-06-27	0741960101	19.0/22.5/22.7
1C	*Chandra*	ACIS	2001-05-02	2029	9.0
2C	*Chandra*	ACIS	2003-08-06	3933	46.2
3CC	*Chandra*	ACIS	2003-08-14	3936	4.6
	Chandra	ACIS	2003-08-17	3937	4.6
4C	*Chandra*	ACIS	2003-09-05	3940	4.8
5C	*Chandra*	ACIS	2003-09-14	3941	4.9
6C	*Chandra*	ACIS	2003-09-23	3942	5.2
7C	*Chandra*	ACIS	2003-10-03	3943	4.9
M83 ULX1 (D = 4.66 Mpc^a, $n_{\rm H}$ = 4.0 × 10^{20} cm^{-2})					
1X	*XMM-Newton*	pn/MOS1/MOS2	2013-08-07	0723450101	44.7/51.1/51.1
2X	*XMM-Newton*	pn/MOS1/MOS2	2014-01-11	0723450201	37.7/53.4/52.8
3X	*XMM-Newton*	pn/MOS1/MOS2	2014-07-06	0729561201	24.0/28.2/28.2
4X	*XMM-Newton*	pn/MOS1/MOS2	2015-02-02	0729561001	15.4/20.1/19.8
5X	*XMM-Newton*	pn/MOS1/MOS2	2015-08-07	0761620101	53.1/59.7/61.0
6X	*XMM-Newton*	pn/MOS1/MOS2	2016-01-20	0761620201	31.9/57.9/65.1
NGC 5408 X−1 (D = 4.80 Mpc^e, $n_{\rm H}$ = 5.2 × 10^{20} cm^{-2})					
1X	*XMM-Newton*	pn/MOS1/MOS2	2001-07-31	0112290501	3.5/6.1/6.5
2X	*XMM-Newton*	pn/MOS1/MOS2	2001-08-08	0112290601	4.5/6.2/6.2
3X	*XMM-Newton*	-/MOS1/MOS2	2001-08-24	0112290701	-/7.3/7.5
4X	*XMM-Newton*	pn/MOS1/MOS2	2003-01-28	0112291201	2.7/4.2/4.2
5X	*XMM-Newton*	pn/MOS1/MOS2	2006-01-13	0302900101	90.6/104.3/105.1
6X	*XMM-Newton*	pn/MOS1/MOS2	2008-01-13	0500750101	45.2/62.5/62.6
7X	*XMM-Newton*	pn/MOS1/MOS2	2010-07-17	0653380201	76.6/89.2/113.3
8X	*XMM-Newton*	pn/MOS1/MOS2	2010-07-19	0653380301	96.3/111.0/111.1
9X	*XMM-Newton*	pn/MOS1/MOS2	2011-01-26	0653380401	79.7/109.1/111.9
10X	*XMM-Newton*	pn/MOS1/MOS2	2011-01-28	0653380501	83.5/108.3/110.5
11XX	*XMM-Newton*	pn/MOS1/MOS2	2014-02-11	0723130301	30.4/35.9/36.2
	XMM-Newton	pn/MOS1/MOS2	2014-02-13	0723130401	29.5/34.1/34.1
1CC	*Chandra*	ACIS	2010-05-02	11032	11.0
	Chandra	ACIS	2010-05-15	11033	11.1
2C	*Chandra*	ACIS	2010-05-28	11034	10.9
NGC 1313 X−1 (D = 4.25 Mpc^a, $n_{\rm H}$ = 4.2 × 10^{20} cm^{-2})					
1X	*XMM-Newton*	pn/MOS1/MOS2	2000-10-17	0106860101	18.3/22.3/23.9
2XX	*XMM-Newton*	pn/-/-	2003-12-21	0150280301	7.4/-/-
	XMM-Newton	pn/-/-	2003-12-23	0150280401	3.2/-/-
3XX	*XMM-Newton*	pn/MOS1/-	2004-01-08	0150280601	7.1/11.1/-
	XMM-Newton	pn/MOS1/MOS2	2004-01-17	0150281101	3.1/6.6/6.7
4X	*XMM-Newton*	pn/MOS1/MOS2	2004-05-01	0205230201	0.6/7.1/7.0
5X	*XMM-Newton*	pn/MOS1/MOS2	2004-06-05	0205230301	8.7/11.5/11.6
6X	*XMM-Newton*	pn/MOS1/MOS2	2004-08-23	0205230401	4.4/13.0/13.3
7X	*XMM-Newton*	-/MOS1/MOS2	2004-11-23	0205230501	-/15.5/15.5
8X	*XMM-Newton*	pn/MOS1/MOS2	2005-02-07	0205230601	8.9/11.4/11.5
9X	*XMM-Newton*	pn/MOS1/MOS2	2006-10-16	0405090101	81.1/100.2/102.8
10XN	*XMM-Newton*	pn/MOS1/MOS2	2012-12-16	0693850501	90.9/112.0/115.1
	NuSTAR	FPMA/FPMB	2012-12-16	30002035002	100.9/100.8
11XN	*XMM-Newton*	pn/MOS1/MOS2	2012-12-22	0693851201	85.4/120.8/122.5
	NuSTAR	FPMA/FPMB	2012-12-21	30002035004	127.0/127.0
12XN	*XMM-Newton*	pn/MOS1/MOS2	2014-07-05	0742590301	53.7/61.0/61.1
	NuSTAR	FPMA/FPMB	2014-07-05	80001032002	63.5/63.4
13X	*XMM-Newton*	-/MOS1/MOS2	2015-12-05	0764770101	-/68.6/71.8
14XN	*XMM-Newton*	pn/MOS1/MOS2	2017-03-29	0794580601	26.1/37.5/40.4
	NuSTAR	FPMA/FPMB	2017-03-29	90201050002	72.8/72.7
15XN	*XMM-Newton*	pn/MOS1/MOS2	2017-06-14	0803990101	110.8/128.3/131.5
	NuSTAR	FPMA/FPMB	2017-06-14	30302016002	94.2/93.9
16X	*XMM-Newton*	pn/MOS1/MOS2	2017-06-20	0803990201	110.9/129.1/128.7
17XXN	*XMM-Newton*	pn/MOS1/MOS2	2017-08-31	0803990301	47.2/73.9/70.9
	XMM-Newton	pn/MOS1/MOS2	2017-09-02	0803990401	30.1/47.5/51.1

Table 5.1: Continued.

	NuSTAR	FPMA/FPMB	2017-09-03	30302016006	73.0/72.7
18X	*XMM-Newton*	pn/MOS1/MOS2	2017-12-07	0803990501	60.1/89.9/97.4
19XN	*XMM-Newton*	pn/MOS1/MOS2	2017-12-09	0803990601	71.8/118.2/123.2
	NuSTAR	FPMA/FPMB	2017-12-09	30302016010	79.3/79.1
Circinus ULX5 (D = 4.20 Mpc[d], $n_{\mathrm{H}} = 50.6 \times 10^{20}$ cm^{-2})					
1X	*XMM-Newton*	-/MOS1/-	2001-08-06	0111240101	-/98.2/-
2XNN	*XMM-Newton*	pn/MOS1/MOS2	2013-02-03	0701981001	33.0/43.4/42.0
	NuSTAR	FPMA/FPMB	2013-02-03	30002038004	40.3/40.2
	NuSTAR	FPMA/FPMB	2013-02-02	30002038002	18.3/18.3
3X	*XMM-Newton*	pn/MOS1/MOS2	2014-03-01	0656580601	23.8/30.9/30.7
4XN	*XMM-Newton*	pn/MOS1/MOS2	2016-08-23	0792382701	17.2/19.0/19.0
	NuSTAR	FPMA/FPMB	2016-08-23	90201034002	49.8/49.7
5X	*XMM-Newton*	pn/MOS1/MOS2	2018-02-07	0780950201	5.0/25.3/27.3
6X	*XMM-Newton*	pn/MOS1/MOS2	2018-09-16	0824450301	88.8/109.7/113.2
1C	*Chandra*	ACIS	2010-12-24	12824	38.9
M81 X−6 (D = 3.61 Mpc[a], $n_{\mathrm{H}} = 9.8 \times 10^{20}$ cm^{-2})					
1X	*XMM-Newton*	pn/-/MOS2	2001-04-22	0111800101	73.6/-/15.1
2X	*XMM-Newton*	pn/MOS1/MOS2	2002-04-10	0112521001	7.0/10.0/10.0
3X	*XMM-Newton*	pn/MOS1/MOS2	2002-04-16	0112521101	7.6/9.4/9.3
4X	*XMM-Newton*	-/MOS1/MOS2	2004-09-26	0200980101	-/89.0/93.8
5X	*XMM-Newton*	pn/-/MOS2	2011-03-24	0657802001	2.9/-/5.4
6X	*XMM-Newton*	pn/MOS1/MOS2	2011-09-26	0657801801	5.8/15.3/15.3
7X	*XMM-Newton*	pn/-/-	2011-11-23	0657802201	13.0/-/-
8X	*XMM-Newton*	pn/MOS1/MOS2	2012-10-23	0693850801	5.8/8.7/10.8
9XX	*XMM-Newton*	pn/MOS1/MOS2	2012-10-27	0693851001	3.9/9.3/10.5
	XMM-Newton	pn/MOS1/MOS2	2012-10-25	0693850901	2.2/11.6/13.0
10XXX	*XMM-Newton*	-/MOS1/-	2012-11-12	0693851701	-/9.5/-
	XMM-Newton	-/MOS1/-	2012-11-14	0693851801	-/8.8/-
	XMM-Newton	pn/MOS1/-	2012-11-16	0693851101	2.8/4.9/-
NGC 55 ULX1 (D = 2.11 Mpc[b], $n_{\mathrm{H}} = 1.4 \times 10^{20}$ cm^{-2})					
1X	*XMM-Newton*	pn/MOS1/MOS2	2001-11-14	0028740201	27.3/32.7/32.7
2X	*XMM-Newton*	-/MOS1/MOS2	2001-11-15	0028740101	-/30.2/30.0
3X	*XMM-Newton*	pn/MOS1/MOS2	2010-05-24	0655050101	98.9/117.6/118.0
NGC 6946 X−1 (D = 5.52 Mpc[b], $n_{\mathrm{H}} = 2.2 \times 10^{20}$ cm^{-2})					
1X	*XMM-Newton*	pn/MOS1/MOS2	2004-06-13	0200670301	7.9/12.2/11.9
2XX	*XMM-Newton*	-/MOS1/MOS2	2007-11-02	0500730201	-/31.6/31.8
	XMM-Newton	pn/MOS1/MOS2	2007-11-08	0500730101	19.5/27.0/28.3
3X	*XMM-Newton*	pn/MOS1/MOS2	2012-10-21	0691570101	88.0/104.1/110.4
4XNN	*XMM-Newton*	pn/MOS1/MOS2	2017-06-01	0794581201	35.5/43.6/44.0
	NuSTAR	FPMA/FPMB	2017-05-21	90302004002	66.8/66.6
	NuSTAR	FPMA/FPMB	2017-06-01	90302004004	47.8/47.7
1C	*Chandra*	ACIS	2001-09-07	1043	58.3
2C	*Chandra*	ACIS	2004-10-22	4631	29.7
3CC	*Chandra*	ACIS	2004-11-06	4632	28.0
	Chandra	ACIS	2004-12-03	4633	26.6
4C	*Chandra*	ACIS	2016-09-28	17878	40.0
NGC 1313 X−2 (P) (D = 4.25 Mpc[a], $n_{\mathrm{H}} = 4.2 \times 10^{20}$ cm^{-2})					
1X	*XMM-Newton*	pn/-/MOS2	2000-10-17	0106860101	18.2/-/23.9
2X	*XMM-Newton*	pn/MOS1/MOS2	2003-12-21	0150280301	7.4/10.1/10.1
3X	*XMM-Newton*	pn/MOS1/MOS2	2003-12-23	0150280401	3.2/4.9/5.1
4X	*XMM-Newton*	pn/MOS1/MOS2	2003-12-25	0150280501	5.8/8.7/8.9
5X	*XMM-Newton*	pn/MOS1/MOS2	2004-01-08	0150280601	7.1/11.1/12.9
6X	*XMM-Newton*	pn/MOS1/MOS2	2004-01-17	0150281101	3.1/6.6/6.7
7X	*XMM-Newton*	pn/MOS1/MOS2	2004-06-05	0205230301	8.7/11.5/11.5
8X	*XMM-Newton*	-/MOS1/MOS2	2004-08-23	0205230401	-/13.0/13.3
9X	*XMM-Newton*	pn/MOS1/MOS2	2004-11-23	0205230501	12.5/15.5/15.5
10X	*XMM-Newton*	pn/MOS1/MOS2	2005-02-07	0205230601	8.9/11.3/11.5
11X	*XMM-Newton*	pn/-/-	2006-03-06	0301860101	17.3/-/-
12X	*XMM-Newton*	pn/-/-	2006-10-16	0405090101	80.4/-/-

Table 5.1: Continued.

13XN	*XMM-Newton*	pn/MOS1/MOS2	2012-12-16	0693850501	90.9/112.0/115.1
	NuSTAR	FPMA/FPMB	2012-12-16	30002035002	100.9/100.8
14XN	*XMM-Newton*	pn/MOS1/MOS2	2012-12-22	0693851201	85.4/120.8/122.5
	NuSTAR	FPMA/FPMB	2012-12-21	30002035004	127.0/127.0
15X	*XMM-Newton*	pn/-/-	2013-06-08	0722650101	12.2/-/-
16X	*XMM-Newton*	pn/-/-	2014-07-05	0742590301	53.5/-/-
17X	*XMM-Newton*	pn/-/-	2015-03-30	0742490101	78.9/-/-
18X	*XMM-Newton*	pn/MOS1/MOS2	2015-12-05	0764770101	53.5/68.6/71.7
19X	*XMM-Newton*	pn/MOS1/MOS2	2016-03-23	0764770401	16.7/22.8/21.7
20X	*XMM-Newton*	pn/MOS1/MOS2	2016-10-08	0782310101	76.2/88.4/88.4
21XN	*XMM-Newton*	pn/-/-	2017-03-29	0794580601	26.0/-/-
	NuSTAR	FPMA/FPMB	2017-03-29	90201050002	72.8/72.7
22X	*XMM-Newton*	-/MOS1/MOS2	2017-06-14	0803990101	-/128.2/131.5
23X	*XMM-Newton*	pn/-/-	2017-06-20	0803990201	110.4/-/-
24X	*XMM-Newton*	-/-/MOS2	2017-08-31	0803990301	-/-/71.0
25X	*XMM-Newton*	-/-/MOS2	2017-09-02	0803990401	-/-/51.1
26XXN	*XMM-Newton*	pn/MOS1/MOS2	2017-12-07	0803990501	60.1/89.8/97.4
	XMM-Newton	pn/MOS1/MOS2	2017-12-09	0803990601	71.8/118.1/123.2
	NuSTAR	FPMA/FPMB	2017-12-09	30302016010	79.3/79.1
NGC 300 ULX1 (P) (D = 2.08 Mpc^b, $n_{\rm H} = 4.1 \times 10^{20}$ cm^{-2})					
1XN	*XMM-Newton*	pn/MOS1/MOS2	2016-12-17	0791010101	96.4/117.2/127.8
	NuSTAR	FPMA/FPMB	2016-12-16	30202035002	163.1/162.8
2X	*XMM-Newton*	pn/MOS1/MOS2	2016-12-19	0791010301	46.1/63.4/68.7
1CC	*Chandra*	ACIS	2018-02-11	20966	9.1
	Chandra	ACIS	2018-02-08	20965	9.1
NGC 5907 ULX1 (P) (D = 17.06 Mpc^a, $n_{\rm H} = 2.1 \times 10^{20}$ cm^{-2})					
1X	*XMM-Newton*	pn/MOS1/MOS2	2003-02-20	0145190201	10.1/18.0/19.1
2X	*XMM-Newton*	pn/MOS1/MOS2	2003-02-28	0145190101	10.9/16.2/16.7
3XXCC	*XMM-Newton*	pn/MOS1/MOS2	2012-02-09	0673920301	12.8/18.2/18.3
	XMM-Newton	pn/MOS1/MOS2	2012-02-05	0673920201	5.3/10.5/16.2
	Chandra	ACIS	2012-02-11	12987	16.0
	Chandra	ACIS	2012-02-11	14391	13.1
4XN	*XMM-Newton*	pn/MOS1/MOS2	2013-11-12	0724810401	18.9/32.3/31.6
	NuSTAR	FPMA/FPMB	2013-11-12	30002039005	112.9/112.8
5XNN	*XMM-Newton*	pn/MOS1/MOS2	2014-07-09	0729561301	37.6/43.2/43.2
	NuSTAR	FPMA/FPMB	2014-07-09	80001042002	57.1/57.0
	NuSTAR	FPMA/FPMB	2014-07-12	80001042004	56.3/56.2
6X	*XMM-Newton*	pn/MOS1/MOS2	2017-07-02	0804090301	21.3/33.8/33.8
7X	*XMM-Newton*	pn/MOS1/MOS2	2017-07-05	0804090401	31.3/36.5/36.5
8XX	*XMM-Newton*	pn/MOS1/MOS2	2017-07-08	0804090501	34.1/40.4/40.4
	XMM-Newton	pn/MOS1/MOS2	2017-07-15	0804090601	32.5/38.0/38.0
NGC 7793 P13 (P) (D = 3.63 Mpc^c, $n_{\rm H} = 1.2 \times 10^{20}$ cm^{-2})					
1X	*XMM-Newton*	pn/MOS1/MOS2	2013-11-25	0693760401	41.1/47.1/47.1
2X	*XMM-Newton*	pn/MOS1/MOS2	2014-12-10	0748390901	42.0/48.2/48.2
3XN	*XMM-Newton*	pn/MOS1/MOS2	2016-05-20	0781800101	23.1/42.4/44.4
	NuSTAR	FPMA/FPMB	2016-05-20	80201010002	106.3/105.9
4X	*XMM-Newton*	pn/-/MOS2	2017-05-13	0804670201	5.2/-/13.6
5XN	*XMM-Newton*	pn/MOS1/MOS2	2017-05-20	0804670301	44.9/54.4/54.4
	NuSTAR	FPMA/FPMB	2017-05-19	30302005002	83.6/83.3
6X	*XMM-Newton*	pn/MOS1/MOS2	2017-05-31	0804670401	25.0/31.0/31.4
7X	*XMM-Newton*	pn/MOS1/MOS2	2017-06-12	0804670501	19.9/32.9/32.5
8X	*XMM-Newton*	pn/MOS1/MOS2	2017-06-20	0804670601	23.0/30.7/30.7
9XN	*XMM-Newton*	pn/MOS1/MOS2	2017-11-25	0804670701	41.8/50.6/50.9
	NuSTAR	FPMA/FPMB	2017-11-25	30302005004	76.7/76.4
1C	*Chandra*	ACIS	2003-09-06	3954	48.9
M51 ULX−7 (P) (D = 7.60 Mpc^f, $n_{\rm H} = 3.3 \times 10^{20}$ cm^{-2})					
1X	*XMM-Newton*	pn/MOS1/MOS2	2003-01-15	0112840201	17.1/20.5/20.5
2X	*XMM-Newton*	pn/MOS1/MOS2	2005-07-01	0212480801	24.0/34.6/34.8
3X	*XMM-Newton*	pn/MOS1/MOS2	2006-05-20	0303420101	29.4/36.7/38.2
4X	*XMM-Newton*	pn/MOS1/MOS2	2006-05-24	0303420201	20.2/27.0/27.4

Table 5.1: Continued.

5X	*XMM-Newton*	pn/MOS1/MOS2	2018-05-13	0824450901	64.7/75.5/75.6
6XX	*XMM-Newton*	pn/MOS1/MOS2	2018-06-13	0830191501	51.6/59.8/59.8
	XMM-Newton	pn/MOS1/MOS2	2018-06-15	0830191601	51.7/59.8/59.8
1C	*Chandra*	ACIS	2003-08-07	3932	48.0
2C	*Chandra*	ACIS	2012-09-09	13813	179.2
3C	*Chandra*	ACIS	2012-09-12	13812	157.5
4CC	*Chandra*	ACIS	2012-09-19	15496	41.0
	Chandra	ACIS	2012-09-20	13814	189.9
5C	*Chandra*	ACIS	2012-09-23	13815	67.2
M51 ULX−8 (NS^g) (D = 7.60 Mpc^f, $n_{\rm H}$ = 3.3 × 10^{20} cm^{-2})					
1X	*XMM-Newton*	-/MOS1/MOS2	2005-07-01	0212480801	-/34.6/34.8
2X	*XMM-Newton*	pn/MOS1/MOS2	2006-05-20	0303420101	29.4/36.7/38.2
3X	*XMM-Newton*	pn/MOS1/MOS2	2006-05-24	0303420201	20.2/27.0/27.4
4X	*XMM-Newton*	pn/MOS1/MOS2	2018-05-13	0824450901	64.5/75.5/75.6
5X	*XMM-Newton*	pn/-/-	2018-05-25	0830191401	80.1/-/-
6XX	*XMM-Newton*	pn/-/-	2018-06-13	0830191501	51.4/-/-
	XMM-Newton	pn/-/-	2018-06-15	0830191601	51.4/-/-
1C	*Chandra*	ACIS	2003-08-07	3932	48.0
2C	*Chandra*	ACIS	2012-09-12	13812	157.5
3CCC	*Chandra*	ACIS	2012-09-19	15496	41.0
	Chandra	ACIS	2012-09-20	13814	189.9
	Chandra	ACIS	2012-09-23	13815	67.2
4C	*Chandra*	ACIS	2012-09-26	13816	73.1

Notes. Observations for which an instrument was not available because it was not active or because the source was not in the field of view are marked with "-". (P) indicates a source for which pulsations have been identified. Distances from: $^{(a)}$ Tully et al. (2016) , $^{(b)}$ Lelli et al. (2015) , $^{(c)}$ Karachentsev et al. (2017) , $^{(d)}$ Tully et al. (2008) , $^{(e)}$ Karachentsev et al. (2002) and $^{(f)}$ Cappellari et al. (2011) . $^{(g)}$ No pulsations have been detected in this source but it was identified as a NS through the detection of a cyclotron line (Brightman et al., 2018).

Table 5.2: Best-fit spectral fit parameters. Errors are quoted at a 90% confidence level. The first epochs in each source correspond to the high-quality datasets that were jointly fitted and from which we determine Γ and $n_{\rm H}$. The rest of the data were fitted individually by freezing $n_{\rm H}$ and/or Γ to the best-fit value found in the joint fit of the high-quality data.

Epoch	$n_{\rm H}$ 10^{20} cm^{-2}	kT$_{\rm soft}$ keV	norm	kT$_{\rm hard}$ keV	norm 10^{-2}	Γ	f_{scat} %	χ^2_r/dof
Holmberg II X-1								
1X	4.3±0.5	$0.26\ ^{+0.03}_{-0.08}$	$39\ ^{+18}_{-10}$	$0.47^{+0.2}_{-0.3}$	333^{+2592}_{-262}	$2.5\ ^{+0.2}_{-0.5}$	62^{+a}_{-30}	1.01/ 2182
2X		0.27±0.02	38^{+11}_{-8}	$0.8^{+0.4}_{-0.3}$	35^{+199}_{-26}		70^{+a}_{-37}	
4X		0.29±0.01	35^{+6}_{-5}	$0.8^{+0.2}_{-0.3}$	35^{+92}_{-16}		47^{+41}_{-21}	
5X		0.23±0.01	43^{+7}_{-6}	$0.87^{+0.09}_{-0.10}$	11^{+7}_{-4}		30±10	
6XNN		0.27±0.01	31^{+6}_{-5}	$1.14^{+0.22}_{-0.01}$	8^{+2}_{-3}	3.2±0.1	100^{+a}_{-30}	
7XN		0.26±0.01	36^{+8}_{-7}	$1.07^{+0.30}_{-0.07}$	10^{+3}_{-5}		100^{+a}_{-50}	
3X	4.3^b	0.22±0.01	39^{+11}_{-9}	$0.85^{+0.09}_{-0.08}$	7^{+4}_{-3}	-	-	1.07/125
Holmberg IX X-1								
4X	$9.8^{+0.6}_{-0.5}$	0.32±0.01	9±1	$1.77^{+0.63}_{-0.03}$	$2.2^{+0.6}_{-1.3}$	$2.9^{+0.2}_{-0.3}$	100^{+a}_{-60}	1.07/3721
9XNN		0.46±0.02	$3.7^{+0.7}_{-0.6}$	2.0±0.2	$2.3^{+1.1}_{-0.7}$		56^{+18}_{-16}	
10XNN		0.80±0.08	$0.67^{+0.19}_{-0.07}$	1.8±0.2	5^{+4}_{-2}	$3.4^{+0.2}_{-0.3}$	51^{+22}_{-16}	
11XXNN		$0.41^{+0.07}_{-0.06}$	3^{+2}_{-1}	$1.55^{+0.09}_{-0.10}$	15^{+4}_{-3}		39^{+13}_{-10}	
1X	9.8^b	0.6±0.1	$1.4^{+1.0}_{-0.5}$	1.7±0.2	7±4	-	-	1.212/199
2X	9.8^b	0.37±0.02	6±1	$1.48^{+0.57}_{-0.06}$	4^{+1}_{-3}	2.90^b	99^{+a}_{-58}	1.05/342
3X	9.8^b	0.42±0.02	$4.3^{+0.9}_{-0.7}$	$1.40^{+0.48}_{-0.04}$	6^{+2}_{-4}	2.90^b	99^{+a}_{-49}	1.02/353
5X	9.8^b	0.46±0.05	3±1	$3.6^{+a}_{-0.8}$	$0.3^{+0.4}_{-0.2}$	-	-	0.80/82
6X	9.8^b	0.46±0.03	$3.6^{+0.8}_{-0.6}$	$1.22^{+0.31}_{-0.03}$	15^{+662}_{-8}	2.90^b	100^{+a}_{-36}	1.15/398

Table 5.2: Continued.

Epoch	$n_{\rm H}$ 10^{20} cm^{-2}	kT$_{\rm soft}$ keV	norm	kT$_{\rm hard}$ keV	norm 10^{-2}	Γ	f_{scat} %	χ^2_r/dof
7X	9.8^{b}	0.58±0.04	$1.8^{+0.4}_{-0.3}$	2.4±0.2	$1.9^{+0.7}_{-0.6}$	-	-	0.97/373
8X	9.8^{b}	0.41±0.03	5±1	2.8±0.3	$0.7^{+0.3}_{-0.2}$	-	-	1.047/302
IC 342 X-1								
2X	55±3	$0.58^{+0.08}_{-0.07}$	$0.9^{+0.5}_{-0.3}$	2.1±0.2	$1.3^{+0.5}_{-0.4}$	-	-	1.03/2488
3X		$0.45^{+0.04}_{-0.03}$	$1.8^{+0.8}_{-0.5}$	$2.8^{+0.3}_{-0.2}$	0.2±0.1	-	-	
4X		0.6±0.1	$0.7^{+0.7}_{-0.3}$	$2.3^{+0.3}_{-0.2}$	$1.4^{+0.7}_{-0.3}$	-	-	
5XNN		0.39±0.02	$3.0^{+1.1}_{-0.8}$	$2.0^{+0.2}_{-0.3}$	$0.8^{+0.6}_{-0.2}$	2.9±0.1	60^{+a}_{-20}	
6XN		0.41±0.03	$2.6^{+1.1}_{-0.8}$	$1.27^{+0.29}_{-0.02}$	$4.1^{+0.3}_{-2.0}$		100^{+a}_{-30}	
1X	55^{b}	$0.41^{+0.07}_{-0.06}$	$1.9^{+1.8}_{-0.9}$	$2.8^{+0.7}_{-0.4}$	$0.2^{+0.2}_{-0.1}$	-	-	0.89/157
1C	55^{b}	$0.41^{+0.12}_{-0.09}$	2^{+4}_{-1}	$2.7^{+2.0}_{-0.7}$	$0.3^{+0.6}_{-0.3}$	-	-	0.80/85
2C	55^{b}	0.5±0.1	$1.0^{+1.4}_{-0.5}$	$2.9^{+a}_{-0.8}$	$0.3^{+0.5}_{-0.2}$	-	-	1.08/78
3C	55^{b}	$0.3^{+0.3}_{-0.1}$	5^{+112}_{-5}	$0.93^{+0.11}_{-0.06}$	25^{+10}_{-13}	-	-	1.01/75
NGC 5204 X-1								
4X	3.0±0.6	$0.31^{+0.02}_{-0.03}$	10^{+3}_{-2}	0.9±0.2	12^{+17}_{-7}	$2.1^{+0.2}_{-0.8}$	27^{+6}_{-12}	1.00/1453
5X		0.34±0.02	$5.2^{+1.1}_{-0.7}$	1.1±0.2	4^{+4}_{-2}		34^{+12}_{-13}	
6X		$0.28^{+0.02}_{-0.03}$	8±2	$0.65^{+0.58}_{-0.05}$	17^{+55}_{-13}		90^{+a}_{-54}	
7XXNN		$0.27^{+0.01}_{-0.001}$	8^{+2}_{-1}	$1.13^{+0.003}_{-0.11}$	$2.4^{+1.1}_{-0.6}$	$3.22^{+0.25}_{-0.07}$	97^{+a}_{-62}	
1X	3.0^{b}	0.28±0.01	7±1	1.7±0.1	$0.6^{+0.2}_{-0.1}$	-	-	1.05/249
2X	3.0^{b}	0.30±0.02	7±2	1.7±0.2	$0.8^{+0.5}_{-0.3}$	-	-	1.21/158
3X	3.0^{b}	0.33±0.02	6±1	1.6±0.2	$1.0^{+0.6}_{-0.4}$	-	-	1.08/181
8X	3.0^{b}	0.28±0.01	7±1	1.8±0.1	0.5±0.1	-	-	1.11/261
1C	3.0^{b}	0.21±0.04	13^{+14}_{-6}	$0.7^{+0.2}_{-0.1}$	9^{+10}_{-6}	-	-	0.86/51
2C	3.0^{b}	0.27±0.02	8±2	$1.01^{+0.10}_{-0.08}$	3^{+2}_{-1}	-	-	1.05/149
3CC	3.0^{b}	0.32±0.03	9^{+4}_{-2}	$1.3^{+0.3}_{-0.2}$	3^{+3}_{-2}	-	-	0.95/153
4C	3.0^{b}	$0.30^{+0.06}_{-0.05}$	7^{+6}_{-3}	$1.2^{+0.4}_{-0.2}$	3^{+5}_{-2}	-	-	0.98/48
5C	3.0^{b}	$0.32^{+0.07}_{-0.06}$	7^{+6}_{-3}	$1.0^{+0.3}_{-0.2}$	9^{+10}_{-6}	-	-	1.15/79
6C	3.0^{b}	0.31±0.05	7^{+6}_{-3}	$1.5^{+1.0}_{-0.4}$	$0.9^{+2.3}_{-0.8}$	-	-	1.05/48
7C	3.0^{b}	$0.29^{+0.06}_{-0.05}$	9^{+8}_{-4}	$1.0^{+0.2}_{-0.1}$	11^{+9}_{-6}	-	-	0.75/69
M83 ULX1								
1X	4±1	$0.29^{+0.04}_{-0.03}$	$1.6^{+1.2}_{-0.7}$	1.63±0.05	0.8±0.1	-	-	0.97/1487
2X		0.27±0.03	$1.2^{+0.8}_{-0.5}$	$1.12^{+0.10}_{-0.08}$	0.6±0.2	-	-	
3X		$0.28^{+0.04}_{-0.03}$	$1.8^{+1.4}_{-0.8}$	$1.53^{+0.08}_{-0.07}$	0.8±0.2	-	-	
4X		$0.23^{+0.04}_{-0.03}$	3^{+2}_{-1}	$1.17^{+0.10}_{-0.09}$	0.9±0.3	-	-	
5X		$0.26^{+0.03}_{-0.02}$	$1.9^{+1.2}_{-0.7}$	$1.41^{+0.04}_{-0.03}$	1.0±0.1	-	-	
6X		$0.27^{+0.04}_{-0.03}$	$1.6^{+1.2}_{-0.7}$	$1.44^{+0.07}_{-0.06}$	$0.8^{+0.2}_{-0.1}$	-	-	
NGC 5408 X-1								
5X	5.0±0.4	0.172±0.005	166^{+25}_{-21}	$0.53^{+0.06}_{-0.07}$	45^{+34}_{-15}	$2.82^{+0.07}_{-0.06}$	50^{+14}_{-8}	1.16/2732
6X		$0.178^{+0.005}_{-0.006}$	126^{+21}_{-17}	$0.59^{+0.07}_{-0.09}$	32^{+28}_{-9}		49^{+18}_{-11}	
7X		$0.176^{+0.003}_{-0.007}$	155^{+30}_{-23}	0.5±0.1	92^{+173}_{-47}		71^{+a}_{-18}	
8X		0.173±0.006	160^{+27}_{-23}	$0.36^{+0.07}_{-0.04}$	217^{+119}_{-99}		100^{+a}_{-20}	
9X		0.176±0.005	147^{+24}_{-19}	$0.51^{+0.07}_{-0.15}$	63^{+143}_{-24}		62^{+a}_{-11}	
10X		0.178±0.005	134^{+21}_{-18}	$0.40^{+0.09}_{-0.03}$	131^{+53}_{-65}		100^{+a}_{-a}	
11XX		0.180±0.006	120^{+21}_{-17}	0.5±0.1	53^{+90}_{-25}		71^{+a}_{-17}	
1X	5.0^{b}	0.180±0.006	235^{+44}_{-36}	$0.82^{+0.08}_{-0.07}$	9^{+5}_{-3}	-	-	1.34/139
2X	5.0^{b}	0.194±0.006	148^{+25}_{-21}	$0.98^{+0.10}_{-0.09}$	4±2	-	-	1.23/140
3X	5.0^{b}	0.182±0.008	216^{+53}_{-42}	$0.92^{+0.10}_{-0.08}$	7^{+4}_{-2}	-	-	1.16/98
4X	5.0^{b}	0.22±0.01	53^{+15}_{-11}	1.1±0.2	$1.8^{+1.5}_{-0.9}$	-	-	0.96/107
1CC	5.0^{b}	0.12±0.01	73^{+21}_{-16}	$1.03^{+0.08}_{-0.07}$	5^{+2}_{-1}	-	-	1.15/202
2C	5.0^{b}	0.12±0.01	84^{+34}_{-24}	1.1±0.1	4^{+3}_{-2}	-	-	1.07/100
NGC 1313 X-1								
10XN		0.31±0.01	$11.1^{+1.0}_{-0.9}$	$1.33^{+0.20}_{-0.01}$	$2.9^{+0.3}_{-1.1}$		100^{+a}_{-25}	
11XN		0.30±0.01	12±1	$1.28^{+0.16}_{-0.01}$	$3.44^{+0.38}_{-1.06}$		100^{+a}_{-26}	
	$22.1^{+0.3}_{-0.4}$					$2.90^{+0.05}_{-0.04}$		1.19/4781

Table 5.2: Continued.

Epoch	$n_{\rm H}$ 10^{20} cm^{-2}	kT$_{\rm soft}$ keV	norm	kT$_{\rm hard}$ keV	norm 10^{-2}	Γ	f_{scat} %	χ^2_r/dof
12XN		0.34±0.01	9±1	$0.77^{+0.12}_{-0.01}$	40^{+9}_{-14}		100^{+a}_{-21}	
14XN		0.34±0.01	$8.4^{+1.1}_{-0.9}$	$1.23^{+0.21}_{-0.02}$	$4.1^{+0.8}_{-1.6}$		100^{+a}_{-29}	
15XN		0.36±0.01	$7.7^{+0.8}_{-0.7}$	$0.93^{+0.14}_{-0.01}$	19^{+3}_{-7}		100^{+a}_{-20}	
17XXN		0.29±0.01	13±1	$1.32^{+0.24}_{-0.01}$	$2.8^{+0.3}_{-1.1}$		100^{+a}_{-29}	
19XN		0.34±0.01	$8.7^{+1.0}_{-0.9}$	$0.80^{+0.18}_{-0.02}$	33^{+8}_{-16}		97^{+a}_{-26}	
1X	22.1^b	0.28±0.01	14±2	2.2±0.1	$0.60^{+0.11}_{-0.09}$	-	-	1.19/339
2XX	22.1^b	0.43±0.03	5^{+2}_{-1}	1.6±0.2	3^{+2}_{-1}	-	-	0.87/151
3XX	22.1^b	0.40±0.03	5±1	$1.1^{+0.6}_{-0.2}$	8^{+7}_{-6}	2.90^b	91^{+a}_{-67}	0.99/343
4X	22.1^b	0.35±0.04	7^{+5}_{-3}	$2.3^{+0.9}_{-0.5}$	$0.5^{+0.7}_{-0.3}$	-	-	0.91/110
5X	22.1^b	$0.43^{+0.03}_{-0.02}$	6±1	1.6±0.1	3±1	-	-	1.01/287
6X	32±5	0.25±0.03	51^{+53}_{-25}	$0.92^{+0.10}_{-0.08}$	9^{+5}_{-3}	-	-	1.18/166
7X	22.1^b	0.33±0.02	8^{+3}_{-2}	$2.1^{+0.3}_{-0.2}$	$0.7^{+0.4}_{-0.3}$	-	-	1.01/158
8X	22.1^b	0.30±0.02	12±3	$1.30^{+0.65}_{-0.08}$	3±2	2.90^b	100^{+a}_{-72}	1.07/218
9X	22.1^b	0.27±0.01	14±1	$1.30^{+0.19}_{-0.02}$	$2.9^{+0.3}_{-1.0}$	2.90^b	100^{+a}_{-24}	1.23/457
13X	22.1^b	0.34±0.01	8±1	2.5±0.2	$0.40^{+0.11}_{-0.09}$	-	-	0.99/257
16X	22.1^b	0.35±0.01	8.0±0.5	$0.95^{+0.09}_{-0.01}$	$13.5^{+0.4}_{-3.5}$	2.90^b	97^{+a}_{-15}	1.32/487
18X	22.1^b	0.34±0.01	$8.8^{+0.7}_{-0.6}$	$1.02^{+0.15}_{-0.01}$	$9.2^{+0.4}_{-3.2}$	2.90^b	100^{+a}_{-22}	1.17/457
Circinus ULX 5								
2XNN	37±12	$0.26^{+0.19}_{-0.04}$	8^{+32}_{-8}	$1.71^{+0.1}_{-0.2}$	$4.4^{+1.6}_{-0.8}$	3±1	17^{+29}_{-10}	1.21/674
1X	37^b	$0.56^{+0.07}_{-0.06}$	$0.6^{+0.3}_{-0.2}$	$2.1^{+0.4}_{-0.3}$	$0.5^{+0.3}_{-0.2}$	-	-	0.82/120
3X	37^b	0.42±0.03	$2.0^{+0.8}_{-0.6}$	$2.2^{+0.3}_{-0.2}$	$0.3^{+0.2}_{-0.1}$	-	-	1.06/272
4XN	37^b	$0.39^{+0.06}_{-0.05}$	$2.3^{+1.7}_{-0.9}$	$1.24^{+0.06}_{-0.04}$	$4.5^{+1.0}_{-0.9}$	-	-	1.00/305
5X	37^b	0.29±0.03	7^{+5}_{-3}	$2.3^{+0.3}_{-0.2}$	$0.24^{+0.12}_{-0.09}$	-	-	0.99/202
6X	37^b	0.26±0.02	11^{+6}_{-4}	1.83±0.02	3.3±0.1	-	-	1.35/487
1C	37^b	$0.43^{+0.02}_{-0.06}$	$1.4^{+1.4}_{-0.3}$	5^{+a}_{-2}	$0.02^{+0.08}_{-0.002}$	-	-	0.80/85
M81 X-6								
1X	$11.7^{+1.6}_{-1.4}$	$0.49^{+0.12}_{-0.08}$	$0.45^{+0.4}_{-0.2}$	$1.42^{+0.08}_{-0.06}$	$2.8^{+0.6}_{-0.8}$	-	-	1.18/466
4X		0.6±0.1	$0.4^{+0.3}_{-0.2}$	$2.3^{+0.3}_{-0.2}$	$0.8^{+0.4}_{-0.3}$	-	-	
2X	11.7^b	$0.6^{+a}_{-0.2}$	$0.3^{+0.4}_{-0.1}$	$2.3^{+0.9}_{-0.4}$	$0.6^{+0.7}_{-0.4}$	-	-	1.08/163
3X	11.7^b	$0.4^{+0.2}_{-0.1}$	$1.2^{+3.5}_{-0.9}$	$1.7^{+0.3}_{-0.2}$	$1.6^{+0.8}_{-0.7}$	-	-	1.02/162
5X	11.7^b	$0.40^{+0.05}_{-0.06}$	$1.5^{+1.2}_{-0.6}$	4^{+a}_{-2}	$0.02^{+0.20}_{-0.01}$	-	-	0.60/46
6X	11.7^b	$0.5^{+0.2}_{-0.1}$	$0.4^{+0.5}_{-0.2}$	$1.7^{+0.3}_{-0.2}$	$1.9^{+0.9}_{-1.0}$	-	-	0.87/234
7X	11.7^b	$0.42^{+0.05}_{-0.04}$	$1.2^{+0.6}_{-0.4}$	$2.5^{+1.3}_{-0.6}$	$0.12^{+0.20}_{-0.09}$	-	-	0.75/65
8X	11.7^b	$0.3^{+0.2}_{-0.1}$	2^{+5}_{-1}	$1.7^{+0.3}_{-0.2}$	2±1	-	-	0.98/139
9XX	11.7^b	$0.5^{+0.2}_{-0.1}$	$0.5^{+0.5}_{-0.2}$	$2.2^{+0.9}_{-0.4}$	$0.6^{+0.7}_{-0.4}$	-	-	1.12/192
10XXX	11.7^b	$0.4^{+0.4}_{-0.2}$	2^{+14}_{-1}	$1.5^{+0.6}_{-0.2}$	3±2	-	-	0.80/132
NGC 55 ULX1								
1X	$26.2^{+1.4}_{-1.3}$	0.25±0.01	59^{+19}_{-10}	$0.77^{+0.03}_{-0.06}$	39^{+6}_{-8}	$1.1^{+3.0}_{-0.1}$	3±2	1.13/472
2X		0.26±0.02	48^{+23}_{-14}	$0.80^{+0.03}_{-0.23}$	50^{+10}_{-18}		7^{+3}_{-4}	
3X	$32.5^{+1.2}_{-0.3}$	$0.20^{+0.004}_{-0.01}$	141^{+32}_{-16}	$0.60^{+0.01}_{-0.02}$	$51.6^{+0.6}_{-7.6}$	$1.06^{+1.64}_{-0.06}$	3±1	1.55/470
NGC 6946 X-1								
1C	6.1±1.2	0.23±0.02	21^{+8}_{-6}	$0.72^{+0.41}_{-0.05}$	9^{+37}_{-7}	$2.9^{+0.7}_{-1.2}$	90^{+a}_{-60}	1.26/1402
1X		0.24±0.02	19^{+10}_{-5}	$0.68^{+0.64}_{-0.04}$	8^{+238}_{-7}		100^{+a}_{-90}	
2C		0.24±0.02	17^{+10}_{-6}	$0.75^{+0.76}_{-0.05}$	6^{+240}_{-4}		100^{+a}_{-a}	
2XX		0.23±0.01	22^{+6}_{-4}	$0.78^{+0.43}_{-0.07}$	5^{+14}_{-3}		90^{+a}_{-70}	
3X		0.24±0.01	22^{+5}_{-4}	$0.9^{+0.2}_{-0.3}$	4^{+9}_{-2}		50^{+a}_{-40}	
4XNN		0.24±0.01	22^{+6}_{-5}	$1.1^{+0.2}_{-0.4}$	$2.1^{+4.4}_{-0.9}$		30^{+a}_{-20}	
3CC	6.1^b	0.23±0.01	22^{+5}_{-4}	1.4±0.1	$0.9^{+0.4}_{-0.3}$	-	-	1.15/216
4C	6.1^b	0.24±0.03	22^{+18}_{-10}	$1.2^{+0.2}_{-0.1}$	$1.7^{+1.0}_{-0.7}$	-	-	0.94/103
NGC 1313 X-2								

Table 5.2: Continued.

Epoch	$n_{\rm H}$ 10^{20} cm^{-2}	kT$_{\rm soft}$ keV	norm	kT$_{\rm hard}$ keV	norm 10^{-2}	Γ	f_{scat} %	χ^2_r/dof
12X	$17.4^{+0.9}_{-0.8}$	0.35±0.06	$1.5^{+1.2}_{-0.6}$	$1.0^{+0.2}_{-0.3}$	10^{+23}_{-5}	$2.3^{+0.3}_{-0.5}$	66^{+a}_{-25}	1.10/2232
13XN		0.40±0.04	$1.0^{+0.4}_{-0.3}$	1.33±0.05	$3.6^{+0.7}_{-0.6}$		7^{+4}_{-3}	
20X		$0.37^{+0.04}_{-0.02}$	$1.6^{+0.6}_{-0.4}$	$1.2^{+0.2}_{-0.3}$	4^{+5}_{-2}		50^{+33}_{-18}	
21XN		$0.28^{+0.09}_{-0.08}$	3^{+7}_{-2}	$0.8^{+0.3}_{-0.4}$	13^{+77}_{-9}		43^{+a}_{-19}	
14XN		0.40±0.03	1.2±0.3	$1.16^{+0.05}_{-0.04}$	$2.6^{+0.6}_{-0.5}$	-	-	
26XXN		0.37±0.03	$1.1^{+0.3}_{-0.2}$	1.15±0.05	2.0±0.4	-	-	
1X	17.4^b	0.37±0.02	$2.1^{+0.6}_{-0.4}$	$1.9^{+0.4}_{-0.3}$	$0.2^{+0.2}_{-0.1}$	-	-	0.97/136
2X	17.4^b	0.40±0.06	$1.3^{+0.9}_{-0.5}$	1.9±0.1	$1.4^{+0.4}_{-0.3}$	-	-	0.89/280
3X	17.4^b	$0.41^{+0.10}_{-0.08}$	$1.3^{+1.6}_{-0.7}$	2.0±0.2	1.3±0.5	-	-	1.05/200
4X	17.4^b	$0.36^{+0.05}_{-0.04}$	$2.2^{+1.3}_{-0.8}$	1.5±0.2	$1.2^{+0.7}_{-0.5}$	-	-	0.91/171
5X	17.4^b	0.39±0.04	$1.6^{+0.8}_{-0.5}$	$1.6^{+0.3}_{-0.2}$	$0.8^{+0.6}_{-0.4}$	-	-	0.93/176
6X	17.4^b	$0.34^{+0.06}_{-0.05}$	$2.3^{+1.7}_{-0.9}$	$1.5^{+0.4}_{-0.2}$	$0.7^{+0.8}_{-0.5}$	-	-	1.00/111
7X	17.4^b	$0.47^{+0.08}_{-0.07}$	$0.7^{+0.5}_{-0.3}$	1.9±0.1	1.6±0.4	-	-	0.78/294
8X	17.4^b	0.31±0.03	4^{+2}_{-1}	$1.9^{+0.4}_{-0.3}$	$0.3^{+0.2}_{-0.1}$	-	-	1.07/137
9X	17.4^b	0.36±0.02	$2.1^{+0.6}_{-0.4}$	$1.9^{+0.3}_{-0.2}$	$0.3^{+0.2}_{-0.1}$	-	-	1.17/182
10X	17.4^b	$0.41^{+0.08}_{-0.07}$	$1.0^{+0.8}_{-0.4}$	2.0±0.1	1.4±0.3	-	-	0.93/303
11X	17.4^b	0.6±0.1	$0.32^{+0.38}_{-0.04}$	$2.0^{+0.1}_{-0.2}$	$1.1^{+0.8}_{-0.1}$	-	-	1.05/119
15X	17.4^b	0.29±0.03	3^{+2}_{-1}	$2.0^{+0.5}_{-0.3}$	$0.2^{+0.2}_{-0.1}$	-	-	1.07/60
16X	17.4^b	0.46±0.06	$0.6^{+0.3}_{-0.2}$	$1.36^{+0.09}_{-0.07}$	$2.7^{+0.8}_{-0.7}$	-	-	1.30/128
17X	17.4^b	0.46±0.07	$0.5^{+0.3}_{-0.2}$	$1.4^{+0.3}_{-0.2}$	$1.0^{+0.9}_{-0.6}$	-	-	1.10/86
18X	17.4^b	0.32±0.01	$2.6^{+0.4}_{-0.3}$	2.3±0.2	0.13±0.03	-	-	0.89/336
19X	17.4^b	0.41±0.05	$1.1^{+0.5}_{-0.3}$	$1.19^{+0.12}_{-0.09}$	$2.4^{+1.2}_{-0.9}$	-	-	1.12/233
22X	17.4^b	0.43±0.05	$0.7^{+0.3}_{-0.2}$	$1.39^{+0.09}_{-0.08}$	$2.0^{+0.6}_{-0.5}$	-	-	1.07/247
23X	17.4^b	0.52±0.05	$0.40^{+0.12}_{-0.08}$	$1.45^{+0.09}_{-0.07}$	1.9±0.5	-	-	1.51/129
24X	17.4^b	0.42±0.04	$1.4^{+0.6}_{-0.4}$	$2.2^{+0.8}_{-0.4}$	$0.2^{+0.3}_{-0.1}$	-	-	1.05/101
25X	17.4^b	$0.48^{+0.09}_{-0.08}$	$0.9^{+0.7}_{-0.4}$	$1.9^{+0.5}_{-0.3}$	$0.8^{+0.8}_{-0.5}$	-	-	0.94/109
NGC 300 ULX1								
1XN	3.7±0.5	0.31±0.01	$6.4^{+0.9}_{-0.8}$	2.30±0.07	0.8±0.1	1.6±0.5	12^{+5}_{-20}	1.26/1305
2X		0.31±0.01	8±1	$2.51^{+0.06}_{-0.29}$	$0.7^{+0.4}_{-0.2}$		0.0003^{+20}_{-a}	
1CC	3.7^b	$0.6^{+a}_{-0.1}$	$0.3^{+0.3}_{-0.1}$	4^{+a}_{-1}	$0.10^{+0.20}_{-0.05}$	-	-	1.08/167
NGC 5907 ULX1								
1X	70^{+6}_{-5}	$0.6^{+0.2}_{-0.1}$	$0.2^{+0.3}_{-0.1}$	$2.6^{+0.5}_{-0.3}$	0.2±0.1	-	-	0.98/1126
2X		$0.4^{+0.2}_{-0.1}$	$0.5^{+1.2}_{-0.3}$	2.2±0.2	0.4±0.1	-	-	
4XN		$0.38^{+0.06}_{-0.05}$	$0.7^{+0.8}_{-0.4}$	2.2±0.1	$0.15^{+0.04}_{-0.03}$	-	-	
5XNN		$0.41^{+0.09}_{-0.06}$	$0.6^{+0.9}_{-0.4}$	1.9±0.4	$0.8^{+0.6}_{-0.4}$	$3.1^{+0.5}_{-1.1}$	60^{+a}_{-40}	
3XXCC	70^b	$0.4^{+0.3}_{-0.1}$	$0.1^{+0.6}_{-0.1}$	$3.3^{+1.0}_{-0.4}$	$0.05^{+0.02}_{-0.03}$	-	-	0.91/240
1C	70^b	$0.6^{+a}_{-0.2}$	$0.04^{+0.14}_{-0.02}$	5^{+a}_{-1}	$0.013^{+0.026}_{-0.001}$	-	-	0.87/56
6X	70^b	$0.34^{+0.07}_{-0.05}$	$0.9^{+1.1}_{-0.5}$	$1.9^{+0.3}_{-0.2}$	0.2±0.1	-	-	1.08/152
7X	70^b	0.27±0.04	2^{+2}_{-1}	1.7±0.2	0.1±0.1	-	-	0.97/123
8XX	70^b	$0.21^{+0.04}_{-0.03}$	4^{+7}_{-3}	1.6±0.2	$0.08^{+0.05}_{-0.03}$	-	-	1.25/126
NGC 7793 P13								
1C	10.7±0.7	$0.32^{+0.05}_{-0.04}$	$1.3^{+0.9}_{-0.5}$	$3.9^{+0.8}_{-0.5}$	$0.07^{+0.04}_{-0.03}$	-	-	1.12/4421
1X		$0.27^{+0.02}_{-0.01}$	$2.8^{+0.8}_{-0.6}$	$2.7^{+0.2}_{-0.1}$	0.11±0.02	-	-	
2X		0.29±0.02	$2.7^{+0.9}_{-0.7}$	3.3±0.2	0.15±0.02	-	-	
3XN		0.24±0.01	8±2	$3.05^{+0.04}_{-0.05}$	0.36±0.02	-	-	
4X		$0.31^{+0.05}_{-0.04}$	3^{+2}_{-1}	$3.1^{+0.5}_{-0.3}$	$0.17^{+0.08}_{-0.06}$	-	-	
5XN		$0.27^{+0.02}_{-0.01}$	$3.3^{+0.9}_{-0.7}$	$2.92^{+0.07}_{-0.06}$	$0.19^{+0.02}_{-0.01}$	-	-	
6X		0.30±0.02	$3.3^{+1.2}_{-0.9}$	3.2±0.1	$0.27^{+0.04}_{-0.03}$	-	-	
7X		0.29±0.02	5^{+2}_{-1}	3.2±0.1	0.32±0.04	-	-	
8X		0.29±0.02	5±1	3.2±0.1	0.31±0.04	-	-	
9XN		0.27±0.01	$4.7^{+1.2}_{-0.9}$	$2.99^{+0.06}_{-0.05}$	0.26±0.02	-	-	
M51 ULX-7								
1X		$0.4^{+0.2}_{-0.1}$	$0.12^{+0.30}_{-0.09}$	3^{+3}_{-1}	$0.01^{+0.04}_{-0.01}$	-	-	

13.7±1.3 1.06/2407

Table 5.2: Continued.

Epoch	$n_{\rm H}$ 10^{20} cm^{-2}	kT$_{\rm soft}$ keV	norm	kT$_{\rm hard}$ keV	norm 10^{-2}	Γ	f_{scat} %	χ^2_r/dof
1C		$0.31^{+0.07}_{-0.06}$	$0.7^{+0.9}_{-0.4}$	$2.7^{+1.3}_{-0.6}$	$0.04^{+0.06}_{-0.03}$	-	-	
2X		0.37 ± 0.04	$0.61^{+0.34}_{-0.22}$	$2.7^{+0.5}_{-0.4}$	$0.06^{+0.04}_{-0.03}$	-	-	
3X		0.36 ± 0.03	$0.6^{+0.3}_{-0.2}$	$3.7^{+1.0}_{-0.6}$	0.02 ± 0.01	-	-	
4X		$0.31^{+0.04}_{-0.03}$	$1.2^{+0.7}_{-0.5}$	$2.8^{+0.4}_{-0.3}$	0.06 ± 0.03	-	-	
2C		$0.36^{+0.04}_{-0.03}$	$0.7^{+0.3}_{-0.2}$	$3.2^{+0.6}_{-0.4}$	0.04 ± 0.02	-	-	
3C		$0.33^{+0.04}_{-0.03}$	$0.8^{+0.5}_{-0.3}$	$2.8^{+0.4}_{-0.3}$	$0.06^{+0.03}_{-0.02}$	-	-	
4CC		$0.35^{+0.04}_{-0.03}$	0.5 ± 0.2	$2.9^{+0.5}_{-0.3}$	0.04 ± 0.02	-	-	
5C		$0.34^{+0.11}_{-0.08}$	$0.34^{+0.7}_{-0.2}$	$3.1^{+a}_{-0.9}$	$0.02^{+0.05}_{-0.02}$	-	-	
5X		0.34 ± 0.02	$0.8^{+0.3}_{-0.2}$	$2.7^{+0.3}_{-0.2}$	$0.05^{+0.02}_{-0.01}$	-	-	
6XX		0.32 ± 0.02	$1.3^{+0.4}_{-0.3}$	$2.6^{+0.2}_{-0.1}$	0.08 ± 0.02	-	-	
M51 ULX-8								
1C	$2.0^{+0.9}_{-0.8}$	0.5 ± 0.1	$0.12^{+0.12}_{-0.05}$	$2.0^{+2.3}_{-0.6}$	$0.06^{+0.21}_{-0.06}$	-	-	1.00/1474
1X		$0.26^{+0.04}_{-0.03}$	$1.4^{+1.1}_{-0.6}$	$2.1^{+0.6}_{-0.4}$	$0.05^{+0.05}_{-0.03}$	-	-	
2X		$0.35^{+0.04}_{-0.03}$	$0.4^{+0.2}_{-0.1}$	$1.9^{+0.5}_{-0.3}$	$0.05^{+0.06}_{-0.03}$	-	-	
3X		0.40 ± 0.05	$0.3^{+0.2}_{-0.1}$	$2.6^{+a}_{-0.8}$	$0.02^{+0.06}_{-0.02}$	-	-	
2C		$0.41^{+0.08}_{-0.07}$	$0.21^{+0.15}_{-0.09}$	1.2 ± 0.1	0.8 ± 0.4	-	-	
3CCC		0.43 ± 0.05	$0.22^{+0.10}_{-0.06}$	$1.1^{+0.2}_{-0.1}$	$0.5^{+0.4}_{-0.3}$	-	-	
4C		$0.33^{+0.10}_{-0.07}$	$0.4^{+0.5}_{-0.2}$	$1.06^{+0.17}_{-0.09}$	$1.0^{+0.6}_{-0.5}$	-	-	
4X		$0.30^{+0.05}_{-0.04}$	$0.5^{+0.4}_{-0.2}$	$1.14^{+0.08}_{-0.06}$	0.8 ± 0.2	-	-	
5X		$0.35^{+0.11}_{-0.08}$	$0.2^{+0.3}_{-0.1}$	$1.48^{+0.09}_{-0.07}$	0.6 ± 0.1	-	-	
6XX		0.38 ± 0.03	$0.35^{+0.12}_{-0.09}$	$1.9^{+0.3}_{-0.2}$	$0.07^{+0.05}_{-0.03}$	-	-	

Notes. $^{(a)}$ Parameter frozen at the value determined in the joint fits. $^{(b)}$ Unbound parameter.

Table 5.3: Estimated unabsorbed luminosities in units of 10^{39} erg/s for each epoch using the distances from Table 5.1 and models from Table 5.2. For jointly fit data, the error estimation takes into account the errors on the joint parameters. Uncertainties are quoted at 90% confidence level. First column indicates the epoch given in Table 5.1 sorted chronologically. The `simpl` flux luminosity corresponds to the entire `diskbb`⊗`simpl` component.

Epoch	L$_{\rm soft}$ (0.3-1.5 keV)	L$_{\rm hard}$ (1.5-10 keV)	L$_{\rm tot}$ (0.3 – 10 keV)	L$_{\rm soft\ diskbb}$ (0.01 – 100 keV)	L$_{\rm hard\ diskbb}$ (0.01 – 100 keV)	L$_{\rm simpl}$ (0.01 – 100 keV)
Holmberg II X-1						
1X	6.1 ± 0.2	4.3 ± 0.1	10.4 ± 0.2	5^{+1}_{-3}	5^{+2}_{-1}	9^{+4}_{-2}
2X	5.5 ± 0.2	4.5 ± 0.2	10.0 ± 0.2	$5.6^{+0.4}_{-0.7}$	3.8 ± 0.9	8 ± 1
3X	1.87 ± 0.05	0.57 ± 0.04	2.44 ± 0.06	2.4 ± 0.1	1.0 ± 0.1	-
4X	6.56 ± 0.14	4.52 ± 0.06	11.1 ± 0.2	$7.0^{+0.3}_{-0.4}$	$4.6^{+0.3}_{-1.0}$	$8.0^{+1.5}_{-0.6}$
5X	$2.87^{+0.08}_{-0.06}$	1.43 ± 0.03	$4.30^{+0.09}_{-0.04}$	3.4 ± 0.1	$1.79^{+0.08}_{-0.09}$	$2.6^{+0.4}_{-0.2}$
6XNN	$4.17^{+0.05}_{-0.11}$	4.23 ± 0.06	$8.40^{+0.07}_{-0.13}$	4.7 ± 0.2	$3.6^{+0.6}_{-0.1}$	$6.4^{+0.3}_{-0.2}$
7XN	$3.98^{+0.09}_{-0.11}$	4.02 ± 0.06	8.0 ± 0.01	4.5 ± 0.2	$3.4^{+0.8}_{-0.2}$	6.1 ± 0.3
Holmberg IX X-1						
1X	$7.6^{+0.3}_{-0.2}$	18.3 ± 0.6	26.0 ± 0.6	6^{+3}_{-2}	22 ± 2	-
2X	$4.60^{+0.07}_{-0.08}$	$9.3^{+0.1}_{-0.2}$	14.0 ± 0.2	4.4 ± 0.2	$7.8^{+2.6}_{-0.3}$	$15.8^{+0.6}_{-1.3}$
3X	$5.11^{+0.06}_{-0.08}$	10.8 ± 0.2	$15.9^{+0.1}_{-0.2}$	4.9 ± 0.3	$8.7^{+2.5}_{-0.3}$	$17.5^{+0.5}_{-1.0}$
4X	$3.70^{+0.04}_{-0.08}$	$8.5^{+0.04}_{-0.07}$	$12.20^{+0.06}_{-0.10}$	3.6 ± 0.1	$8.0^{+2.0}_{-0.2}$	$14.6^{+0.5}_{-0.8}$
5X	4.7 ± 0.2	10.6 ± 0.6	15.3 ± 0.6	$5.6^{+0.7}_{-0.6}$	15^{+5}_{-3}	-
6X	$6.95^{+0.07}_{-0.08}$	$15.6^{+0.2}_{-0.3}$	$22.6^{+0.2}_{-0.3}$	6.0 ± 0.6	$12.1^{+2.4}_{-0.3}$	$24.5^{+0.5}_{-0.8}$
7X	7.3 ± 0.1	19.7 ± 0.4	27.0 ± 0.3	$7.7^{+0.9}_{-0.8}$	23.5 ± 0.8	-
8X	5.16 ± 0.12	11.8 ± 0.3	17.0 ± 0.3	5.4 ± 0.3	16 ± 1	-
9XXNN	$5.91^{+0.12}_{-0.07}$	13.2 ± 0.1	19.1 ± 0.2	6.2 ± 0.2	$11.3^{+2.3}_{-0.4}$	20.6 ± 0.7
10XNN	8.3 ± 0.2	23.7 ± 0.2	32.1 ± 0.3	7 ± 2	20^{+3}_{-1}	32 ± 2
11XXNN	8.8 ± 0.2	27.1 ± 0.2	35.9 ± 0.3	$3.3^{+0.6}_{-0.5}$	30^{+1}_{-2}	39 ± 1

Table 5.3: Continued.

Epoch	L_{soft} (0.3-1.5 keV)	L_{hard} (1.5-10 keV)	L_{tot} (0.3 – 10 keV)	$L_{soft\ disk}$ (0.01 – 100 keV)	$L_{hard\ disk}$ (0.01 – 100 keV)	L_{simpl} (0.01 – 100 keV)
IC 342 X-1						
1X	1.5±0.1	3.1±0.2	4.5±0.1	1.6±0.2	$4.1^{+0.5}_{-0.4}$	-
1C	1.82±0.2	$3.8^{+0.3}_{-0.4}$	5.6±0.2	1.9±0.3	$4.8^{+2.3}_{-0.6}$	-
2C	1.61±0.2	4.0±0.3	$5.7^{+0.3}_{-0.2}$	$1.8^{+0.5}_{-0.4}$	$5.3^{+2.7}_{-0.8}$	-
2X	2.9±0.1	6.8±0.1	9.7±0.1	$3.0^{+0.4}_{-0.3}$	$7.8^{+0.3}_{-0.4}$	-
3X	1.8±0.1	3.41±0.09	5.2±0.1	2.2±0.2	4.2±0.2	-
4X	$3.3^{+0.1}_{-0.2}$	9.2±0.2	12.5±0.2	$3.2^{+0.8}_{-0.6}$	11.0±0.5	-
5XNN	1.8±0.1	3.54±0.03	5.4±0.1	$1.9^{+0.2}_{-0.1}$	$3.6^{+0.3}_{-0.5}$	5.9±0.2
6XN	$2.17^{+0.03}_{-0.1}$	4.06±0.04	$6.2^{+0.1}_{-0.2}$	2.1±0.2	$3.1^{+0.6}_{-0.1}$	6.5±0.3
3C	$2.9^{+0.2}_{-0.3}$	3.2±0.2	6.1±0.3	$1.2^{+1.3}_{-0.8}$	$5.59^{+0.4}_{-1.3}$	-
NGC 5204 X-1						
1C	1.54±0.08	0.62±0.07	2.2±0.1	$1.5^{+0.2}_{-0.3}$	$1.4^{+0.2}_{-0.3}$	-
1X	2.08±0.04	2.34±0.07	4.42±0.08	2.26±0.07	3.0±0.1	-
2X	2.96±0.08	$2.7^{+0.2}_{-0.1}$	5.7±0.2	3.4±0.2	3.4±0.2	-
3X	3.45±0.08	2.8±0.1	6.3±0.1	4.0±0.2	3.4±0.2	-
2C	2.28±0.05	1.23±0.05	3.51±0.07	2.3±0.2	1.9±0.2	
3CC	5.1±0.2	3.9±0.3	9.0±0.3	5.5±0.5	5.1±0.5	-
4C	3.0±0.2	2.4±0.3	5.45±0.3	3.0±0.5	$3.4^{+0.5}_{-0.6}$	-
5C	4.7±0.2	3.7±0.3	8.4±0.4	$4.1^{+1.1}_{-0.9}$	$5.6^{+0.9}_{-1.1}$	-
6C	2.8±0.2	$2.23^{+0.28}_{-0.27}$	5.0±0.3	3.3±0.4	$2.8^{+0.5}_{-0.4}$	-
7C	4.4±0.2	3.5±0.3	7.9±0.3	$3.6^{+0.8}_{-0.7}$	$5.6^{+0.7}_{-0.9}$	-
4X	$4.5^{+0.2}_{-0.1}$	3.27±0.05	$7.8^{+0.2}_{-0.1}$	$4.6^{+0.5}_{-0.2}$	$3.6^{+0.5}_{-0.2}$	$6.6^{+7.8}_{-0.6}$
5X	3.61±0.09	3.07±0.02	6.7±0.1	4.0±0.2	$3.0^{+1.1}_{-0.3}$	$5.75^{+5.00}_{-0.7}$
6X	$2.65^{+0.08}_{-0.07}$	2.76±0.08	5.4±0.1	$2.28^{+0.13}_{-0.05}$	$1.71^{+1.65}_{-0.03}$	7^{+11}_{-1}
7XXNN	$2.10^{+0.06}_{-0.05}$	$2.45^{+0.04}_{-0.02}$	$4.52^{+0.06}_{-0.07}$	$2.24^{+0.11}_{-0.04}$	$2.06^{+0.03}_{-0.09}$	3.7±0.2
8X	2.00±0.03	2.25±0.07	4.25±0.07	2.20±0.07	2.9±0.1	-
M83 ULX1						
1X	1.10±0.03	2.46±0.05	3.56±0.06	$0.60^{+0.09}_{-0.08}$	3.32±0.07	-
2X	0.42±0.02	0.37±0.02	0.79±0.02	$0.36^{+0.05}_{-0.04}$	0.56±0.04	-
3X	0.93±0.03	1.75±0.06	2.68±0.06	$0.59^{+0.09}_{-0.08}$	2.39±0.08	-
4X	0.55±0.03	0.61±0.04	1.16±0.04	$0.42^{+0.08}_{-0.07}$	0.93±0.06	-
5X	0.88±0.03	1.56±0.03	2.44±0.04	$0.50^{+0.08}_{-0.07}$	2.20±0.05	-
6X	0.78±0.03	1.34±0.04	2.12±0.04	$0.50^{+0.07}_{-0.06}$	1.87±0.06	-
NGC 5408 X-1						
1X	8.9±0.2	1.34±0.08	10.2±0.2	14.6±0.6	2.5±0.2	-
2X	7.9±0.2	1.43±0.08	9.3±0.2	$12.4^{+0.5}_{-0.4}$	2.3±0.2	-
3X	8.8±0.3	1.7±0.1	10.5±0.3	14.2±0.8	2.9±0.2	-
4X	4.8±0.2	1.5±0.1	6.4±0.2	6.9±0.4	2.2±0.2	-
5X	$5.66^{+0.10}_{-0.09}$	1.54±0.02	$7.19^{+0.11}_{-0.09}$	$8.0^{+0.3}_{-0.2}$	$2.13^{+0.08}_{-0.10}$	$3.3^{+0.2}_{-0.1}$
6X	5.20±0.09	$1.71^{+0.04}_{-0.03}$	6.9±0.1	7.0±0.2	$2.3^{+0.1}_{-0.2}$	3.5±0.2
1CC	5.1±0.2	2.0±0.1	7.1±0.2	6.8±0.4	3.3±0.2	-
2C	5.7±0.3	$2.1^{+0.2}_{-0.1}$	7.7±0.3	$7.9^{+0.7}_{-0.6}$	3.3±0.3	-
7X	6.4±0.1	2.20±0.03	8.6±0.1	$8.2^{+0.3}_{-0.2}$	$2.7^{+0.2}_{-0.5}$	$4.6^{+0.3}_{-0.2}$
8X	$6.10^{+0.10}_{-0.09}$	2.13±0.03	8.2±0.1	$7.8^{+0.3}_{-0.2}$	$2.19^{+0.27}_{-0.05}$	$4.7^{+0.3}_{-0.2}$
9X	$5.81^{+0.10}_{-0.09}$	1.92±0.03	$7.73^{+0.10}_{-0.09}$	$7.8^{+0.3}_{-0.2}$	$2.4^{+0.1}_{-0.3}$	4.0±0.2
10X	$5.51^{+0.09}_{-0.08}$	$2.00^{+0.03}_{-0.01}$	$7.53^{+0.09}_{-0.13}$	7.3±0.2	$2.00^{+0.29}_{-0.05}$	4.2±0.2
11X	$5.22^{+0.09}_{-0.08}$	1.92±0.03	$7.15^{+0.09}_{-0.11}$	6.9±0.2	$2.2^{+0.2}_{-0.4}$	$3.9^{+0.2}_{-0.1}$
NGC 1313 X-1						
1X	$3.65^{+0.07}_{-0.06}$	4.7±0.1	8.3±0.1	4.1±0.1	6.0±0.2	-
2XX	7.1±0.2	8.1±0.3	15.3±0.3	8.2±0.7	9.0±0.7	-
3XX	5.4±0.1	6.6±0.2	12.0±0.2	6.1±0.5	$4.66^{+1.8}_{-0.2}$	$9.5^{+0.4}_{-1.2}$
4X	4.1±0.3	5.4±0.4	9.5±0.4	4.8±0.6	$6.6^{+1.7}_{-1.0}$	-
5X	8.0±0.2	10.0±0.2	18.0±0.3	8.9±0.6	11.2±0.6	-
6X	6.6±0.8	1.85±0.08	8.5±0.8	9^{+3}_{-2}	2.90±0.4	-
7X	4.2±0.2	5.12±0.2	9.4±0.2	4.9±0.3	6.2±0.4	-
8X	$3.94^{+0.11}_{-0.12}$	$5.0^{+0.1}_{-0.2}$	8.9±0.2	4.4±0.2	$4.0^{+1.6}_{-0.2}$	$8.1^{+0.5}_{-1.0}$

Table 5.3: Continued.

Epoch	$L_{\rm soft}$ (0.3-1.5 keV)	$L_{\rm hard}$ (1.5-10 keV)	$L_{\rm tot}$ (0.3 – 10 keV)	$L_{\rm soft\ disk}$ (0.01 – 100 keV)	$L_{\rm hard\ disk}$ (0.01 – 100 keV)	$L_{\rm simpl}$ (0.01 – 100 keV)
9X	3.37±0.03	$4.65^{+0.04}_{-0.05}$	$8.02^{+0.05}_{-0.06}$	3.66±0.06	$3.83^{+0.53}_{-0.06}$	7.8±0.1
10XN	$4.13^{+0.05}_{-0.06}$	$5.39^{+0.04}_{-0.06}$	9.52±0.07	$4.60^{+0.10}_{-0.09}$	$4.35^{+0.61}_{-0.07}$	8.8±0.1
11XN	$4.33^{+0.05}_{-0.07}$	5.46±0.04	9.79±0.07	$4.82^{+0.10}_{-0.09}$	$4.38^{+0.51}_{-0.07}$	$8.9^{+0.1}_{-0.2}$
12XN	6.5±0.1	8.28±0.07	14.8±0.1	5.4±0.2	$6.5^{+0.8}_{-0.1}$	$13.4^{+0.3}_{-0.4}$
13X	4.16±0.08	5.8±0.1	9.9±0.1	4.8±0.1	$7.3^{+0.4}_{-0.3}$	-
14XN	4.48±0.08	5.67±0.06	$10.16^{+0.08}_{-0.10}$	5.0±0.1	$4.4^{+0.6}_{-0.1}$	8.9±0.2
15XN	$6.12^{+0.09}_{-0.08}$	$8.38^{+0.03}_{-0.05}$	$14.50^{+0.09}_{-0.10}$	5.7±0.1	$6.42^{+0.78}_{-0.07}$	$13.2^{+0.2}_{-0.3}$
16X	5.62±0.03	$6.92^{+0.04}_{-0.05}$	$12.54^{+0.05}_{-0.06}$	$5.68^{+0.09}_{-0.10}$	$5.20^{+0.46}_{-0.05}$	10.7±0.1
17XXN	3.57±0.06	$4.81^{+0.03}_{-0.04}$	$8.38^{+0.05}_{-0.07}$	$3.92^{+0.10}_{-0.09}$	$3.95^{+0.64}_{-0.06}$	$8.0^{+0.1}_{-0.2}$
18X	$5.12^{+0.04}_{-0.05}$	$6.16^{+0.04}_{-0.06}$	$11.28^{+0.06}_{-0.07}$	5.4±0.1	$4.66^{+0.59}_{-0.06}$	9.5±0.1
19XN	$6.36^{+0.10}_{-0.05}$	7.83±0.05	$14.22^{+0.09}_{-0.13}$	5.5±0.2	$6.11^{+1.03}_{-0.08}$	$12.6^{+0.3}_{-0.4}$
Circinus ULX5						
1X	2.2±0.1	4.1±0.1	6.3±0.1	2.6±0.3	$4.3^{+0.2}_{-0.3}$	-
1C	$1.62^{+0.23}_{-0.06}$	3.1±0.2	4.8±0.2	2.1±0.2	$5.7^{+0.4}_{-2.0}$	-
2XNN	$4.5^{+0.4}_{-0.5}$	13.6±0.1	16.6±0.1	2^{+3}_{-2}	$17.0^{+0.6}_{-1.2}$	$20.0^{+1.6}_{-0.7}$
3X	2.3±0.1	3.00±0.09	5.3±0.1	2.8±0.2	$3.4^{+0.2}_{-0.1}$	-
4XN	2.94±0.07	3.59±0.06	6.53±0.09	2.3±0.2	4.9±0.3	-
5X	1.8±0.1	2.3±0.1	4.1±0.1	$2.1^{+0.4}_{-0.3}$	$2.9^{+0.3}_{-0.2}$	-
6X	4.63±0.06	$12.64^{+0.08}_{-0.07}$	17.27±0.09	2.4±0.3	16.9±0.1	-
M81 X-6						
1X	1.47±0.03	2.91±0.04	4.38±0.05	$0.9^{+0.3}_{-0.2}$	$3.8^{+0.2}_{-0.3}$	-
2X	1.35±0.06	$4.0^{+0.2}_{-0.3}$	5.4±0.2	$1.2^{+0.6}_{-0.4}$	4.9±0.5	-
3X	1.42±0.06	3.7±0.2	5.1±0.2	$0.7^{+0.3}_{-0.2}$	4.9±0.3	-
4X	$1.74^{+0.05}_{-0.06}$	5.7±0.2	7.4±0.2	$1.3^{+0.4}_{-0.3}$	7.1±0.3	-
5X	0.97±0.08	1.6±0.2	2.6±0.2	$1.2^{+0.1}_{-0.2}$	$2.6^{+0.7}_{-1.1}$	-
6X	1.53±0.04	3.9±0.2	5.4±0.2	$0.8^{+0.7}_{-0.3}$	$5.0^{+0.3}_{-0.5}$	-
7X	1.01±0.05	1.4±0.1	2.4±0.1	1.3±0.1	$1.7^{+0.4}_{-0.2}$	-
8X	1.69±0.08	4.5±0.3	6.2±0.3	$0.7^{+0.4}_{-0.2}$	6.1±0.4	-
9XX	$1.40^{+0.06}_{-0.07}$	3.7±0.2	5.1±0.2	$1.2^{+0.6}_{-0.4}$	$4.6^{+0.6}_{-0.5}$	-
10XXX	$1.81^{+0.09}_{-0.10}$	$4.3^{+0.4}_{-0.3}$	$6.1^{+0.4}_{-0.3}$	$0.7^{+1.2}_{-0.3}$	$5.8^{+0.4}_{-0.9}$	-
NGC 55 ULX1						
1X	2.5±0.1	0.87±0.02	3.4±0.1	$2.8^{+0.3}_{-0.2}$	1.6±0.1	$1.9^{+0.4}_{-0.3}$
2X	$2.7^{+0.2}_{-0.1}$	1.37±0.06	4.0±0.2	2.6±0.3	$2.42^{+0.05}_{-0.41}$	4^{+5}_{-2}
3X	$1.98^{+0.07}_{-0.08}$	0.31±0.01	$2.30^{+0.07}_{-0.09}$	$2.69^{+0.02}_{-0.03}$	$0.77^{+0.02}_{-0.04}$	$0.9^{+0.1}_{-0.2}$
NGC 6946 X-1						
1C	$3.8^{+0.2}_{-0.1}$	$2.32^{+0.2}_{-0.1}$	6.2±0.3	4.7±0.4	$1.9^{+9.4}_{-0.4}$	$3.97^{+3.1}_{-0.6}$
1X	3.8±0.3	$1.68^{+0.2}_{-0.1}$	5.5±0.3	$5.0^{+0.4}_{-1.1}$	$1.32^{+0.69}_{-0.08}$	$2.8^{+1.2}_{-0.5}$
2C	$3.3^{+0.3}_{-0.2}$	1.8±0.2	5.1±0.3	$4.3^{+0.3}_{-0.4}$	$1.4^{+0.8}_{-0.4}$	$2.9^{+2.3}_{-0.9}$
3CC	3.9±0.1	1.96±0.09	5.8±0.1	5.1±0.3	2.6±0.1	-
2XX	3.8±0.2	$1.75^{+0.09}_{-0.08}$	$5.5^{+0.3}_{-0.2}$	5.0±0.4	$1.5^{+1.2}_{-0.1}$	$2.9^{+1.9}_{-0.5}$
3X	$4.5^{+0.3}_{-0.2}$	2.09±0.05	$6.6^{+0.3}_{-0.2}$	5.8±0.4	2.1±0.5	$3.4^{+1.4}_{-0.3}$
4C	4.3±0.4	2.0±0.1	6.3±0.3	$5.5^{+1.1}_{-0.8}$	2.9±0.2	-
4XNN	$4.6^{+0.4}_{-0.3}$	2.05±0.05	6.7±0.3	$6.1^{+0.5}_{-0.2}$	$2.4^{+0.2}_{-0.6}$	$3.1^{+0.4}_{-0.2}$
NGC 1313 X-2						
1X	1.43±0.05	$1.38^{+0.07}_{-0.06}$	2.81±0.07	$1.75^{+0.09}_{-0.10}$	1.6±0.1	-
2X	$2.47^{+0.05}_{-0.06}$	6.2±0.2	8.7±0.2	$1.6^{+0.3}_{-0.2}$	8.0±0.3	-
3X	2.63±0.08	7.4±0.3	10.0±0.3	$1.6^{+0.4}_{-0.3}$	9.5±0.5	-
4X	1.89±0.07	2.4±0.1	4.3±0.1	1.8±0.2	3.0±0.2	-
5X	1.65±0.06	1.82±0.08	3.48±0.09	1.8±0.2	2.1±0.2	-
6X	1.42±0.08	1.5±0.1	2.9±0.1	1.5±0.2	1.9±0.2	-
7X	2.74±0.05	7.6±0.2	10.3±0.2	$1.7^{+0.4}_{-0.3}$	$9.7^{+0.3}_{-0.4}$	-
8X	1.34±0.06	1.31±0.08	2.65±0.09	1.6±0.1	$1.6^{+0.2}_{-0.1}$	-
9X	1.40±0.04	1.41±0.06	2.80±0.07	1.66±0.09	1.6±0.1	-
10X	2.46±0.05	7.3±0.2	9.8±0.2	$1.3^{+0.3}_{-0.2}$	9.6±0.3	-
11X	2.39±0.05	6.6±0.2	9.0±0.2	$1.6^{+0.4}_{-0.5}$	8.1±0.4	-
12X	$2.40^{+0.08}_{-0.07}$	6.08±0.09	8.5±0.1	1.1±0.3	$5.3^{+0.8}_{-1.6}$	13^{+4}_{-2}
13XN	2.12±0.03	4.02±0.04	6.14±0.05	1.1±0.1	5.3±0.1	$6.0^{+0.4}_{-0.3}$

Table 5.3: Continued.

Epoch	$L_{\rm soft}$ (0.3-1.5 keV)	$L_{\rm hard}$ (1.5-10 keV)	$L_{\rm tot}$ (0.3 – 10 keV)	$L_{\rm soft\ disk}$ (0.01 – 100 keV)	$L_{\rm hard\ disk}$ (0.01 – 100 keV)	$L_{\rm simpl}$ (0.01 – 100 keV)
14XN	1.62±0.03	1.65±0.02	3.27±0.04	1.5±0.1	2.2±0.1	-
15X	1.01±0.06	1.2±0.1	2.2±0.1	1.1±0.1	1.5±0.2	-
16X	1.91±0.03	3.25±0.07	5.15±0.07	$1.3^{+0.3}_{-0.2}$	$4.3^{+0.2}_{-0.3}$	-
17X	1.09±0.04	1.38±0.06	2.47±0.07	$1.1^{+0.3}_{-0.2}$	$1.7^{+0.2}_{-0.3}$	-
18X	1.10±0.02	1.23±0.03	2.33±0.03	1.31±0.03	1.52±0.06	-
19X	1.61±0.04	1.73±0.05	3.34±0.06	1.4±0.2	$2.3^{+0.2}_{-0.3}$	-
20X	2.15±0.06	4.61±0.06	$6.76^{+0.10}_{-0.09}$	1.5±0.2	$4.4^{+0.4}_{-0.8}$	9^{+2}_{-1}
21XN	$1.90^{+0.09}_{-0.08}$	2.78±0.07	4.7±0.1	$1.0^{+0.4}_{-0.3}$	$3.0^{+0.3}_{-0.9}$	$5.8^{+0.8}_{-0.6}$
22X	1.63±0.03	2.66±0.06	4.28±0.06	1.2±0.2	3.5±0.2	-
23X	1.78±0.02	3.15±0.05	4.93±0.05	$1.4^{+0.3}_{-0.2}$	$3.9^{+0.2}_{-0.3}$	-
24X	$1.59^{+0.07}_{-0.06}$	1.79±0.09	3.4±0.1	2.0±0.2	$1.9^{+0.3}_{-0.2}$	-
25X	2.16±0.09	3.9±0.2	6.1±0.2	$2.2^{+0.5}_{-0.4}$	4.6±0.3	-
26XXN	1.11±0.02	1.15±0.02	2.26±0.02	0.92±0.07	1.61±0.08	-
NGC 300 ULX1						
1XN	0.79±0.01	2.00±0.01	2.79±0.02	$0.67^{+0.03}_{-0.02}$	$2.6^{+0.9}_{-0.1}$	$3.7^{+0.5}_{-0.3}$
2X	$0.92^{+0.02}_{-0.01}$	2.27±0.03	$3.20^{+0.04}_{-0.02}$	$0.81^{+0.02}_{-0.04}$	$3.07^{+0.05}_{-0.21}$	$3.06^{+0.06}_{-0.05}$
1CC	0.44±0.03	1.66±0.08	2.09±0.08	0.5±0.1	2.5±0.5	-
NGC 5907 ULX1						
1X	18±1	57±2	75±2	17^{+5}_{-4}	71±4	-
2X	15±1	46±2	61±2	10^{+4}_{-3}	60±3	-
3XXCC	5.6±0.3	26±1	32±1	$3^{+0.6}_{-0.9}$	40^{+7}_{-4}	
4XN	11.9±0.7	20.7±0.6	33±1	12^{+3}_{-2}	26±1	-
5XNN	21^{+3}_{-2}	68.5±0.9	90^{+3}_{-2}	14^{+4}_{-3}	73^{+12}_{-14}	112^{+14}_{-7}
6X	$9.9^{+0.6}_{-0.7}$	14.7±0.8	24.6±0.7	10±1	18±1	-
7X	8.2±0.6	7.8±0.5	16.0±0.5	9^{+2}_{-1}	10.0±0.6	-
8XX	$4.6^{+0.5}_{-0.4}$	2.9±0.2	7.6±0.4	6^{+3}_{-2}	3.9±0.3	-
NGC 7793 P13						
1C	0.75±0.03	3.4±0.2	4.2±0.2	0.50±0.06	$5.8^{+1.2}_{-0.8}$	-
1X	0.58±0.02	1.47±0.04	2.06±0.03	0.53±0.03	$2.06^{+0.09}_{-0.08}$	-
2X	0.98±0.02	3.95±0.07	4.93±0.07	$0.66^{+0.05}_{-0.04}$	6.0±0.2	-
3XN	1.62±0.04	$7.17^{+0.05}_{-0.06}$	8.79±0.06	$0.92^{+0.09}_{-0.08}$	10.6±0.2	-
4X	1.05±0.04	3.6±0.2	4.7±0.2	0.80±0.09	$5.3^{+0.6}_{-0.5}$	-
5XN	0.88±0.02	3.23±0.04	4.11±0.04	0.60±0.04	4.7±0.1	-
6X	1.48±0.03	6.4±0.1	7.9±0.1	0.89±0.07	9.6±0.3	-
7X	1.87±0.04	7.9±0.1	9.8±0.1	$1.18^{+0.09}_{-0.08}$	12.0±0.4	-
8X	1.84±0.04	7.5±0.1	9.4±0.1	$1.20^{+0.09}_{-0.08}$	$11.3^{+0.4}_{-0.3}$	-
9XN	1.31±0.02	4.91±0.04	6.21±0.05	0.89±0.06	7.2±0.1	-
M51 ULX-7						
1X	0.32±0.06	0.7±0.1	1.0±0.1	0.3±0.1	$0.8^{+1.0}_{-0.1}$	-
1C	1.04±0.08	2.7±0.3	3.7±0.2	0.9±0.2	$3.7^{+1.4}_{-0.6}$	-
2X	1.7±0.1	3.5±0.2	5.2±0.2	1.7±0.2	$4.6^{+0.5}_{-0.4}$	-
3X	$1.36^{+0.09}_{-0.08}$	$2.9^{+0.2}_{-0.1}$	4.3±0.2	1.5±0.1	$4.5^{+1.0}_{-0.6}$	-
4X	1.8±0.1	4.1±0.2	5.9±0.2	1.7±0.2	$5.6^{+0.6}_{-0.5}$	-
2C	$1.76^{+0.09}_{-0.08}$	4.8±0.2	6.6±0.2	1.7±0.1	$7.0^{+1.0}_{-0.7}$	-
3C	1.51±0.07	3.8 ±0.2	5.3±0.2	1.4±0.1	$5.2^{+0.6}_{-0.4}$	-
4CC	1.13±0.05	2.9±0.1	4.0±0.1	1.06±0.09	$4.0^{+0.5}_{-0.3}$	-
5C	0.77±0.08	$2.1^{+0.2}_{-0.3}$	2.9±0.2	0.7±0.1	$3.0^{+2.7}_{-0.6}$	-
5X	1.55±0.07	3.2±0.1	4.8±0.1	1.6±0.1	$4.3^{+0.3}_{-0.2}$	-
6XX	2.11±0.07	4.1±0.1	6.2±0.1	$2.2^{+0.2}_{-0.1}$	5.4±0.2	-
M51 ULX-8						
1C	0.92±0.05	1.5±0.1	2.4±0.1	1.1±0.3	$1.6^{+0.6}_{-0.3}$	-
1X	$0.91^{+0.07}_{-0.06}$	1.3±0.1	2.9±0.1	1.0±0.1	$1.7^{+0.3}_{-0.2}$	-
2X	0.78±0.04	0.93±0.07	1.70±0.07	0.87±0.09	1.1±0.1	-
3X	0.85±0.05	1.08±0.10	1.9±0.1	1.1±0.1	$1.3^{+0.9}_{-0.2}$	-
2C	1.20±0.04	1.46±0.06	2.66±0.06	$0.9^{+0.3}_{-0.2}$	$2.1^{+0.2}_{-0.3}$	-
3CCC	1.04±0.04	0.89±0.03	1.93±0.05	1.1±0.2	1.1±0.2	-

Table 5.3: Continued.

Epoch	L_{soft} (0.3-1.5 keV)	L_{hard} (1.5-10 keV)	L_{tot} (0.3 – 10 keV)	$L_{\mathrm{soft\ disk}}$ (0.01 – 100 keV)	$L_{\mathrm{hard\ disk}}$ (0.01 – 100 keV)	L_{simpl} (0.01 – 100 keV)
4C	1.12 ± 0.05	$1.24^{+0.08}_{-0.07}$	2.36 ± 0.08	$0.7^{+0.3}_{-0.2}$	$1.9^{+0.2}_{-0.3}$	-
4X	0.99 ± 0.03	1.28 ± 0.05	2.27 ± 0.05	$0.57^{+0.10}_{-0.09}$	2.0 ± 0.1	-
5X	1.26 ± 0.04	$2.94^{+0.10}_{-0.09}$	4.2 ± 0.1	$0.5^{+0.2}_{-0.1}$	$4.1^{+0.1}_{-0.2}$	-
6XX	0.97 ± 0.04	1.10 ± 0.05	2.06 ± 0.06	1.11 ± 0.08	$1.26^{+0.08}_{-0.09}$	-

Table 5.7: Results of the F-test between `tbabs`⊗`tbabs`⊗(`diskbb`+ `diskbb`) (1) and `tbabs`⊗`tbabs`⊗(`diskbb`+ `simpl`⊗`diskbb`) (2) models. Epochs are sorted chronologically and the nomenclature indicates the number of *XMM-Newton*, *Chandra*, and *NuSTAR* observations fit together (see Table 5.1).

Epoch	χ_{r1}/dof_1[a]	χ_{r2}/dof_2[b]	$\Delta\chi$	[1-Prob(F-test)] × 100 (%)	`simpl` ?
Holmberg II X–1					
1X	1.01/281	0.90/279	32.8	100.0	yes
2X	1.06/246	1.02/244	10.7	99.40	yes
3X	1.07/124	1.08/122	1.3	45.02	no
4X	1.32/392	1.15/390	70.9	100.0	yes
5X	1.12/316	1.06/314	22.6	100.0	yes
6XNN	1.31/490	0.99/488	159.2	100.0	yes
7XN	1.17/467	0.91/465	125.5	100.0	yes
Holmberg IX X–1					
1X	1.19/198	1.20/196	0.9	31.29	no
2X	1.08/342	1.04/340	13.2	99.80	yes
3X	1.05/353	0.98/351	25.4	100.0	yes
4X	1.25/502	1.20/500	30.0	100.0	yes
5X	0.82/81	0.80/79	3.1	85.00	no
6X	1.19/398	1.09/396	40.3	100.0	yes
7X	0.97/372	0.97/370	3.6	84.24	no
8X	1.05/301	1.05/299	2.6	70.80	no
9XXNN	1.24/1211	1.07/1209	208.0	100.0	yes
10XNN	1.22/956	1.04/954	175.8	100.0	yes
11XXNN	1.18/1055	0.98/1053	211.0	100.0	yes
IC 342 X–1					
1X	0.89/156	0.90/154	-	0.00	no
1C	0.80/84	0.82/82	0.0	0.00	no
2C	1.07/77	1.10/75	0.0	0.00	no
2X	1.00/336	1.00/334	1.9	61.32	no
3X	1.11/286	1.11/284	1.2	41.54	no
4X	0.98/288	0.97/286	4.0	87.06	no
5XNN	1.09/775	0.95/773	111.0	100.0	yes
6XN	1.29/802	1.10/800	154.5	100.0	yes
3C	1.04/74	1.01/72	4.4	87.94	no
NGC 5204 X–1					
1C	0.86/50	0.89/48	0.1	5.46	no
1X	1.04/249	1.04/247	2.34	67.45	no
2X	1.22/157	1.21/155	4.0	80.66	no
3X	1.08/180	1.08/178	2.0	60.09	no
2C	1.27/151	1.27/149	1.7	48.59	no
3CC	0.94/152	0.95/150	0.1	5.12	no
4C	0.97/47	1.01/45	0.0	0.00	no
5C	1.06/78	1.09/76	0.4	16.77	no
6C	1.08/47	1.04/45	3.9	83.55	no
7C	0.66/68	0.68/66	0.0	0.00	no
4X	0.97/185	0.94/183	7.8	98.28	yes
5X	1.01/339	0.97/337	15.3	99.96	yes

Table 5.7: Continued.

Epoch	χ_{r1}/dof_1[a]	χ_{r2}/dof_2[b]	$\Delta\chi$	[1-Prob(F-test)] × 100 (%)	`simpl` ?
6X	1.03/307	1.00/305	12.1	99.74	yes
7XXNN	1.13/625	1.02/623	72.5	100.0	yes
8X	1.07/260	1.06/258	4.7	88.84	no
			NGC5408X–1		
1X	1.18/138	1.16/136	4.7	86.41	no
2X	1.01/139	1.01/137	1.2	44.48	no
3X	1.13/97	1.12/95	2.9	71.99	no
4X	0.97/106	0.97/104	2.4	70.65	no
5X	1.86/352	1.57/350	106.4	100.0	yes
6X	1.56/314	1.41/312	48.9	100.0	yes
1CC	1.15/201	1.15/199	3.9	81.52	no
2C	1.07/99	1.04/97	5.5	92.42	no
7X	1.65/379	1.45/377	79.9	100.0	yes
8X	1.85/382	1.58/380	105.4	100.0	yes
9X	1.79/366	1.40/364	145.8	100.0	yes
10X	1.75/377	1.42/375	129.1	100.0	yes
11XX	1.51/568	1.36/566	86.3	100.0	yes
			NGC 1313 X–1		
1X	1.16/338	1.15/336	4.8	87.49	no
2XX	0.85/150	0.84/148	3.7	88.67	no
3XX	1.00/343	0.98/341	6.9	99.05	yes[c]
4X	0.91/109	0.86/107	7.8	98.73	no
5X	1.01/286	1.01/284	0.7	29.23	no
6X	1.18/166	1.19/164	-	0.00	no
7X	1.01/157	1.02/155	-	0.00	no
8X	1.09/218	1.06/216	9.3	98.67	yes[c]
9X	1.27/457	1.21/455	30.0	100.0	yes
10XN	1.43/649	1.20/647	157.3	100.0	yes
11XN	1.43/678	1.15/676	189.5	100.0	yes
12XN	1.61/558	1.18/556	244.2	100.0	yes
13X	0.98/256	0.98/254	1.8	60.07	no
14XN	1.38/512	1.11/510	142.6	100.0	yes
15XN	1.71/759	1.16/757	415.8	100.0	yes
16X	1.58/487	1.30/485	139.2	100.0	yes
17XXN	1.39/983	1.24/981	148.8	100.0	yes
18X	1.31/457	1.12/455	87.3	100.0	yes
19XN	1.82/655	1.26/653	368.1	100.0	yes
			Circinus ULX5		
1X	0.78/119	0.80/117	0.0	64.12	no
1C	0.78/84	0.77/82	1.9	70.14	no
2XNN	1.30/678	1.21/676	67.9	100.0	yes
3X	1.04/271	1.01/269	12.2	99.73	no[d]
4XN	0.99/305	0.98/303	3.6	83.73	no
5X	0.99/201	0.99/199	2.0	63.55	no
6X	1.30/486	1.30/484	5.4	87.40	no
			NGC 55 ULX1		
1X	1.11/293	1.06/291	17.5	99.97	yes
2X	1.36/178	1.32/176	11.2	98.44	yes[c]
3X	1.43/317	1.36/315	26.9	99.99	yes
			NGC 6946 X–1		
1C	1.1/162	1.0/160	19.1	100.0	yes
1X	1.1/130	1.0/128	8.6	98.7	yes[c]
2C	1.1/97	1.0/95	11.5	99.5	yes
3CC	1.0/103	0.9/101	6.2	95.9	no
2XX	1.1/329	1.1/327	19.0	100.0	yes
3X	1.4/357	1.2/355	72.0	100.0	yes
4C	1.0/102	0.9/100	3.6	84.82	no
4XNN	1.3/328	1.2/326	29.6	100.0	yes

Table 5.7: Continued.

Epoch	χ_{r1}/dof$_1$^{a}	χ_{r2}/dof$_2$^{b}	$\Delta\chi$	[1-Prob(F-test)] × 100 (%)	`simpl` ?
NGC 1313 X–2					
1X	0.98/135	0.97/133	3.3	81.43	no
2X	0.89/279	0.89/277	0.0	0.00	no
3X	1.06/199	1.06/197	2.7	71.91	no
4X	0.91/170	0.92/168	0.0	0.00	no
5X	0.91/175	0.90/173	3.8	87.53	no
6X	1.00/110	0.97/108	5.6	93.99	no
7X	0.78/293	0.79/291	0.4	22.49	no
8X	1.22/95	1.21/93	3.6	76.86	no
9X	1.18/181	1.18/179	2.1	58.75	no
10X	0.93/302	0.93/300	1.1	44.53	no
11X	1.05/118	1.05/116	2.0	61.00	no
12X	1.10/154	0.92/152	29.7	100.0	yes
13XN	1.11/484	1.09/482	8.3	97.69	yes
14XN	1.15/393	1.15/391	4.8	87.56	no
15X	1.09/59	1.12/57	0.0	0.00	no
16X	1.30/127	1.29/125	3.1	69.48	no
17X	1.11/85	1.14/83	0.0	0.00	no
18X	0.88/335	0.88/333	2.0	67.96	no
19X	1.11/232	1.12/230	0.0	0.00	no
20X	1.09/433	1.03/431	26.2	100.0	yes
21XN	1.14/160	1.04/158	17.4	99.96	yes
22X	1.06/246	1.07/244	0.0	0.00	no
23X	1.51/135	1.48/133	0.0	87.02	no
24X	1.02/100	1.01/98	2.8	74.54	no
25X	0.90/108	0.91/106	1.1	45.26	no
26XXN	1.23/625	1.23/623	1.3	66	no
NGC 300 ULX1					
1XN	1.59/857	1.34/855	221.3	100.0	yes
2X	1.1/450	1.1/448	12.1	99.6	yes
1CC	1.05/165	1.06/163	-	0.00	no
NGC 5907 ULX-1					
1X	0.80/215	0.81/213	0.0	0.00	no
2X	1.11/187	1.12/185	0.0	0.00	no
3XXCC	0.91/239	0.92/237	0.0	-	no
4XN	1.12/232	1.11/230	5.2	90.13	no
5XNN	1.03/491	0.94/489	47.7	100.0	yes
6X	1.06/151	1.03/149	6.4	95.19	no
7X	0.93/122	0.94/120	0.0	0.00	no
8XX	1.14/125	1.15/123	2.2	61.46	no
NGC 7793 P13					
1C	1.05/221	1.06/219	0.2	8.98	no
1X	1.07/336	1.08/334	0.0	0.00	no
2X	1.25/401	1.25/399	1.3	40.56	no
3XN	1.13/812	1.12/810	6.8	95.10	no
4X	0.90/168	0.91/166	0.6	28.11	no
5XN	1.17/579	1.18/577	-0.5	-	no
6X	1.23/403	1.23/401	4.6	84.56	no
7X	1.04/423	1.05/421	-3.0	-	no
8X	1.09/422	1.09/420	3.6	80.70	no
9XN	1.10/661	1.10/659	2.9	73.12	no

Notes: $^a\chi_r$ and degrees of freedom of the `tbabs`⊗`tbabs`⊗(`diskbb`+ `diskbb`) model. ^{b} Similarly for model `tbabs`⊗`tbabs`⊗(`diskbb`+ `simpl`⊗`diskbb`). ^{c}`simpl` model included as we could constrain it with another observation where the source was similar in flux and hardness ratio. ^{d}`simpl` model not included as we could not constrain its parameters with other observations where the source was similar in flux and hardness ratio.

5.1.6 Additional commentary on the paper

T. Roberts pointed out that the soft disk component in NGC 7793 P13 and M51 ULX7 exceeds the Eddington luminosity for a NS and that therefore, if this component represents the outer disk beyond R_{m}, it cannot remain thin as argued above. Indeed, given that a disk stops remaining thin when $L > L_{\mathrm{Edd}}$, if these luminosities are taken at face value, then this may point to an inconsistency in our line of reasoning above. It must be noted that in general, for a Eddington luminosity of 3×10^{38} erg/s, these disks exceed this limit by a factor of ~ 5 at most. Considering uncertainties on the distance, the absorption column, the exact modeling of this component and the fact that we are not using a self-consistent physically motivated model, whether these differences can be considered sufficient to claim that the outer disk is thick is debatable.

Nevertheless, if we ascribe this luminosity as the outer disk being super-Eddington, then it may be possible that these two sources do have $R_{\mathrm{sph}} < R_{\mathrm{m}}$ as was suggested for NGC 1313 X–2. Obviously we do not expect a perfect dichotomy in the relationship between R_{m} and R_{sph} and instead, it is possible instead that NGC 7793 P13 and M51 ULX7 do have supercritical disks, but that in these cases R_{sph} is close to R_{m} whereas for NGC 1313 X–2 $R_{\mathrm{m}} < R_{\mathrm{sph}}$. Indeed, the soft component in NGC 1313 X–2 are in general much brighter than those of NGC 7793 P13 and M51 ULX7, supporting that R_{sph} in NGC 1313 X–2 is much larger than in the other two sources. To summarize, it is possible that as opposed as having some sources where $R_{\mathrm{m}} > R_{\mathrm{sph}}$, instead all fulfil the condition $R_{\mathrm{sph}} > R_{\mathrm{m}}$ and what we are seeing are varying degrees of differences between R_{m} and R_{sph}, for which we expect NGC 1313 X–2 to have the largest R_{sph} compared to R_{m} based on the soft component luminosity i.e. NGC 1313 X–2 has the largest accretion rate or lowest magnetic field, as was argued above based on the spectral variability.

5.2 Discovery of a recurrent spectral evolutionary cycle in the ultraluminous X-ray sources Holmberg II X–1 and NGC 5204 X–1

A. Gúrpide[1], O. Godet[1], G. Vasilopoulos[2,3], N. A. Webb[1], J.-F. Olive[1]

[1]Institut de Recherche en Astrophysique et Planétologie, Université de Toulouse, UPS/CNRS/CNES, 9 Avenue du Colonel Roche, BP44346, F-31028 Toulouse Cedex 4, France
[2] Department of Astronomy, Yale University, PO Box 208101, New Haven, CT 06520-8101, USA
[3]Université de Strasbourg, CNRS, Observatoire astronomique de Strasbourg, UMR 7550, 67000, Strasbourg, France

Accepted to A&A the 4th of June of 2021

Abstract

Most ultra-luminous X-ray sources (ULXs) are now thought to be powered by stellar-mass compact objects accreting at super-Eddington rates. While the discovery of evolutionary cycles have marked a breakthrough in our understanding of the accretion flow changes in the sub-Eddington regime in Galactic black hole binaries, their evidence in the super-Eddington regime has so far remained elusive. However, recent circumstantial evidence hinted at the presence of a recurrent evolutionary cycle in two archetypal ULXs: Holmberg II X–1 and NGC 5204 X–1. We aim to build on our previous work and exploit the long-term high-cadence monitoring of *Swift*-XRT in order to provide robust evidence of the evolutionary cycle in these two sources and investigate the main physical parameters inducing their spectral transitions. We studied the long-term evolution of both sources using hardness-intensity diagrams (HID) and by means of Lomb-Scargle periodograms and Gaussian process modelling to look for periodic variability. We also applied a physically motivated model to the combined *Chandra*, *XMM-Newton*, *NuSTAR*, and *Swift*-XRT data of each of the source spectral states. We robustly show that both sources follow a clear and recurrent evolutionary pattern in the HID that can be characterised by the hard ultra-luminous (HUL) and soft ultra-luminous (SUL) spectral regimes, and a third state with characteristics similar to the super-soft ultra-luminous (SSUL) state. The transitions between the soft states seem consistent with aperiodic variability, as revealed by a timing analysis of the light curve of Holmberg II X–1; albeit, further investigation is warranted. The light curve of NGC 5204 X–1 shows a stable periodicity on a longer baseline of ~ 200 days, possibly associated with the duration of the evolutionary cycle. The similarities between both sources provide strong evidence of both systems hosting the same type of accretor and/or accretion flow geometry. We support a scenario in which the spectral changes from HUL to SUL are due to a periodic increase of the mass-transfer rate and subsequent narrowing of the opening angle of the super-critical funnel. The narrower funnel, combined with stochastic variability imprinted by the wind, might explain the rapid and aperiodic variability responsible for the SUL–SSUL spectral changes. The nature of the longer periodicity of NGC 5204 X–1 remains unclear, and robust determination of the orbital period of these sources could shed light on the nature of the periodic modulation found. Based on the similarities between the two sources, a long periodicity should be detectable in Holmberg II X–1 with future monitoring.

5.2.1 Introduction

Extensive monitoring of black hole (BH) and neutron star (NS) X-ray binaries has marked a breakthrough in our understanding of the accretion flow changes driving the flux variability in the sub-Eddington regime (e.g. Done & Gierliński, 2003; Remillard & McClintock, 2006; Gladstone et al., 2007) thanks to the discovery of the hysteresis cycles. For instance, the discovery of the hysteresis cycle or 'q-shape' diagram found in BH X-ray Binaries (BHXBs) (e.g. Fender et al., 2004; Belloni, 2010) has allowed us to build a coherent picture of the physical changes in the accretion flow responsible for the multi-wavelength observational properties of each spectral state (associated with the presence or absence of radio jet emission, for instance). The importance of such evolutionary tracks is such that it is still used as a tool to identify accreting stellar-mass BHs today (e.g. Zhang et al., 2020). For the same reason, the spectral changes observed in HLX-1 (Farrell et al., 2009; Godet et al., 2009; Servillat et al., 2011), reminiscent of those observed in BHXBs but at three orders of magnitude higher in luminosity, remain one of the most compelling arguments in favour of the system harbouring an accreting intermediate-mass BH (IMBH: $\sim 100 - 10^5$ $M_\odot$; see Mezcua, 2017, for a review).

At the same time, it was the atypical spectral states of ultra-luminous X-ray sources (ULXs), most of them being extragalactic, off-nuclear, point-like X-ray sources with an X-ray luminosity in excess of $\sim 10^{39}$ erg/s (see Kaaret et al., 2017, for a review), which suggested that the majority of these objects with $L_X < 10^{41}$ erg/s could be powered by super-Eddington accretion onto stellar-mass compact objects (e.g. Stobbart et al., 2006; Gladstone et al., 2009; Sutton et al., 2013). In this still poorly understood extreme regime, the intense radiation pressure caused by the high-mass transfer rate is expected to drive powerful and conical outflows (Shakura & Sunyaev, 1973; Poutanen et al., 2007; Ohsuga & Mineshige, 2007; Narayan et al., 2017). The atypical ULX spectral states were thus empirically classified as hard or soft ultra-luminous (HUL and SUL regimes), which were argued to depend on whether the observer had a clean view of the inner regions of the accretion flow or instead the source was viewed through the wind (Sutton et al., 2013). The wind cone is expected to narrow with the accretion rate (King, 2009; Kawashima et al., 2012) and may explain the spectral transitions frequently observed in ULXs (Sutton et al., 2013; Middleton et al., 2015a; Gúrpide et al., 2021a). It has been argued that at higher inclinations or mass-accretion rates a ULX may appear as an ultra-luminous super-soft source (ULSs; e.g. Urquhart & Soria, 2016). This scenario is supported by the transitions from the SUL to the super-soft ultra-luminous (SSUL) regime observed in a handful of sources such as NGC 247 ULX-1 (e.g. Feng et al., 2016; Pinto et al., 2021) and NGC 55 ULX (Pinto et al., 2017).

Multi-wavelength observations provide indirect evidence of such outflows or winds, in the form of inflated bubbles of ionised gas around a handful of ULXs (e.g. Pakull & Mirioni, 2002; Abolmasov et al., 2007b) or optical (Fabrika et al., 2015) and X-ray spectral lines (e.g. Pinto et al., 2020a). The detection of X-ray pulsations in the light curve of six ULXs (Bachetti et al., 2013; Fürst et al., 2016; Israel et al., 2017a; Carpano et al., 2018; Sathyaprakash et al., 2019; Rodríguez-Castillo et al., 2020) and possibly in another one (Quintin et al., 2021) identified the accretor as an NS and provided direct evidence of super-Eddington accretion for at least a fraction of the objects. The existing evidence, together with the sustained luminosities above 10^{39} erg/s over timescales of years (e.g. Kaaret & Feng, 2009; Grisé et al., 2013) and their relative proximity, make ULXs excellent laboratories for studying super-Eddington accretion.

However, as opposed to Galactic X-ray binaries, the irregular monitoring of ULXs has precluded the study of any such evolutionary tracks, which are so important for our understanding of the accretion flow properties in the super-Eddington regime. For this reason, previous studies focussed mainly on discussing the different spectral states observed in ULXs (Sutton et al., 2013; Middleton et al., 2015a). Therefore, these studies lacked information about the timescales and duration of each spectral state, that still hampers a full understanding of the nature of these transitions.

For this reason, long-term monitoring programmes have proven particularly useful in our understanding of the mechanisms responsible for the variability in ULXs. These have revealed the presence of super-orbital periods on timescales of months (see e.g. Vasilopoulos et al. (2019) and Townsend & Charles (2020) and references within), which are often variable (Kong et al., 2016; An et al., 2016; Vasilopoulos et al., 2020a). The nature of these super-orbital periods remains unclear, but it has recently been proposed that a Lense-Thirring precession of a super-critical disc and outflows (Middleton et al., 2018, 2019b) could explain the modulation seen in the light curves of PULXs (Dauser et al., 2017). This model has been proposed to explain the extreme flux modulation of factor >50 due to obscuration seen in the case of NGC 300 ULX1, where a stable spin-up rate has been maintained during epochs of variable flux (Vasilopoulos et al., 2019). In addition, NGC 300 ULX1 is perhaps the only ULX system where an orbital period has been proposed to be longer than one year based on both X-ray (Vasilopoulos et al., 2018; Ray et al., 2019) and infrared properties (Heida et al., 2019; Lau et al., 2019).

In Gúrpide et al. (2021a), we studied the long-term variability of a sample of 17 ULXs in order to understand the accretion flow geometry that could be responsible for the spectral variability observed in each source. In particular, we showed that certain ULXs followed an interesting evolutionary track in the hardness-luminosity diagram (HLD). Of particular interest were two archetypal ULXs, NGC 5204 X–1 and Holmberg II X–1, whose evolution could be clearly summarised in three states: 'hard-intermediate', 'soft-bright' and 'soft-dim' (see Figure 6 from Gúrpide et al., 2021a).

However, the limited cadence offered by *XMM-Newton* and *Chandra* precluded us from constraining the exact temporal evolution of the sources and therefore the nature of these transitions. In this work, we build on that of our previous paper by exploiting the high-cadence monitoring offered by *Swift*-XRT (Burrows et al., 2005) in

Table 5.8: Observation log used for each state.

State	Telescope	Obs. ID	Date	Good Exp (ks)	Detector/Filter^{a}	$(M–S)/T^{b}$
			NGC 5204 X–1			
SUL	*XMM-Newton*	0405690101	2006-11-16	7.82/5.85/5.82	pn/MOS1/MOS2	–0.32
	Chandra	3936	2003-08-14	4.56	ACIS	–0.49
	Chandra	3937	2003-08-17	4.64	ACIS	–0.49
	Chandra	3941	2003-09-14	4.88	ACIS	–0.43
	Chandra	3943	2003-10-03	4.90	ACIS	–0.44
SSUL	*Chandra*	2029	2001-05-02	9.01	ACIS	–0.62
	Chandra	3934	2003-08-09	4.74	ACIS	–0.73
	Chandra	3935	2003-08-11	4.5	ACIS	–0.61
	Chandra	3938	2003-08-19	5.15	ACIS	–0.73
	Chandra	3939	2003-08-27	5.14	ACIS	–0.79
HUL	*XMM-Newton*	0142770101	2003-01-06	15.33/18.49/18.50	pn/MOS1/MOS2	-0.26
	XMM-Newton	0741960101	2014-06-27	19.01/22.54/22.73	pn/MOS1/MOS2	–0.29
	XMM-Newton	0693851401	2013-04-21	13.37/16.40/16.46	pn/MOS1/MOS2	–0.28
	XMM-Newton	0693850701	2013-04-29	9.97/14.24/15.45	pn/MOS1/MOS2	–0.29
	NuSTAR	30002037002	2013-04-19	95.96/95.80	FPMA/FPMB	
	NuSTAR	30002037004	2013-04-29	88.98/88.85	FPMA/FPMB	
			Holmberg II X–1			
SUL	*XMM-Newton*	0200470101	2004-04-15	34.95/49.61/51.10	pn/MOS1/MOS2	–0.27
	XMM-Newton	0112520601	2002-04-10	4.64/9.45/9.65	pn/MOS1/MOS2	–0.31
	Swift	00035475019	2009-12-01	23.40	XRT	
SSUL	*XMM-Newton*	0112520901	2002-09-18	3.78/5.85/6.45	pn/MOS1/MOS2	-0.51
HUL	*XMM-Newton*	0724810101	2013-09-09	4.65/6.63/6.63	pn/MOS1/MOS2	–0.25
	XMM-Newton	0724810301	2013-09-17	5.81/8.61/9.31	pn/MOS1/MOS2	–0.29
	NuSTAR	30001031002	2013-09-09	31.38/31.32	FPMA/FPMB	
	NuSTAR	30001031003	2013-09-09	79.44/79.34	FPMA/FPMB	
	NuSTAR	30001031005	2013-09-17	111.10/111.00	FPMA/FPMB	
	HST	j9dr03r1q	2013-08-24	1.505	ACS/WFC/F550M	
	HST	icdm60ipq	2006-01-28	2.424	WFC3/UVIS/F275W	
	HST	icdm60j0q	2013-08-24	1.146	WFC3/UVIS/F336W	
	HST	icdm60j6q	2013-08-24	0.992	WFC3/UVIS/F438W	

Notes. (a) Only for the *HST* data. (b) Softness computed as per Urquhart & Soria (2016), but only for *XMM-Newton* and *Chandra* observations. M, S, and T refer to the net count rates in the 0.3–1.1 keV, 1.1–2.5 keV, and 0.3–10 keV, respectively.

order to constrain the temporal timescale of the transitions. We will show that these two sources describe a very similar and well-defined recurrent evolutionary cycle. Moreover, we show that the whole cycle is likely periodic, providing a clear connection between long-term periodicities and spectral changes in these ULXs.

Section 5.2.2 outlines the data reduction process. Section 5.2.3 presents the data analysis and results. In Section 5.2.4, we discuss our findings. Finally, in Section 5.2.5 we summarise our conclusions.

5.2.2 Data reduction

For this work, we used the dataset analysed in Gúrpide et al. (2021a) to which we added long-term monitoring provided by archival *Swift*-XRT data. The details of our data reduction for *XMM-Newton* (Jansen et al., 2001), *NuSTAR* (Harrison et al., 2013), and *Chandra* (Weisskopf et al., 2000) can be found in Gúrpide et al. (2021a). Here, we briefly summarise the main steps followed. The data used in this work is summarised in Table 5.8.

5.2.2.1 *XMM-Newton*

For the EPIC-pn (Strüder et al., 2001) and MOS (Turner et al., 2001) cameras we selected events with the standard filters, removing pixels flagged as bad and those close to a CCD gap. We filtered periods of high background flaring by removing times where the count rate was above a chosen threshold by visually inspecting the background high-energy light curves. Source products were extracted from a circular region with a radius of 40" and 30" for pn and MOS, respectively. The background region was selected from a larger, circular, source-free region on the same chip as the source (when possible). We generated response files using the tasks `rmfgen` (version 2.8.1) and

Table 5.9: *Chandra* observations of NGC 5204 X–1 considered in this work that were not included in Gúrpide et al. (2021a). The number of Cs indicates the number of observations fitted together after checking their consistency.

Epoch	Date	Obs. ID	Good Exp. (ks)	Total Counts
1CC	2003-08-09	3934	4.7	539
	2003-08-11	3935	4.5	616
2C	2003-08-19	3938	5.1	567
3C	2003-08-27	3939	5.1	586

`arfgen` (version 1.98.3). Finally, we regrouped our spectra to have a minimum of 20 counts per bin to allow the use of χ^2statistics and also avoid oversampling the instrumental resolution by setting a minimum channel width of 1/3 of the FWHM energy resolution.

5.2.2.2 *Chandra*

All *Chandra* data were reduced using the CIAO software version 4.11 with calibration files from *CALDB* 4.8.2. We used extraction regions given by the tool *wavdetect* to extract source events. Background regions were selected from circular nearby source-free regions that were roughly three times larger. For this work, we included four *Chandra* observations of NGC 5204 X–1 that were not considered by Gúrpide et al. (2021a) due to their limited number of counts (< 700). These are presented in Table 5.9. All data were re-binned to a minimum of 20 counts per bin so as to use χ^2 statistics, except for these low count observations that are re-binned to two counts per bin and analysed using the pseudo C-statistic (Cash, 1979), W-stat in XSPEC [15], which is suitable for the analysis of low count spectra when the background is not being modelled. The choice of two counts per bin was made in order to reduce the biases associated with the W-stat[16]. We note that W-stat is the default statistic used when the C-stat option is selected and a background file is read in.

5.2.2.3 *NuSTAR*

The *NuSTAR* data were extracted with the *NuSTAR* Data Analysis Software version 1.8.0 with *CALDB* version 1.0.2. Source and background spectra were extracted using the task *nuproducts* with the standard filters. Source events were selected from a circular of $\sim 60"$ centred on the source. Background regions were selected from larger, circular, source-free regions and on the same chip as the source but as far away as possible to avoid contamination from the source itself. We re-bin *NuSTAR* data to 40 counts per bin, owing to the lower energy resolution compared to the *EPIC* cameras.

5.2.2.4 *Swift*

We retrieved all publicly available snapshots from the UK *Swift*-XRT data centre[17] as of 1 August 2020. Each *Swift* observation is split into several snapshots, each of which we considered separately in our periodicity analysis (Section 5.2.3.2). In order to build products (i.e. light curves and/or spectra), we used the standard tools outlined in Evans et al. (2007, 2009), considering all detections above the 95% confidence level. We further discarded two snapshots that had a signal-to-noise below 2 from the dataset of NGC 5204 X–1 for our periodicity analysis (Section 5.2.3.2). We also extracted the count rate in two energy bands, a soft band (0.3 – 1.5 keV range) and a hard band (1.5 – 10 keV range), to build a hardness–intensity diagram (HID) (Section 5.2.3.1). We were left with 152 snapshots with a mean cadence between observations of 4.7 days for NGC 5204 X–1 and 303 snapshots with a mean cadence between observations of 1.6 days for Holmberg II X–1.

5.2.3 Data analysis and results

5.2.3.1 Long-term variability

In order to investigate the long-term variability of both sources, we inspected the *Swift*-XRT light curves and built HIDs for both sources (Figure 5.14). Here, we considered the data binned by observations to ensure that the source was well detected in each of the energy bands.

The *Swift*-XRT data for Holmberg II X–1 reveal two distinct trends, one from the 2009–2010 data in which the source switched quickly and repeatedly, within a few days (see also Grisé et al., 2010), between a bright and soft state (soft-bright state: HR ~ 0.5, count rate in the 0.3 – 10 keV band ~ 0.28 cts/s) and a dim and softer

---

[15] https://heasarc.gsfc.nasa.gov/xanadu/xspec/manual/XSappendixStatistics.html

[16] https://giacomov.github.io/Bias-in-profile-poisson-likelihood/

[17] https://www.swift.ac.uk/user_objects/

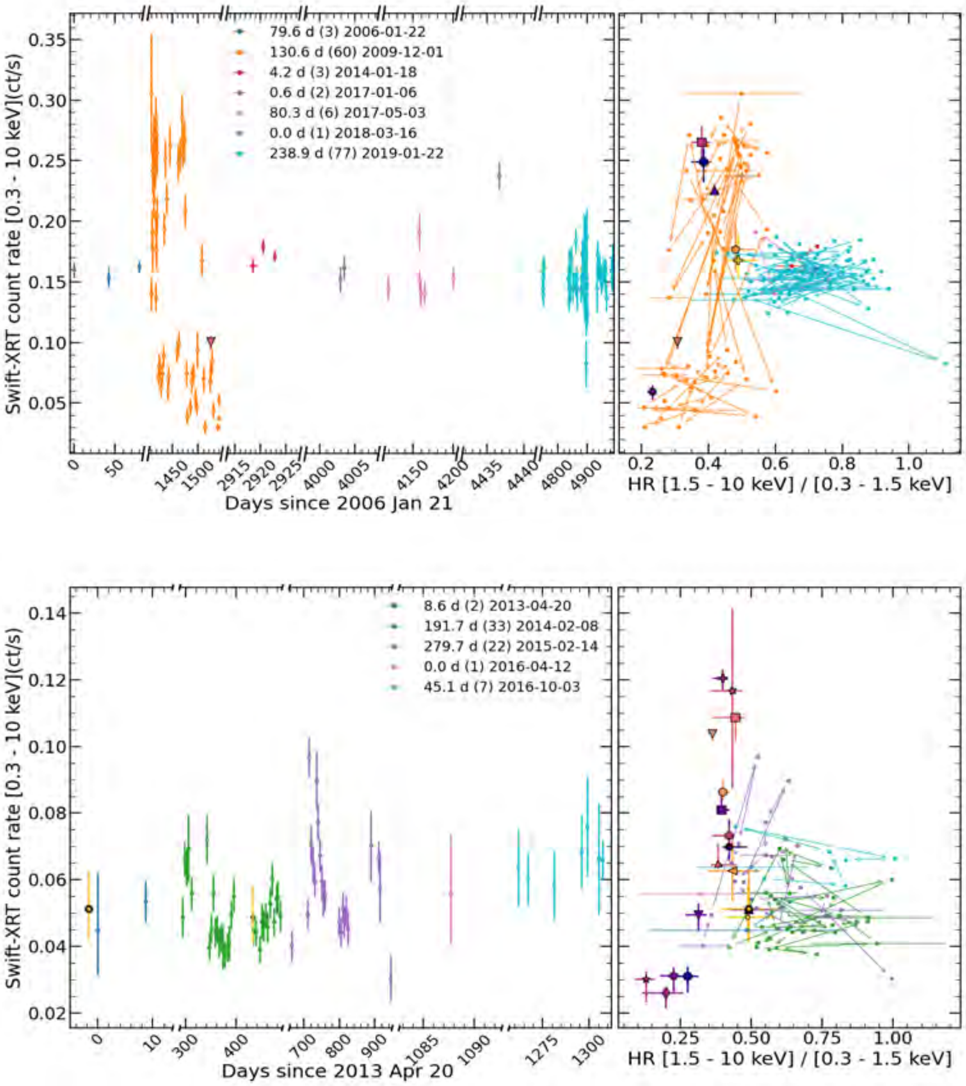

Figure 5.14: *Left*: *Swift*-XRT light curve in the 0.3 – 10 keV band for Holmberg II X–1 (top) and NGC 5204 X–1 (bottom) with its associated HID (right). Continuous monitoring intervals with data gaps of less than 12 weeks have been coloured accordingly and the legend indicates the duration in days, the number of observations, and starting date of each continuous period. Arrows in the HID indicate chronological order and errors are given every eight datapoints for clarity. Big coloured markers correspond to the *Swift*-XRT 0.3–10 keV count-rate estimates of the *XMM-Newton* and *Chandra* observations based on best-fit models from Gúrpide et al. (2021a) (see text for details). Errors are at 1 σ confidence level. We note that the X-axis has been split on the left panels.

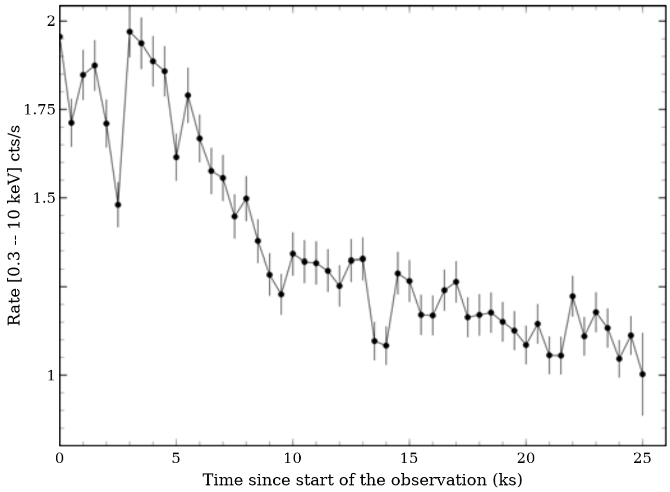

Figure 5.15: 0.3 – 10 keV background-subtracted EPIC-pn light curve of Holmberg II X–1 (obs id 0561580401) binned to 500 s and corrected using the task `epiclccorr`.

state (soft-dim state: HR ∼ 0.25, count rate of ∼ 0.05 cts/s). This variability is also observed intra-observation in the long (30 ks good exposure; Gúrpide et al., 2021a) obs id 0561580401 (this observation is indicated as a pink triangle pointing downwards in Figure 5.14).

The second trend is well sampled in the 2019 monitoring and shows that the source remained stable with HR ∼ 0.75 and a 0.3–10 keV count rate of ∼ 0.15 – 0.2 cts/s (hard-intermediate state). The source has been repeatedly observed in this state on several occasions prior to 2019, in 2006, 2014, and 2017. From the 2009–2010 monitoring, the duration of whole soft state transitions seems to last at least 131 days, whereas the 2019 monitoring indicates that the duration of the hard state seems to be of at least 240 days.

The identification of any pattern in the *Swift*-XRT data is not straightforward in the case of NGC 5204 X–1 because *Swift* caught the source mostly in the hard-intermediate state, albeit Gúrpide et al. (2021a) showed that Holmberg II X–1 and NGC 5204 X–1 evolved in a similar manner from the analysis of archival *XMM-Newton* and *Chandra* data. To illustrate this, we adapted Figure 6 from Gúrpide et al. (2021a) in our Figure 5.16 by considering the full *Chandra* monitoring of NGC 5204 X–1 presented by Roberts et al. (2006) (see Table 5.9) to highlight the short-term variability the source underwent in 2003. We fitted these new *Chandra* observations using the same model as in Gúrpide et al. (2021a), an absorbed dual-thermal component in XSPEC (Arnaud, 1996) version 12.10.1f. We fixed the galactic $n_{\rm H}$ and the local $n_{\rm H}$ to the same values found in Gúrpide et al. (2021a). The best-fit parameters are summarised in Table 5.10. For our aim, we retrieved unabsorbed fluxes using `cflux` in the 0.3 – 1.5 keV and the 1.5 – 10 keV bands, and we show them together with the previous observations from Gúrpide et al. (2021a) in Figure 5.16.

To put the *XMM-Newton* and *Chandra* observations from Gúrpide et al. (2021a) in perspective with respect to the *Swift*-XRT data, we estimated the count rates in the 0.3 – 1.5 keV, 1.5 – 10 keV and 0.3 – 10 keV bands from the best-fit model parameters from Gúrpide et al. (2021a) by convolving each model with the latest redistribution matrix (swxpc0to12s6_20130101v014.rmf) and ancillary file (swxs6_20010101v001.arf) available as of 1 August 2020. In order to derive the uncertainties, we linearly interpolated the 1σ uncertainties from the observed fluxes to convert them to equivalent *Swift*-XRT count rates. This is represented in Figure 5.14 using the same colour code as in Gúrpide et al. (2021a) in the case of Holmberg II X-1 and that of Figure 5.16 in the case of NGC 5204 X–1.

The pattern revealed by the *Chandra* monitoring is reminiscent of the transitions observed in the 2009–2010 *Swift*-XRT data of Holmberg II X–1 (Figures 5.14 and 5.16). Once again, the source transits from soft-bright (HR ∼ 0.8, unabsorbed $L_X \sim 9 \times 10^{39}$ erg/s) to soft-dim (HR ∼ 0.2, unabsorbed $L_X \sim 2 \times 10^{39}$ erg/s) on several occasions over ∼ 3 months. The tightest constraints on the duration of these transitions come from the 2003-08-09/19 observations, which show that the source went back and forth from the soft-dim state to the soft-bright state in ten days. The *XMM-Newton* observations from Figure 5.16 (coloured markers) show how the source went from the hard-intermediate state (epoch 2003-01-06) to the soft-bright state and started transiting from soft-bright to soft-dim from epoch 2003-05-01 onwards. Another transition from bright/soft to hard-intermediate was also observed by *XMM-Newton* in 2006. Given that the source was found in the soft-dim state in 2001 and back in that state in 2003-08-06 (Figure 5.16), the full cycle seems to have a duration of less than 2 years. It is also observed that NGC 5204 X–1 was not detected in the soft-dim state by *Swift*-XRT.

Overall, the multi-instrument data presented reveal that the evolution of both NGC 5204 X–1 and Holmberg II X–1 are akin and can be characterised in three states: soft-bright, soft-dim, and hard-intermediate. The 2006 transitions of NGC 5204 X–1 were also discussed by Sutton et al. (2013), and thus it is easy to see that the soft-bright state corresponds to the soft ultra-luminous (SUL) regime defined by these authors, whereas the hard-intermediate states correspond to the hard ultra-luminous (HUL) regime. The soft-dim state instead shows

Table 5.10: Results of the fit of the *Chandra* observations considered in this work that were not included in Gúrpide et al. (2021a). Errors are quoted at the 90% confidence level. The number of Cs indicates the number of observations jointly fitted.

Epoch	$kT_{\rm soft}$ keV	norm	$kT_{\rm hard}$ keV	norm 10^{-2}	$L^a_{\rm soft}$ (0.3–1.5 keV)	$L^a_{\rm hard}$ (1.5–10 keV)	$L^a_{\rm tot}$ (0.3 – 10 keV)	C-stat(dof)
				NGC 5204 X–1				
1CC	0.26 ± 0.03	8^{+6}_{-3}	$1.0^{+0.5}_{-0.2}$	2^{+4}_{-2}	1.6 ± 0.1	$0.57^{+0.09}_{-0.08}$	2.2 ± 0.1	1.24/218
2C	0.28 ± 0.04	6^{+6}_{-3}	$1.2^{+b}_{-0.5}$	$0.50^{+1.7}_{-0.5}$	1.4 ± 0.1	0.4 ± 0.1	1.8 ± 0.2	1.03/104
3C	0.26 ± 0.04	10^{+9}_{-4}	$0.9^{+b}_{-0.4}$	1^{+26}_{-1}	$1.8^{+0.2}_{-0.1}$	$0.32^{+0.10}_{-0.08}$	2.1 ± 0.2	0.79/94

Notes. The Galactic $n_{\rm H}$ and the local $n_{\rm H}$ were frozen to 1.75×10^{20} cm^{-2} Kalberla et al. (2005) and to 3.0×10^{20} cm^{-2}, respectively, following Gúrpide et al. (2021a). $^{(a)}$ In units of 10^{39} erg/s. $^{(b)}$ We set an upper limit of 5 keV.

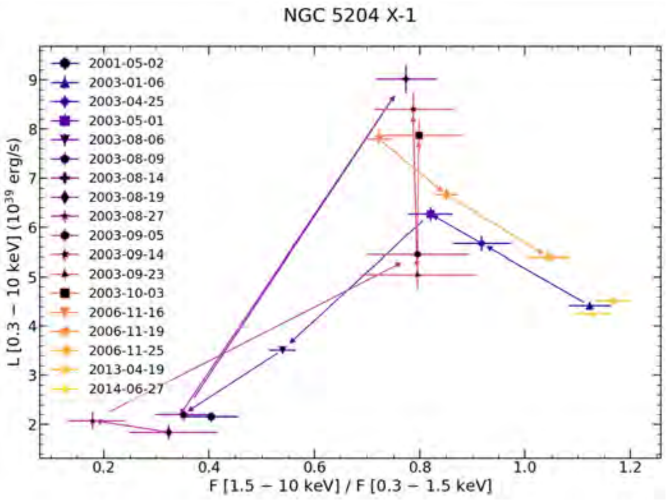

Figure 5.16: Temporal tracks on the HLD adapted from Gúrpide et al. (2021a) for NGC 5204 X–1. New *Chandra* observations have been included to illustrate the short-term variability in 2003 (see Tables 5.9 and 5.10). Black and coloured markers indicate *Chandra* and *XMM-Newton* observations, respectively. Arrows indicate the chronological order and are only plotted for observations closer in time than four months.

several characteristics similar to the SSUL regime (Feng et al., 2016; Urquhart & Soria, 2016; Pinto et al., 2017), namely a luminosity around 10^{39} erg/s (Figure 5.16) and little emission above 2 keV (see Figure 6 in Gúrpide et al., 2021a). To illustrate this further, we measured net count rates in the same three energy bands as Urquhart & Soria (2016): 0.3.–1.1 keV (S), 1.1–2.5 keV (M), and 0.3–7.0 keV (T). We computed $(M-S)/T$ for each of the *XMM-Newton* and *Chandra* observation available for each state (Table 5.8). We see that the values for the soft-dim state of NGC 5204 X–1 reach $(M-S)/T \approx$ – 0.8, the approximate threshold the authors used to classify ULX sources as super-soft. The lowest value of Holmberg II X–1 registered by *XMM-Newton* is –0.5, which overlaps with some super-soft sources, depending on the model considered (see their Figure 1). We also note that *Swift* observed Holmberg II X–1 at even lower fluxes than those observed by *XMM-Newton* (Figure 5.14) and that Holmberg II X–1 is generally softer than NGC 5204 X–1(Gúrpide et al., 2021a), suggesting that these differences in $(M-S)/T$ might be mostly instrumental and that the properties of the SSUL state are broader than based on hardness alone. We discuss in Section 5.2.4 why Holmberg II X–1 and NGC 5204 X–1 appear slightly harder in the SSUL state than canonical ULS sources.

Additional evidence for the similarity between these states and the ULS regime comes from the rapid < 2-day variability observed in the soft-bright to soft-dim transitions in the *Swift*-XRT light curve of Holmberg II X–1 (see also Grisé et al., 2010). This is reminiscent of the transitions observed in the ULS in M81 (Liu, 2008), which shows sudden flux drops and rises on timescales of ∼ 1 ks, similarly to those seen in Holmberg II X–1 (Figure 5.15). The ULX-ULS transitions seen in NGC 247 ULX-1 and NGC 55 ULX are also associated with the brightest states (Feng et al., 2016; Pinto et al., 2017, 2021), which is exactly what is observed in Holmberg II X–1 and NGC 5204 X–1. Thus, Holmberg II X–1 and NGC 5204 X–1 may be the first ULXs observed to switch through all these three canonical ULX spectral states. Hereafter, we use the terms SUL, HUL, and SSUL to refer to the spectral states seen in Holmberg II X–1 and NGC 5204 X–1 for consistency with previous works.

5.2.3.2 Periodicity analysis

5.2.3.2.1 Lomb-Scargle periodograms: To investigate the presence of any periodicity in the long-term evolution of NGC 5204 X–1 and Holmberg II X–1, we performed Lomb-Scargle periodograms[18] (Lomb, 1976; Scargle, 1982), which is suitable to look for stable sinusoidal periodicities. In this implementation of the Lomb-Scargle periodogram, the uncertainties in the measurements are used to weight the differences between the sinusoidal model and the data, as with a classical least-squares estimation. We also adopted the floating-mean periodogram, in which the mean count rate is fitted in the model instead of being subtracted as for the classical periodogram, which has been shown to give higher accuracy, especially when the data does not have full phase coverage (VanderPlas, 2018). For this analysis, we used the data from the *Swift*-XRT as it has the highest cadence and longest monitoring.

In the case of unevenly sampled data, there is no well-defined Nyquist frequency and thus the maximum frequency explored in the periodogram has to be set according to some physical and/or observing constraints. In this case, we restricted the maximum frequency explored to 5 $^{-1}$days, which is slightly above the typical cadence at which *Swift* visited each source. The minimum frequency explored is set to 1/T$_{\text{segment}}$ where T$_{\text{segment}}$ is the duration of the continuous light-curve segment considered in each case. We oversampled the periodogram by a factor of five (i.e. $\Delta f = 1/nT_{\text{segment}}$ where n = 5).

5.2.3.2.2 False-alarm probability: Bootstrap method: A common challenge in the Lomb-Scargle periodogram is to estimate the significance of a peak in the power spectrum. In the presence of white noise, Scargle (1982) showed that the false-alarm probability of a single peak with power P is $F(P) = 1 - e^{-P}$. However, because we are essentially trying to detect a peak over a certain frequency range, one should account for the fact that several frequencies are being explored. This is challenging because the frequencies in the Lomb-Scargle periodogram are not independent, and thus one cannot compute the false-alarm probability simply by assuming that several independent frequencies (i.e. trials) have been looked for. Some empirical estimates of the number of independent frequencies exist (e.g. Horne & Baliunas, 1986), but the most robust method is to rely on Monte Carlo simulations to calibrate the reference distribution as it makes few assumptions on the number of independent frequencies and considers the observing cadence of the real data, so the effects of the observing window are taken into account.

We thus estimated 2σ and 3σ false alarm probabilities in the absence of a signal by using the bootstrap method outlined in VanderPlas (2018). This method generates N light curves by drawing random samples from the original measurements to generate light curves with the same time coordinates as for the original data. For each randomised light curve, the same Lomb-Scargle periodogram is performed as for the real data. From the maxima of these fake periodograms, the reference distribution is built. Another advantage of this method is that the null-hypothesis model is not based on pure white noise, since the reference distribution is built on randomised data, although there are other limitations to consider (which we discuss in Section 5.2.3.2.3). We performed 3500 simulations to ensure that at least ten peaks are found above the 3σ level and thus that the reference distribution was well sampled (VanderPlas, 2018).

For Holmberg II X–1, in order to avoid aliasing effects caused by the large data gaps, we analysed the data separately in two segments of continuous monitoring. The first segment included the data from 2009 to 2010 and the second one comprised the 2019 data. The resulting periodograms are shown in Figures 5.17 and 5.18. In the inset of the Figures we also show the structure of the observing window, which is computed by performing the Lomb-Scargle periodogram on a light curve of constant flux and the same time coordinates as for the real data.

The periodogram of the 2009–2010 segment reveals two strong peaks at around 21 and 28 days both with a significance above the 3σ level. However, the observing window has a strong power at $\sim$ 25 days (Figure 5.17), which may be introducing some aliasing. We also note that Grisé et al. (2010) analysed the same dataset and found no evidence of any periodicity. However, the discrepancy between these results might be simply due to the differences in the periodogram implementation used by the authors (the prescription by Horne & Baliunas, 1986), the sampling grid, the way the false alarm probabilities were computed, and the fact that their implementation did not take into account the uncertainties in the measurements.

The best solution given by the 28-day peak is shown in Figure 5.17 (see the light purple solid line in the top right panel). The variability is clearly more complex than described by the simple sinusoidal profile. It is also observed that the source variability changed after 2 February 2010 (see the blue dashed vertical line in the top right panel of Figure 5.17). Since there is now compelling evidence of variable periodicities in ULXs (Kong et al., 2016; An et al., 2016; Brightman et al., 2019; Vasilopoulos et al., 2020a) with an as yet unclear origin, we repeated our analysis by considering the data before and after 2 February 2010 separately. The results are presented in the top right and bottom panels of Figure 5.17. The peak from the first segment is consistent with the one at 28 days previously found, albeit now is found slightly below the 3σ level. For the second segment after the blue dashed line, we found no evidence of any periodicity above the 2σ level. We still show the best solution from the highest peak found in the periodogram (yellow solid line in the top right panel of Figure 5.17) to illustrate that if the oscillation is still present, its amplitude must have significantly decreased. Finally, the 2019 data showed no evidence of any periodicity, which may indicate that the oscillation has decreased significantly or disappeared entirely (see Figure 5.18).

---

[18] `https://docs.astropy.org/en/stable/timeseries/lombscargle.html`(VanderPlas, 2018)

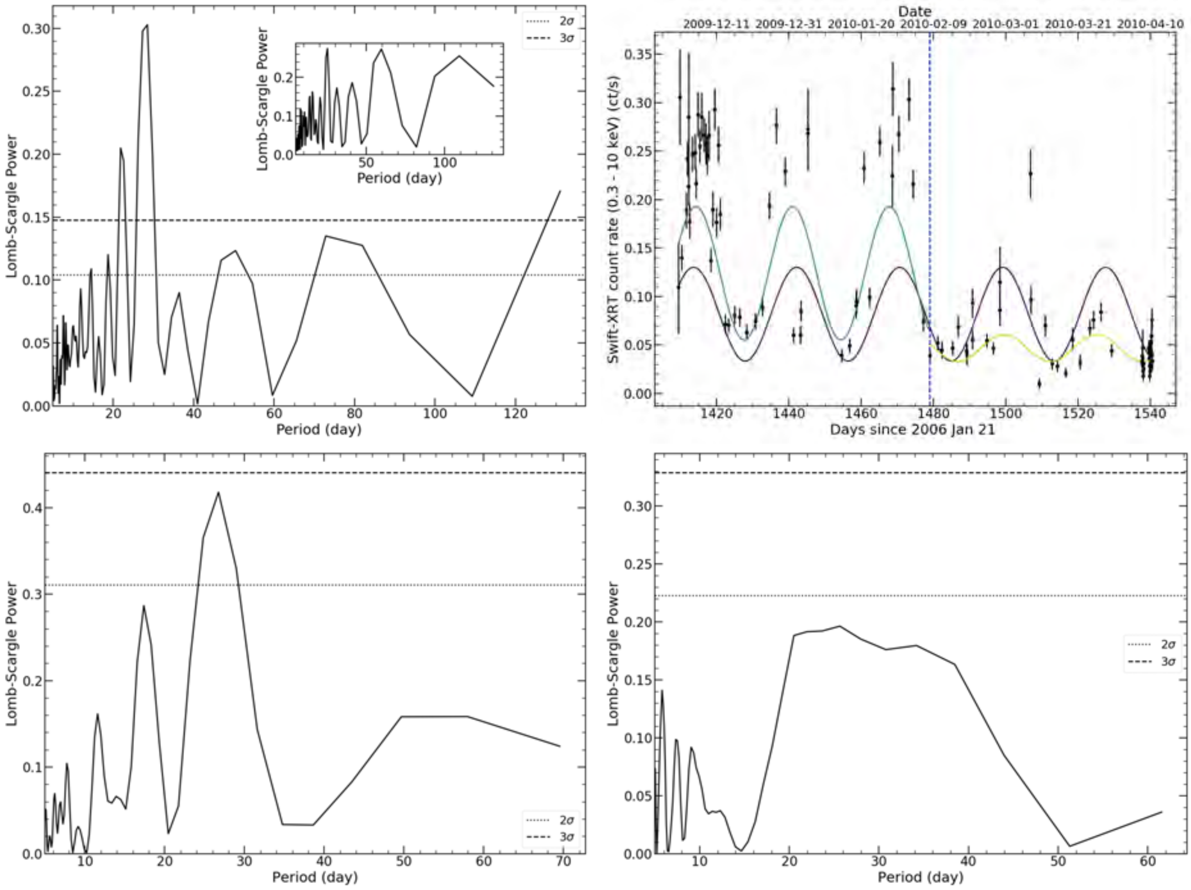

Figure 5.17: Top left: Lomb-Scargle periodogram for the entire 2009–2010 *Swift*-XRT dataset of Holmberg II X-1 (black solid line). The 2σ and 3σ levels (dashed and dotted lines, respectively) mark the false alarm probability computed from bootstrapped samples (see text for details). The inset shows the structure of the observing window. Top right: *Swift*-XRT light curve corresponding to the 2009–2010 segment. The solid purple line indicates the best-fit period from the periodogram of the whole light-curve segment. The solid light blue line indicates the best-fit period from the periodogram considering only the light curve segment to the left of the blue dashed line, while the yellow solid line indicates the best-fit period from the light-curve segment to the right of the blue dashed line. Bottom: Lomb-Scargle periodograms of two sub-segments of the 2009–2010 data separated by the blue dashed line in the top right panel (left and right panels correspond to the data prior to and after ∼ day 1480).

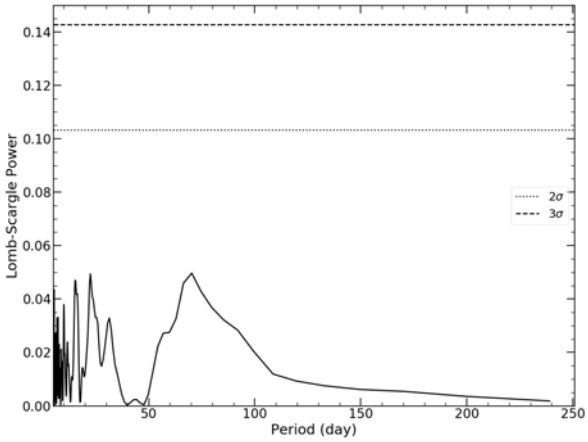

Figure 5.18: As per Figure 5.17, but for the 2019 *Swift*-XRT dataset of Holmberg II X–1.

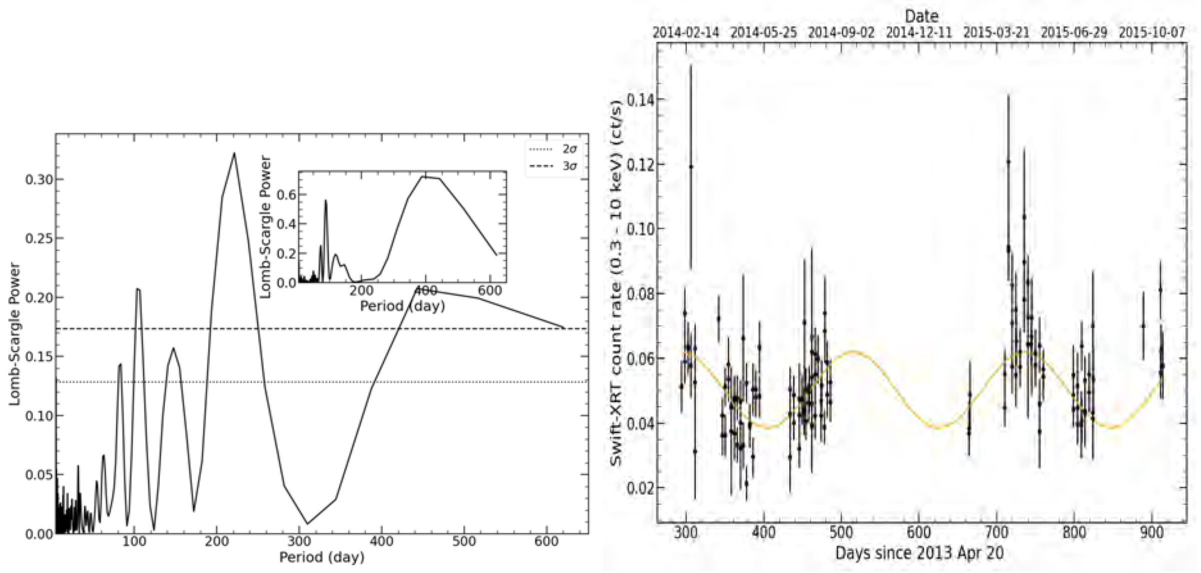

Figure 5.19: *Left*: Lomb-Scargle periodogram of the 2014–2015 *Swift*-XRT light curve of NGC 5204 X–1 in solid black. The 2σ and 3σ mark the false alarm probability levels computed from bootstrapped samples (see text for details). The inset plot shows the structure of the observing window. *Right*: *Swift*-XRT light curve with the best-fit period from the periodogram (orange solid line).

For NGC 5204 X–1, we analysed only the continuous and densely sampled part of the light curve from $\sim$ day 300 until $\sim$ day 900 after the start of the monitoring (green and purple segments in Figure 5.14). The Lomb–Scargle periodogram reveals a strong peak at around 221 days (Figure 5.19), which is not coincident with any structure from the observing window. The peaks at 444 days and 103 days above the 3σ are almost exactly or very close to 2×221 days and 221/2 days, respectively, suggesting that they could be harmonics of the period at 221 days. The peak at 444 days is also highly uncertain as it is only supported by 1.5 cycles, and stronger noise is expected towards longer periodicities given the sparsity of our data and the structure of the observing window. We also observe some variability on top of the sinusoidal variation at around 700–800 days after the beginning of the monitoring.

5.2.3.2.3 False-alarm probability: REDFIT: We note, however, that in the presence of aperiodic variability, the measurements could have some degree of correlation (i.e. in the presence of a flare) and by design, any correlation will be lost in the bootstrapped samples. In fact, red-noise, commonly observed in accreting sources, can often appear periodic (e.g. Scargle, 1981; Vaughan et al., 2016), and tests against the null-hypothesis of white noise often underestimate the false-alarm probability of the peaks in the periodogram (e.g. Liu, 2008).

We therefore performed a second test to derive the significance of the peaks in the periodogram under the null-hypothesis of red noise. To do so, we based ourselves on the publicly available `R` code REDFIT developed by Schulz & Mudelsee (2002)[19], in which red noise is modelled as a first-order autoregressive process (termed AR(1) for short), a model commonly used in astrophysics to model stochastic time series (see e.g. Scargle (1981) and also An et al. (2016) for a similar approach). In AR(1) processes, the time series (x_i) at a given time (t_i) depend on the previous sample as $x_i = \rho_i x_{i-1} + \epsilon_i$, where ρ is the autocorrelation coefficient and ϵ is the random component with zero mean and a given variance σ^2. The case in which $\rho = 1$ simply describes a random walk. For unevenly sampled data, the AR(1) can be modelled with a variable autocorrelation coefficient that depends on the sampling time difference $\rho = e^{-(t_i - t_{i-1})/\tau}$ (Robinson, 1977), where τ is the characteristic time of the AR(1) process, a measure of its memory and σ^2 is set equal to $1 - e^{-2(t_i - t_{i-1})/\tau}$ to ensure that the AR(1) process has a variance equal to unity and is stationary. τ can be calculated directly from the time series using the least-squares algorithm of Mudelsee (2002). From the AR(1) model, an ensemble of Monte Carlo simulations of time series with the same sampling as for the original light curve can be created to test whether the presence of a peak in the periodogram is consistent with an AR(1) process. However, the Lomb-Scargle implementation proposed by Schulz & Stattegger (1997) does not take into account the uncertainties in the data, and the mean of the measurements is not fitted as for the floating-mean periodogram. Additionally, REDFIT might underestimate the significance of the peaks in the periodogram as it computes the false alarm probabilities based on the entire distribution of the simulated periodograms rather than on the largest peak in each synthetic periodogram.

Because of the caveats outlined above, we replicated the same approach but instead simulated the ensemble of AR(1)-generated light curves by setting the variance of the noise $\sigma^2 = \sigma_d^2 \left(1 - \mathrm{e}^{-2(t_i - t_{i-1})/\tau}\right)$, where σ_d is the variance of the data, so that the simulated data has a variance equal to that of the real measurements. We

---

[19] `https://rdrr.io/cran/dplR/src/R/redfit.R`

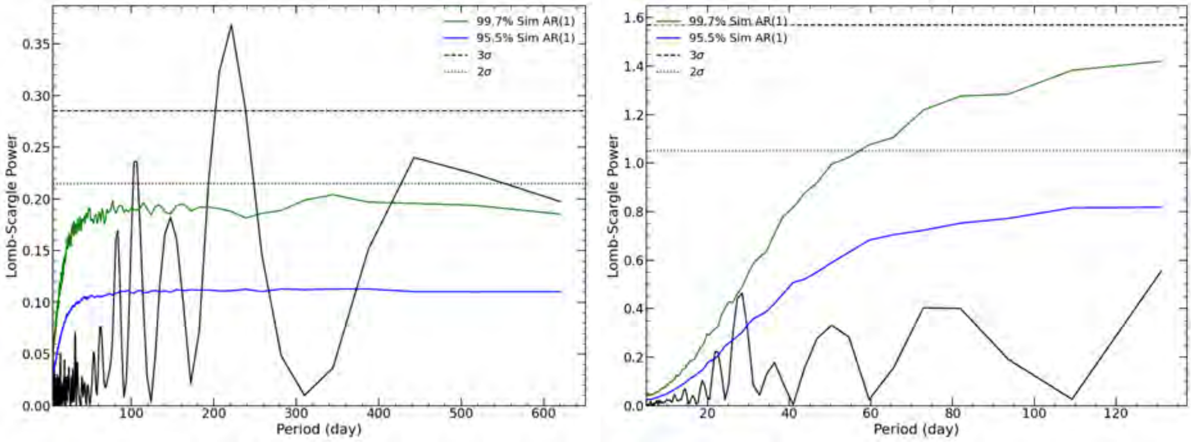

Figure 5.20: False-alarm probabilities for the Lomb-Scargle periodogram based on an adaptation of the REFIT code (see text for details) for NGC 5204 X–1 (left) for the 2014–2015 monitoring and for Holmberg II X–1 (right) for the 2009–2010 monitoring under the null-hypothesis of red noise. The coloured 95.5% and 99.7% mark the distribution of the 10000 synthetic periodograms, whereas the black dashed line marks 2σ and 3σ false-alarm probabilities, which have been determined from the maximum of the peaks of the synthetic periodograms.

then added an offset to the simulated data equal to the mean of the real measurements, so the simulated data also has approximately the same mean. We then computed uncertainties on x_i assuming Poissonian statistics. In cases where x_i happens to be negative, we simply set the uncertainty equal to that of the observed data at i. We note that there is no issue in introducing negative rates in the Lomb-Scargle calculation, although the simulations should ideally be flux limited to match the real measurements more closely.

We then conducted the same Lomb-Scargle periodograms on these light curves as for the real data, taking into account the uncertainties. Following Schulz & Mudelsee (2002), we scaled the synthetic periodograms to match the area under the power spectrum of the real data and computed a bias-corrected version of the periodograms. We finally derived the false-alarm probability levels from each of the largest peaks in the synthetic periodograms. Results are shown in Figure 5.20 for 10000 Monte Carlo simulations.

As expected, the false alarm probabilities under the null-hypothesis of red noise are more stringent than those from the bootstrap method. For Holmberg II X–1, the peak is well below the 3σ false-alarm probability. If we consider the less stringent false-alarm probability computed from the entire distribution of simulations (green line), the peak is only slightly below this limit. It is possible that the variability exhibited by the source (Figure 5.17, right panel) is complicating the detection of the quasi-periodicity if the latter is not strictly coherent. Thus, more monitoring might be needed to clarify whether the variability is indeed quasi-periodic. Instead, for NGC 5204 X–1 the red-noise AR(1) process cannot account for the variability observed, suggesting that the periodicity in the periodogram might be real.

5.2.3.2.4 Uncertainties on the period: In order to derive meaningful uncertainties on the periodicity of NGC 5204 X–1, we followed Brightman et al. (2019) and used a fitting procedure based on Gaussian process modelling proposed by Foreman-Mackey et al. (2017). Gaussian processes offer several advantages over the classical Lomb–Scargle periodogram, namely the possibility to test more refined models than the implicitly assumed stable sinusoid in the Lomb–Scargle periodogram, and the possibility to retrieve meaningful errors on the best period estimate, which are not well defined in the case of the periodogram VanderPlas (2018). We used the python implementation `celerite` proposed by Foreman-Mackey et al. (2017) and considered three different models consisting of one or two components for our data.

The first model (model a) has a single term to capture the oscillatory behaviour by means of a damped simple harmonic oscillator (SHO), whose power spectral density is given by

$$S(\omega) = \sqrt{\frac{2}{\pi}} \frac{S_0 \omega_0^4}{(\omega^2 - \omega_0^2)^2 + \omega_0^2 \omega^2 / Q^2}, \tag{5.5}$$

where S_0 is the amplitude of the oscillation, ω_0 is the frequency of the undamped oscillator, and Q is the quality factor, which indicates how peaked the periodicity is in the PSD and gives a measure of the stability of the periodicity. For the second and third models, we added a noise component on top of the SHO to consider the variations not captured by the Lomb–Scargle solution (see e.g. Figure 5.19 around 700–800 days after the beginning of the monitoring). In one of the models, this noise was modelled with a white noise or jitter term (model b) with amplitude σ. For the other model (model c), we considered a red-noise component that can be modelled in `celerite` with the same kernel as for the damped harmonic oscillator, but fixing $Q_N = 1 / \sqrt{2}$ (Foreman-Mackey et al., 2017), and leaving the other parameters of the oscillator (S_N, ω_N) free to vary during

Table 5.11: Best-fit parameters from the minimisation routine for the three different models tested and the corresponding Bayesian information criterion (BIC) for each of them to model the 2014–2015 light curve of NGC 5204 X–1.

Model	P (days)	log S_0	log Q	log σ	log S_N	log ω_N	BIC
NGC 5204 X–1							
SHO	186.5	4.0	3.0	-	-	-	–772
SHO + white noise	196.8	3.7	3.0	–5.1	-	-	–788
SHO + red-noise	196.8	3.7	3.0	-	–6.9	-2.9	–783

fit. To summarise, we thus tested three different models: a) a single SHO term, b) the same SHO term but with a white noise term, and, finally, c) the SHO term with the red-noise component.

In order to select the most suitable model for our datasets, we fitted each of the three models to the light curve using the L-BFGS-B minimisation method from `scipy` and retrieved the Bayesian information criterion (BIC) (Schwarz, 1978) as given in Equation 54 of Foreman-Mackey et al. (2017), meaning lower BIC values indicating preferred models. We set the following uniform priors on the parameters:$10 < P < 700$ days, $0.1 < S_0 < 10000$, and $20 < Q < 2000$. That is, all parameters are essentially unconstrained except for the lower bound of Q, which we limited, as low values of Q lose the oscillatory behaviour that we want to describe (Foreman-Mackey et al., 2017). For the red-noise component, S_N and ω_N are arbitrarily started at $\log \omega_N = –0.1$ and $\log S_N = –5$ with the following uniform priors (again essentially unconstrained): $–10 < \log \omega_N < 15$ and $–10 < \log S_0 < 15$. The amplitude of the white noise term σ is set initially to the mean value of the count-rate errors and is allowed to vary between $–10 < \log \sigma < 15$. We performed several runs varying the initial parameters to ensure that the minimisation routine finds the global minimum for each model. The best-fit parameters and the BIC calculations are presented in Table 5.11.

Based on the BIC values, the model with the addition of white noise (model b) seems to be the preferred model. The addition of a more complex red-noise component (model c) seems not to be justified by the quality of data since a similar solution is found to that of model b (Table 5.11), with the addition of an extra parameter. Therefore, the simpler white noise component seems to be the preferred model, and we thus considered only this model for the subsequent analysis. The best-fit model is shown in Figure 5.21.

In order to estimate errors on the best fit parameters of the model with the added white noise, we initialised 32 walkers (or chains) to sample the posterior probability distribution by drawing 20000 MCMC samples using the `emcee` library in `python`. Each walker is initialised by randomly drawing a sample from the uniform priors defined above to ensure that parameter space is adequately sampled by the chains. In order to estimate an adequate burn-in period, we visually inspected the convergence of the chains and discarded the first 10000 samples of each of them. From the remaining samples, we selected one every 20 samples to derive the posterior probability density that is shown in Figure 5.21. The periodicity found above in the light curve of NGC 5204 X–1 is of 197^{+27}_{-31} days (1 σ error), which is consistent with the 221-day peak found in the Lomb–Scargle periodogram (Section 5.2.3.2.3) at the 1 σ level.

5.2.3.3 Spectral analysis

Here, we attempt to spectrally characterise each of the states found in Section 5.2.3.1 (HUL, SUL, and SSUL regimes) with a physically motivated model. To do so, we made use of the *XMM-Newton*, *Chandra*, and *NuSTAR* data used in Gúrpide et al. (2021a), and the additional *Chandra* and *Swift*-XRT data of this work. We considered all the available datasets for each state, regardless of their date, and fitted them assuming the same model. This selection is driven by the results from Section 5.2.3.1 and the analysis presented in Gúrpide et al. (2021a). We also extracted *Swift*-XRT spectra for each source state by stacking individual observations using the online tools (Evans et al., 2009). The count rates and hardness used to classify the observations can be found in Table 5.12. For NGC 5204 X–1, we found the data quality of *Swift*-XRT spectra to be too low for a meaningful analysis. For Holmberg II X–1, we only found good agreement between the *Swift*-XRT data and the other mission datasets for the SUL regime, and thus this was the only *Swift*-XRT spectrum that we finally used. In the other cases, we found the *Swift*-XRT data to be significantly dimmer below 1 keV compared to the other datasets (residuals of $\gtrsim 3\sigma$) and the floating cross-calibration constant is above 10% with respect to the *XMM-Newton* data, even when taking into uncertainties. This disagreement is consistent with the scatter seen in the *Swift*-XRT observations with respect to the *XMM-Newton* observations of the SSUL and HUL regimes (Figure 5.14).

We also inspected the *XMM-Newton* optical monitor and the *Swift*-UVOT images looking for observations that could help to constrain the broadband emission. However, given the limited spatial resolution of the instruments (PSF $\sim$ 1 arcsec), both ULXs are completely blended with nearby sources in the field of view preventing a clean determination of the direct contribution from the ULX. We therefore searched for *Hubble* optical/UV data using the MAST portal[20] and selected observations when the source state was known. We restricted the search to the

---

[20] `https://mast.stsci.edu/portal/Mashup/Clients/Mast/Portal.html`

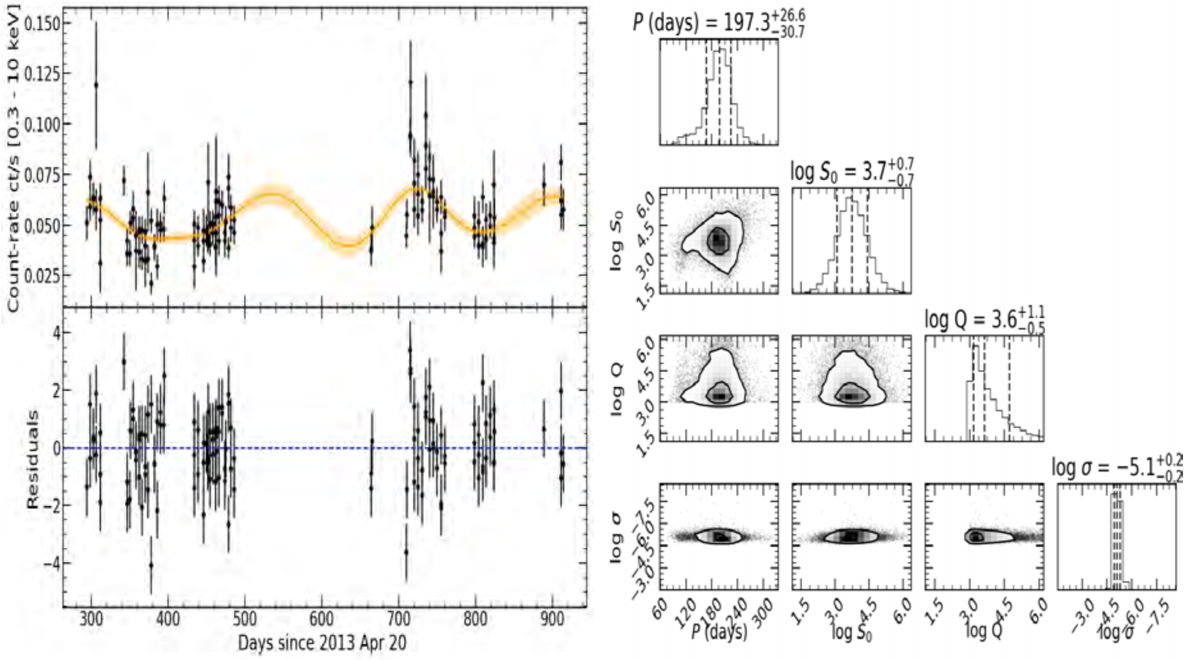

Figure 5.21: *Left:* Best-fit solution of the `celerite` modelling (orange solid line) with the 1σ shaded contours for the light curve of NGC 5204 X–1: The model shows the SHO with additional white noise (model b), for which we only show the oscillatory component. *Right*: Posterior probability distributions of the parameters of the `celerite` model in the right panel. The histograms along the diagonal show the marginalised posterior distribution for each parameter with dashed lines indicating the median and the 1σ errors. The two-dimensional histograms show the marginalised regions for each pair of parameters with the contours showing the 1 and 2σ confidence intervals.

Table 5.12: *Swift*-XRT count rates and hardness ratios used to extract stacked spectra.

	NGC 5204 X–1		Holmberg II X-1	
State	Count rate cts/s	HR	Count rate cts/s	HR
SUL	0.06–0.11	0.4–0.8	0.225–0.35	0.3–0.7
HUL	0.05–0.06	0.45–1.1	0.105–0.205	0.44–1.0
SSUL	0.4–1.1	0.035–0.05	0–0.105	0–0.8

Table 5.13: Best-fit results for the HUL states seen in NGC 5204 X–1 and Holmberg II X–1 using the `sirf` model. All uncertainties are given at the 90% confidence level.

State	$n_{\rm H}$ 10^{20} cm^{-2}	$T_{\rm in}$ keV	$R_{\rm in}$ 10^{-3} $R_{\rm sph}$	θ_f °	i °	$\dot{m}_{\rm ejec}$	norm	χ^2_r / dof
				NGC 5204 X–1				
HUL	7±1	$1.45^{+0.12}_{-0.09}$	$0.8^{+0.3}_{-0.2}$	39.4±0.4	< 12.2	29^{+10}_{-4}	$4.9^{+4.3}_{-2.2}$	1.12 (1136)
				Holmberg II X–1				
HUL	11.4±0.7	$1.48^{+0.05}_{-0.04}$	$0.15^{+0.04}_{-0.01}$	41.0±0.4	< 9.1	169±25	$544.2^{+183.1}_{-157.6}$	0.99 (960)

Notes. $^{(a)}$ Unconstrained parameter. $^{(b)}$ Fixed parameter. We set a lower limit on i of 0.5 degrees.

wide or medium filters as we were interested in the continuum emission. Unfortunately, we only found quasi-simultaneous *HST* data for the hard-intermediate state of Holmberg II X-1 in the F275W, F336W, F438W, and F550M filters. We used a 0.255" radius circular aperture for the source and an annulus of 0.37" and 0.58" inner and outer radius for the background, to consider some of the nebular emission in the background subtraction. We applied the appropriate aperture correction for each filter [21] and converted the telescope counts to fluxes using the calibration *PHOTFLAM* keywords found in the file headers[22]. We obtained background-corrected fluxes in units of erg/cm^{-2}s^{-1}Å^{-1} of $(6 \pm 2) \times 10^{-17}$, $(3.6 \pm 0.8) \times 10^{-17}$, $(1.6 \pm 0.4) \times 10^{-17}$, and $(7\pm 2) \times 10^{-18}$ for the F275W, F336W, F438W, and F550M filters, respectively. The different datasets considered together to characterise each state can be found in Table 5.8.

Previous broadband spectral analysis by Tao et al. (2012) of NGC 5204 X–1 indicated that the emission could be consistent with an irradiated standard accretion disc and that a stellar origin was unlikely. Here, we chose to model our data with the physically motivated model `sirf` (Abolmasov et al., 2009, available in XSPEC), which provides a self-consistent analytical solution to the super-critical funnel geometry based on the theoretical works of Shakura & Sunyaev (1973) and Poutanen et al. (2007) to see if the broadband emission could instead be explained as arising from a self-irradiated super-critical disc.

This model considers black-body emission from the outer wind photosphere, the walls of the super-critical funnel, and the photosphere at the bottom of the funnel, taking into account self-irradiation effects. The model has nine variable parameters: namely, the temperature and the distance from the source of the funnel bottom photosphere ($T_{\rm in}$ and $R_{\rm in}$), the outer wind photospheric radius ($R_{\rm out}$), the half-opening angle of the funnel (θ_f), the velocity-law exponent for the wind (α) that is, $v_{\rm wind} \propto r^{\alpha}$, the adiabatic index ($\gamma$), the mass-ejection rate ($\dot{m}_{\rm ejec}$), and the normalisation of the model. As a caveat, we note that the model does not take into account Comptonisation, which is likely to be an important source of opacity in the super-Eddington regime (e.g. Kawashima et al., 2012).

We modelled interstellar X-ray absorption with two `tbabs` components, one frozen at the Galactic value along the line of sight (2.72×10^{20} cm^{-2} and 5.7×10^{20} cm^{-2} for NGC 5204 X–1 and Holmberg II X-1, respectively; HI4PI Collaboration et al., 2016) and another one free to vary. For the dataset containing *HST* data, we considered interstellar extinction by adding the `redden` model in `XSPEC` with E(V-B) fixed to 0.074, based on the measured H_α/H_β ratio from the nebular emission of Vinokurov et al. (2013) and using the extinction curve from Cardelli et al. (1989) of $R_V = 3.1$.

The nine parameters of the `sirf` model could not all be constrained if left free to vary, even for the hard-intermediate state of Holmberg II X–1, where we had the best data quality. Therefore, following Abolmasov et al. (2009), in all fits we fixed the velocity law exponent of the wind (α) to –0.5, the adiabatic index (γ) to 4/3, and R$_{\rm out}$ to 100 $R_{\rm sph}$, as the latter parameter is insensitive to the spectra unless its value is below 1, according to the authors. However, we found that for the soft and super-soft states, due to the lack of optical coverage and the poor data quality, we could not discriminate between different solutions, with the fit often being insensitive to several parameters and resulting in large parameter uncertainties. Another complication arose due to the fact that the model favours solutions in which $i \sim \theta_f$ when θ_f was not well constrained. This occurs due to the fact that a sharp transition is created in the χ^2 space when the model changes from a solution where our line of sight is within the the wind cone to a solution with the wind cone out of the line of sight, creating an artificial minimum in the χ^2 space at $i \sim \theta_f$. We therefore decided to restrict the spectral analysis to the hard-intermediate states, which are the only states for which we have good quality broadband data. Obtaining *HST* observations of both ULX in the different spectral states should help to allow us to constrain the broadband emission.

The `sirf` model offered a good fit (χ^2_r= 1.00 for 960 degrees of freedom) to the broadband emission (see Figure 5.22 and Table 5.13) of Holmberg II X–1 in the HUL state. Thus, while emission from the donor star or an irradiated disc could be consistent with the UV/optical emission (e.g. Tao et al., 2012), self-irradiation by a

---

[21] `https://www.stsci.edu/hst/instrumentation/acs/data-analysis/aperture-corrections` and `https://www.stsci.edu/hst/instrumentation/wfc3/data-analysis/photometric-calibration/uvis-encircled-energy`

[22] `https://www.stsci.edu/hst/wfpc2/Wfpc2_dhb/wfpc2_ch52.html`

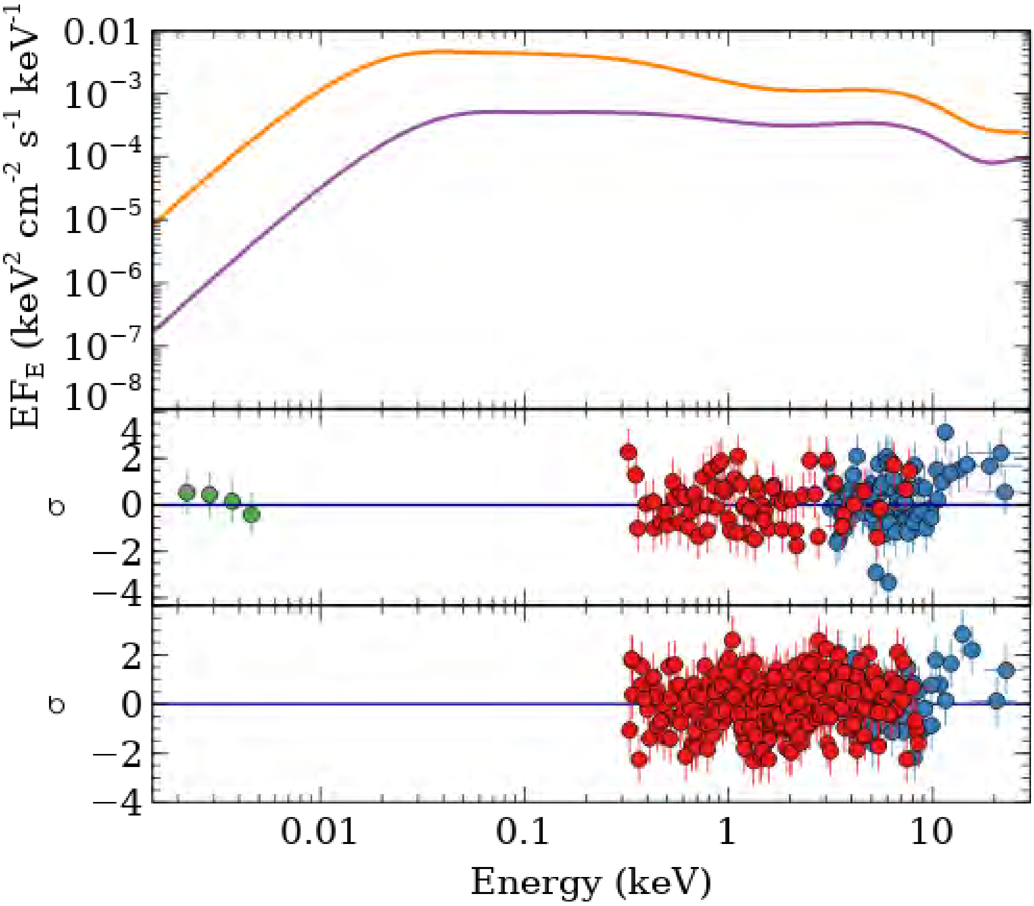

Figure 5.22: (Top) Broadband best-fit (solid lines) to the HUL states of Holmberg II X-1 (orange) and NGC 5204 X–1 (purple line) with the self-irradiated super-critical funnel model (`sirf` in XSPEC) for i $\sim$ 10 degrees (see Table 5.13). The models in the upper panel have been corrected for X-ray and optical absorption. The lower panels show the best-fit residuals for Holmberg II X–1 (middle panel) and NGC 5204 X–1 (bottom panel) without any correction for X-ray absorption. Green, red, and blue circles show the *HST*, *XMM-Newton* EPIC-pn, and FPMA *NuSTAR* data, respectively (see Table 5.13)

super-critical disc seems another plausible scenario based on the broadband emission. We found an upper limit on i of 9.1°. This is slightly below the lower limit of 10° suggested by Cseh et al. (2014), assuming that the radio jet detection is not strongly Doppler boosted, although we note that if the source precesses, the viewing angle could be variable. Therefore, a viewing angle looking down the funnel ($\theta_f\sim$ 40 degrees) seems to be supported. For NGC 5204 X–1, we similarly obtained an upper limit on i of $\sim 12°$. Interestingly, the set of parameters obtained are very similar to those obtained for Holmberg II X–1, except for a factor of $\sim$ 7 lower $\dot{m}_{\rm ejec}$ and a factor of $\sim$ 5 higher $R_{\rm in}$ (see Table 5.13). Therefore, the spectral differences between NGC 5204 X–1 and Holmberg II X–1 could be accounted for by a lower $\dot{m}_{\rm ejec}$ and a thicker bottom of the funnel in the case of NGC 5204 X–1 with an unobscured view of the bottom of the funnel in both cases.

5.2.4 Discussion

The multi-instrument data analysed in this work has allowed us to firmly establish, for the first time, the presence of a recurrent evolutionary cycle in ULXs. The similarities that exist in the temporal (Figures 5.14 and 5.16) and spectral (Figure 5.22 and Table 5.13; see also Figure 6 in Gúrpide et al., 2021a) properties of Holmberg II X–1 and NGC 5204 X–1 allow us to describe the evolution of the cycle as follows: starting from the HUL state, the sources transit to the SUL state (Figure 5.16). There, the sources will transit back and forth from the SUL regime to the SSUL regime (Figures 5.14 and 5.16), and finally the sources will return to the HUL state from the SUL state (Figure 5.16). These findings offer a unique opportunity to constrain the timescale and nature of the transitions frequently observed in these sources (e.g. Roberts et al., 2006; Grisé et al., 2010) and could potentially be extended to similar transitions seen in other ULXs as well (e.g. Middleton et al., 2015b; Gúrpide et al., 2021a; Mondal et al., 2021).

Spectral transitions in ULXs have been frequently discussed invoking geometrical effects induced by the wind/funnel structure (e.g. Sutton et al., 2013; Middleton et al., 2015a; Pinto et al., 2021) expected to form as the mass-transfer rate approaches the Eddington limit and radiation pressure starts to drive a conical outflow (Shakura & Sunyaev, 1973; Poutanen et al., 2007). Building a coherent picture of the long-term spectral evolution of these two ULXs was attempted in Gúrpide et al. (2021a), where it was suggested that the transition from the hard to the soft ULX regime was due to an increase of the mass-transfer rate and corresponding decrease of the opening angle of the funnel, based on the HUL-SUL softening from a rather sparse monitoring provided by *XMM-Newton* and *Chandra*. The authors also suggested that a line of sight grazing the wind walls in the SUL state could explain the rapid transitions observed to the SSUL state as we switch between peering down the optically thin funnel and observing the wind photosphere as the source processed (e.g. Abolmasov et al., 2009). We note that a viewing angle grazing the wind walls is also supported by the lack of short-term variability in the SUL state of Holmberg II X–1 and NGC 5204 X–1 (e.g. Heil et al., 2009; Sutton et al., 2013), which is at odds with the high short-term variability seen in softer of the soft ULXs (e.g. Middleton et al., 2011a) argued to be viewed through the wind. However, the lack of periodic variability (Figure 5.20) in the SUL–SSUL transitions found here suggests that precession of the accretion flow might not be responsible for the spectral changes. Instead, a scenario in which the short-term variability may be ascribed to the presence of wind clumps crossing our line of sight (Takeuchi et al., 2013; Middleton et al., 2015a) as a result of the narrower funnel is supported by the aperiodic transitions.

Similar transitions from SUL to SSUL are seen in the ULS NGC 247 ULX–1 (Urquhart & Soria, 2016; Feng et al., 2016) and NGC 55 ULX (Pinto et al., 2017), which are also observed during the bright states (Pinto et al., 2021), suggesting a tight link between standard ULXs and ULSs. However, as opposed to NGC 247 ULX-1, Holmberg II X–1 and NGC 5204 X–1 are the first sources observed to switch through all these three canonical ULX states, possibly due to the lower viewing angle compared to ULSs. Moreover, dips frequently seen in ULSs (e.g. Stobbart et al., 2006; Urquhart & Soria, 2016; Alston et al., 2021) are not observed in the light curves of Holmberg II X–1 and NGC 5204 X–1, supporting this interpretation. It is thus likely that the dipping activity in ULSs is associated with direct obscuration of the inflated accretion disc as a result of the increased mass-accretion rate (Guo et al., 2019). Hence, the increase in mass-accretion rate confers Holmberg II X–1 and NGC 5204 X–1 with a somewhat harder ULS aspect, because the SSUL aspect of these standard ULXs is not due to a high inclination angle, but rather due to the extreme narrowing of the funnel. This might imply that ULSs are characterised by both a high inclination angle and a high mass-accretion rate.

The amplitude of the jittering decays towards the end of the 2009–2010 monitoring of Holmberg II X–1 (Figure 5.17). This might imply that the mass-transfer rate has increased and narrowed the funnel further; so, towards the end of the 2009–2010 monitoring our line of sight no longer sees the inner regions of the accretion flow and instead mostly sees the wind photosphere, reducing the observed variability. Such dimming and reduced variability caused by an increase of the mass-accretion rate is in good agreement with the predictions made by Middleton et al. (2015a) for sources at moderate inclinations. This is illustrated in Figure 5.23, panels b and c.

The spectral analysis might support a low viewing angle for Holmberg II X–1 and NGC 5204 X–1, at least for the HUL state (Section 5.2.3.3), and a moderate opening angle of the funnel ($\theta_f \sim 40°$). The lack of clear jittering behaviour in the 2019 data (see Figure 5.14) may be explained by the larger opening angle of the funnel as a result of the lower mass-transfer rate, implying that the wind is unlikely to enter the line of sight. This is consistent with the reduced short-term variability seen in hard ULXs (e.g. Middleton et al., 2015a; Sutton et al., 2013), frequently argued to be viewed face-on, and is consistent with the suggestion that the increase of mass-transfer rate and narrowing of the opening angle of the funnel causes the HUL–SUL spectral change (Figure 5.16). This interpretation naturally accounts for the lack of direct transitions from the SSUL regime to the HUL regime (Figures 5.14 and 5.16). A cartoon illustrating the source variability and its relation to the different spectral states is depicted in Figure 5.23.

The ~ 200-day periodicity found in the light curve of NGC 5204 X–1 is possibly associated with the timescale of the whole cycle (Figure 5.21); albeit, further investigation is needed. While the nature of this periodicity remains unclear, should our interpretation of the evolutionary cycle be correct, we would expect some mechanism of periodic mass-transfer increase to be responsible for it and cause the source to switch from the HUL regime to the SUL state. This could be the case in an eccentric orbit in which the mass-transfer rate is expected to be maximal as the companion passes through the periapsis. This scenario would likely require a super-giant star, as for large eccentricities $e > 0.5$ we find that the star would need to have a radius in excess of $\sim 200\ R_\odot$ to fill its Roche-Lobe overflow for compact objects of masses as low as 1.4 $\mathrm{M}_\odot$. This large radius is at odds with the suggested radius of 30 $R_\odot$ for the companion based on the UV spectrum of the counterpart (Liu et al., 2004). Additionally, orbital solutions in ULXs (only available thanks to a timing solution in ULXs showing pulsations) require modest eccentric orbits ($e \lesssim 0.1$ Bachetti et al., 2014; Fürst et al., 2018; Rodríguez-Castillo et al., 2020) and generally shorter orbital periods ($P \lesssim 60$ days) are found, although the orbital period of NGC 300 ULX1 is expected to be of ~ 1 year based on the red super-giant companion (Heida et al., 2019).

Another mechanism that could induce periodic increases in the mass-transfer rate is the Kozai mechanism (Kozai, 1962), in which the presence of a third body causes modulation of the eccentricity of the inner binary. The changes in eccentricity will affect the distance between the inner L1 Lagrangian point and the centre of mass of the companion, therefore modulating the mass-transfer rate. This mechanism has been proposed to explain the super-orbital X-ray modulation of ~ 176 days associated with mass-transfer rate variations in the triple system 4U1820-303 (see Zdziarski et al. (2007) and references therein). It has also been suggested that this mechanism could explain the ~ 60-day quasi-periodicity responsible for the strong bi-modal flux modulation of the PULX M82 X–2 (Brightman et al., 2019; Bachetti et al., 2020), which has been argued to be due to the NS switching

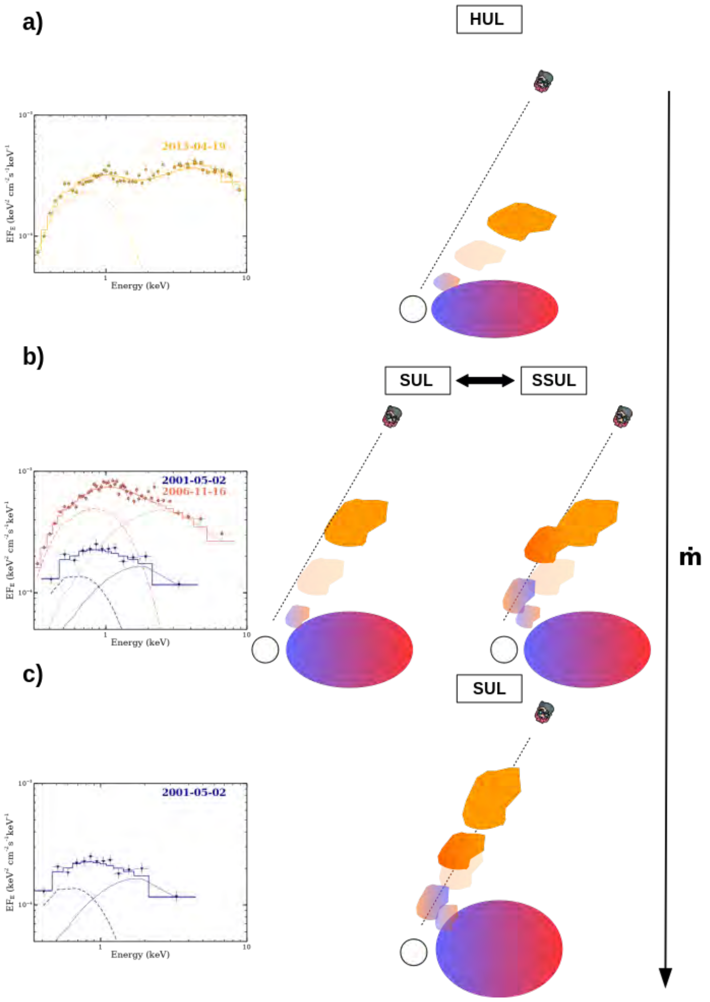

Figure 5.23: Cartoon illustrating the different spectral states observed in Holmberg II X–1 and NGC 5204 X–1 as a function of the mass-transfer rate and wind clumps crossing the line of sight. The compact object (NS or a BH) is represented by a white sphere. From top to bottom, the mass transfer increases as indicated by the black arrow on the right. In panel a), the funnel is wide open due to the low accretion rate, and the observer sees the inner regions of the accretion flow and little variability is observed (HUL regime; 2019 *Swift* monitoring of Holmberg II X–1), because the wind is unlikely to enter the line of sight. The left graph shows the corresponding spectral state (adapted from Gúrpide et al., 2021a). In panel b), the mass-transfer rate increases and narrows the opening angle of the funnel (SUL regime; SSUL regime), so wind clumps might now start to enter the line of sight and produce the spectral changes from soft to the SSUL regime observed (right and left panels and as seen in the 2009 *Swift* monitoring of Holmberg II X–1). Finally, in panel c), the mass-transfer rate increases further and the wind cone is now in the line of sight. The observer mostly sees the wind and the colder outer parts of the inflated disc, so the effect of absorption by wind clumps is dampened (end of the 2009–2010 *Swift* monitoring of Holmberg II X–1).

back and forth from the accretor phase to the propeller regime (Tsygankov et al., 2016b).

It is also worth noting that a linear relationship has been found between super-orbital and orbital periods in Be/X-ray binaries, SGXBs, and ULXs (see Corbet & Krimm, 2013; Townsend & Charles, 2020, and references therein). Assuming the 200-day periodicity is super-orbital in nature, we would expect an orbital period in NGC 5204 X–1 of the order of ∼ 10 days. This is in agreement with the estimate made by Liu et al. (2004), based on the UV spectrum of the counterpart and on the assumption that the companion fills its Roche Lobe. Indeed, the relationship between the orbital and super-obital periods would imply that NGC 5204 X–1 is a system with a super-giant filling its Roche Lobe (Townsend & Charles, 2020). We note that the linear relationship between the period and super-orbital period in super-giant Roche-Lobe filling systems is yet unclear, although the presence of a third body could account for the super-orbital periodicity (Corbet & Krimm, 2013), as stated also above.

Finally, we note that further monitoring of the soft spectral transitions would be of interest to robustly determine whether the spectral changes are associated with a quasi-periodicity. It has recently been proposed that a possible mechanism to account for the observed superorbital periods in ULXs could be the Lense-Thirring effect (Middleton et al., 2018). If so, precession of the accretion flow induced by the Lense-Thirring effect may explain the spectral changes from SUL to SSUL as the wind cone comes into and out of the line of sight throughout the precession cycle, strongly modulating the flux (Abolmasov et al., 2009; Dauser et al., 2017). The decay of the amplitude of the putative modulation towards the end of 2009–2010 could be similarly accounted for by an increase in the mass-accretion rate associated with a reduction of the opening angle of the funnel, meaning that throughout the whole cycle we only see the wind. Conversely, the lack of modulation during the HUL state of 2019 (Figure 5.18) could be due to the opposite effect, that is, a larger opening angle of the funnel resulting from a decrease of the mass-transfer rate. In this case, our line of sight observes the optically thin funnel (e.g. Narayan et al., 2017) throughout the whole precessing cycle, again effectively diminishing the amplitude of the oscillation (Abolmasov et al., 2009).

5.2.5 Conclusions

We show the striking similarities of Holmberg II X–1 and NGC 5204 X–1 in their long-term evolution as they transit through the canonical hard, soft, and super-soft ULX spectral regimes. This is the first time that such recurrent evolutionary cycle is observed in ULXs and that all three states are observed in a single ULX, strengthening the hypothesis that ULSs are standard ULXs viewed at high inclinations. We argue that the sources transit from hard to soft ULX as the mass-transfer rate increases and the funnel closes. There, the source will exhibit jittering, as wind clumps start to cross the line of sight due to the now narrower funnel, explaining the spectral transitions from soft to super-soft ULX. As the mass-accretion rate increases further and the funnel closes, our line of sight mostly sees the wind photosphere, with the subsequent reduction of short-term variability. The absence of SSUL–HUL state transitions are naturally explained by this scenario.

This interpretation is supported by the *Swift*-XRT light curve of Holmberg II X–1, which shows a lack of strong variability in the hard ULX state and a strong rapid variability responsible for the spectral changes between soft and super-soft states. The light curve of NGC 5204 X–1 shows instead a periodicity on a long timescale of ∼ 200 days, which is likely associated with the duration of the full hard—soft–super-soft cycle; albeit, further monitoring is needed to robustly confirm this association. We argue that the transitions from hard to soft ULX are likely associated with some periodic increase of the mass-transfer rate, yet the nature of this modulation remains unclear. Similar periodicity may be present in the long-term evolution of Holmberg II X–1 based on its similarities with NGC 5204 X–1. We therefore encourage *Swift*-XRT monitoring of Holmberg II X–1 over longer timescales to detect it.

Acknowledgements

We would like to thank the anonymous reviewer for comments and suggestions that improved this manuscript. The authors are grateful to H. Carfantan for his help with the timing analysis. GV acknowledges support by NASA Grant numbers 80NSSC20K1107, 80NSSC20K0803 and 80NSSC21K0213. NAW acknowledges support by the CNES.
Software used: HEASoft v6.26.1, Python v3.8, Veusz 3.3.1 (J. Sanders).

5.2.6 Additional commentary on the paper

T. Roberts pointed out that the association of the 200 d periodicity found in the lightcurve of NGC 5204 X–1 with the cycle is not robust. While perhaps the most obvious explanation for this periodicity is its association with the evolutionary cycle, this still remains uncertain and other scenarios are possible. First, it must be clarified that further monitoring is likely needed to robustly confirm it. That said, if the ULX cycle bears any similarity with the cycle in BHXRBs, then it would make sense for the cycle to be simply recurrent as opposed to periodic. This may strengthen the onset of the spectral changes as due to increases of mass-transfer, as argued above, and may suggest that the periodicity is due to an entirely different mechanism. Another thing that must be noted is that if the cycle is periodic, given the spectral changes observed (HUL–SUL, rapid SUL–SSUL changes and finally SUL–HUL) then the periodicity should follow a more complex profile than a simple sinusoid. Therefore further monitoring on NGC 5204 X–1 would certainly be of interest in the future to a) confirm the periodicity itself and b) whether it is associated with the evolutionary cycle.

5.3 Complementary studies

In an effort to understand better the accretion flow geometry and nature of ULXs, I also had the opportunity to collaborate in other projects where I carried a small part of the main analysis. These results were published in (Vasilopoulos et al., 2021) (Section 5.3.1) and (Quintin et al., 2021) (Section 5.3.2).

5.3.1 Dips in the Pulsating Ultraluminous X-ray source M51 ULX–7

The study of Gúrpide et al. (2021a) (Section 5.1) led to G. Vasilopoulos and F. Koliopanos to investigate in more details some of the transitions observed in M51 ULX–7. This was reported in Vasilopoulos et al. (2021) in which it was found that the source showed periodic dips associated with the orbital period in the *Chandra* light curves. In this work I carried out the count-rate and flux determination from the *Chandra* observations. Some of the drops in flux by a factor ~ 8 in the *Chandra* observations were shown not to be consistent with the superorbital flux modulation of the source (Vasilopoulos et al., 2020a) or the periodic dips, and thus a likely explanation is that the source is entering the propeller regime. This allowed us to estimate the strength of the magnetic field of the source to be around $4–9 \times 10^{13}$ G and to rule out strong beaming effects due to the orbital constraints inferred from the presence of dips. This was in very good agreement with the low degree of beaming inferred in (Gúrpide et al., 2021a) (Section 5.1.4.1) based on the lack of marked hardness variability. Also importantly, the presence of dips implies that the source cannot be viewed at low inclinations, and challenges the notion that a low-viewing angle is required to identify a supercritical accretor as a ULX (e.g. Middleton & King, 2016; King, 2009).

5.3.2 A New Pulsating and Transient Ultraluminous X-ray Source

While studying long-term highly variable X-ray sources by cross-correlating several X-ray catalogs, E. Quintin found a highly variable ULX (Quintin et al., 2021) (variations by a factor of ~ 100 in flux) in the same field of view of the well known PULXs NGC 7793 P13 (e.g. Fürst et al., 2016). High levels of long-term variability are a signature commonly seen in PULXs (e.g. Israel et al., 2017a) and has been considered a potential signature for the accretor hosting a NS (e.g. Song et al., 2020). Therefore, I investigated whether pulsations were present in the light curve of the source at its X-ray (0.3–10 keV) peak (unabsorbed luminosity of $\sim 3 \times 10^{39}$ erg/s), an epoch when the source has been serendipitously caught by a ~ 29 ks *XMM-Newton* observation. I used `HENDRICS` (Bachetti, 2018) as outlined in Section 5.1.4.3. A potential pulsation candidate was found at ~ 0.4 s. The solution and proper estimation of the significance was later refined by M. Bachetti. Additionally, I also carried out the determination of the *Chandra* 3σ upper limits and the power spectral densities calculations, for which we found no significant peaks.

Chapter 6

Looking for Optical Bubbles in the MUSE Archive

As we have seen in Section 3.2.3, ULX nebulae are a powerful tool to diagnose the true energy throughput of the source and hence constrain the energetics and overall properties of the super-Eddington accretion flows. The simultaneous spectro-imaging capabilities of IFU instruments and in particular the MUSE (Section 4.2.2) coverage of the main nebular lines used for gas diagnostics make it an ideal instrument for the study of ULXs bubbles. Additionally, the gas diagnostics employed to study the bubble may potentially reveal evidence for the presence of collimated jet activity, which is still a rather elusive phenomena in ULXs. We will see that these types of study can also yield interesting clues about the birthplace of the ULX, by studying the metallicity of the gas around the source and its relative motion to the ISM (see e.g. Egorov et al., 2017).

Another important aspect of the simultaneous spectro-imaging capabilities is the possibility to obtain redshift measurements of the source of interest with a single observation, which otherwise require a two step process combining photometric and spectroscopic observations. Redshift measurements are crucial to clean the ULX sample from contaminants as they allow us to robustly determine the association of the X-ray source with the putative host galaxy. However, we will see later in Section 6.2.3.7 that given the ULX counterpart faintness and MUSE limited spatial resolution (PSF FWHM $\sim 1''$ in seeing limited conditions) this will not be feasible unless for rather close targets ($D \lesssim 2\,\mathrm{Mpc}$) (see also Quintin et al., 2021). Nevertheless, the identification of ULX nebulae, provided they can be associated with the source in question, can provide indirect evidence for the association of the source with the galaxy. By the same token, the absence of a nebula around the ULX might cast some doubts about the association of the source with the galaxy, although as we shall see in Section 6.4 not all ULXs show associated nebular emission.

6.1 Catalog search

As a first step, I explored what data was already available in the archives. To this end, I cross-matched the ULX catalogs produced by Liu & Mirabel (2005); Swartz et al. (2011); Earnshaw et al. (2019) with the ESO science archive[1] with a search radius of 1 arcmin, corresponding roughly to the MUSE FOV width. The cross-match returned 117 ULXs that had been observed by MUSE at least once. Figure 6.1 shows the distribution of distances, offsets from the host galaxy center and luminosities in the X-ray band (for details on how the latter was derived see the aforementioned catalogs, in particular Earnshaw et al. (2019) quote observed luminosities, whereas Swartz et al. (2011); Liu & Mirabel (2005) quote unabsorbed luminosities).

The pixel scale of MUSE in the seeing limited mode (0.2") represents a physical scale of 25 pc at 25 Mpc, whereas a typical PSF of ∼1" represents ∼ 120 pc. Thus the ULXs below $D < 25$ Mpc are those more promising for the study, given that we are interested in studying structures of around $30 - 450\,\mathrm{pc}$. Those above $D > 25$ Mpc might be more suited to study metallicity gradients around them to understand the conditions that gave birth to the putative ULX.

In the remainder, I present some interesting targets that I had the opportunity to study during this thesis. At the beginning of this work (around 2019), only serendipitously targets were available and thus the observations analysed were of considerably worse quality (further distances, objects close to the edge of the FOV, etc...). For instance, the ULXs in NGC 1068 ($D = 14.6\,\mathrm{Mpc}$[2]) reported by Liu & Mirabel (2005) were all too close to the bright AGN and their study was not feasible. From the serendipitously observed targets, I had time to analyse in depth a few targets: the ULXs in NGC 1672 (Section 6.3) and the PULX in NGC 300 (Section 6.4). Later on, data cubes for a few interesting targets with known nebulae became publicly available such as NGC 1313 X–2

---

[1] `http://archive.eso.org/scienceportal/home`

[2] Average of the values reported in Simbad.

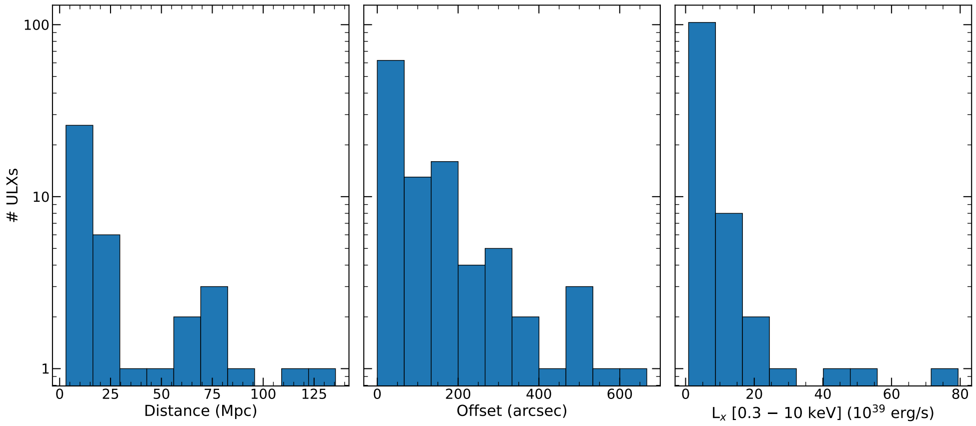

Figure 6.1: Distributions of some of the properties of the sample of ULX which have at least one MUSE data cube associated. Distances are only given for each unique host galaxy and offsets only for those ULXs found in the catalog by Liu & Mirabel (2005).

and NGC 1313 X–1 (see Table 3.2 in Section 3.2.3) which were also studied in Chapter 5 and thus are excellent targets given that their X-ray properties have been fully characterized. Section 6.2 describes the work done to characterize the nebula around NGC 1313 X-1. Given the data quality and the findings, this is the analysis for which I was able to provide more details and hence it is presented first, as most of the subsequent analyses largely follow the same procedure.

NGC 1313 X–1 was among the few sources for which high-resolution spectroscopy in X-rays had hinted the presence of powerful winds indicative of super-Eddington accretion (Pinto et al., 2016, 2020b). Given the available data for this source, this was an excellent opportunity to examine the impact of these winds in the environment. There was no confirmed bubble nebula around this source and only abnormally high [OI]λ6300/Hα ratios around the source had been reported by Pakull & Mirioni (2002). We discovered the presence of a huge shock-powered bubble, extending 452 × 266 pc in size. The bubble and the kinematic data left no doubt of the presence of powerful winds, in agreement with the studies in X-rays. From these observations, we could estimate the average mechanical power that goes into powering the winds to be around 2×10^{40} erg/s. Surprisingly, our estimates showed good agreement with those presented by Pinto et al. (2016); Walton et al. (2016b), indicating that these winds are able to exert an enormous impact on the ISM. This mechanical power is higher than the radiative luminosity of the source, which suggests that in the super-Eddington regime the mechanical feedback might be more relevant that the radiative one. The morphology of the nebula and the kinematic data suggest that there might be evidence for jet activity too, although this remains to be investigated. Finally, we also detected a high excitation region produced by the X-ray radiation from the source, indicating that the source is influencing its environment via shocks and radiation.

In this study, I carried out the initial data investigation, reduction and extraction of the main quantities of interest (e.g. fluxes, velocities) from the cube and from the *Chandra* data. I also performed the reddening correction and the numerical estimates of the ISM densities and mechanical powers and the analysis of the SNRs. I prepared and designed the first manuscript, producing all the Figures and leading the overall investigation. I produced the initial code to compare the extracted line ratios to the classical BPT diagrams (Baldwin et al., 1981) which later M. Parra, a master student supervised by O. Godet, modified and refined to adapt them to the newest classification proposed by Law et al. (2021) as advised by T. Contini. M. Parra also lead the investigation of the various metallicity methods available and wrote the very first version of the metallicity Section. He also performed the initial spatial analysis of the *Chandra* data to look for extended emission, which I later refined, although this part was later dropped due to inconclusive results. M. Parra also carried out the initial investigation on the use of the MAPPINGS libraries as well as finding the new compiled library by Alarie & Morisset (2019), easing substantially the comparison I later carried out. O. Godet provided the initial idea to use MUSE for this investigation whereas he and all the rest of the co-authors contributed to the discussion of the manuscript adding ideas, suggestions and overall improving substantially the final manuscript.

6.2 MUSE spectroscopy of the ULX NGC 1313 X-1: a shock-ionised bubble, an X-ray photoionised nebula and two supernova remnants

A. Gúrpide[1], M.Parra[1,2], O. Godet[1], T. Contini[1] and J.-F. Olive[1]

[1]Institut de Recherche en Astrophysique et Planétologie, Université de Toulouse, UPS/CNRS/CNES, 9 Avenue du Colonel Roche, BP44346, F-31028 Toulouse Cedex 4, France
[2]Univ. Grenoble Alpes, CNRS, IPAG, 38000 Grenoble, France

Accepted to A&A 21th of January 2022

Abstract

The presence of large ionised gaseous nebulae found around some Ultraluminous X-ray sources (ULXs) provides means to assess the mechanical and radiative feedback of the central source, and henceforth constrain the efficiency and impact on the surroundings of the super-Eddington regime powering most of these sources. NGC 1313 X–1 is an archetypal ULX which had been reported to be surrounded by abnormally high [O I]λ6300/H$\alpha > 0.1$ ratios and for which high-resolution spectroscopy in X-rays had hinted the presence of powerful outflows. We report observations taken with the integral field unit (IFU) Multi-Unit Spectroscopic Explorer (MUSE) mounted at the Very Large Telescope (VLT) of NGC 1313 X–1 in order to confirm the presence of a nebula inflated by the winds, investigate its main sources of ionisation and estimate the mechanical output of the source. We investigate the morphology, kinematics and sources of ionisation of the bubble through the study of the main nebular lines. We compare the main line ratios with spatially resolved BPT diagrams and with the prediction from radiative shock libraries, which allows us to differentiate regions excited by shocks from those excited by EUV/X-ray radiation. We detect a bubble of 452×266 pc in size, roughly centred around the ULX, which shows clear evidence for shock ionisation in the outer edges. We estimate shock velocities to be in the $\approx 160 - 180$ km/s range based on the line ratios. This suggests that an average and continuous outflow power of $\sim (2 - 4.5) \times 10^{40}$ erg/s over a timescale of $(4.5 - 7.8) \times 10^{5}$ yr is required to inflate the bubble. In the interior of the bubble and closer to the ULX we detect an extended ($\sim$140 pc) X-ray ionised region. Additionally, we detect two supernova remnants coincidentally close to the ULX bubble of which we also report age and explosion energy estimates. The elongated morphology and the kinematics of the bubble strongly suggest that the bubble is being inflated by winds and/or jets emanating from the central source, supporting the presence of winds found through X-ray spectroscopy. The estimated mechanical power is comparable or higher than the X-ray luminosity of the source, providing additional evidence in support of NGC 1313 X–1 harbouring a super-Eddington accretor.

6.2.1 Introduction

Ultraluminous X-ray sources (ULXs) are an enigmatic class of objects empirically defined as extragalactic, point-like, off-nuclear and with an X-ray luminosity exceeding the classical Eddington limit for a $\sim 20\,\mathrm{M}_\odot$ black hole (BH) (see Fabrika et al., 2021, for the most recent review). While this empirical definition alone does not convey much information about the nature of these objects, there is now firm evidence suggesting that a fraction of them are powered by super-Eddington accretion onto stellar-compact objects. Evidence in support of this picture comes from their atypical X-ray spectral states compared to sub-Eddington X-ray binaries (e.g. Gladstone et al., 2009; Bachetti et al., 2013; Gúrpide et al., 2021b), the discovery of X-ray pulsations in several ULXs with luminosities exceeding the classical Eddington limit for a neutron star (NS) by orders of magnitude (e.g. Bachetti et al., 2014; Fürst et al., 2016; Israel et al., 2017a; Carpano et al., 2018; Sathyaprakash et al., 2019; Rodríguez-Castillo et al., 2020; Quintin et al., 2021), the detection of strongly Doppler shifted X-ray lines indicative of super-Eddington winds with speeds reaching fractions of the speed of light (e.g. Pinto et al., 2016, 2020b, 2021), the inflated or photo-ionised 40–400 pc optical and radio bubbles found around them (Pakull & Mirioni, 2002; Abolmasov et al., 2007a; Berghea et al., 2020) and their similarities with the supercritically accreting Galactic source SS433 (Fabrika, 2004; Liu et al., 2015; Waisberg et al., 2019; Middleton et al., 2021). While these observational clues appear to match our understanding of the super-Eddington accretion regime to some extent (e.g. Shakura & Sunyaev, 1973; Poutanen et al., 2007; Takeuchi et al., 2013; Jiang et al., 2014; Middleton et al., 2015a; Narayan et al., 2017), many questions about the super-Eddington regime and its connection with ULXs remain open such as the degree to which the emission is beamed (e.g. King et al., 2001; Kaaret et al., 2004; Jiang et al., 2014; Mushtukov et al., 2021), the fraction of energy carried in the outflows, the mechanical and radiative feedback induced by ULXs and the exact accretion flow geometry allowing them to reach such high luminosities.

Because the X-ray luminosity is the defining property of a ULX, it is natural that most studies attempting to tackle these issues have focused on the X-ray band (e.g. Middleton et al., 2015a; Koliopanos et al., 2017; Walton et al., 2018c; Gúrpide et al., 2021a). However, observations in this band are generally limited by our ability to obtain information restricted to our line of sight. For this reason, testing the degree of anisotropy of the X-ray emission remains challenging (e.g. Middleton et al., 2021), yet strong anisotropy is predicted in many theoretical studies of the super-Eddington accretion regime (e.g. Shakura & Sunyaev, 1973; Poutanen et al., 2007; Narayan et al., 2017) and is a fundamental piece of information to determine the true radiative output in this poorly understood accretion regime.

On the other hand, the study of ULX bubbles offers means to infer this energetic output by observing the impact of the ULX on the environment. Because the bubble nebula sees the full emission from the ULX, it essentially offers a 2D map of the ionising photon field emitted by the ULX, while also probing the presence and the impact of the super-Eddington winds or jets on the environment. Therefore, ULX nebulae can be used to constrain the energetics and overall properties of the super-Eddington accretion flows powering ULXs. A prime example is the study of the ULX nebula around the ULX NGC 6946 X–1 by Abolmasov et al. (2008), who showed that the presence of a UV source with $L \sim 10^{40}$ erg/s was needed to explain the high-excitation lines of the nebula. Indeed, later *HST* observations in the far UV by Kaaret et al. (2010) confirmed the presence of the first ultraluminous UV source, in good agreement with the predictions made by Abolmasov et al. (2008). Observations of the HeIIλ4686 recombination line of the X-ray photoionised nebula around Holmberg II X–1 have also been used to constrain the intrinsic X-ray flux of the source, finding that the degree of beaming of the X-ray emission must be small (Pakull & Mirioni, 2002; Kaaret et al., 2004; Berghea et al., 2010). ULX nebulae are also of interest because they allow to probe faint X-ray sources with luminosities below the ULX threshold, but for which most of the X-ray radiation might be simply not directed into our line of sight, or for which most of the energy might be released mechanically (Dubner et al., 1998; Pakull et al., 2010; Urquhart et al., 2019).

With Integral Field Unit instruments (IFUs), the study of ULX nebulae becomes even more attractive as all the information needed to diagnose the physical conditions of the gas can be accessed with a single exposure. Indeed, several promising results can already be found in the literature (e.g. Egorov et al., 2017; McLeod et al., 2019). For this reason, we are undertaking a program to search for ULXs directly or serendipitously observed by the Multi Unit Spectroscopic Explorer (MUSE, Bacon et al., 2017), an IFU instrument at the Very Large Telescope (VLT) covering the 480–930 nm range, with a resolving power of ~ 2484 at 650 nm.

In this paper, we report the first of such analysis focusing on the well-known ULX NGC 1313 X–1 (e.g. Feng & Kaaret, 2006; Bachetti et al., 2013). NGC 1313 X–1 has a persistent unabsorbed luminosity in the 0.3–10 keV band above $\sim 8 \times 10^{39}$ erg/s, with a mean luminosity of 1.1×10^{40} erg/s (Gúrpide et al., 2021a) and is among the few ULXs for which high-resolution spectroscopy has hinted the presence of powerful winds with velocities $\simeq 0.2\,c$ (Pinto et al., 2016, 2020b, see also Walton et al. (2016b)), suggesting that the source harbours a supercritically accreting source, but whose nature remains unclear (Walton et al., 2020). The source is frequently argued to be viewed at low inclinations, through the optically thin funnel formed by the wind around the rotational axis of the compact object (e.g. Sutton et al., 2013; Middleton et al., 2015a; Gúrpide et al., 2021a). While these winds have been suggested to be powerful enough to carve the aforementioned ~100 pc bubbles sometimes seen around ULXs (Pinto et al., 2020a), this had not been directly confirmed so far. The presence of a nebula around NGC 1313 X–1 was hinted in the seminal study of Pakull & Mirioni (2002), who noted an exceptional high [O I]λ6300/H$\alpha > 0.1$ ratio surrounding the ULX. Here we report the detection and analysis of a well defined elongated 452 × 266 pc shock-ionised bubble, providing the first link between wind detections in X-rays and their large-scale impact on the surroundings. In the interior of the bubble we find line ratios typical of an X-ray photoionised nebula, consistent with the results from Pakull & Mirioni (2002).

Our focus here lies in investigating the main sources of ionisation of the bubble. Through different diagnostics and thanks to the MUSE data we are able to spatially resolve and distinguish regions excited by shocks from those excited by EUV/X-ray photoionisation from the ULX, providing important clues about the energy feedback of the source. We will show that while the bubble is likely to have been inflated by a wind, the inner regions show clear evidence for hard photoionisation from the ULX.

Coincidentally, we detect two supernova remnants (SNRs) at the edge of the bubble, of which we also provide line ratios and estimates of their kinetic explosion energy. An illustrative comparison between the energy required to inflate the ULX bubble invoking a SNR and these bona-fide SNRs is provided. We show that the explosion energy required to inflate the ULX bubble is orders of magnitude higher than that of the SNRs, strongly disfavouring this hypothesis, in agreement with previous works.

NGC 1313 ($z = 0.001568$) is a face-on SB(s)d spiral galaxy at a distance of 4.25 Mpc (Tully et al., 2016) with an inclination $i = 48°$ Ryder et al. (1995). NGC 1313 X–1 is located in the northern part of the galaxy, within the inner 46" ($\sim$ 950 pc) radius from the nucleus of NGC 1313, where Ryder et al. (1995) determined the rotational velocity to be 46.5 km/s. This gives a line-of-sight velocity at the source position of $V_{\text{rot}} \sin i \cos\theta \sim 30$ km/s over the systemic velocity, where θ is the azimuth angle in the disk plane as defined by (Ryder et al., 1995) and at the position of NGC 1313 X–1 $\theta = 30°$.

This paper is organised as follows: Section 6.2.2 presents the observations considered and the data reduction. Section 6.2.3 presents our analysis and results of the ULX bubble and the SNRs. In Section 6.2.4 we discuss our results and implications. Finally we present our conclusion in Section 6.2.5.

6.2.2 Data reduction

NGC 1313 X–1 has been observed by MUSE in the Wide Field Mode (WFM) in three instances (PI F.P.A. Vogt) of 1.4 ks exposure time each. Two of these observations were taken in extended mode, which extends the observable bandpass in the blue part of the spectrum down to $\sim$ 465 nm, compared to the nominal mode that reaches only to $\sim$ 480 nm. The data cubes were downloaded from the ESO Science Portal[3], which provides the data reduced by the automatic dedicated pipeline (Weilbacher et al., 2020) and ready for scientific analysis.

After inspection of the cubes, we discarded cube ADP.2019-12-20T09 12 08.117 from the analysis as $\sim$ 92% of the spaxels had negative values, rendering it unusable. We therefore considered only cubes ADP.2019-12-08T00:33:13.185 (cube 1) and ADP.2019-11-29T11:13:19.106 (cube 2) for the analysis (see Table 6.1 for details). We found that both cubes had around 5% of invalid pixels, which we interpolated using the 3×3×3 nearest pixels using the method available in the Zurich Atmosphere Purge (ZAP) tool (Soto et al., 2016).

Cube 1 had slightly better spatial resolution (FWHM PSF $\sim$ 1" vs 1.2") and appeared of overall higher data quality as the sky subtraction had mostly affected the spectrum in the red part above $\sim$ 7000 Å, whereas in cube 2 the sky residuals are also observed around the Hα-[N II] complex. However, because the spatial distribution of the noise in each cube is different and the quality of each of the lines of interest depends strongly on the success of the sky correction, in some cases we could improve the results by combining the information from both cubes (see Section 6.2.3.1). For this reason, we decided to analyse independently both cubes and use them to cross-validate our results, although we mainly present the results from cube 1 for the reasons outlined above. We focused on the main nebular lines used for gas diagnostics covered by MUSE i.e. Hβ, [O III]λ5007, [O I]λ6300, the Hα-[N II] complex and the [S II] doublet. While cube 2 was taken in extended mode, in principle allowing us to measure HeIIλ4686, a relevant emission line in high-excitation nebulae (e.g. Kaaret et al., 2004), edge effects and uncertainties in the flux calibration seemed to be affecting the cube in the blue part of the spectrum below 4700 Å (Figure 6.2), and thus we were unable to use this line in our analysis. The MUSE/WFM pixel scale of 0.2" and the PSF FWHM of $\sim$ 1" represent respectively a physical distance of 4.2 pc and $\sim$ 20 pc at the distance of NGC 1313 X–1 of 4.25 Mpc.

Along with the MUSE observations, we made use of archival *HST* data to correct the astrometry of the MUSE cubes and inspect the field around NGC 1313 X–1. In particular, we retrieved calibrated *HST* images from the Hubble Legacy Archive[4] in the *ACS/WFC/F555W* filter and in the *WFC3/UVIS/F657N* and *WFC3/UVIS/547M* filters. The former filter was chosen as it has substantial overlap with the MUSE wavelength range (Table 6.1), which was required to perform the astrometric correction, whereas the latter filters allowed us to inspect the morphology of the nebular emission with a higher spatial resolution than provided by MUSE, in particular to aid in the identification of the SNRs (Section 6.2.3.2).

Finally, we also retrieved the longest available *Chandra* observation of NGC 1313 X–1 in order to inspect for the presence of nearby X-ray sources (see Section 6.2.3.2) associated with the identified SNRs. We reprocessed these observations using the script `chandra_repro` using CIAO v. 4.12 and CALDB 4.9.3. Table 6.1 provides a summary of all the data used in this work.

The optical counterpart of NGC 1313 X–1 was identified by Yang et al. (2011), which is depicted in the *HST* image in Figure 6.3. To identify the position of the counterpart in the MUSE cube, we used the *HST* image taken in the ACS/F555W filter to correct the astrometry of the cube and register it to the *HST* coordinates (Figure 6.3 left). To do so, we used the `python` package `mpdaf` (Piqueras et al., 2017) to integrate the MUSE cube in

---

[3] http://archive.eso.org/scienceportal/home

[4] https://hla.stsci.edu/

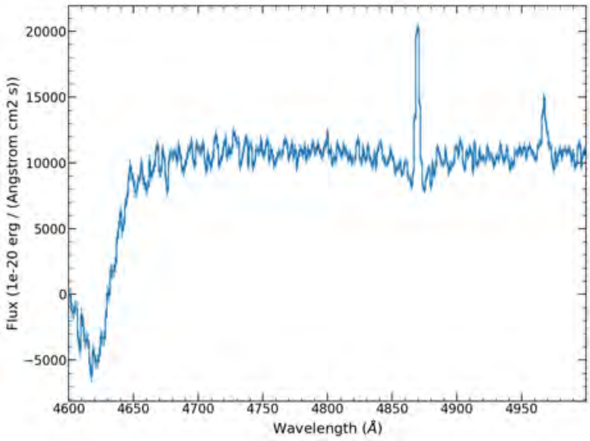

Figure 6.2: Spectrum extracted from a pixel of cube id ADP.2019-11-29T11:13:19.106 strongly affected by flux miscalibration effects at the blue edge of the wavelength range.

Table 6.1: Log of the observations used in this work.

Telescope	Detector	Obs id	Date	Band	Exposure ks
Chandra	ACIS-S	2950	2002-10-13	0.3–10 keV	19.9
HST	ACS/WFC/F555W	hst_9796_01_acs_wfc_f555w	2003-11-17	4777–6017 Å	1.16
HST	WFC3/UVIS/F657N	hst_13773_15_wfc3_uvis_f657n	2015-02-24	6503–6628	1.5
HST	WFC3/UVIS/F547M	hst_13773_15_wfc3_uvis_f547m	2015-02-24	5108–5821	0.55
VLT	MUSE	ADP.2019-12-08T00:33:13.185	2019-10-17	4750-9350 Å	1.4
VLT	MUSE	ADP.2019-11-29T11:13:19.106	2019-10-16	4600–9350 Å	1.4

wavelength space, weighting each wavelength by the ACS/F555W filter throughput in order to generate a MUSE image in the F555W filter (central wavelength of 5360 Å with a bandwidth of 360 Å). Then, we used the task `adjust_coordinates` from the same package, to run an autocorrelation function between the F555W MUSE and the *HST* images. The maximum of the autocorrelation function was used to shift the cube coordinates relative to the *HST* image and register its coordinates to this reference image. The resulting alignment is shown in Figure 6.3 and showed excellent agreement with the *HST* image. We considered the uncertainty on the position of the counterpart in the cube to be the nominal *HST* PSF added in quadrature to the pixel scale of MUSE (0.2"). We fit a 2D Gaussian profile to the optical counterpart in the *HST* image to determine the PSF FWHM = 0.110±0.003". Thus the 3σ uncertainty of the position of the optical counterpart in the MUSE cube was found to be ∼0.61". We note that the counterpart was not clearly detected in this MUSE image (but see Section 6.2.3.7).

6.2.3 Data analysis and results

6.2.3.1 Line maps

In order to derive physical quantities from the main nebular lines, we used the publicly available code CAMEL[5] which is described in Epinat et al. (2012). CAMEL performs pixel by pixel Gaussian line fitting to derive flux and kinematic maps for each fitted line. We enhanced the signal to noise ratio (S/N) of the faint lines in the cubes by applying a 2D spatial Gaussian smoothing with FWHM = 2 pixels, as the spatial resolution of the cube (PSF FWHM ∼ 1") was well above the pixel scale of MUSE (0.2"). A single Gaussian component was chosen to fit the lines and CAMEL was run in five independent spectral cuts so the continuum could be easily modelled with a one degree polynomial in each cut. The only exception to this was the Hβ line that presented some Balmer absorption (see the dipping structure around the Hβ in Figure 6.2) that we took into account using a Gaussian absorption line together with a zero-degree polynomial to model the continuum. We found that the relative differences in Hβ flux between the approach where the continuum was modelled with a one degree polynomial and the approach taking into account the Balmer absorption were 1–50% (10% and 90% percentiles) with a median value of ∼ 10%. Cuts in the spectral space were performed around the Hβ line, both [O III] lines, the [O I]λ6300 line, the [N II]-Hα complex and finally one for the [S II] doublet. In each case we assumed the same line width for each pair of forbidden lines and same line-of-sight velocity for the whole set of lines fitted in each cut.

The dispersion maps were corrected for instrumental broadening by subtracting the instrumental line spread function (LSF) FWHM in quadrature. In order to estimate the LSF FWHM, we computed the median and

---

[5] `https://gitlab.lam.fr/bepinat/CAMEL`

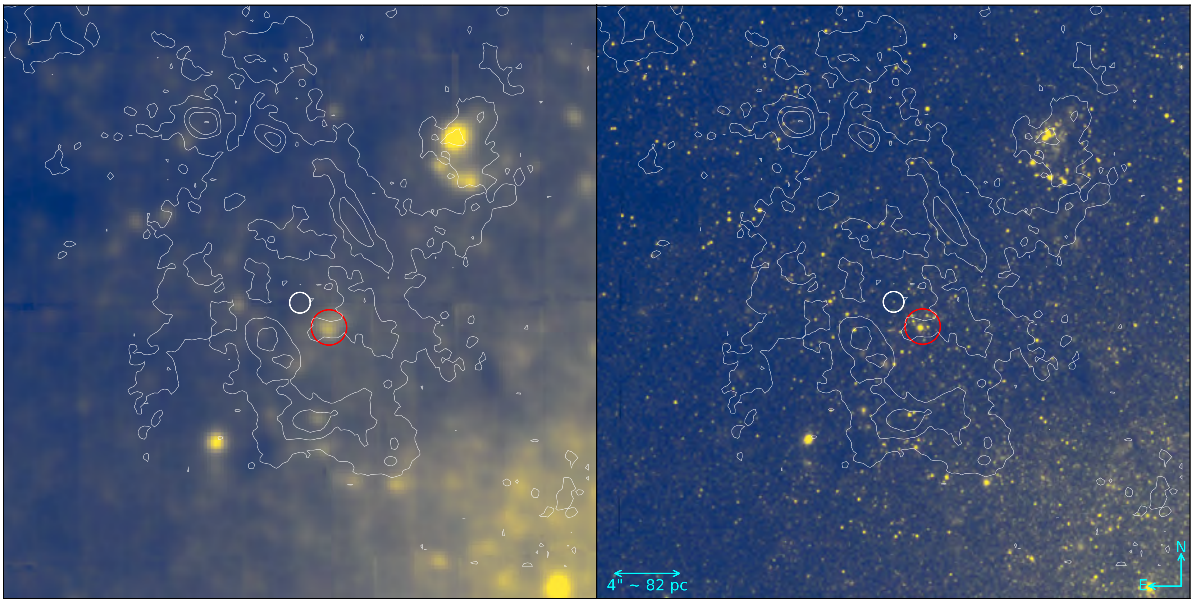

Figure 6.3: (left) MUSE image in the HST/ACS/F555W bandwidth after alignment with the *HST* image in the F555W filter (right). The white circle has 0.61" in radius and shows the 3σ uncertainty on the position of the ULX NGC 1313 X–1 in the MUSE cube. The red circle indicates a bright star of a young cluster of massive stars (Ryon et al., 2017) to aid the comparison between the images. The contours show the flux of the [O I]λ6300 line (see Figure 6.6). (right) *HST*/ACS image in the F555W filter. The same white circle as for the right panel is shown, showing the position of the optical counterpart of NGC 1313 X–1, which was determined by Yang et al. (2011). Both images have the same orientation and show a region of 30"×30".

the standard deviation of the 10% bottom percentile FWHM of the dispersion maps produced by CAMEL for all the lines we measured. We additionally included the sky line at [O I]λ6300 which was present throughout the spatial extent of the cube at its rest-frame wavelength. We only considered lines with a S/N $>$ 5 to avoid introducing noise in the calculation. Table 6.2 reports the determined FWHM for the different lines along with the number of pixels from the dispersion map used in the calculation whereas Figure 6.4 shows a comparison with the parametrisation from Bacon et al. (2017) (see their Equations 7 and 8) for cube 1. The results for cube 2 were similar and we do not report them for brevity.

The discrepancy found in the Hβ line might be due to the stellar absorption around this wavelength, affecting the estimation of its FWHM. The discrepancy between the other lines FWHM and the parametrisation of Bacon et al. (2017) is unclear. The parametrisation from Bacon et al. (2017) was derived by fitting the sky lines from a combined cube composed of 25 minute exposures totalling 10–37h with a specific observation pattern, where the field was rotated by 90° between exposures, an observing strategy far more complex than our single exposure data cubes. It is possible that the recipe derived by Bacon et al. (2017) might not be suited for our more simplistic case. We decided to focus only the FWHM of the [N II]-Hα and [S II] lines, which showed good agreement with the parametrisation proposed by Bacon et al. (2017). We corrected the observed FWHM using our own estimation of the LSF FWHM, although the results are unchanged if instead we used the values obtained from Bacon et al. (2017).

The resulting line-of-sight and dispersion maps were more severely affected by the invalid pixels and noise present in the cubes in comparison with the flux maps. We therefore decided to use the information from cube 2 to improve them. As stated in Section 6.2.2, because the spatial distribution of the noise is unique to each cube, we found that we could improve the S/N of these maps by averaging the information obtained from cube 1 and cube 2. For the velocity maps, we further noted that the [N II]-Hα and [S II] were consistent with each other, both spatially and numerically (the median and the standard deviation of the velocity differences between the two maps were –0.09±5 km/s). We therefore decided to combine the information from the [N II]-Hα and [S II] maps from cube 1 and cube 2, in order to create an average map of these lines. The [O III] and [O I]λ6300 maps were also produced by averaging cubes 1 and 2. We similarly averaged the maps from the Hα, [S II]λ6716 and [N II]λ6583 lines for the dispersion maps to obtain a smoother map, as the maps showed again good consistency between them (the median and standard deviation of the differences between the Hα and [S II]λ6716 maps were 13±12 km/s, with same values found for the differences between the Hα and [N II]λ6583 maps). In this case we did not use the information from cube 2 as it was considerably affected by noise, not providing any significant improvement.

The resulting maps for the line flux, dispersion and line-of-sight velocity are shown in Figures 6.6, 6.7 and

Table 6.2: Results from the instrumental LSF FWHM estimation (see text for details). For the forbidden doublets only one line is shown as the same FWHM value was assumed.

Line	FWHM[a] Å	N[b]
Hβ	2.1±0.5	2289
[O I]λ6300[†]	2.20±0.08	2880
[O I]λ6300	2.05±0.09	2734
[O III]λ5007	2.5±0.2	3101
Hα	2.55±0.06	3276
[N II]λ6583	2.4±0.1	3276
[S II]λ6716	2.54±0.08	3276

Notes. (a) Average and standard deviation of the pixels used. (b) Number of pixels from the dispersion map used. (†) Sky line

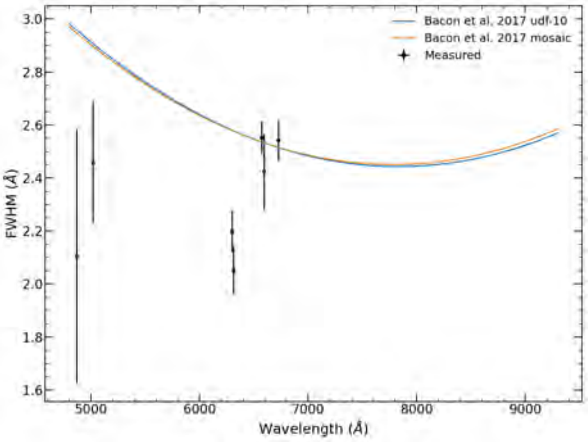

Figure 6.4: Estimated FWHM (see text for details) compared to the parametrization of Bacon et al. (2017). The FWHM estimated from the data cube does not show a good agreement with the parametrization of Bacon et al. (2017) towards the blue part of the spectrum.

Table 6.3: Observed fluxes of the different nebular lines relative to Hβ, integrated in each of the regions highlighted in the right panel of Figure 6.7. Uncertainties are given at the 1σ level by adding the uncertainty on each pixel in quadrature.

Line	SNR 1	SNR 2	Region 3	Region 4	Region 5	Region 6	Region 7	Bubble
Hβ (10^{-15} ergs s^{-1} cm^{-2})	1.5±0.1	0.95±0.08	2.1±0.1	3.2±0.2	2.4±0.1	2.2±0.1	1.7±0.1	24.1±0.4
[O III]λ4959	0.698±0.002	0.713±0.003	0.500±0.002	0.589±0.001	0.707±0.002	0.386±0.002	0.470±0.002	0.550±0.001
[OIII]λ5007	2.175±0.010	2.156±0.011	1.543±0.007	1.799±0.006	2.143±0.008	1.154±0.006	1.449±0.008	1.674±0.002
[O I]λ6300	0.414±0.002	0.433±0.002	0.455±0.001	0.474±0.001	0.722±0.002	0.770±0.002	0.417±0.002	0.496±0.001
[N II]λ6548	0.191±0.001	0.192±0.001	0.207±0.001	0.232±0.001	0.276±0.001	0.252±0.001	0.220±0.001	0.227±0.001
Hα	3.614±0.005	3.718±0.004	3.490±0.002	3.688±0.002	3.555±0.002	3.741±0.002	3.687±0.003	3.580±0.001
[N II]λ6583	0.610±0.006	0.610±0.005	0.646±0.003	0.732±0.003	0.850±0.004	0.794±0.003	0.691±0.004	0.711±0.001
[S II]λ6716	1.304±0.003	1.284±0.004	1.374±0.002	1.387±0.002	1.522±0.002	1.804±0.002	1.305±0.003	1.388±0.001
[S II]λ6731	0.954±0.002	0.920±0.002	0.962±0.001	0.976±0.001	1.079±0.001	1.263±0.001	0.924±0.001	0.980±0.001

6.8 for some of the nebular lines with best S/N. Pixels with a line detection S/N below 5 have been masked. Figure 6.5 shows a composite image of the Hα, [O III]λ5007 and [S II]λ6716 lines. For the line-of-sight velocity maps, we subtracted the median value measured from the map after excluding the central parts of the bubble in order to reflect more closely local velocities. This value was found to be 25 km/s, which is in good agreement with the estimated 30 km/s based on the measurements from Ryder et al. (1995) in Section 6.2.1.

The right panel of Figure 6.7 shows some regions of interest which will be discussed throughout the paper and in particular in Sections 6.2.3.5 and 6.2.4.1. These were obtained by fitting 2D Gaussian ellipsoidal profiles to the [O I]λ6300 flux map, except for SNR 1 for which we used the Hα map instead (see Section 6.2.3.4) and a circular Gaussian given its apparently symmetric profile. The radii of the regions were set equal to their respective FWHMs obtained, with the exception of regions 5, 6 and 7. For the former two we reduced the sizes obtained to avoid overlapping between them, whereas region 7 was simply determined visually. Integrated fluxes of these regions and the bubble are quoted in Table 6.3 while sizes are given in Table 6.5. The two bright [S II] and [O I]λ6300 northernmost blobs are likely two SNRs coincidentally close to the ULX bubble as we explain below in Section 6.2.3.2. We describe first the regions concerning the interaction of the ULX with the interstellar medium (ISM).

The Hα, [O I]λ6300 and [S II]λ6716 flux maps clearly reveal an elongated bubble in the south-west north-east direction, of 452 × 266 pc in size (highlighted in the right panel of Figure 6.7 in cyan). The ULX is roughly at 1.2" from the centre of the ellipsoidal shape marked by the bright [O I]λ6300 regions, corresponding to a physical distance of 25 pc.

Figure 6.7 shows that the lines are broadened just inside the edges marked by the [O I]λ6300 and [S II]λ6716 flux maps (see particularly the strong broadening FWHM $\sim$ 100 km/s towards the south near region 6, north east near region 3 and east to the NGC 1313 X–1 near region 5). This is a telltale that the gas is being shocked in these regions and defines the limit of the interaction of the ULX with the surrounding medium. The maximum FWHM measured in these regions (3, 4, 5, 6 and 7) were in the 90–130 km/s range (Table 6.5 gives the maximum FWHM values measured in each of the regions of interest). Instead, the [O III]λ5007 flux map shows slightly different morphology, with a brighter region just south of the ULX position, also clearly visible in Figure 6.5 as a blue-ish blob.

The line-of-sight velocity (V_{los}) fields (Figures 6.8) show a structure roughly contained inside the [O I]λ6300 contours, with V_{los} about 30–40 km/s higher than those of the surrounding gas, indicating that the gas inside the bubble is being dynamically perturbed by the ULX via outflows. This is clearly seen in the combined [N II]-Hα and [S II] and [O III]λ5007 V_{los} fields. This is illustrated more clearly in Figure 6.9, which is a close-up of the two maps around the ULX position. Note also the distinct structure of the two maps, which suggests that the [O III]λ5007 map is tracing different gas compared to the combined Hα[N II][S II] map. The combined [N II]-Hα and [S II] velocity fields show peak velocities of $\sim$ 20 km/s whereas the surrounding gas shows slower velocities reaching at most $\sim$ 0 km/s with a typical 1σ uncertainty of $\sim$ 1 km/s. The [O III]λ5007 shows higher velocities reaching up to $\sim$ 35 km/s whereas the gas in the outer regions of the bubble has velocities of at most $\sim$ 5 km/s. The typical 1σ uncertainty of the maps of the individual cubes here is slightly higher of $\sim$ 4 km/s. The [O I]λ6300 map shows somewhat similar structure to the Hα[N II][S II] maps, with two distinct regions north and south from the ULX, albeit the level of noise is considerably higher.

Finally we note that the dispersion map in the [O I]λ6300 line reveals some strong broadening (uncorrected FWHM $\gtrsim$ 200 km/s) at the position of NGC 1313 X–1 (see Figure 6.18). We note that as stated in Section 6.2.2 the exact value of the instrumental-corrected FWHM is uncertain. Nevertheless, because this broadening is coincident with the source position, we used it in Section 6.2.3.7 to extract a spectrum of the optical counterpart.

6.2.3.2 Supernova remnants in disguise

Figures 6.5 and 6.6 reveal two compact spots bright in the [S II] and [O I]λ6300 lines, located north of the ULX (marked as SNR 1 and SNR 2 in the right panel of Figure 6.7). These are at $\sim$ 12" and 9.8" from the ULX position, corresponding to a physical distance of $\sim$ 250 pc and 200 pc respectively. Here we find intrinsic FWHM

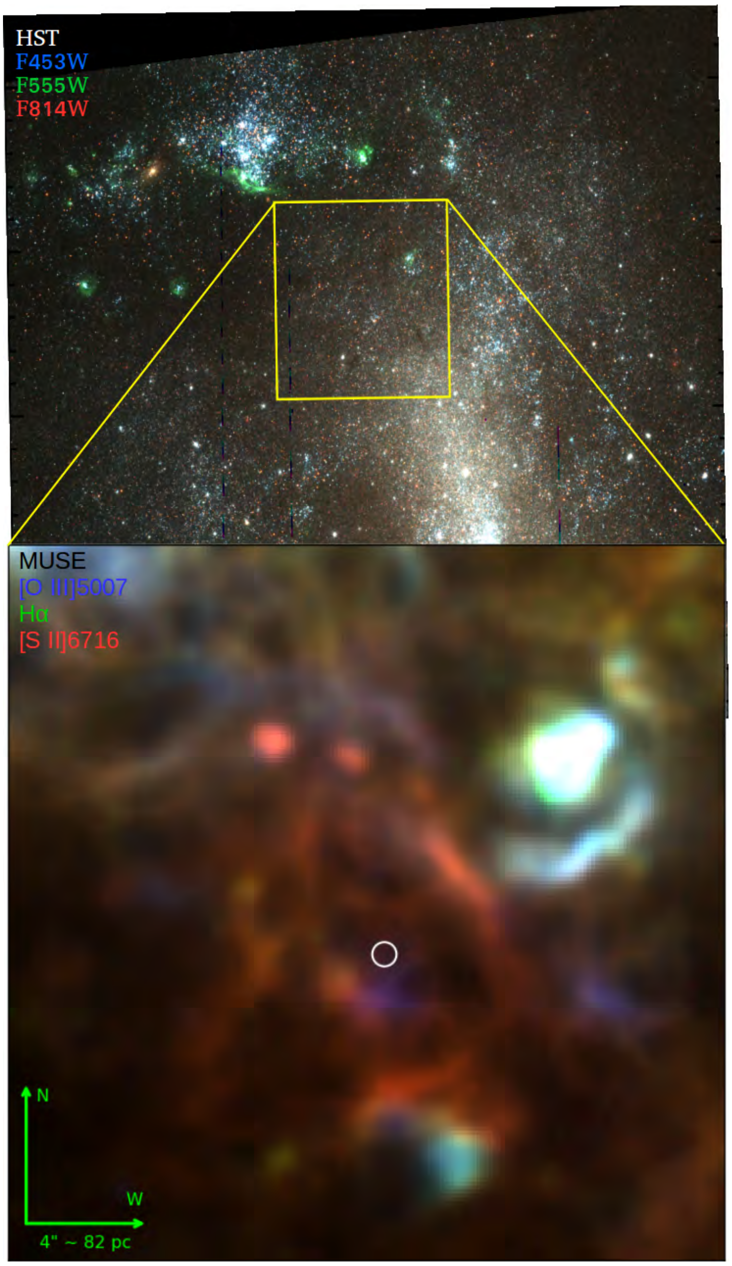

Figure 6.5: (Top) Composite *HST* image showing F435W (Blue), F555W (Green) and F814W (red) ACS/WFC images downloaded from the HLA archive (obsid hst_9796_01_acs_wfc_f814w_f555w_f435w). The yellow square shows the region shown in the MUSE image in the bottom panel. (Bottom) MUSE RGB image of the nebula around NGC 1313 X–1 corresponding to the yellow square in the *HST* image, showing fluxes in Hα (green channel), [O III]λ5007 (blue channel) and [S II]λ6717 (red channel) lines.

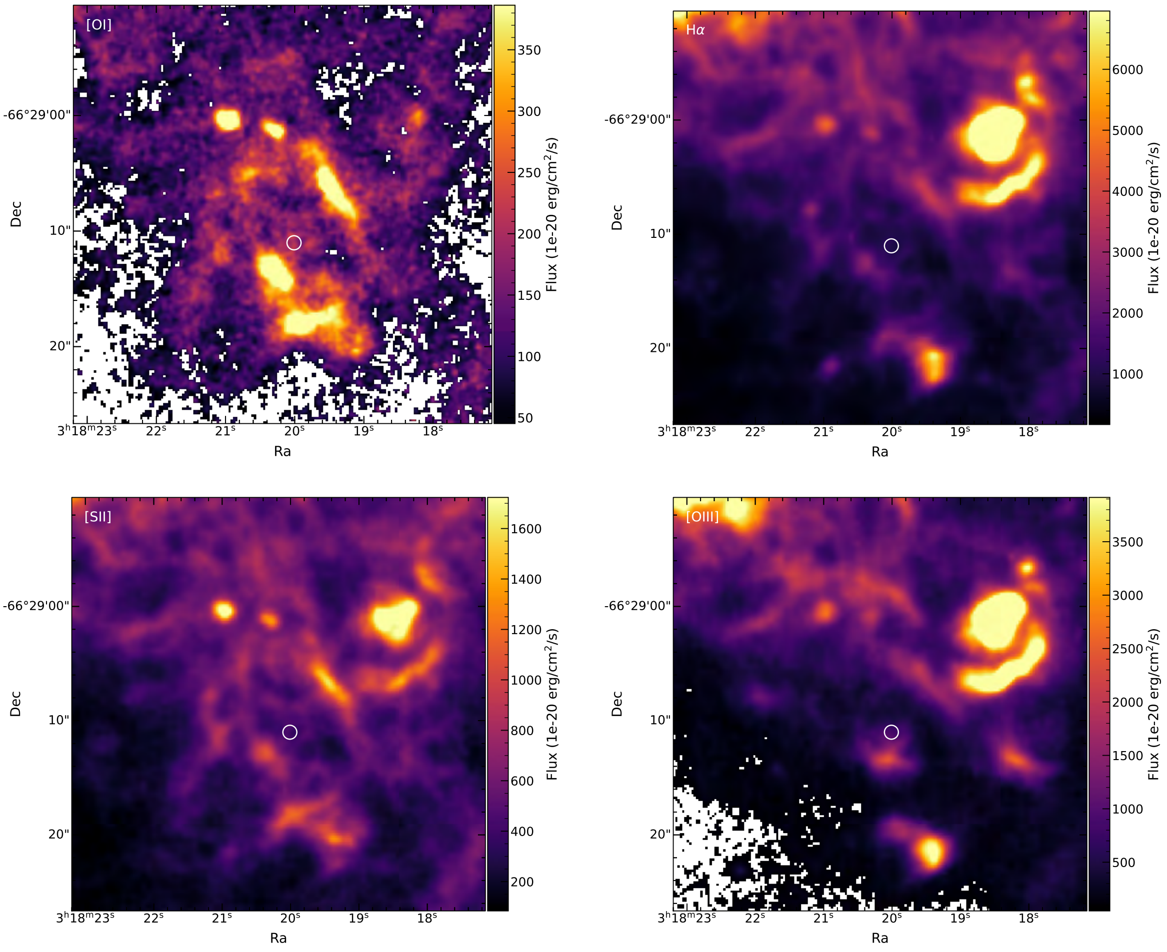

Figure 6.6: Flux maps for [O I]λ6300 (top left), Hα (top right), [S II]λ6716 (bottom left) and [O III]λ5007 (bottom right). The small white circle indicates the position of NGC 1313 X–1and its uncertainty (see text for details). The scale and direction is the same as in Figure 6.5.

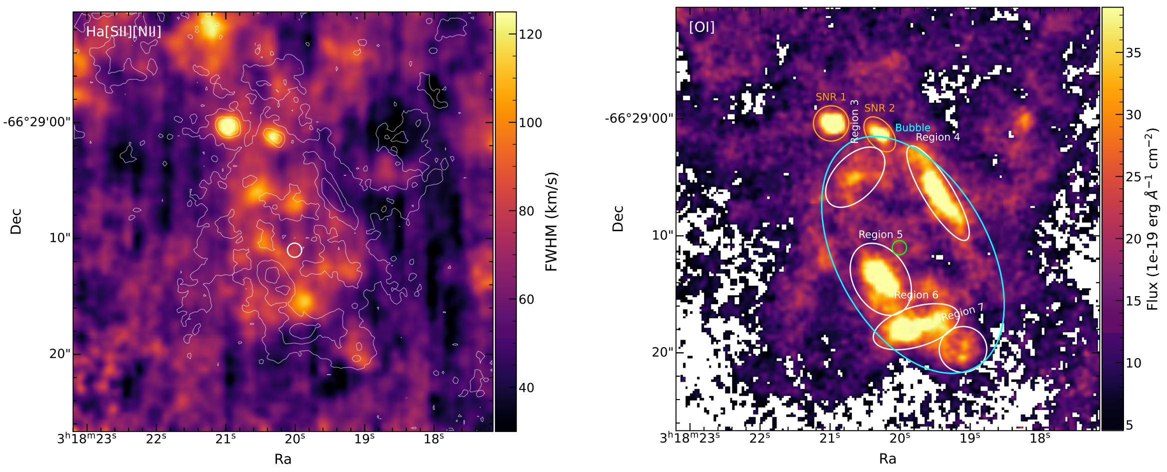

Figure 6.7: (left) Dispersion map of the average of the Hα, [N II]λ6853 and [S II]λ6716 lines, corrected for instrumental broadening. Contours as per Figure 6.3. The map has been smoothed with a Gaussian kernel with $\sigma = 1.5$ pixels. (right) [O I]λ6300 flux map showing some regions discussed throughout the paper, the ULX bubble (cyan) and the coincidentally close SNRs (orange). The position of the ULX is indicated with a green circle.

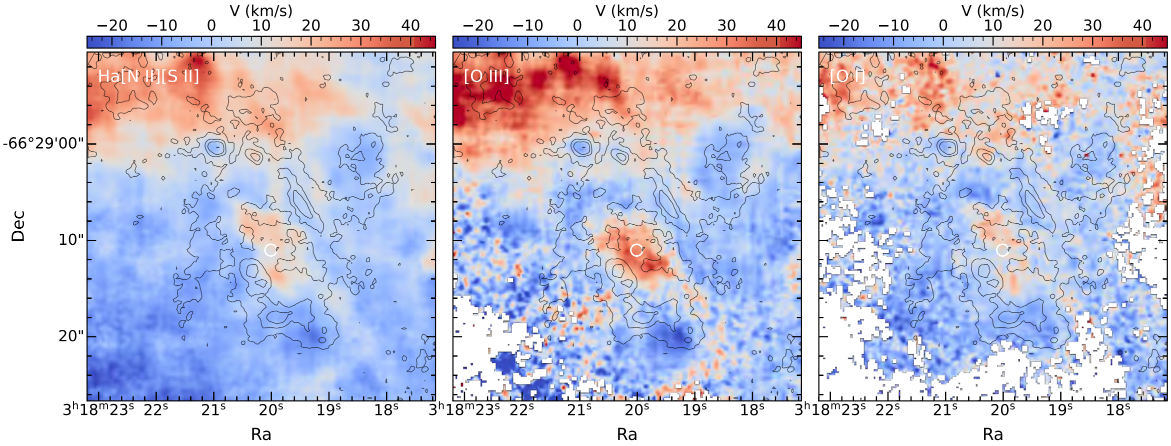

Figure 6.8: Line-of-sight velocity maps over the system velocity of NGC 1313 ($\sim$ 470 km/s) for the combined [N II]-Hα and [S II] lines (left), [O III] (middle) and [O I]λ6300 (right). We have subtracted an offset of 25 km/s (the median value estimated from the whole map after excluding the central bubble) to reflect more closely the local velocities, which is in good agreement with the 30 km/s estimated at the position of NGC 1313 X–1 based on the values given by Ryder et al. (1995) (see the Introduction). The scale is the same in all panels and the contours are as per Figure 6.7.

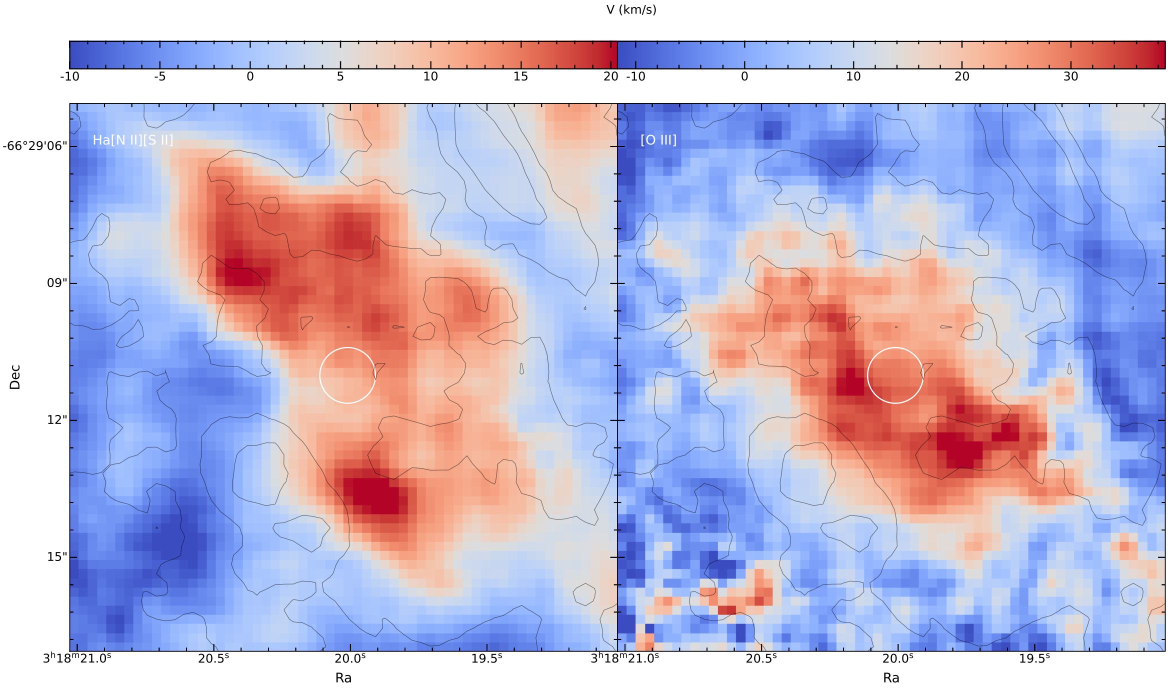

Figure 6.9: Close-up view of the velocity maps for the Hα[N II][S II] (left) and [O III] maps (right). Note the difference in scale between the two maps. The position of the ULX is indicated with a white circle. Contours as per Figure 6.8.

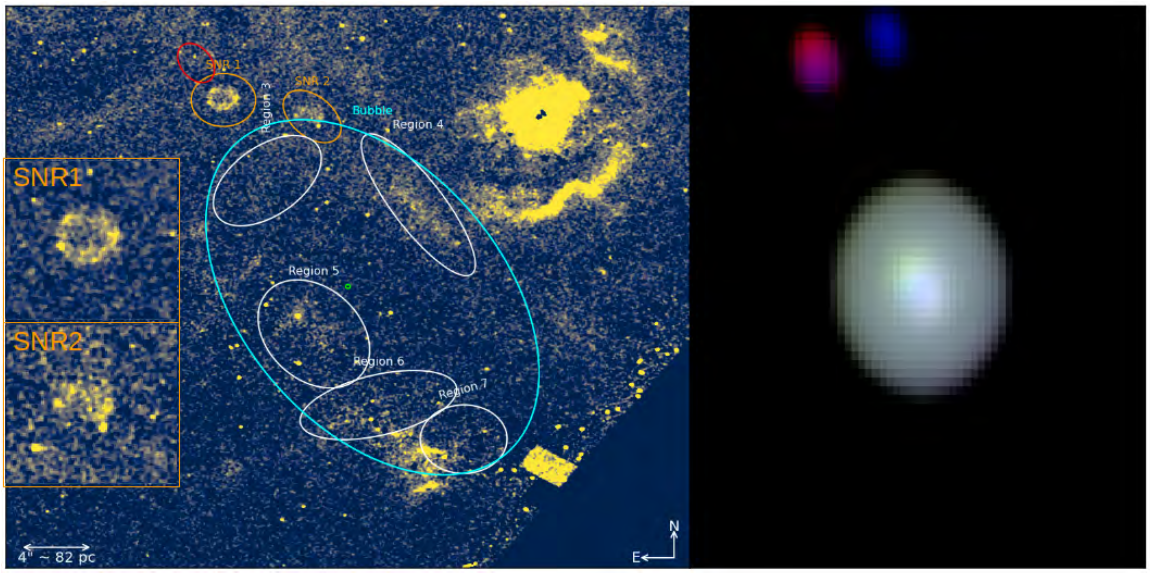

Figure 6.10: (left) *HST* continuum-subtracted WFC3/UVIS/F657N (Hα + [N II]) image of the field around NGC 1313 X–1 (green circle). The WFC3/UVIS/F547M image was used for the continuum approximation. The red ellipse shows the 3σ contour confidence level of the easternmost source with red-ish colours in the *Chandra* image. The same regions from Figure 6.7 are also shown and the insets show close-up looks of the two SNRs as indicated. (right) R,G,B = 0.5–1.2 keV, 1.2–2 keV, 2–7 keV *Chandra* showing the same field. Both images show a of 32"×32" field centred around the ULX and have been smoothed with 2-pixel Gaussian kernel.

values reaching up to $\sim$ 166 km/s in the combined Hα, [N II] and [S II] dispersion map[6], the highest values in the whole nebula. The broadening and the strong [S II] and [O I]λ6300 lines implies that the gas is also being shocked in these regions. However, its association with the ULX is unclear as its distance is extreme even for ULX standards (cf. 150 pc from S26 NGC 7793; Pakull et al., 2010) whereas its round morphology (notably for SNR 1) argues against a jet or wind excitation, for which we would likely expect an arc-shaped structure instead (cf. Regions 3 and 7). A face-on view could still make such arc-shape appear circular, but considering its already large projected distance this is highly unlikely. Recently, these regions have been identified as SNRs by Kopsacheili et al. (2021), based on their [S II]/Hα> 0.4 ratios, a common diagnostic used to identify SNRs. However, most of the gas inside the bubble also shows [S II]/Hα> 0.4 (see Section 6.2.3.3) and in fact many ULX bubbles were initially misclassified as SNRs based on this diagnostic (e.g. Matonick & Fesen, 1997). In this regard, Urquhart et al. (2019) offers an interesting historical discussion on the early identification of several ULX bubbles as SNRs to which we refer the interested reader. For this reason we decided to investigate the nature of these regions to assess whether they were related to the ULX activity. Here we show that their identification as SNRs is nonetheless likely to be robust, based on a more detailed imaging and spectral analysis.

In order to inspect the morphology of the diffuse emission of these regions in more detail, we retrieved a *WFC3/UVIS/F657N* (which isolates the Hα + [N II] lines) image from the HLA archive, together with a *WFC3/UVIS/F547M* image for the continuum subtraction. The details of these observations are reported in Table 6.1. In order to isolate more precisely the Hα + [N II] emission, we subtracted the continuum emission as measured from the F547M image. More specifically, we took into account the different filters bandwidth by measuring the ratio between the intensities in these two images in four different circular regions of 4–5" containing stars and no obvious diffuse emission. The median of these ratios was used as a rescale factor to the continuum image before subtracting it from the narrow-band image (prior to this, the images were aligned as explained below). The subtracted image (Figure 6.10) shows that the emission from SNR 1 is rather spherical, with an angular radius of $\sim$0.85" (17.5 pc), confirming what had been hinted from the MUSE Hα image and strongly supporting its identification as a SNR (Kopsacheili et al., 2021). Based on the morphology alone, the situation might be less clear for SNR 2 due to the low S/N of the diffuse emission, but its shape might also be suggestive of a SNR. Note also the brighter emission from these two regions compared to the rest of the nebula.

We also present spectra of the two SNRs averaged over each of the regions respectively. These are shown in Figure 6.11 along with the average spectrum from region 4 for comparison. The resemblance between the two SNR spectra and the presence of several emission lines typically seen in SNRs (Fesen & Hurford, 1996) strengthens the association of the SNR 2 as a SNR. A detailed analysis of these spectra is beyond the scope of the present paper but based on the similarity between SNR 1 and SNR 2, we believe there is enough evidence to support

---

[6] The colour scale of the Figure does not reflect such high values owing to the chosen scaling, which is meant to aid the visualization of the other areas.

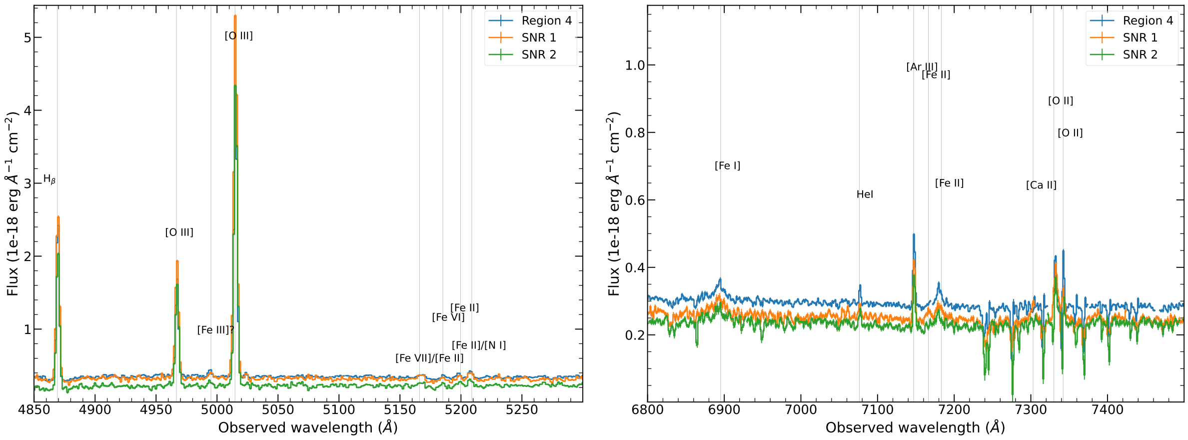

Figure 6.11: Average spectra extracted from regions SNR 1, SNR 2 and region 4 in Figure 6.7 showing the spectral bands between 4850–5300 Å (left) and 6800–7500 Å (right). The thin vertical lines show expected transitions at the redshift of NGC 1313 based on the line catalog from Fesen & Hurford (1996). The spectra have been smoothed with a Gaussian kernel of 2.5 Å. Small gaps mask some pixels having negative values due to low S/N.

the classification of SNR 2 as a SNR. Even if this is not the case, we note that our main conclusions remain unaffected. These spectra also illustrate the well-known difficulty in distinguishing ULX bubbles from SNRs (e.g. Pakull & Grisé, 2008), and provide further evidence for region 4 as being excited by shocks.

For completeness, we also decided to inspect the *Chandra* images for any evidence of associated X-ray emission which could strengthen their classification as SNRs. To this end, we used archival obsid 2950 as it had the longest exposure time and the smallest PSF distortion around the ULX, owing to its off-axis angle of 2.317', compared to 6.884' for the other two available observations in the archives (obsids 3550 and 3551). The details of this observation is also reported in Table 6.1.

To precisely align the optical and X-ray images to a common reference frame, we matched the sources detected in both wavelengths to the *Gaia* DR2 source catalogue (Gaia Collaboration et al., 2018). For the three *HST* images (F555W, F547M and F657N filters), we used the tool `tweakreg` from the `astrodrizzle` package[7], which allows to perform both source detection and cross-matching. We tested different set of parameters and decided to use a detection threshold of 75σ as well as to restrict the number of sources used in the matching stage to the 846 brightest sources (set to twice the amount of *Gaia* sources in the F555W field of view). This was in order to restrict the matching stage to the brighter sources more readily detected by *Gaia*. After cross-matching each of the images, we allowed the task to subsequently incorporate the new sources (not included in the original reference *Gaia* catalog) detected in the previous images to build a larger reference catalog for the next image. Owing to its larger field of view the F555W image was used first, followed by the F547M image and lastly the F657N due its narrower filter. We found 85, 33 and 307 matches for the F555W, F547M and F657N filters respectively, resulting in rms residuals all below 0.007".

For the *Chandra* images, we used the `ciao` task `wavdetect` on the 0.5–7 keV band for source detection. A faint ($\sim$ 13 net counts) source north-east of the ULX is detected[8] (Figure 6.10), with a 1σ statistical uncertainty on the position of δ R.A. = 0.36" and δ DEC = 0.19". To examine whether this source could be the X-ray counterpart of SNR 1, we used the task `wcsmatch` with an initial search radius of 4" to match the X-ray sources to the *Gaia* catalog. After an initial transformation, an iterative process discards all matches with a radii above a certain value and re-updates the solution until no more matches are discarded. We visually inspected the resulting matches obtained for different radii and settled for a value of 0.6". This resulted in five matches: two background AGNs, two foreground stars (one used in the work of Yang et al. (2011) for this same correction) and the supernova remnant SN1978K (e.g. Kuncarayakti et al., 2016). The rms residuals were 0.16". Adding all the uncertainties in quadrature the final 3σ uncertainty on the position of the source is δ R.A. = 1.2" and δ DEC = 0.8". Based on the 3σ confidence contour depicted in Figure 6.10, we rule out the association of the X-ray emission with SNR 1.

6.2.3.3 BPT diagrams

In order to study the physical conditions of the gas around NGC 1313 X–1, we exploited MUSE access to the main nebular lines to derive spatially-resolved [O III]λ5007/Hβ vs [N II]/Hα, [O III]λ5007/Hβ vs [S II]/Hα and [O III]λ5007/Hβ vs [O I]/Hα Baldwin–Phillips–Terlevich (BPT) diagrams (Baldwin et al., 1981; Veilleux & Osterbrock, 1987). These diagrams use the flux ratios of the Balmer lines to the forbidden lines to distinguish regions of gas ionised by stars (HII regions) from regions ionised by hard X-ray emission and/or shocks (AGN

---

[7] https://drizzlepac.readthedocs.io/en/latest/index.html

[8] This source is CXOU J031821.2–662858 in the work of Mineo et al. (2012), identified as a high-mass X-ray binary.

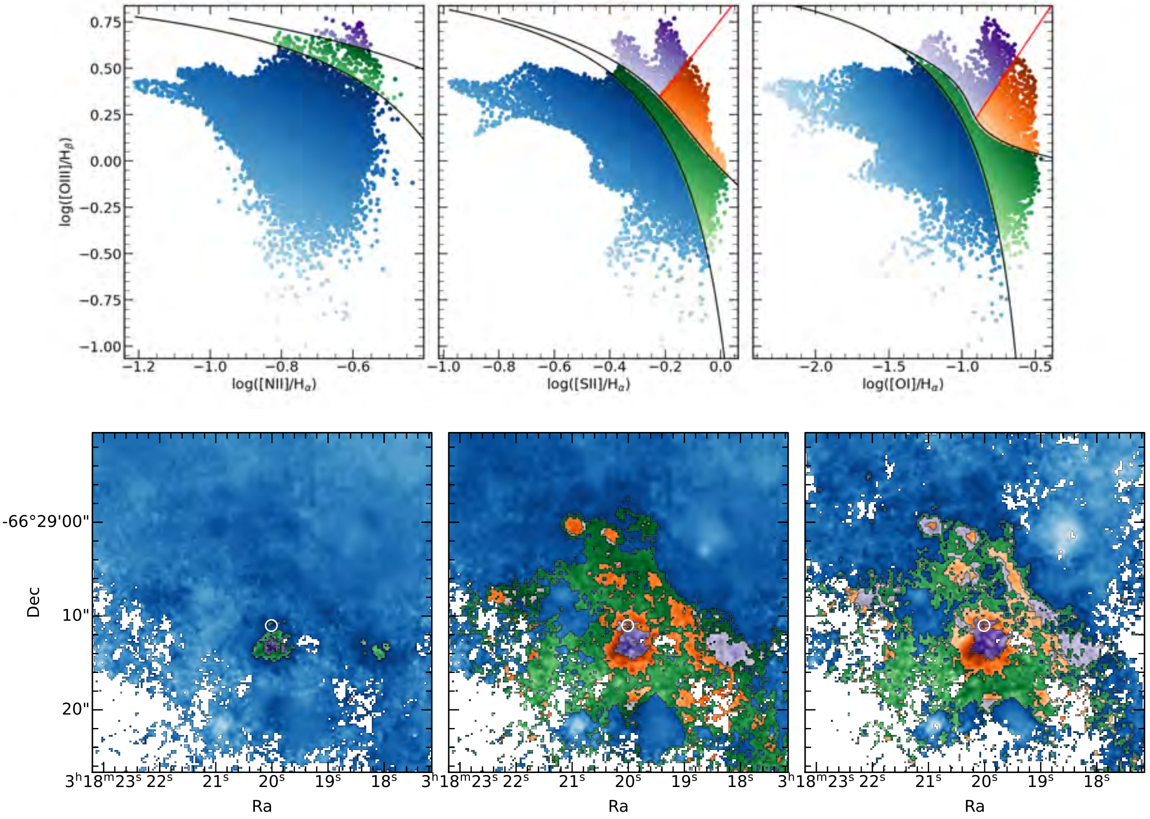

Figure 6.12: (Top) Spatially resolved BPT diagrams derived using the classification proposed by Law et al. (2021). Regions classified as HII, intermediate, AGN and LINER are shown in blue, green, purple and orange colours respectively. Each pixel has been colour coded proportionally to the sum of the x and y values in each BPT diagram to aid the visualization and localisation of each pixel in the bottom panel. (Bottom) The region around the ULX has been colour coded according to the upper diagrams, to show the spatial distribution of AGN, LINER, intermediate and HII regions. The colour coding is the same as in the upper panels.

regions and LINER). To classify the regions based on these line ratios, a theoretical and empirical classification scheme has been commonly used based on the works of Kewley et al. (2001); Kauffmann et al. (2003); Kewley et al. (2006). For instance, Kewley et al. (2001) derived the theoretical maximum ratios expected from regions photoionised solely by stars, using photoionisation and stellar synthesis population codes. This line is termed the maximum starburst line and it is used to differentiate between HII regions from intermediate regions (where hard X-ray radiation and/or shocks start to contribute) and/or AGN-dominated regions (mainly ionised by shocks and/or hard X-ray radiation). However, these early works were based purely on line ratios of integrated spectra of galaxies, resulting in mixing of various components. By using IFU data from the MaNGA galaxy survey, Law et al. (2021) recently refined these classification schemes by combining spatially resolved line ratios and the kinematic information provided by the dispersion along the line of sight of the Hα line. This classification results in a cleaner separation between the different components compared to early works and we therefore made use of it to derive the BPT diagrams shown in Figure 6.12. We note also that these diagrams are essentially independent of the exact reddening correction, since the lines ratios employed are sufficiently close in wavelength such that the correction can be safely ignored.

The diagrams clearly highlight that most of the pixels around the ULX are classified as AGN/LINER or intermediate, indicating that the ULX is contributing heavily to the ionisation budget of the surrounding environment. The [N II]/Hα BPT diagram is more sensitive to metallicity. For this reason, at low oxygen abundances ($\log(\mathrm{O/H}) + 12 \lesssim 8.4$), AGN regions become difficult to distinguish from classical HII regions, mostly owing to the dependency of the [N II]λ6583/Hα ratio with metallicity (Kewley et al., 2013). We show in Section 6.2.3.6 that the metallicity around NGC 1313 X–1 is $\log(\mathrm{O/H}) + 12 \approx 8.1$–$8.4$. This likely explains why many of the regions classified as AGN/LINER in the other two BPT diagrams are found in the HII/intermediate region in the [N II]λ6583/Hα diagram. Nevertheless, this diagram is useful because the pixels classified as AGN likely trace the hard EUV/X-ray radiation from the source, as the hardness of the ionisation field tends to increase the [O III]λ5007/Hβ ratio (Kewley et al., 2013), given the high ionisation potential needed to doubly ionize oxygen.

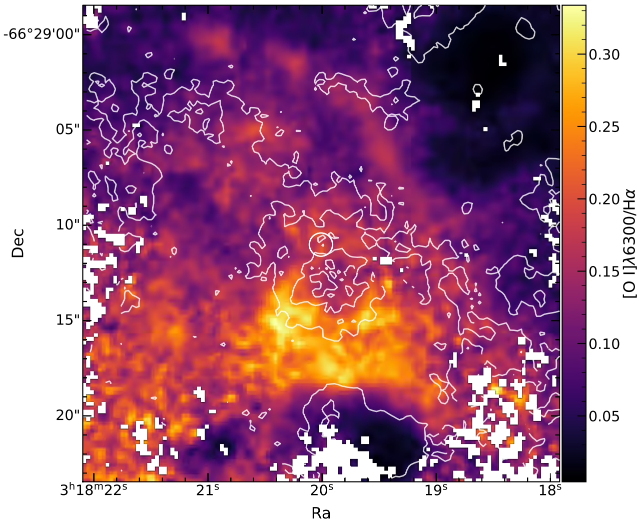

Figure 6.13: [O I]λ6300/Hα map with the [O III]λ5007/Hβ contours overlaid in white showing a region of 25"×25" around the ULX (white circle). Extended emission with high [O I]λ6300/Hα ratios is seen south to the peak of the [O III]λ5007/Hβ indicating X-ray excitation.

Thus essentially the [N II]λ6583/Hα BPT diagram offers a map of the regions strongly excited by EUV/X-rays from the ULX.

The other two diagrams show a central roughly circular region slightly offset to the south from the position of NGC 1313 X–1, where the gas is classified as AGN and LINER. This classification is also observed in regions SNR 1 and SNR 2. Comparison of these diagrams with the kinematic data and the [O I]λ6300 and [S II]λ6716 flux maps (see Section 6.2.3.1) suggest that lightly coloured regions found at the boundary of the AGN regions and LINER mostly highlight regions excited by shocks. To further illustrate this point, we show the [O I]λ6300/Hα BPT diagram coloured based on the FWHM values from Figure 6.7 in Figure 6.14, whereas in Figure 6.21 from the Appendix the same result is shown, but for each of the regions highlighted in the right panel of Figure 6.7. We can clearly see that pixels with largest FWHM values are concentrated close to the intermediate boundary, in the between AGN and LINER regions. These correspond mainly to regions SNR 1 and SNR 2 and regions close to 3 and 4 where the strong broadening is seen, which all have values $-1 < \log([\text{O I}]\lambda6300/\text{H}\alpha) < -0.75$.

Regions 5 and 6 include some of the strong broadening seen in these areas, but the ratios where FWHM is strongest are instead pushed to higher [O I]λ6300/Hα ratios ([O I]λ6300/Hα > 0.25 or $\log([\text{O I}]\lambda6300/\text{H}\alpha) >$ –0.6) compared to the other regions (Figure 6.21), most notably for region 6. These regions show also a clear dependence with distance to the ULX, with the pixels closer to the ULX showing high $\log([\text{O III}]\lambda5007/\text{H}\beta) \gtrsim$ 0.25 as a result of the higher excitation by the ULX, whereas pixels further from the ULX are again found at the boundary between AGN/LINER and intermediate regions. Note in particular how the [O III]λ5007/Hβ ratio is much lower in region 6 whereas the [O I]λ6300/Hα has increased. These pixels with [O I]λ6300/Hα are located to the south and east of the region classified as LINER in the [S II]/Hα or [O I]λ6300 diagrams. To illustrate this in more detail, we show in Figure 6.13 the [O III]λ5007/Hβ contours over the [O I]λ6300/Hα image. This shows the presence of a highly ionised zone (in this case traced by the high [O III]λ5007/Hβ ratio) surrounded by regions of bright forbidden transitions of neutrals atoms (here traced by the [O I]λ6300/H$\alpha \gtrsim$ 0.25 ratio). This is consistent with the expectation of an X-ray ionised nebula (Halpern & Grindlay, 1980), in very good agreement with the weakly ionised region reported by Pakull & Mirioni (2002). Therefore in regions 5 and 6 we are likely seeing a mixture of shock- and X-ray ionised gas. In region 7 we note some of the pixels include the contribution from the stellar cluster located east of it, which explains the array of values found in the HII region, but again we observe some the pixels located at the AGN/LINER/Intermediate boundary. In summary, we see that the environment of the ULX shows indication of being ionised by both hard EUV/X-ray radiation and shocks. While we do observe some pixels with FWHM ~ 80–120 km/s within the HII region in Figure 6.14 (see the yellow coloured datapoints at $-1.5 < \log([\text{O I}]\lambda6300/\text{H}\alpha) < -1.25$), associated with the northernmost region in Figure 6.14, we can rule out these as due to shocks due to their position in the BPT diagrams.

6.2.3.4 Comparison with the MAPPINGS libraries

BPT diagrams are a powerful tool to separate regions excited by stars from those excited by EUV/X-ray radiation and/or shocks (LINER and AGN regions). However, these diagrams cannot cleanly separate regions excited by shocks from EUV/X-ray radiation, although in Sections 6.2.3.1 and 6.2.3.3 we saw that the kinematic data can help in this discrimination. For this reason, it is often valuable to complement these diagrams with the predictions from radiative shock libraries. Here we chose to do so with the up-to-date set of pre-run shock-

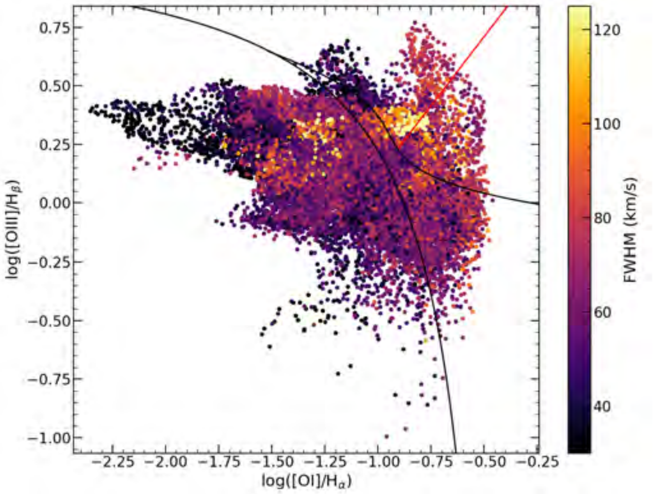

Figure 6.14: Spatially resolved [O III]λ5007/Hβ vs [O I]λ6300/Hα BPT diagram coloured as a function of the intrinsic FWHM of the Hα line. The solid lines show the classification scheme proposed by Law et al. (2021) as in Figure 6.12.

ionisation MAPPINGS V (Sutherland et al., 2018) models compiled by Alarie & Morisset (2019), which is an extension of the MAPPINGS III (Allen et al., 2008) models to a wider range of abundances from the work of Gutkin et al. (2016). With this analysis we can also attempt to provide an independent estimate of the shock velocities in the bubble ($v_{\rm shock}$), which will be relevant to evaluate the mechanical power needed to inflate the bubble (Section 6.2.4.1) as well as the explosion energy of the SNRs (Section 6.2.4.2).

We show in Section 6.2.3.6 that the metallicity around NGC 1313 X–1 is 12+log(O/H) $\approx$ 8.1–8.4. We therefore considered models for SMC (log(O/H) + 12 = 8.03±0.10) and LMC abundances (log(O/H) + 12 = 8.35±0.6) (Russell & Dopita, 1992) from the updated Allen et al. (2008) set, which have the closest set of abundances to our estimates. From the Gutkin et al. (2016) abundances, we considered four abundances to match roughly the observed range: Z = 0.002, 0.004 and 0.01 which correspond approximately to $12 + \log(\mathrm{O/H}) = 7.91$, 8.21 and 8.61 respectively[9]. We also consider a representative range of pre-shock magnetic fields given in Figure 6.15. Using the Gutkin et al. (2016) models, for which the pre-shock density ($n_{\rm ISM}$) can be varied logarithmically in the 1–10000 cm^{-3} range, we found that the best match to the data was given for $n_{\rm ISM}$ = 1 cm^{-3}. Models with $n_{\rm ISM}$ = 10 cm^{-3} were also acceptable, but mostly had the effect of making the line ratios less sensitive to variations of the pre-shock magnetic value than $v_{\rm shock}$. Therefore, the range of velocities found were roughly the same as the ones recovered for $n_{\rm ISM}$ = 1 cm^{-3}. We also note that our estimates from Section 6.2.3.5 suggest $n_{\rm ISM} \lesssim 5$ cm^{-3} even for velocities as low as ~100 km/s and thus we considered only models with $n_{\rm ISM}$ = 1 cm^{-3}. The predicted line ratios from the libraries are compared with our line ratio estimates in Figure 6.15.

From the [S II]/Hα and [O I]λ6300/Hα diagrams, it is clear that velocities in excess of $v_{\rm shock} \gtrsim 150$ km/s are needed to produce the observed line ratios close to the AGN, LINER and intermediate boundaries, especially for the range of metallicities which match more closely our estimates (Section 6.2.3.6). The LMC or $12 + \log(\mathrm{O/H})$ = 8.24 set of abundances with velocities $v_{\rm shock} \sim 200$ km/s or the SMC abundances with slightly higher velocities $v_{\rm shock} \sim 250$ km/s, seem to provide a good match to our data (cf. Figure 6.21). It is also clear that values with log([O III]λ5007/Hβ) $\gtrsim$ 0.45 cannot be explained by shocks alone, as they either require shock velocities $\gtrsim$ 300 km/s, which can be ruled out by our kinematic data, or a set of abundances with abnormally high metallicity (cf. Figure 6.2.3.6), also ruled out by our estimates. Therefore, pixels at the uppermost right region of the BPT diagrams seem consistent with mainly EUV/X-ray excitation. Similar argument can be made about the pixels with the highest [O I]λ6300/Hα ratios seen in Regions 5 and 6. This is in line with the analysis presented in Sections 6.2.3.1 and 6.2.3.3, in which it was shown that shocked regions are instead close to the AGN/LINER–Intermediate boundary delimitation. Considering the [N II]/Hα diagram, it seems that the best match to the data would be given by the set of LMC abundances, in good agreement with our metallicity estimates (Section 6.2.3.6). The set of points with FWHM $\gtrsim$ 120 km/s seen in Figure 6.14 closer to the AGN/LINER and intermediate boundaries is clustered around $-0.8 < \log([\mathrm{N\,II}]/\mathrm{H}\alpha) < -0.6$ and $0.25 < \log([\mathrm{O\,III}]\lambda5007/\mathrm{H}\beta) < 0.5$ in this diagram, which again would suggest 175 km/s $< v_{\rm shock} <$ 200 km/s. In summary, the line ratios with values at rightmost part of the [O I]λ6300/Hα and [S II]/Hα diagrams or with very high ($\gtrsim$ 0.45) values of log([O III]λ5007/Hβ) ratio cannot be explained by shocks, suggesting that these are regions excited by EUV/X-ray radiation. Instead, regions closer to the AGN/LINER–Intermediate boundary line are well matched by shocks with velocities in the $\sim$ 165 $< v_{\rm shock} <$ 225 km/s range.

It is often worth comparing these estimates with the kinematical data. In this regard, Soria et al. (2021) provides an interesting discussion on how to relate the measured line FWHMs to the shock velocity in their

---

[9] We have assumed a dust-to-metal mass ratio of 0.1 for the conversion (see Gutkin et al., 2016).

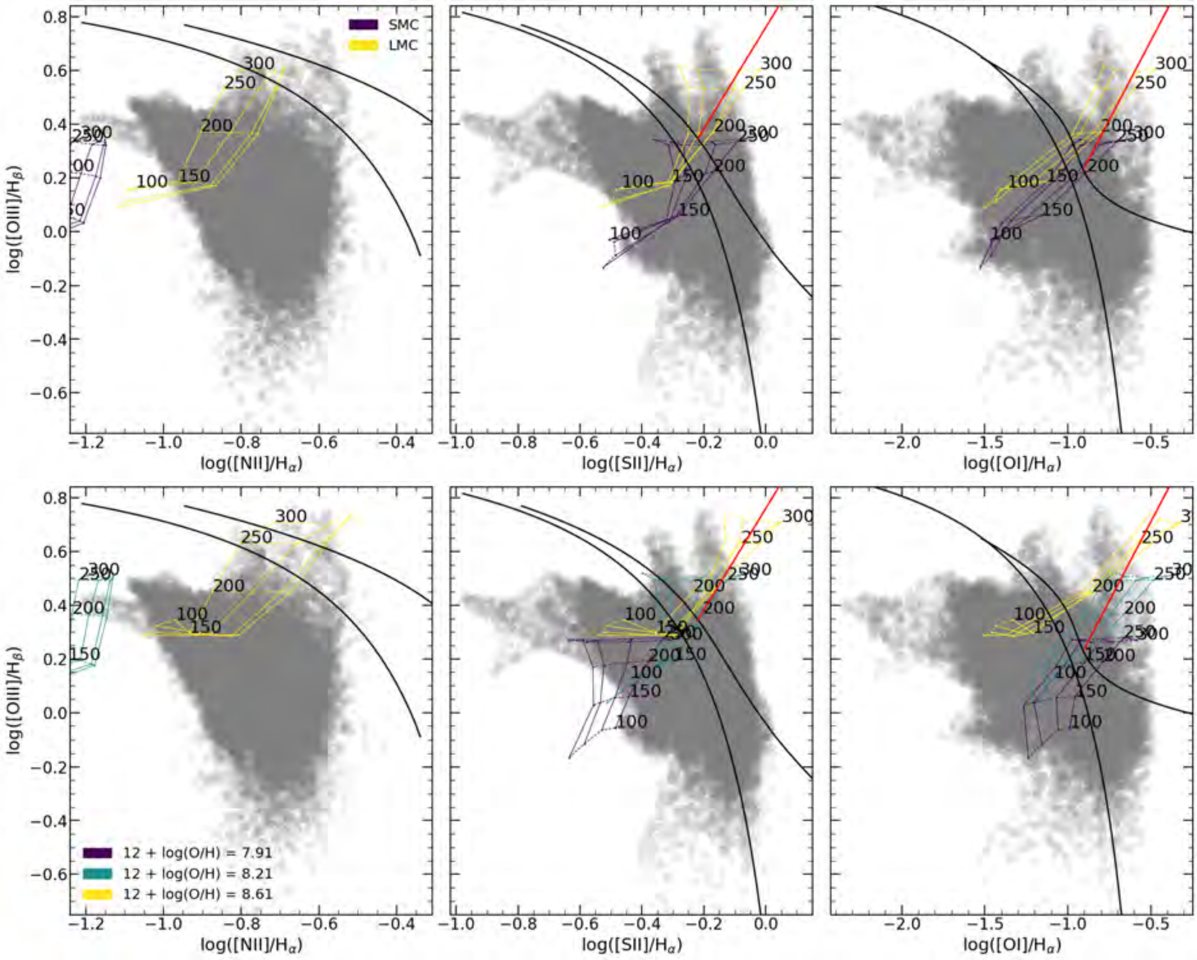

Figure 6.15: Comparison between the theoretical ratios predicted by the radiative shock libraries compiled by Alarie & Morisset (2019) for the precursor + shock models from abundances from Allen et al. (2008) (top) and abundances from Gutkin et al. (2016) (bottom) and the observed ones. Each colour shows the predictions for a set of abundances (see text for details). Each line connects the predictions for shock velocities ranging from 100 to 300 km/s in steps of 50 km/s as indicated in the Figure. The models for a given velocity are connected by a dashed line, indicating the effect of varying the pre-shock magnetic field for 10^{-4}, 1, 3.23 and 5 μG cm$^{3/2}$. The grey datapoints and the black solid lines correspond to the data and region delimitations from Figure 6.12.

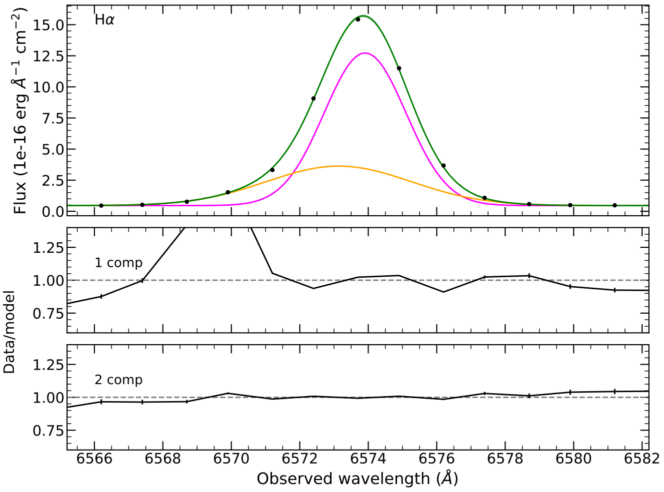

Figure 6.16: (top) Best-fit (green solid line) to the integrated Hα emission from region SNR 1 (Figure 6.7) using two Gaussian components (shown in pink and yellow colours). The lower panels show the ratio plots of one or two component fits respectively.

Appendix, to which we refer the interested reader for more details. Briefly, if we are observing the projected central region of a thin spherically expanding bubble, we expect to observe a distribution function $f_c = \frac{1}{2}[\delta(v - v_{\rm exp}) + \delta(v + v_{\rm exp})]$ where $v_{\rm exp}$ is the expanding velocity of the bubble. For radiative shocks, $v_{\rm exp} = v_s$ (Dewey, 2010) and one finds $v_{\rm shock} = 0.425\,$FWHM. Considering the fact that in reality we observe a finite region with range of velocities instead of a delta function and that some gas lags the shock, Soria et al. (2021) suggested that $v_{\rm shock} = 0.47\,$FWHM is a more appropriate relationship. Another possibility is to take a spectrum of the entire bubble, instead of observing a finite region. In this case, assuming there is a single expansion velocity for the whole bubble, the observed velocity distribution is a uniform distribution $f_{\rm T} = \frac{1}{2}\, v_{\rm exp}$, which leads to $v_{\rm shock} = 0.735\,$FWHM. Given the morphology of the nebula, we considered only a circular region centred at the centre of the cyan ellipse in the right panel of Figure 6.7 with radius 7.5" ($\sim$ 150 pc), roughly delimited by regions 4, 5 and 6. Here we measured a maximum FWHM of 127 km/s and a mean of 70 km/s from the mean Hα, [N II] and [S II] map. Assuming the case of a spherically thin expanding nebula, this would suggest $v_{\rm shock} \sim 55$ km/s using either of both estimates. However, such slow $v_{\rm shock}$ values are at odds with the measured line ratios as we have shown in Section 6.2.3.4. Note also that a radial expansion does not appear to be supported by the $V_{\rm los}$ maps, which shows instead some sort of outflowing gas emanating from the ULX (see the trough in the velocity field at the ULX position in Figure 6.9).

It is also possible that in our case, given the high shock velocity inferred from the line ratios, the FWHM we are measuring is a blending of the broadened line from the shock and the narrow component from the photoionised precursor, only broadened by thermal Doppler effect. We note that the presence of the shock precursor is strongly supported by the fact that this component is needed to match the line ratios in the LINER and AGN regions. Given the moderate resolution of MUSE (instrumental FWHM of $\sim$ 116 km/s at 6560 Å) it is likely that we cannot resolve both of these components. If the narrow component from the precursor dominates the emission, this can result in a narrower Gaussian fit to the blended line profile than if the shocked component could be resolved and modelled alone. We may see some evidence in support of this phenomenon in SNR 1 (Figure 6.7), where the FWHM measured with a single Gaussian component was the strongest and where we found the strongest fit residuals, which could indicate the presence of a more complex line profile. We focused on the Hα as it is the line with the strongest S/N and extracted a spectrum from the region shown in Figure 6.7, determined by fitting a 2D Gaussian profile as explained in Section 6.2.3.1.

We performed Gaussian fits of the Hα line using the `python` package `lmfit`[10] considering one or two Gaussian components. The continuum was modelled using a constant around the line centroid. The best-fit parameters for the one and two model components are reported in Table 6.4. Figure 6.16 shows the best-fit two-Gaussian model component, with the corresponding residuals for one and two Gaussian components shown in the panels below. We also tried more complex profiles such as a Lorentzian or a Voigt profile but these yielded worst fits than the single Gaussian model.

The single Gaussian component deviates strongly from the line profile at the blue-wing of the line profile, suggesting the presence of a second broad component. In line with the above argumentation, the second broad component alone is broader (FWHM = 196±8 km/s) than the single-Gaussian model component (FWHM = 98±6 km/s). The former FWHM-value is in turn much closer to the shock velocities inferred from the MAPPINGS libraries. We conclude that it is possible that the narrow component of the precursor is causing the FWHM of the lines to be underestimated. It must also be noted that a one to one correspondence between $v_{\rm shock}$ and

---

[10] https://lmfit.github.io/lmfit-py/

Table 6.4: Best-fit parameters to the integrated Hα line of region SNR 1 (Figure 6.7 right panel) for one and two Gaussian components. Uncertainties at the 1 σ level.

	Wavelength Å	$V_{\rm los}{}^{a}$ km/s	FWHM km/s	Flux 10^{-15} erg cm^{-2} s^{-1}
1 Component	6573.78±0.07	31±3	98±6	5.2±0.1
2 Components	6573.92±0.03	38±1	56±5	3.7±0.2
	6573.15±0.09	3±4	196±8	1.7±0.2

Notes. [a] Line-of-sight velocity over the galaxy redshift ($z = 0.001568$).

FWHM is not expected given that the FWHM might not necessary sample the direction of maximum expansion. Considering the uncertainties associated with relating FWHM to the shock velocity, we decided to rely on the shock velocities inferred from MAPPINGS, rather than from the kinematic data.

Based on the different positions of the selected regions in the BPT diagrams (Figure 6.21) we assigned them a shock velocity depending on the typical values found for the SMC, LMC and 12 + log(O/H) = 7.91, 8.21 abundances. These are shown in Table 6.5. We also report in Table 6.5 the maximum FWHM found in the selected regions. There is clear trend in the sense that regions with higher FWHM show higher shock velocity values as derived using the line ratios. This suggests that the estimated shock velocities based on the MAPPINGS libraries are reasonable. The shock velocities found are typically a factor ~1.4 higher than the measured FWHMs. Similar factors were also found by Dopita et al. (2012) in the study of the microquasar NGC 7793 S26. Given that region 6 does not show much overlap with the line ratios predicted by the MAPPINGS libraries, notably where FWHM is strongest (Figure 6.21), owing to the likely contribution from X-ray ionisation (Section 6.2.3.3), we simply assigned it $v_{\rm shock}$= 1.4 FWHM. We note also that the differences between the FWHM-values and the shock velocities inferred from the line ratios we found are much smaller than in other previous works such as Urquhart et al. (2018) or Soria et al. (2021), who found $v_{\rm shock}$ based on the line ratios to be $\gtrsim 5$ FWHM. Note however that as stated earlier these values are less certain for regions 5 and 6 given the likely contribution from X-ray radiation.

6.2.3.5 ISM Density estimates

A key physical quantity necessary to estimate the energetics of the bubble (see Section 6.2.4) and that of the SNRs (Section 6.2.4.2) is the pre-shock density of the ISM ($n_{\rm ISM}$). This quantity can be estimated using Equation 3.4. from Dopita & Sutherland (1996), who provide a relationship between the surface brightness of the Hβ line in the shock, $v_{\rm shock}$ and $n_{\rm ISM}$:

$$f_{H\beta \rm shock} = 7.44 \times 10^{-6}\ v_{100}^{2.41} \times \frac{n_{\rm ISM}}{cm^{-3}}\ \text{erg s}^{-1}\text{cm}^{-2} \tag{6.1}$$

where v_{100} is the shock velocity in units of 100 km/s. In cases where $v_{\rm shock} > 150$ km/s, the shock will create a photoionised precursor that needs to be taken into account (Dopita & Sutherland, 1996). The same relationship as above but for the precursor term reads (their Equation 4.4.):

$$f_{H\beta \rm precursor} = 9.85 \times 10^{-6}\ v_{100}^{2.28} \times \frac{n_{\rm ISM}}{\rm cm^{-3}}\ \text{erg s}^{-1}\text{cm}^{-2} \tag{6.2}$$

combining both equations, $n_{\rm ISM}$ can be expressed as:

$$\frac{n_{\rm ISM}}{\rm cm^{-3}} = \frac{10^6 L_{\rm H\beta}}{A(7.44 v_{100}^{2.41} + 9.85 v_{100}^{2.28})} \tag{6.3}$$

where A is the surface area of the emitting region. The surface area of each region was estimated assuming a prolate ellipsoid i.e. we assumed the shorter of the semi-axis for the third dimension of the ellipsoid. We estimated the density of the ISM for the two SNRs and the bubble as well as each of the elliptical regions shown in the right panel of Figure 6.7, where we have found clear signs of shock excitation as argued in Sections 6.2.3.1 and 6.2.3.3. We caution again that these estimates might be less robust for regions 5 and 6 given that a fraction of the Hβ luminosity might be produced by X-ray excitation. We return to this point in Section 6.2.4.1.

The integrated flux in the Hβ line map in each of the aforementioned regions was corrected for reddening using the observed Balmer decrement map. To this end, we followed Momcheva et al. (2013), who provide a relationship between the observed Balmer decrement and the colour excess:

$$E(B-V) = \frac{-2.5}{k(H\beta) - k(H\alpha)} \times \log_{10}\left(\frac{(H\alpha/H\beta)_{int}}{(H\alpha/H\beta)_{obs}}\right) \tag{6.4}$$

where we used the extinction curve of Calzetti et al. (2000) with $R_v = 4.05$ to obtain $k(H\beta) = 4.6$ and $k(H\alpha) = 3.3$. For the intrinsic Hα/Hβ ratio, the MAPPINGS libraries suggested values of $\approx$ 2.95–3.0 for SMC and LMC

Table 6.5: Estimated pre-shock ISM densities in the regions shown the right panel of Figure 6.7. We have assumed a distance to NGC 1313 X–1 of 4.25 Mpc in the calculations of the Hβ luminosities. a and b are the semi-major and semi-minor radii of the elliptical regions considered. For the third dimension of the spheroid we have assumed a radius equal to b i.e. a prolate spheroid. The values of $\Sigma L_{\mathrm{H}\beta}$ indicate the integrated extinction-corrected luminosity in the region and the error is propagated from the error flux map and takes into account the uncertainty on <E(B-V)>. <E(B-V)> indicates the mean and its standard deviation in each region to provide some reference values, although the extinction correction has been applied on a pixel-by-pixel basis. The error on n_{ISM} takes into account the error on v_{shock} and the error on $L_{\mathrm{H}\beta}$. All uncertainties are at the 1σ level.

Region	a arcsec	b arcsec	Area 10^{40} cm^2	R^a pc	$\Sigma L_{\mathrm{H}\beta}$ 10^{36} erg/s	< E(B-V)>	FWHM^b km/s	$v_{\mathrm{shock}}{}^c$ km/s	n_{ISM} cm^{-3}	t^d 10^5 yr	$P_{\mathrm{mec}}{}^e$ 10^{39} erg/s	E^f 10^{51} erg
SNR 1	1.51	1.51	11.6	257±6	6.37±0.02	0.16±0.06	166±27	220±25	0.5±0.1	0.24–0.27	–	0.3–0.8
SNR 2	1.72	1.06	8.1	211±5	4.64±0.02	0.20±0.08	136±20	200±25	0.7±0.2	0.27–0.34	–	0.3–0.8
3	3.12	1.81	25.1	164±9	8.35±0.02	0.12±0.08	119±13	165±25	0.6±0.2	–	–	–
4	4.68	1.26	24.2	116± 1	15.25±0.03	0.18±0.08	110±12	170±25	1.1±0.4	–	–	–
5	3.30	2.33	35.5	69±3	10.66±0.03	0.16±0.07	110±13	170±25	0.5±0.2	–	–	–
6	3.80	1.70	27.6	137±5	11.16±0.04	0.2±0.1	130±15	180±25	0.6±0.2	–	–	–
7	2.03	1.96	19.9	199±8	7.90±0.04	0.2±0.1	100±17	160±25	0.8±0.3	–	–	–
Bubble	11	6.5	318.6	134–227	105.6±0.12	0.16±0.1	130	170±25	0.6±0.2	4.6±0.7–7.8±1.2	19±10–55±30	~188–990

Notes. (a) Average distance from the centre of the region to the average between the centre of the bubble and the position of the ULX. For the bubble we quote instead the range between the major and minor axis. (b) Maximum FWHM measured in each region. The error is the the typical spread in the region. (c) Shock velocity estimated from the observed line ratios in each region after comparison with the MAPPINGS libraries (see text for details). (d) Estimated age of the bubble or, in the case of the SNRs, time since the initial explosion. (e) Estimated average mechanical power required to inflate the bubble. (f) Estimated explosion energy in the case of an evolved SNR in the pressure-driven snow-plough phase (see Section 6.2.4.2 for details).

abundances (see Sections 6.2.3.4 and 6.2.3.6) and for shock velocities v_{shock} = 175–225 km/s. We therefore assumed an intrinsic ratio Hα/Hβ = 3.0 for the extinction correction.

The estimated n_{ISM} values are in overall good agreement with the 0.1–1 cm^{-3} values typically found in other ULX bubbles (e.g. Pakull et al., 2005). In general the values found are in good agreement between all regions across the bubble except for Region 4, where the slightly higher n_{ISM}-value might explain its higher surface brightness.

6.2.3.6 Metallicity

The presence of shocks heavily affects abundances in nebulae (e.g. Peimbert et al., 1991) and requires specific modelling (Allen et al., 2008). Consequently, empirical metallicity diagnostics remain restricted to photo-ionisation zones, and are built with careful samples of reliable HII (or similar) regions. The most prevalent tools currently in use (e.g. Pérez-Montero, 2017) are often based on temperature and density estimations originating from weak recombination lines (Osterbrock & Ferland, 2006). However, these lines are either outside the observed bandpass of MUSE (e.g. the [O III]λ4363 and [S III]λ9532 lines) or are too weak to be detected above the continuum (e.g. [N II]λ5755). We therefore used the strong line method, through the S (empirical) calibration provided by Pilyugin & Grebel (2016), which only relies on strong lines (Hβ [O III]λ4959,5007, [N II]λ6548,6584 and [S II]λ6717,6371), well detected in our data cube. More specifically, as suggested by the authors, we used two different calibrations (their Equations 6 and 7) for the so-called upper ($\log N_2 \geqslant -0.6$) and lower ($\log N_2 < -0.6$) branches respectively, where N_2 = ([N II]λ6548 + [N II]λ6584) / Hβ, (see Pilyugin & Grebel, 2016, for more details), to calculate $12 + \log(\mathrm{O/H})$.

Because this method is only calibrated for HII regions, we restricted our analysis to the dynamically "cold" regions. We followed the principle used in Dors et al. (2017), who considered the cold-warm delimitation of the [S II]/Hα BPT diagram of Kewley et al. (2006) (see also Lara-López et al. (2021) for a similar approach). Here we also excluded the new intermediate delimitation of Law et al. (2021), as we have seen that this delimitation region is affected by the X-ray ionisation of the source (Section 6.2.3.3). Hence we restricted the analysis to the regions strictly classified as HII.

Given that some of the line ratios involved in the metallicity computation are rather distant in wavelength, we corrected the corresponding fluxes for extinction using the methodology outlined in Section 6.2.3.5, this time adopting the theoretical value for Case B recombination of Hα/Hβ = 2.86, more suitable for HII-like regions (Osterbrock & Ferland, 2006). The values obtained for E(B-V) in the regions of interest in this case are in the 0.15–0.8 range. The resulting metallicity map is shown in Figure 6.17.

We find a 3σ-clipped median and standard deviation of $12 + \log(\mathrm{O/H}) = 8.18 \pm 0.04$. These estimates are slightly below the values reported by Walsh & Roy (1997), who found that the metallicity in NGC 1313 followed a nearly flat profile with $12 + \log(\mathrm{O/H}) \approx 8.4 \pm 0.1$. We note that in the bright HII regions created by the stellar cluster north-west and south of the ULX the metallicity is closer to the values reported by Walsh & Roy (1997) (purples areas in the map). Therefore, while some of these differences in metallicity are likely due to the difference

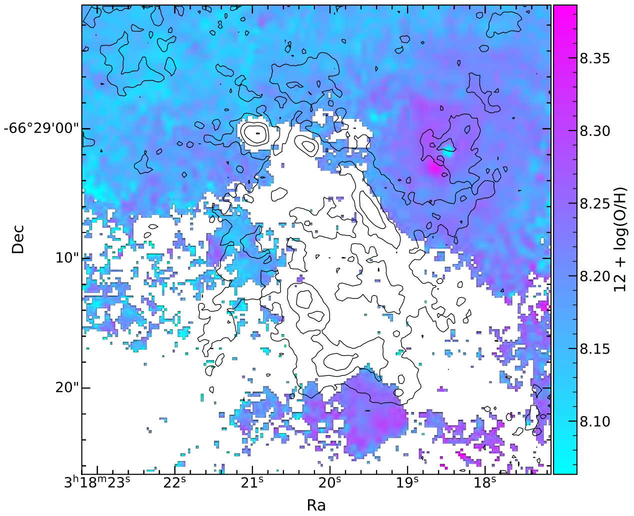

Figure 6.17: Metallicity map around NGC 1313 X–1 only for those regions classified as HII regions (see text for details) based on the [S II]/Hα vs [O III]λ5007/Hβ BPT diagram (Figure 6.12). Contours as per Figure 6.3.

in the reddening correction and the metallicity calibration used, it may be possible that the method we employed is less suited for these diffuse regions. Nevertheless, a plausible range for the metallicity around NGC 1313 X–1 seems 8.1–8.4, which is in line with the estimates from the MAPPINGS libraries (Section 6.2.3.4). We can also confidently say that NGC 1313 X–1 was formed in a subsolar environment.

6.2.3.7 Optical counterpart

As stated earlier, the optical counterpart is not detected in the ACS/F555W equivalent MUSE image (Figure 6.3), neither in the white light MUSE image. The lowest Vega magnitude in any of the U, V, I filters reported by Yang et al. (2011) from analyses of the 2004 *HST* data was $\sim$ 22.6 in the U filter. The MUSE cube has a limiting AB magnitude of ~20.6 as determined by the automatic pipeline (Weilbacher et al., 2020), which translates to a $\sim$ 20 Vega magnitude. Thus our sensitivity is too low to assess whether the optical counterpart has varied with respect to the 2004 observations. The counterpart might be additionally blurred due to the limited spatial resolution (FWHM PSF $\sim$ 1") of the MUSE data cube.

However, while the counterpart is not detected, as stated in Section 6.2.3.1, we observed an enhancement of the width of the [O I]λ6300 line at the position of NGC 1313 X–1, with the FWHM reaching a peak value of 200 km/s as stated in Section 6.2.3.1 (see Figure 6.18). We determined the peak and the FWHM of this enhancement by fitting a 2D Moffat profile to the region around the peak emission to select a suitable extraction region for the spectrum of the optical counterpart. We used a circular region centred at the peak with a ~0.5" radius for both semi-axes, as given by the estimated FWHM. We chose the background from an annulus centred at the source position to encompass some of the nebular emission. We set the inner radius to be equal to the source radius and the outer radius to 1.5", in order to avoid the significantly brighter south/east rim of the nebula.

Figure 6.18 shows the background-subtracted spectrum around the Hα-[N II] complex, which shows that the resulting spectrum is dominated by noise and oversubtracted. There were no obvious features in the spectrum of the optical counterpart besides the sky residuals, suggesting that the emission is dominated by the nebular emission, which precluded us from characterizing the optical counterpart.

6.2.4 Discussion

The simultaneous spectral and imaging capabilities of MUSE have allowed to analyse in detail the complex morphology of the bubble around NGC 1313 X–1, first noticed by Pakull & Mirioni (2002). The nebula shows indication of excitation by both shocks and EUV/X-rays. Shock excitation is seen at outer edges of the nebula close to the NGC 1313 X–1, revealed by the strong [O I]λ6300/Hα and [S II]/Hα ratios, together with the strong broadening (FWHM $\gtrsim$ 100 km/s) of the Hα, [N II] and [S II] lines near those regions (see Figures 6.6, 6.7 and 6.21). This strong broadening at the edges of the bubble is also seen in other ULX bubbles where the kinematics have been studied, such as the one around NGC 1313 X–2 (Ramsey et al., 2006) and NGC 5585 X–1 (Soria et al., 2021). We have also seen that the gas in a region of $\sim$ 7.5" around the ULX shows a high line-of-sight velocity compared to the surrounding gas (Figure 6.8). In particular, the Hα[N II][S II] and [O III] velocity maps show two high-velocity regions with a trough at the source position (Figure 6.9), which argues against a radial expansion, which could be the case for a SNR. This strongly suggests that the gas inside the bubble is being

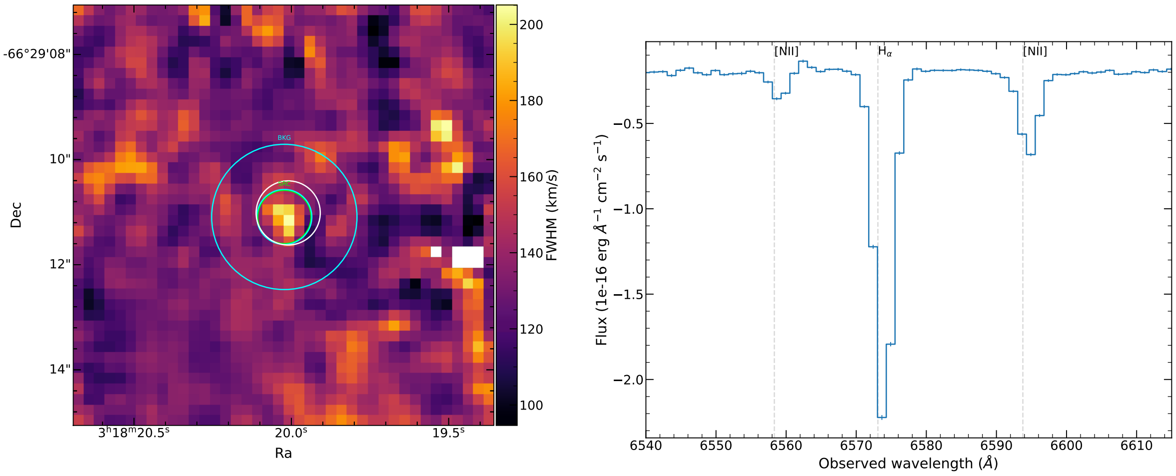

Figure 6.18: (left) Dispersion map for the [O I]λ6300 line showing the enhancement around the ULX position and the extraction regions used. The extraction regions for the source and background are shown in green and cyan respectively, whereas the white circle shows the ULX positions as determined in Section 6.2.2. (right) MUSE background-subtracted spectrum of the optical counterpart around the Hα-[N II] complex. The main nebular lines are labelled and their expected position based on the redshift of the galaxy is indicated with a grey dashed line.

dynamically perturbed by winds emanating from the ULX, creating the cavity around it. The strong broadening at the edges of the bubble is then thought to be an indication of the gas being decelerated at the shock front, strongly supporting that the bubble has been (and is being) inflated by a wind or/and jets. Therefore these results provide direct and supporting evidence to the presence of powerful winds in NGC 1313 X–1, so far only revealed through X-ray spectroscopy (Walton et al., 2016b; Pinto et al., 2016, 2020b). We show below that the estimated mechanical power of the wind in these previous works is in remarkable agreement with that estimated from the bubble. The elongated shape and the roughly diametrically opposite regions 3 and 7 (see in particular the [O I]λ6300 contours in Figure 6.7) might suggest that we are witnessing the activity of a jet. Follow-up radio observations would therefore be of great interest to confirm this. Given the clear evidence for shocks, below we compute the age and mechanical power of the bubble following previous works on shock-ionised bubbles (e.g. Pakull et al., 2010; Soria et al., 2021).

Interestingly, the inner parts of the nebula also show clear indication of strong EUV/X-ray excitation. This is revealed by the high [O III]λ5007/Hβ > 5 close to the source and south of it (Figure 6.12), surrounded by a region of weakly ionised gas (Figure 6.13), indicative of hard ionising radiation, in good agreement with the findings from Pakull & Mirioni (2002). This morphology, a cavity with an X-ray ionised nebula in its interior is in many respects very similar to the bubble around IC 342 X–1 reported by Roberts et al. (2003). The morphology of the X-ray ionised region is also reminiscent of the prototypical photoionised nebula around Holmberg II X–1, which shows an area of high-excitation close to the source (traced by the He II λ4686 line), and strong [O I]λ6300 emission in the outer pars (Pakull & Mirioni, 2002; Kaaret et al., 2004; Lehmann et al., 2005). We have seen also that some of these regions fall in the AGN/LINER classification locus according to the BPT diagrams (Figure 6.12). Similar classification was found by Berghea & Dudik (2012) using infrared observations of Holmberg II X–1 and NGC 6946 X–1, which are typical photo-ionised dominated nebulae (e.g. Abolmasov et al., 2006). EUV/X-ray excitation is also supported by the line ratios predicted by the MAPPINGS libraries, which cannot account for the combined high [O I]λ6300/Hα or [O III]λ5007/Hβ ratios, ruling out shocks as the main source of ionisation. Thus NGC 1313 X–1 shows signs of ionising the surrounding medium by means of both shocks and EUV/X-ray radiation, which highlights the complex morphology of the nebula and enormous power of ULXs in ionising the ISM. This has been recently highlighted in the work of Simmonds et al. (2021), which have shown that a combination of realistic ULX broadband and stellar population spectra can reproduce the nebular He II λ4686 emission seen in low-metallicity galaxies, whose origin remains unclear.

Our study also suggest that ULX bubbles might be more complex than revealed by long-slit spectroscopy alone. In this regard, it is surprising that the nebula around NGC 5408 X–1 seems to show no signs of shock excitation (Cseh et al., 2012) and displays a much smaller bubble ($\sim$ 60 pc; Grisé et al., 2012), given the detection of winds in X-rays (Pinto et al., 2016) with similar outflow velocities ($\sim 0.2\,c$). We note that Cseh et al. (2012) probed a small (2" × 1") region around NGC 5408 X–1 based on the [O III]λ5007 line map, whereas here we have shown that the [O III]λ5007 emission is concentrated close to the source in the high excitation regions. In fact, a similar conclusion was reached by Mirioni (2002) after performing long-slit spectroscopy of the high excitation region around NGC 1313 X–1, thereby missing the shock-excited regions at further distances from the source. We believe that a more thorough study using IFU spectroscopy is needed to completely rule out the presence of shocks in sources such as NGC 5408 X–1.

The 452 × 266 pc bubble around NGC 1313 X–1 sits at the high end of the largest optical nebulae ever detected to date, comparable in size to the shocked bubble around the ULX in NGC 1313 X–2 (Pakull et al., 2005) or the one around Holmberg IX X–1 (Grisé et al., 2011). The detailed analysis of the nebula around NGC 5585 X–1 presented by Soria et al. (2021) allows to compare the X-ray properties and bubble characteristics between these two sources. The bubble around NGC 5585 X–1 is also similar in size and morphology with respect to that of NGC 1313 X–1 and, as stated above, shows similar strong broadening towards the edges of the bubble with similar FWHM values and [S II]/Hα and [O I]λ6300/Hα ratios, typical of shock-dominated bubbles. However, it is interesting to observe that the bubble around NGC 5585 X–1 shows no signs of EUV/X-ray excitation, with [O III]λ5007/Hβ only reaching values of $\sim$ 1.6 (log([O III]/Hβ) $\sim$ 0.2) well within the HII region classification in the [N II]/Hα diagram (cf. Figure 6.12). While NGC 1313 X–1 reaches unabsorbed luminosities of $\sim 1.8 \times 10^{40}$ erg/s (Gúrpide et al., 2021a), NGC 5585 X–1 only reaches $\sim 4 \times 10^{39}$ erg/s (Soria et al., 2021). The difference in ionising photons between these two sources may therefore account for the different [O III]λ5007/Hβ ratios. This may suggest that the dimmer luminosity of NGC 5585 X-1 is intrinsic and not due to a geometrical effect due to an unfavourable viewing angle, in which the funnel axis could have been strongly misaligned with respect to our line-of-sight. Interestingly, NGC 1313 X–1 switches between soft and hard ultraluminous states (Sutton et al., 2013), thought to belong to the ULXs for the which the intense accretion rate leads to the formation of a supercritical disk-wind funnel (Shakura & Sunyaev, 1973; Poutanen et al., 2007), whereas NGC 5585 X-1 belongs to the so-called broadened disk type (Soria et al., 2021), which are thought to be sources close or at the Eddington limit (e.g. Middleton et al., 2013). This may be consistent with the implied higher accretion rate in NGC 1313 X–1. Alternatively, the gas in the cavity created by NGC 5585 X–1 might more rarefied than that of NGC 1313 X–1. We show below that the mechanical power of NGC 1313 X–1 is comparable to that of NGC 5585 X–1. If the outflow rate depends on the Eddington accretion rate (e.g. Shakura & Sunyaev, 1973; Poutanen et al., 2007), this may instead imply that the Eddington accretion rates of both sources is similar, and that NGC 5585 X–1 might be viewed through an unfavourable viewing angle compared to NGC 1313 X–1. Another possibility, if indeed both sources have similar Eddington accretion rates, is that NGC 5585 X–1 hosts a lighter compact object, which could also account for its dimmer luminosity.

In this respect, it is unclear whether from the morphology of the X-ray ionised nebula we can derive some conclusions with regards the level of anisotropy of the X-ray emission in NGC 1313 X–1. The offset between the peak of the [O III]λ5007/Hβ ratio and the ULX position is expected given the rather low ionisation potential to doubly ionize oxygen (35.1 eV). The fact that the X-ray ionised region is only seen south of the ULX is likely due to the nebula being density-bounded in the north direction, given the absence of significant Hα emission there (Figure 6.6). Therefore the nebula might not probe directly the degree of anisotropy of the X-ray emission. Observations in the [O IV] 25.89 μm or the He II λ4686 lines would be of interest as they should trace more closely the high-excitation regions closer to the ULX. The flux of the He II λ4686 photo-counting line (e.g. Pakull & Angebault, 1986) or photoionisation modelling of these regions might provide useful constraints on the EUV/X-ray spectra of the source, degree of anisotropy and/or inclination (e.g. Kaaret et al., 2004; Abolmasov et al., 2008, 2009; Berghea et al., 2010). MUSE observations of the nebulae around the Galactic supercritically accreting source SS433 (Dubner et al., 1998), long speculated to be an edge-on ULX (King, 2002; Fabrika, 2004; Middleton et al., 2021), and ULXs for which the inclination is suspected to be higher than for NGC 1313 X–1, such as NGC 5408 X–1 (Middleton et al., 2011a), might also offer interesting comparisons with that of NGC 1313 X–1 to constrain the inclination of these systems and the relationship between the bubbles morphology and the accretion flow geometry.

6.2.4.1 Age and mechanical power of the ULX bubble

The characteristic age of the bubble can be estimated assuming a spherically expanding bubble has been carved by a steady wind with mechanical power $P_{\rm mec}$ over the bubble lifetime (t) (Weaver et al., 1977). The evolution of the bubble radius (R) over time as a function of $P_{\rm mec}$ and the mass density of the unshocked ISM (ρ) is given by:

$$R = \left(\frac{125}{154\pi}\right)^{1/5} (P_{\rm mec}/\rho_0)^{1/5}\, t^{3/5} \tag{6.5}$$

. We assume that the bubble expands into a neutral ISM, which has a mean molecular weight $\mu = 1.38$ and thus $\rho_0 = \mu m_p n_{\rm ISM}$, where m_p is the proton mass and $n_{\rm ISM}$ is the hydrogen number density estimated in Section 6.2.3.5. The expansion velocity is therefore:

$$v_{\rm exp} = \frac{dR}{dt} = \frac{3}{5}R/t \tag{6.6}$$

which we take as $v_{\rm shock}$. The age of the bubble is then $t = \frac{3R}{5v_{\rm exp}}$. From these expressions the mechanical power can be estimated as:

$$P_{\rm mec} = \left(\frac{154\pi}{125}\right) R^2 v_{\rm shock}^3 (\mu m_p n_{\rm ISM}) \tag{6.7}$$

With these formulae we estimate the age and the mechanical power considering the major and minor semi-axes of the bubble for a typical $v_{\rm shock} = 170$ km/s. The results are given in Table 6.5. The estimated ages are found to be (4.6±0.7) × 10^5 yr and (7.8±1.2) × 10^5 yr for the minor and major axes respectively, so a typical age would

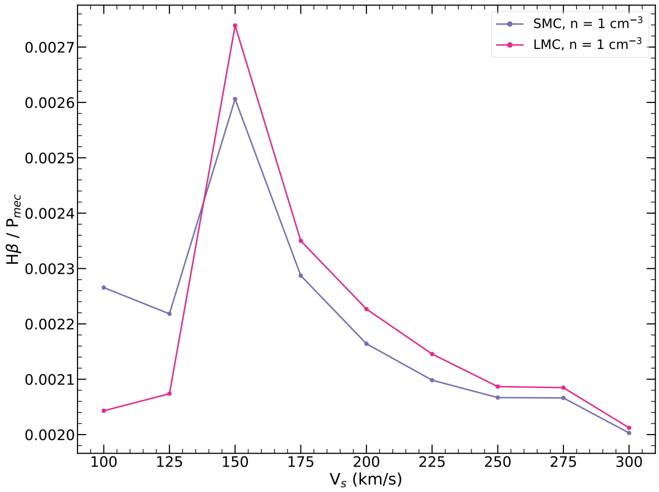

Figure 6.19: Ratio between Hβ luminosity and the mechanical power as a function of $v_{\rm shock}$ for a plausible range of metallicities (SMC and LMC as derived in Section 6.2.3.4) assuming equipartition for the magnetic field value.

be $\sim$ 6.2 $\times$ 10^5 yr. For the mechanical power, we find (1.9±1) $\times 10^{40}$ erg/s and (5.5±3) $\times 10^{40}$ erg/s, essentially consistent within uncertainties for both semi-axes.

As stated in Section 6.2.3.5, the exact factor relating $v_{\rm shock}$ and FWHM is rather uncertain. Assuming the perhaps more conservative case in which $v_{\rm shock}$= FWHM, which we take as ~110 km/s, the average FWHM from all regions (Table 6.5), we find slightly larger mechanical power for the larger axis, but in good agreement within uncertainties with the estimates given above. This is partially because the estimated $n_{\rm ISM}$ are higher for lower shock velocities (cf. Equation 6.3), and offset the lower shock velocity when estimating the mechanical power. We thus consider the estimates given above as a good figure for the mechanical power of the source. The age of the bubble would obviously increase by a factor $\sim$ 1.47, thus a reasonable range may be $t \sim$ (6.2–8.7) $\times$ 10^5 yr.

Another method commonly used to estimate the mechanical power is to use some of the optical lines as a proxy (e.g. Pakull et al., 2010; Soria et al., 2014). To this end, we used the Hβ line as it has a weak dependence on the shock velocity, whereas we have already determined the pre-shock gas density of the ISM (which we take as $n_{\rm ISM}$= 1 cm^{-3}) and the metallicity around NGC 1313 X–1. From standard bubble theory (Weaver et al., 1977) we expect the total radiative luminosity of the shock to be $L_{\rm T}$ = 27/77 $P_{\rm mec}$. The total radiative luminosity of the shock as a function of $v_{\rm shock}$ can be estimated from Dopita & Sutherland (1996) Equation 3.3. (see also Soria et al., 2014):

$$L_{\rm T} = \frac{1}{2}(\mu m_p n_{\rm ISM})\, v_s^3 = \\ 1.14 \times 10^{-3} \left(\frac{v_s}{100\,{\rm kms}^{-1}}\right)^3 n_{\rm ISM}\ {\rm erg\,cm^{-2}\,s^{-1}} \tag{6.8}$$

where we have assumed μ = 1.38 as above. The total radiative luminosity of the Hβ line as a function of $v_{\rm shock}$ can be obtained from the MAPPINGS libraries (Allen et al., 2008)[11]. We therefore calculated the fraction of power radiated in the Hβ line as a function of $v_{\rm shock}$ for the best set of abundances as derived in Section 6.2.3.4 (LMC and SMC). The resulting calculation is shown in Figure 6.19. We have assumed equipartition magnetic field values in the calculation but the results are equivalent for ISM magnetic field values in the 1–10 μG range. From the shock velocities derived in Table 6.5, we found $L_{\rm H\beta} \simeq$ (2.3–2.6) $\times$ 10^{-3} $P_{\rm mec}$.

We now need to estimate the total luminosity in the Hβ emitted by shocks in the bubble. For this we simply add the $L_{\rm H\beta}$ of each of the five shocked regions discussed in Figure 6.7 (Table 6.5) which gives $\Sigma L_{\rm H\beta}$ = (5.33 ± 0.01) $\times$ 10^{37} erg/s. We note that while there might be some contribution to the Hβ luminosity coming from EUV/X-ray excitation, notably for region 5, this is likely compensated by the fact that we might be missing some Hβ flux around regions 3, 4 and 6 given the coarser regions employed (Figure 6.7). We thus consider these regions adequate in order to provide an order of magnitude estimate on $P_{\rm mec}$. With these values we obtained $P_{\rm mec} \simeq$ (3.8–4.3) $\times$ 10^2 $\Sigma L_{\rm H\beta} \simeq$ (2.2±0.3) $\times$ 10^{40} erg/s. An approximate upper limit on the mechanical power using this method may be obtained by considering all the flux emitted in the whole bubble – approximated as the cyan ellipse in Figure 6.7– and subtracting the flux emitted due to EUV/X-ray excitation, which we approximate as the polygon classified as intermediate and AGN in the [N II]/Hα BPT diagram (Figure 6.12) south of the ULX. We measure $\Sigma L_{\rm H\beta}$ = 1 $\times$ 10^{38} erg/s, and therefore we estimate $P_{\rm mec} \lesssim$ 4.0–4.5 $\times$ 10^{40} erg/s. If we additionally

---

[11] Here we use the Allen et al. (2008) tables as the tables compiled by Alarie & Morisset (2019) do not include these values.

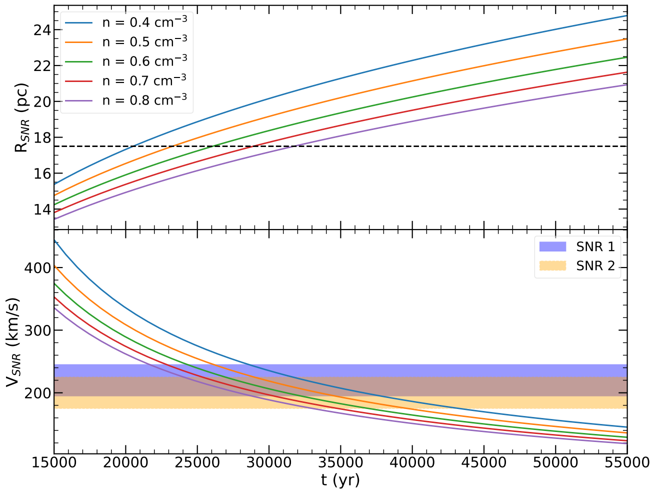

Figure 6.20: Evolution of the radius and expansion velocity of a SNR (green shaded areas) as a function of time for the pressure-drive snow-plow phase using the analytical expressions from Cioffi et al. (1988) for an initial explosion energy of 0.5 × 10^{51}. The evolution is calculated for the typical range of values found for $n_{\rm ISM}$ in Section 6.2.3.5 (Table 6.5). The dashed line marks the radii of the SNRs measured from the *HST* images (Figure 6.10) and the blue and yellow shaded areas represent the range of shock velocities determined in Section 6.2.3.4 (Table 6.5) for SNR 1 and 2 respectively.

exclude the flux from region 5 which we saw is likely dominated by X-ray ionisation, we obtain $P_{\rm mec} \lesssim 3.5$–4.0×10^{40} erg/s.

We thus conclude that the estimated mechanical power is comparable or higher than the X-ray luminosity of the source. This is in agreement with the estimates obtained from wind detections using X-ray spectroscopy (Pinto et al., 2016; Walton et al., 2016b), which also found that the wind dominates the energy output of the source. Note that this agreement is remarkable given that these estimates are completely independent. The mechanical power of the NGC 1313 X–1 is comparable to that found for microquasars such as NGC 7793–S26 or M83 Q1 (Soria et al., 2014), which also display mechanical powers exceeding their radiative luminosities, whereas the estimated age is commensurate with other ULX bubbles such as the one around the ULX in NGC 5585 (Soria et al., 2021) or IC 342 X–1 (Cseh et al., 2012).

6.2.4.2 Age and explosion energy of the supernova remnants

We first consider the case in which these SNRs are in the free-adiabatic expanding phase, in which the expansion can be described by the well-known Sedov-Taylor self-similar solution. The radius of the SNR since the time of explosion (t) is defined solely by the initial explosion energy E and the density of the ambient medium (ρ):

$$R = \left(\frac{2.026E}{\rho}\right) = \left(\frac{2.026E}{\mu n_{\rm ISM} m_p}\right)^{1/5} t^{2/5} \tag{6.9}$$

for which we have assumed neutral hydrogen as in the previous Section. The expansion velocity is therefore:

$$V = \frac{2R}{5t} \tag{6.10}$$

. Using our estimates from Section 6.2.3.4 for the shock velocity and our estimates for $n_{\rm ISM}$ from Section 6.5, for a radius of 17.5 pc, we estimate $t_{\rm SNR1} = (16 \pm 2) \times 10^4$ yr and $t_{\rm SNR2} = (17 \pm 2) \times 10^4$ yr. However, the energies obtained under this assumption are $\sim 10^{49}$ erg, two orders of magnitude below the canonical value of 10^{51} erg. In fact, assuming a canonical energy of 10^{51} erg and using the analytical expressions from Cioffi et al. (1988), we find that the radius at which the Sedov-Taylor expansion stage ends are ∼ 19 pc and ∼17 pc for SNR 1 and SNR 2, respectively. It is thus possible that these are evolved SNRs that have already entered the so-called pressure-driven snow-plow phase, in which radiative losses become important (Cioffi et al., 1988). This might also be supported by the presence of several strong forbidden lines in their spectra (Figures 6.6 and 6.11).

We therefore refine our calculation by using the analytical expressions from (Cioffi et al., 1988, see also Fesen et al. (2020b)). Figure 6.20 shows the evolution of the radius and the SNR expansion velocity as a function of time. We find good agreement with the calculations for both the radii and the velocities assuming an initial explosion energy of 0.5 × 10^{51} erg. From the Figure, we estimate $t_{\rm SNR1} = 2.4 - 2.7 \times 10^4$ yr and $t_{\rm SNR2} = 2.5 - 3.4 \times 10^4$ yr (for a fixed $E = 0.5 \times 10^{51}$ erg). We find $0.3 < E < 0.8 \times 10^{51}$ erg as a plausible range of energies to match the observed radii and derived velocities.

We can do a similar exercise for the ULX bubble, assuming again that given its large size ($R > 130\,\text{pc}$; Table 6.5), it is also an evolved remnant in the snow-plough phase. The expression for the energy explosion in the radiative phase is (Cioffi et al., 1988):

$$E_{51} = 6.8 \times 10^{43} \left(\frac{R}{\text{pc}}\right)^{3.16} \left(\frac{v_{\text{exp}}}{\text{kms}^{-1}}\right)^{1.35} \left(\frac{n_{\text{ISM}}}{\text{cm}^{-3}}\right)^{1.16} \text{erg} \tag{6.11}$$

where following Cseh et al. (2012) we have also adopted the metallicity factor ξ_{m} as unity for simplicity. Taking the values from Table 6.5 we arrive at $E = 188$–990×10^{51} erg for the minor and major axes respectively, more than two orders of magnitude above the typical SNR explosion energy and in the range of estimates of other ULX bubbles (e.g. Pakull & Mirioni, 2002; Berghea et al., 2020). This is perhaps not surprising as SNRs are not expected to remain optically bright once expanded beyond $\sim 100\,\text{pc}$ for an input canonical energy of 10^{51} erg (Braun et al., 1989) and indeed the largest and oldest known SNRs have radii of just $\simeq 50\,\text{pc}$ (see e.g. Leahy et al., 1986; Williams et al., 2004; Fesen et al., 2020a, and references therein). Therefore these results are in good agreement with previous works (e.g. Pakull & Mirioni, 2002; Cseh et al., 2012; Urquhart et al., 2019; Berghea et al., 2020) which suggest instead that a continuous injection of energy is more likely to explain the cavities found around some ULXs. However, we note that we cannot exclude the possibility that the ULX perturbed the SNR that gave birth to the compact object. This would be akin to the case of the SS433/W50 nebula (Goodall et al., 2011, although see also Ohmura et al. (2021)) or its potentially younger version Circinus X–1 (Heinz et al., 2015; Coriat et al., 2019).

6.2.5 Conclusions

We have shown that NGC 1313 X–1 ionizes a region of 452 × 266 pc via EUV/X-ray excitation and shocks. Thanks to the simultaneous spectro-imaging capabilities of MUSE we have been able to diagnose the main sources of ionisation of the bubble in a spatially resolved manner: the inner regions close to the ULX show all the hallmarks of an X-ray ionised region, whereas the outer edges shows clear signs of shock-excitation. The latter is revealed by the strong broadening of the nebular lines at the edges of the bubble combined with the high line-of-sight velocity measured inside the bubble cavity close to the source, strongly suggesting that the bubble is being inflated by a wind. The elongated shape of the nebula may point to the presence of jet activity and thus radio observations would be of great interest here. Future observations probing high-excitation lines of the X-ray ionised nebula inside the bubble might be of interest to constrain the degree of beaming of the source.

The mechanical power is found to be in excess of 10^{40} erg/s, suggesting that the mechanical power of the source is comparable or even higher than the radiative throughput. This is in line with other estimates made by Pakull et al. (2010); Soria et al. (2014, 2021), suggesting that the mechanical feedback in the super-Eddington regime is superior to the radiative one. Obtaining a statistical sample of ULXs with estimated mechanical and radiative powers will be of interest to constrain the energy that goes into powering the wind, its dependency with the mass-accretion rate and its link with the class of less-luminous but with equally super-Eddington mechanical powers microquasars such as SS433 or NGC 300 S10 (Urquhart et al., 2019; McLeod et al., 2019). The high mechanical power of ULXs make them good sources for cosmic-ray acceleration (Inoue et al., 2017; Abeysekara et al., 2018), which could be targeted in the future with the Cherenkov Telescope Array (Consortium, 2011), the next-generation of ground-based gamma-ray observatories.

With this work we hope to have highlighted the promising avenue that IFU spectroscopy provides in our understanding of the ULX bubble nebulae and the energetic feedback of the super-Eddington regime.

Acknowledgements

The authors are deeply grateful to M. Pakull and R. Soria for their careful read and constructive comments on an earlier version of this manuscript. We would also like to thank M. Coriat for his helpful comments on the discussion related to the presence of any jet-like signature. We finally thank I. Pastor-Marazuela for her comments which lead us to investigate and discover the two SNRs. This work has made use of data obtained from the Chandra Data Archive as well as observations made with the NASA/ESA Hubble Space Telescope and obtained from the Hubble Legacy Archive, which is a collaboration between the Space Telescope Science Institute (STScI/NASA), the Space Telescope European Coordinating Facility (ST-ECF/ESA), and the Canadian Astronomy Data Centre (CADC/NRC/CSA). Software used: Python v3.8, mpdaf (Piqueras et al., 2017).

Appendix A: Line ratios of the shocked regions

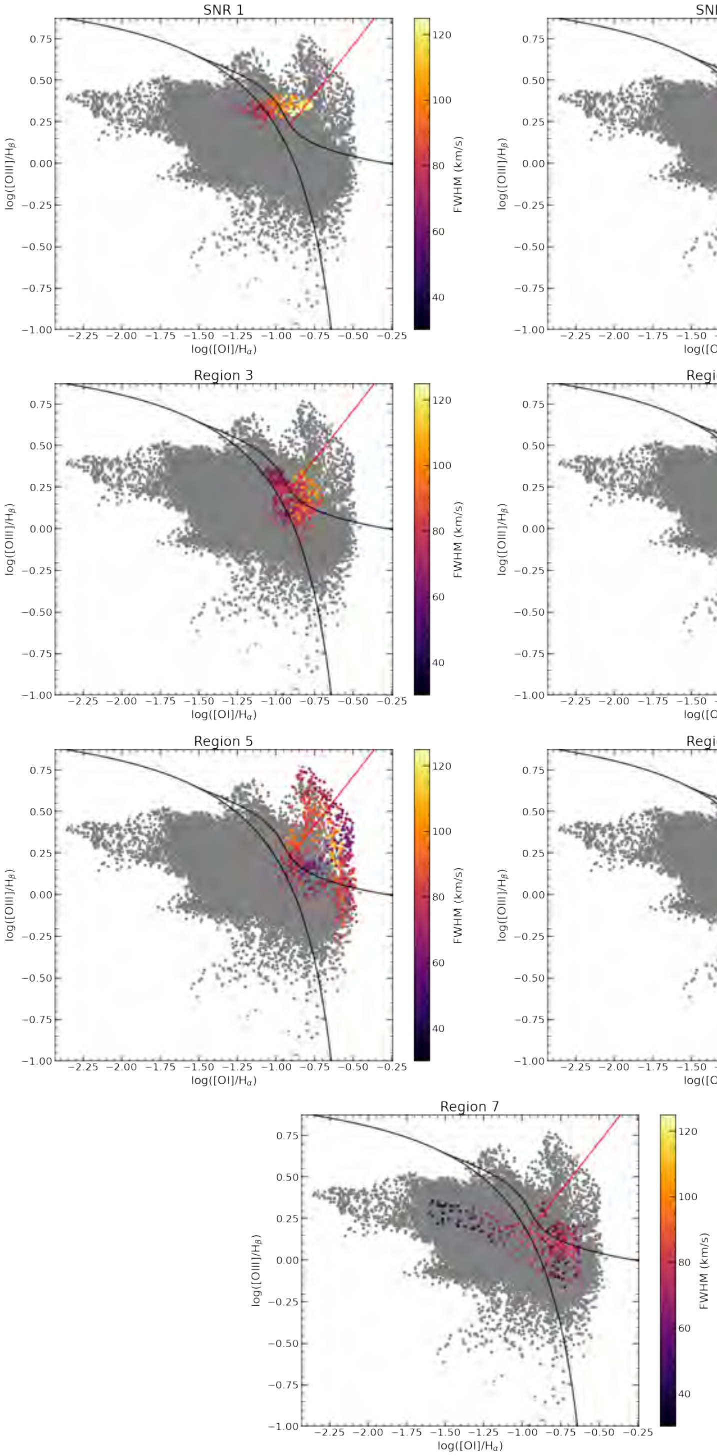

Figure 6.21: As per Figure 6.14 but showing only the different regions from Figure 6.7

6.3 The ‘Ultraluminous X-ray Sources’ in NGC 1672

NGC 1672 is a face-on barred spiral galaxy at a distance of $\sim$ 16.5 Mpc[12] with vigorous star-forming activity in its outer regions and a central low-luminosity AGN (Jenkins et al., 2011). The authors studied the impact of the bar structure on the nuclear activity using X-ray, infrared and radio data. They reported nine X-ray sources reaching observed luminosities $\gtrsim 10^{39}$ erg/s, with three notably brighter sources ($L_X > 5{\times}10^{39}$ erg/s). These sources were also reported in the catalogue of Liu & Mirabel (2005) as IXO 25, 26 and 27 which correspond to sources 4, 5 and 25 in the work of Jenkins et al. (2011). The galaxy had been observed by the VLT/MUSE in several occasions (PI E. Schinnerer), serendipitously caughting the sources in the FOV. Each source had a single data cube available, except for IXO 27 which was observed in three instances. Given the available MUSE, *HST* and *Chandra* data (see Section 6.3.1), I decided these sources could represent interesting targets to investigate any optical counterpart, check the robustness of the association with the galaxy and look for evidence for associated nebula emission. Each source had a single associated cube, except for IXO 27 that had three cubes available. However in this case I simply analysed the one which had better spatial resolution than the other two[13] (PSF FWHM $\sim$ 1" vs 1.4" corresponding to a physical distance of $\sim$ 80 pc and 112 pc respectively). Table 6.6 summarizes the details of the data cubes.

Table 6.6: Log of observations analysed in the study of the ULXs in NGC 1672.

Telescope	Detector	Obs id	Date	Exposure ks	Band	PSF arcsec	Source^a
VLT	MUSE	ADP.2018-01-15T14:29:04.642	2018-01-11	2.58	475-930 nm	0.75	IXO 25
VLT	MUSE	ADP.2018-01-09T21:47:27.849	2017-12-19	2.58	475-930 nm	0.9	IXO 26
VLT	MUSE	ADP.2018-01-09T17:16:55.903	2017-12-26	2.58	475-930 nm	1.06	IXO 27
HST	ACS/WFC/F550M	j95801020	2005-08-01	2.444	5500-5662 Å	~0.1	All
HST	ACS/WFC/F658N	j95801040	2005-08-01	2.444	6834-6871 Å	~0.1	All
Chandra	ACIS	5932	2006-04-30	40.16	0.3-10 keV	-	All

Notes. $^{(a)}$ Source observed.

As stated in Section 6.2.2 I needed *HST* images to correct the astrometry of the cube. I therefore retrieved an image in the F550M (5247–5930 Å) filter for the astrometric correction and counterpart identification, and one in the F568N (6510–6659 Å) to inspect any evidence of diffuse Hα emission around the sources. Because the counterparts of the sources in question had not been identified, I also retrieved the only *Chandra* observation available for the galaxy, in order to identify the position of the X-ray sources in the optical images. I also studied their X-ray spectra in order to gain insight into their nature. The specifics of these observations are also listed in Table 6.6.

The astrometric alignment between the *HST* and the *Chandra* images was carried out by aligning both images to the *Gaia* (Prusti et al., 2016) DR2 catalogue (Gaia Collaboration et al., 2018), as not enough source pairs were found between the *Chandra* and the *HST* images. The source detection in the *Chandra* images and alignment was performed using `CALDB` 4.9.3 and `CIAO` 4.12 with the tasks `wavdetect` and `wcs_match` respectively. Six source pairs were found between the *Chandra* and the *Gaia*, leaving a 1σ residual of 0.24". The position of the ULXs in the *Chandra* image had all a comparable statistical 1σ uncertainty of ~0.02". For the alignment between the *HST* image and the *Gaia* catalogue, I used the task `tweakreg` from the `AstroDrizzle` package[14]. 22 and 32 matches were found between the sources in the F550M and F658N images and the *Gaia* sources, with residuals all below 0.01" (3σ level), adding a negligible contribution to the total positional uncertainty. Adding all the errors in quadrature, I estimated a 3σ uncertainty of 0.73" for the X-ray position of the ULXs in the *HST* images. I considered the same uncertainty for the data cube. Even if there is some additional uncertainty in the alignment between the MUSE and the *HST* images, since these two images cover approximately the same wavelength range the result can be easily visually inspected and the agreement was found to be satisfactory. Furthermore, as we will see, the exact uncertainty level on the position of the data cube is not as relevant as for the *HST* images, since at these distances the counterpart is far from being resolved in the MUSE data cube. It is only in the *HST* images where we can aim to identify the counterpart and thus where the error circle is be more relevant. The *HST* images along with the MUSE equivalent *HST*/ACS/F550M image are shown in Figure 6.22 for the three ULXs.

There are several sources within each error circle and thus the counterpart cannot be uniquely identified in any case. Extracting the main properties of the counterpart candidates is left for a future work. Here I focus on deriving the main physical conditions of the gas around the sources in order to look for evidence of nebular emission associated with the ULXs.

---

[12] Average of the two measurements found in Simbad.

[13] The exposure time was the same in all three cubes.

[14] https://drizzlepac.readthedocs.io/en/latest/tweakreg.html

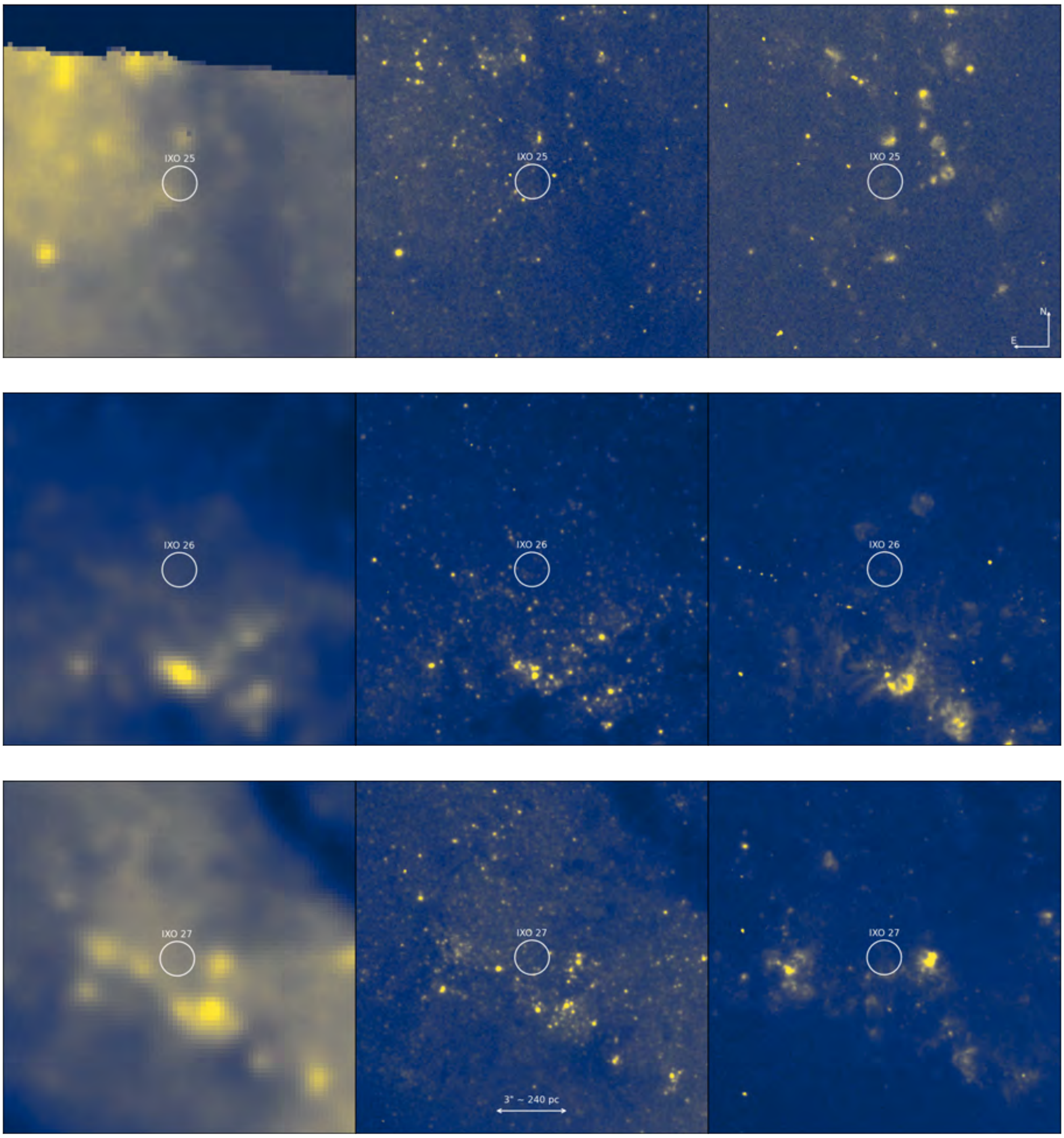

Figure 6.22: MUSE image in the equivalent *HST*/ACS/F550M filter (left), *HST*/ACS/F550M (middle) and *HST*/ACS/F658N images showing a 15"×15" FOV around each of the ULXs. The white circle in all images shows the 3σ positional uncertainty. From top to bottom, the images show the fields around IXO 25, 26 and 27 respectively. The orientation and scale are the same for all images.

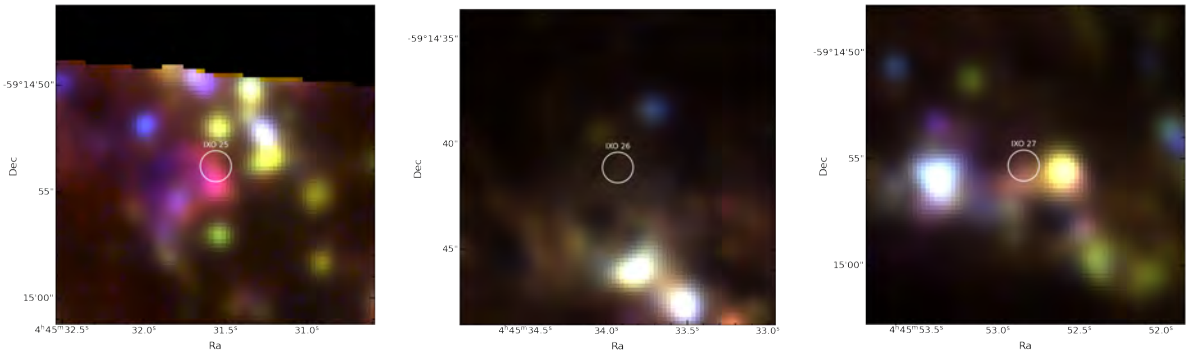

Figure 6.23: RGB images combining the Hα (green channel), the [OIII]λ5007 (blue channel) and the [SII]λ6731 (red channel) lines for the IXO 25 (left), IXO 26 (middle) and IXO 27 (right), showing the same FOV as per Figure 6.22.

Fluxes and kinematics from the main nebular lines were extracted using CAMEL as described in Section 6.2.3.1 and pixels with a S/N $<$ 5 were masked. Figures 6.23 show RGB images for the three ULXs combining the Hα (green channel), the [O III]λ5007 (blue channel) and the [SII]λ6731 (red channel) lines.

Inspection of these images shows that there seems to be some enhanced [SII]λ6731 emission around IXO 25, which may point to the presence of shocks. Conversely, there is no clear enhanced emission around IXO 26 (note the large scales involved as 15" $\sim$ 1200 pc). For IXO 27, the bright spots at the east and west of the source correspond to the bright sources clearly resolved in the *HST* images (Figure 6.22), thus again there does not seem to be apparent nebular emission associated with this ULX.

To obtain a more quantitative view on the different contributions of each nebular line, I finally derived spatially resolved BPT diagrams around each of the ULXs as explained in Section 6.2.3.3. Figures 6.24, 6.25 and 6.26 show the resulting diagrams for IXO 25, 26 and 27 respectively. These maps essentially confirm what was already hinted in the RGB images. Briefly, IXO 25 seems to be associated with a region were shocks and/or EUV/X-ray excitation might be important, as the nearby pixels are classified as Intermediate/AGN or LINER. The region were the pixels are classified as AGN is at $\sim$ 40 pc from the ULX, which is a reasonable distance considering the sizes of known ULX nebulae (cf. Table 3.2). However, this elongated region seems to be associated with a larger structure from the galaxy, and it is not clear whether we can associated the excitation to the ULX itself. For the ULXs IXO 26 and 27, there is no indication of activity of the ULXs themselves. This could indicate that these sources are instead background AGNs, something that seems to be supported by the X-ray analysis in the case of IXO 26 (Section 6.3.1).

I finally present the line-of-sight velocity maps for the Hα-[NII] complex in Figure 6.27. At least from these maps, we cannot rule out any of the ULXs as *not* belonging to the galaxy, but if some of these are background objects, it could well be that we are simply observing the foreground stars or gas from the galaxy itself. There seems to be some motion around IXO 25, which could hint the presence of shocks. IXO 26 shows two spots east and west to the source, but the absence of shocks in these regions suggest that this is a mere spatial coincidence. Finally there is no appreciable difference between the velocities around IXO 27 with respect to the nearby gas.

Investigation of these sources is ongoing. The nebular emission near IXO 25 warrants further investigation. Gas temperature estimates using the [N II] lines (which I note they are all well detected) and comparison with radiative shock libraries will allow to discern whether the gas is being shocked or ionized, although it might be challenging to robustly confirm the association of this ionized gas with the source. I will also derive metallicity maps around the sources, which could also provide some clues as to whether the sources belong to the galaxy. As stated above, metallicity estimates are also of interest to understand the formation pathways that lead to ULX-like binary systems.

6.3.1 X-ray spectral analysis

In order to gain more insight in the nature of these sources, I reanalysed the X-ray data that had been presented by Jenkins et al. (2011). The authors noted that owing to the low number of counts, a simple powerlaw offered a satisfactory fit to the data and did not investigate the spectral shape any further. For this reason, I decided to investigate whether I could provide more evidence in favour of some sources being bona-fide ULXs. The data was reduced as outlined in Section 6.2.3, but with updated `CALDB` 4.9.3 and `CIAO` 4.12. As stated in Section 6.2.3 I used the regions given by the `wavdetect` tool to extract the source events. The number of total counts for IXO 25, 26 and 27 were $\sim$800, 800 and 1300 respectively. Because of the rather limited number of counts, I rebinned the data with the rebinning method proposed by Kaastra & Bleeker (2016), which takes into account the response matrix of the instrument as well as the number of counts in each bin to provide an optimal rebinning scheme.

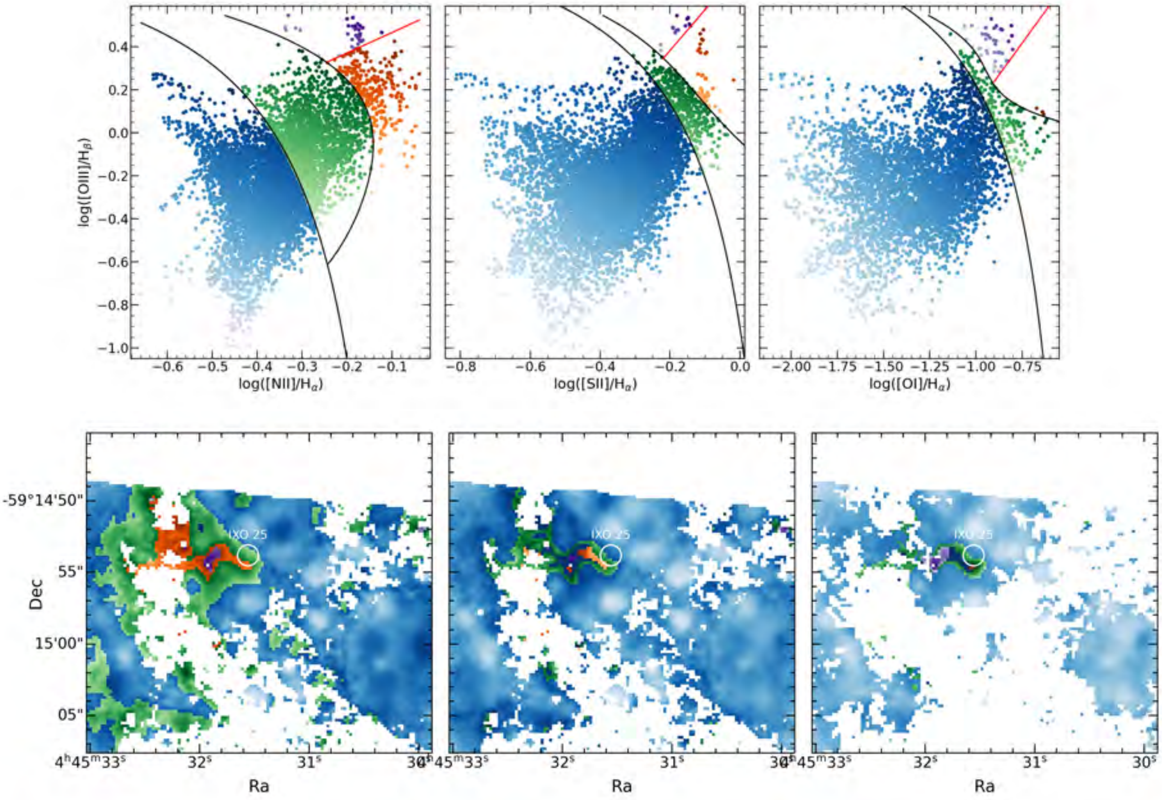

Figure 6.24: Spatially resolved BPT diagrams using the classification scheme from Law et al. (2021). Blue, green, purple and orange colored regions show regions classified as HII, intermediate, AGN or LINER, respectively. Each data point is colored as the sum of the x and y axis (from the top panel) to ease the visualization. White regions had some lines with S/N < 5.

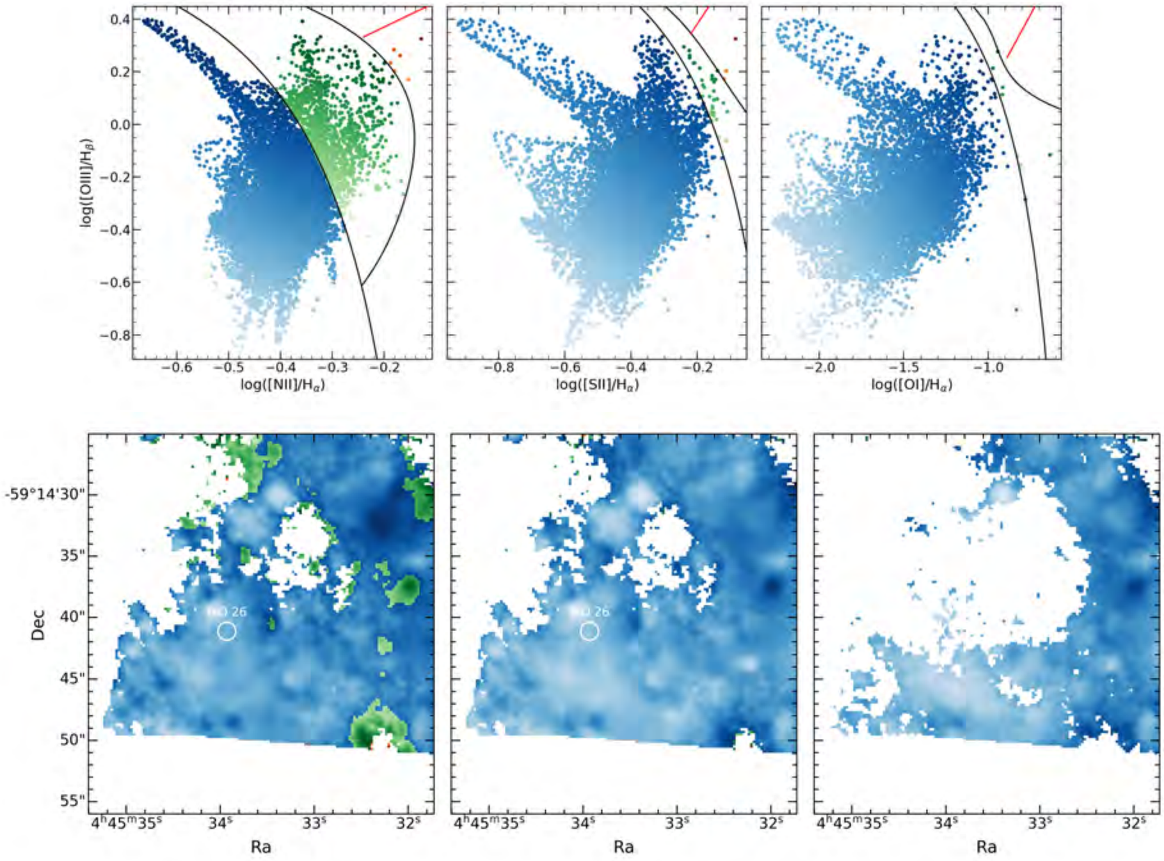

Figure 6.25: As per Figure 6.24 but for IXO 26.

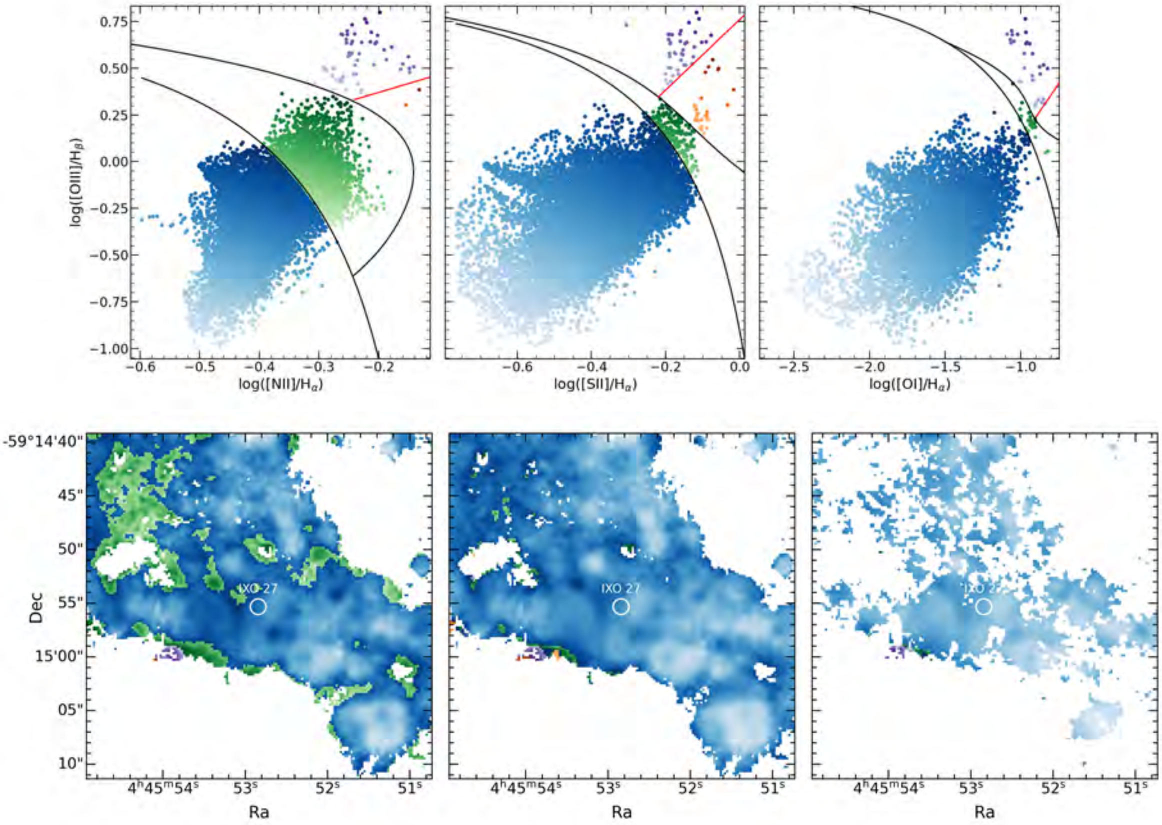

Figure 6.26: As per Figure 6.24 but for IXO 27.

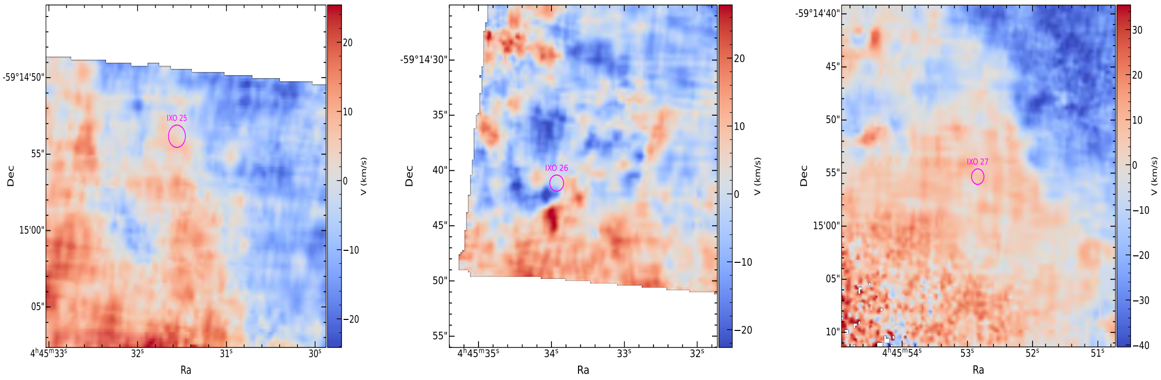

Figure 6.27: Velocity along the line of sight over the systemic velocity of NGC 1672. The median value has been subtracted to reflect local velocities more closely. The grid-like structure seen in some areas is due to noise. The typical 1σ on these maps is 1 km/s.

Table 6.7: Best-fit parameters and their uncertainties (90% confidence level) from the X-ray analysis of the *Chandra* data.

Source	$n_{\rm H}$ 10^{21}cm^{-2}	Γ	E_c keV	kT$_{\rm in}$ keV	L[0.5-7 keV]^a 10^{39} erg /s	$\chi^2_{\rm r}$/dof
			`powerlaw`			
IXO 25	3.2 ± 0.9	2.1 ± 0.2	-	-	5.1 ± 0.4	1.02/47
IXO 26	$0.1^{+0.9}_{b}$	$1.08^{+0.2}_{-0.1}$	-	-	5.7 ± 0.5	0.94/54
IXO 27	$3.4^{+0.9}_{-0.8}$	1.7 ± 0.2	-	-	$11.3^{+0.8}_{-0.7}$	0.87/48
			`cutoffpl`			
IXO 25	$1.4^{+1.8}_{b}$	0.9 ± 1	2.2^{+15}_{-1}	-	5.1 ± 0.4	0.97/46
IXO 26	0^b	$1.02^{+0.2}_{-0.1}$	50^{b}_{-39}	-	5.7 ± 0.5	0.96/53
IXO 27	2^{+2}_{-1}	$0.5^{+0.8}_{-0.9}$	2^{+5}_{-1}	-	9.3 ± 1	0.77/47
			`diskbb`			
IXO 25	0.6 ± 0.6	-	-	1.1 ± 0.1	5.0 ± 0.4	0.97/47
IXO 26	0^b	-	-	$2.6^{+0.8}_{-0.5}$	5.5 ± 0.6	1.12/54
IXO 27	$1.4^{+0.6}_{-0.5}$	-	-	1.4 ± 0.2	9.1 ± 0.6	0.75/48

Notes. $^{(a)}$ Absorption-corrected luminosity. $^{(b)}$ Unconstrained parameter.

This maximizes the data quality and avoids oversampling problems. Because this rebinning scheme does not guarantee the ∼20 counts/bin needed to use χ^2 statistics (Cash, 1979), I inspected the spectra and verified that this was the case over the 0.5–7 keV band. The sources were thus fitted in this band using χ^2 statistics in XSPEC version 12.11.1, with three different simple models: a powerlaw, a powerlaw with a high energy cutoff (`cutoffpl` in XSPEC) or a standard thin accretion disk model (`diskbb` in XSPEC) all subject to interstellar absorption modelled with `tbabs` (Wilms et al., 2000), using the abundances of Verner et al. (1996). Note that owing to the low effective area of *Chandra* above 7 keV and the relatively low number of counts it is unlikely that we will be able to detect the downturn characteristic of the ULX spectra, as this is only seen in high-quality *XMM-Newton* data (e.g. Gladstone et al., 2009). Nevertheless, I also tested this model for completeness. The results are shown in Table 6.7 and Figure 6.28.

From these results, it is clear that IXO 25 and IXO 27 show very similar properties. When using a powerlaw or a cutoff powerlaw, a certain level of absorption above the Galactic line-of-sight value[15] is needed to provide the curvature at soft energies. The powerlaw or the cutoff powerlaw offer equally satisfactory fits, so neither the cutoff at high-energies or a pure powerlaw can be rejected on the basis of this data. In contrast, it is clear that IXO 26 is harder and well modelled with a simple powerlaw with negligible absorption (inconsistent with the Galactic value), as it does not present neither curvature at low or high energies. The inner disk temperature obtained with the `diskbb` model ($kT_{\rm in} > 2.1$ keV) seems also abnormally high when compared to XRBs or ULXs (cf. Sections 2.1.1 and 3.2.1). Based on the absence of associated nebular optical emission and the X-ray powerlaw-like spectrum, I suggest that IXO 26 likely represents a background AGN. Instead IXO 25 and IXO 27 could be bona-fide ULXs, albeit further investigation is needed. Based on this analysis, we may expect IXO 26 to be rather constant over year timescales, whereas high-levels of variability in IXO 25 and 27 may be in line with our expectation. From the work of Jenkins et al. (2011), who also fit an *XMM-Newton* observation taken two years prior to the *Chandra* observation using powerlaws, we can see that IXO 26 was found at the same luminosity level in both epochs, whereas IXO 25 and 27 were dimmer by a factor ∼ 5 and 2–3 respectively, which may support these findings. I note here that *Swift* has monitored NGC 1672 for a cumulative exposure of 36.6 ks, which may provide some additional hints on the nature of these sources. Lastly, studying the spectral variability from the *XMM-Newton* observation will also provide additional information on these sources.

6.4 Evidence for a Young System in the Pulsating NGC 300 ULX1?

NGC 300 ULX1 is one of the few known pulsating ULXs (see Section 5.1.4.1 and Binder et al., 2020, for a review on the source). The system was first misclasssified as supernova (SN 2010da) when it went into outburst in 2010. Four months later an associated X-ray source was found by Binder et al. (2011), who suggested that the system could instead be a HMXB hosting an accreting NS, based on the hardness of the X-ray spectrum. Pulsations ($P \sim 31$ s) in X-rays were detected by Carpano et al. (2018), establishing the nature of the accretor as a NS. The system reached an unabsorbed X-ray luminosity of $\sim 4 \times 10^{39}$ erg/s during the 2016 outburst when the pulsations were detected, establishing the source as a ULX. The companion was later revealed to be a

---

[15] This is $\sim 1.7 \times 10^{20}$ cm^{-2} for all three sources (HI4PI Collaboration et al., 2016).

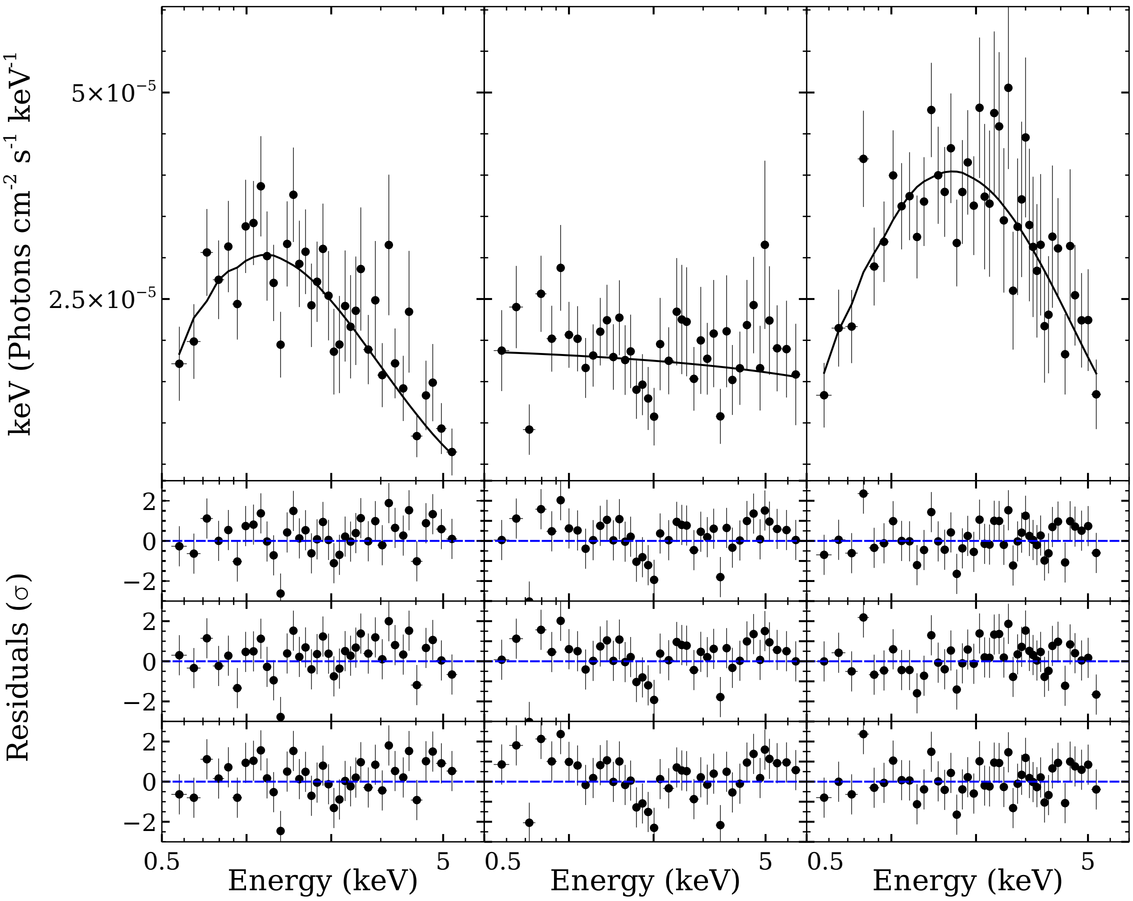

Figure 6.28: (top) Best-fit cutoff powerlaw model for the three ULXs in NGC 1672. The lower panels show the residuals for the `cutoffpl` (top), powerlaw (middle) and `diskbb` (bottom) models.

Table 6.8: Log of observations used in the study of NGC 300 ULX1.

Telescope	Detector	Obs id	Date	Exposure ks	Band	PSF arcsec
VLT	MUSE	ADP.2018-01-15T14:29:04.642	2016-10-05	2.7	475-930 nm	1.4
HST	ACS/WFC/F606W	jcfp04010	2014-07-02	2.4	5585-6257 Å	~0.1

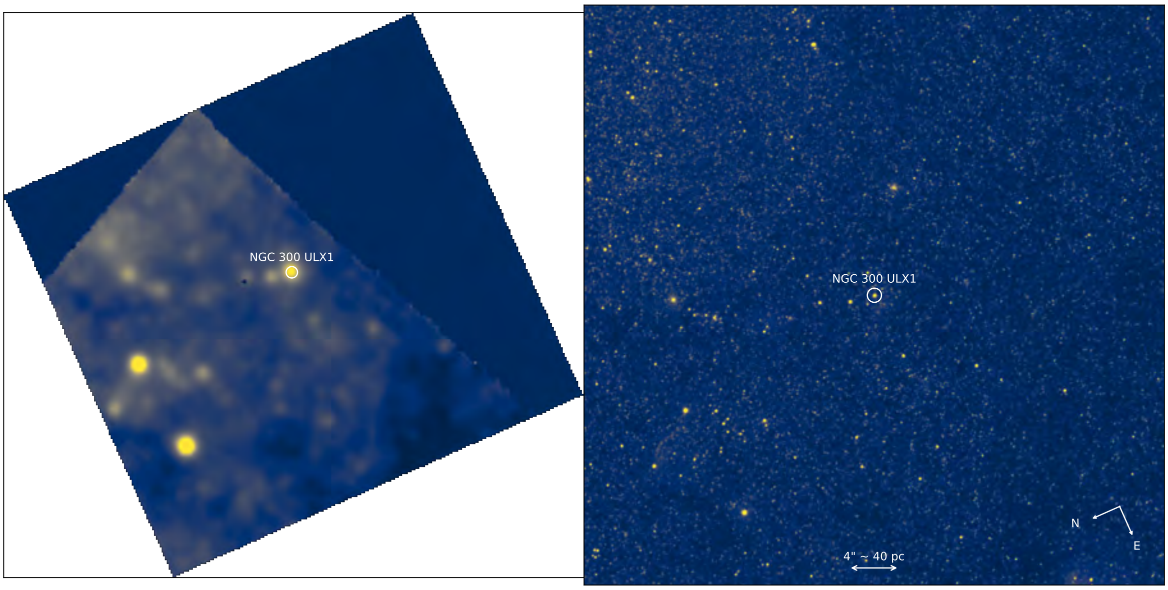

Figure 6.29: (left) MUSE ACS/WFC/F606W equivalent image and the *HST*/WFC/ACS/F606W (right) showing a 50"×50" field around NGC 300 ULX1 (indicated with a white circle in both images).

red supergiant through IR spectroscopy (Heida et al., 2019), confirming the that the system is a HMXB. Binder et al. (2016) put an upper limit on the age of the system of 5 My using colour-magnitude diagrams. The absence of X-ray emission prior to the 2010 outburst and the relatively young age of the system suggest that this event might have represented the onset of the mass-transfer from the companion to the NS (see Binder et al., 2016, and references therein).

MUSE mapped the NGC 300 spiral galaxy in 2016-2018 (PI A.F. McLeod) in the WFM, observing NGC 300 ULX1 serendipitously in one instance. Given the relatively proximity of the galaxy (D = 2.08 Mpc; Lelli et al., 2015), it represented an excellent target to study the presence of a bubble around a PULX. Given that the optical counterpart had been identified (Binder et al., 2011), I only aligned the MUSE cube with an *HST* image to correct its astrometry. I used an *HST* image in the F606W (4626–7179.31 Å) for the reasons outlined in Section 6.2.2. Table 6.8 summarizes the details of the data cube and the *HST* image. At a distance of 2.08 Mpc, the MUSE WFM pixel scale of 0.2" and the 1.4" FWHM PSF represent a physical distance of 2 pc and 14 pc respectively.

Fluxes and kinematics from the main nebular lines were extracted using CAMEL as described in Section 6.2.3.1 and pixels with a S/N $<$ 5 were masked. Figure 6.30 shows a RGB image of the field around NGC 300 ULX1 combining the Hα (green channel), the [O III]λ5007 (blue channel) and the [S II]λ6731 (red channel) lines. We can see that the emission is dominated by the Hα line and small amount of [O III]λ5007, but there is barely any [S II]λ6731 emission (this is shown more clearly below when extracting the spectrum of the counterpart). From this image it is not strictly clear whether the emission is extended or point like.

I therefore inspected whether the emission was consistent with the PSF of the data cube. To do so, for a given line (e.g. Hβ in Figure 6.31 left panel), I compared the encircled flux fraction as a function of radius of each line map with the PSF. The PSF was derived by identifying a star in the FOV and creating an image around the line of interest (e.g. Hβ, Figure 6.31 middle panel) by summing all the pixels in a $[-5\sigma_{\mathrm{H}\beta},\ 5\sigma_{\mathrm{H}\beta}]$ window to enhance the S/N, where $\sigma_{\mathrm{H}\beta}$ is the standard deviation of the fitted line centroid in the original map. I fitted a 2D circular Moffat profile (suitable to model the MUSE PSF) to this Hβ image. Then I derived the flux encircled in this 2D Moffat profile within the same radii as for the observed line map. To estimate the uncertainties in the observed profile, I created 1000 images by drawing fluxes and central wavelengths for each pixel based on the uncertainties of these two parameters in the observed maps.

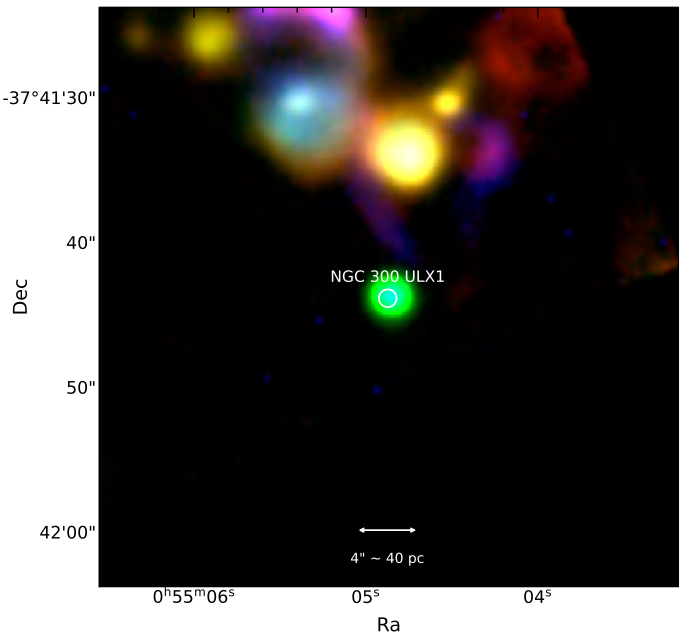

Figure 6.30: RGB image of the field around NGC 300 ULX1 combining the Hα (green channel), the [OIII]λ5007 (blue channel) and the [SII]λ6731 (red channel). The image shows a 40"×40" region.

For each sample image, I then repeated the same estimation of the encircled flux fraction as for the original image, retrieving the 68% confidence level on the derived profiles as the uncertainty for the observed profile. Similarly for the PSF, the same approach was followed by creating 1000 images by sampling from the uncertainties on the Moffat profile parameters (the continuum, the FWHM, and atmospheric scattering coefficient). The results for the Hβ line is shown in Figure 6.31 in the right panel. Similar results were found for the other lines.

We see now robustly that there is no sign for extended emission as the source is consistent with being point like. This is consistent with the work of Binder et al. (2018) and the *HST* observations, which show no evidence for nebular emission. Binder et al. (2018) suggested that the light from the 2010 outburst could have travelled only to a radius of ~2.5 pc in 8 years, which is well below the MUSE PSF of 14 pc. Therefore, NGC 300 ULX1 might be a young ULX which has yet to create a nebula!

We can finally extract a spectrum of the counterpart. To do so, I integrated the pixels enclosing 90% of the flux around the peak emission of NGC 300 ULX1, and weighted the contribution of each annulus using the PSF profile. The resulting spectrum is shown in Figure 6.32[16]. A full analysis of the spectrum is beyond the scope of this work but I mention here a few interesting points. A very detailed optical spectral analysis of the counterpart (and with much higher spectral resolution) was presented by Villar et al. (2016). Most of the lines identified in the MUSE spectrum were also reported by these authors and Binder et al. (2018). Remarkable is the lack of strong [SII] lines, indicating that contribution from shocks is negligible. The [OIII]λ5007/Hβ is $\sim$ 0.4 (consistent with the 0.5 value reported by Binder et al., 2018), which is not particular high. Compared to the $\gtrsim$ 3 value found for NGC 1313 X-1 (Section 6.2), we can see that EUV/X-ray photoionization is not particularly important. This is consistent with the notably higher and much persistent L_X of NGC 1313 X–1 (a factor 10 or more). The Balmer lines are extremely broadened and three to four Gaussian components are required to fit them (FWHM $\gtrsim$ 400 km/s) (see also Villar et al., 2016).

---

[16] The background subtraction was neglected owing to the brightness of the source.

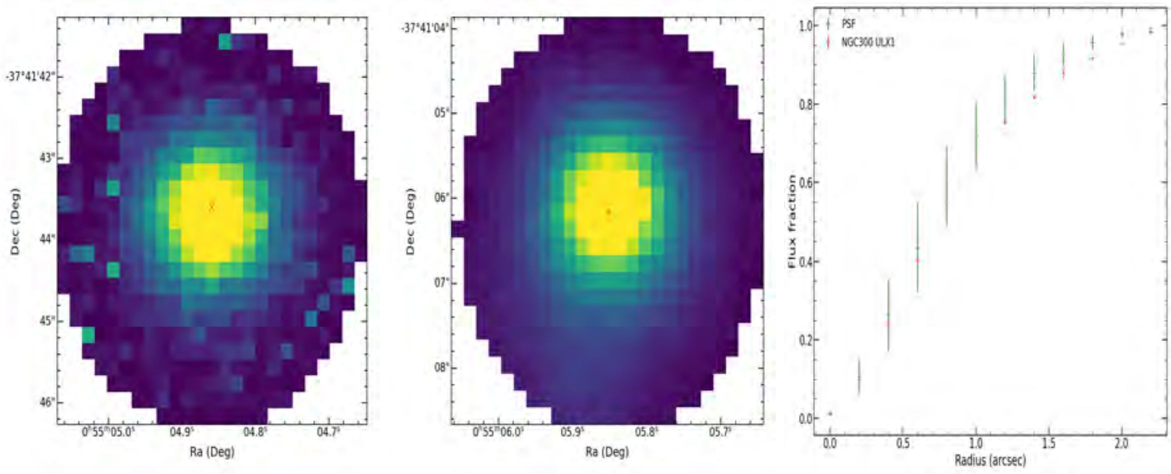

Figure 6.31: (left) Hβ flux map centered at the position of NGC 300 ULX1. (middle) Integrated image around the Hβ line for a star in the FOV of the MUSE data cube, which was used to estimate the PSF profile. (right) Comparison between the observed Hβ PSF profile for NGC 300 ULX1 and the PSF derived using the star. The uncertainties are given at the 1σ level. There is no indication of extended emission in the profile of NGC 300 ULX1.

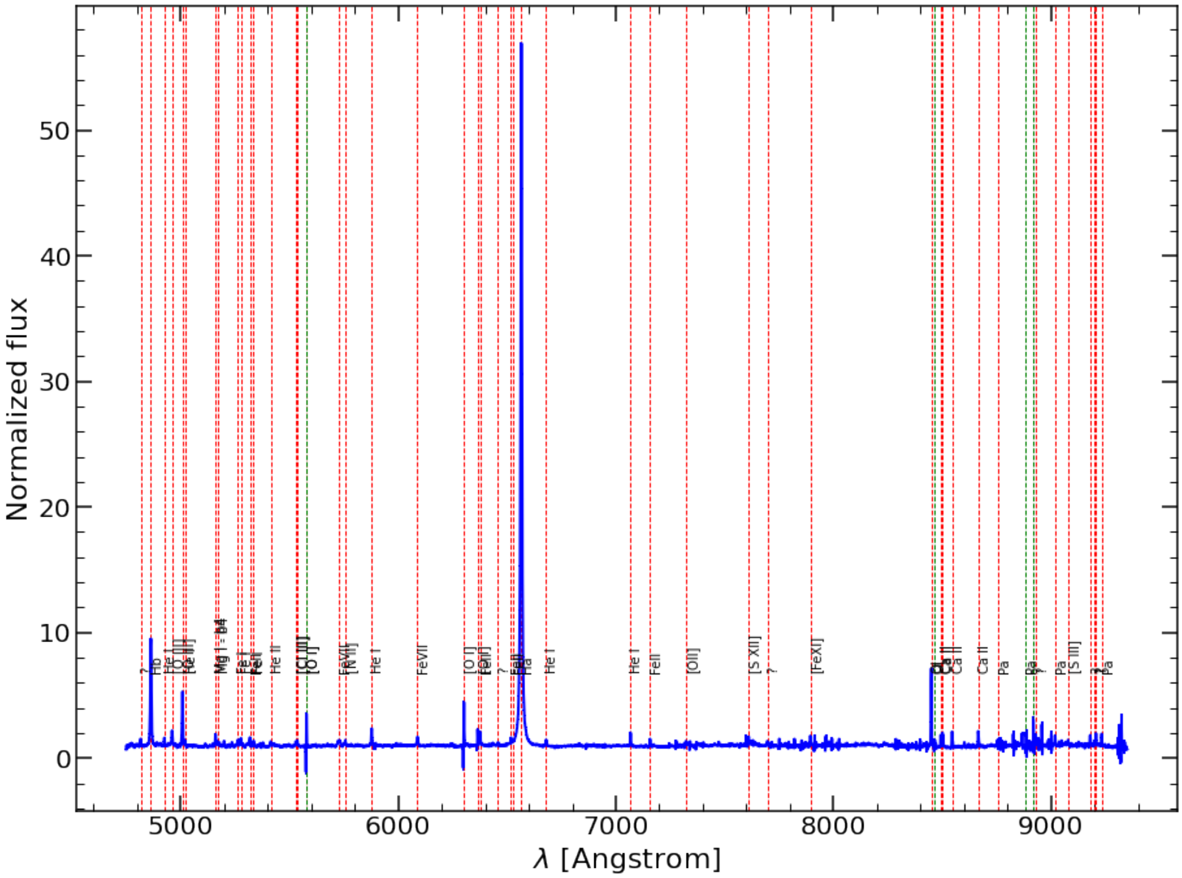

Figure 6.32: The optical spectrum of NGC 300 ULX1 with some identified lines. Red shows emission lines and green absorption lines. The spectrum has been normalized by the estimated continuum. Residuals around the [OI]λ6300 are due to the sky correction.

Chapter 7

Conclusions & Perspectives

As we have seen, thanks to the gradual accumulation of data, ULXs, notably those with $L_X \lesssim 10^{41}$ erg/s, have evolved from a mere empirical definition to a class of its own: stellar-compact objects power by sustained super-Eddington accretion over year/decade timescales. Thereby ULXs offer an accessible observational template to study this poorly understood accretion regime, thought to have played a role in the rapid growth of SMBHs.

Through a multi-wavelength study in X-rays, optical and to lesser extent UV, employing X-ray spectral modelling and timing analysis, IFU spectroscopy, and optical photometry, I carried out a study of several ULXs in order to investigate the accretion flow geometry in the super-Eddington regime, the nature of the accretor and their powerful radiative and mechanical feedback on the parsec-scale environment. Answering these issues is on itself relevant to ULXs, to improve our understanding of ULX physics and to draw interesting implications of their role in shaping their host galaxy properties (e.g. Simmonds et al., 2021), in hope that we can extrapolate back to the case of the high-redshift SMBHs, and understand whether super-Eddington accretion could have been an efficient process to grow these BHs and to what extent the radiation and outflows shaped their host galaxies.

In the first part of this thesis, in Chapter 5, I focused on tackling the first two issues by using X-ray spectroscopy and timing analysis. In the first part, I built a sample of 17 ULXs with 6 known NS-ULXs to present a comprehensive study of their spectral transitions. Here I have shown that PULXs are among the hardest sources in my ULX sample. According to the most recent models (e.g. Mushtukov et al., 2019), high magnetic fields ($B \gtrsim 10^{12}$ G) can suppress the development of outflows, if the disk is truncated before becoming supercritical. I suggested that the differences in hardness and hardness variability could be due to this interplay between the magnetospheric and spherization radius. Weakly magnetised NSs ($B \lesssim 10^{12}$ G), of which I argued NGC 1313 X–2 was a prototypical example, can develop a supercritical disk/funnel geometry before the disk is truncated. In such cases, Compton-down scattering by the cool electrons within the optically thick walls of the funnel and the outflow itself can explain the source low pulsed fraction, softer appearance and high-hardness variability as a result of the highly anisotropic emission. Therefore, the source properties will in turn depend strongly on the inclination of the line of sight with respect to the inner structures of the in-/out-flow. Conversely, strongly magnetised NSs, have reduced outflows, larger pulsed fractions, hard spectrum and low-hardness variability as a result of their much less anisotropic emission expected in this case. While the difference in hardness in ULXs were previously attributed to an inclination-dependent effect (e.g. Sutton et al., 2013), this has been challenged by the detection of orbital dips in M51 ULX–7 (Vasilopoulos et al., 2021), which is among the hardest ULXs. This could indicate that indeed there are other variables at play, such as the magnetic field as suggested. With only around seven known PULXs, the sample is still very limited, and more objects are needed to explore these differences in detail. Constraining the inclination of these systems is also crucial to help reducing degeneracies when attempting to understand what parameters drive the differences between these systems (e.g. mass-accretion rate, nature of the accretor, inclination, etc).

For this reason, I also investigated the nature of the accretor. I provided indirect evidence for one BH- and one NS-ULX candidates based on their spectral properties. M81 X–6 was deemed as the best NS-ULX candidate of the sample due to their similar long-term spectral evolution to that seen in NGC 1313 X–2. This sparked the interest of Gianluca Israel and Guillermo Andrés Rodriguez-Castillo (from the Osservatorio Astronomico di Roma and Istituto di Astrofisica Spaziale e Fisica Cosmica di Milano respectively), who kindly searched for pulsations in the longest *XMM-Newton* observation taking into account orbital corrections. This yielded a 3σ upper limit on the pulsed fraction of 10%. Investigation on this source is still ongoing: recently, Roberta Amato (postdoc at IRAP) has found additional unpublished archival *Chandra* observations on the source, which have confirmed that the source follows the same bi-modal behaviour presented in Section 5.3.2. A preliminary search for pulsations has not yielded any detection, but this might be due to *Chandra*'s limited timing resolution ($\sim$ 3.2 s). Another *XMM-Newton* observation has recently become publicly available, but unfortunately, the source is caught at the edge of the FOV and with only ~27 ks of total exposure, this observation is unlikely to provide a clear answer, as we have already seen how challenging it is to detect pulsations. Requesting new *XMM-Newton* observations remains also challenging as the source is only observable during brief periods of time (<40 ks) with *XMM-Newton*. Another challenge is posed by the fact that we do not know why or what is causing the appearance/disappearance of pulsations. It is possible that a definite answer on the nature of the accretor in M81 X–6 will have to await the ESA's upcoming cornerstone Advanced Telescope for High-ENergy Astrophysics (*Athena*) mission. *Athena* is expected to fly in early 2030 and it will carry the X-ray IFU (X-IFU; Barret et al., 2018) instrument, which will provide high resolution X-ray spectroscopy ($\delta E \sim$ 2.5eV < 7 keV) over the 0.2–10 keV band with an effective area ∼ 15 times that of *XMM-Newton* EPIC–PN, representing a giant leap in performance with respect to any precedent and upcoming mission for the next decade. Coupled with its good timing resolution of ∼ 10 μs and fine spatial resolution of 5", the X-IFU will be a game changer in the quest for NS-ULXs.

I also noted a lack of variability at high-energies (> 10 keV) in NGC 1313 X-1 and Holmberg IX X–1, whose origin is still unclear, but seems to support a low inclination angle. Unfortunately I could not support this with the MUSE observations of NGC 1313 X-1, which I discuss below. I also suggested that the stability at high-energy may be more easily understood if the accretor in these sources are BHs, as they can swallow the excess energy produced in their vicinity through advection, but again this will depend on the exact mechanism creating this emission. Beyond indirect evidence on ULXs slightly above the Eddington limit (e.g. Middleton et al., 2013), the case for a firm BH-ULX still awaits definite confirmation. In this regard, radio variability of the proposed BH-ULX candidate might be of interest to see if it belongs to the same category as the microquasar in M31 (XMMU J004243.61412519;; Middleton et al., 2013).

I also segregated the sample into sources sharing similar properties, which will be useful in future in cases where information from one source is missing but is available for another one that is akin. This is exemplified in the follow-up study I performed on Holmberg II X–1 and NGC 5204 X–1, where I showed the first evidence for an evolutionary cycle by combining all the X-ray data available in these two sources (Section 5.2). This cycle might be the analogue of the q-shape diagram seen in BH binaries (Section 2.1.1), but for the super-Eddington regime. It remains to be seen what is conferring these two sources such striking similarities, is it the same orbit/companion configuration and therefore similar mass-transfer rates? Is it simply similar mass-transfer rate albeit having different accretor-to-companion mass ratios? If we can draw an analogy from the q-shape diagram, in which the cycle outlines a common accretion flow properties and accretor (i.e. a BH), we may suggest that these two sources host the same accretor. While this remains to be investigated, these two sources provide an excellent benchmark to test theories of the super-Eddington accretion, by coordinating multi-wavelength observations when the sources are found in the different spectral states. The supercritical funnel is compelling because it may account for the observed variability, due to the dependency of the opening angle of the funnel with the mass-accretion rate and the short-term variability induced by wind clumps. If the broadband emission (including optical and UV) can be modelled in all three states with the same physically motivated model, these claims could be corroborated by examining the spectral parameter variations. It is also likely that some improvement in the current available models might be needed.

Moreover, precession of the accretion flow could not be completely ruled out to explain the transitions between the two soft states (the soft and the supersoft states). Albeit I was not able to confirm this scenario, it is interesting to note that Holmberg II X–1, the source for which I could study in more detail these transitions, always reaches similar maxima and minima between the soft transitions, which may argue in favour of precession (Figure 7.1). Qualitatively, the behaviour is in good agreement with the lightcurves modelled by Dauser et al. (2017) expected from a precessing supercritical funnel. In essence, even if the inner accretion flow precesses, we do not expect variability in the hard state due to the high opening angle, whereas strong flux variations are expected as soon as the inclination is higher than the half-opening angle, likely with additional stochastic variability imprinted by the wind (which are not taken into account in the Dauser et al. (2017) model). In this regard, Holmberg II X–1 is still being monitored by *Swift*, and I could confirm that the source has gone back to transiting between the two soft states as shown in Figure 7.1. This also confirms that indeed the cycle is recurrent and could help constraining its timescale.

I plan to investigate whether the spectral changes between the soft states show any evidence for a periodicity consistent with the ∼ 28-day periodicity found in (Gúrpide et al., 2021b). This will settle whether these transitions are periodic or not, and I will be able to consider whether wind clumps or precession are a more viable mechanism to explain them. With the new lightcurve, I will also be able to investigate the presence of a long-term periodicity associated with the cycle, and constrain the duration of each state better. If I manage to establish main timescale of the cycle, it will become possible to conduct multi-wavelength campaigns along the cycle branches more efficiently. In particular, Holmberg II X–1 is known to display intermittent jet activity (Cseh et al., 2015). Finding a connection between the jet activity and the specific spectral states of the cycle will represent a milestone coupling accretion and ejection phenomena in ULXs, like in BH-XRBs. Such studies would surely improve the characterization of such evolutionary cycles and our understanding of the main physical processes driving the cycle.

It is also likely that improvement in the available models is needed, as the only attempt to model the

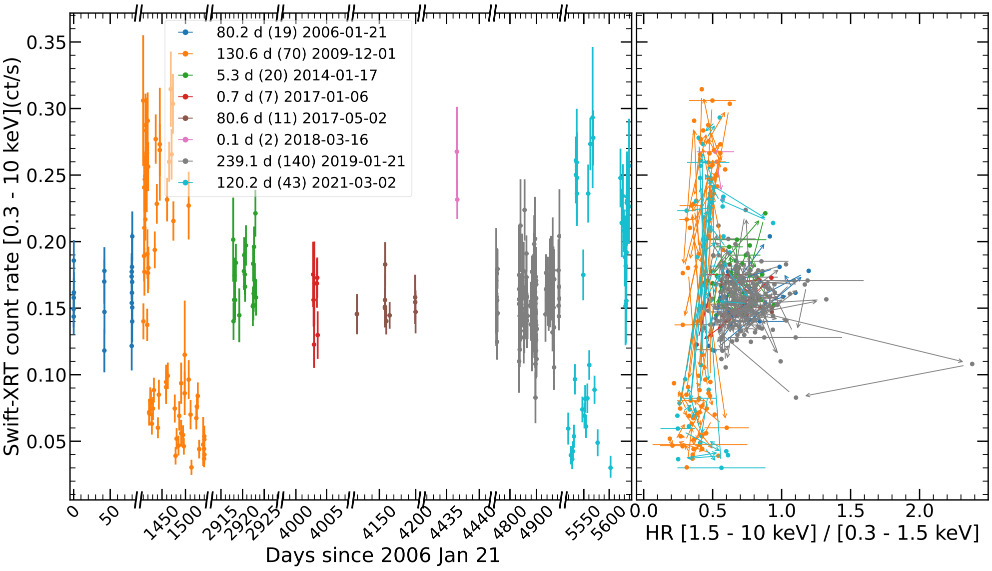

Figure 7.1: *Left*: Updated *Swift*-XRT light curve in the 0.3–10 keV band of Holmberg II X–1 with its associated HID (right) (cf. Figure 5.14). Continuous monitoring intervals with data gaps of less than 12 weeks have been coloured accordingly and the legend indicates the duration in days, the number of observations, and starting date of each continuous period. Arrows in the HID indicate chronological order and errors are given every eight datapoints for clarity. Errors are at 1 σ confidence level. Note that the x-axis has been split on the left panel. *Left* : Mise à jour de la courbe de lumière *Swift*-XRT dans la bande 0.3–10 keV de Holmberg II X–1 avec son HID associé (à droite) (cf. Figure 5.14). Les intervalles de surveillance continue avec des lacunes dans les données de moins de 12 semaines ont été colorés en conséquence et la légende indique la durée en jours, le nombre d'observations et la date de début de chaque période continue. Les flèches dans le HID indiquent l'ordre chronologique et les erreurs sont données tous les huit points de données pour plus de clarté. Les erreurs sont au niveau de confiance de 1 σ. Notez que l'axe des x a été divisé sur le panneau de gauche.

supercritical funnel available in XSPEC (Abolmasov et al., 2009) does not take into account Comptonization effects. I also note that in this model, the opening angle of the funnel and the mass outflow rate are not linked. To test this scenario properly, a model where these two variables are linked would be needed so ideally the results from the two models could be compared, but an analytical expression linking these two parameters is lacking. This could be of the form of $\theta_f \propto \dot{m}^{-\beta}$, where β could be a variable parameter in the model. In this way the scaling proposed by (King, 2009) where $\beta = 2$ could be tested to some degree. Note that while my analysis supports a certain degree of anisotropy, the orbital parameters of M51 ULX–7 suggest that at least in this source beaming must be mild (Vasilopoulos et al., 2021). The case of highly magnetised NSs is also lacking a self-consistent model (Mushtukov et al., 2017), which makes it difficult to properly test this scenario.

Another important consequence of this work is that observations taken in different epochs but for which the source is in the same spectral state can now be combined to improve the signal-to-noise ratio. For instance, I note that NGC 5204 X–1 has a cumulative net exposure of ∼57 ks in the hard ultraluminous state, spread in four different observations. These datasets could be stacked to obtain a high signal-to-noise ratio RGS spectrum, ensuring to some extent that the lines are not washed away by changes in the source properties. I note here that during my Master internship (5 months) and the beginning of this thesis I analysed RGS data of ULXs to look for lines that could indicate the presence of ionized winds. For this, I implemented a method to detect the faint features against the strong background (by stepping a Gaussian line on the continuum) and then run the Posterior Predictive P-value outlined in Protassov et al. (2002) to determine their significance based on Monte Carlo simulations. There are still some technical aspects to be fine tuned, but in the future I plan to use the now fully characterise spectral states of some ULXs to attempt to look for wind features in their stacked RGS spectra. Once again, *Athena* will allow to resolve multiple lines blended in the RGS data and obtain high signal-to-noise ratio with relatively short exposures (see the simulations from Pinto et al., 2020a). Moreover, time-resolved spectroscopy over short timescales will become feasible, which will enable to track how dynamical and patchy are super-Eddington winds, measuring the wind clump properties and its effects on the continuum in a dynamical way, as it is done for AGNs. These results can be compared to numerical simulations (e.g. Takeuchi et al., 2013) to test our understanding of the super-Eddington regime.

Due to their high radiative and mechanical output, a single ULX can influence its environment up to parsec scales, suggesting that they might even influence some galaxy properties! In this regard, it has recently suggested that ULXs may account for the He II λ4686 line seen in low-metallicity galaxies, whose origin remains unclear (Simmonds et al., 2021). To understand the impact on the environment of ULXs and more broadly of the super-Eddington regime, I have used data from the *HST* and the IFU MUSE instrument at the VLT. I have shown that new-generation of IFU instruments will prove immensely valuable for the study of the ULX bubbles. In the first part, the detection of a shocked bubble around NGC 1313 X–1 has allowed me to independently confirm the presence of outflows in this source, becoming the first ULX in which evidence for outflows are detected at multiple scales, close to the accretion disk and up to hundreds of parsecs. The morphology of the shocked regions may suggest the presence of jet activity, but this remains to be investigated with follow-up radio observations. I have also revealed that the source has created an X-ray ionized region in the cavity of the bubble, suggesting that ULX bubbles are more complex than revealed by long-slit spectroscopy alone. We have also shown that all the observable needed to estimate the mechanical power are accessible with a single MUSE observation. From the literature and this study, it seems that the mechanical power in ULXs is comparable or higher than the radiative one. This suggests that a significant fraction of the energy is channeled into powering the outflow, suggesting that purely advective models might not be a good match to the properties of the super-Eddington regime (e.g. Abramowicz et al., 1988; Madau et al., 2014). These observational constraints, if applicable to the case of SMBHs, are crucial for simulations that try to extrapolate back in time and understand how galaxy coevolve with the growth of SMBHs. Because more estimates of the mechanical power are needed to have a statistically significant sample, I plan to perform similar studies on the nebula around NGC 1313 X–2 (Grisé et al., 2008) and discover new nebulae by exploring the existing MUSE archival data.

I also plan to ask for future observations to image the nebula around NGC 5408 X–1 (Grisé et al., 2012), for which high-resolution spectroscopy in X-rays has also revealed the presence highly-blueshifted lines (Pinto et al., 2016) but surprisingly no sign of shock excitation have been found in its vicinity (Cseh et al., 2012) as discussed in Section 6.2. However, this result was obtained using an averaged spectrum of the nebula and we have seen that the nebula around NGC 1313 X–1 shows various excitation mechanisms working simultaneously at different sites. IFU spectroscopy may therefore provide a clearer view on the excitation mechanism of the nebula around NGC 5408 X–1. Lastly, I plan to also request observations of the SS433/W50 nebula (Dubner et al., 1998) in the NFM. This will be of great interest to compare the properties of the well known W50 nebula with those from NGC 1313 X-1. For SS433, given its known low inclination, we might expect two aligned blobs of gas showing high-excitation at each side of the source, provided it has the long-invoked funnel-like geometry (Abolmasov, 2011). Moreover, I will be able to investigate any evidence for super-Eddington winds and the formation mechanism of the W50 bubble, which is currently debated. As stated in Section 3.2.5, hydrodynamical simulations have shown that the collision between the jets and the supernova explosion can explain the morphology of the nebula Goodall et al. (2011), whereas other similar works (Ohmura et al., 2021) argue that interaction of the jets with the ISM through backflows and lateral expansion suffices to reproduce the morphology.

This can be investigated by studying the motion of the gas inside the bubble by measuring its line-of-sight velocity.

In the future, I would also like to get familiar with the use of photoionization codes, such as `CLOUDY` (Ferland et al., 2017), so I can couple them with my observations. `CLOUDY` can be used with existing X-ray ULX spectra and physically motivated models to try to match the observed lines in the regions of high-excitation found around NGC 1313 X–1 or NGC 5408 X–1 (Grisé et al., 2012). This can provide some constraints on the EUV emission of these sources, and hence on their nature and inclination.

Lastly, I have shown that with MUSE, combined with X-ray spectroscopy, can be useful in cleaning the sample of ULXs from contaminants. Exploration of the available *XMM-Newton* and *Swift* data for the ULXs in NGC 1672 is likely to help discriminate whether these are bona-fide ULXs. The exploration of the MUSE archive will thus provide useful results for the community, in the form of newly discovered bubbles or by cleaning the ULX sample from contaminants.

Conclusions et Perspectives

A partir des travaux de ces dernières années, les sources ultra-lumineuses en X (ULXs), notamment celles avec $L_X \lesssim 10^{41}$ erg/s, sont passées d'une simple définition empirique à une classe à part : des objets compacts stellaires (trous ou étoile à neutrons) accrétant de la matière d'une étoile compagnon à des taux super-Eddington sur des échelles de temps couvrant des années, voire des décennies. Ainsi, les ULXs constituent un laboratoire "idéal" pour étudier ce régime d'accrétion encore mal compris.

En adoptant une approche multi-longueurs d'onde (optique, rayons X et dans une moindre mesure UV) combinant de la modélisation spectrale et l'analyse temporelle en rayons X, de la spectroscopie IFU en optique ainsi que de la photométrie multi-bande en optique, j'ai réalisé une étude en deux parties sur plusieurs ULX afin d'étudier : 1) les géométries des flots d'accrétion (dans le disque ainsi que les vents/jets) dans le régime super-Eddington et 2) la nature de l'accréteur (trou noir/étoile à nautrons); 3) les effets de rétroaction induits par l'injection d'énergie radiative et mécanique des ULX dans leur environnement sur des échelles de quelques dizaines/centaines de parsec. Ces différentes questions ouvertes sont pertinentes car les réponses à ces questions permettront d'améliorer notre compréhension de la physique des ULXs d'une part et d'autre part d'explorer leurs impacts à de multiples échelles sur les propriétés de leur galaxie hôte (eg Simmonds et al., 2021), participant ainsi à une meilleure connaissance de l'évolution des galaxies. Mieux comprendre l'accrétion super-Eddington dans les ULXs est également un enjeu d'importance pour aider à mieux comprendre la pertinence et l'efficacité de ce processus dans la croissance des trous noirs supermassifs à haut redshift et dans l'évolution de leur galaxie hôte.

Dans la première partie de ma thèse, dans le chapitre 5, je me suis focalisé sur les deux premiers points mentionnés ci-dessus en utilisant la spectroscopie et l'analyse temporelle en rayons X. J'ai ainsi construit un échantillon de 17 ULXs incluant 6 ULXs pulsantes dont l'accréteur est une étoile à neutrons (PULXs) pour présenter une étude complète de leurs transitions spectrales sur différentes échelles de temps, notamment les temps longs (i.e. plusieurs années). Dans cette étude, j'ai montré que les PULXs sont parmi les sources les plus dures de mon échantillon. Selon certains modèles (eg Mushtukov et al., 2019), des champs magnétiques élevés ($B \gtrsim 10^{12}$ G) peuvent supprimer le développement des vents, si le disque est tronqué avant de devenir supercritique. J'ai suggéré que les différences de dureté et de variabilité de la dureté pourraient être dues à l'interaction entre la magnétosphère de l'étoile à neutrons et le rayon de sphérisation à partir du duquel les vents peuvent être lancés par la très forte pression de radiation. Dans le cas d'étoiles à neutrons faiblement magnétisées ($B \lesssim 10^{12}$ G) la géométrie des flots d'accrétion est plus complexe arbhorant un disque depuis lequel de puissants vents sont lancés formant une sorte d'"entonnoir" (*funnel*) autour de l'axe de rotation de l'étoile à neutrons. La source NGC 1313 X–2 est pour moi un bon exemple d'ULX arbhorant ce type de géométrie autour d'une étoile à neutrons faiblement magnétisée. Dans de tels cas, les photons issus des bords internes du disque d'accrétion vont se propager à travers l'"entonnoir" (*funnel*). Si certains de ces photons s'approchent de ou pénètrent les parois des vents optiquement épais, ils subiront une série de diffusions Compton par les électrons froids de ces vents. Cela pourrait expliquer la faible fraction pulsée de la source, son apparence spectrale plus molle et la grande variabilité de sa dureté en raison d'une émission fortement anisotrope. Par conséquent, les propriétés de la source dépendront à leur tour fortement de l'inclinaison de la ligne de visée par rapport aux structures internes des flots d'accrétion (disques/*funnel*/vents). A l'inverse pour les étoiles à neutrons fortement magnétisées accrétantes, les vents sont a priori supprimés. Dans ce cas, nous pouvons nous attendre à avoir des fractions pulsées plus importantes, un spectre dur et une variabilité de la dureté plus faible en raison de leur émission beaucoup moins anisotrope. Alors que la différence de dureté dans les ULXs était auparavant attribuée à un effet dépendant de l'inclinaison (eg Sutton et al., 2013), cela a été contesté par la détection de creux dans la courbe de lumière de la source M51 ULX–7 (Vasilopoulos et al., 2021), qui est parmi les ULXs les plus dures connues. Cela pourrait indiquer qu'en effet il existe d'autres paramètres d'influence, tels que le champ magnétique comme je l'ai suggéré. Avec seulement sept PULXs connues, l'échantillon est encore très limité, et plus d'objets sont nécessaires pour explorer ces différences en détail. Contraindre l'inclinaison de ces systèmes est également cruciale pour aider à réduire les dégénérescences lorsque l'on essaie de comprendre quels paramètres déterminent les différences entre ces systèmes (par exemple, le taux d'accrétion, la nature de l'accréteur, ...).

Au cours de cette étude, j'ai également recherché à contraindre la nature de l'accréteur. J'ai fourni des preuves indirectes pour un candidat ULX à trou noir et un autre à étoile à neutrons à partir de leurs propriétés spectrales. J'ai montré que M81 X–6 est un des meilleurs candidats de l'échantillon pour abriter une étoile à neutrons accrétante en raison de son évolution spectrale à long terme similaire à celle observée dans NGC 1313 X–2. Cela a suscité l'intérêt de Gianluca Israel et Guillermo Andrés Rodriguez-Castillo (respectivement de l'Osservatorio Astronomico di Roma et de l'Istituto di Astrofisica Spaziale e Fisica Cosmica di Milano), qui ont gentiment recherché des pulsations dans l'observation la plus longue de *XMM-Newton* en tenant compte des corrections orbitales. Cela a donné une limite supérieure à 3σ sur la fraction pulsée de 10%. Les investigations sur cette source continuent : récemment, Roberta Amato (post-doctorante à l'IRAP) a trouvé des observations d'archive prises par *Chandra* supplémentaires et non publiées sur cette source, qui ont confirmé que celle-ci suit le même comportement bimodal présenté dans la Section 5.3.2. Une recherche préliminaire de pulsations n'a donné aucun résultat probant, mais cela pourrait être dû à la résolution temporelle limitée de *Chandra* (~ 3.2 s). Une observation prise par *XMM-Newton* est récemment devenue publique, malheureusement la source est placée au bord du champ de vue et le temps d'observation est relativement court ($\sim$27 ks); ce qui rendrait cette observation moins utile que prévu initialement compte tenu de la difficulté pour détecter des pulsations. Faire des demandes de temps d'observation avec *XMM-Newton* reste compliqué car la source n'est observable que pendant de brèves périodes de temps ($<$40 ks). Un autre problème vient du fait que nous ne savons pas ce qui provoque l'apparition/la disparition des pulsations. Il est possible qu'une réponse définitive sur la nature de l'accréteur dans M81 X–6 doive attendre la prochaine mission clé de l'ESA *Athena*. *Athena* devrait voler au début de prochaine décennie et transportera notamment l'instrument à rayons X-IFU (X-IFU Barret et al., 2018), qui permettra de faire de la spectroscopie à haute résolution ($\delta E \sim 2.5$ eV < 7 keV) sur la bande 0.2–10 keV couplant une surface efficace $\sim$ 15 fois supérieure à celle de *XMM-Newton* EPIC–PN. Couplé à sa bonne résolution temporelle de $\sim 10\,\mu$s et à sa résolution spatiale fine de 5", le X-IFU changera la donne dans la quête des ULX à étoiles à neutrons.

Lors de mon étude, j'ai également remarqué un manque de variabilité aux hautes énergies ($>$ 10 keV) dans NGC 1313 X-1 et Holmberg IX X–1, dont l'origine est encore incertaine. Néanmoins ce manque de variabilité semble supporter l'idée selon laquelle le système est vu à une faible inclinaison. Malheureusement, cela n'a pas pu être confirmé avec les observations de MUSE de NGC 1313 X-1 (cf. ci-dessous). J'ai suggéré que la stabilité de l'émission à haute énergie pourrait être plus facilement comprise si l'accréteur dans ces sources est un trou noir, car ils peuvent "avaler" l'excès d'énergie produit dans leur voisinage par advection, mais encore une fois cela dépendra de l'exact mécanisme créant cette émission. Ce dernier point pourrait être investigué plus en détail dans les simulations numériques de disques d'accrétion super-Eddington. Au-delà des preuves circonstancielles sur les ULXs ayant des luminosités en X légèrement au-dessus de la limite d'Eddington (e.g. Middleton et al., 2013), l'existence d'ULX à trou noir reste à confirmer. À cet égard, étudier la variabilité radio du candidat ULX à trou noir proposé pourrait être intéressant pour voir s'il appartient à la même catégorie que le microquasar dans M31 (XMMU J004243.61412519; Middleton et al., 2013).

Un corollaire intéressant de cette étude est que j'ai séparé l'échantillon de sources en fonction des similitudes observées de leurs propriétés. Compte tenu des informations parcellaires dont nous disposons sur les ULXs, ceci pourrait s'avérer fort utile à l'avenir pour faire des intercomparaisons entre ces sources en utilisant leurs similitudes. Ceci est illustré dans l'étude de suivi que j'ai effectuée sur Holmberg II X–1 et NGC 5204 X–1, dans laquelle j'ai montré pour la première fois l'existence d'un cycle évolutif dans l'espace dureté–luminosité en combinant toutes les données en rayons X disponibles pour ces deux sources (Section 5.2). Ce cycle pourrait être l'analogue du diagramme en forme de q observé dans les binaires X à trou noir accrétant principalement dans le régime sous-Eddington (Section 2.1.1), mais pour le régime super-Eddington. Reste à savoir ce qui confère à ces deux sources des similitudes si frappantes, est-ce la même configuration orbite/compagnon et donc des taux de transfert de masse similaires ? S'agit-il simplement d'un taux de transfert de masse similaire, bien qu'ayant des rapports de masse accréteur/compagnon différents ? Si nous faisons une analogie du diagramme en forme de q pour les binaires X à trou noir, dans lequel le cycle décrit des propriétés spécifiques des flots d'accrétion pour un accréteur commun (c'est-à-dire un trou noir), nous pourrions suggérer que ces deux sources hébergent le même accréteur. Bien que cela reste à étudier, ces deux sources constituent une excellente référence pour tester les théories de l'accrétion super-Eddington, en coordonnant des observations multi-longueurs d'onde lorsque les sources se trouvent dans des états spectraux différents à l'instar de ce qui a été fait pour les binaires X à trou noir. Invoquer une géométrie des flots d'accrétion incluant la présence d'un *funnel* est séduisant car la variabilité à long terme observée pourrait alors être le résultat de la dépendance de l'angle d'ouverture du *funnel* avec le taux d'accrétion alors que la variabilité à court terme pourrait être induite par les propriétés filamentaires/granuleuses des vents. Si l'émission dans une large bande d'énergie (y compris optique et UV) peut être modélisée dans les trois états avec le même modèle physiquement motivé, ces affirmations pourraient être testées en examinant les variations des paramètres spectraux. Il faut aussi souligner l'importance de continuer à améliorer par leurs contenus physiques les modèles actuellement disponibles.

De plus, la précession des parties internes des flots d'accrétion n'a pas pu être totalement exclue pour expliquer les transitions entre les deux états mous. Bien que nous n'ayons pas pu confirmer ce scénario, il est intéressant de noter que Holmberg II X–1, la source pour laquelle j'ai pu étudier plus en détail ses transitions, atteint toujours des maxima et des minima en luminosité similaires entre les deux transitions molles, ce qui peut plaider en faveur de la précession (Figure 7.1). Qualitativement, ce comportement est en bon accord avec les courbes de lumière modélisées par Dauser et al. (2017) pour une géométrie des flots d'accrétion avec un *funnel* qui précesse. En substance, nous ne nous attendons pas à une variabilité du flux de la source dans l'état dur à cause d'un angle d'ouverture élevé du *funnel*, alors que de fortes variations du flux de la source sont attendues dès que l'inclinaison est supérieure à l'angle de demi-ouverture de ce dernier.

Il faudrait probablement rajouter à cela une variabilité stochastique supplémentaire imprimée par le caractère filamentaire/granuleux des vents (qui ne sont pas pris en compte dans le modèle de Dauser et al. (2017)). À cet égard, la source Holmberg II X–1 est toujours suivie par *Swift*, et j'ai pu confirmer que la source a recommencé à transiter entre les deux états mous, comme cela est indiqué sur la Figure 7.1. Cela confirme également qu'en effet le cycle est récurrent et ces nouvelles données pourraient aider à contraindre son échelle de temps.

Je prévois d'étudier si les changements spectraux entre les états mous montrent des preuves d'une périodicité cohérente avec la périodicité $\sim$ de 28 jours trouvée dans (Gúrpide et al., 2021b). Cela déterminera si ces transitions sont périodiques ou non, et je serai en mesure d'examiner quel mécanisme (discutés ci-dessus) serait le plus viable. A partir de la nouvelle courbe de lumière du *Swift*-XRT, je pourrai également étudier la présence d'une périodicité à long terme associée au cycle, et mieux contraindre la durée de chaque état. Si je parviens à établir l'échelle de temps principale du cycle, il deviendra possible de mener plus efficacement des campagnes multi-longueurs d'onde le long des branches du cycle. En particulier, Holmberg II X–1 est connu pour afficher une activité de jet intermittente (Cseh et al., 2015). Trouver un lien entre l'activité du jet et les états spectraux spécifiques du cycle représenterait une étape importante couplant les phénomènes d'accrétion et d'éjection dans les ULX, comme dans le cas des binaires X à trou noir. De telles études amélioreraient sûrement la caractérisation de ces cycles évolutifs et notre compréhension des principaux processus physiques à l'origine de ce cycle.

Ceci passera également par une amélioration des modèles décrivant l'émission issue des flots d'accrétion super-Eddington. En effet, le seul modèle d'émission incluant la présence d'un *funnel* disponible dans XSPEC (Abolmasov et al., 2009) ne prend pas en compte les effets de la Comptonisation. Je note aussi que dans ce modèle, l'angle d'ouverture du *funnel* et le taux de masse éjectée ne sont pas liés. Pour tester correctement ce scénario, un modèle où ces deux variables sont liées serait nécessaire, mais une expression analytique reliant ces deux paramètres fait défaut. Cela pourrait être de la forme $\theta_f \propto \dot{m}^{-\beta}$, où β pourrait être un paramètre variable dans le modèle. De cette façon, la mise à l'échelle proposée par (King, 2009) où $\beta = 2$ pourrait être testée dans une certaine mesure. Bien que mon analyse soit en faveur d'un certain degré d'anisotropie, les paramètres orbitaux de M51 ULX–7 suggèrent qu'au moins dans cette source les effets de collimation doivent être modérés (Vasilopoulos et al., 2021). Pour le moment, il n'existe pas de modèle simple décrivant l'émission attendue dans Le cas d'étoiles à neutrons hautement magnétisées accrétant à des taux super-critiques (Mushtukov et al., 2017); ce qui rend difficile de tester correctement ce scénario.

Une autre conséquence importante de ce travail est que des observations prises à des époques différentes mais pour lesquelles la source est dans le même état spectral peuvent désormais être combinées pour améliorer le rapport signal sur bruit. Par exemple, je note que NGC 5204 X–1 a une exposition nette cumulée de ∼57 ks à l'état ultra-lumineux dur, répartie en quatre observations différentes. Ces jeux de données pourraient être combinés pour obtenir un spectre RGS avec un rapport signal/bruit élevé, en supposant que dans une certaine mesure les signatures discrètes d'intérêt ne sont pas modifiées d'un jeu de données à l'autre. Je remarque ici que lors de mon stage de Master 2 (5 mois) et au début de cette thèse j'ai analysé les données RGS de plusieurs ULXs pour rechercher des signatures spectrales discrètes qui pourraient indiquer la présence de vents ionisés. Pour cela, j'ai implémenté une méthode pour détecter ces caractéristiques faibles noyées dans un bruit de fond dominant (en balayant une certaine bande d'énergie avec une ligne gaussienne d'énergie superposé au continu), puis j'ai mis en place la méthode décrite par Protassov et al. (2002) pour déterminer leur degré de significativité en utilisant des simulations Monte-Carlo. Il reste encore quelques aspects techniques à peaufiner, mais à l'avenir, je prévois d'utiliser les états spectraux désormais entièrement caractérisés de certaines ULXs pour tenter de rechercher les caractéristiques spectrales discrètes induites par les vents dans les spectres RGS empilés. Encore une fois, *Athena* permettra de résoudre avec l'instrument X-IFU ces caractéristiques spectrales qui dans les données RGS sont parfois mélangées et d'obtenir un rapport signal/bruit élevé grâce à sa grande surface efficace pour des temps d'exposition relativement courts (voir les simulations de Pinto et al., 2020a). De plus, la spectroscopie résolue en temps sur de courtes échelles de temps deviendra possible, ce qui permettra d'étudier le caractère dynamique de ces vents super-Eddington ainsi que leurs structures fines filamentaires/granuleuses, en mesurant les propriétés de ces structures et leurs effets sur l'émission continu provenant du disque d'accrétion, comme cela est fait pour certains noyaux actifs de galaxie. Ces résultats pourront alors être comparés à des simulations numériques (e.g. Takeuchi et al., 2013); ce qui in fine améliorera notre compréhension de la physique du régime d'accrétion super-Eddington.

En raison de l'importance de la quantité d'énergie radiative et mécanique produite, une seule ULX peut influencer son environnement jusqu'à l'échelle du parsec (voire plus), ce qui suggère qu'il pourrait même influencer certaines propriétés de leur galaxie hôte ! À cet égard, il a récemment suggéré que les ULXs pourraient expliquer la raie He II observée dans les galaxies de faible métallicité, dont l'origine reste incertaine (Simmonds et al., 2021). Pour comprendre l'impact sur l'environnement des ULXs et plus largement du régime super-Eddington, j'ai utilisé les données de l'instrument *HST* et de l'instrument IFU MUSE au VLT. J'ai montré que la nouvelle génération d'instruments IFU s'avérera extrêmement précieuse pour l'étude des bulles ULX. Dans la première partie, la détection d'une bulle de gaz choqués autour de NGC 1313 X–1 m'a permis de confirmer de manière indépendante la présence de vents dans cette source, devenant ainsi la première ULX dans lequelle des preuves de la présence de vents sont détectées à plusieurs échelles, proches du disque d'accrétion en rayon X et jusqu'à des centaines de parsecs en optique. La morphologie des régions choquées peut suggérer la présence d'une activité de jet, mais cela reste à étudier avec des observations radio de suivi. J'ai également révélé que la source a créé une région ionisée par rayons X dans la cavité de la bulle, suggérant que les bulles ULX sont plus complexes que révélées par la spectroscopie à fente longue. Nous avons également montré que toutes les observables nécessaires à l'estimation de la puissance mécanique sont accessibles avec une seule observation MUSE. La puissance mécanique dans cette ULXs semble comparable, voire supérieure à la puissance radiative; ce qui concorde avec des résultats trouvés dans la littérature. Cela suggère qu'une fraction importante de l'énergie sert à alimenter les vents; ce qui implique que les modèles purement advectifs pourraient ne pas correspondre aux propriétés du régime super-Eddington (eg Abramowicz et al., 1988; Madau et al., 2014). Ces contraintes observationnelles, si elles s'appliquent au cas des trous noirs supermassifs, sont cruciales pour les simulations cosmologiques s'intéressant à la croissance des trous noirs massifs et leur co-évolution avec leur galaxie hôte. Il est important d'accroître le nombre d'estimations de la puissance mécanique dans les ULX pour construire un échantillon statistiquement significatif. Je prévois ainsi d'effectuer des études similaires sur la nébuleuse autour de NGC 1313 X–2 (Grisé et al., 2008) et découvrir de nouvelles nébuleuses en explorant les données d'archives MUSE existantes.

Je prévois également de demander de futures observations pour observer la nébuleuse autour de NGC 5408 X–1 (Grisé et al., 2012), pour laquelle la spectroscopie à haute résolution en rayons X a également révélé la présence de raies fortement décalées vers le bleu (Pinto et al., 2016) mais étonnamment aucun signe d'excitation/ionisation par choc n'a été trouvé dans son voisinage (Cseh et al., 2012) comme cela a été discuté à la Section 6.2. Cependant, ce résultat a été obtenu en utilisant un spectre moyen de la nébuleuse et nous avons vu que la nébuleuse autour de NGC 1313 X–1 montre divers mécanismes d'excitation/ionisation opérant simultanément sur différents sites. La spectroscopie IFU peut donc fournir une image plus claire sur le mécanisme d'excitation/ionisation de la nébuleuse autour de NGC 5408 X–1. Enfin, je prévois de demander également des observations de la nébuleuse SS433/W50 (Dubner et al., 1998) dans le mode NFM de MUSE. Cela sera d'un grand intérêt pour comparer les propriétés de la bien connue nébuleuse W50 avec celles de NGC 1313 X-1. Pour la source SS433, qui semble être vue de côté, nous pourrions nous attendre à observer deux zones d'émission alignées montrant une excitation élevée de chaque côté de la source, à condition qu'elle ait le même type de géométrie des flots d'accrétion que pour NGC 1313 X–1 (Abolmasov, 2011). De plus, je pourrai investiguer les mécanismes de formation de la bulle W50, qui est toujours débattu. A cet égard, des simulations hydrodynamiques ont montré que la collision entre les jets et l'explosion de la supernova peut expliquer la morphologie de la nébuleuse Goodall et al. (2011), alors que d'autres travaux similaires (Ohmura et al., 2021) soutiennent que l'interaction des jets avec le milieu interstellaire suffisent à reproduire la morphologie. Cela peut être étudié en étudiant le mouvement du gaz à l'intérieur de la bulle en mesurant sa vitesse le long de la ligne de visée.

Dans le futur, j'aimerais aussi me familiariser avec l'utilisation des codes de photoionisation, comme `CLOUDY` (Ferland et al., 2017), afin de pouvoir les coupler avec mes observations. `CLOUDY` peut être utilisé avec des spectres de rayons X existants d'ULXs et des modèles physiquement motivés pour essayer de faire correspondre les raies observées dans les régions de haute excitation trouvées autour de NGC 1313 X–1 et NGC 5408 X–1 (Grisé et al., 2012). Cela peut fournir des contraintes sur l'émission EUV de ces sources, et donc sur leur nature et leur inclinaison.

Enfin, j'ai montré qu'avec MUSE, combiné à la spectroscopie en rayons X, il est possible de nettoyer les échantillons d'ULXs de leurs contaminants.

Bibliography

Abarca, D., Parfrey, K., & Kluźniak, W. 2021, arXiv:2107.01149 [astro-ph], arXiv: 2107.01149

Abbott, B. P., Abbott, R., Abbott, T. D., et al. 2019, ApJL, 882, L24, publisher: American Astronomical Society

Abbott, R., Abbott, T. D., Abraham, S., et al. 2020, The Astrophysical Journal, 900, L13, aDS Bibcode: 2020ApJ...900L..13A

Abeysekara, A. U., Albert, A., Alfaro, R., et al. 2018, Nature, 562, 82, bandiera_abtest: a Cg_type: Nature Research Journals Number: 7725 Primary_atype: Research Publisher: Nature Publishing Group Subject_term: High-energy astrophysics;Particle astrophysics Subject_term_id: high-energy-astrophysics;particle-astrophysics

Abolmasov, P. 2011, New Astronomy, 16, 138

Abolmasov, P., Fabrika, S., Sholukhova, O., & Afanasiev, V. 2007a, Astrophys. Bull., 62, 36

Abolmasov, P., Fabrika, S., Sholukhova, O., & Kotani, T. 2008, arXiv:0809.0409 [astro-ph], arXiv: 0809.0409 version: 1

Abolmasov, P., Karpov, S., & Kotani, T. 2009, Publications of the Astronomical Society of Japan, 61, 213

Abolmasov, P. K., Fabrika, S. N., & Sholukhova, O. N. 2006, Proceedings of the International Astronomical Union, 2, 229, publisher: Cambridge University Press

Abolmasov, P. K., Swartz, D. A., Fabrika, S., et al. 2007b, ApJ, 668, 124

Abramowicz, M. A., Czerny, B., Lasota, J. P., & Szuszkiewicz, E. 1988, The Astrophysical Journal, 332, 646

Agarwal, B., Khochfar, S., Johnson, J. L., et al. 2012, Monthly Notices of the Royal Astronomical Society, 425, 2854

Alarie, A. & Morisset, C. 2019, Revista Mexicana de Astronomia y Astrofisica, 55, 377

Allen, M. G., Groves, B. A., Dopita, M. A., Sutherland, R. S., & Kewley, L. J. 2008, The Astrophysical Journal Supplement Series, 178, 20

Alston, W. N., Pinto, C., Barret, D., et al. 2021, arXiv:2104.11163 [astro-ph], arXiv: 2104.11163

An, T., Lu, X.-L., & Wang, J.-Y. 2016, A&A, 585, A89, publisher: EDP Sciences

Arnaud, K. A. 1996, Astronomical Data Analysis Software and Systems V, 101, 17

Bachetti, M. 2018, Astrophysics Source Code Library, ascl:1805.019

Bachetti, M., Harrison, F. A., Walton, D. J., et al. 2014, Nature, 514, 202

Bachetti, M., Maccarone, T. J., Brightman, M., et al. 2020, ApJ, 891, 44, publisher: American Astronomical Society

Bachetti, M., Markwardt, C. B., Grefenstette, B. W., et al. 2021, The Astrophysical Journal, 908, 184

Bachetti, M., Rana, V., Walton, D. J., et al. 2013, ApJ, 778, 163

Bacon, R., Accardo, M., Adjali, L., et al. 2010, in Ground-based and Airborne Instrumentation for Astronomy III, Vol. 7735 (International Society for Optics and Photonics), 773508

Bacon, R., Conseil, S., Mary, D., et al. 2017, A&A, 608, A1

Balbus, S. A. & Hawley, J. F. 1991, The Astrophysical Journal, 376, 214

Baldwin, J. A., Phillips, M. M., & Terlevich, R. 1981, Publications of the Astronomical Society of the Pacific, 93, 5

Barret, D., Lam Trong, T., den Herder, J.-W., et al. 2018, 10699, 106991G, conference Name: Space Telescopes and Instrumentation 2018: Ultraviolet to Gamma Ray Place: eprint: arXiv:1807.06092 ADS Bibcode: 2018SPIE10699E..1GB

Barthelmy, S. D., Barbier, L. M., Cummings, J. R., et al. 2005, Space Sci Rev, 120, 143

Basko, M. M. & Sunyaev, R. A. 1976, Mon Not R Astron Soc, 175, 395

Bañados, E., Venemans, B. P., Mazzucchelli, C., et al. 2017, Nature, 553, 473

Becker, P. A. & Wolff, M. T. 2007, The Astrophysical Journal, 654, 435

Begelman, M. C. 1979, Monthly Notices of the Royal Astronomical Society, 187, 237

Begelman, M. C. 2003, arXiv:astro-ph/0303040, arXiv: astro-ph/0303040

Belloni, T., Klein-Wolt, M., Méndez, M., van der Klis, M., & van Paradijs, J. 2000, Astronomy and Astrophysics, 355, 271

Belloni, T. M. 2010, 794, 53

Berghea, C. T. & Dudik, R. P. 2012, ApJ, 751, 104, publisher: IOP Publishing

Berghea, C. T., Dudik, R. P., Weaver, K. A., & Kallman, T. R. 2010, The Astrophysical Journal, 708, 364

Berghea, C. T., Johnson, M. C., Secrest, N. J., et al. 2020, ApJ, 896, 117, publisher: American Astronomical Society

Binder, B., Levesque, E. M., & Dorn-Wallenstein, T. 2018, ApJ, 863, 141

Binder, B., Williams, B. F., Kong, A. K. H., et al. 2011, ApJ, 739, L51

Binder, B., Williams, B. F., Kong, A. K. H., et al. 2016, Mon. Not. R. Astron. Soc., 457, 1636

Binder, B. A., Carpano, S., Heida, M., & Lau, R. 2020, arXiv:2002.04113 [astro-ph], arXiv: 2002.04113

Blair, W. P., Fesen, R. A., & Schlegel, E. M. 2001, The Astronomical Journal, 121, 1497

Blandford, R. D. & Payne, D. G. 1982, Monthly Notices of the Royal Astronomical Society, 199, 883, aDS Bibcode: 1982MNRAS.199..883B

Blandford, R. D. & Znajek, R. L. 1977, Monthly Notices of the Royal Astronomical Society, 179, 433, aDS Bibcode: 1977MNRAS.179..433B

Bondi, H. 1952, Monthly Notices of the Royal Astronomical Society, 112, 195

Braun, R., Goss, W. M., & Lyne, A. G. 1989, The Astrophysical Journal, 340, 355, aDS Bibcode: 1989ApJ...340..355B

Brightman, M., Earnshaw, H., Fürst, F., et al. 2020a, ApJ, 895, 127, publisher: American Astronomical Society

Brightman, M., Harrison, F., Walton, D. J., et al. 2016a, ApJ, 816, 60

Brightman, M., Harrison, F. A., Bachetti, M., et al. 2019, The Astrophysical Journal, 873, 115

Brightman, M., Harrison, F. A., Barret, D., et al. 2016b, ApJ, 829, 28, arXiv: 1607.03903

Brightman, M., Harrison, F. A., Fürst, F., et al. 2018, Nat Astron, 2, 312, number: 4 Publisher: Nature Publishing Group

Brightman, M., Walton, D. J., Xu, Y., et al. 2020b, ApJ, 889, 71, publisher: IOP Publishing

Brinkman, B. C., Gunsing, T., Kaastra, J. S., et al. 2000, 4012, 81, conference Name: X-Ray Optics, Instruments, and Missions III

Buccheri, R., Bennett, K., Bignami, G. F., et al. 1983, A&A, 128, 245

Burrows, D. N., Hill, J. E., Nousek, J. A., et al. 2005, Space Science Reviews, 120, 165

C. McKinney, J., Tchekhovskoy, A., Sadowski, A., & Narayan, R. 2013, Monthly Notices of the Royal Astronomical Society, 441

Caballero, I. & Wilms, J. 2012, arXiv:1206.3124 [astro-ph], arXiv: 1206.3124

Calzetti, D., Armus, L., Bohlin, R. C., et al. 2000, ApJ, 533, 682, publisher: American Astronomical Society

Campana, S., Stella, L., Israel, G. L., et al. 2002, The Astrophysical Journal, 580, 389

Canizares, C. R., Davis, J. E., Dewey, D., et al. 2005, Publications of the Astronomical Society of the Pacific, 117, 1144

Canuto, V., Lodenquai, J., & Ruderman, M. 1971, Physical Review D, 3, 2303

Cappellari, M., Emsellem, E., Krajnović, D., et al. 2011, Monthly Notices of the Royal Astronomical Society, 413, 813

Cardelli, J. A., Clayton, G. C., & Mathis, J. S. 1989, The Astrophysical Journal, 345, 245

Carpano, S., Haberl, F., Maitra, C., & Vasilopoulos, G. 2018, Monthly Notices of the Royal Astronomical Society: Letters, 476, L45

Casares, J., Jonker, P. G., & Israelian, G. 2017, arXiv:1701.07450 [astro-ph], 1499, arXiv: 1701.07450

Cash, W. 1979, The Astrophysical Journal, 228, 939

Chandrasekhar, S. 1931, The Astrophysical Journal, 74, 81, aDS Bibcode: 1931ApJ....74...81C

Chashkina, A., Abolmasov, P., & Poutanen, J. 2017, Mon Not R Astron Soc, 470, 2799, publisher: Oxford Academic

Chashkina, A., Lipunova, G., Abolmasov, P., & Poutanen, J. 2019, Astronomy and Astrophysics, 626, A18

Cherepashchuk, A. M., Belinski, A. A., Dodin, A. V., & Postnov, K. A. 2021, Monthly Notices of the Royal Astronomical Society: Letters, slab083, arXiv: 2107.09005

Cioffi, D. F., McKee, C. F., & Bertschinger, E. 1988, The Astrophysical Journal, 334, 252, aDS Bibcode: 1988ApJ...334..252C

Coburn, W., Heindl, W. A., Rothschild, R. E., et al. 2002, The Astrophysical Journal, 580, 394

Colbert, E. J. M. & Mushotzky, R. F. 1999, ApJ, 519, 89

Consortium, T. C. 2011, Exp Astron, 32, 193, arXiv: 1008.3703

Corbet, R. H. D. & Krimm, H. A. 2013, The Astrophysical Journal, 778, 45

Coriat, M., Fender, R. P., Tasse, C., et al. 2019, Monthly Notices of the Royal Astronomical Society, 484, 1672

Corral-Santana, J. M., Casares, J., Muñoz-Darias, T., et al. 2016, Astronomy and Astrophysics, 587, A61

Crook, A. C., Huchra, J. P., Martimbeau, N., et al. 2007, ApJ, 655, 790

Cseh, D., Corbel, S., Kaaret, P., et al. 2012, ApJ, 749, 17

Cseh, D., Grisé, F., Kaaret, P., et al. 2013, Monthly Notices of the Royal Astronomical Society, 435, 2896

Cseh, D., Kaaret, P., Corbel, S., et al. 2014, Mon Not R Astron Soc Lett, 439, L1

Cseh, D., Miller-Jones, J. C. A., Jonker, P. G., et al. 2015, Mon Not R Astron Soc, 452, 24, publisher: Oxford Academic

Dall'Osso, S., Perna, R., & Stella, L. 2015, Mon Not R Astron Soc, 449, 2144

Dauser, T., Garcia, J., Wilms, J., et al. 2013, Monthly Notices of the Royal Astronomical Society, 430, 1694, aDS Bibcode: 2013MNRAS.430.1694D

Dauser, T., Middleton, M., & Wilms, J. 2017, Mon Not R Astron Soc, 466, 2236, publisher: Oxford Academic

Dewey, D. 2010, Space Science Reviews, Volume 157, Issue 1-4, pp. 229-248, 157, 229

Dolan, J. F., Boyd, P. T., Fabrika, S., et al. 1997, Astronomy and Astrophysics, 327, 648

Done, C. & Gierliński, M. 2003, Mon Not R Astron Soc, 342, 1041

Done, C., Gierliński, M., & Kubota, A. 2007, Astron Astrophys Rev, 15, 1

Done, C., Wardziński, G., & Gierliński, M. 2004, Monthly Notices of the Royal Astronomical Society, 349, 393

Dopita, M. A., Payne, J. L., Filipović, M. D., & Pannuti, T. G. 2012, Monthly Notices of the Royal Astronomical Society, 427, 956, aDS Bibcode: 2012MNRAS.427..956D

Dopita, M. A. & Sutherland, R. S. 1996, The Astrophysical Journal Supplement Series, 102, 161

Doroshenko, V., Santangelo, A., & Ducci, L. 2015, Astronomy & Astrophysics, 579, A22

Dors, O. L., Hägele, G. F., Cardaci, M. V., & Krabbe, A. C. 2017, Monthly Notices of the Royal Astronomical Society, 466, 726, aDS Bibcode: 2017MNRAS.466..726D

Dressel, L. 2012, Wide Field Camera 3, HST Instrument Handbook

Dubner, G. M., Holdaway, M., Goss, W. M., & Mirabel, I. F. 1998, AJ, 116, 1842, publisher: American Astronomical Society

Díaz Trigo, M. & Boirin, L. 2016, Astronomische Nachrichten, 337, 368, aDS Bibcode: 2016AN....337..368D

Earnshaw, H. P., Roberts, T. P., Middleton, M. J., Walton, D. J., & Mateos, S. 2019, Monthly Notices of the Royal Astronomical Society, 483, 5554

Egorov, O. V., Lozinskaya, T. A., & Moiseev, A. V. 2017, Mon Not R Astron Soc Lett, 467, L1, publisher: Oxford Academic

Eisenstein, D. J. & Loeb, A. 1995, Astrophys. J., 443, 11, _eprint: astro-ph/9401016

Epinat, B., Tasca, L., Amram, P., et al. 2012, Astronomy and Astrophysics, 539, A92

Evans, P. A., Beardmore, A. P., Page, K. L., et al. 2009, Mon Not R Astron Soc, 397, 1177, publisher: Oxford Academic

Evans, P. A., Beardmore, A. P., Page, K. L., et al. 2007, A&A, 469, 379, number: 1 Publisher: EDP Sciences

Event Horizon Telescope Collaboration, Akiyama, K., Alberdi, A., et al. 2019, The Astrophysical Journal, 875, L1

Fabbiano, G. 1989, Annual Review of Astronomy and Astrophysics, 27, 87

Fabrika, S. 2004, Astrophysics and Space Physics Reviews, 12, 1

Fabrika, S., Ueda, Y., Vinokurov, A., Sholukhova, O., & Shidatsu, M. 2015, Nature Phys, 11, 551, number: 7 Publisher: Nature Publishing Group

Fabrika, S. N., Atapin, K. E., Vinokurov, A. S., & Sholukhova, O. N. 2021, Astrophys. Bull., 76, 6, arXiv: 2105.10537

Farrell, S. A., Webb, N. A., Barret, D., Godet, O., & Rodrigues, J. M. 2009, Nature, 460, 73

Fender, R. P., Belloni, T. M., & Gallo, E. 2004, Monthly Notices of the Royal Astronomical Society, 355, 1105

Fender, R. P., Garrington, S. T., McKay, D. J., et al. 1999, Monthly Notices of the Royal Astronomical Society, 304, 865

Feng, H. & Kaaret, P. 2006, ApJ, 650, L75

Feng, H. & Kaaret, P. 2008, The Astrophysical Journal, 675, 1067

Feng, H. & Kaaret, P. 2009, ApJ, 696, 1712

Feng, H. & Kaaret, P. 2010, ApJL, 712, L169

Feng, H., Tao, L., Kaaret, P., & Grisé, F. 2016, ApJ, 831, 117

Feng, J., Cao, X., Gu, W.-M., & Ma, R.-Y. 2019, ApJ, 885, 93, publisher: American Astronomical Society

Ferland, G. J., Chatzikos, M., Guzmán, F., et al. 2017, Revista Mexicana de Astronomia y Astrofisica, 53, 385

Fesen, R. A. & Hurford, A. P. 1996, The Astrophysical Journal Supplement Series, 106, 563, aDS Bibcode: 1996ApJS..106..563F

Fesen, R. A., Weil, K. E., Raymond, J. C., et al. 2020a, Monthly Notices of the Royal Astronomical Society, 498, 5194, aDS Bibcode: 2020MNRAS.498.5194F

Fesen, R. A., Weil, K. E., Raymond, J. C., et al. 2020b, Monthly Notices of the Royal Astronomical Society, 498, 5194

Foreman-Mackey, D., Agol, E., Ambikasaran, S., & Angus, R. 2017, AJ, 154, 220, publisher: American Astronomical Society

Fowler, R. H. 1926, Monthly Notices of the Royal Astronomical Society, 87, 114, aDS Bibcode: 1926MNRAS..87..114F

Frank, J., King, A., & Raine, D. J. 2002, Accretion Power in Astrophysics, by Juhan Frank and Andrew King and Derek Raine, pp. 398. ISBN 0521620538. Cambridge, UK: Cambridge University Press, February 2002., num Pages: 398

Fryer, C. L. & Kalogera, V. 2001, The Astrophysical Journal, 554, 548, aDS Bibcode: 2001ApJ...554..548F

Fuchs, Y., Koch Miramond, L., & Ábrahám, P. 2006, Astronomy and Astrophysics, 445, 1041

Fuerst, F., Walton, D. J., Heida, M., et al. 2021, arXiv:2105.04229 [astro-ph], arXiv: 2105.04229

Fürst, F., Walton, D., Harrison, F., et al. 2016, The Astrophysical Journal, 831

Fürst, F., Walton, D. J., Heida, M., et al. 2018, Astronomy & Astrophysics, 616, A186

Fürst, F., Walton, D. J., Stern, D., et al. 2017, ApJ, 834, 77

Gaia Collaboration, A. G. A. Brown, Vallenari, A., et al. 2018, A&A, 616, A1, publisher: EDP Sciences

Galloway, D. K., Muno, M. P., Hartman, J. M., Psaltis, D., & Chakrabarty, D. 2008, The Astrophysical Journal Supplement Series, 179, 360, aDS Bibcode: 2008ApJS..179..360G

Gao, Y., Wang, Q. D., Appleton, P. N., & Lucas, R. A. 2003, ApJ, 596, L171

García, J. A., Steiner, J. F., McClintock, J. E., et al. 2015, The Astrophysical Journal, 813, 84, aDS Bibcode: 2015ApJ...813...84G

Gehrels, N., Chincarini, G., Giommi, P., et al. 2004, The Astrophysical Journal, 611, 1005

Ghez, A. M., Klein, B. L., Morris, M., & Becklin, E. E. 1998, ApJ, 509, 678, arXiv: astro-ph/9807210

Ghosh, P. & Lamb, F. K. 1978, The Astrophysical Journal, 223, L83

Ghosh, P., Lamb, F. K., & Pethick, C. J. 1977, The Astrophysical Journal, 217, 578

Giacconi, R., Branduardi, G., Briel, U., et al. 1979, The Astrophysical Journal, 230, 540

Gierliński, M. & Done, C. 2004, Monthly notices of the Royal Astronomical Society., 347, 885

Gilfanov, M. 2010, Lecture Notes in Physics, Berlin Springer Verlag, 794, 17, aDS Bibcode: 2010LNP...794...17G

Gladstone, J., Done, C., & Gierlinski, M. 2007, Monthly Notices of the Royal Astronomical Society, 378, 13

Gladstone, J. C., Copperwheat, C., Heinke, C. O., et al. 2013, The Astrophysical Journal Supplement Series, 206, 14

Gladstone, J. C., Roberts, T. P., & Done, C. 2009, Mon Not R Astron Soc, 397, 1836

Godet, O., Barret, D., Webb, N. A., Farrell, S. A., & Gehrels, N. 2009, ApJ, 705, L109

Godet, O., Plazolles, B., Kawaguchi, T., et al. 2012, ApJ, 752, 34

Gonçalves, A. C. & Soria, R. 2006, Monthly Notices of the Royal Astronomical Society, 371, 673

Goodall, P. T., Alouani-Bibi, F., & Blundell, K. M. 2011, Monthly Notices of the Royal Astronomical Society, 414, 2838

Goranskij, V. 2011, Peremennye Zvezdy, 31, 5

Greene, J. E., Strader, J., & Ho, L. C. 2020, Annual Review of Astronomy and Astrophysics, 58, 257, _eprint: https://doi.org/10.1146/annurev-astro-032620-021835

Grisé, F., Kaaret, P., Corbel, S., Cseh, D., & Feng, H. 2013, Mon Not R Astron Soc, 433, 1023

Grisé, F., Kaaret, P., Corbel, S., et al. 2012, ApJ, 745, 123

Grisé, F., Kaaret, P., Feng, H., Kajava, J. J. E., & Farrell, S. A. 2010, The Astrophysical Journal, 724, L148

Grisé, F., Kaaret, P., Pakull, M. W., & Motch, C. 2011, The Astrophysical Journal, 734, 23

Grisé, F., Pakull, M. W., Soria, R., et al. 2008, A&A, 486, 151

Guo, J., Sun, M., Gu, W.-M., & Yi, T. 2019, Monthly Notices of the Royal Astronomical Society, 485, 2558

Gutkin, J., Charlot, S., & Bruzual, G. 2016, Monthly Notices of the Royal Astronomical Society, 462, 1757

Gúrpide, A., Godet, O., Koliopanos, F., Webb, N., & Olive, J.-F. 2021a, A&A, 649, A104, publisher: EDP Sciences

Gúrpide, A., Godet, O., Vasilopoulos, G., Webb, N. A., & Olive, J.-F. 2021b, A&A, 654, A10

Gültekin, K., Richstone, D. O., Gebhardt, K., et al. 2009, The Astrophysical Journal, 698, 198

Habouzit, M., Volonteri, M., Latif, M., Dubois, Y., & Peirani, S. 2016, Monthly Notices of the Royal Astronomical Society, 463, 529

Halpern, J. P. & Grindlay, J. E. 1980, The Astrophysical Journal, 242, 1041, aDS Bibcode: 1980ApJ...242.1041H

Harrison, F. A., Craig, W. W., Christensen, F. E., et al. 2013, The Astrophysical Journal, 770, 103

Hawking, S. W. 1975, Communications in Mathematical Physics, 43, 199, aDS Bibcode: 1975CMaPh..43..199H

Heger, A., Fryer, C. L., Woosley, S. E., Langer, N., & Hartmann, D. H. 2003, The Astrophysical Journal, 591, 288, aDS Bibcode: 2003ApJ...591..288H

Heida, M., Lau, R. M., Davies, B., et al. 2019, ApJL, 883, L34, publisher: IOP Publishing

Heil, L. M., Vaughan, S., & Roberts, T. P. 2009, Mon Not R Astron Soc, 397, 1061

Heinz, S., Burton, M., Braiding, C., et al. 2015, ApJ, 806, 265, publisher: American Astronomical Society

Heinz, S., Sell, P., Fender, R. P., et al. 2013, The Astrophysical Journal, 779, 171, aDS Bibcode: 2013ApJ...779..171H

Herder, J. W. d., Brinkman, A. C., Kahn, S. M., et al. 2001, A&A, 365, L7, number: 1 Publisher: EDP Sciences

HI4PI Collaboration, Bekhti, N. B., Flöer, L., et al. 2016, A&A, 594, A116, publisher: EDP Sciences

Hickox, R. C., Narayan, R., & Kallman, T. R. 2004, ApJ, 614, 881

Higginbottom, N., Proga, D., Knigge, C., & Long, K. S. 2017, ApJ, 836, 42, publisher: American Astronomical Society

Homan, J., Wijnands, R., van der Klis, M., et al. 2001, The Astrophysical Journal Supplement Series, 132, 377, aDS Bibcode: 2001ApJS..132..377H

Horne, J. H. & Baliunas, S. L. 1986, The Astrophysical Journal, 302, 757

Huppenkothen, D., Bachetti, M., Stevens, A. L., et al. 2019, ApJ, 881, 39, publisher: American Astronomical Society

Illarionov, A. F. & Sunyaev, R. A. 1975, A&A, 39, 185

Inoue, A., Ohsuga, K., & Kawashima, T. 2020, Publications of the Astronomical Society of Japan, 72

Inoue, Y., Lee, S.-H., Tanaka, Y. T., & Kobayashi, S. B. 2017, Astroparticle Physics, 90, 14, aDS Bibcode: 2017APh....90...14I

Israel, G. L., Belfiore, A., Stella, L., et al. 2017a, Science, 355, 817

Israel, G. L., Papitto, A., Esposito, P., et al. 2017b, Mon Not R Astron Soc Lett, 466, L48, publisher: Oxford Academic

Jansen, F., Lumb, D., Altieri, B., et al. 2001, Astronomy & Astrophysics, 365, L1

Jenkins, L. P., Brandt, W. N., Colbert, E. J. M., et al. 2011, ApJ, 734, 33

Jiang, Y.-F., Stone, J. M., & Davis, S. W. 2014, ApJ, 796, 106

Kaaret, P., Corbel, S., Prestwich, A. H., & Zezas, A. 2003, Science, 299, 365

Kaaret, P. & Feng, H. 2009, ApJ, 702, 1679, publisher: IOP Publishing

Kaaret, P., Feng, H., & Roberts, T. P. 2017, Annual Review of Astronomy and Astrophysics, 55, 303, _eprint: https://doi.org/10.1146/annurev-astro-091916-055259

Kaaret, P., Feng, H., Wong, D. S., & Tao, L. 2010, ApJL, 714, L167

Kaaret, P., Ward, M. J., & Zezas, A. 2004, Mon Not R Astron Soc, 351, L83

Kaastra, J. S. & Bleeker, J. a. M. 2016, A&A, 587, A151, publisher: EDP Sciences

Kajava, J. J. E. & Poutanen, J. 2009, Mon Not R Astron Soc, 398, 1450

Kalberla, P. M. W., Burton, W. B., Hartmann, D., et al. 2005, Astronomy and Astrophysics, 440, 775

Karachentsev, I. D., Dolphin, A. E., Geisler, D., et al. 2002, Astronomy and Astrophysics, 383, 125

Karachentsev, I. D., Kaisina, E. I., & Kashibadze Nasonova, O. G. 2017, The Astronomical Journal, 153, 6

Kauffmann, G., Heckman, T. M., Tremonti, C., et al. 2003, Monthly Notices of the Royal Astronomical Society, 346, 1055

Kawashima, T., Mineshige, S., Ohsuga, K., & Ogawa, T. 2016, Publ Astron Soc Jpn Nihon Tenmon Gakkai, 68, publisher: Oxford Academic

Kawashima, T., Ohsuga, K., Mineshige, S., et al. 2012, ApJ, 752, 18

Kewley, L. J., Dopita, M. A., Leitherer, C., et al. 2013, The Astrophysical Journal, 774, 100

Kewley, L. J., Dopita, M. A., Sutherland, R. S., Heisler, C. A., & Trevena, J. 2001, The Astrophysical Journal, 556, 121

Kewley, L. J., Groves, B., Kauffmann, G., & Heckman, T. 2006, Monthly Notices of the Royal Astronomical Society, 372, 961

King, A. 2002, Monthly Notices of the Royal Astronomical Society, 335

King, A. & Lasota, J.-P. 2016, Mon Not R Astron Soc Lett, 458, L10

King, A. & Lasota, J.-P. 2019, Mon Not R Astron Soc, 485, 3588

King, A. & Lasota, J.-P. 2020, Monthly Notices of the Royal Astronomical Society, 494, 3611

King, A., Lasota, J.-P., & Kluźniak, W. 2017, Mon Not R Astron Soc Lett, 468, L59, publisher: Oxford Academic

King, A. & Muldrew, S. I. 2016, Mon Not R Astron Soc, 455, 1211

King, A. R. 2008, Monthly Notices of the Royal Astronomical Society, 385, L113

King, A. R. 2009, Mon Not R Astron Soc Lett, 393, L41

King, A. R., Davies, M. B., Ward, M. J., Fabbiano, G., & Elvis, M. 2001, ApJ, 552, L109

King, A. R. & Pounds, K. A. 2003, Mon Not R Astron Soc, 345, 657, publisher: Oxford Academic

King, A. R., Pringle, J. E., & Livio, M. 2007, Monthly Notices of the Royal Astronomical Society, 376, 1740

King, A. R. & Puchnarewicz, E. M. 2002, Mon Not R Astron Soc, 336, 445

Kitaki, T., Mineshige, S., Ohsuga, K., & Kawashima, T. 2017, Publ Astron Soc Jpn Nihon Tenmon Gakkai, 69, publisher: Oxford Academic

Koliopanos, F., Vasilopoulos, G., Buchner, J., Maitra, C., & Haberl, F. 2019, A&A, 621, A118

Koliopanos, F., Vasilopoulos, G., Godet, O., et al. 2017, A&A, 608, A47

Kong, A. K. H., Hu, C.-P., Lin, L. C.-C., et al. 2016, Monthly Notices of the Royal Astronomical Society, 461, 4395

Kopsacheili, M., Zezas, A., Leonidaki, I., & Boumis, P. 2021, Monthly Notices of the Royal Astronomical Society, 507, 6020

Kormendy, J. & Ho, L. C. 2013, Annual Review of Astronomy and Astrophysics, 51, 511

Kovlakas, K., Zezas, A., Andrews, J. J., et al. 2020, Monthly Notices of the Royal Astronomical Society, 498, 4790

Kozai, Y. 1962, The Astronomical Journal, 67, 591

Kraft, R. P., Kregenow, J. M., Forman, W. R., Jones, C., & Murray, S. S. 2001, The Astrophysical Journal, 560, 675, aDS Bibcode: 2001ApJ...560..675K

Krivonos, R. & Sazonov, S. 2016, Monthly Notices of the Royal Astronomical Society, 463, 756

Kubota, A. & Makishima, K. 2004, The Astrophysical Journal, 601, 428

Kubota, A., Makishima, K., & Ebisawa, K. 2001, ApJ, 560, L147, publisher: IOP Publishing

Kudritzki, R. P. 2002, The Astrophysical Journal, 577, 389, aDS Bibcode: 2002ApJ...577..389K

Kuncarayakti, H., Maeda, K., Anderson, J. P., et al. 2016, Monthly Notices of the Royal Astronomical Society, 458, 2063

Kuntz, K. D., Gruendl, R. A., Chu, Y.-H., et al. 2005, The Astrophysical Journal, 620, L31

Lang, C. C., Kaaret, P., Corbel, S., & Mercer, A. 2007, ApJ, 666, 79, publisher: IOP Publishing

Lara-López, M. A., Zinchenko, I. A., Pilyugin, L. S., et al. 2021, The Astrophysical Journal, 906, 42

Lau, R. M., Heida, M., Walton, D. J., et al. 2019, ApJ, 878, 71, publisher: American Astronomical Society

Laurent, F., Renault, E., Anwand, H., et al. 2014, 9151, 91511U, conference Name: Advances in Optical and Mechanical Technologies for Telescopes and Instrumentation

Law, D. R., Ji, X., Belfiore, F., et al. 2021, arXiv:2011.06012 [astro-ph], arXiv: 2011.06012

Laycock, S. G. T., Maccarone, T. J., & Christodoulou, D. M. 2015, Monthly Notices of the Royal Astronomical Society, 452, L31

Leahy, D. A., Naranan, S., & Singh, K. P. 1986, Monthly Notices of the Royal Astronomical Society, 220, 501

Lehmann, I., Becker, T., Fabrika, S., et al. 2005, A&A, 431, 847, number: 3 Publisher: EDP Sciences

Lelli, F., McGaugh, S. S., & Schombert, J. M. 2015, ApJL, 816, L14

Lin, D., Strader, J., Romanowsky, A. J., et al. 2020, ApJL, 892, L25, publisher: American Astronomical Society

Lipunova, G. V. 1999, Astronomy Letters, 25, 508

Liu, J., Bregman, J. N., & McClintock, J. E. 2008, ApJ, 690, L39, publisher: IOP Publishing

Liu, J.-F. 2008, The Astrophysical Journal Supplement Series, 177, 181

Liu, J.-F., Bai, Y., Wang, S., et al. 2015, Nature, 528, 108, number: 7580 Publisher: Nature Publishing Group

Liu, J.-F., Bregman, J. N., Bai, Y., Justham, S., & Crowther, P. 2013, Nature, 503, 500

Liu, J.-F., Bregman, J. N., & Seitzer, P. 2004, ApJ, 602, 249, publisher: IOP Publishing

Liu, Q. Z. & Mirabel, I. F. 2005, Astronomy and Astrophysics, 429, 1125

Lodato, G. & Natarajan, P. 2006, Monthly Notices of the Royal Astronomical Society, 371, 1813, aDS Bibcode: 2006MNRAS.371.1813L

Lomb, N. R. 1976, Astrophysics and Space Science, 39, 447

Luangtip, W., Roberts, T. P., & Done, C. 2016, Monthly Notices of the Royal Astronomical Society, 460, 4417

Lynden-Bell, D. 1969, Nature, 223, 690

Madau, P., Haardt, F., & Dotti, M. 2014, ApJL, 784, L38, publisher: American Astronomical Society

Madsen, K. K., Harrison, F. A., Markwardt, C. B., et al. 2015, ApJS, 220, 8

Makishima, K., Kubota, A., Mizuno, T., et al. 2000, ApJ, 535, 632

Marconi, A., Pastorini, G., Pacini, F., et al. 2006, A&A, 448, 921, number: 3 Publisher: EDP Sciences

Margon, B. & Anderson, S. F. 1989, The Astrophysical Journal, 347, 448

Marino, A., Barnier, S., Petrucci, P. O., et al. 2021, Tracking the evolution of the accretion flow in MAXI J1820+070 during its hard state with the JED-SAD model, Tech. rep., publication Title: arXiv e-prints ADS Bibcode: 2021arXiv210900218M Type: article

Mason, K. O., Breeveld, A., Much, R., et al. 2001, A&A, 365, L36, number: 1 Publisher: EDP Sciences

Matonick, D. M. & Fesen, R. A. 1997, The Astrophysical Journal Supplement Series, 112, 49, aDS Bibcode: 1997ApJS..112...49M

Matsumoto, H., Tsuru, T., Matsushita, S., et al. 2001, 251, 60

McClintock, J. E. & Remillard, R. A. 2006, Compact stellar X-ray sources, 157, iSBN: 9780521826594

McLeod, A. F., Scaringi, S., Soria, R., et al. 2019, Monthly Notices of the Royal Astronomical Society, 485, 3476, arXiv: 1903.00005

Mezcua, M. 2017, Int. J. Mod. Phys. D, 26, 1730021

Middleton, M., Done, C., Gierliński, M., & Davis, S. W. 2006, Monthly Notices of the Royal Astronomical Society, 373, 1004

Middleton, M. J., Brightman, M., Pintore, F., et al. 2019a, Mon Not R Astron Soc, 486, 2, publisher: Oxford Academic

Middleton, M. J., Fragile, P. C., Bachetti, M., et al. 2018, Mon Not R Astron Soc, 475, 154, publisher: Oxford Academic

Middleton, M. J., Fragile, P. C., Ingram, A., & Roberts, T. P. 2019b, Mon Not R Astron Soc, 489, 282, publisher: Oxford Academic

Middleton, M. J., Heil, L., Pintore, F., Walton, D. J., & Roberts, T. P. 2015a, Monthly Notices of the Royal Astronomical Society, 447, 3243

Middleton, M. J. & King, A. 2016, Mon Not R Astron Soc Lett, 462, L71, publisher: Oxford Academic

Middleton, M. J. & King, A. 2017, Mon Not R Astron Soc Lett, 470, L69, publisher: Oxford Academic

Middleton, M. J., Miller-Jones, J. C. A., Markoff, S., et al. 2013, Nature, 493, 187

Middleton, M. J., Roberts, T. P., Done, C., & Jackson, F. E. 2011a, Mon Not R Astron Soc, 411, 644, publisher: Oxford Academic

Middleton, M. J., Sutton, A. D., & Roberts, T. P. 2011b, Mon Not R Astron Soc, 417, 464, publisher: Oxford Academic

Middleton, M. J., Walton, D. J., Alston, W., et al. 2021, arXiv:1810.10518 [astro-ph], arXiv: 1810.10518

Middleton, M. J., Walton, D. J., Fabian, A., et al. 2015b, Monthly Notices of the Royal Astronomical Society, 454, 3134

Middleton, M. J., Walton, D. J., Roberts, T. P., & Heil, L. 2014, Mon Not R Astron Soc Lett, 438, L51

Migliari, S. & Fender, R. P. 2006, Monthly Notices of the Royal Astronomical Society, 366, 79, aDS Bibcode: 2006MNRAS.366...79M

Miller, B. W. 1995, The Astrophysical Journal Letters, 446, L75

Miller, J. M., Cackett, E. M., & Reis, R. C. 2009, ApJ, 707, L77

Miller, J. M., Fabian, A. C., & Miller, M. C. 2004, ApJ, 607, 931

Miller, J. M., Raymond, J., Fabian, A., et al. 2006, Nature, 441, 953, aDS Bibcode: 2006Natur.441..953M

Miller, J. M., Walton, D. J., King, A. L., et al. 2013, The Astrophysical Journal, 776, L36

Miller, M. C. & Hamilton, D. P. 2002, Monthly Notices of the Royal Astronomical Society, 330, 232, aDS Bibcode: 2002MNRAS.330..232C

Mineo, S., Gilfanov, M., & Sunyaev, R. 2012, Monthly Notices of the Royal Astronomical Society, 419, 2095

Mirioni, L. 2002, PhD thesis

Mitsuda, K., Inoue, H., Koyama, K., et al. 1984, Publications of the Astronomical Society of Japan, 36, 741

Momcheva, I., Lee, J. C., Ly, C., et al. 2013, AJ, 145, 47, arXiv: 1207.5479

Mondal, S., Rozanska, A., Baginska, P., Markowitz, A., & De Marco, B. 2021, arXiv e-prints, 2104, arXiv:2104.12894

Mortlock, D. J., Warren, S. J., Venemans, B. P., et al. 2011, Nature, 474, 616

Motch, C., Pakull, M. W., Soria, R., Grisé, F., & Pietrzyński, G. 2014, Nature, 514, 198

Mudelsee, M. 2002, Computers & Geosciences, 28, 69

Mukherjee, E. S., Walton, D. J., Bachetti, M., et al. 2015, ApJ, 808, 64

Mushtukov, A. A., Ingram, A., Middleton, M., Nagirner, D. I., & van der Klis, M. 2019, Mon Not R Astron Soc, 484, 687, publisher: Oxford Academic

Mushtukov, A. A., Portegies Zwart, S., Tsygankov, S. S., Nagirner, D. I., & Poutanen, J. 2021, Monthly Notices of the Royal Astronomical Society, 501, 2424

Mushtukov, A. A., Suleimanov, V. F., Tsygankov, S. S., & Ingram, A. 2017, Mon Not R Astron Soc, 467, 1202

Mushtukov, A. A., Suleimanov, V. F., Tsygankov, S. S., & Poutanen, J. 2015, Monthly Notices of the Royal Astronomical Society, 454, 2539

Narayan, R., Sadowski, A., & Soria, R. 2017, Mon Not R Astron Soc, 469, 2997, publisher: Oxford Academic

Narayan, R. & Yi, I. 1995, The Astrophysical Journal, 452, 710

Ogawa, T., Mineshige, S., Kawashima, T., Ohsuga, K., & Hashizume, K. 2017, Publications of the Astronomical Society of Japan, 69

Ohkubo, T., Nomoto, K., Umeda, H., Yoshida, N., & Tsuruta, S. 2009, ApJ, 706, 1184, publisher: American Astronomical Society

Ohmura, T., Ono, K., Sakemi, H., et al. 2021, The Astrophysical Journal, 910, 149

Ohsuga, K. & Mineshige, S. 2007, ApJ, 670, 1283, publisher: IOP Publishing

Ohsuga, K., Mineshige, S., Mori, M., & Umemura, M. 2002, ApJ, 574, 315, publisher: IOP Publishing

Ohsuga, K., Mori, M., Nakamoto, T., & Mineshige, S. 2005, ApJ, 628, 368

Oppenheimer, J. R. & Snyder, H. 1939, Phys. Rev., 56, 455, publisher: American Physical Society

Oppenheimer, J. R. & Volkoff, G. M. 1939, Phys. Rev., 55, 374, publisher: American Physical Society

Osterbrock, D. E. & Ferland, G. J. 2006, Astrophysics of gaseous nebulae and active galactic nuclei, 2nd. ed. by D.E. Osterbrock and G.J. Ferland. Sausalito, CA: University Science Books, 2006

Pakull, M. W. & Angebault, L. P. 1986, Nature, 322, 511

Pakull, M. W., Grise, F., & Motch, C. 2005, Proc. IAU, 1, 293, arXiv: astro-ph/0603771

Pakull, M. W. & Grisé, F. 2008, 1010, 303, conference Name: A Population Explosion: The Nature & Evolution of X-ray Binaries in Diverse Environments Place: eprint: arXiv:0803.4345

Pakull, M. W. & Mirioni, L. 2002, arXiv:astro-ph/0202488, arXiv: astro-ph/0202488

Pakull, M. W., Soria, R., & Motch, C. 2010, Nature, 466, 209

Paragi, Z., Vermeulen, R. C., Fejes, I., et al. 1999, Astronomy and Astrophysics, 348, 910

Parfrey, K. & Tchekhovskoy, A. 2017, ApJL, 851, L34, publisher: American Astronomical Society

Pasham, D. R., Strohmayer, T. E., & Mushotzky, R. F. 2014, Nature, 513, 74, number: 7516 Publisher: Nature Publishing Group

Pastor-Marazuela, I., Webb, N. A., Wojtowicz, D. T., & Leeuwen, J. v. 2020, A&A, 640, A124, publisher: EDP Sciences

Peimbert, M., Sarmiento, A., & Fierro, J. 1991, Publications of the Astronomical Society of the Pacific, 103, 815, aDS Bibcode: 1991PASP..103..815P

Pilyugin, L. S. & Grebel, E. K. 2016, Monthly Notices of the Royal Astronomical Society, 457, 3678

Pinto, C., Alston, W., Soria, R., et al. 2017, Mon Not R Astron Soc, 468, 2865, publisher: Oxford Academic

Pinto, C., Mehdipour, M., Walton, D. J., et al. 2020a, Mon Not R Astron Soc, 491, 5702, publisher: Oxford Academic

Pinto, C., Middleton, M. J., & Fabian, A. C. 2016, Nature, 533, 64

Pinto, C., Soria, R., Walton, D., et al. 2021, arXiv:2104.11164 [astro-ph], arXiv: 2104.11164

Pinto, C., Walton, D. J., Kara, E., et al. 2020b, Mon Not R Astron Soc, 492, 4646, publisher: Oxford Academic

Pintore, F., Esposito, P., Zampieri, L., Motta, S., & Wolter, A. 2015, Mon Not R Astron Soc, 448, 1153

Pintore, F. & Zampieri, L. 2012, Mon Not R Astron Soc, 420, 1107

Pintore, F., Zampieri, L., Stella, L., et al. 2017, The Astrophysical Journal, 836, 113

Pintore, F., Zampieri, L., Wolter, A., & Belloni, T. 2014, Monthly Notices of the Royal Astronomical Society, 439, 3461

Piqueras, L., Conseil, S., Shepherd, M., et al. 2017, arXiv:1710.03554 [astro-ph], arXiv: 1710.03554

Ponti, G., Fender, R. P., Begelman, M. C., et al. 2012, Mon Not R Astron Soc Lett, 422, L11

Popham, R. & Sunyaev, R. 2001, The Astrophysical Journal, 547, 355

Poutanen, J., Lipunova, G., Fabrika, S., Butkevich, A. G., & Abolmasov, P. 2007, Monthly Notices of the Royal Astronomical Society, 377, 1187

Pringle, J. E. & Rees, M. J. 1972, A&A, 21, 1

Protassov, R., van Dyk, D. A., Connors, A., Kashyap, V. L., & Siemiginowska, A. 2002, The Astrophysical Journal, 571, 545

Prusti, T., Bruijne, J. H. J. d., Brown, A. G. A., et al. 2016, A&A, 595, A1, publisher: EDP Sciences

Pérez-Montero, E. 2017, PASP, 129, 043001, publisher: IOP Publishing

Quintin, E., Webb, N., Gúrpide, A., Bachetti, M., & Fürst, F. 2021, arXiv:2103.11650 [astro-ph], arXiv: 2103.11650

Ramsey, C. J., Williams, R. M., Gruendl, R. A., et al. 2006, ApJ, 641, 241

Rana, V., Harrison, F. A., Bachetti, M., et al. 2015, The Astrophysical Journal, 799, 121

Rappaport, S. A., Podsiadlowski, P., & Pfahl, E. 2005, Monthly Notices of the Royal Astronomical Society, 356, 401

Ray, P. S., Guillot, S., Ho, W. C. G., et al. 2019, ApJ, 879, 130

Remillard, R. A. & McClintock, J. E. 2006, Annual Review of Astronomy and Astrophysics, 44, 49

Roberts, T., Gladstone, J., Goulding, A., et al. 2011, Astron. Nachr., 332, 398

Roberts, T. P. & Colbert, E. J. M. 2003, Mon Not R Astron Soc, 341, L49

Roberts, T. P., Goad, M. R., Ward, M. J., & Warwick, R. S. 2003, Monthly Notices of the Royal Astronomical Society, 342, 709

Roberts, T. P., Kilgard, R. E., Warwick, R. S., Goad, M. R., & Ward, M. J. 2006, Monthly Notices of the Royal Astronomical Society, 371, 1877

Roberts, T. P., Warwick, R. S., Ward, M. J., Goad, M. R., & Jenkins, L. P. 2005, Monthly Notices of the Royal Astronomical Society, 357, 1363

Robinson, P. M. 1977, Stochastic Processes and their Applications, 6, 9

Rodríguez-Castillo, G. A., Israel, G. L., Belfiore, A., et al. 2020, ApJ, 895, 60, publisher: American Astronomical Society

Roming, P. W. A., Kennedy, T. E., Mason, K. O., et al. 2005, Space Science Reviews, 120, 95

Russell, D. M., Fender, R. P., Gallo, E., & Kaiser, C. R. 2007, Monthly Notices of the Royal Astronomical Society, 376, 1341

Russell, S. C. & Dopita, M. A. 1992, The Astrophysical Journal, 384, 508

Ryder, S. D., Staveley-Smith, L., Malin, D., & Walsh, W. 1995, The Astronomical Journal, 109, 1592

Ryon, J. E. 2021, Advanced Camera for Surveys HST Instrument Handbook

Ryon, J. E., Gallagher, J. S., Smith, L. J., et al. 2017, The Astrophysical Journal, 841, 92

Sathyaprakash, R., Roberts, T. P., Walton, D. J., et al. 2019, Monthly Notices of the Royal Astronomical Society, 488, L35

Scargle, J. D. 1981, The Astrophysical Journal Supplement Series, 45, 1

Scargle, J. D. 1982, The Astrophysical Journal, 263, 835

Schulz, M. & Mudelsee, M. 2002, Computers & Geosciences, 28, 421

Schulz, M. & Stattegger, K. 1997, Computers & Geosciences, 23, 929

Schwarz, G. 1978, Ann. Statist., 6, 461, publisher: Institute of Mathematical Statistics

Schödel, R., Ott, T., Genzel, R., et al. 2002, Nature, 419, 694, aDS Bibcode: 2002Natur.419..694S

Servillat, M., Farrell, S. A., Lin, D., et al. 2011, ApJ, 743, 6

Shahbaz, T., Ringwald, F. A., Bunn, J. C., et al. 1994, Monthly Notices of the Royal Astronomical Society, 271, L10

Shakura, N. I. & Sunyaev, R. A. 1973, Astronomy and Astrophysics, 24, 337

Shimura, T. & Takahara, F. 1995, The Astrophysical Journal, 445, 780

Silverman, J. M. & Filippenko, A. V. 2008, ApJ, 678, L17, publisher: IOP Publishing

Simmonds, C., Schaerer, D., & Verhamme, A. 2021, Can nebular HeII emission be explained by ultra-luminous X-ray sources?, Tech. rep., publication Title: arXiv e-prints ADS Bibcode: 2021arXiv210812438S Type: article

Song, X., Walton, D. J., Lansbury, G. B., et al. 2020, Monthly Notices of the Royal Astronomical Society, 491, 1260

Soria, R. & Kong, A. 2016, Mon Not R Astron Soc, 456, 1837, publisher: Oxford Academic

Soria, R., Kuntz, K. D., Long, K. S., et al. 2015, ApJ, 799, 140

Soria, R., Long, K. S., Blair, W. P., et al. 2014, Science, 343, 1330

Soria, R., Pakull, M. W., Motch, C., et al. 2021, Monthly Notices of the Royal Astronomical Society, 501, 1644

Soto, K. T., Lilly, S. J., Bacon, R., Richard, J., & Conseil, S. 2016, Monthly Notices of the Royal Astronomical Society, 458, 3210, arXiv: 1602.08037

Staubert, R., Klochkov, D., Vasco, D., et al. 2013, A&A, 550, A110, publisher: EDP Sciences

Steiner, J. F., Narayan, R., McClintock, J. E., & Ebisawa, K. 2009, PASP, 121, 1279

Steinhardt, C. L. & Elvis, M. 2010, Monthly Notices of the Royal Astronomical Society, 402, 2637, arXiv: 0911.1355

Stobbart, A.-M., Roberts, T. P., & Wilms, J. 2006, Mon Not R Astron Soc, 368, 397

Strüder, L., Briel, U., Dennerl, K., et al. 2001, Astronomy & Astrophysics, 365, L18

Sutherland, R., Dopita, M., Binette, L., & Groves, B. 2018, Astrophysics Source Code Library, ascl:1807.005, aDS Bibcode: 2018ascl.soft07005S

Sutton, A. D., Roberts, T. P., & Middleton, M. J. 2013, Monthly Notices of the Royal Astronomical Society, 435, 1758

Swartz, D. A., Ghosh, K. K., McCollough, M. L., et al. 2003, ApJS, 144, 213, publisher: American Astronomical Society

Swartz, D. A., Soria, R., Tennant, A. F., & Yukita, M. 2011, ApJ, 741, 49, publisher: American Astronomical Society

Sądowski, A. & Narayan, R. 2016, Monthly Notices of the Royal Astronomical Society, 456, 3929

Sądowski, A., Narayan, R., Tchekhovskoy, A., et al. 2015, Mon Not R Astron Soc, 447, 49, publisher: Oxford Academic

Takahashi, H. R., Mineshige, S., & Ohsuga, K. 2018, ApJ, 853, 45

Takahashi, H. R. & Ohsuga, K. 2017, ApJ, 845, L9

Takahashi, H. R., Ohsuga, K., Kawashima, T., & Sekiguchi, Y. 2016, ApJ, 826, 23, publisher: American Astronomical Society

Takeuchi, S., Ohsuga, K., & Mineshige, S. 2013, Publ Astron Soc Jpn Nihon Tenmon Gakkai, 65, publisher: Oxford Academic

Tanaka, Y., Inoue, H., & Holt, S. S. 1994, Publications of the Astronomical Society of Japan, 46, L37

Tao, L., Kaaret, P., Feng, H., & Grisé, F. 2012, ApJ, 750, 110, publisher: American Astronomical Society

Teukolsky, S. A. & Shapiro, S. L. 1983, Black holes, white dwarfs, and neutron stars : the physics of compact objects (Wiley)

Tolman, R. C. 1939, Phys. Rev., 55, 364, publisher: American Physical Society

Townsend, L. J. & Charles, P. A. 2020, Monthly Notices of the Royal Astronomical Society: Letters, 495, L139

Tsygankov, S. S., Lutovinov, A. A., Doroshenko, V., et al. 2016a, Astronomy & Astrophysics, 593, A16

Tsygankov, S. S., Mushtukov, A. A., Suleimanov, V. F., & Poutanen, J. 2016b, Mon Not R Astron Soc, 457, 1101

Tully, R. B., Courtois, H. M., & Sorce, J. G. 2016, AJ, 152, 50

Tully, R. B., Shaya, E. J., Karachentsev, I. D., et al. 2008, The Astrophysical Journal, 676, 184

Turner, M. J. L., Abbey, A., Arnaud, M., et al. 2001, A&A, 365, L27

Urquhart, R. & Soria, R. 2016, MNRAS, 456, 1859

Urquhart, R., Soria, R., Johnston, H. M., et al. 2018, Monthly Notices of the Royal Astronomical Society, 475, 3561

Urquhart, R., Soria, R., Pakull, M. W., et al. 2019, Monthly Notices of the Royal Astronomical Society, 482, 2389

van den Heuvel, E. P. J. 1981, Vistas in Astronomy, 25, 95

van der Klis, M. 1989, 1, 203, conference Name: Two Topics in X-Ray Astronomy, Volume 1: X Ray Binaries. Volume 2: AGN and the X Ray Background

VanderPlas, J. T. 2018, ApJS, 236, 16, publisher: American Astronomical Society

Vasilopoulos, G., Haberl, F., Carpano, S., & Maitra, C. 2018, A&A, 620, L12, publisher: EDP Sciences

Vasilopoulos, G., Koliopanos, F., Haberl, F., et al. 2021, ApJ, 909, 50, publisher: American Astronomical Society

Vasilopoulos, G., Lander, S. K., Koliopanos, F., & Bailyn, C. D. 2020a, Mon Not R Astron Soc, 491, 4949, publisher: Oxford Academic

Vasilopoulos, G., Petropoulou, M., Koliopanos, F., et al. 2019, Mon Not R Astron Soc, 488, 5225, publisher: Oxford Academic

Vasilopoulos, G., Ray, P. S., Gendreau, K. C., et al. 2020b, arXiv:2004.03022 [astro-ph], arXiv: 2004.03022

Vaughan, S., Uttley, P., Markowitz, A. G., et al. 2016, Monthly Notices of the Royal Astronomical Society, 461, 3145

Vedrenne, G. & Atteia, J.-L. 2009, Gamma-Ray Bursts, publication Title: Gamma-Ray Bursts: The Brightest Explosions in the Universe ADS Bibcode: 2009grb..book.....V

Veilleux, S. & Osterbrock, D. E. 1987, The Astrophysical Journal Supplement Series, 63, 295

Verner, D. A., Ferland, G. J., Korista, K. T., & Yakovlev, D. G. 1996, The Astrophysical Journal, 465, 487

Vierdayanti, K., Done, C., Roberts, T. P., & Mineshige, S. 2010, Monthly Notices of the Royal Astronomical Society, 403, 1206

Villar, V. A., Berger, E., Chornock, R., et al. 2016, The Astrophysical Journal, 830, 11

Vinokurov, A., Fabrika, S., & Atapin, K. 2013, Astrophys. Bull., 68, 139

Volonteri, M. 2010, The Astronomy and Astrophysics Review, 18, 279

Waisberg, I., Dexter, J., Olivier-Petrucci, P., Dubus, G., & Perraut, K. 2019, Astronomy and Astrophysics, 624, A127

Walsh, J. R. & Roy, J.-R. 1997, Monthly Notices of the Royal Astronomical Society, 288, 726

Walton, D. J., Bachetti, M., Fürst, F., et al. 2018a, ApJL, 857, L3, publisher: American Astronomical Society

Walton, D. J., Fürst, F., Bachetti, M., et al. 2016a, ApJL, 827, L13

Walton, D. J., Fürst, F., Harrison, F. A., et al. 2017, ApJ, 839, 105

Walton, D. J., Fürst, F., Harrison, F. A., et al. 2018b, Monthly Notices of the Royal Astronomical Society, 473, 4360

Walton, D. J., Fürst, F., Heida, M., et al. 2018c, ApJ, 856, 128

Walton, D. J., Harrison, F. A., Grefenstette, B. W., et al. 2014, ApJ, 793, 21

Walton, D. J., Middleton, M. J., Pinto, C., et al. 2016b, ApJL, 826, L26

Walton, D. J., Middleton, M. J., Rana, V., et al. 2015, The Astrophysical Journal, 806, 65

Walton, D. J., Pinto, C., Nowak, M., et al. 2020, Monthly Notices of the Royal Astronomical Society, 494, 6012

Walton, D. J., Roberts, T. P., Mateos, S., & Heard, V. 2011, Mon Not R Astron Soc, 416, 1844, publisher: Oxford Academic

Wang, J., Mastroserio, G., Kara, E., et al. 2021, ApJL, 910, L3, publisher: American Astronomical Society

Watarai, K.-y., Fukue, J., Takeuchi, M., & Mineshige, S. 2000, Publications of the Astronomical Society of Japan, 52, 133, aDS Bibcode: 2000PASJ...52..133W

Weaver, R., McCray, R., Castor, J., Shapiro, P., & Moore, R. 1977, The Astrophysical Journal, 218, 377

Weilbacher, P. M., Palsa, R., Streicher, O., et al. 2020, A&A, 641, A28, arXiv: 2006.08638

Weisskopf, M. C., Tananbaum, H. D., Van Speybroeck, L. P., & O'Dell, S. L. 2000, 4012, 2, conference Name: X-Ray Optics, Instruments, and Missions III Place: eprint: arXiv:astro-ph/0004127

Weiß, A., Kovács, A., Güsten, R., et al. 2008, A&A, 490, 77, number: 1 Publisher: EDP Sciences

Weng, S.-S. & Feng, H. 2018, ApJ, 853, 115

Wiktorowicz, G., Lasota, J.-P., Middleton, M., & Belczynski, K. 2019, The Astrophysical Journal, 875, 53

Wiktorowicz, G., Sobolewska, M., Sa\kdowski, A., & Belczynski, K. 2015, ApJ, 810, 20, publisher: IOP Publishing

Williams, R. M., Chu, Y.-H., Dickel, J. R., et al. 2004, ApJ, 613, 948, publisher: IOP Publishing

Wilms, J., Allen, A., & McCray, R. 2000, The Astrophysical Journal, 542, 914

Wilson-Hodge, C. A., Malacaria, C., Jenke, P. A., et al. 2018, The Astrophysical Journal, 863, 9

Xu, H., Wise, J. H., & Norman, M. L. 2013, ApJ, 773, 83

Yang, L., Feng, H., & Kaaret, P. 2011, ApJ, 733, 118, publisher: American Astronomical Society

Zampieri, L., Impiombato, D., Falomo, R., Grisé, F., & Soria, R. 2012, Monthly notices of the Royal Astronomical Society, 419, 1331, publisher: Oxford University Press

Zdziarski, A. A., Wen, L., & Gierliński, M. 2007, Monthly Notices of the Royal Astronomical Society, 377, 1006

Zhang, L., Altamirano, D., Cúneo, V. A., et al. 2020, Monthly Notices of the Royal Astronomical Society, 499, 851

Zhou, Y., Feng, H., Ho, L. C., & Yao, Y. 2019, ApJ, 871, 115

Zimmerman, E. R., Narayan, R., McClintock, J. E., & Miller, J. M. 2005, ApJ, 618, 832

Zwart, S. F. P. & McMillan, S. L. W. 2002, ApJ, 576, 899, arXiv: astro-ph/0201055